Cardiac Electro-Mechanics:
From cellML to theWhole Heart

by D. P. Nickerson.

Supervised by Professor P. J. Hunter.

A thesis submitted in partial fulfilment of the requirements for the degree of
Doctor of Philosophy in Bioengineering, The University of Auckland, 2004.

Bioengineering Institute

The University of Auckland

New Zealand

March 2005

Abstract

We have developed a computational modelling and simulation framework for cardiac electromechanics which for the first time tightly couples cellular, tissue, and whole heart modelling paradigms. Application of the framework has been demonstrated in simulations of the electrical activation and mechanical contraction of cardiac myocytes, myocardial tissue, and models of ventricular structure and function.

The framework has been implemented as part of the CMISS computational modelling environment. This allows for detailed specification of tissue microstructure and the variation of cellular models and their material parameters over a geometric domain of interest. Through previous work in CMISS we have access to a large pool of existing models and methods on which to base this work.

A key aspect of our framework is the implementation of methods allowing the dynamic specification of mathematical models at run-time using CellML – an XML language designed to store and exchange computer based biological models. We use these methods to enable the specification of cellular level models using CellML, thus providing a very powerful method to simply *"plug"* cellular models into the distributed tissue and organ level models. While in this work we have developed specific cellular models, and their CellML description, the framework is now developed to the point where a non-expert user could pull out a given model and plug-in their own model. This allows cellular modellers to develop their models and then bring them into a distributed model of tissue or organ physiology.

We present a review of cellular electrophysiology and mechanics models. As a demonstration of the ability of CellML to describe cardiac cellular models in a computationally useful manner we have encoded the majority of these models into CellML. The CellML descriptions of these models are provided as they were used in the computational simulations which generated all results presented for the models directly from the CellML encoded models.

While the work described in this thesis focuses on cardiac electro-mechanics, the framework has much wider applicability. As such, this work forms the beginning of a generalised simulation framework for the IUPS Physiome Project, with the goal being models describing entire organisms from proteins through to organ systems.

Acknowledgements

None of this work would have been possible without all the work that has been done before me in the Bioengineering Institute (formerly the Bioengineering Research Group). For that, I am thankful for all the staff and students who have contributed to the fantastic base for mathematical modelling, computational simulation, and visualisation that exists in the Institute.

Distinguished Professor Peter J. Hunter – mentor, inspiration, friend. Thanks for everything.

Contents

List of Figures

List of Tables

Glossary of Acronyms

AP action potential

APD action potential duration

API Application Program Interface

AVN atrioventricular node

BCL basic cycle length

BiV bi-ventricular

CESE Cell Electrophysiology Simulation Environment

CRT cardiac resynchronisation therapy

CMISS Continuum Mechanics, Image analysis, Signal processing, and System identification

COR Cellular Open Resource

DM Distribution-Moment

DOM Document Object Model

ECG electrocardiogram

FE finite element

FD finite difference

GBFE grid-based finite element

iCell Interactive cell modelling software

IUPS International Union of Physiological Sciences

LA left atrium

LBBB left bundle branch block

LV left ventricle

LVb left ventricular base

MRI magnetic resonance imaging

ODE ordinary differential equation

RA right atrium

RV right ventricle

RVa right ventricular apex

RC rectangular Cartesian

RMS root mean squared

SAN sinoatrial node

SI International System of Units

SR sarcoplasmic reticulum

VT ventricular tachycardia

W3C World Wide Web consortium

XML eXtensible Markup Language

XSLT eXtensible Stylesheet Language Transformation

Model Abbreviations

BR Beeler & Reuter

DFN di Francesco & Noble

FK Fenton & Karma

FK-HMT Fenton & Karma–Hunter, McCulloch & ter Keurs

HMT Hunter, McCulloch & ter Keurs

JRW Jafri, Rice & Winslow

LRd dynamic Luo & Rudy

N98 Noble *et al.* 1998

N-LRd Nickerson – Clancy & Rudy

N-LRd-HMT Nickerson – Clancy & Rudy – Hunter, McCulloch & ter Keurs

Chapter 1

Introduction

The human heart has just one function – to contract approximately once per second for every minute in every day for every year in your lifetime: more than 2.2 billion contractions over seventy years. These contractions are required to pump blood around the body. Failure in this single function caused an estimated 16.5 million deaths in the year 2001, or 29.3 % of deaths worldwide (World Health Organization 2002) and heart disease is the single largest killer of men in New Zealand. With better understanding of cardiac function will come the possibility of improved detection and treatment of such diseases and hopefully a reduction of the mortality rate.

Mathematical models and simulation techniques are developed in this thesis which extend the current cardiac models to encompass electro-mechanical aspects of cardiac function from the cellular to whole organ spatial and temporal scales. Through extension of the current models and simulation tools we are better able to investigate phenomena in which capturing the interaction of electrophysiology and mechanics is crucial to the models ability to predict physiological function. Some examples where inclusion of this interaction offers greater insight are models of cardiac arrhythmia, ventricular pacing when undergoing cardiac resynchronisation therapy, and the effect of mechanosensitive ion channels on tissue and organ behaviour underdifferent conditions.

The quantity of molecular and cellular detail required in a tissue or organ model depends very much on what one is trying to model. We have, therefore, developed and implemented a framework which enables a modeller to easily change the cellular model(s) underlying their tissue or organ model. This thesis presents the development of this framework based on its

application to cardiac electro-mechanics, but as discussed in Section 4.5 this work has already been applied in other models and will be used even more as the IUPS Physiome Project moves forward. As part of the feasibility study performed using this framework, we investigate both a lightweight and a very computationally demanding cellular electro-mechanics model in tissue models. We will also examine various models based on a simplified left ventricle (LV) geometry.

Modelling of biological tissue requires the use of simplifying approximations which maintain a balance between computability and physiological accuracy. The approximations occur at both the cellular and tissue levels. At the cellular level, it is currently inconceivable to attempt to track an individual ion's actual movements through the cellular membrane and within subcellular compartments and its interactions with various proteins while trying to model the billions of interacting cells in a piece of tissue. Then at the tissue level it is currently computationally impossible to accurately model the complete, deforming, three dimensional geometry of all the cells and connective tissue which combine to form a piece of cardiac tissue. In both these cases, approximations must be made which simplify the physiology into a system that is both computationally feasible and yet capable of representing the fundamental physiology of the system with sufficient detail to simulate cardiac function in health and disease. In addition to providing a description of the modelling and simulation framework developed to simulate cardiac electro-mechanics, this thesis describes the approximations made in the development of such models and shows that the models are both computationally feasible and capable of reproducing the observed physiological reactions of cardiac muscle to multiple and varied experimental stimuli.

We now present a brief overview of the physiology and anatomy of the heart and then provide an overview of the main method on which the techniques developed are based – the finite element method. Finally, a general description of the remainder of this thesis is given.

1.1   The Heart

The heart is a four chambered pump, with the two smaller chambers (atria) used to prime the larger chambers (ventricles). The right ventricle (RV), filled by the right atrium (RA) through the tricuspid valve, pumps blood to the lungs via the pulmonary artery through the pulmonary valve. The oxygen enriched blood then returns from the lungs into the left atrium (LA), from where the left ventricle (LV) is filled through the mitral valve. The oxygenated blood is then pumped through the body by the LV via the aorta. Figure 1.1 shows a schematic illustration detailing the anatomy of the heart.
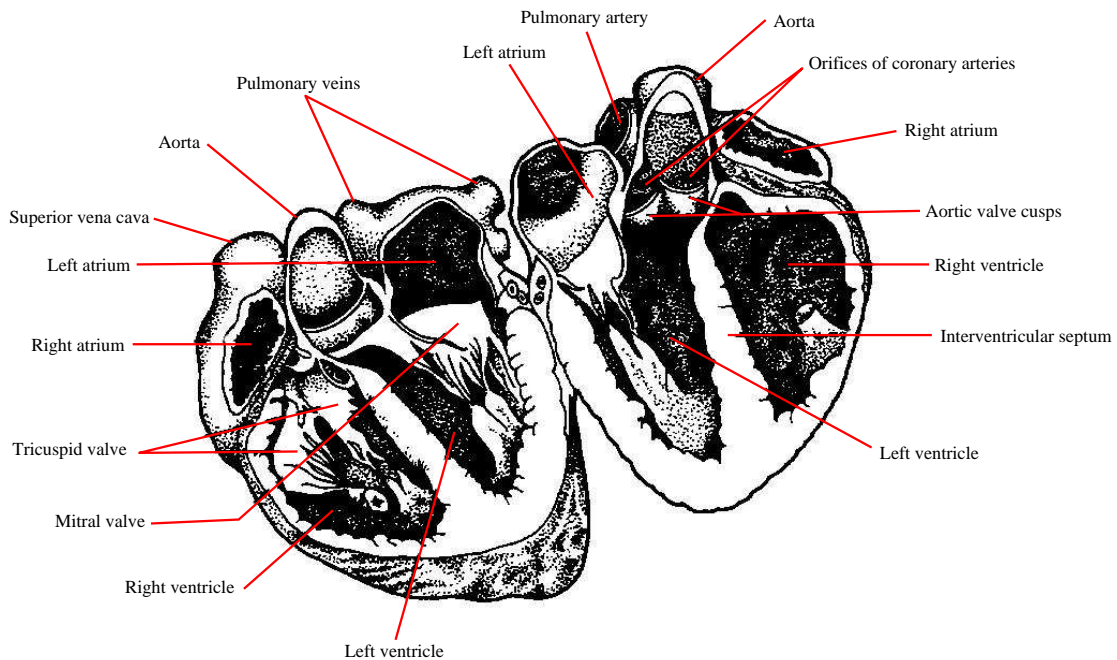
FIGURE 1.1: Anatomy of the heart (Katz 1992).

The contraction of the heart is initiated by a wave of electrical excitation travelling through the myocardium in the sequence illustrated by Figure 1.2. Neither the initiation nor the conduction of this excitation involves the central nervous system. Specialised heart cells initiate an electrical signal which is propagated throughout the heart via a specialised conduction system. The conduction of this electrical signal determines the sequence of the muscular contraction. Disruption of the electrical conduction, therefore, can have grave consequences for the mechanical function of the heart.

Electrical excitation in a healthy heart begins at the sinoatrial node (SAN), the normal cardiac pacemaker giving rise to the term "sinus rhythm" to describe normal electrical excitation. Following Figure 1.2, the excitation wavefront takes approximately 45 ms to emerge from the SAN, 40 ms to travel across the atria to the atrioventricular node (AVN). In normal hearts, the AVN is the only region of electrical conductivity between the atria and ventricles. Electrical excitation takes at least 100 ms to pass through the AVN, then 30 ms to be conducted through the Purkinje system and a final 30 ms to propagate throughout the ventricular myocardium (Brown & Kozlowski 1997). These numbers are approximate and average for adult human hearts.

The myocardium is a very complex and heterogeneous tissue, consisting of layers of interconnected sheets of tissue separated by cleavage planes (Hooks, Tomlinson, Marsden, LeGrice, Smaill, Pullan & Hunter 2002, Dokos, Smaill, Young & LeGrice 2002, LeGrice, Hunter, Young
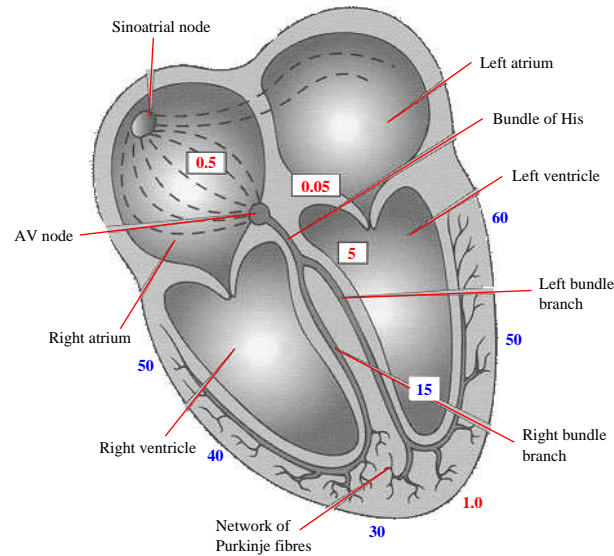
FIGURE 1.2: Schematic illustration of the activation sequence of the heart (Brown & Kozlowski 1997). The red figures are the speed of the electrical wave in $\mathrm{m \cdot s^{-1}}$; blue figures are the time to travel from the AV node to various points in the myocardium, in ms.

& Smaill 2001, LeGrice, Smaill, Chai, Edgar, Gavin & Hunter 1995). Each sheet is 3 to 4 cells thick and loosely coupled together by the perimysial collagen network. Myocytes are arranged longitudinally in fibres which lie in the plane of the sheets. The fibres are bound together by the endomysial collagen network. Thus, adjacent fibres are coupled, electrically and mechanically, more strongly in the plane of the sheet than transverse to it. When describing material properties of the myocardium it is therefore required to do so with respect to the three micro-structural axes evident in the tissue: fibre, sheet, and normal. This micro-structure is schematically illustrated in Figure 1.3.

As shown in Figure 1.3(a), the orientation of the material axes varies through the wall of the LV. Using detailed measurements, geometric models have been created which include the variation of the material axes throughout the porcine (Stevens 2002) and canine (Nash 1998) ventricles. Illustrations of the variation is provided in Figure 1.4.

Following the rapid spread of electrical excitation through the specialised conduction system of the ventricles, the electrical wave propagates through the myocardium. Conduction of the wave is fastest along the fibre axis, due to the strong electrical coupling between the myocytes through gap junctions. Lower conductivity is shown between fibres within a sheet, and lower still between sheets. This preferential electrical conduction can be represented by orthotropic conductivity tensors related to the micro-structural material axes.
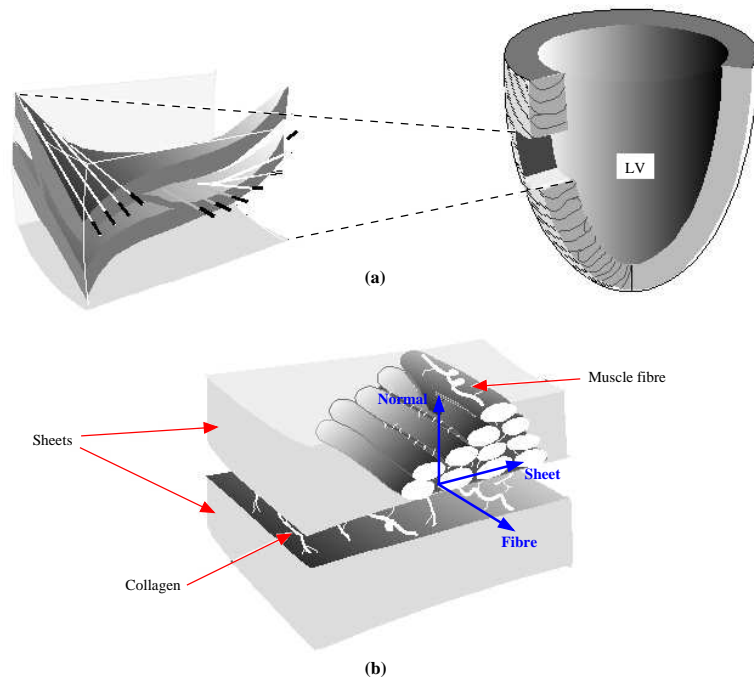
FIGURE 1.3: A illustration of the heterogeneous micro-structural detail of cardiac tissue. (a) shows a section of the LV wall to illustrate the variation of the fibre and sheet orientation through the wall of the ventricle. A detailed view of the micro-structure is shown in (b), demonstrating the micro-structurally based material coordinate system consisting of the fibre, sheet, and normal axes.

(a) Canine.   (b) Porcine.
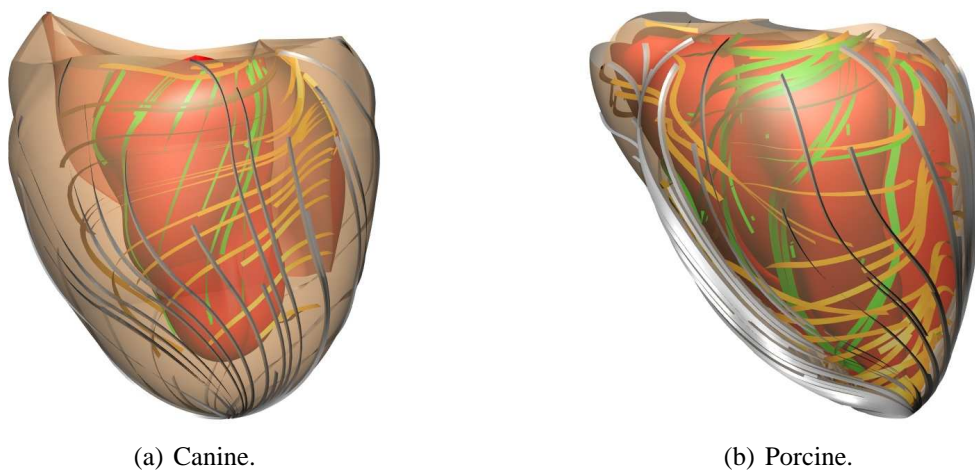
FIGURE 1.4: Anatomically based finite element models of canine and porcine ventricles. Three layers of streamlines are used to visualise the epicardial (silver), mid-wall (gold), and endocardial (green) fibre directions which vary continuously through the wall. The red surfaces are the endocardial left and right ventricular surfaces in both models.

Conduction of the wave of excitation through the myocardium is based on depolarisation of myocytes beyond a threshold causing the initiation of an action potential. The action potential propagates over the cellular membrane without significant delay (Berne & Levy 1993) before propagating to connected myocytes through gap junctions. Action potentials are caused by the opening and closing of particular populations of ion channels in the cellular membrane. Ions passing through these channels from the extracellular volume to the intracellular, or vice versa, give rise to currents causing changes to the transmembrane potential which defines the action potential.

Of particular importance to this work is the calcium ion. In myocardial cells, a small influx of calcium ions into the cell at the beginning of the action potential triggers a huge release of calcium from internal stores. The binding of these calcium ions to the cellular contractile proteins initiates active contraction of the myocyte. The amount of calcium released determines the force that can be generated by the cell (amongst many other contributing factors). Following contraction, the calcium is returned to the intracellular stores and primed for the next contraction.

1.2   Finite Element Modelling

The development of anatomically based representations of organ geometry and tissue properties is the essential first step in the construction of an integrated model of whole organ function. We now introduce a finite element method for representation of these fields.

The finite element method is one of the most commonly used approaches to numerically represent spatially distributed fields. Traditionally, finite element models use low-order Lagrangian interpolation and, with very few exceptions, only one type of interpolation scheme in the solution domain. For a detailed introduction to the finite element method readers are referred to Zienkiewicz & Taylor (1994). We present here a different approach which uses high-order Hermitian interpolation to provide improved efficiency and convergence properties (Hunter 1975, Bradley, Pullan & Hunter 1997) for representing the nonlinear and C^1-continuous variation typical of many biological fields.

In the notation used below, ξ_i is the local finite element coordinate in the ith direction ($0 \leq \xi_i \leq 1$), u represents the field variable and u_n its value at local node n of a given element. $\Delta(n, e)$ maps the local node n of element e to its unique global number for a particular

mesh. Continuity of the derivative of u with respect to ξ_i across element boundaries is achieved by defining additional nodal parameters which are the partial derivatives of the field variable u with respect to the local coordinate $\left(\dfrac{\partial u}{\partial \xi_i}\right)_n$. Illustrating this concept in one dimension, basis functions are chosen to ensure that nodal derivatives which contribute to the interpolation within an element are shared by two adjacent elements in order to maintain derivative continuity across different boundaries. Derivative continuity requires cubic interpolation and therefore four element parameters. These parameters are specified as the nodal value and its derivative with respect to ξ for two nodes per element in one dimension. Thus:

$$u(\xi) = a + b\xi + c\xi^2 + d\xi^3, \quad \text{and therefore} \quad \frac{du}{d\xi} = b + 2c\xi + 3d\xi^2,$$

where

$$a = u_1, b = u'_1, c = 3u_2 - 3u_1 - 2u'_1 - u'_2, d = u'_1 + u'_2 + 2u_1 - 2u_2,$$

or, rearranging,

$$u(\xi) = H_1^0(\xi)u_1 + H_1^1(\xi)u'_1 + H_2^0(\xi)u_2 + H_2^1(\xi)u'_2 \tag{1.2.1}$$

where H_n^1 represents the derivative of H_n^0 with respect to ξ and $u'_n = \left(\dfrac{du}{d\xi}\right)_n$. The four one dimensional cubic-Hermite basis functions are drawn in Figure 1.5.
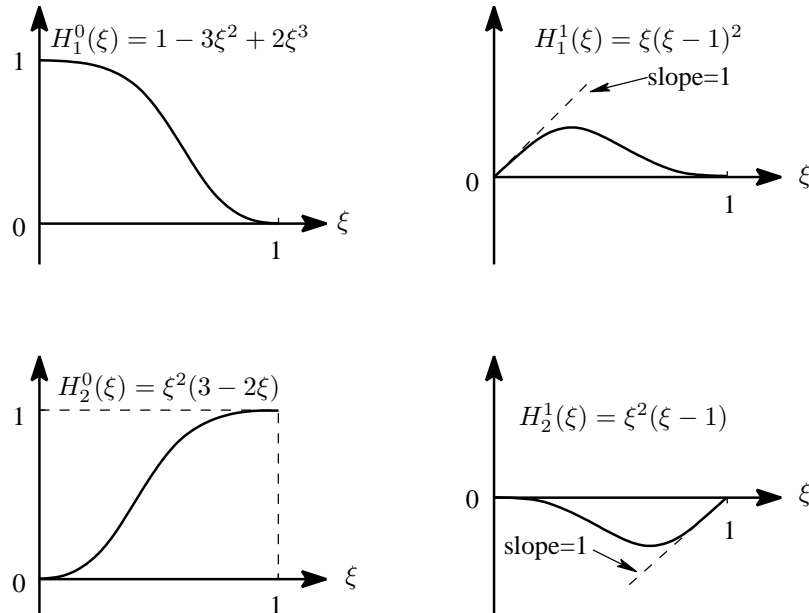
FIGURE 1.5: One-dimensional cubic-Hermite basis functions.

To constrain continuity across element boundaries in the global coordinate system, rather than in the local ξ coordinate system, a further modification is required. The derivative $\left(\dfrac{du}{d\xi}\right)_n$

defined at node n is dependent upon the element ξ-coordinate in the two adjacent elements. It is more useful to define a global node derivative $\left(\frac{du}{ds}\right)_n$ where s is arc-length and then use

$$\left(\frac{du}{d\xi}\right)_n = \left(\frac{du}{ds}\right)_{\Delta(n,e)} \cdot \left(\frac{ds}{d\xi}\right)_n \tag{1.2.2}$$

where $\left(\frac{ds}{d\xi}\right)_n$ is an element "scale factor" which scales the arc-length derivative of global node Δ to the ξ-coordinate derivative of element node n.
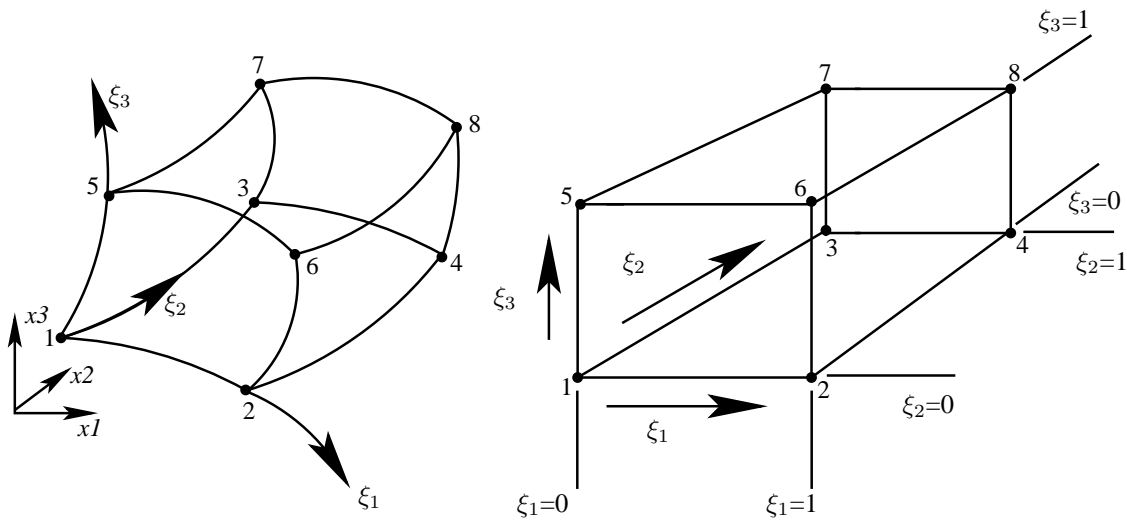
FIGURE 1.6: Schematic and local node numbering of a three dimensional element shown in physical space on the left and transformed into ξ-space on the right.

Achieving derivative continuity in three dimensions for the element shown in Figure 1.6 requires eight values per node:

$$u, \frac{\partial u}{\partial \xi_1}, \frac{\partial u}{\partial \xi_2}, \frac{\partial u}{\partial \xi_3}, \text{ and } \frac{\partial^2 u}{\partial \xi_1 \partial \xi_2}, \frac{\partial^2 u}{\partial \xi_1 \partial \xi_3}, \frac{\partial^2 u}{\partial \xi_2 \partial \xi_3}, \frac{\partial^3 u}{\partial \xi_1 \partial \xi_2 \partial \xi_3}$$

The second-order cross-derivative terms arise from the need to maintain cubic interpolation along every element edge in each ξ direction. To illustrate, if we consider a particular edge of a three dimensional element where moving between nodes corresponds to only increasing in ξ_1. The cubic variation in u can be uniquely specified by u and $\frac{\partial u}{\partial \xi_1}$ at each node. However, $\frac{\partial u}{\partial \xi_2}$, $\frac{\partial u}{\partial \xi_3}$ and $\frac{\partial^2 u}{\partial \xi_2 \partial \xi_3}$ should also vary cubically and are completely independent of these parameters. Thus six additional parameters are specified for each node. Thus tricubic interpolation of these

nodal parameters is given by

$$
\begin{aligned}
u(\xi_1, \xi_2, \xi_3) = \sum_{k=1}^{2} \sum_{j=1}^{2} \sum_{i=1}^{2} \Bigg[& H_i^0(\xi_1)H_j^0(\xi_2)H_k^0(\xi_3)u_n + H_i^1(\xi_1)H_j^0(\xi_2)H_k^0(\xi_3)\left(\frac{\partial u}{\partial \xi_1}\right)_n + \\
& H_i^0(\xi_1)H_j^1(\xi_2)H_k^0(\xi_3)\left(\frac{\partial u}{\partial \xi_2}\right)_n + H_i^0(\xi_1)H_j^0(\xi_2)H_k^1(\xi_3)\left(\frac{\partial u}{\partial \xi_3}\right)_n + \\
& H_i^1(\xi_1)H_j^1(\xi_2)H_k^0(\xi_3)\left(\frac{\partial^2 u}{\partial \xi_1 \partial \xi_2}\right)_n + H_i^1(\xi_1)H_j^0(\xi_2)H_k^1(\xi_3)\left(\frac{\partial^2 u_n}{\partial \xi_1 \partial \xi_3}\right)_n + \\
& H_i^0(\xi_1)H_j^1(\xi_2)H_k^1(\xi_3)\left(\frac{\partial^2 u_n}{\partial \xi_2 \partial \xi_3}\right)_n + H_i^1(\xi_1)H_j^1(\xi_2)H_k^1(\xi_3)\left(\frac{\partial^3 u}{\partial \xi_1 \partial \xi_2 \partial \xi_3}\right)_n \Bigg]
\end{aligned}
$$
(1.2.3)

where the nodal index $n = 4(k-1) + 2(j-1) + i$ and

$$
H_1^0(\xi) = 1 - 3\xi^2 + 2\xi^3, \; H_1^1(\xi) = \xi(\xi-1)^2, \; H_2^0(\xi) = \xi^2(3-2\xi) \text{ and } H_2^1(\xi) = \xi^2(\xi-1) \quad (1.2.4)
$$

as shown in Figure 1.5. To simplify notation, let

$$
u\left(\xi_1, \xi_2, \xi_3\right) = \sum_{m} \psi_m\left(\boldsymbol{\xi}\right) \boldsymbol{u}_m, \tag{1.2.5}
$$

where $\boldsymbol{u}_m$ represents the vector of nodal values and their derivatives and ψ_m are formed from the products of the one dimensional basis functions given in Equation (1.2.4), and the summation over m is taken over all these quantities.

As in the one dimensional case, to preserve derivative continuity in physical x-coordinate space rather than in ξ-coordinate space the global node derivatives need to be specified with respect to physical arc-length. There are now three arc-lengths to consider: s_i, measuring arc-

length along the ξ_i-coordinate, for $i = 1, 2, 3$. Thus

$$
\begin{aligned}
\left(\frac{\partial u}{\partial \xi_1}\right)_n &= \left(\frac{\partial u}{\partial s_1}\right)_{\Delta(n,e)} \cdot \left(\frac{ds_1}{d\xi_1}\right)_n \\[2mm]
\left(\frac{\partial u}{\partial \xi_2}\right)_n &= \left(\frac{\partial u}{\partial s_2}\right)_{\Delta(n,e)} \cdot \left(\frac{ds_2}{d\xi_2}\right)_n \\[2mm]
\left(\frac{\partial u}{\partial \xi_3}\right)_n &= \left(\frac{\partial u}{\partial s_3}\right)_{\Delta(n,e)} \cdot \left(\frac{ds_3}{d\xi_3}\right)_n \\[2mm]
\left(\frac{\partial^2 u}{\partial \xi_1 \partial \xi_2}\right)_n &= \left(\frac{\partial^2 u}{\partial s_1 \partial s_2}\right)_{\Delta(n,e)} \cdot \left(\frac{ds_1}{d\xi_1}\right)_n \cdot \left(\frac{ds_2}{d\xi_2}\right)_n \\[2mm]
\left(\frac{\partial^2 u}{\partial \xi_1 \partial \xi_3}\right)_n &= \left(\frac{\partial^2 u}{\partial s_1 \partial s_3}\right)_{\Delta(n,e)} \cdot \left(\frac{ds_1}{d\xi_1}\right)_n \cdot \left(\frac{ds_3}{d\xi_3}\right)_n \\[2mm]
\left(\frac{\partial^2 u}{\partial \xi_2 \partial \xi_3}\right)_n &= \left(\frac{\partial^2 u}{\partial s_2 \partial s_3}\right)_{\Delta(n,e)} \cdot \left(\frac{ds_2}{d\xi_2}\right)_n \cdot \left(\frac{ds_3}{d\xi_3}\right)_n \\[2mm]
\left(\frac{\partial^3 u}{\partial \xi_1 \partial \xi_2 \partial \xi_3}\right)_n &= \left(\frac{\partial^3 u}{\partial s_1 \partial s_2 \partial s_3}\right)_{\Delta(n,e)} \cdot \left(\frac{ds_1}{d\xi_1}\right)_n \cdot \left(\frac{ds_2}{d\xi_2}\right)_n \cdot \left(\frac{ds_3}{d\xi_3}\right)_n
\end{aligned}
$$

$$(1.2.6)$$

Equations (1.2.3)–(1.2.6) provide a means of interpolating spatially varying fields that are C^1-continuous.

Previously, two alternative approaches to modelling the geometry of the heart have been used. The original canine heart was modelled using a prolate spheroidal coordinate system with bicubic-linear field interpolation (Nielsen, LeGrice, Smaill & Hunter 1991, Nash 1998). Use of the LV like prolate spheroidal coordinate system reduced the number of degrees of freedom in the model allowing for a concise and compact computational description of the canine ventricles but imposed some non-physiological constraints on the model (Stevens 2002). More recently, models have been developed using the rectangular Cartesian (RC) coordinate system as the need for this compact computational description no longer outweighs the increasing need for physiological complexity in the models. The canine model has now been transformed to the RC coordinate system (Tomlinson 2000) and the porcine ventricular model was developed completely in RC coordinates (Stevens 2002) using tricubic-Hermite field interpolation.

As with geometry, cubic-Hermite interpolation can effectively be used to represent the variation in microstructurally based material directions. This is demonstrated in Figure 1.4 which shows the microstructural fibre field in the prolate spheroidal canine model and the RC porcine model.

An overview of the application of cubic-Hermite finite elements to finite deformation elasticity and electrical activation models is provided in Appendices B and C, respectively. Greater detail on the implementation and use of cubic-Hermite finite elements can be found in many of the theses from our group (*e.g.,* Bradley 1998, Nash 1998, Buist 2001, Stevens 2002).

1.3 Thesis Overview

The research encompassed in this thesis can be divided into three components: development of a method for dynamic specification of mathematical models at run-time through the use of CellML; development of a mathematical modelling and numerical simulation framework for cardiac electro-mechanics at the cellular, tissue, and organ spatial and temporal scales; and the application of these tools to specific models of cardiac electro-mechanics. This work is targeted at providing an initial simulation environment capable of bringing together different aspects of the IUPS Physiome Project, which is described in Chapter 4.

To test the methods we have developed and implemented which enable the use of CellML in this work (Section 4.3), we present in Chapter 2 a comprehensive review of published cellular models. All simulation results presented in this chapter are generated directly from the CellML, as are the model descriptions provided in Appendix A.

Chapter 3 builds on the base of models provided in Chapter 2, and demonstrates how models of cellular electrophysiology and mechanics can be coupled together. Several cellular electro-mechanics models are presented that are capable of reproducing some key experimental data. We then describe the modelling and simulation framework we have developed for cardiac electro-mechanics based on tightly coupling the cellular level active tension dynamics into tissue and organ level continuum models. Simulations are presented which test the models developed and ensure the accuracy and reliability of the numerical results.

This work forms part of the IUPS Physiome Project. In Chapter 4 we present an overview of the Physiome Project and provide more information about the CellML language. The models described in this thesis are all simulated using the CMISS computational biology package which is also described in this chapter. Chapter 4 describes our implementation of an initial simulation framework suitable for a wide range of the multi-scale modelling being done as part of the Physiome Project. We use cardiac electro-mechanics as a case study for the use of the framework. We also discuss the future of this framework and its application to other modelling

areas.

In Chapter 5, the models of cardiac electro-mechanics developed are used with the framework we have developed to provide insight to some real physiological problems. Discussion of these results follows in Chapter 6, where we also discuss some future uses of the models developed. A list of publications from this work is provided in Section 6.3.

Full descriptions of all the cellular models used in this thesis are provided in Appendix A, generated from the CellML version of each of the models. Appendices B and C provide some background information on the theory and implementation of finite elasticity and electrical activation finite element modelling. Appendix D provides a description of the contents of the compact disc that accompanies this thesis.

Chapter 2

Cellular Modelling Review

This chapter attempts to summarise the development of cellular electrical and mechanical modelling from the work of Hill (1938), Hodgkin & Huxley (1952), and Huxley (1957) through to today's sophisticated models. While the focus of this thesis is on cardiac cells, some non-cardiac cellular models are included here as many cardiac cellular models are derived from earlier work on nerve and muscle cells (Fozzard & Lipkind 1995). The models presented here are designed to represent the average properties of a group of cells forming part of a tissue, rather than one particular cell. The heart contains 10^{10} cells and it is infeasible to model each one individually, nor is it necessary because all the cells are tightly coupled both electrically and mechanically and one cell behaves like its neighbours.

2.1   Introduction

In a very general sense, cellular models can be separated into two broad categories: biophysical and simplified models. Biophysical models attempt to accurately model the underlying physiology whereas simplified models mathematically represent a particular cellular property – typically the cardiac action potential in the case of electrophysiological models. Biophysically based models tend to have the advantage of greater predictive power but are fairly computationally intensive while simplified models are ideal for certain simulations where resources are limited, either physically or due to the simultaneous solution of multiple cell simulations, and only a specific aspect of the system is being investigated. For example, if one is only interested in the propagation of the activation wave along a one-dimensional fibre, a simple polynomial

model of activation (Hunter, McNaughton & Noble 1975) might be appropriate.

As well as the distinction between biophysical and simplified, models also tend to be thought of in terms of the particular aspect of the cellular physiology they are modelling. In this work we concentrate on modelling the electrophysiology and mechanical behaviour. Also, there are models which model the cell as a whole and those which model just one component of the cell, where a component is a general term which could mean anything from a single transmembrane ion channel model to the full calcium dynamics subsystem of the cell. There are also models which combine multiple component models together and/or model both the electrophysiology and mechanical behaviour and their interaction – looking at excitation contraction coupling and mechano-electrical feedback.

An important feature of this review is that all the mathematical models have been marked-up in CellML (Section 4.1.1). Thus, all simulations presented in this chapter and the mathematical equations provided in Appendix A are consistent. The CellML models are all provided on the attached CD, see Section D.2 for more information.

2.1.1   Overview

Figure 2.1 graphically illustrates the time line of the development of the cellular models reviewed or developed in this thesis. While this figure (and this section) attempts to encompass the significant models in this area, the figure is by no means a complete listing of all cardiac cellular models. In Figure 2.1 the coloured arrows are used to indicate that a given model has some connection to an earlier model or models. For example, the Luo & Rudy (1991) model was further developed and presented as the Luo & Rudy (1994) model which was again further developed into the Jafri, Rice & Winslow (1998) model.

Also shown in Figure 2.1 is a time line of the development of the Intel®[1] microprocessors. This development can be interpreted as a general indication of the typical computational power a scientist of the time would have had available in their laboratory or on their desktop. It is interesting to note that the complexity of the mathematical models at least keeps up with the development of the microprocessor, such that for a modeller to be able to solve a single cell model in real time they would need the most powerful desktop computer at that time, if not something more advanced. Certainly with the pure computational power accessible in most

---

[1]Intel, 386, 486, Pentium, and Celeron are trademarks or registered trademarks of Intel Corporation or its subsidiaries in the United States of America and other countries.
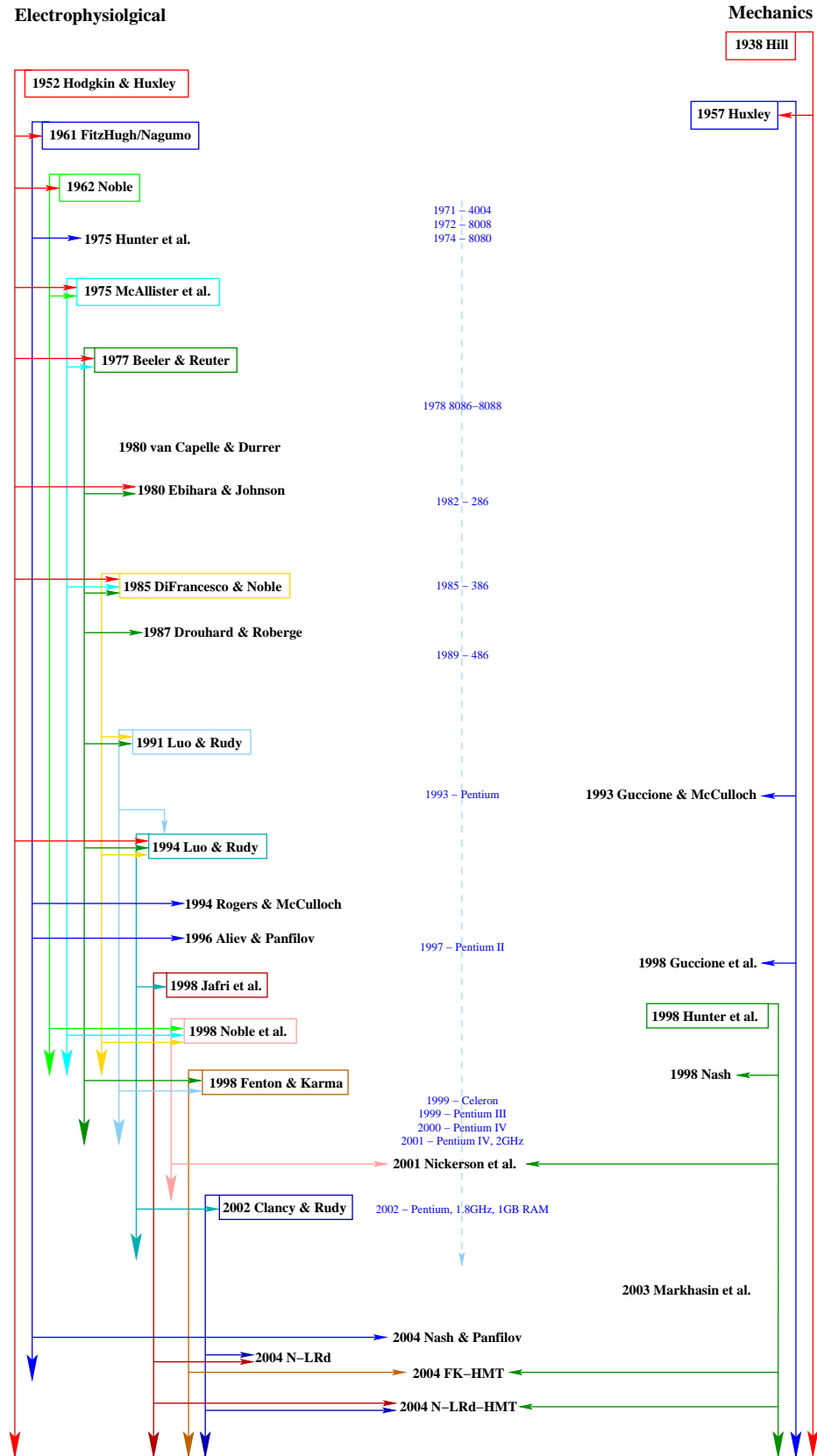
FIGURE 2.1: Time line of the development of the cellular models reviewed and developed in this thesis. The models on the left are focused on electrophysiology, those on the right on mechanical behaviour, and those down the middle are coupled electro-mechanics models. The blue text through the centre of the figure provides the progressive development of Intel microprocessors.

homes today a modeller is able to accomplish the solution of models that could not even be attempted when the first Hodgkin & Huxley (1952) or Noble (1962) simulations were run on huge, punch-card based mainframe computers.

The remainder of this chapter reviews the most of the models illustrated in Figure 2.1 describing their development and any improvement made to them over the years. The exceptions are the two coupled electro-mechanics models developed as part of this work (FK-HMT and N-LRd-HMT), which are covered in Section 3.1.

2.1.2   Nomenclature and Conventions

Generally most cellular models use similar nomenclature and conventions. To aid the use of the models reviewed here, the model descriptions have all been adjusted from the original publications to ensure consistency throughout all the models reviewed. Particular care has been taken to ensure that the similar conventions are used across all the models and that the models are self-consistent for units and dimensionality.

Conventions

All the models reviewed below have been formulated using the electrophysiological convention described by Noble (1962). The transmembrane electric potential (denoted as V_m) is the potential of the bulk intracellular cytoplasm with respect to the extracellular space, the resting potential is a negative quantity, and the action potential is a positive variation – requiring outward currents to be positive. This needs to be consistent when comparing different cellular electrophysiology models and also when using the models in distributed simulations.

The main requirement for the cellular mechanical models is that the model's representation of stress and strain is consistent with that at the tissue and organ levels. We achieve this through the use of the fibre extension ratio, described in Section 2.1.3 below, at both the tissue and cellular modelling levels. As will be described, the fibre extension ratio is readily calculated for a given tissue strain state.

Units and Dimensionality

With the development of standards such as CellML, which requires every quantity to be associated with an appropriate unit definition, it is hoped that model definitions will become much more specific in terms of units. The models reviewed here all predate a common specification of such standards to represent them – which sometimes leads to incompatibilities between the models. To avoid such compatibility issues and to ensure models may be easily compared all models below have been described in terms of a common underlying set of units. The base set of units are defined in Table 2.1 and those derived from these are given in Table 2.2.

Quantity	S.I. Base Units		Cellular Modelling Units	
	Name	**Symbol**	**Multiplier**	**Symbol**
Amount of substance	mole	mol	10^{-9}	nmol
Electric current	Ampere	A	10^{-6}	μA
Length	metre	m	10^{-3}	mm
Mass	kilogramme	kg	10^{-9}	ng
Temperature	Kelvin	K		K
Time	second	s	10^{-3}	ms

TABLE 2.1: The standard base units used in all the cellular modelling in this thesis and their relationship to base S.I. units.

2.1.3   Fibre Extension Ratio

The fibre extension ratio is a non-dimensional localised measure of uniaxial cellular deformation. A value of 1.0 corresponds to a cell at its resting length, typically taken as 100.0 μm. Values greater than 1.0 indicate the cell is being stretched and a value less than 1.0 implies the cell is being compressed in the fibre direction. While a cardiac cell is usually only stretched through the application of external forces, compression can be caused either passively by the surrounding tissue or through active contraction of the cell.

In cellular models the fibre extension ratio is defined as the ratio of the current length of the cell, L, to the cellular resting length, L_0, and is denoted λ,

$$\lambda = \frac{L}{L_0}. \tag{2.1.1}$$

This is, of course, another way of expressing material strain with respect to the fibre axis. When modelling myocardial tissue, there are three microstructural axes and the strain in each of these

Derived Quantity	Cellular Modelling Units	
	Units	**Synonym**
Area	mm^2	
Volume	mm^3	
Voltage	$\mathrm{mm}^2 \cdot \mathrm{ng} \cdot \mathrm{ms}^{-3} \cdot \mu\mathrm{A}^{-1}$	mV
Conductivity	$\mathrm{mm}^{-2} \cdot \mathrm{ng}^{-1} \cdot \mathrm{ms}^3 \cdot \mu\mathrm{A}^2$	mS
Membrane conductance	$\mathrm{mm}^{-4} \cdot \mathrm{ng}^{-1} \cdot \mathrm{ms}^3 \cdot \mu\mathrm{A}^2$	$\mathrm{mS} \cdot \mathrm{mm}^{-2}$
Tissue conductivity	$\mathrm{mm}^{-3} \cdot \mathrm{ng}^{-1} \cdot \mathrm{ms}^3 \cdot \mu\mathrm{A}^2$	$\mathrm{mS} \cdot \mathrm{mm}^{-1}$
Current density	$\mu\mathrm{A} \cdot \mathrm{mm}^{-2}$	
Volume current	$\mu\mathrm{A} \cdot \mathrm{mm}^{-3}$	
Charge	$\mathrm{ms} \cdot \mu\mathrm{A}$	nC
Capacitance	$\mathrm{mm}^{-2} \cdot \mathrm{ng}^{-1} \cdot \mathrm{ms}^4 \cdot \mu\mathrm{A}^2$	$\mu\mathrm{F}$
Specific capacitance	$\mathrm{mm}^{-4} \cdot \mathrm{ng}^{-1} \cdot \mathrm{ms}^4 \cdot \mu\mathrm{A}^2$	$\mu\mathrm{F} \cdot \mathrm{mm}^{-2}$
Concentration	$\mathrm{nmol} \cdot \mathrm{mm}^{-3}$	mM
Concentration rate	$\mathrm{nmol} \cdot \mathrm{mm}^{-3} \cdot \mathrm{ms}^{-1}$	$\mathrm{mM} \cdot \mathrm{ms}^{-1}$
Force	$\mathrm{mm} \cdot \mathrm{ng} \cdot \mathrm{ms}^{-2}$	nN
Stress (pressure)	$\mathrm{mm}^{-1} \cdot \mathrm{ng} \cdot \mathrm{ms}^{-2}$	mPa
Energy	$\mathrm{mm}^2 \cdot \mathrm{ng} \cdot \mathrm{ms}^{-2}$	pJ
Power	$\mathrm{mm}^2 \cdot \mathrm{ng} \cdot \mathrm{ms}^{-3}$	nW

TABLE 2.2: The standard derived units for the cellular modelling in this thesis, both in terms of the base units from Table 2.1 and the commonly used synonyms.

axes can be expressed as extension ratios,

$$\lambda_{ii} = \sqrt{2E_{ii} + 1}, \tag{2.1.2}$$

where E_{ii} are the axial strain components from the Green strain tensor, Equation (B.1.4).

In the fibre direction, it is generally assumed that intact cells can be passively stretched to approximately 2.4 μm and internal structure prevents compression and/or contraction below approximately 1.6 μm. This results in a physiological range of

$$0.8 \lesssim \lambda \lesssim 1.2$$

Knowledge of the range of λ is important in the simulation of tissue models and is used to impose physiological constraints on the numerical methods used in such simulations (Section 3.2.2).

2.2   1952 Hodgkin & Huxley

Over the period $1935 - 1952$ Hodgkin & Huxley performed a series of experiments concerned with the flow of electric current through the surface membrane of a squid giant nerve fibre. These experiments led to the publication in 1952 of the first biophysically based model of the electrophysiology of a single cell (Hodgkin & Huxley 1952). This model laid the foundation for much of the electrical modelling of cardiac cells, with some of the mechanisms from this model still in use today – most models incorporate at least a few "Hodgkin-Huxley" type gating variables (see Equation (2.2.2)).

Given the relevance of this spectacularly successful paradigm model (Noble & Rudy 2001) to all of the following electrophysiology models, we devote more attention to its description.

In this model Hodgkin & Huxley presented the idea that the electrical behaviour of the axon membrane may be represented by the equivalent electrical circuit shown in Figure 2.2. This analogy shows that current can be carried through the membrane by charging the membrane capacity or by movement of ions through resistances in parallel to the capacity.

Hodgkin & Huxley break the membrane current into three components: sodium, potassium, and a leak current (made up by chloride and other ions). Each component current is determined by a driving force conveniently measured as an electrical potential difference and a permeability coefficient which has the dimensions of conductance. Their experiments suggested that the
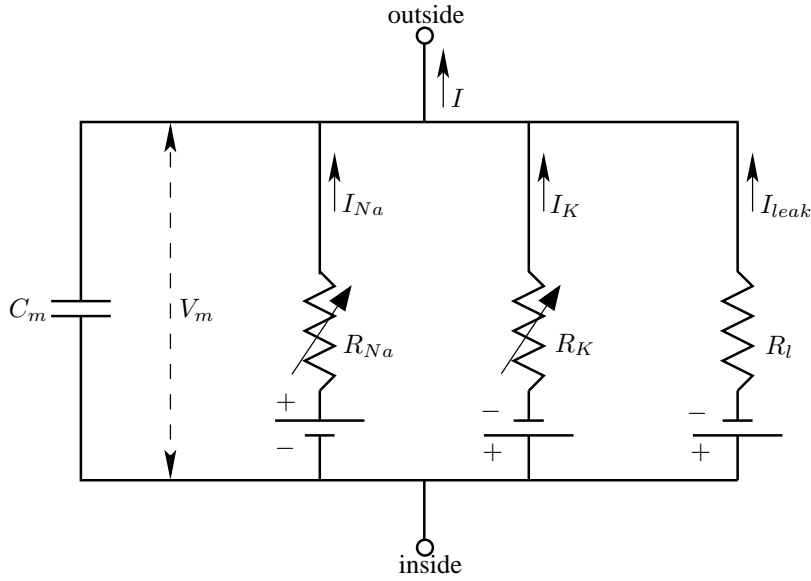
FIGURE 2.2: Electrical circuit representing the membrane. $R_{Na} = g_{Na}^{-1}$, $R_K = g_K^{-1}$, and $R_l = \overline{g_{leak}}^{-1}$.

conductance for the sodium and potassium currents were functions of time and membrane potential while that of the leakage current was constant, as were the equilibrium potentials for all three components of the membrane current. They also observed that changes in membrane permeability were dependent on membrane potential, not membrane current.

Possibly the most significant contribution of their work was the suggestion that changes in ionic permeability depended on the movement of some component of the membrane which behaved as though it had a large charge or dipole moment. With this suggestion, they also state that for such components to exist it would be necessary to suppose that their density is relatively low and that a number of ions cross the membrane at a single (selective) active patch – *i.e.,* a selective transmembrane ion channel. In their model Hodgkin & Huxley describe two such components – one sodium sensitive, with both activation and inactivation molecules, and one potassium sensitive, with slower kinetics and no blocking or inactivation molecules.

This model and all the following electrophysiology models make extensive use of an ion's equilibrium, or Nernst, potential. An ion's equilibrium potential is calculated using the Nernst equation, which describes the relationship between the ratio of concentrations of an ion across a membrane and the electrical potential difference across the membrane when the ion is distributed in equilibrium. The Nernst potential for ion X is given by:

$$E_X = \frac{RT}{z_X F} \ln \left(\frac{[X]_o}{[X]_i} \right), \tag{2.2.1}$$

where R is the natural gas constant, T is the absolute temperature, z_X is the ion's valence, $[X]_o$ denotes extracellular concentration of the ion, and $[X]_i$ is the intracellular concentration.

The complete Hodgkin & Huxley mathematical model of a squid giant axon is given in Section A.2. In summary, the activation variables of the Na^+ (m) and K^+ (n) currents and the inactivation variable of the Na^+ current (h) are governed by an ordinary differential equation of the form

$$\frac{dx}{dt} = \alpha \left(1 - x\right) - \beta x, \tag{2.2.2}$$

where x is one of m, h, or n and t is time. α and β are the voltage-dependent opening and closing rates, respectively, of the molecular gates (see Section A.2 for their formulations). As mentioned, the ionic currents are defined as the product of a permeability coefficient and the potential difference between the membrane potential and the ion's equilibrium potential

$$I_{Na} = g_{Na} \left(V_m - E_{Na}\right) \tag{2.2.3}$$

$$I_K = g_K \left(V_m - E_K\right) \tag{2.2.4}$$

$$I_{leak} = \overline{g_{leak}} \left(V_m - E_{leak}\right), \tag{2.2.5}$$

where V_m is the membrane potential, E_{Na}, E_K, and E_{leak} are the constant equilibrium potentials of the channels. $\overline{g_{leak}}$ is the constant conductance for the leakage channel and g_{Na} and g_K are given by

$$g_{Na} = \overline{g_{Na}} m^3 h \tag{2.2.6}$$

$$g_K = \overline{g_K} n^4. \tag{2.2.7}$$

The kinetics of the membrane potential are then defined as the sum of the ionic currents

$$\frac{dV_m}{dt} = \frac{I_{stim} - \left(I_{Na} + I_K + I_{leak}\right)}{C_m}. \tag{2.2.8}$$

I_{stim} is an applied stimulus current and C_m is the membrane capacitance per unit area.

Figure 2.3 shows the results Hodgkin & Huxley model simulations with a repetitive stimulus of $400 \ \mu A \cdot mm^{-3}$ applied at a frequency of 10 Hz.

2.3   Simplified Models of Cardiac Cellular Electrophysiology

This section reviews models derived to represent cardiac cellular electrophysiology without explicit inclusion of ion channel mechanisms. These simplified models attempt to replicate

PSfrag replacements

V_m
C_m
I
I_{ion}
I_{Na}
I_K
I_{leak}

$\mu A \cdot mm^{-2}$

ms

$(I_{leak}) \, \mu A \cdot mm^{-2}$

(a) Membrane potential, V_m

PSfrag replacements

V_m
C_m
I
I_{ion}
I_{Na}
I_K
I_{leak}

mV

$\mu A \cdot mm^{-2}$

ms

$(I_{leak}) \, \mu A \cdot mm^{-2}$

(b) Gating variables

PSfrag replacements

V_m
C_m
I
I_{ion}

$\mu A \cdot mm^{-2}$

mV

(c) Transmembrane ionic currents
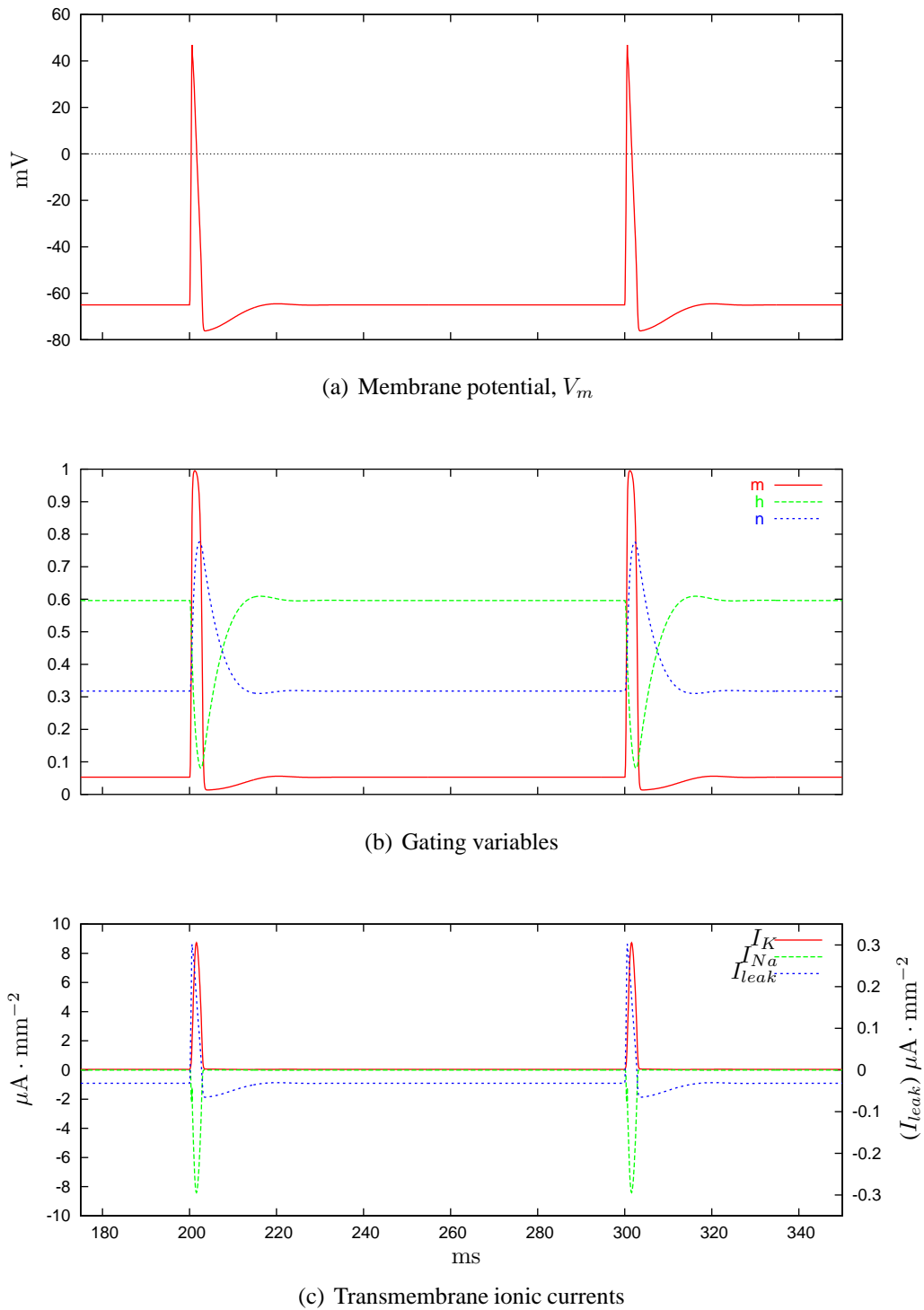
FIGURE 2.3: Results from simulating the Hodgkin & Huxley (1952) model. The I_{leak} current is amplified, right scale, to better illustrate its time course. The model is stimulated at a frequency of 10 Hz with a current of $400 \, \mu A \cdot mm^{-3}$ for a duration of 0.5 ms.

certain key features of the electrophysiology, such as propagation, restitution behaviour, and activation properties. The distinction in complexity between these "simple" models and the later biophysical models is not always clear but is illustrated by comparing the three differential equations in the Fenton & Karma (1998) model (Sections 2.3.4 and A.16) to the 31 in the Jafri et al. (1998) model (Sections 2.4.7 and A.18).

2.3.1   1961 FitzHugh/Nagumo

FitzHugh (1961) and Nagumo, Animoto & Yoshizawa (1962) independently published a generalisation of van der Pol's equation for a relaxation oscillator to provide a simplified unifying concept for the theoretical study of axon physiology. This model has become known as the FitzHugh-Nagumo model of nerve membrane.

By considering the Hodgkin & Huxley (1952) model as one member of a large class of non-linear systems showing excitable and oscillatory behaviour and through the application of phase space methods, FitzHugh reduced the four state variable Hodgkin & Huxley model to a two state variable model. This model can be taken as representative of a wide class of non-linear excitable-oscillatory systems which show threshold and refractory properties as well as oscillations or infinite trains of responses.

Section A.3 presents the full mathematical model of FitzHugh and Nagumo, Animoto & Yoshizawa, but rather than using the non-dimensional equations given in the original publication of these models the equations have been formulated in terms of the "real" membrane potential. Results of simulating with this model are presented in Figure 2.4.

1994 Rogers & McCulloch

In 1994 Rogers & McCulloch published a modification of the FitzHugh-Nagumo model designed to make the model more characteristic of cardiac electrical behaviour. As shown in Figure 2.5, the modified model (Section A.14) removes the hyperpolarisation from the refractory part of the action potential.

The modification Rogers & McCulloch made was to the second term in the I_{ion} equation, with the additional multiplication by the activation variable (Equation (A.14.4)), and changes in model parameter values.

(a) Membrane potential and ionic current

(b) Recovery variable
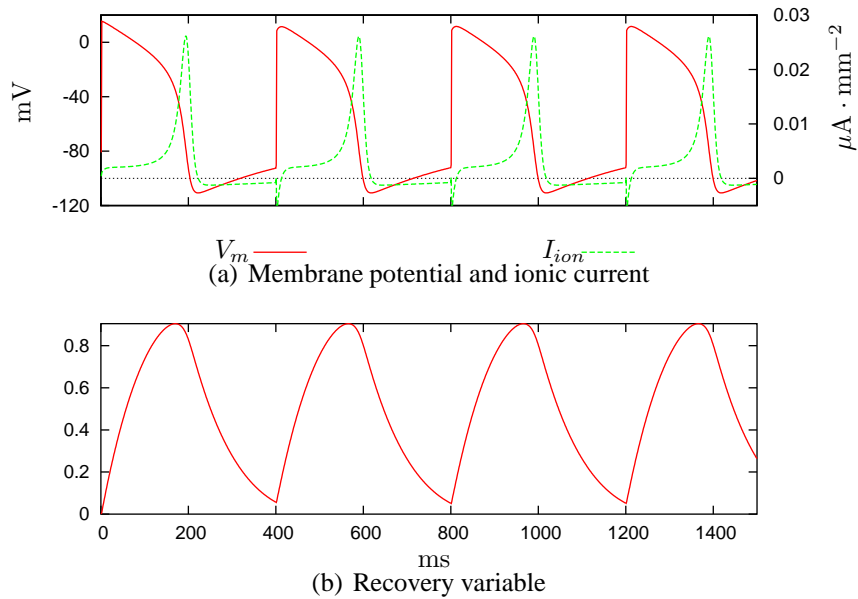
FIGURE 2.4: Results from the FitzHugh-Nagumo model, for an applied stimulus of $400\,\mu\text{A} \cdot \text{mm}^{-3}$ at a frequency of 2.5 Hz with a duration of 0.5 ms.

(a) Membrane potential

(b) Recovery variable
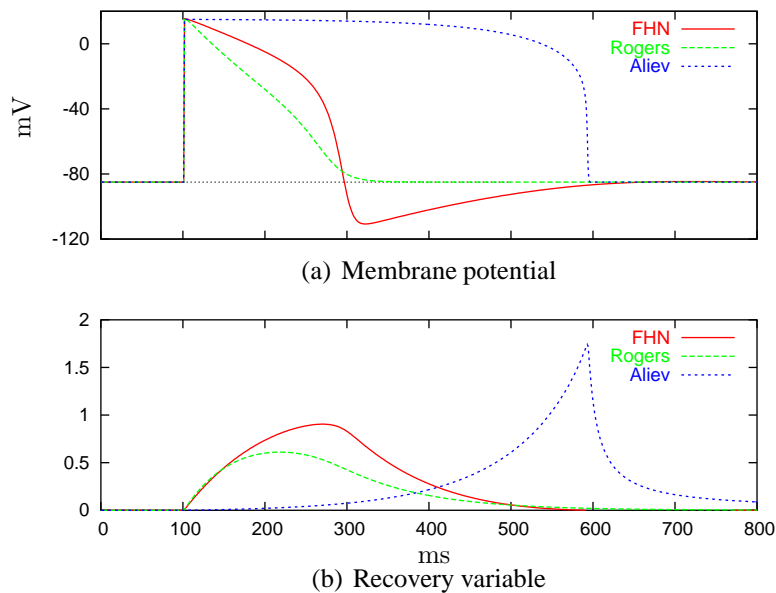
FIGURE 2.5: Results from the Rogers & McCulloch (1994) and Aliev & Panfilov (1996) modified FHN models plotted with the original FHN model. Notice the lack of the hyperpolarisation region in the tail of the action potential for the modified models. For all models, a stimulus of $400\,\mu\text{A} \cdot \text{mm}^{-3}$ is applied at 100 ms for 0.5 ms.

1996 Aliev & Panfilov

Aliev & Panfilov (1996) proposed another modification of the FitzHugh-Nagumo model which simulates the restitution property of cardiac tissue, adequately represents the shape of the action potential, and can be used effectively in computer simulations, particularly, in whole heart modelling. The model is given in Section A.15, with the simulated action potential presented in Figure 2.5.

The restitution properties of this model are shown in Figure 2.6. Electrical restitution is the property in cardiac tissue where the action potential duration (APD) is dependent on the stimulus frequency, characterised here by the basic cycle length (BCL) (the period between stimuli).
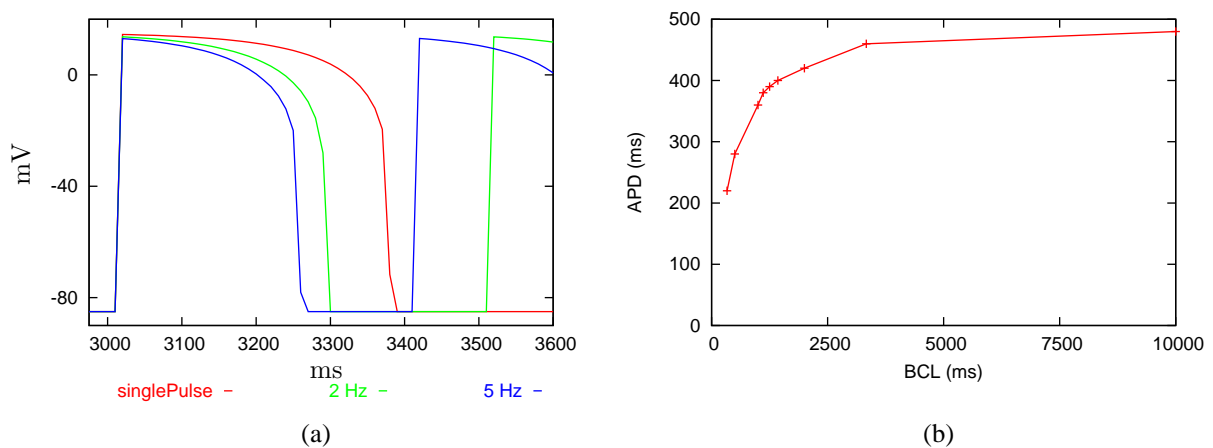
FIGURE 2.6: An illustration of the restitution ability of the Aliev & Panfilov (1996) modified FitzHugh-Nagumo model. (a) presents sample action potentials at three stimulus frequencies and (b) provides a summary of the restitution properties of the model (*cf.* Aliev & Panfilov (1996, Fig. 3). In all simulations a $400\,\mu\text{A} \cdot \text{mm}^{-3}$ stimulus current is applied at required frequency for a duration of $0.5\,\text{ms}$.

2.3.2 1975 Hunter *et al.*

Hunter et al. (1975) look at the mathematics of electrical impulse propagation in excitable cells, namely conduction in fibres of uniform geometry. One motivation for this work was establishing a quantitative technique for calculation of conduction velocities in nerve fibres.

The model Hunter et al. (1975) developed built on earlier work which assumed that at a given threshold potential an instantaneous change in membrane electromotive force occurs – which is incorrect, as the ionic current was known to be a smooth (even if sometimes steep) function of potential. Thus, Hunter et al. (1975) propose various continuous polynomial functions for the ionic current. Polynomial functions were used as they could be chosen to give very good fits to current-voltage relations found in excitable cells without having to include more than a few powers in the polynomial equation.

Like the earlier discontinuous models however, the polynomial models still model the ionic current as purely voltage-dependent, whereas in real cells the ionic current is also an independent function of time. Hunter et al. (1975) mention some contemporary models which include time dependence through the addition of a recovery variable. However, for the purposes of reproducing the conduction process Hunter et al. (1975) state that this is an unnecessary modification since at normal temperatures it is the activation properties that limit conduction.

The third order polynomial model is presented in Section A.5 – this version of the model has become known as the cubic model of electrical activation and used in various studies of electrical propagation in continuum tissue models. Plotting the current-voltage relationship for this model illustrates the cubic nature of this model, as shown in Figure 2.7(a), and the continuous activation of the membrane potential can be seen in Figure 2.7(b).

(a) Current-Voltage relationship.　　　(b) Membrane potential.
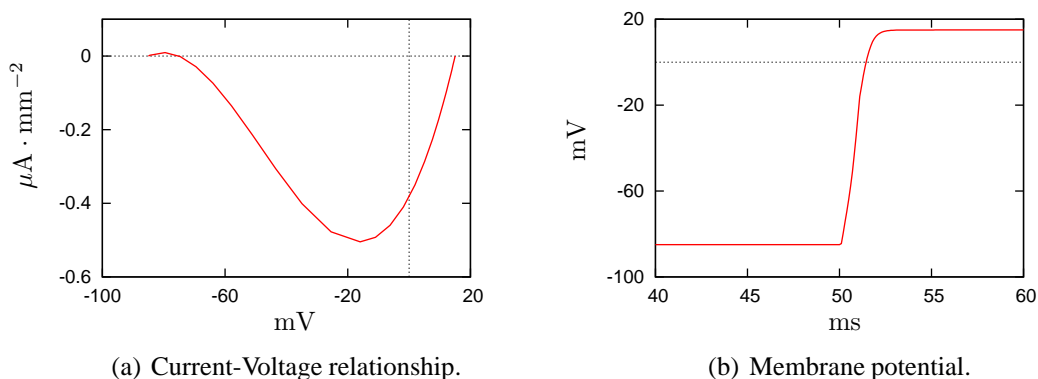
FIGURE 2.7: Results from simulation of the Hunter et al. (1975) cubic polynomial model of activation. The activation is initiated with an applied $1\ \mathrm{ms}$ duration stimulus of $100\ \mu\mathrm{A} \cdot \mathrm{mm}^{-3}$.

2.3.3   1980 van Capelle & Durrer

In a study of the role of spatial interaction among excitable elements in the mechanisms underlying cardiac arrhythmia, van Capelle & Durrer (1980) developed a simplified membrane electrical activation model. Like the FitzHugh-Nagumo type models, their model consists of two variables of state: the transmembrane potential (V_m) and a generalised excitability variable, (Y). Y can have any value between 0 (maximal excitability) and 1 (complete in-excitability). The state of a "cell" in this model, is then completely determined at any time by V_m and Y. In this way, Y is essentially playing the role of the m, h, and n gating variables in the Hodgkin & Huxley kinetics.

The full van Capelle & Durrer (1980) model is given in Section A.9, and the results of simulating this model are presented in Figure 2.8.
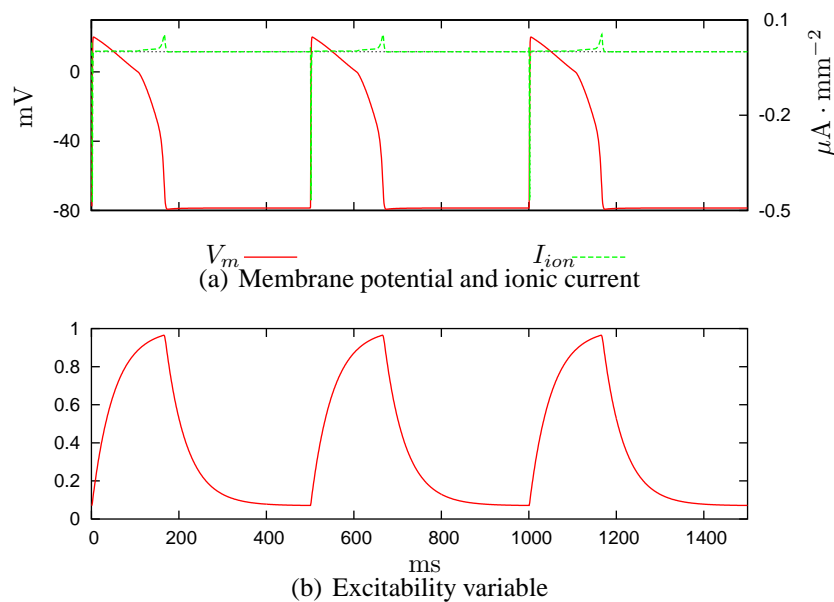
FIGURE 2.8: Results from the van Capelle & Durrer (1980) model, for an applied stimulus of $100\,\mu\mathrm{A}\cdot\mathrm{mm}^{-3}$ at a frequency of 2 Hz with a duration of 1.0 ms.

2.3.4   1998 Fenton & Karma

In a study examining reentry phenomenon in cardiac tissue, Fenton & Karma (1998) developed an ionic activation model that retains the minimal ionic complexity necessary to reproduce quantitatively the restitution curves that describe how the pulse duration and its propagation

velocity depend on the time interval after repolarisation during which the membrane recovers its resting properties. They concentrate on the action potential duration and conduction velocity restitution curves because these dictate the dynamics of the depolarisation wavefront and repolarisation wave-back, and the interaction between these two fronts – most important for modelling reentry. When modelling wave dynamics, these two properties are more fundamental quantities than the shape of the action potential.

The model, given in full in Section A.16, consists of three ionic currents: a fast inward current that is responsible for depolarisation of the membrane and only depends on one inactivation-reactivation gate (v); a slow, time-independent, outward current that is responsible for repolarisation of the membrane; and a slow inward current activated during the plateau phase of the action potential and only depends on one inactivation-reactivation gate (w).

Fenton & Karma chose their model parameters to fit the restitution curves from four sources. Three of the sources were previously published biophysical ventricular cell models: the Beeler & Reuter (1977) model (BR), and modified versions of the Beeler & Reuter (MBR) and Luo & Rudy (1991) (MLR-I) models. The modification made to the models was to speed up the calcium dynamics by a factor of two. The fourth source (GP) was some experimental steady-state curves from optical recordings of membrane potentials on the epicardial surface of the left ventricle of a guinea pig during plane wave pacing at fixed cycle lengths. The results of the model for each of the versions are presented in Figure 2.9.

In Figure 2.10, the action potential for the BR version of the Fenton & Karma model is plotted with that from the full Beeler & Reuter (1977) ventricular myocyte model.

2.4 Biophysically Based Models of Cardiac Cellular Electrophysiology

Biophysically based cellular models are derived from extensive experimental observations and are designed to model, in varying amounts of detail, the underlying physiological mechanisms (especially gated ion channels) rather than just reproduce the action potential. Due to the inclusion of the physiological detail these models tend to have much greater predictive power than the simplified models presented in the previous section, but that same detail leads to very large (and typically stiff) systems of ordinary differential equations – which is still a limiting factor in the use of this class of model in large scale tissue and organ models.

(a) Membrane potential.

(b) Ionic currents.

(c) Gating variables.
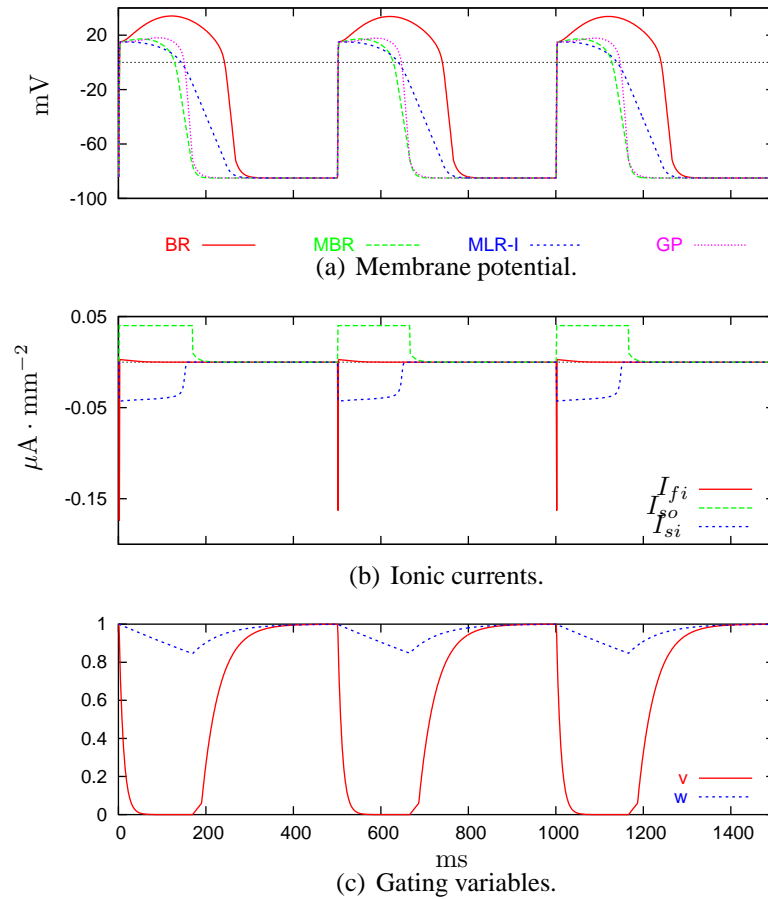
FIGURE 2.9: Results from the Fenton & Karma (1998) model, for an applied stimulus of $80\ \mu\mathrm{A}\cdot\mathrm{mm}^{-3}$ at a frequency of 2 Hz with a duration of 1.0 ms. (a) shows the action potential for each of the four versions of the model – Beeler & Reuter (1977) (BR/MBR), Luo & Rudy (1991) (MLR-I), and the experimentally derived version (GP); (b) and (c) present the ionic currents and the gating variables, respectively, for the GP version of the model.
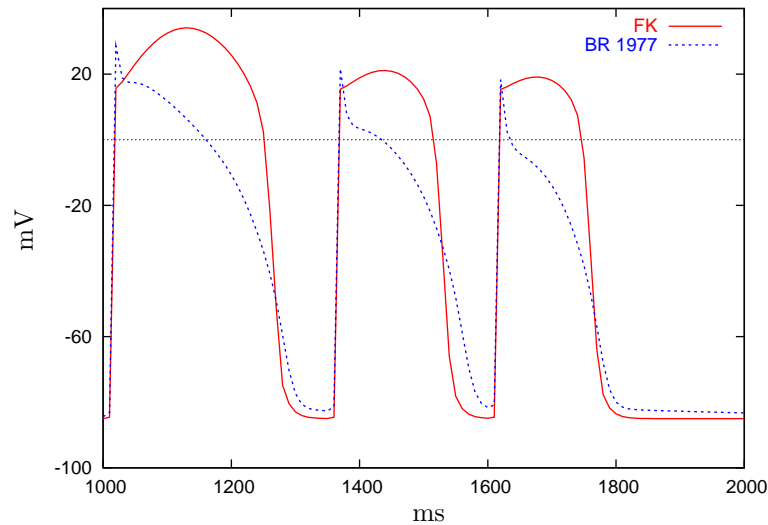
FIGURE 2.10: Comparison of the action potentials calculated from the BR version of the Fenton & Karma model and those from the original Beeler & Reuter (1977) model, for a S1-S2-S3 stimulus protocol (*cf.* Fenton & Karma (1998, Fig. 4))

As mentioned previously, these models were largely based on the model of the squid axon by Hodgkin & Huxley (1952). But with ever improving experimental techniques the models are gradually leaning more and more toward stochastic modelling of populations of individual channels governed by more biochemically-oriented models. Differential equations can then be formulated from these stochastic channel population models to give approximations for inclusion into whole cell models.

2.4.1   1962 Noble

Following the discovery that there were at least two K^+ conductances in the heart, I_{K1} and I_K (initially known as I_{K2}), Noble (1962) developed a model to test whether this combination of K^+ currents plus a Hodgkin & Huxley type Na^+ channel could be used to describe the long-lasting action and pacemaker potentials of the Purkinje fibres of the heart.

The sodium current equations in this model are very similar to the Hodgkin & Huxley (1952) description, with the curves now fitted to voltage-clamp data from Purkinje fibre experiments. The I_{K1} current is assumed to be an instantaneous function of the membrane potential and falls when the membrane is depolarised (a time-independent rectification current). The I_{K2} current slowly rises when the membrane is depolarised, described using Hodgkin & Huxley's (1952) potassium current equations (see Section 2.2), with two main modifications: the maximum

value, $\overline{g_{K_2}}$, was made much smaller than in nerve in order that the increase in g_{K_2} produced by depolarisation should not offset the decrease in g_{K_1}; and the rate constants were divided by 100 in order to take account of the very much slower onset of this effect in Purkinje fibres.

The full Noble (1962) model is given in Section A.4, with results from simulating the model presented in Figure 2.11. Figure 2.11(a) shows the action potentials generated for the free running (pacemaker) version of the model and those for the quiescent version. Noble (1962) obtain a quiescent version of their model by adding $0.001\,\mathrm{mS}\cdot\mathrm{mm}^{-2}$ to the K^+ conductance – see the g_K_add parameter in Section A.4.

(a) Membrane potential, V_m

(b) Gating variables

(c) Transmembrane ionic currents
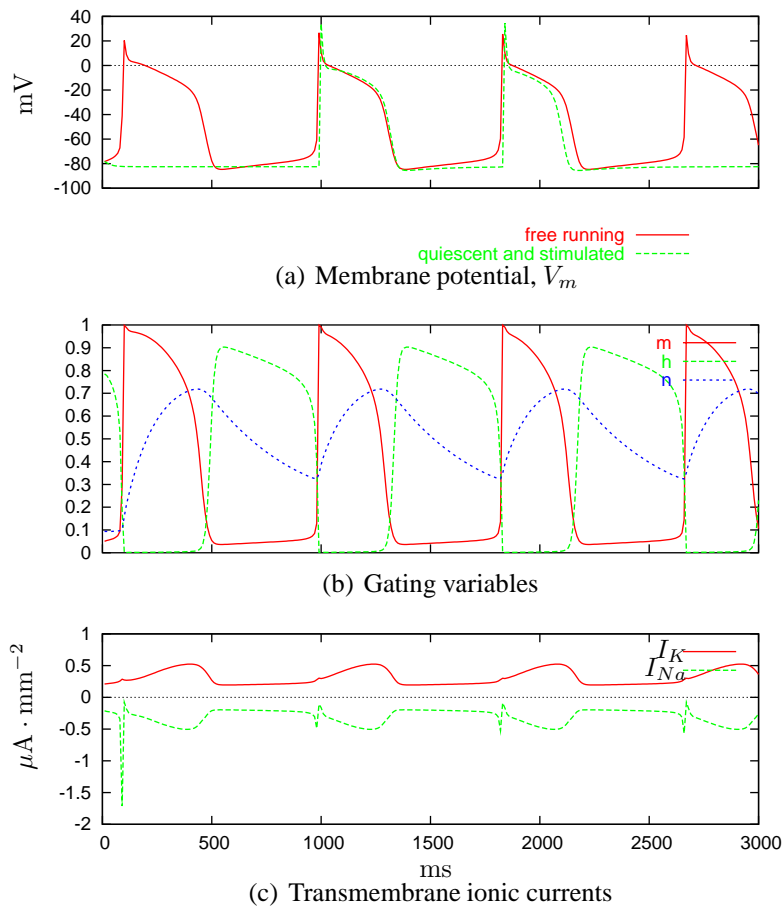
FIGURE 2.11: Results from simulating the Noble (1962) model. (a) shows the action potentials generated by the free running (pacemaker) version of the model and those for the quiescent version of the model with two stimuli of $400\,\mu\mathrm{A}\cdot\mathrm{mm}^{-3}$ with a duration of $1\,\mathrm{ms}$. (b) and (c) are results for the free running model.

2.4.2   1975 McAllister *et al.*

With the development of better and more extensive experiments on cardiac membranes, McAllister, Noble & Tsien (1975) found that previous cardiac models based on modifications to the Hodgkin & Huxley (1952) nerve model were inadequate in important ways. Using the wealth of data then available, McAllister et al. (1975) developed a new model of cardiac Purkinje fibres containing many significant advances from the Noble (1962) model.

The model contains two time-dependent inward currents: a fast sodium current (I_{Na}, similar to that of Hodgkin & Huxley (1952)); and a secondary inward current (I_{si}) with slower kinetics was identified and is partly carried by calcium ions. There is a transient outward chloride current (I_{qr}) activated during strong depolarisations. Finally, instead of the single K^+ current of Hodgkin & Huxley (1952) and Noble (1962), McAllister et al. (1975) found three distinguishable time-dependent potassium currents (I_{K2}, I_{x_1}, and I_{x_2}). None of these potassium currents quantitatively resembled the squid potassium current.

In addition to these currents, McAllister et al. (1975) expand the time-independent leakage current from the Hodgkin & Huxley (1952) nerve model into three distinct components, based on the possible ionic composition of the currents. The outward background current is carried mainly by K^+ (I_{K1}) and corresponds to the outward membrane current that may be recorded below the I_{x_1} and I_{x_2} threshold in Na^+-free solutions. They also define an inward background current carried by Na^+ which gives the measured resting potential deviation from that of the potassium equilibrium potential (the primary cause of the resting potential value). The third component came from experimental evidence that Cl^- contribute to the current flow during the pacemaker and plateau phases of the action potential. While McAllister et al. (1975) formulated the three background time-independent currents in terms of specific ions, they note that there was at that time no reliable means to experimentally dissect the total background current so their formulation was rather tentative and does not imply that there necessarily exists such distinct membrane channels.

Figure 2.12 presents the results this model, which is given in full in Section A.6. The currents and gating variables are all shown along with the spontaneous action potentials.

(a) Membrane potential, V_m

(b) Fast sodium channel

(c) Secondary inward current

(d) Pacemaker current

(e) Plateau potassium currents

(f) Transient chloride channel

(g) Background currents
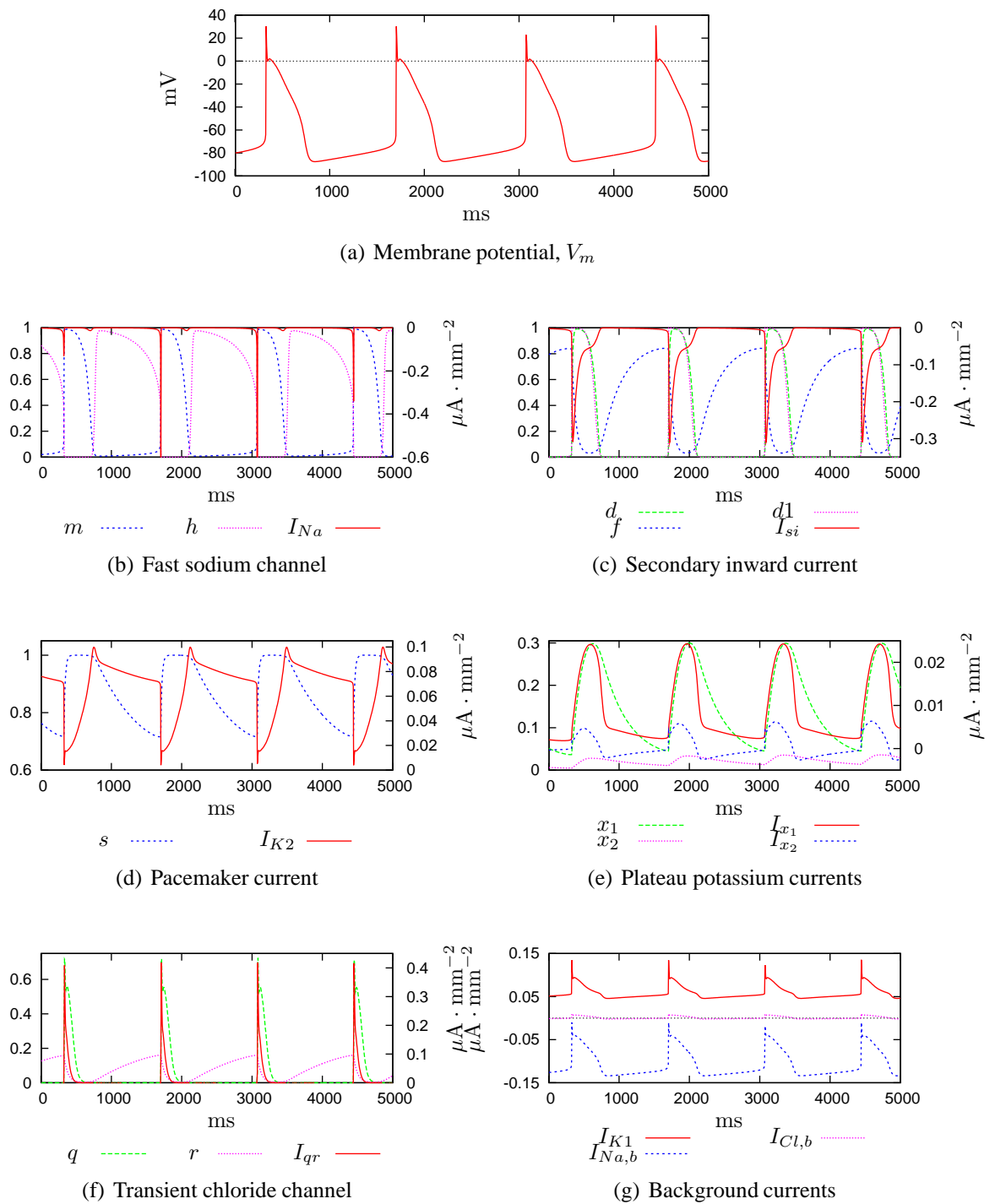
FIGURE 2.12: Simulation results for all the currents and gating variables in the McAllister et al. (1975) Purkinje fibre model, illustrating the pacemaker functionality of the model. In figures (b)–(f) the left hand axis denotes the scale for the gating variables and the right hand denotes the current scale.

2.4.3   1977 Beeler & Reuter

In 1977 Beeler & Reuter published the first mathematical model of the cardiac ventricular action potential. This model formulated the cardiac ventricular action potential from transmembrane ionic currents using Hodgkin & Huxley (1952) type equations, in a similar manner to the model by McAllister et al. (1975) for the cardiac Purkinje fibre. The Beeler & Reuter (1977) model became the framework for the development of later more comprehensive models of cardiac ventricular action potentials and has been used extensively in simulations of action potential propagation in multicellular models of cardiac tissue (Noble & Rudy 2001).

The model includes four individual components of ionic current. The two inward voltage- and time-dependent currents are the excitatory sodium current (I_{Na}) and a secondary or slow current primarily carried by calcium ions (I_s). For outward currents, there is a time-independent potassium current (I_{K1}) which exhibits inward-going rectification, and a voltage- and time-dependent current primarily carried by potassium ions (I_{x_1}). Both I_{K1} and I_{x_1} were adopted from the McAllister et al. (1975) model, while the pacemaker current (I_{K2}) and I_{x_2} were dropped as there was no convincing experimental evidence for the presence of these currents in ventricular myocardium.

The fast sodium current (I_{Na}) was adapted from Hodgkin & Huxley (1952) with the addition of a slow inactivation gating variable (j) based on experimental evidence that re-activation of I_{Na} was much slower than inactivation. The secondary inward current (I_s) was the main focus of the Beeler & Reuter (1977) model and included an initial model of intracellular calcium handling (Figure 2.13(b)). The full model is given in Section A.7 and the results from simulation with this model are presented in Figure 2.13.

1980 Ebihara & Johnson

In 1980, Ebihara & Johnson published possibly the first mathematical model focused on a single cardiac transmembrane ionic current – the fast sodium channel (I_{Na}). While previous models had been developed for this current, the lack of experimental data for the kinetics of the channel under physiological conditions led to *ad hoc* assumptions in such models (Ebihara & Johnson 1980).

The aim of the Ebihara & Johnson (1980) model was to provide a quantitative description of the kinetics of the fast sodium channel using voltage-clamp data obtained from small spherical

(a) Membrane potential, V_m

(b) Intracellular calcium, $[\text{Ca}^{2+}]_i$

(c) Fast sodium channel

(d) Secondary inward current

(e) Time-dependent outward current, I_{x_1}

(f) Time-independent potassium current, I_{K1}
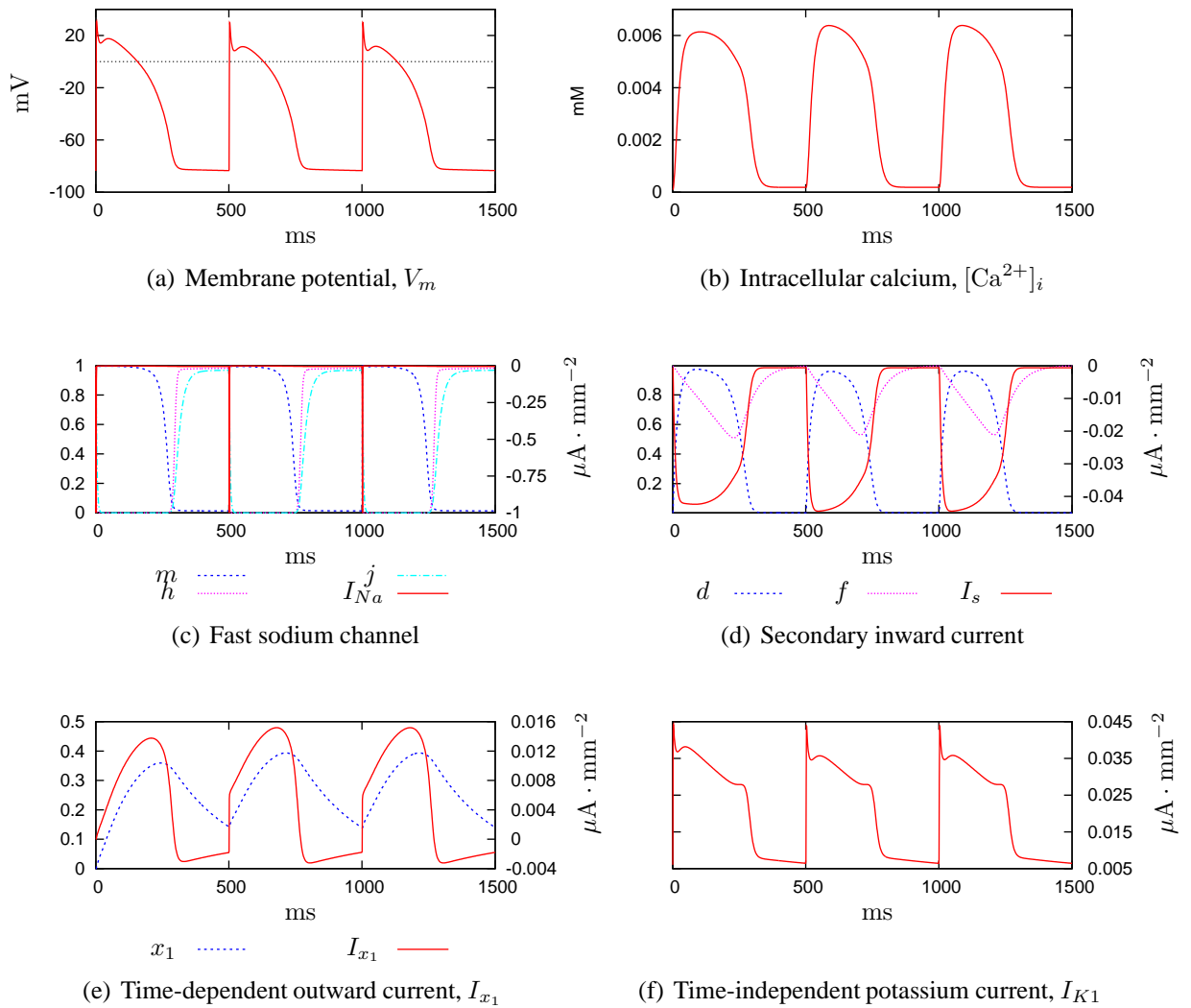
FIGURE 2.13: Simulation results for all the currents and gating variables in the Beeler & Reuter (1977) ventricular model. In figures (c)–(f) the left hand axis denotes the scale for the gating variables and the right hand denotes the current scale. (b) gives the intracellular calcium concentration.

clusters of tissue-cultured heart cells. The kinetic data were fit to the Hodgkin & Huxley (1952) model to facilitate comparison of the kinetics to those of other studies.

While the model given by Ebihara & Johnson (1980) was only for the I_{Na} current, this model can be treated as a direct replacement for I_{Na} in the Beeler & Reuter (1977) ventricular myocyte model. This full cellular model (including corrections published in Spach & Heidlage (1993)) is given in Section A.8. Figure 2.14 shows a comparison of the Ebihara & Johnson modified model with the original Beeler & Reuter model.

1987 Drouhard & Roberge

Using more recent and extensive voltage-clamp data, Drouhard & Roberge (1987) further revised the Hodgkin-Huxley formulation of the I_{Na} current for ventricular myocardial cells. They developed the kinetics of the fast sodium channel to represent a good compromise between available experimental data and to lead to a reasonable average representation of the cardiac Na^+ current.

As with the Ebihara & Johnson (1980) model, that of Drouhard & Roberge can be used as a replacement for the fast sodium channel in the original Beeler & Reuter ventricular myocyte model. The full cellular model is given in Section A.11 and Figure 2.14 compares this version of the Beeler & Reuter model with the previous Ebihara & Johnson version, as well as the original Beeler & Reuter (1977) model.

(a) Membrane potential, V_m

(b) I_{Na}
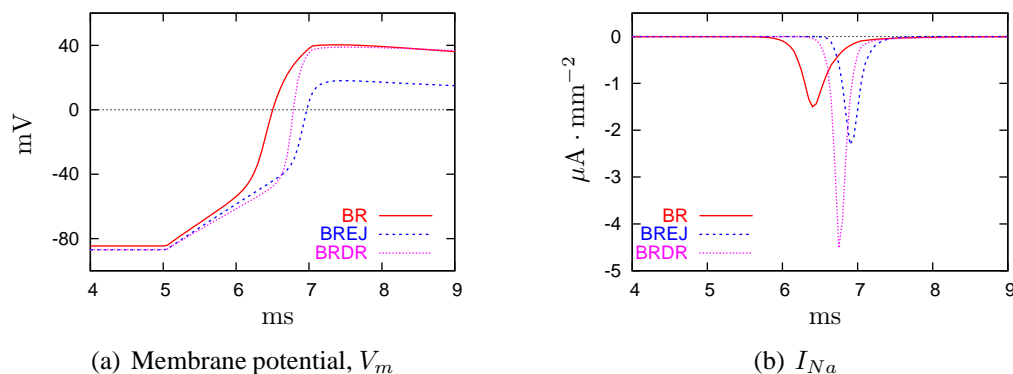
FIGURE 2.14: Comparison of the original Beeler & Reuter model with the I_{Na} modified Ebihara & Johnson (BREJ) and Drouhard & Roberge (BRDR) versions (*cf.* Drouhard & Roberge (1987, Fig. 6)). The stimuli used follow that specified by Drouhard & Roberge (1987, Table 2) – BR 64.8 $\mu A \cdot mm^{-3}$, BREJ 80 $\mu A \cdot mm^{-3}$, and BRDR 72 $\mu A \cdot mm^{-3}$, all with a 2 ms duration.

1999 Defibrillation BR

The Drouhard & Roberge modified Beeler & Reuter model (Drouhard & Roberge 1987) was further modified by Skouibine, Trayanova & Moore (2000) to handle potentials outside the normal physiological range, allowing the model to be used in defibrillation studies. The full defibrillation model is given in Section A.21.

2.4.4   1985 DiFrancesco & Noble

Making use of the extensive developments in experimental work since the development of the McAllister et al. (1975) cardiac Purkinje model (*e.g.,* Fabiato & Fabiato 1975, Colatsky 1980, Gadsby 1980), DiFrancesco & Noble published a new model of cardiac Purkinje fibre electrophysiology (DiFrancesco & Noble 1985) – a model which remains the most comprehensive of all Purkinje fibre ionic current models. The full description of the model can be found in Section A.10, and some results from model simulations are shown in Figure 2.15.

This model provided the first description of ion exchangers in a cellular model – the sodium pump (Na^+-K^+ exchange), Na^+-Ca^{2+} exchanger and the SR calcium pump. The development of this model involved a modelling avalanche (Noble & Rudy 2001), in which the addition of Na^+-K^+ exchange to match experimental data for K^+ concentrations in the extracellular spaces led to the inclusion of other mechanisms to maintain the intracellular cation balances (Na^+ and Ca^{2+}) since they are all linked via the sodium pump and Na^+-Ca^{2+} exchanger. The model also, in another first, included intracellular events through the incorporation of a model of calcium release from the SR.

In a good example of the model's predictive power, the DiFrancesco & Noble (1985) model showed that in order to maintain a resting intracellular Ca^{2+} concentration below $1\,\mu M$ the Na^+-Ca^{2+} exchanger must operate with a $3 : 1$ (Na^+:Ca^{2+}) stoichiometry rather than the widely accepted (at that time) 2:1. This stoichiometry predicts that there must be a current carried by the Na^+-Ca^{2+} exchanger and that, if dependent on intracellular calcium, it must be strongly time dependent. Shortly after the publication of this model experimental data showing the validity of these predictions was published (Kimura, Noma & Irisawa 1986).

However, while the model keeps the resting calcium concentration within physiologically acceptable limits, the peak value reached ($\sim$7 μM) is outside those limits (Figure 2.15(d)). This inaccuracy in the model was corrected in the development of the Hilgemann & Noble (1987)

(a) Membrane potential.

(b) Sarcolemmal ionic currents.

(c) SR calcium fluxes.

(d) Intracellular calcium transients.
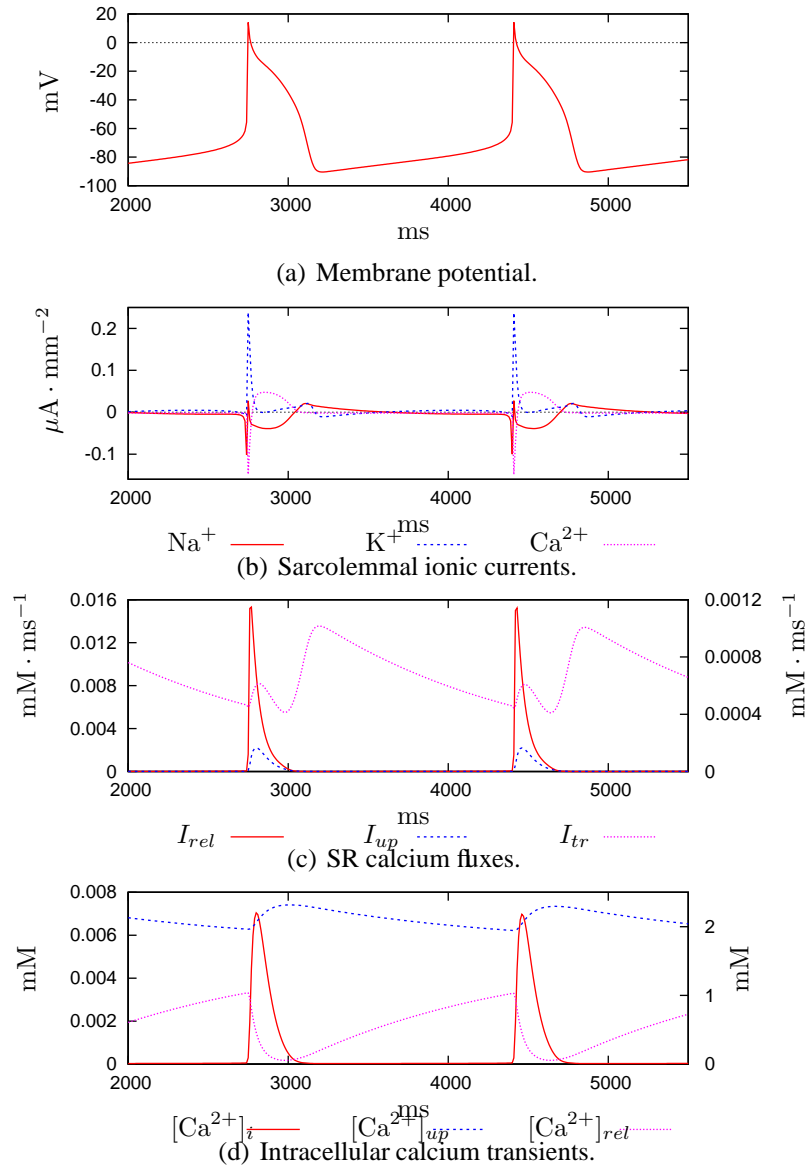
FIGURE 2.15: Results from simulating the DiFrancesco & Noble (1985) cardiac Purkinje ionic current model. In (c), the left axis shows the scale for I_{rel} and the right axis the scale for I_{up} and I_{tr}. The left axis in (d) gives the scale for the intracellular calcium transient ($[\mathrm{Ca}^{2+}]_i$) with the scale for the SR uptake and release calcium stores ($[\mathrm{Ca}^{2+}]_{up}$ and $[\mathrm{Ca}^{2+}]_{rel}$, respectively) is shown on the right axis. These results are for the pacemaker version of the model, obtained by shifting the y gating variable 10 mV (DiFrancesco & Noble 1985).

atrial cell model (and later versions of the Noble model, *i.e.,* Noble, Varghese, Kohl & Noble (1998), Section 2.4.8) through the inclusion of intracellular calcium buffers.

2.4.5   1991 Luo & Rudy

In 1991 Luo & Rudy reformulated the Beeler & Reuter (1977) ventricular myocyte model using new experimental data provided by single cell and single channel recordings. The model included formulations of the fast sodium current (I_{Na}), delayed rectifier potassium current (I_K), and the inward rectifier current (I_{K1}). The plateau potassium current (I_{K_p}) from Yue & Marban (1988) was also included in the model.

A summary of the results of simulating the Luo & Rudy (1991) model is presented in Figure 2.16 and the full model is provided in Section A.12.

(a) Membrane potential

(b) Transmembrane ionic currents
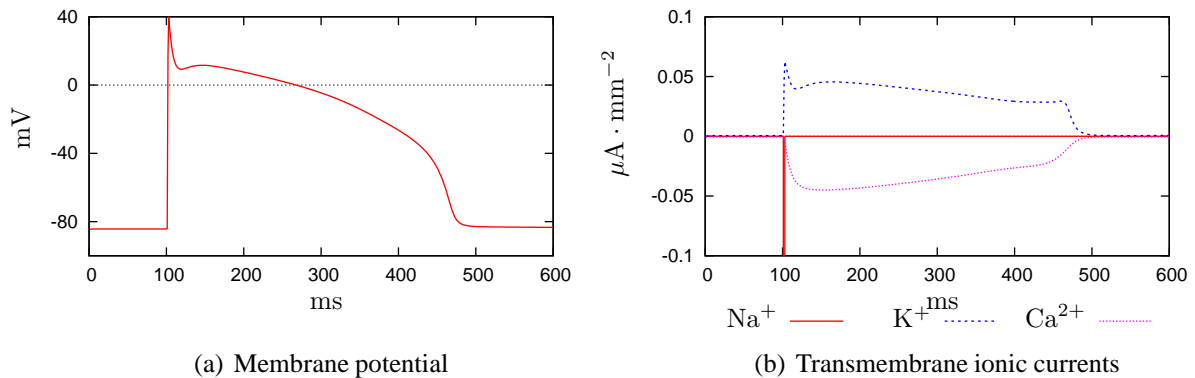
FIGURE 2.16: Results from simulations with the Luo & Rudy (1991) ventricular myocyte model. In (b) the total current for each of the three ionic species is shown, the Na^+ current is not shown to its full peak so the Ca^{2+} and K^+ currents can be seen. A stimulus current of $100\ \mu A \cdot mm^{-3}$ is applied with a duration of $1\ ms$.

Following the formulation of Beeler & Reuter, the Luo & Rudy (1991) model also takes into account changes in intracellular calcium concentration ($[Ca^{2+}]_i$). The Luo & Rudy model, however, also incorporates the possibility of changing extracellular potassium concentration ($[K^+]_o$), an important factor in ischaemic tissue. The action potential simulations of this model duplicates the experimentally observed effects of changes in $[K^+]_o$ on action potential duration and resting potential (Figure 2.17).
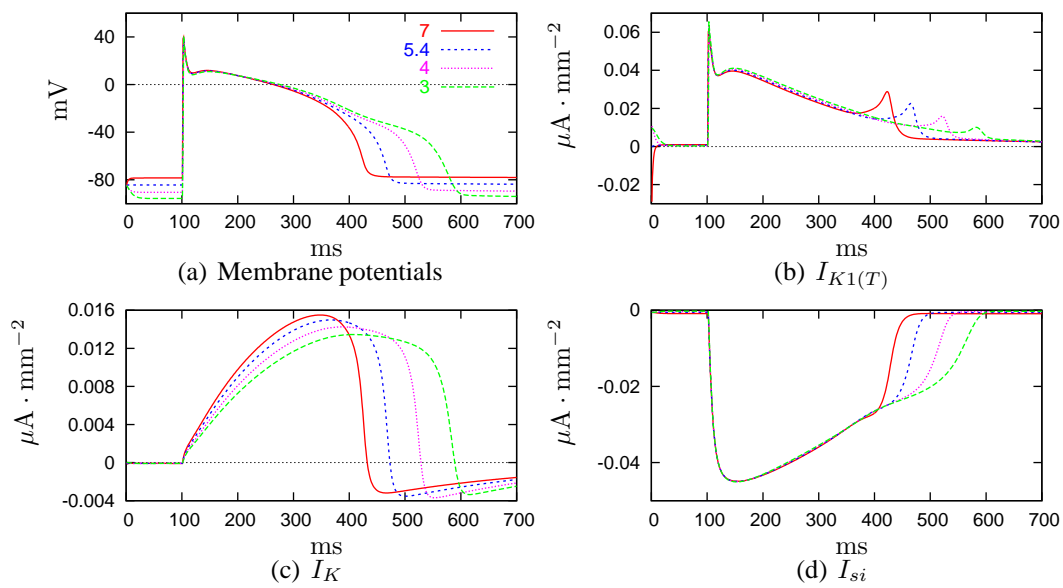
FIGURE 2.17: Results from simulations of the Luo & Rudy (1991) ventricular myocyte model with different values for extracellular potassium concentration ($[K^+]_o$) – *cf.* Luo & Rudy (1991, Figure 4). The legend in (a) gives the $[K^+]_o$ values, in mM, used for the simulations. (a) shows the change in action potential duration and resting potential for the different values of $[K^+]_o$. In (b), $I_{K1(T)}$ is the total time-independent potassium current which shows a strong dependence on $[K^+]_o$, while (c) and (d) show only a weak dependence of I_K and I_{si} on $[K^+]_o$. In all the simulations a stimulus current of $100~\mu A \cdot mm^{-3}$ is applied with a duration of 1 ms.

2.4.6   1994 Luo & Rudy

Continuing the development of the Luo & Rudy (1991) cardiac ventricular action potential model, Luo & Rudy (1994) introduced processes that control the dynamically changing concentrations of intracellular ions (Ca^{2+}, Na^{+}, K^{+}) and their effects on transmembrane currents. The model also included cell compartmentalisation (myoplasm and junctional and network sarcoplasmic reticulum – JSR and NSR respectively) and models the Ca^{2+} concentration in each of the three compartments with an initial model of calcium-induced calcium release from the JSR. Buffering of Ca^{2+} in the myoplasm (by calmodulin and troponin) and in the JSR (by calsequestrin) was also incorporated into the model. The full model is presented in Section A.13 with some summary results in Figure 2.18.

(a) Membrane potential

(b) Transmembrane ionic currents
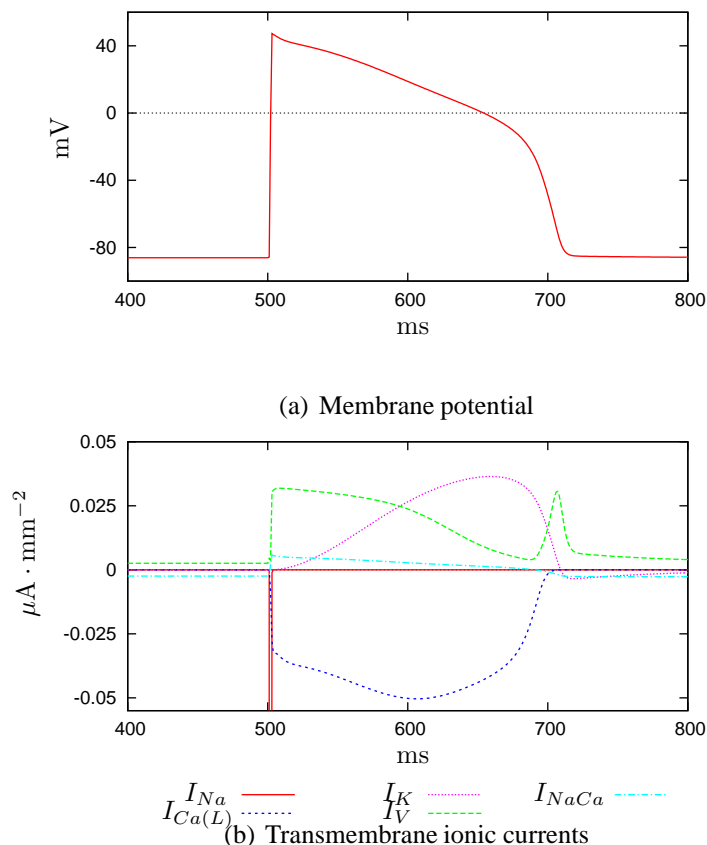
FIGURE 2.18: Results from simulations with the Luo & Rudy (1994) ventricular myocyte model. I_V is the total time-independent current, and the peak I_{Na} is not shown to allow the other currents to be seen. A stimulus current of $100\,\mu A \cdot mm^{-3}$ is applied with a duration of 1 ms.

Due to the extent to which the membrane current formulations and model predictions have been validated against experimental data the Luo & Rudy (1994) model has become the most

widely used model of cardiac ventricular myocyte electrophysiology (Winslow, Scollan, Holmes, Yung, Zhang & Jafri 2000). While the model was originally formulated from guinea-pig data, it has since been fitted to several species. Due to its prolific use, the base Luo & Rudy (1994) action potential model has been, and continues to be, developed to remain consistent with accepted experimental data as it becomes available. Some of the advances in the model by Rudy and colleagues are described below (see also Sections 2.4.7 and 2.4.9)

Zeng, Laurita, Rosenbaum & Rudy (1995) split the delayed rectifier current (I_K) into two components – I_{Kr} (rapid) and I_{Ks} (slow), and added the T-type calcium channel ($I_{Ca(T)}$). I_{Kr} incorporated a $[K^+]_o$-dependent conductance and the I_{Ks} conductance was $[Ca^{2+}]_i$-dependent. Viswanathan, Shaw & Rudy (1999) refined I_{Ks} with the addition of a second gating variable and reformulated the channel conductance and its $[Ca^{2+}]_i$ dependence. This version of the model also included a reformulation of the calcium-induced calcium release process to provide a graded response for even a small entry of Ca^{2+} into the cell. The Viswanathan et al. (1999) model provided formulations for three different cell types (epi-, mid-, and endocardial cells) by scaling the I_{Ks} current to represent the differing density of these channels through the ventricular wall.

Faber & Rudy (2000) studied the effect on the action potential and contraction with changes caused by intracellular sodium overload. This required several modifications to the previous version of the Luo & Rudy model. Calcium-induced calcium release was once again reformulated to give graded release without threshold, and calcium uptake into the NSR was increased. The Na^+-K^+ exchanger current (I_{NaK}) was increased and I_{NaCa} was also reformulated. For the case when the cell was experiencing sodium overload, a Na^+ activated K^+ channel was introduced.

The continual reformulation of the calcium-induced calcium release process used in the various Luo & Rudy models is related to the focus of these models being on whole cell electrophysiology rather than on biophysical details of the mechanisms involved in calcium handling. This allows for the best use of computational and numerical resources in modelling the electrophysiology at the cost of excluding possible effects of detailed calcium models.

2.4.7   1998 Jafri *et al.*

The Luo & Rudy models described in the previous section contain a lot of biophysical detail in the cellular electrophysiology but represent the calcium subsystem with phenomenological

models. The Jafri et al. (1998) model adds biophysical detail to the calcium subsystem in the Luo & Rudy (1994) model. In the Jafri, Rice & Winslow model, several modifications and additions are made to the Luo & Rudy model:

- the L-type Ca^{2+} current is replaced with a new formulation based on the mode-switching Markov-state model of Imredy & Yue (1994);
- the SR calcium release mechanism is replaced with the Markov state model of ryanodine receptor Ca^{2+} release channels in the junctional SR membrane (Keizer & Levine 1996);
- ryanodine receptors and L-type Ca^{2+} channels are assumed to empty into a restricted subspace located between the junctional SR and T-tubules;
- both high- and low-affinity Ca^{2+} binding sites for troponin are included; and
- the magnitudes of the I_{K_p}, I_{Na}, I_{NaCa}, $I_{ns(Ca)}$, and $I_{Ca,b}$ currents are scaled to preserve myoplasmic ionic concentrations and action potential shape.

Figure 2.19 illustrates some simulation results from the Jafri et al. (1998) model, with emphasis on the calcium subsystem. The full model is given in Section A.18. A comparison with the original Luo & Rudy (1994) model simulated action potential is presented in Figure 2.19(a).

When investigating excitation-contraction coupling, many of the phenomena of interest depend on the interval between stimuli and hence evolve over the time course of multiple action potentials. These phenomena are known as interval-force relations. Due to force generation in a myocyte being roughly proportional to intracellular Ca^{2+} concentration and the inclusion of a detailed calcium subsystem in their model, Jafri et al. (1998) were able to investigate the effects of pacing rate on force generation.

One of the simulations Jafri et al. (1998) presented examined the transition period between increasing and decreasing the pacing frequency of the model. This simulation illustrated the extended range of applicability of the Jafri et al. (1998) model over the Luo & Rudy (1994) model by producing results comparable to those seen experimentally. The model also allowed a prediction to be made as to the mechanisms involved in producing the experimentally observed phenomena.

2.4.8   1998 Noble *et al.*

The Noble et al. (1998) guinea-pig ventricular cell electrophysiology model is an extension and update of the earlier Noble, Noble, Bett, Earm, Ho & So (1991) ventricular model built from

(a) Membrane potential

(b) $[\mathrm{Ca}^{2+}]_i$

(c) RyR_{open}

(d) $[\mathrm{Ca}^{2+}]_{SS}$

(e) $I_{Ca(L)_{Ca}}$

(f) SR Ca^{2+}

(g) Troponin Ca^{2+} buffers
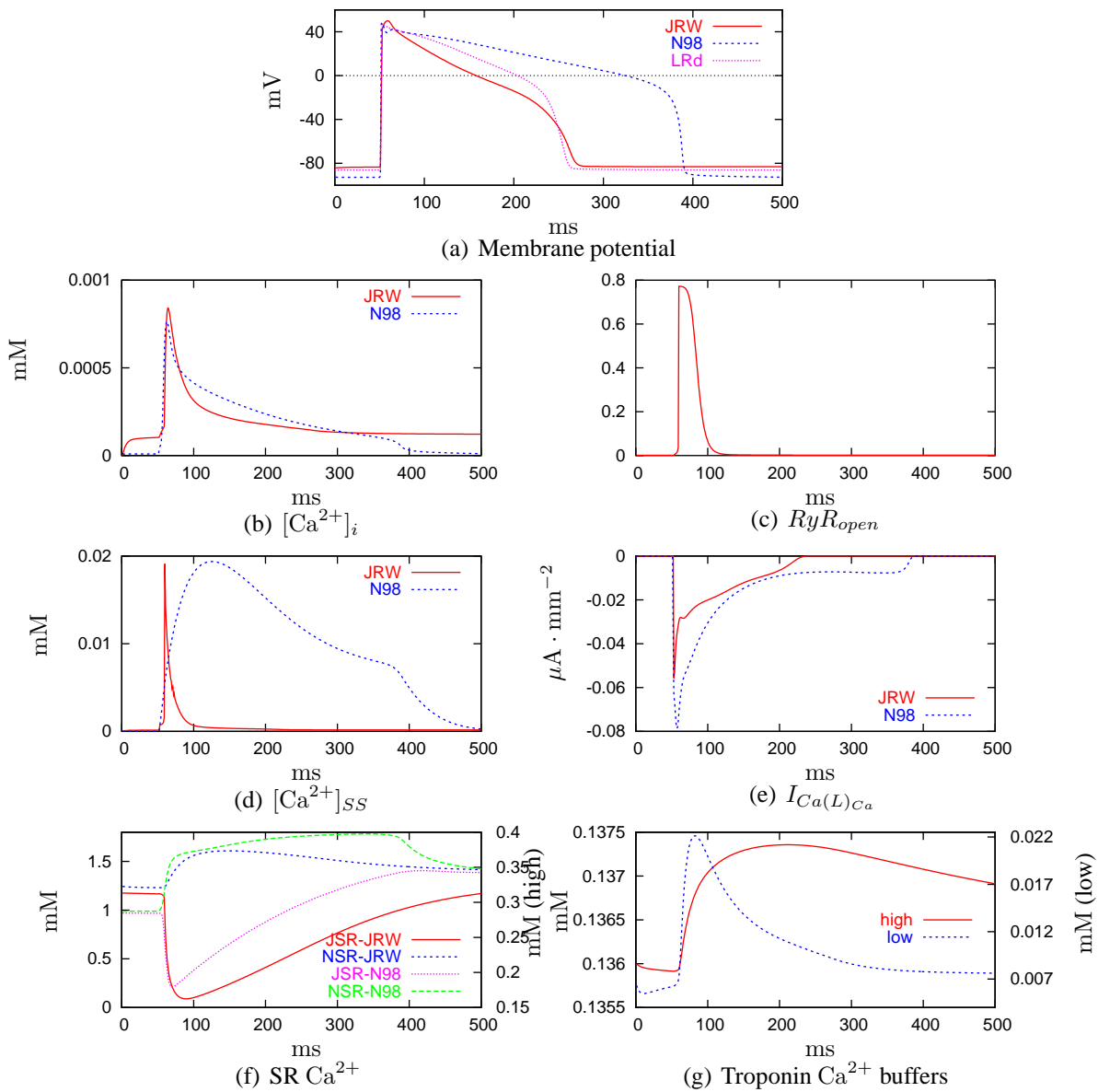
FIGURE 2.19: Results from simulations with the Jafri et al. (1998) and Noble et al. (1998) ventricular myocyte models. (a) shows the simulated action potential from the Jafri et al. (1998) (JRW), Noble et al. (1998) (N98) and Luo & Rudy (1994) (LRd) models. In (c), RyR_{open} is the sum of the fraction of ryanodine receptors in an open state (JRW only). (d) is the Ca^{2+} concentration transient from the restricted subspace (diadiac space in Noble et al. (1998) model) and (f) shows the Ca^{2+} concentrations in the junctional (JSR) and network (NSR) compartments of the SR. The concentration of Ca^{2+} bound to the high- and low-affinity troponin buffers in the myoplasm are shown in (g) (JRW only), with the high transient using the left scale and the low transient using the right scale. A stimulus current of $250\ \mu\mathrm{A}\cdot\mathrm{mm}^{-3}$ is applied with a duration of $1\ \mathrm{ms}$ for the Jafri et al. (1998) and Noble et al. (1998) models and $100\ \mu\mathrm{A}\cdot\mathrm{mm}^{-3}$ for the Luo & Rudy (1994) model.

the initial Purkinje fibre (*e.g.,* Noble 1962, McAllister et al. 1975, DiFrancesco & Noble 1985) and atrial (*e.g.,* Hilgemann & Noble 1987, Earm & Noble 1990) cellular models.

This version of the Noble model includes a diadic space between the sarcolemma and junctional SR – equivalent to the restricted subspace of the Jafri et al. (1998) model. In the Noble et al. (1998) model, the L-type Ca^{2+} channels (or at least a large fraction of them) empty into the diadic space and the concentration of Ca^{2+} in the diadic space is used to both initiate calcium-induced calcium release from the SR and to terminate the L-type Ca^{2+} current ($I_{Ca(L)}$). Unlike the Jafri et al. (1998) model, however, the Noble et al. (1998) assumes that activation of SR calcium release sites by the diadic space Ca^{2+} triggers release into the bulk myoplasm.

In addition to the diadic space, the Noble et al. (1998) model splits the delayed potassium current (I_K) into a rapidly activating component (I_{Kr}) and a slowly activating component (I_{Ks}). The rapidly activating component is divided into two further components: I_{Kr1} for the fast deactivation component; and I_{Kr2} for the slow component. The slow component of the deactivation, I_{Kr2}, is slower than the deactivation rate of I_{Ks}.

The Noble et al. (1998) model also includes mechanisms for cellular contraction and tension generation, stretch- and tension-dependent processes, and drug-receptor interactions. For the case of normal, healthy myocytes these processes have little or no effect on the bulk cellular electrophysiology.

Section A.20 presents the full Noble et al. (1998) model. Some simulation results from this model are given in Figure 2.19 for comparison with the Jafri et al. (1998) and Luo & Rudy (1994) models.

2.4.9   2002 Clancy & Rudy

With the exception of the Jafri et al. (1998) model, the above biophysical models were formulated using the traditional Hodgkin & Huxley (1952) scheme – *i.e.,* the whole cell action potential is simulated from macroscopic descriptions of transmembrane currents generated by a large ensemble of ion channels. Recently, a large body of knowledge has been accumulated on the relationships between ion channel structure and function, on the kinetic properties of single ion channels, and on the modification of ion channels structure and function by genetic defects. Most of these data were obtained in expression systems (*e.g.,* Xenopus Oocyte), away from the actual physiological environment where the channel interacts with other types of channels and

the dynamically changing ionic composition of its environment. Thus, a major challenge is the integration of this single channel information into the functioning cardiac cell in an effort to mechanistically relate molecular level findings to whole cell function (Noble & Rudy 2001).

Jafri et al. (1998) used such information in the formulation of their calcium subsystem model for normal guinea-pig ventricular myocytes. Clancy & Rudy (1999) presented the first application of such molecular level data to the formulation of a state specific Markov model of the cardiac sodium channel (I_{Na}). They formulated models for wild-type sodium channels and ΔKPQ mutant channels, a three amino-acid deletion that affects the channel inactivation and is associated with a congenital form of the long-QT syndrome, LQT3. The Clancy & Rudy (1999) study showed how a genetic defect in a single type of ion channel could be incorporated into a whole cell model of electrophysiology.

The model of Clancy & Rudy (1999) was then extended to include models of wild-type and mutant I_{Kr} channels, again using a Markovian state based model (Clancy & Rudy 2001). This model was used to investigate the effect of HERG[2] mutations on the action potential and to provide insight into the mechanism by which each defect results in a net loss of repolarising current and prolongation of the action potential duration.

In an excellent example of the usefulness of computational approaches in establishing a mechanistic link between genetic defects and functional abnormalities, Clancy & Rudy (2002) performed simulations showing that a single sodium channel mutation can cause both long-QT (LQT) and Brugada syndromes. Coexistence of these two syndromes seems paradoxical, with LQT associated with enhanced sodium channel function while Brugada is associated with reduced function. Clancy & Rudy (2002) demonstrated in their study that the 1795insD mutation[3] of the sodium channel can cause both LQT and Brugada syndromes through interaction with the heterogeneous myocardium in a rate-dependent manner (see discussion in Section 2.4.10). This result highlights the complexity and multiplicity of genotype-phenotype relationships.

Clancy & Rudy (2002) conducted simulations of isolated epicardial, endocardial, and mid-myocardial (M) cells using a model based on the Clancy & Rudy (2001) modified version of the Luo & Rudy (1994) ventricular cell model. The three cell types are defined by varying the maximum conductance of the slowly activating delayed rectifier current, I_{Ks}, as described by Viswanathan et al. (1999). A transient outward current (I_{to}) was also added to the model with

---

[2]HERG is the major subunit of the rapidly activating component of the cardiac delayed rectifier, I_{Kr}.

[3]1795insD results from the insertion of aspartic acid in the C terminus of SCN5A, the cardiac sodium channel gene.

varying maximal conductances in the three cell types. The previous Markov formulation of I_{Na} from Clancy & Rudy (1999) was extended to incorporate new experimental observations and to better represent various states in both the wild-type and mutant models (see Clancy & Rudy (2002, Figure 1) for the full models).

The following section describes a model based on the combination of these Markov state models of I_{Kr} and I_{Na} with the calcium subsystem model of Jafri et al. (1998). The simulations presented in this section illustrate the effects of some of these channel mutations on whole cell action potential simulations.

2.4.10   2004 Nickerson – Clancy & Rudy

Here we present a model developed through the combination of the Markov state models based on the Luo & Rudy (1994) ventricular cell model. The wild-type and mutant I_{Na} and I_{Kr} models of Clancy & Rudy (1999, 2001, 2002) are combined with the detailed calcium subsystem model of Jafri et al. (1998) to produce a very detailed biophysical model of ventricular cell electrophysiology and calcium dynamics, with the ability to link in several specific genetic mutations. The spatial variation of channel properties described by Viswanathan et al. (1999) and Clancy & Rudy (2002) provides the basis for a specification of epicardial, endocardial, and midmyocardial cell types.

The starting point for this model was the Jafri et al. (1998) model, with the detailed calcium dynamics model and the Markov state models for the ryanodine release channels in the SR membrane and the L-type calcium channel in the sarcolemma. From this base model, I_K was divided into the rapidly (I_{Kr}) and slowly (I_{Ks}) activating components described by Zeng et al. (1995) with the calcium-dependent maximal conductivity of the I_{Ks} current from Viswanathan et al. (1999). The I_{Kr} current was then replaced with the Markov state model formulated by Clancy & Rudy (2001), and the I_{Na} current was replaced with either the wild-type or 1795insD mutant Markov state models of Clancy & Rudy (2002). $I_{Ca(T)}$ from Zeng et al. (1995) was included in the model, as was the I_{to} current used by Clancy & Rudy (2002) (Dumaine, Towbin, Brugada, Vatta, Nesterenko, Nesterenko, Brugada, Brugada & Antzelevitch 1999). Figure 2.20 gives a schematic view of the complete cell model with the Markov state models, including both the wild-type and mutant I_{Na} channels.

The full model descriptions are given in Section A.24 for the wild-type model and Section A.25 for the 1795insD sodium channel mutation. Figure 2.21 shows some results from the
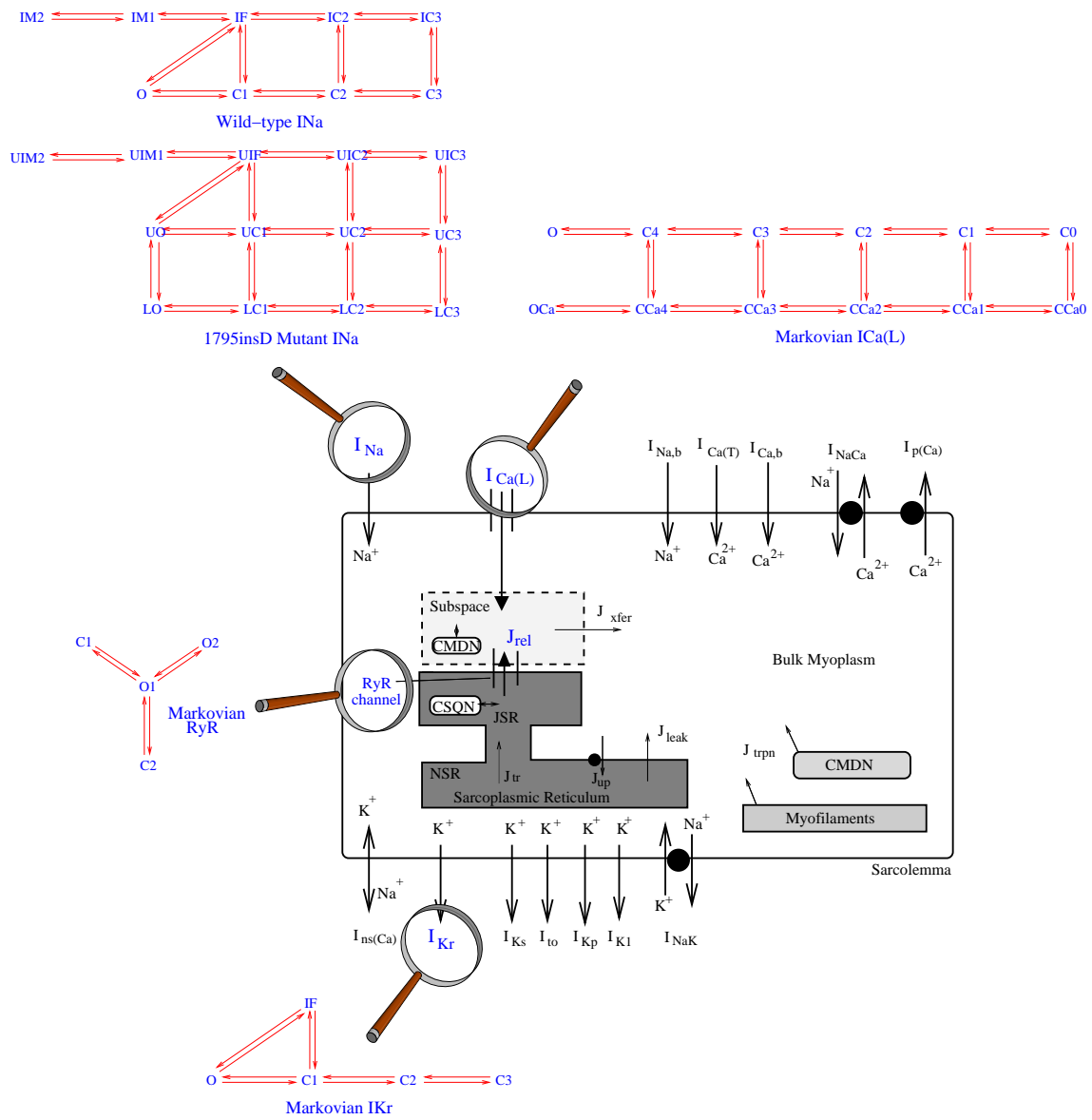
FIGURE 2.20: Schematic diagram of the N-LRd cellular model. The red and blue diagrams show the Markov state channel models included in the model, with both the wild-type and 1795insD mutant I_{Na} channel models shown.

simulation of the wild-type Nickerson – Clancy & Rudy (N-LRd) model. Results are shown for the three cell types described by the model: endocardial, midmyocardial, and epicardial cells. The cell types are distinguished by differences in density of I_{Ks} and I_{to} channels. In epicardial cells the density ratio of I_{Ks} to I_{Kr} is $G_{Ks}/G_{Kr} = 23$ and the maximal conductance of I_{to} is $G_{to} = 0.011 \, \mathrm{mS \cdot mm^{-2}}$. For midmyocardial cells $G_{Ks}/G_{Kr} = 7$ and $G_{to} = 0.005 \, \mathrm{mS \cdot mm^{-2}}$, and for endocardial cells $G_{Ks}/G_{Kr} = 19$ and $G_{to} = 0.0005 \, \mathrm{mS \cdot mm^{-2}}$ (Viswanathan et al. 1999, Clancy & Rudy 2002). In epicardial cells, the maximal permeability of $I_{Ca(L)}$ was reduced by $50 \, \%$ to obtain realistic durations of simulated action potentials (Dumaine et al. 1999).

In their study, Clancy & Rudy (2001) showed that as the density of functional I_{Kr} channels was reduced in midmyocardial cells the generated action potentials lengthened. They found that a $75 \, \%$ reduction in I_{Kr} channel density resulted in early after depolarisations, when the model was paced with a period of $1000 \, \mathrm{ms}$. A similar simulation is presented in Figure 2.22, with comparable results.

Clancy & Rudy (2001) studied several HERG mutations, including the T474I and R56Q kinetic mutations. The T474I mutation alters the gating properties and reduces the macroscopic I_{Kr}, and was modelled by changing the voltage dependence of the activation transition rates and by reducing G_{kr} by $35 \, \%$. R56Q is a mutation in the PAS domain of the amino terminal which has the effect of greatly increasing the rate of deactivation of I_{Kr}. This mutant was modelled by increasing the transition rates between the open and closed states. In their simulations, Clancy & Rudy (2001) showed that these two mutations affected the action potential duration in a rate dependent manner, with the largest effect seen in midmyocardial cells with decreasing rate. Figure 2.23 shows this effect for the case when the cycle length is $2000 \, \mathrm{ms}$, which gives rise to the early after depolarisations with the R56Q mutant channel.

The Clancy & Rudy (2002) model described Markov state models for the wild-type I_{Na} channel and the 1795insD mutant channel, which results from the insertion of aspartic acid in the C terminus of the I_{Na} gene (SCN5A). In their simulations, Clancy & Rudy (2002) show that the morphology of the mutant's action potential changes with pacing rate. They found that at fast rates ($300 \, \mathrm{ms}$), the epicardial cells with the 1795insD mutant I_{Na} channel had an action potential that alternated between the characteristic spike-and-dome and the loss of the dome. At slower rates (750–$1000 \, \mathrm{ms}$), however, the characteristic morphology returns. Figure 2.24 presents the results of simulating the N-LRd model at these pacing rates in epicardial cells with the wild-type and 1795insD mutant models.

Figure 2.25 presents a simulation which demonstrates the cellular basis of one of the ECG

(a) Membrane potential

(b) $[Ca^{2+}]_i$

(c) $I_{Ca(L)Ca}$

(d) I_{Kr}

(e) I_{Ks}

(f) I_{Na}

(g) I_{to}
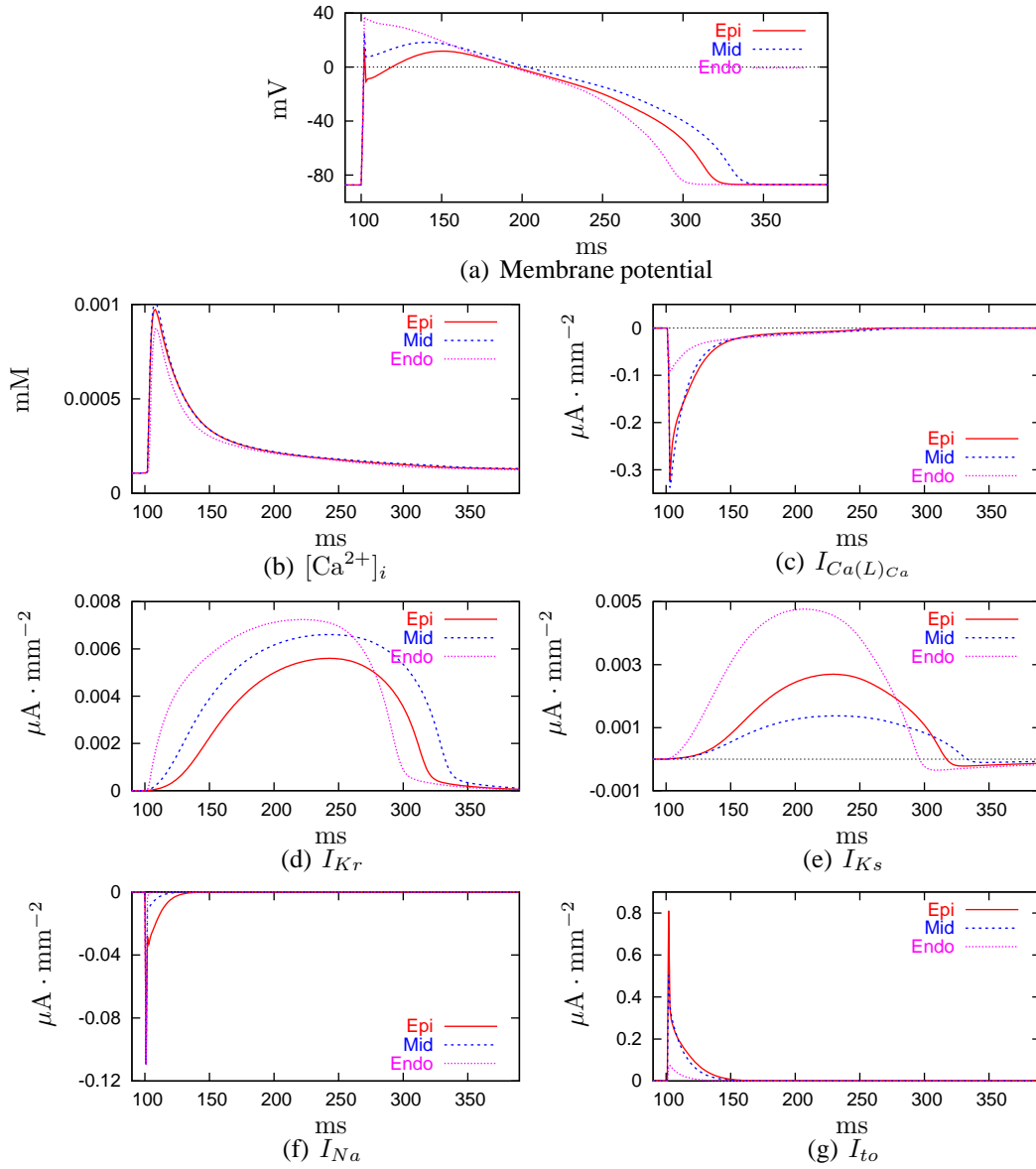
FIGURE 2.21: Results from the wild-type N-LRd model for the different cell types: epicardial (epi), midmyocardial (mid), and endocardial (endo). For all cell types a stimulus of $250\,\mu A \cdot mm^{-3}$ is applied for 1 ms. Epicardial cells $G_{Ks}/G_{Kr} = 23$, $G_{to} = 0.011$ mS$\cdot$mm^{-2}; midmyocardial $G_{Ks}/G_{Kr} = 7$, $G_{to} = 0.005$ mS$\cdot$mm^{-2}; and endocardial $G_{Ks}/G_{Kr} = 19$, $G_{to} = 0.0005$ mS$\cdot$mm^{-2}.
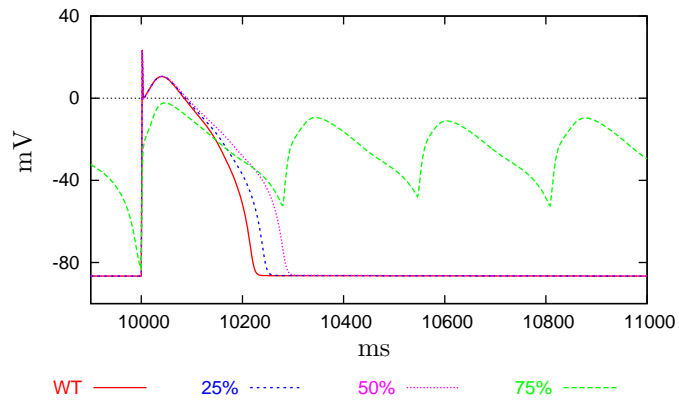
FIGURE 2.22: The effect of reducing the density of functional I_{Kr} channels on the midmyocardial action potential. Results are shown for reductions of 25, 50, and 75 % and for the wild-type (WT) midmyocardial cell. The model is paced with a period of 1000 ms with a stimulus of $250 \, \mu A \cdot mm^{-3}$ applied for 1.0 ms.
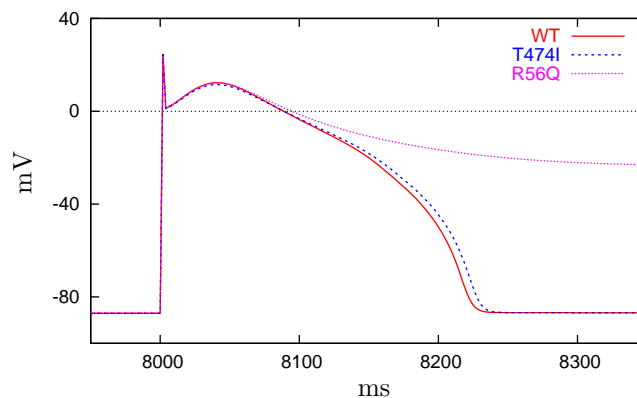
FIGURE 2.23: The effect of the T474I and R56Q kinetic mutations of the I_{Kr} channel, compared to the wild-type (WT) model. The model is paced with a period of 2000 ms with a stimulus of $250 \, \mu A \cdot mm^{-3}$ applied for 1.0 ms.

(a) CL = 300 ms

(b) CL = 750 ms

(c) CL = 1000 ms
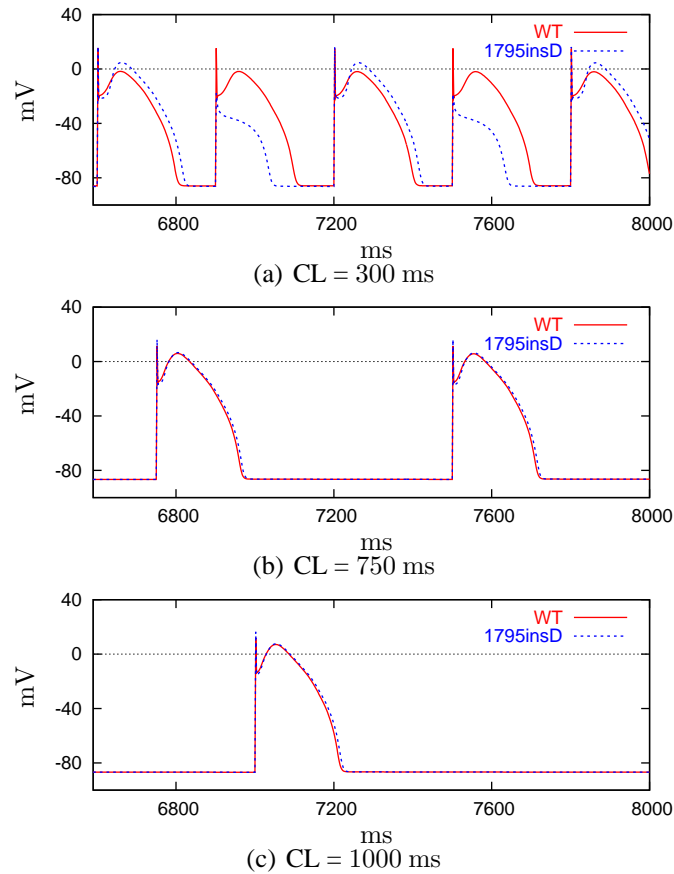
FIGURE 2.24: The 1795insD mutation of the I_{Na} channel affects the action potential of epicardial cells in a rate dependent manner. Here we show the results of simulating the N-LRd epicardial cell model with the wild-type (WT) and 1795insD mutant I_{Na} channel at various pacing rates. The alternating morphology of the mutant action potential at the fast rate (300 ms) is clearly visible in (a). The effect of this mutation at slower rates ((b),(c)) is not as large. In all cases the model is stimulated with an applied current of 250 μA $\cdot$ mm^{-3} with a duration 1 ms.

changes associated with the 1795insD mutation, that indicative of Brugada syndrome. The results shown in Figure 2.25 would manifest on the ECG as ST-segment elevation, a phenomena associated with Brugada syndrome (*cf.* Clancy & Rudy (2002, Figure 8(a))).

PSfrag replacements
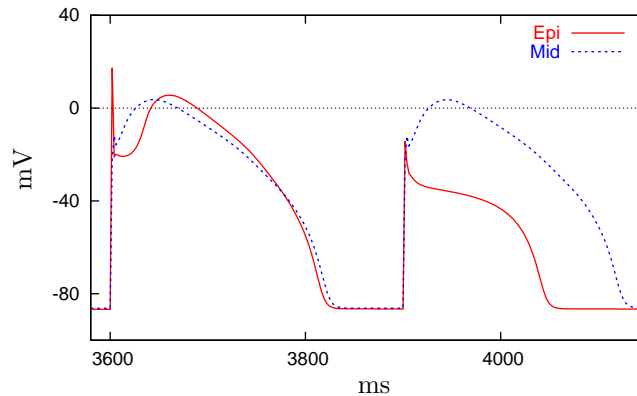
FIGURE 2.25: Comparison of 1795insD mutant epicardial (Epi) and midmyocardial (Mid) cellular action potentials. At fast rates, mutation induced changes in epicardial action potential morphologies cause dispersion of plateau potentials and a voltage gradient from epicardial to midmyocardial cells. The model is paced with a period of 300 ms with a stimulus of $250 \, \mu\text{A} \cdot \text{mm}^{-3}$ applied for 1.0 ms.

Special Note

The model described here is simply an example of how the various Markov state models of specific processes can be combined into a model of cellular electrophysiology. While this model is capable of reproducing some of the results of the Clancy & Rudy (2001, 2002), there is still work to be done validating and stabilising the model. Of particular note is that the Markov state models of I_{Na} and I_{Kr} (and their associated mutant variations) were developed using the phenomenological intracellular calcium dynamics model incorporated in the Luo & Rudy models. This phenomenological model has been replaced here with the biophysically detailed model of Jafri et al. (1998), resulting in substantially different calcium kinetics. These differences tend to lead to unstable behaviour of the model when combined with some of the channel mutations and pacing rates, where the instability comes from intracellular calcium oscillations. This suggests that further fine-tuning of the interaction between the calcium subsystem and the Markov state models of I_{Na} and I_{Kr} and their mutations is required.

Furthermore, the length of the two models presented in Sections A.24 and A.25 highlights the usefulness of CellML 1.1 over 1.0 (Section 4.1.1). If these models were to be implemented in CellML 1.1, the bulk of the model would not need to be duplicated. Given the two models

are identical except for the I_{Na} channel states component, a common base model could be used to specify the common components. The specialised wild-type and 1795insD mutant models would then import the common base model and add the specialised I_{Na} channel state component.

2.5 Cardiac Mechanics

2.5.1 1938 Hill

The work of modelling the mechanical behaviour of muscle began with the work of A. V. Hill who studied both the mechanical and thermal consequences of muscular contraction. A historical and personal perspective of this work can be found in Hill (1970). With the publication of his seminal article in 1938, the Hill model was firmly established as what was to become one of the great models of classical muscle mechanics.

Hill (1938) described active skeletal muscle as being the combination of a undamped elastic component in series with a damped contractile component (Figure 2.26). Resting muscle consists of the elastic element but only to a minor degree the damped element. Hill (1938) examined three cases of sustained contraction suited to this two component model. Here we illustrate the Hill (1938) model for the isometric contraction example.
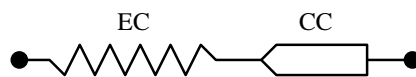
FIGURE 2.26: Schematic of the Hill (1938) model of skeletal muscle, consisting of a undamped EC and a damped CC in series.

During isometric contraction the total length of the muscle remains constant. Assume the contractile component (CC), with initial length l_c, stretches the elastic component (EC), initial length l_e. The subsequent lengths at time t are y_c and y_e, respectively. The active state of the CC is is defined by Hill's characteristic equation

$$(T + a)(v + b) = const \tag{2.5.1}$$

and we assume that the response of this equation is instantaneous upon stimulation and is maintained by tetanus. The total force, T, exerted by the muscle is proportional to the stretch of the EC if we assume the EC is perfectly elastic ($T = \alpha(y_e - l_e)$, where α is constant).

In isometric contraction, the rate of lengthening of the EC is equal to the rate of shortening of the CC, giving

$$v = -\frac{dy_c}{dt} = \frac{dy_e}{dt} = \frac{dT}{dt}\alpha^{-1}. \tag{2.5.2}$$

Substituting for v into the characteristic Equation (2.5.1) results in

$$(T + a)\left(\frac{dT}{dt} + \alpha b\right) = const = (T_0 + a)\,\alpha b \tag{2.5.3}$$

where T_0 is the full tension for the given total muscle length. Rearranging this equation gives

$$\frac{dT}{dt} = \frac{(T_0 + a)\,\alpha b}{T + a} - \alpha b, \tag{2.5.4}$$

which is the model presented in Section A.1.

Results from solution of this model are presented in Figure 2.27 using the material parameters from Hill (1938) for frog sartorius muscle at $0\ ^\circ$C and $23\ ^\circ$C. Material parameters for the $0\ ^\circ$C simulation are given in Section A.1 and those for $23\ ^\circ$C can be found on the attached compact disc Section D.2.
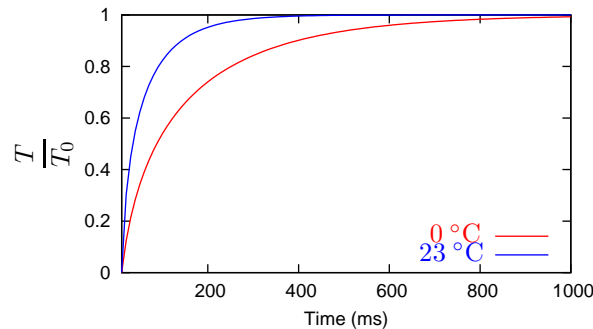
FIGURE 2.27: Development of isometric tension following activation of the contractile component in frog satorius muscle. *cf.* Hill (1938, Figure 15)

The two important concepts in the Hill model are that the EC is a passive element whose properties are independent of contraction and the CC force-velocity relationship is instantaneous. Later experimental data has since disproved these concepts leading to the demise of the classical approach to muscle mechanics (Simmons & Jewel 1974). This led to a paradigm shift to the contemporary approach to muscle mechanics based upon known structure of striated muscle in addition to the observed behaviour upon which the classical models were built. At the core of the new paradigm was the sliding filament theory first proposed by H. E. Huxley (Huxley 1953, Huxley & Hanson 1954), which was first formulated into a theory of muscular contraction by A. F. Huxley (Huxley 1957).

2.5.2   1957 A. F. Huxley

Based on the sliding filament theory (Huxley & Hanson 1954), Huxley (1957) developed a new theory for the mechanism of contraction in striated muscle. This theory was based on the observed microstructure of myofibrils, shown here in Figure 2.28. Many myofibrils combine to provide the contractile machinery of a muscle cell.
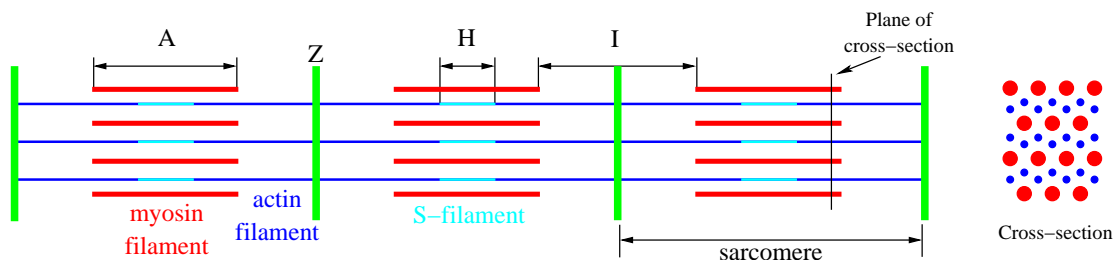
FIGURE 2.28: A schematic view of the arrangement of the filaments within a myofibril, as shown by Huxley (1957). When the muscle length changes, the myosin (red) and actin (blue) filaments slide past one another in each of the zones where they overlap. Only the S-filaments are actually stretched or shortened.

As shown in Figure 2.28, Huxley (1957) described the myofibrils as a series of sarcomeres connected at the Z lines. Within a sarcomere, the A band is the region of overlap between the myosin and actin filaments. The actin filaments are anchored in the Z lines and extend into the A band as far as the beginning of the less dense H region. When the muscle lengthens or shortens, the myosin and actin filaments slide past each other. The myosin and actin proteins are the principal constituents of their respective filaments. Corresponding I filaments of the two ends of a sarcomere are connected by a very extensible connection, the S filament.

Rather than the then accepted view that contraction on the molecular level occurred via some kind of protein folding or coiling, Huxley (1953) proposed that contraction occurred via the myosin and actin filaments sliding past one another. The basis of this theory is that each of the myosin filaments has side pieces which can slide along the main backbone of the thick filament, with the extent of the movement being limited by an elastic connection. These sliding members can bind temporarily with sites on adjacent actin filaments, the connections being made spontaneously but broken only by a reaction, requiring energy to be supplied from metabolic sources. The essential feature of this system is that the rates of the reactions by which connections are made or broken are assumed to depend on the position of the sliding member relative to the backbone of its myosin filament. Figure 2.29 provides an illustration of this system. Huxley (1957) presents a detailed description of the operation of this system and its mathematical formulation, briefly summarised below.
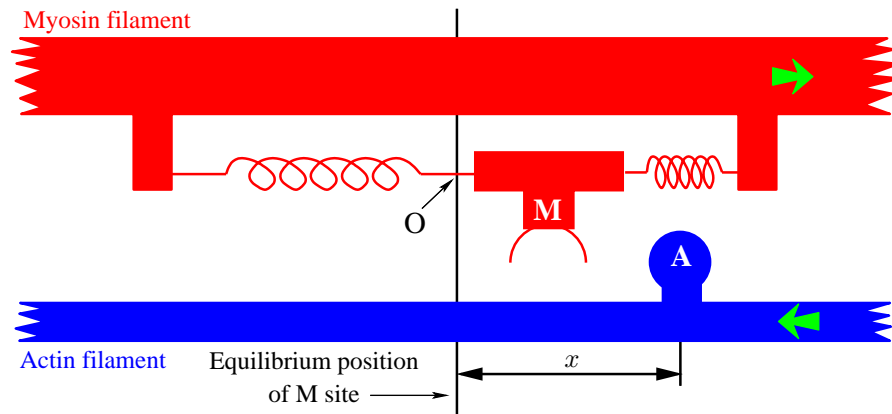
FIGURE 2.29: Diagram illustrating the mechanism which Huxley (1957) proposed for the development of tension in striated muscle. The section of filament shown is in the right hand half of an A band (Figure 2.28), so the actin filament is attached to a Z line which is out of the picture to the right. The green arrows indicated the relative motion between the filaments when the muscle shortens.

With reference to Figure 2.29, Huxley (1957) theorised that M and A are initially detached. M oscillates about its equilibrium position, O, as a result of thermal agitation, and if A is ever within range of M there is a chance that combination will occur. The combination can only occur in the region to the right of O (Figure 2.30, f rate relation). If combination occurs the tension in the elastic element will be exerted on the actin filament and the AM combination moves toward O as the muscle shortens. While there is always the chance that the link between M and A will be broken, the rate constant is small until AM passes O, at which point the link is soon broken to prevent the elastic link, now in the reverse direction, resisting shortening (Figure 2.30, g rate relation). The AM link is broken by the binding of a high energy phosphate compound, XP, to a site near A. This system is summarised in Equations (2.5.5)–(2.5.7) with the f and g rate relations shown in Figure 2.30.

$$A + M \xrightarrow{f} AM \qquad (2.5.5)$$

$$AM + XP \xrightarrow{g} AXP + M \qquad (2.5.6)$$

$$AXP \longrightarrow A + X + PO_4 \qquad (2.5.7)$$
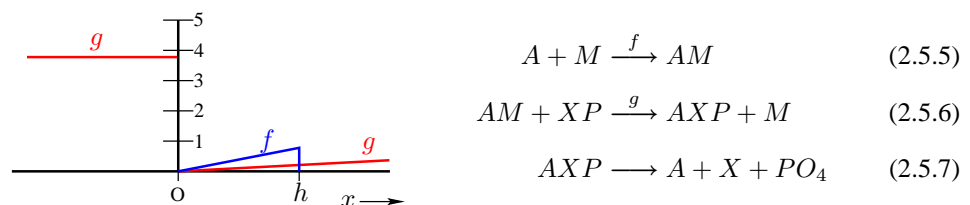
FIGURE 2.30: Dependence of the binding (Equation (2.5.5), f) and dissociation (Equation (2.5.6), g) reaction rates on x (Figure 2.29). The vertical scale is such that $(f + g)$ at $x = h$ is 1.

Now it is assumed that the elastic elements obey Hooke's law with a spring stiffness of $k \, \mathrm{nN \cdot mm^{-1}}$ and n is the proportion of the contraction sites at which M is combined with the

corresponding A. The average value of the work done at one myosin site as one actin site is carried past it by the shortening of the muscle is then given by

$$\int\limits_{-\infty}^{\infty} nkx \, dx, \tag{2.5.8}$$

and the corresponding average force is obtained by dividing by the distance between A sites along the actin filament, l. The total tension in the muscle is the sum of the tensions generated by all the contraction sites within one half-sarcomere. The number of these sites for a muscle of 1 mm^2 cross-sectional area is $ms/2$, where m is the number of M sites per unit volume of muscle and s is the sarcomere length. The tension per unit area is, therefore, given by:

$$T = \frac{msk}{2l} \int\limits_{-\infty}^{\infty} nkx \, dx. \tag{2.5.9}$$

Huxley (1957) went on to describe how Equation (2.5.9) could be used in energy calculations using various forms of the f and g reaction rates, with the best relations being those shown in Figure 2.30. In doing this it was also shown that the sliding filament theory could provide a good fit to the relationships derived by Hill (1938).

2.5.3   1993 Guccione & McCulloch

Guccione & McCulloch (1993) recognised that the most significant problem in developing a continuum mechanics model of the beating heart was the lack of knowledge concerning the constitutive relation for active stress in cardiac muscle. To plug this gap Guccione & McCulloch (1993) proposed constitutive relations for active stress in cardiac muscle and fit the material parameters of these relations to experimental data from the literature. Unlike previous models, primarily based on the skeletal muscle models of Hill (Section 2.5.1) and Huxley (Section 2.5.2), the Guccione & McCulloch model was able to describe the deactivation effect experimentally observed following rapid length perturbations.

The Guccione & McCulloch (1993) model predicted active tension developed by a cardiac muscle fibre from peak intracellular calcium ion concentration, time after onset of contraction, and sarcomere length history. The intracellular free calcium transient was independent of length and calcium ions were able to bind to two sites on troponin-C, with length dependent association and dissociation. The availability of actin sites for interaction with myosin was determined

from the total number of actin sites, free calcium, and calcium bound to troponin-C, and was modelled with a first order differential equation. Active tension is then related to actin binding site availability by a general cross-bridge model where bridges attach in a single configuration at a constant rate while the force in each cross-bridge varies linearly with position, and the rate of detachment depends on both position and time after onset of contraction. The fibre active tension is the integral of the individual cross-bridges.

Model parameters were obtained by trial and error so that predictions matched reported experimental observations of active tension development in rat right ventricular trabeculae.

2.5.4   1998 Guccione *et al.*

Guccione, Motabarzadeh & Zahalak (1998) developed a model of active tension development in cardiac muscle through modification of the Distribution-Moment (DM) model (Zahalak & Ma 1990, Zahalak & Motabarzadeh 1997). The DM model was aimed at deriving tractable constitutive relations for skeletal muscle from biophysical cross-bridge theories and in contrast to previous models of striated muscle contraction all model parameters have physical meaning and assumptions concerning biophysical events within the cell are consistent with available data.

The DM model emphasises the important role of the moments of the actin-myosin bond distribution function and the theory leads to a relatively simple third order state variable model for contraction dynamics in which the state variables are the three lowest moments of the bond distribution function (Zahalak & Ma 1990). These three moments have simple macroscopic interpretations as muscle stiffness, force, and elastic energy. With the introduction of free intracellular calcium ion concentration as a fourth state variable, Zahalak & Ma (1990) formulated a compatible model of excitation-contraction coupling for the DM model. Zahalak & Motabarzadeh (1997) then further investigated the mathematical relations between models of calcium activation kinetics and the cross-bridge dynamics.

To adapt the DM model to cardiac muscle, Guccione et al. (1998) modified the number of regulating calcium binding sites on each troponin molecule and the cross-bridge attachment and detachment rate functions for large cross-bridge strains. The model was primarily developed to determine whether or not a model could achieve the deactivation effect (as described above in Section 2.5.3) as a consequence of high cross-bridge detachment rates at high cross-bridge strain, without making any provisions for length dependent calcium-troponin dissociation. Guc-

cione et al. (1998) show that this is, indeed, possible and that their model was the first to be capable of showing this result.

2.5.5 1998 Hunter *et al.*

Hunter, McCulloch & ter Keurs (1998) presented a model of passive and active cardiac muscle mechanics suitable for use in continuum mechanics models of the whole heart. The model was based on an extensive review of experimental data from a variety of preparations, species and temperatures. They developed a model consisting of four components which is capable of reproducing a number of physiologically significant experimental observations.

The four components are: passive elasticity of cardiac tissue; the rapid binding of calcium ions to troponin-C and its slower tension dependent release; the kinetics of tropomyosin movement and availability of cross-bridge binding sites and the length dependence of this process; and the kinetics of cross-bridge tension development under perturbations of muscle length. The modelling of passive elasticity presented by Hunter et al. (1998) is more relevant to models of tissue and interacting cells. As such, it is described in Appendix B (Section B.3).

As described previously, contraction of cardiac myocytes is initiated by calcium ions binding to troponin-C molecules. This initiates a chain of events in the thin filament which results in the availability of binding sites for the myosin heads of the cross-bridges. The model of Hunter et al. (1998) does not include any representation of intracellular calcium kinetics, instead using a simple exponential relationship to specify the calcium ions available for binding to troponin-C during a typical cellular twitch. The version of the Hunter et al. (1998) model presented in Section A.17 assumes this calcium transient is supplied as an input parameter into the model.

The model for calcium binding to troponin-C developed by Hunter et al. (1998) includes rapid binding and tension dependent release as observed in various experiments. The binding of calcium ions to troponin-C is very fast and limited by the diffusion of ions from the release sites on the junctional sarcoplasmic reticulum (SR) (first term of Equation (2.5.10)). The release of calcium ions from troponin-C was known to be dependent on the mechanical state of the muscle, and this dependence was shown to be due to changes in tension rather than length (Hunter et al. 1998), shown in the second term in Equation (2.5.10).

$$\frac{\mathrm{d}[\mathrm{Ca}^{2+}]_b}{\mathrm{d}t} = \rho_0[\mathrm{Ca}^{2+}]_i \left(\overline{[\mathrm{Ca}^{2+}]_b} - [\mathrm{Ca}^{2+}]_b \right) - \rho_1 \left(1 - \frac{T}{\gamma T_o} \right) \qquad (2.5.10)$$

Tropomyosin movement resulting from calcium binding to troponin-C controls the availability of actin sites available for cross-bridge binding. Hunter et al. (1998) introduced a non-dimensional parameter z ($0 \leq z \leq 1$) to represent the proportion of actin sites available for binding. With the observation that tension increases exponentially with a first order rate constant that depends on the level of calcium activation, Hunter et al. (1998) proposed first order kinetics for the form of z. In a significant improvement over previous models, the Hunter et al. (1998) z kinetics are dependent not only upon the concentration of calcium bound to troponin-C, but also the current muscle length:

$$\frac{\mathrm{d}z}{\mathrm{d}t} = \alpha_0 \left[\left(\frac{[\mathrm{Ca}^{2+}]_b}{C_{50}} \right)^n (1 - z) - z \right], \tag{2.5.11}$$

where the material parameters C_{50} and n are also length dependent and fitted from experimental data. Isometric tension was then shown to be the algebraic relationship

$$T_o = T_{ref} \left(1 + \beta_0 \left(\lambda - 1 \right) \right) z. \tag{2.5.12}$$

Like the distribution moment model described in Section 2.5.4, the model of Hunter et al. (1998) was developed for use in large scale macroscopic models. As such, this model presented an empirical description of tension development in myocytes that can be related back to the underlying molecular processes. The basis of this model is the fading memory model (Bergel & Hunter 1979, Hunter 1995), in which a nonlinear function of tension is written as a linear superposition of dynamic length changes. This model makes use of the fading memory assumption that the current tension is influenced more by recent length changes than earlier changes in describing the nonlinear function as

$$Q \left(T, T_o \right) = \sum_{i=1}^{N} A_i \int_{-\infty}^{t} e^{-\alpha_i(t-\tau)} \stackrel{\bullet}{\lambda} \left(\tau \right) d\tau, \tag{2.5.13}$$

where $\stackrel{\bullet}{\lambda} \equiv \frac{\mathrm{d}\lambda}{\mathrm{d}t}$ is the velocity of the current length change and λ is described in Section 2.1.3. Hunter et al. (1998) limit the number of rate constants in Equation (2.5.13) (N) to three, in line with experimental observations. With use of constant velocity experiments, Hunter et al. (1998) derived the following expression for the dynamic active tension

$$T = T_o \frac{1 + aQ}{1 - Q}, \tag{2.5.14}$$

giving the observed tension T as the isometric tension T_o scaled by a nonlinear function of the hereditary integral of length changes (Equation (2.5.13)).

A modified version of the Hunter et al. (1998) model is presented in Section A.17. The modification is to transform the hereditary integral, Equation (2.5.13), into the equivalent differential equation formulation given in Equation (2.5.15). This transformation was done to make it much easier to implement the model in CellML and, thus, include into simulations using CMISS.

$$Q_i = A_i \int_0^t e^{-\alpha_i(t-\tau)} \overset{\bullet}{\lambda}(\tau)\, d\tau \qquad i = 1\ldots3$$

$$\Rightarrow \quad \frac{dQ_i}{dt} = -A_i\alpha_i \int_0^t e^{-\alpha_i(t-\tau)} \overset{\bullet}{\lambda}(\tau)\, d\tau + A_i \overset{\bullet}{\lambda}(t) \tag{2.5.15}$$

$$= -\alpha_i Q_i + A_i \overset{\bullet}{\lambda}(t) \qquad i = 1\ldots3 \quad \text{(no sum on } i\text{)}$$
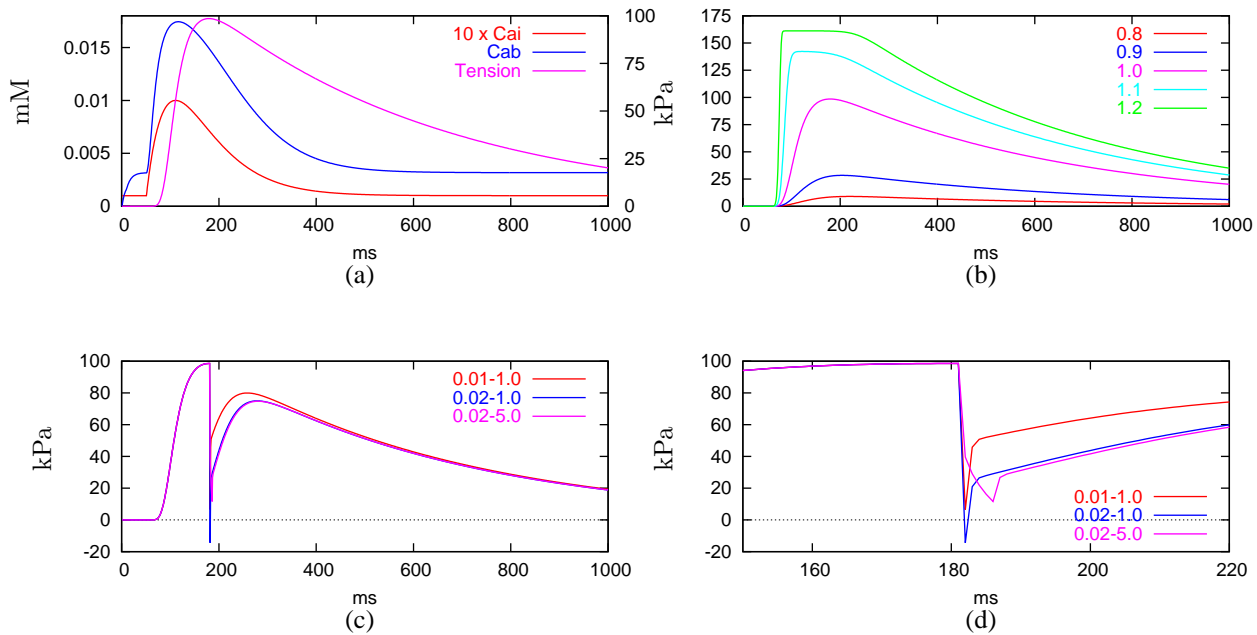
FIGURE 2.31: Results from the solution of the Hunter et al. (1998) model. (a) shows the intracellular calcium transient (Cai, scaled by a factor of 10), the calcium bound to troponin-C (Cab), and the generated active tension (right scale) for an extension ratio of 1.0. (b) illustrates the length dependence of the active tension with a series of isometric twitches (using the calcium transient shown in (a)) at the specified values of the extension ratio (Section 2.1.3). The effects of different length steps on active tension are shown in (c), with a close-up in (d). The three length steps shown are: a 1.0 % shortening over a 1 ms time period (0.01-1.0); a 2.0 % shortening over 1 ms (0.02-1.0); and a 2.0 % shortening over 5 ms (0.02-5.0).

2.5.6   1998 Nash

In developing a mathematical model of the mechanics of the canine ventricles, Nash presented a steady state tension-length-calcium relationship for the active force generated during systole (Nash 1998). Building upon the models developed by Hunter (1995) and Hunter, Nash & Sands (1997), Nash used the following equation for active tension.

$$T\left(\lambda, Ca_{actn}\right) = \frac{Ca_{max}(Ca_{actn})^{h}}{\left(Ca_{actn}\right)^{h} + (C_{50})^{h}} T_{ref}\left[1 + \beta\left(\lambda - 1\right)\right] \tag{2.5.16}$$

Parameter values are given in Section A.19.

Equation (2.5.16) gives the active tension as a function of muscle length, λ, and the activation level of the muscle, Ca_{actn}. The activation level is a measure of the free intracellular calcium ions available for cross bridge binding and tension development. $Ca_{actn} = 0$ for tissue at rest and $Ca_{actn} = 1$ for maximally activated muscle. Thus, by varying the activation level Nash was able to simulate cardiac systole and demonstrate reasonable agreement with experimental observations of the canine cardiac cycle. Figure 2.32 illustrates the relationship between calcium activation level and active tension for the Nash (1998) model.
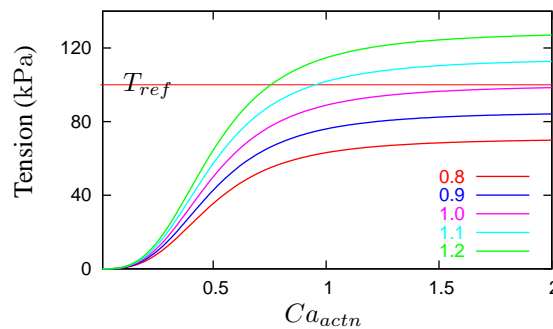
FIGURE 2.32: Illustration of the calcium-tension relationship of the Nash (1998) active tension model for various values of extension ratio (see key for values). Ca_{actn} is the activation level of the muscle, see Section A.19 for parameter values and equations.

Due to its significance in the previous work done in our group, the Nash (1998) is used as part of the validation for the simulation methods developed and implemented in this thesis.

2.5.7   2003 Markhasin *et al.*

Markhasin, Solovyova, Katsnelson, Protsenko, Kohl & Noble (2003) presents a review of the

development of experimental and theoretical duplex models that were conceived to test the hypothesis that well-organised inhomogeneity may be a prerequisite for normal cardiac function. The concept of the duplex comes from the idea that heterogeneity in cardiac tissue can be simulated using two individually controlled and mechanically interacting elements. In the work discussed in Markhasin et al. (2003) either or both of these elements can be biological (*e.g.,* thin papillary muscles or trabeculae) or virtual (a mathematical model).

Duplexes have been developed and characterised in three different configurations: a biological duplex, with both elements biological; a virtual duplex, with both elements being described by models; and a hybrid duplex, with a model element interacting in real-time with a biological duplex. For each of these configurations the two elements can be in either parallel or series.

Initial versions of the virtual elements used a cardiac mechanics and calcium dynamics model of contraction (Katsnelson, Izakov & Markhasin 1990, Izakov, Katsnelson, Blyakhman, Markhasin & Shklyar 1991). This has recently been extended through the merging of the mechanics model with the Noble et al. (1998) electrophysiology model (Solovyova, Vikulova, Katsnelson, Markhasin, Noble, Garny, Kohl & Noble 2003).

Experimental and numerical studies performed using the muscle duplex method has provided support for the hypothesis the well-organised inhomogeneity is required for normal cardiac function and suggested that electrical and mechanical heterogeneity are normally synergistic (Markhasin et al. 2003). Markhasin, Solovyova, Katsnelson, Protsenko, Kohl & Noble also assert that the muscle duplex method is provides a method to assess various mechanisms underlying pathophysiological conditions that have previously been inaccessible concepts.

2.6 Cardiac Electro-Mechanics

2.6.1 2001 Nickerson *et al.*

Nickerson (1998) developed a method of coupling the computationally efficient Hunter et al. (1998) cardiac mechanics model (Section 2.5.5) to the biophysically detailed electrophysiology model of Jafri et al. (1998) (Section 2.4.7). This method was then formalised in Nickerson, Smith & Hunter (2001), but rather than the Jafri et al. (1998) model they used the Noble et al. (1998) electrophysiological cellular model.

This work provided the basis for most of the electro-mechanical coupling between cellular mechanical and electrical models used in this thesis. Nickerson et al. (2001) provide a method whereby electro-mechanical coupling is achieved through the calcium dynamics model, which is usually defined by (or at least heavily reliant on) the electrophysiology model, driving the active tension development. Mechano-electric feedback can also be included through the addition of length-, velocity-, or force-dependent terms or mechanisms in the electrophysiology model. The most notable of these in the model of Nickerson et al. (2001) is the force dependent dissociation of calcium ions from troponin-C. When performing this coupling it was also shown to be important to ensure that the model parameters are consistent between the electrical and mechanical models.

2.6.2   2004 Nash & Panfilov

Nash & Panfilov (2004) presented an electromechanical model of excitable tissue in order to study reentrant cardiac arrhythmia. In this model they developed a cellular electro-mechanics model based on the Aliev & Panfilov (1996) activation model (Section 2.3.1). The Aliev & Panfilov (1996) model was modified to include the effect of mechanical deformation on the activation and recovery kinetics and a new differential equation was introduced to model the time course of active tension.

A version of the full Nash & Panfilov (2004) cellular model is given in Section A.23. This version of the model does not include the mechanical deformation effects on the activation and recovery kinetics as in our tissue and organ level models these effects are included into the continuum activation model (monodomain or bidomain).

Chapter 3

Modelling Cardiac Electro-Mechanics

Previous work (Hunter et al. 1997, Usyk, LeGrice & McCulloch 2002, Kerckhoffs, Bovendeerd, Kotte, Prinzen, Smits & Arts 2003, Kerckhoffs, Faris, Bovendeerd, Prinzen, Smits, McVeigh & Arts 2003) has modelled the electrical excitation and mechanical contraction as two separate processes weakly coupled together through the use of the excitation wavefront to initiate active contraction of the tissue. We extend this work by developing a framework generalising these types of tissue and organ models to allow for varying levels of coupling between the electrophysiology and mechanics at the cellular, tissue, and organ levels. Depending on the cellular model being used, the coupling can also be extended down to the molecular and protein levels.

Appendices B and C provide brief overviews of the theory of finite deformation elasticity and electrical activation and propagation, respectively, and their numerical formulation as used in this work. Section 3.2 details how these two methods can be coupled together and, through inclusion of the cellular models described in Section 3.1, provide the ability to model cardiac electro-mechanics at the tissue and organ levels.

In Section 3.1 we present two cellular level electro-mechanics models developed for use in testing the modelling framework. The first model can be used to obtain tissue and organ models very similar to previous models (Hunter et al. 1997, Usyk et al. 2002, Kerckhoffs, Bovendeerd, Kotte, Prinzen, Smits & Arts 2003, Kerckhoffs, Faris, Bovendeerd, Prinzen, Smits, McVeigh & Arts 2003), where a propagating electrical activation wave is used to drive the mechanical contraction at the cellular level. The second model contains a detailed biophysical description of cellular electrophysiology including the intracellular calcium dynamics. This has the advantage over previous models that it includes some mechano-electric feedback, but the disadvantage that

it is a very computationally demanding model to integrate. Section 3.4.3 provides comparisons of computational performance using the two different models in various tissue level models.

3.1   Cellular Electro-Mechanics

Here we present two models of cellular electro-mechanics developed for use in this thesis. These models will be used in the distributed tissue and ventricular models described later in this section and in Chapter 5. Each of these models demonstrates different aspects of the modelling framework developed in this thesis.

The first model (FK-HMT) is based on coupling the Fenton & Karma (1998) simplified activation model to the Hunter et al. (1998) mechanics model. This illustrates how a simple model of activation can be used to drive the mechanical contraction at the cellular level and then in larger scale distributed models. The second model couples the complex biophysically detailed N-LRd electrophysiology model (Section 2.4.10) to the Hunter et al. (1998) mechanics model. With this model we demonstrate tighter coupling between the electrophysiology and mechanics as well as the introduction of some mechano-electric feedback.

3.1.1   FK-HMT

In some cases simplified cellular models may be desirable to enhance computational performance while still maintaining the electro-mechanics characteristics required for the study being performed. Examples where such models might be useful are: normal sinus activation; electrical reentry phenomena where the reentry is caused by conduction blocks; and localisation of pacing sites for implantable defibrillation devices or resynchronisation therapy.

Here we present a model developed through the coupling of the Fenton & Karma (1998) simplified activation model (Section 2.3.4) to the computationally efficient Hunter et al. (1998) model of cardiac mechanics (Section 2.5.5). Following the method described by Nickerson et al. (2001), the activation model is used to provide the calcium transient input required to drive the active and dynamic development of cellular tension.

The Fenton & Karma (FK) model, however, lacks a calcium transient. As noted in Section 2.3.4, the FK model was derived from the Beeler & Reuter (1977) and Luo & Rudy (1991)

models and these models both use the same model of intracellular calcium changes based on the slow inward current. Thus, through the inclusion of this relatively simple model of calcium dynamics we have a version of the FK activation model which includes enough detail of intracellular calcium dynamics for use in driving the Hunter, McCulloch & ter Keurs (HMT) mechanics model.

The full Fenton & Karma–Hunter, McCulloch & ter Keurs (FK-HMT) model is given in Section A.22 with some illustrative simulation results presented in Figures 3.1 and 3.2.
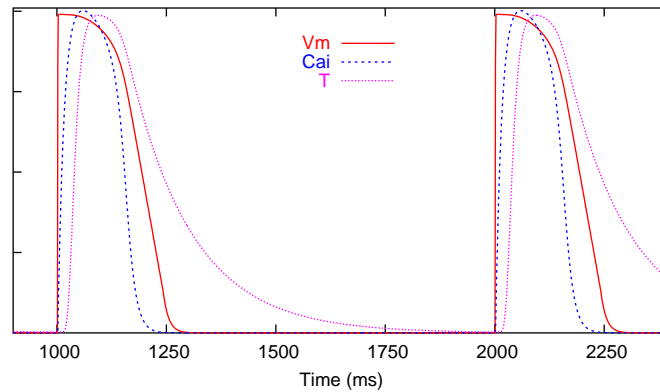
FIGURE 3.1: A train of isometric twitches obtained from simulations with the FK-HMT cellular model. Membrane potential (Vm), intracellular calcium concentration (Cai) and active tension (T) are normalised to illustrate their overlapping time transients. A $1\,\mathrm{ms}\ 80\,\mu\mathrm{A}\cdot\mathrm{mm}^{-3}$ stimulus current is applied with a cycle length of $1000\,\mathrm{ms}$.

The FK-HMT model developed here includes only electromechanical coupling – there is no mechano-electric feedback in this model, as demonstrated by the length steps in Figure 3.2 having no effect on the calcium or membrane potential transients. As such, it is suitable for use in simulations of normal cardiac tissue with application to, for example, studies of: normal activation and contraction in tissue and organ level models; reentry phenomena and the effect of contraction on reentry; and location of pacing sites for implantable defibrillator's and resynchronisation therapy. It would be possible to modify one (or all) of the three "currents" in the model to add a length dependence or add the calcium release from troponin to the intracellular calcium transient, and hence have some measure of mechano-electric feedback in the model. While doing so expands the applicability of this model in tissue and organ level simulations, such modifications rapidly begin to negate the advantages of using such a computationally efficient model.
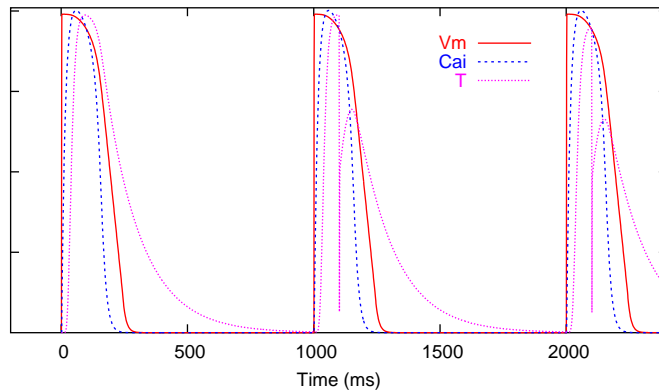
FIGURE 3.2: The same train of action potentials as Figure 3.1 but now showing the effect of two length steps on the actively developed tension, as described by the FK-HMT model. The first twitch is performed with $\lambda = 1.0$ with a step down to $\lambda = 0.99$ occurring during the second twitch with a duration of 1 ms. This new length is retained until a second step during the third twitch down to $\lambda = 0.98$, again over a period of 1 ms.

Cellular Heterogeneity

The variation of cellular behaviour throughout the myocardium is crucial to the normal functioning of the heart. One of the most dramatic intrinsic heterogeneities in the heart is the presence of a layer of cells midmyocardial or M cells, roughly located in the middle of the ventricular wall (Antzelevitch, Sicouri, Litovsky, Lukas, Krishnan, Di Diego, Gintant & Liu 1991). This layer consists of cells which have distinct electrophysiological properties and its presence has been observed in numerous species (*e.g.,* canine (Yan, Shimizu & Antzelevitch 1998) and human (Drouin, Charpentier, Gauthier, Laurent & Le Marec 1995)).

The most notable feature of the midmyocardial cells is the prolongation of the cellular action potential at slow pacing rates compared to the epicardial and endocardial cells. Several modelling studies have been performed examining the effect of this APD distribution through the ventricular wall – see Henry & Rappel (2004) for a recent example. The variation of APD can be included in the FK-HMT model via several mechanisms. In Figure 3.3 we show some results matched to action potential (AP) records from human myocytes performed by Drouin et al. (1995), where the change in APD is achieved through altering the slow outward currents repolarisation time constant.

APD is measured here as the time between maximal positive slope during the AP upstroke and maximal negative slope during the AP repolarisation phase. Analysis of the APs from the simulation illustrated in Figure 3.3 gives APDs of 437 ms for the midmyocardial cell type,
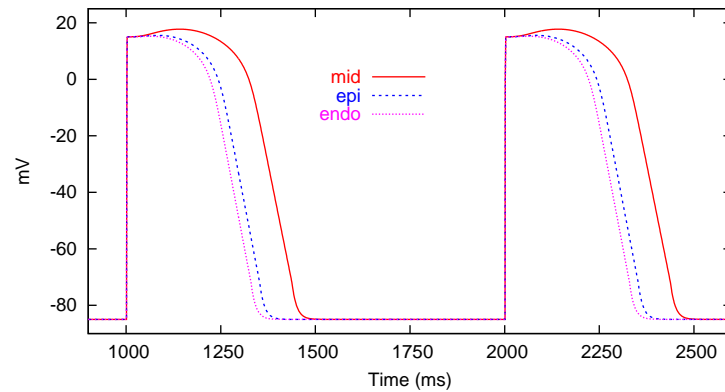
(a) Membrane potential.
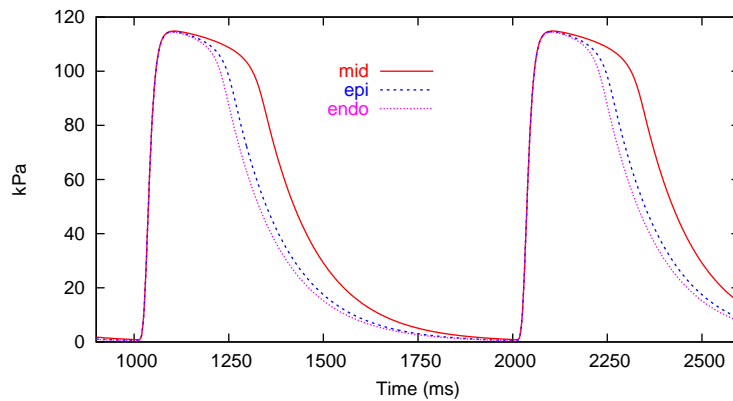
(b) Active tension.

FIGURE 3.3: Following the same pacing protocol as used in Figure 3.1, we show how altering the repolarisation time constant of the slow outward current can give APD results consistent with those recorded from human midmyocardial (mid), epicardial (epi), and endocardial (endo) myocytes (*cf.* Drouin et al. (1995, Figure 2 & Table 2)). The different APDs are obtained with τ_r values of: 150 ms for the midmyocardial cell; 144 ms for the epicardial; and 142 ms for the endocardial. The default value for the modified LR-I version of the FK-HMT model is 130 ms.

352 ms for the epicardial, and 329 ms for the endocardial cell type.

3.1.2 Nickerson – Clancy & Rudy – Hunter, McCulloch & ter Keurs

The FK-HMT model described above is a very useful and computationally efficient model suitable for a wide range of applications involving basically healthy normal tissue. When modelling unhealthy or abnormal tissue, however, it is often critical to be able to capture changes or modifications on the scale of individual mechanisms. To enable the description of such changes, we present here a model of cellular electro-mechanics based on the wild-type N-LRd electrophysiological model (Section 2.4.10). This model describes in great detail the electrophysiology of cardiac cells including a detailed biophysical model of the intracellular calcium subsystem. Cellular heterogeneity is intrinsic in the model based on the density of certain transmembrane ionic channels in the epicardial, endocardial, and midmyocardial cell types (see Figure 2.21). This model also allows for the inclusion of certain well characterised genetic mutations into the electrophysiology (see Figures 2.23 and 2.24).

As with the FK-HMT model above, we couple the N-LRd model to the Hunter et al. (1998) mechanics model. The coupled model is known here as the Nickerson – Clancy & Rudy – Hunter, McCulloch & ter Keurs (N-LRd-HMT) model of cardiac cellular electro-mechanics. The full N-LRd-HMT model is given in Section A.26 and a brief overview of the model is presented here.

The major component of communication between the cellular electrophysiology and mechanics is the intracellular calcium subsystem. In the N-LRd-HMT model the calcium subsystem is derived from the Jafri et al. (1998) model of calcium dynamics. Nickerson (1998) presented an electro-mechanics model which coupled the Jafri, Rice & Winslow (JRW) and HMT models together. Following Nickerson (1998), the calcium binding to troponin-C kinetics from the HMT model is replaced with the kinetics for the low affinity troponin-C binding sites from the JRW model. The JRW kinetics are modified to include the tension dependent release of calcium from the low affinity troponin-C binding sites. Due to differences in the development of the JRW and HMT models, various parameter values require adjusting to correctly match the calcium binding kinetics to the active tension development.

Figure 3.4 presents a series of isometric twitches obtained from solution of the N-LRd-HMT model for the three cell types, as they are described in Section 2.4.10. This shows the electromechanical coupling between the models. The mechano-electric feedback aspects of the

N-LRd-HMT model are presented in Figure 3.5 with simulations where various step decreases in length are performed during an isometric twitch.

(a) Membrane potential.

(b) Active tension.

(c) Intracellular calcium concentration.

(d) Calcium bound to tropinin-C.
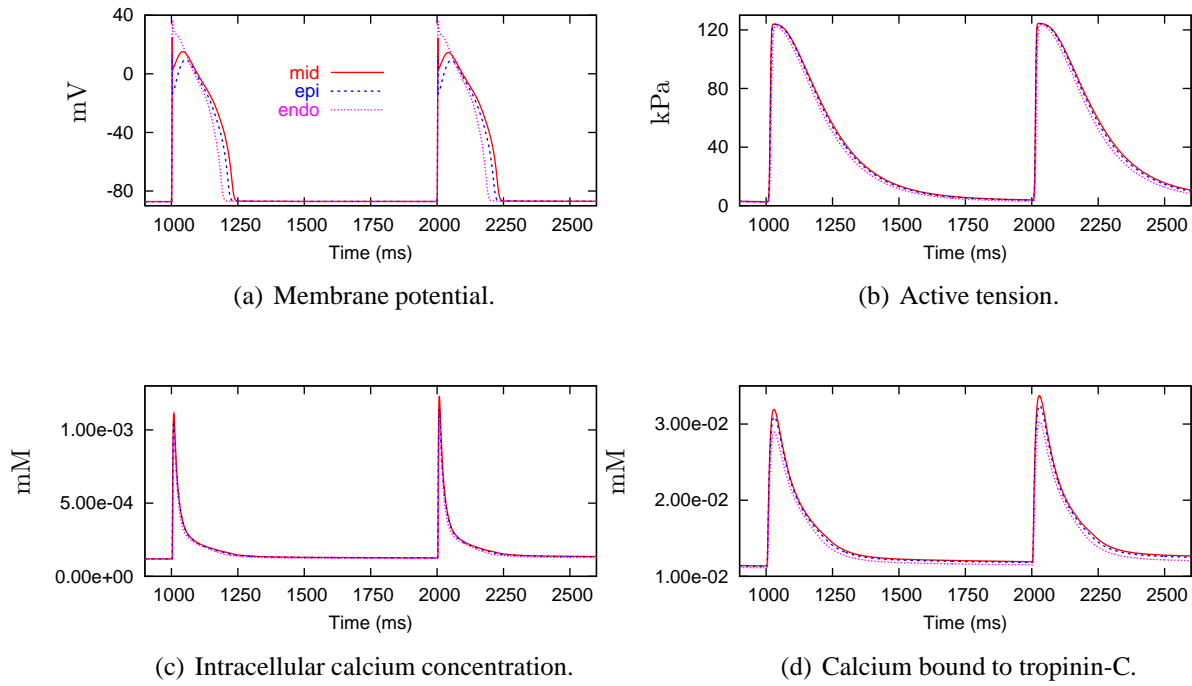
FIGURE 3.4: Isometric twitches as simulated by the N-LRd-HMT electro-mechanics model for epicardial (epi), midmyocardial (mid), and endocardial (endo) cell types.

The results given in Figure 3.5 highlight the mechano-electric feedback in the N-LRd-HMT model. Following a shortening length step, calcium is released from troponin-C (Figure 3.5(d)) and becomes available in the common intracellular calcium pool (Figure 3.5(e)). From the intracellular space the extra calcium is taken up into the SR (Figures 3.5(f) and 3.5(g)). Very little of the extra calcium uptake translocates through to the release channels of the SR (not shown). The calcium uptake into the SR overcompensates once the filaments start binding calcium again, causing the free intracellular calcium concentration to drop below the isometric level (Figures 3.5(e) and 3.5(g)). Increase of the calcium concentration in the SR stores results in an increase in the leakage of calcium from the SR (Figure 3.5(h)).

As shown in Figure 3.5(b), the AP shape and duration are virtually unaffected by these length changes. This is due to the majority of the calcium ions released from troponin-C being absorbed internally by the intracellular calcium subsystem. The largest changes in transmembrane ion transport are seen in the Na^+-Ca^{2+} exchanger current (Figure 3.5(i)), which demonstrates a very minor effect compared to the intracellular calcium dynamics changes. Figure 3.5 also shows that the changes observed in the intracellular calcium handling are dependent on the

severity of the length step.

3.2   Modelling Tissue Electro-Mechanics

Modelling cardiac electro-mechanics on a spatial scale larger than that of the single cell models described above requires the coupling of two processes: the spread of electrical excitation through the tissue; and the mechanical behaviour of the tissue. In a normal mammalian heart, the spreading wave of electrical excitation triggers contraction of the cardiac muscle which is responsible for the pumping of blood required to sustain life. While these processes can be modelled independently, it is well established that feedback occurs in both directions between them (Kohl 1995).

A large body of research exists for modelling the spread of electrical excitation throughout cardiac tissue and the whole heart (for reviews, see Hunter, Pullan & Smaill 2003, Kléber & Rudy 2004, Smith, Nickerson, Crampin & Hunter 2004). Numerous methods have been developed to model the spread of electrical excitation varying from discrete models in which individual cells are electrically coupled to their neighbours via variable resistive elements (gap junctions) through to continuum based models. Continuum models are based on the assumption that the length scales of the physically observable phenomena are large in comparison to the underlying discrete structure of the material. Our group has developed numerical simulation techniques for solving continuum models of electrical excitation, based either on the bidomain model (Appendix C) or an eikonal type model for activation times (Tomlinson 2000, Tomlinson, Pullan & Hunter 2002). While we have the tools to model the full bidomain model, in this work we have used the simplified monodomain model (Section C.2) as we are currently modelling isolated pieces of tissue. This allows a significant saving in terms of computational cost and model complexity. The numerical formulation we have used in this work, known here as the grid-based finite element (GBFE) method, is presented in Section C.3.

Similarly, a large body of research also exists for modelling the mechanical behaviour of cardiac tissue (for example, see Hunter et al. (2003) and Smith et al. (2004) for reviews). In the past, many models of cardiac mechanics considered only the passive properties of the muscle. This was due to both model complexity and the lack of experimental data during the systolic phase of the cardiac cycle (or contraction of isolated tissue preparations). This allowed the use of quasi-static models of finite deformation elasticity to be applied to the heart with great success. Finite element continuum models of cardiac mechanics are the most prevalent in this

(a) Active tension.

(b) Membrane potential.

(c) Active tension.

(d) Calcium bound to tropinin-C.

(e) Intracellular calcium concentration.

(f) SR calcium uptake store.

(g) SR calcium uptake flux.

(h) SR calcium leak flux.

(i) Na^+-Ca^{2+} exchanger current.
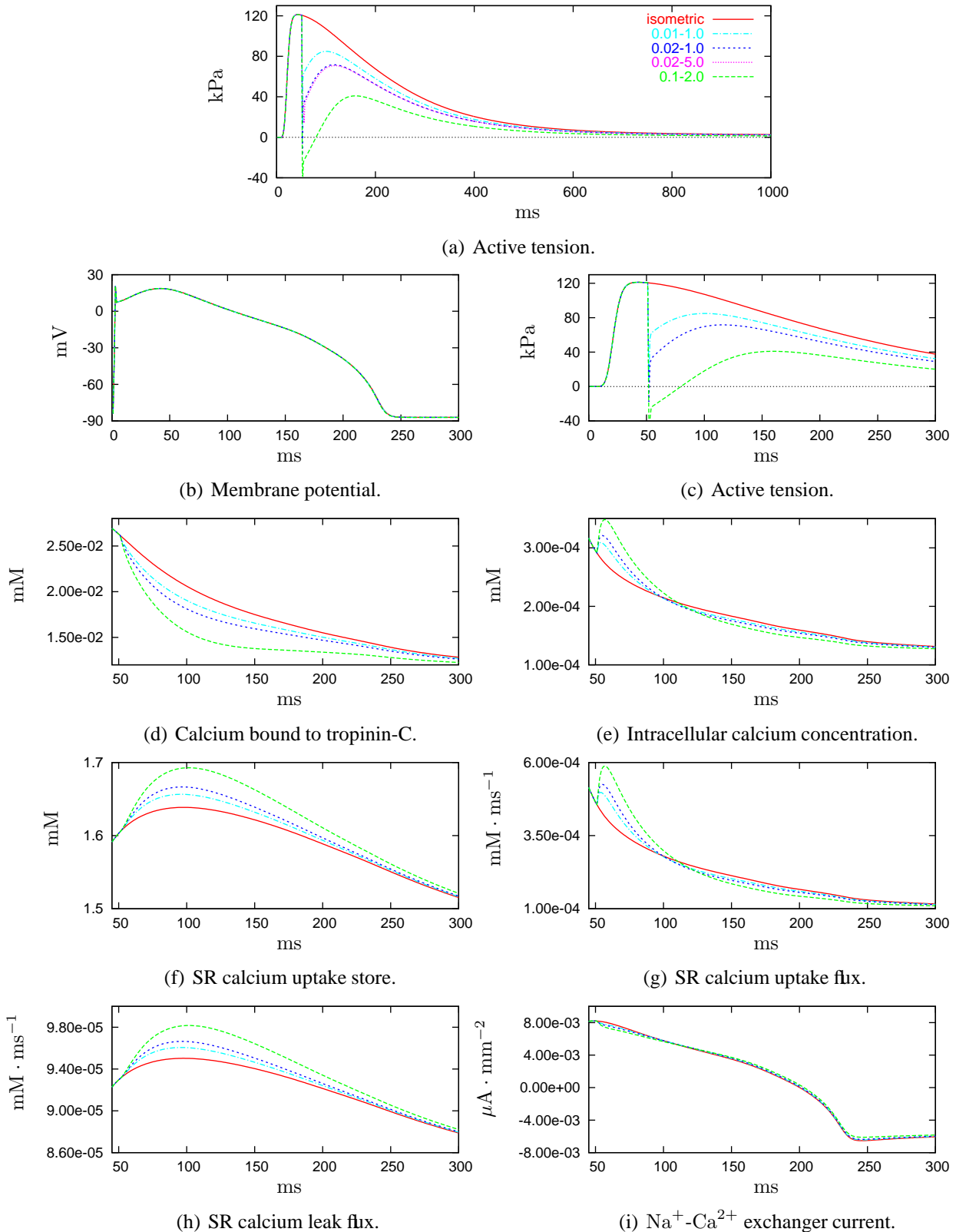
FIGURE 3.5: Comparison of an isometric twitch from the N-LRd-HMT model with transients obtained from simulations with various length steps. The key is given in (a) where the length steps shown are: a 1.0 % shortening over a 1 ms time period (0.01-1.0); a 2.0 % shortening over 1 ms (0.02-1.0); a 2.0 % shortening over 5 ms (0.02-5.0); and a 10.0 % shortening over 2 ms (0.1-2.0) (*cf.* Figure 2.31). These twitches are from the midmyocardial cell type of the N-LRd-HMT model with a stimulus current of 250 $\mu A \cdot mm^{-3}$ applied at 0 ms for a duration of 1 ms.

field and the use of high order interpolation in which our group specialises is well suited to these types of models. The finite elasticity finite element (FE) formulation we have used in this work is given in Appendix B.

The development of models of these two processes has largely occurred independently, and it is only recently that we have begun to obtain the computational power and experimental data required to develop models of electro-mechanics in cardiac tissue. In this work we have taken the two methods described in Appendices B and C and coupled them together to produce a technique for the numerical solution of biophysically detailed cardiac electro-mechanics models. The method developed uses cellular models of electro-mechanics to drive the dynamic active material properties of the model while the cellular models themselves get feedback from both the electrical excitation and the deforming mechanical model. The mechanical deformation of the FE geometric models also feeds into the excitation model affecting the propagation of electrical activation and cellular electrophysiology.

We now describe the technique developed to model cardiac electro-mechanics at the tissue and organ levels using the previously described cellular models. The first step is the inclusion of active contraction in the finite elasticity model. This then provides a full specification of an active mechanics model which can be coupled to the electrical activation model as described below. Implementation of the numerical solution of electro-mechanics models is also discussed.

It is important to note that the methods described below make no use of prior knowledge of the cellular model being used in the tissue model. The only caveat is that it is assumed that the cellular model will be providing the active tension – at a minimum, the active tension component in the fibre material direction is expected but sheet and normal components can also be specified.

3.2.1 Finite Deformation Elasticity with Active Contraction

The cellular mechanisms involved in active contraction of myocytes are discussed in Section 3.1 above. Incorporation of the actively generated cellular tension into models of cardiac tissue requires extending the passive finite elasticity modelling formulation presented in Appendix B. When modelling electro-mechanics we are specifically interested in the dynamic active behaviour of the tissue and the inclusion of active material properties into the finite deformation modelling paradigm is therefore a crucial first step in developing a model of cardiac electro-mechanics.

We assume active contraction of muscle fibres generates force only in the direction of the fibre axis (Figure 1.3), which aligns with the ν_1-coordinate in the deformation theory (Appendix B). Therefore only one term of the true (Cauchy) stress tensor is altered and the the full Piola-Kirchhoff stress tensor with respect to the microstructural axes can be written

$$T^{\alpha\beta} = \frac{1}{2}\left(\frac{\partial W}{\partial E_{\alpha\beta}} + \frac{\partial W}{\partial E_{\beta\alpha}}\right) - pa_{(\nu)}^{\alpha\beta} + T\frac{\rho_o}{\rho}\frac{\partial X^\alpha}{\partial \nu_1}\frac{\partial X^\beta}{\partial \nu_1}, \qquad (3.2.1)$$

where $T = T(t, \lambda_{11}, \ldots)$ is the active tension generated by a fibre at the time for which the stress tensor is being evaluated and $\frac{\rho_o}{\rho} = 1$ as we assume an incompressible material. λ_{11} is the fibre axis extension ratio described in Section 2.1.3. Addition of active tension to the stress tensor seems a minor addition to the model, but we will show how the addition of dynamic behaviour to a traditionally quasi-static method results in a huge increase in the computational cost of the numerical simulation of such models.

For the purposes of this thesis we have followed the above assumption and only included active tension generated in the fibre direction. The implementation of this method, however, allows for active tension components to be specified aligned with any or all of the fibre, sheet, and normal material axes, taking into account the strain in all material directions.

Previous work in our group has used a steady-state tension-length-calcium relationship (Section 2.5.6) for the active tension, T, in Equation (3.2.1) (Nash 1998, Stevens 2002, Remme, Nash & Hunter 2004). This approach has also assumed a near constant activation level over the entire solution domain. The method we develop in this thesis allows for T to be defined directly from cellular models spatially distributed throughout the solution domain.

3.2.2 Coupling Electrical Activation and Finite Elasticity

Although electrical excitation and mechanical contraction are physiologically interdependent, the quasi-static techniques used for the solution of the finite elasticity tissue models and the fact that the electrical and cellular processes take place on much faster timescales allows for some uncoupling in continuum model simulation. Figure 3.6 presents an overview of the algorithm developed for the solution of coupled electro-mechanics in continuum tissue models. This algorithm allows for the semi-independent solution of the finite elasticity and electrical activation models at a given instant in time, resulting in two solution steps separated by an update step in which information is transferred between the models. This is advantageous because it enables us to make use of the code base provided by CMISS for the individual components of the algorithm

with the addition of the communication and updating processes. As discussed in Section 6.1, however, this requires further investigation to determine if this actually inhibits performance of the simulations performed in this thesis. The two solution steps are semi-independent because they both utilise the same underlying cellular model(s) in their respective solutions.

Model specification

Any simulation starts with a description of the model and some initial conditions. In this case the model definition includes a FE geometry (including the continuum representation of the fibrous microstructure), the constitutive material law for the mechanical model, the electrical activation model to use, continuum material parameters for both excitation and mechanics models, and specification of the cellular model. The simulation framework we have developed allows for spatial variation of not only cellular model parameters but cellular models themselves.

Boundary and initial conditions in an electro-mechanics model will typically be restrictions on the movement of sections of the geometric model, possibly an applied pressure to some surfaces, and an electrical stimulus of some kind. The electrical stimulus could be applied internally through the use of pacemaker cells within the solution domain (*e.g.,* SAN cells or Purkinje fibre cells), but in this work transmembrane volume currents will usually be applied at the desired location(s).

Solution procedure specification

Once the model has been specified the numerical techniques to be used in solution of the model need to be specified. The FE method for finite elasticity requires a system of nonlinear equations to be solved over the solution domain. This system is rearranged into a set of residuals which must be minimised with respect to the set of solution variables using a root finding technique. The electrical activation and finite elasticity models both involve, at some point, in a linear system of equations of the form $\boldsymbol{A}\boldsymbol{x} = \boldsymbol{b}$ to be solved for the unknown values of $\boldsymbol{x}$. Due to the structure of the different $\boldsymbol{A}$ matrices, the two models will generally obtain better performance with different linear solvers. These linear solvers and their parameters need to be specified for each of models.

In addition to the solution techniques to be used in the solution of the electrical activation and finite elasticity models, the spatial and temporal discretization to be used by each of the
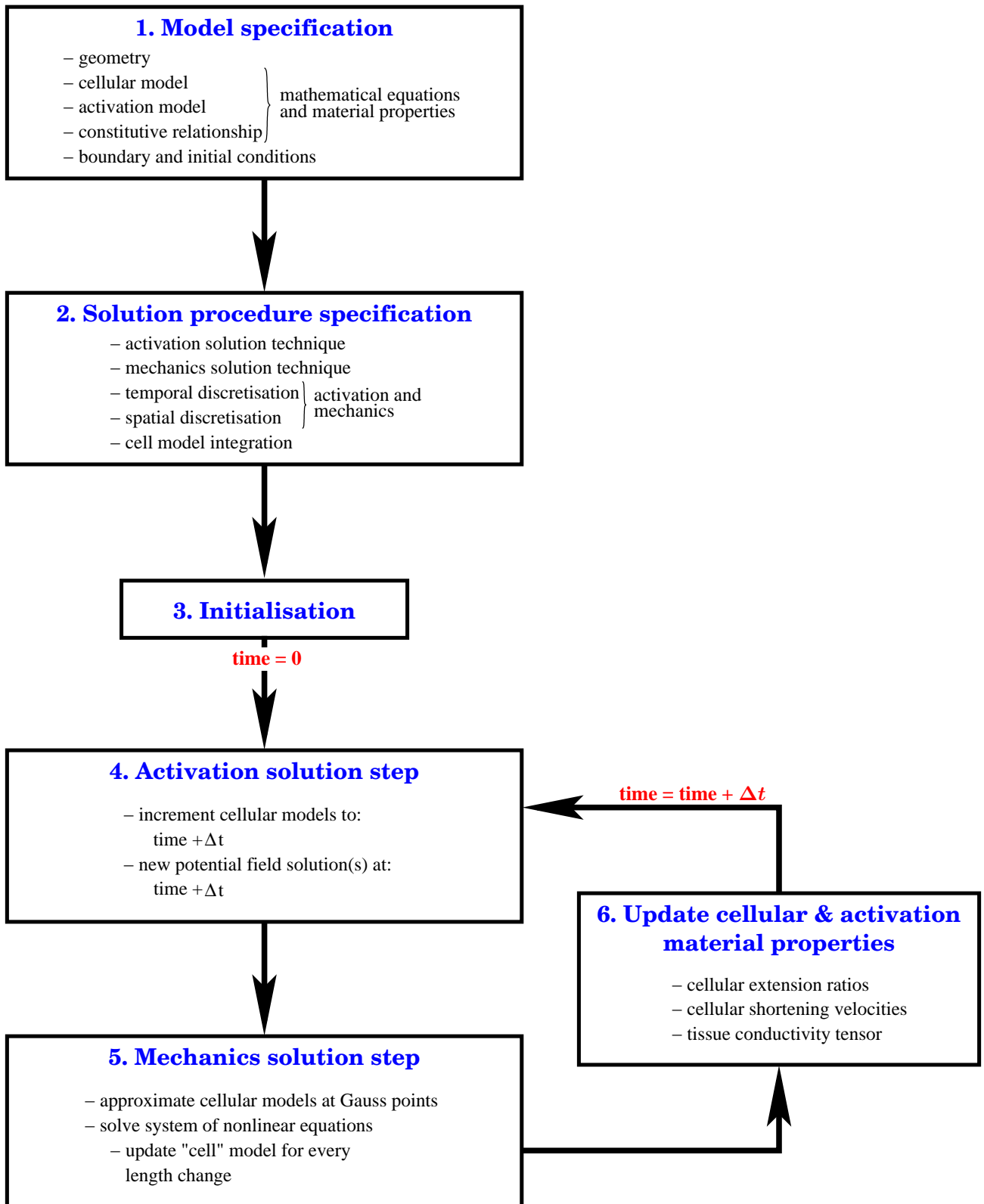
FIGURE 3.6: Overview of the algorithm developed for the coupled solution of cardiac electro-mechanics over a continuum solution domain. See text for detail.

models needs to be specified. The spatial resolution of the finite elasticity model will be given by the interpolating basis functions used for the deformation and pressure fields, where we typically use high order cubic Hermite interpolation (Section 1.2). When using the grid-based finite element (GBFE) method with either the bidomain or monodomain activation models, the solution domain is subdivided into trilinear FEs where the spatial resolution of the model is given by the size of these elements. It has been shown that a spatial resolution on the order of $200 \ \mu$m is required for a converged activation solution (Sands 1997, Buist 2001, Pollard 2003, Hunter et al. 2003). Time discretization on the order of $10 \ \mu$s is required to obtain a converged activation solution (Hunter et al. 2003). The quasi-static nature of the finite elasticity formulation, however, allows for much larger time intervals between solution steps. The limiting size of this interval is, however, still under investigation and will most likely be found to be specific for a given model.

Further to the specification of the solution techniques for the activation and mechanics models, the numerical method used for the solution of the cellular model must also be specified. Cardiac electro-mechanics cell models will consist of a system of ordinary differential equation (ODE)s. This system, which could be very large and very stiff, must be integrated over the desired time interval to give the cellular state at the next time point for use in both the activation and mechanics models. The stiff nature of some cellular models may require even finer time resolution for their integration than the $10 \ \mu$s required by the activation model. Such time resolution can be achieved through the use of adaptive time stepping ODE integrators. For example, the LSODA (Hindmarsh 1983) and RADAU (Hairer & Wanner 1996) integrators have been found to perform well with the range of cellular models presented in Chapter 2.

Initialisation

Having specified the model and solution techniques, there are some initialisations that are only required to be performed once. For the mechanics model, an initial solution step may be required to incorporate any residual strains (Omens & Fung 1990, Rodriguez, Omens, Waldman & McCulloch 1993, Costa, May-Newman, Farr, O'Dell, McCulloch & Omens 1997) into the model in order to obtain a true stress-free reference state required for the finite elasticity (Nash 1998, Stevens 2002). The electrical activation model needs to compute initial tissue conductivities throughout the solution domain and also assemble the initial matrices.

The initialisation stage marks the end of the simulation set-up phase. We are now ready to solve the model. Model solution is split into two parts – first the time dependent electrical

activation model is solved for the current time step and then the mechanics model is solved given the current active state of the cellular model(s). The two solution steps are iterated upon for the duration of the full temporal solution domain with an update at each time step.

Activation solution step

Solution of the electrical activation model takes the current potential field solution and solves for a given time interval (Δt) using the GBFE method (Section C.3). The actual solution of the activation model and the integration of the ionic current model will need to be performed on a very fine temporal scale ($\delta t \approx 10\ \mu s$) whereas in this algorithm we are interested in a larger scale time resolution. Thus, Δt is usually in the range 1–10 ms.

This solution step will result in new potential fields over the solution domain at the time $t + \Delta t$. As part of the solution process the cellular fields at each node in the GBFE mesh will be at their $t + \Delta t$ value.

The main feedback from the finite elasticity model into the cellular model will be through the cellular strain, and in some cases the velocity with which the strain is applied. The strain and shortening velocities at each cell in the continuum model is determined in the update step. For the case when there is a dependence on the velocity of length changes, we say the cellular model provides a dynamic active tension and it is this dynamic tension that will generally be used as the initial active tension input into the finite elasticity model.

Mechanics solution step

Section 3.2.1 describes how the active tension is incorporated into the FE formulation of the finite elasticity equations given in Section B.3. Gauss-Legendre quadrature (or Gaussian quadrature) is used to numerically integrate these equations through the use of weighted sums of integrand evaluations using specified sets of independent variables (Nash 1998). The spatial location of the Gauss points at which the integrands are evaluated are determined by an element's interpolating basis function and the resolution of the quadrature scheme. Throughout the solution of the finite elasticity equations at a given point in time, the full stress tensor (Equation (3.2.1)) is evaluated at each of the Gauss points. In the models we have developed in this thesis, the active tension contribution to each of these stress tensor evaluations comes from the cellular model governing the active behaviour of the tissue surrounding the Gauss point.

When using Newton's method to solve the finite elasticity equations, a Jacobian matrix needs to be created for each load step to determine the direction to search for the required root (Section B.3.2). As shown in Equation (B.3.13), the Jacobian matrix is a combination of the rate of change of each solution variable with respect to each of the other solution variables. This matrix is numerically evaluated by perturbing each solution variable by a small amount and calculating the change in each of the other variables, which is used to estimate the required derivatives.

For the formulation of the finite elasticity equations used here, the solution variables mostly consist of displacements of nodal coordinates and nodal derivatives for all the nodes in the solution domain not fixed by a specified boundary condition. As such, the perturbations of the solution variables is analogous to localised application of mechanical deformation of the solution domain. Thus, the perturbations result in changing the length of the cells in the region of tissue surrounding the point being perturbed with those physically closest to the point exhibiting the largest effect, while the effect decreases further from this point. As shown in Section 3.1 the active tension generated by a cell is highly dependent on the cell length with a nonlinear relationship between length and tension.

We have found that the changes in active tension caused by these perturbations are essential to the convergence of Newton's method. If a constant active tension value is used throughout the calculation of the Jacobian matrix, it is very difficult, and in most cases impossible, to obtain a converged solution to the finite elasticity equations. We found that for very small increments of the activation level over the solution domain, converged solutions may be obtained while using a constant value of active tension at a given Gauss point for the Jacobian evaluation. To obtain such small increments over the solution domain given the rapid upstroke of the cellular tension transient, however, would result in a small temporal step between solutions of the finite elasticity model and Δt would tend toward δt. This results in a solution method that is very time consuming and possibly not required.

Through incorporation of the solution of the cellular model for every evaluation of the stress tensor, we have developed a method which provides a converged solution for much larger changes in activation level throughout the solution domain. During the solution of the finite elasticity model the stress tensor evaluations will typically be performed at the Gaussian quadrature points, requiring the calculation of the active tension from the cellular model at a given spatial location. We tested two methods for this calculation, both of which make use of the fact that the active tension at the Gauss point is going to be dominated by the cell physically closest to the Gauss point, with influence from the cells surrounding that cell, and then very little to no

influence from cells more distal (Figure 3.7(a)). Here we refer to the nodes of the GBFE mesh as cells.

Method one, illustrated in Figure 3.7(b), updates the cellular fields based on the current deformation of the geometry given by the finite elasticity model. The cellular model is then integrated at the influential cells and the active tension value is interpolated to the value required at the Gauss point. Method two, Figure 3.7(c), interpolates the cellular fields from the influential cells to values at the Gauss point and then integrates the cellular model at the Gauss point using these values. In three dimensions both methods consist of 27 influential cells.

Method two requires that all the influential cells are modelled with the same cellular model. While this is lacks the generality of method one, it is felt that the case when a Gauss point is spatially located very close to the boundary of two cell types will be very rare and did not occur in any of the models in this thesis. Further refinement of method two could be performed to enable the solution of any such cases that may occur. Method one requires that the local material strain be evaluated at each of the influential cells, which is a particularly time consuming process. In method two, however, we already have the local material strain at the Gauss point as part of the finite elasticity model. In three dimensions, method one involves 27 cellular model solutions whereas method two has 1.

Comparisons of the two methods has shown that method two is significantly less time consuming when running simulations, while obtaining quantitatively the same answer. The time saved in model solution easily compensates for the lack of generality, especially given that in all the models in this thesis we never encountered the problem described above. Thus, we have used method two for all the simulations described in this thesis. Potentially this method will need to be improved to cover future model requirements or techniques could be employed to ensure the more general method one is made computationally tractable. While this discussion has focused on evaluating the full stress tensor at a Gaussian quadrature point, the methods are both applicable to any spatial location in the solution domain given that point's material coordinates in local element space.

The final problem to overcome in the process of coupling cellular dynamics models into the finite elasticity model is the fact that in the calculation of the Jacobian matrix for Newton's method (Section B.3.2) we are essentially applying perturbations of cellular lengths in regions of the tissue model. To the cellular model, these appear as instantaneous length steps which, as shown in Figures 3.2 and 3.5, result in a rapid decrease of the dynamic active tension to near 0 before recovery to the new isometric tension value for the new cellular length. Such
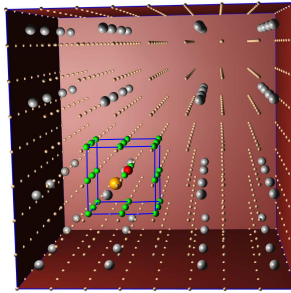
(a) Interpolation from GBFE nodes to Gauss points.
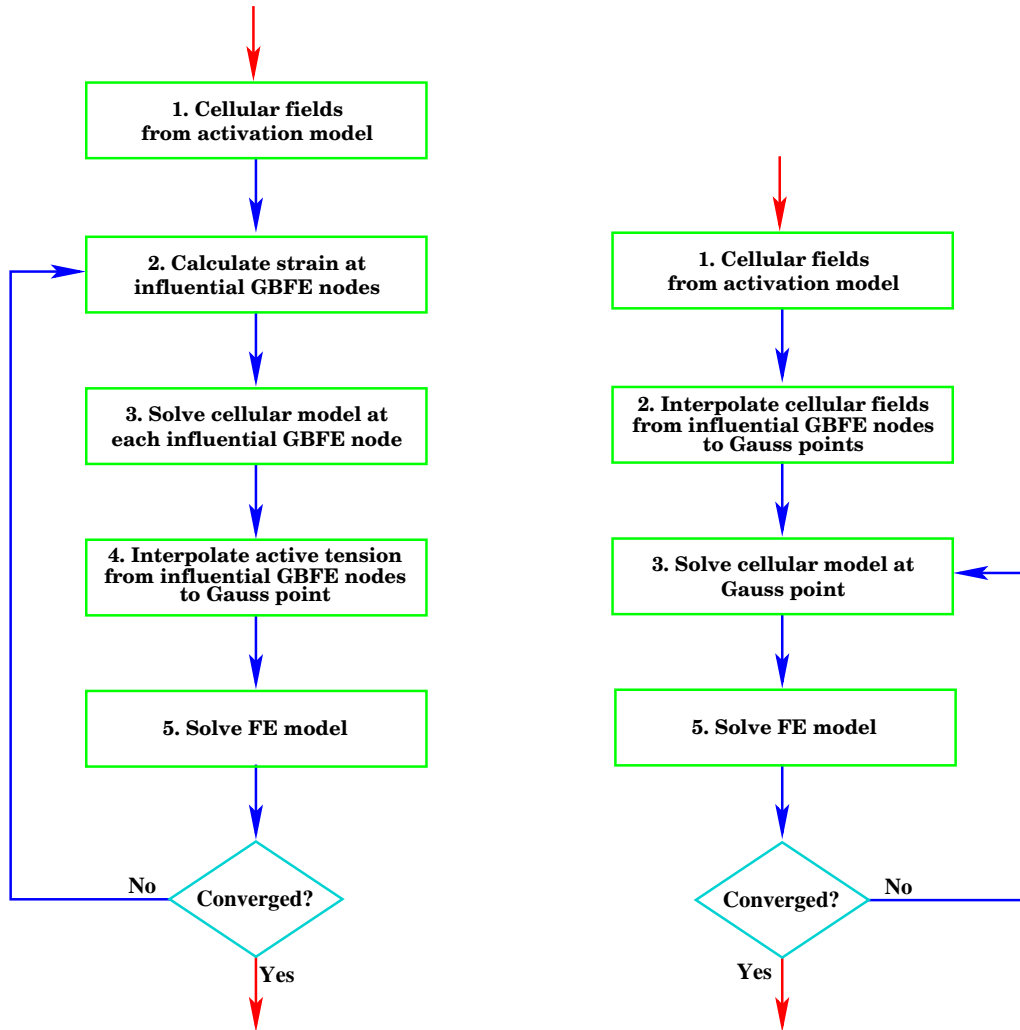
(b) Method one.

(c) Method two.

FIGURE 3.7: The two methods developed for calculating active tension at a Gauss point. (a) shows a cube element with the Gaussian quadrature points shown as large silver spheres and GBFE nodes (or cells) as smaller tan spheres. The cells which influence the active behaviour of the tissue at the gold Gauss point are shown in green, the cell with the greatest influence is shown in red. The blue lines indicate the volume of tissue assumed to influence the active behaviour of the material at the gold Gauss point. This example uses a very coarse GBFE mesh to aid presentation, see Figure 3.8(d) for a grid closer to that required for actual model solution. (b) and (c) show the two methods developed for the calculation of active tension for a given Gauss point (gold) from the cellular values at the influential grid points (green and red).

rapid changes in active tension wreak havoc with the numerical techniques we are employing to solve the finite elasticity equations. We note here that these applied length changes are purely an artifact of the numerical method being used to solve the model. We can therefore neglect any dynamic changes in active tension due to the length changes and use only the non-dynamic active tension from the cellular model in the finite elasticity model solution for a given instant in time. The dynamic component of the active tension is included from the cellular model due to the initial active tension applied to the finite elasticity model from the activation solution step being computed using the full dynamic model.

For some models, it is conceivable that evaluation of active tension may require the integration of some ODEs. To enable this, the framework implementation has the ability to perform a *dummy* integration step of the cellular model for each active tension calculation. Here the dummy step size is assumed large enough to allow transient effects of the applied numerical length steps to dissipate so as to allow a converged finite elasticity solution to be obtainable.

Finally, we note that the length perturbations applied to the cells during the solution of the finite elasticity equations are the basis of a numerical technique and not based on the physiology. As such, the perturbations can possibly result in cellular extension ratios outside the physiological range for cardiac myocytes described in Section 2.1.3. When the value of the extension ratio falls outside the physiological range during the application of the numerical technique non-physiological active tensions will result. In these cases the limiting extension ratio values can be used in the evaluation of active tension – in effect, the maximal and minimal active tensions are capped at their values for the corresponding limiting extension ratio. A converged mechanics solution step is only accepted if the cellular extension ratio values throughout the solution domain are within the physiological limits.

Update cellular and activation material properties

Having completed the activation and mechanics solution steps we have a global activation and cellular solution for the time $t + \Delta t$ but with the deformation from time t and a new deformation solution based on the activation and cellular solution at time $t + \Delta t$. We now update the GBFE mesh to match the new deformed geometry and update the any activation model parameters dependent on geometry (*i.e.,* the conductivity tensor).

Local material strain in each of the material axes is calculated at each of the GBFE nodes and the cellular lengths are updated in line with the new deformation solution. If required,

the velocity of the length changes can also be calculated at each of the nodes from the change in length and the known time step (Δt). Similarly, the sheet and normal axial strains can be transfered to cellular fields for models which include mechanosensitive mechanisms dependent upon other forms of deformation. Membrane area or intracellular volume sensitive ion channels, for example, which are now attracting significant interest in this field (Barritt & Rychkov 2005).

Finally, the current time is incremented ($t = t + \Delta t$) and we return to the activation model solution step to solve for the next time interval.

3.3   Framework Validation

Previous work based on CMISS have presented simulation results using a steady-state tension-length-calcium relationship to provide an approximation of active tension in cardiac tissue (Hunter et al. 1997, Nash 1998, Stevens 2002). These investigations have provided the basis of a basic validation of the numerical implementation of the framework developed in this thesis. We now use the implementation of this tension-length-calcium relationship to compare simulation results with our framework to check the numerical results obtained from our framework. The CellML version of the steady-state tension-length-calcium relationship used in the following simulations is provided in Section A.19 and a description of the model is given in Section 2.5.6.

3.3.1   Tissue Cubes

We begin with possibly the simplest example of active contraction. A cube, measuring $4 \, \text{mm}$ on an edge, is initially at rest in an unloaded state. The calcium activation level is increased in a step-wise manner from the rest value of 0.0 to the fully activated state at 1.0. We compare here the results obtained from simulating the contraction of this cube using the previous implementation (Nash 1998) with those from the cellular based framework developed in this thesis.

With the cellular based model we compare the results obtained using four resolutions of cellular spatial discretization. The first resolution is one which overlays the underlying Gaussian quadrature points for the finite elasticity integration (Figure 3.8(a)) – this results in an identical model to the previous implementation, but now with the active mechanics equation defined via CellML. Then we use three different grid resolutions to confirm that the same solution can be

(a) Gauss points

(b) Coarse grid

(c) Medium grid

(d) Fine grid
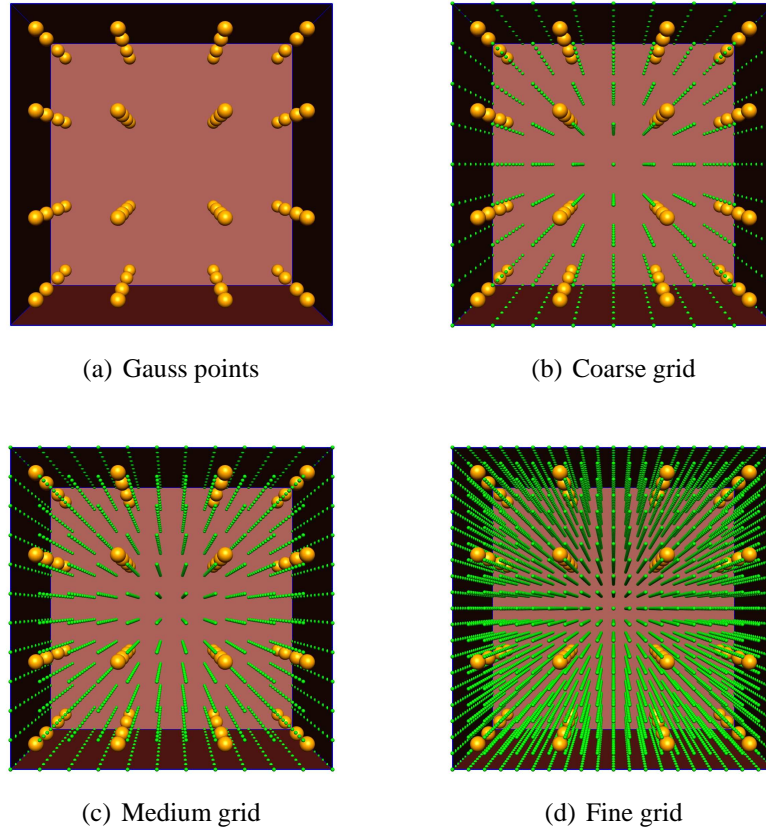
FIGURE 3.8: The five different configurations of a 4x4x4 mm cube of cardiac tissue. (a) shows the Gaussian quadrature points used in the solution of the finite elasticity model. The grid points for the lowest resolution grid lie on the same points in the element. (b)–(d) show the increasing grid resolutions used in the simulations. The coarse grid has an initial grid point spacing of 500 μm, the medium of approximately 364 μm, and the fine grid 200 μm.

obtained when interpolating the active tension from the grid points used in the GBFE used to solve the electrical activation model (Figures 3.8(b)–3.8(d)).

A homogeneous cube

The first simulation performed assumes that the tissue is an isotropic material. We use the pole-zero (Section B.3) material constitutive law with the same parameter values in the fibre, sheet, and sheet-normal directions (Table 3.1). While the material properties are isotropic, the fibre direction is used to specify the axis along which the active contraction occurs. In this simulation the fibres are aligned with the x-axis.

Parameter	Value
$a_{11} = a_{22} = a_{33}$	0.475
$k_{11} = k_{22} = k_{33}$	2.0 kPa
$b_{11} = b_{22} = b_{33}$	1.5

TABLE 3.1: The pole-zero material parameters used for the isotropic tissue cube model. These values correspond to the fibre-axis material parameters from Remme et al. (2004).

Results from this isotropic model, summarised in Figure 3.9, show that for this example an identical solution is achieved for both the original model and the cellular based version of the model, for all the different grid resolutions give the same solution (Figure 3.9(i)). Here we calculate the root mean squared (RMS) error as

$$RMS = \sqrt{\frac{\sum_{i=1}^{N}(G_i - g_i)^2}{N}}, \qquad (3.3.1)$$

where N is the number of nodes, G_i are the original method's deformation solution at each node i (including derivative information where appropriate), and g_i are the current implementation's solution at each node i.

We now repeat the same simulation using the orthotropic material parameters for porcine cardiac tissue (Remme et al. 2004). The material parameters are given in Table 3.2 and the fibre, sheet, and normal axes are aligned with the x, y, and z rectangular Cartesian axes respectively. A summary of the results from simulation of this orthotropic tissue cube model is presented in Figure 3.10. Results from the isotropic cube model are superimposed to illustrate the effect of the orthotropic material properties compared to the isotropic material.

Figures 3.9(h) and 3.10(g) nicely illustrate the combination of the pole-zero constitutive law with an incompressible material. As the sheet and normal extension ratios approach their pole values ($\sqrt{2*a_{ii}+1} \Rightarrow 1.396$ (isotropic) and $1.496, 1.699$ (sheet and normal, respectively, for orthotropic)), the tissue becomes stiffer resulting in a much reduced contraction in the fibre direction despite the increasing calcium level. With the homogeneous material and active mechanics the extension ratio changes are similarly homogeneous and the plots given in Figures 3.9(h) and 3.10(g) are identical at all points within the cube of tissue.

Notice the larger lateral expansion in the normal direction (z-axis) than in the sheet direction (y-axis) shown in Figures 3.10(a)–3.10(g) compared to the matching isotropic results in Figures 3.9(b)–3.9(h). Note also the greater fibre compression achieved at a given calcium ac-
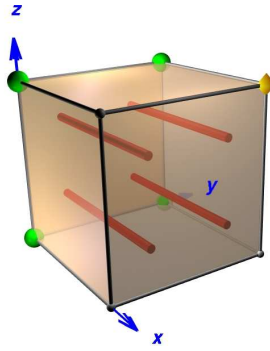
(a) Geometry and boundary conditions for this simulation. The nodes represented by the green spheres are fixed in the y-z plane and that represented by the gold diamond is restricted to slide along the x-axis. The solid cylinders indicate the material fibre axis.
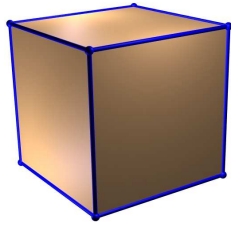
(b) $Ca = 0.0$
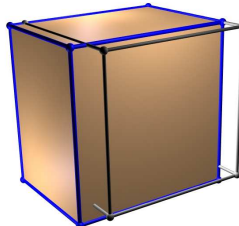
(c) $Ca = 0.2$
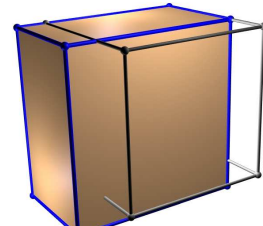
(d) $Ca = 0.4$
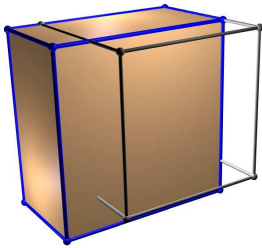
(e) $Ca = 0.6$
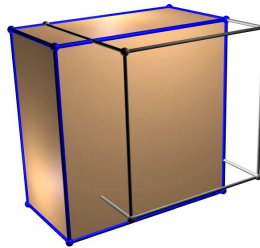
(f) $Ca = 0.8$
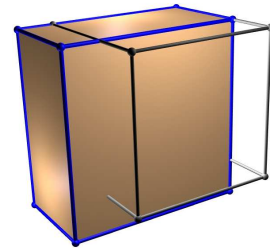
(g) $Ca = 1.0$
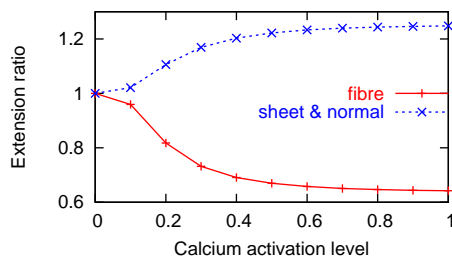
(h) Extension ratios *vs.* calcium activation.
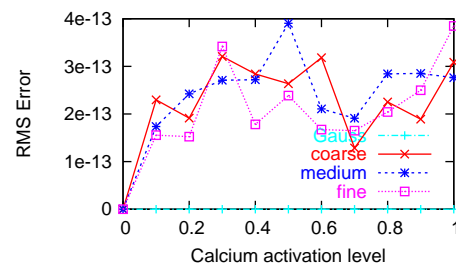
(i) RMS errors comparing the different grid schemes to the original Gauss point method.

FIGURE 3.9: Results from simulating the contraction of an isotropic 4x4x4 mm cube of cardiac tissue using the pole-zero constitutive law, with parameters given in Table 3.1, and the steady-state tension-length-calcium active mechanics model. Figures (b)–(g) are the deformed solutions for the specified calcium activation levels, with the initial geometry superimposed (silver lines). (h) plots the calculated extension ratios against the calcium activation level and (i) plots the RMS errors for the different model configurations.

(a) $Ca = 0.0$ (b) $Ca = 0.2$ (c) $Ca = 0.4$

(d) $Ca = 0.6$ (e) $Ca = 0.8$ (f) $Ca = 1.0$

(g) Extension ratios *vs.* calcium activation.

(h) RMS errors comparing the different grid schemes to the original Gauss point method.
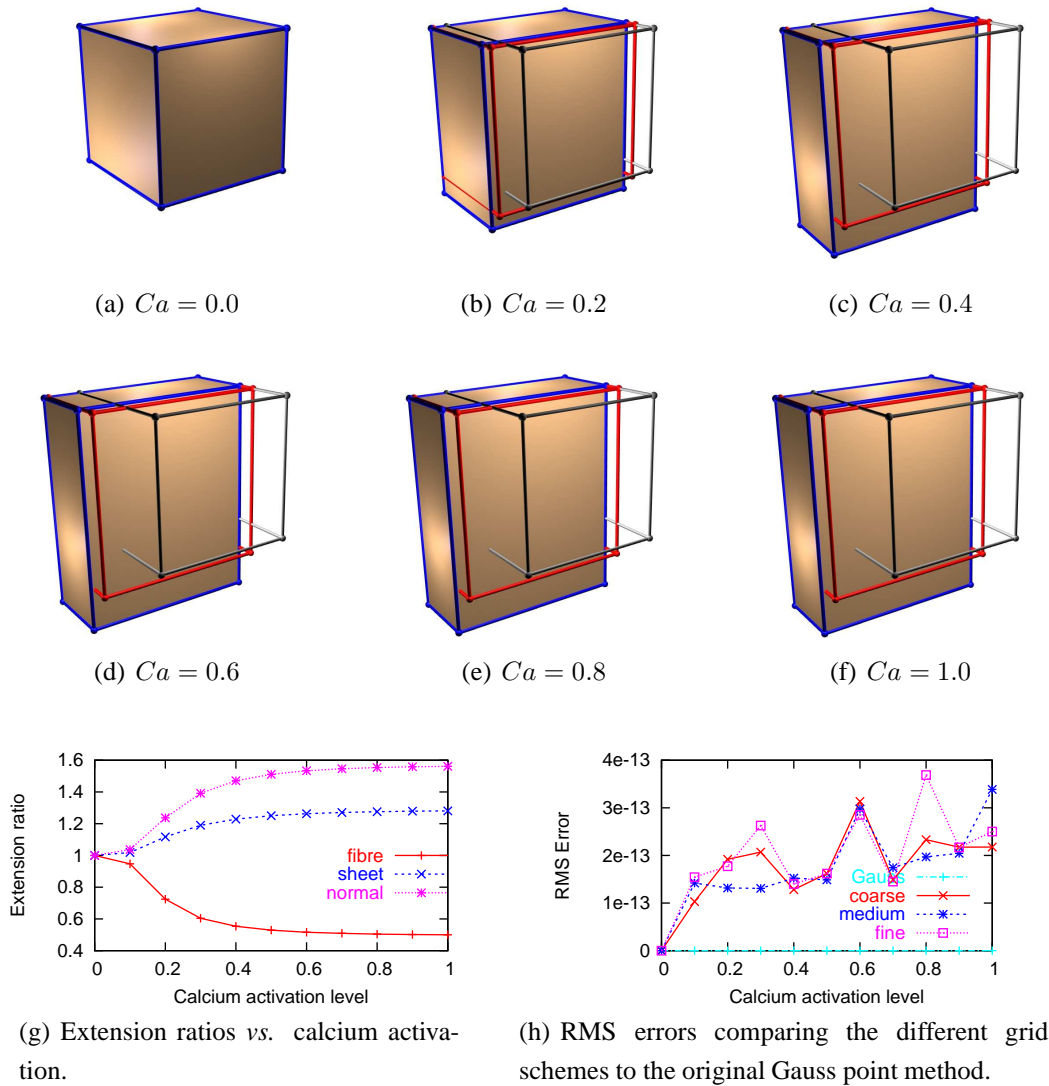
FIGURE 3.10: Results from simulating the contraction of an orthotropic 4x4x4 mm cube of cardiac tissue using the pole-zero constitutive law and the steady-state tension-length-calcium active mechanics model. Material parameters are given in Table 3.2. Initial geometry and boundary conditions are identical to those given in Figure 3.9(a). Figures (a)–(f) are the deformed solutions for the specified calcium activation levels, with the initial geometry (silver lines) and isotropic solutions (red lines) superimposed. (g) plots the calculated extension ratios in each of the three material axes against the calcium activation level and (h) plots the RMS errors for the different model configurations.

Material Axis	Parameter	Value
Fibre	a_{11}	0.475
	k_{11}	2.0 kPa
	b_{11}	1.5
Sheet	a_{22}	0.619
	k_{22}	2.0 kPa
	b_{22}	1.5
Normal	a_{33}	0.943
	k_{33}	2.0 kPa
	b_{33}	0.442

TABLE 3.2: The pole-zero material parameters used for the orthotropic porcine tissue cube model. These values are taken from Remme et al. (2004).

tivation level in the orthotropic model due to the increased expansion in the sheet and normal directions which are less stiff than in the isotropic model. We also note that mass is conserved as shown by the scalar product of the fibre, sheet, and normal extension ratios being equal to 1.0000 at all calcium activation levels.

The effect of fibre angles

We now alter the orthotropic cube model to include a realistic distribution of material fibre axes through the cube, as if the cube was taken from the ventricular wall. The distribution of material axes is illustrated in Figure 3.11(a), showing the rotation of the fibre axes from the epicardial surface through to the endocardial.

For an initial simulation, identical boundary conditions from the previous cube models (Figure 3.9(a)) are applied. As shown in Figures 3.11(b)–3.11(g), this results in some interesting deformation of the cube. Figure 3.11(h) provides an illustrative plot of the three axial extension ratios against the calcium activation level for a point near the initial centre of the cube. Due to the varying orientation of the material axes the deformation is no longer homogeneous and the extension ratio curves vary throughout the cube.

The deformation shown in Figures 3.11(b)–3.11(g) illustrates the large deformations that are possible when simulating the active contraction of a passive piece of tissue. As seen by the shortening of the fibre (red) arrows and lengthening of the sheet (green) and normal (blue) arrows, the material is contracting in the fibre direction and expanding in the other directions due to the incompressible nature of the material. Due to the changing orientation of the fibres the
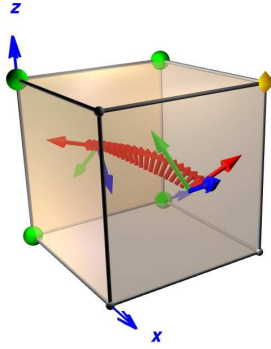
(a) Geometry used in this simulation. The red arrows are aligned with the fibre axis, the green with the sheet axis, and the blue with the normal axis. Larger arrows are shown on the 'epicardial' ($x = 0$) and 'endocardial' ($x = 4$) faces, and the rotation of the fibre axis through the wall is shown with smaller red arrows. Boundary conditions are identical to those in Figure 3.9(a).

(b) $Ca = 0.0$ (c) $Ca = 0.2$ (d) $Ca = 0.4$

(e) $Ca = 0.6$ (f) $Ca = 0.8$ (g) $Ca = 1.0$
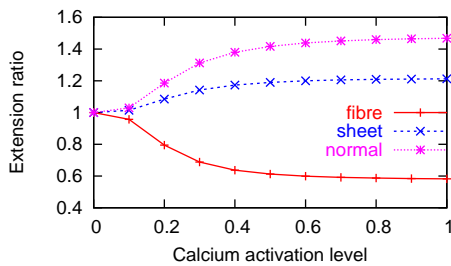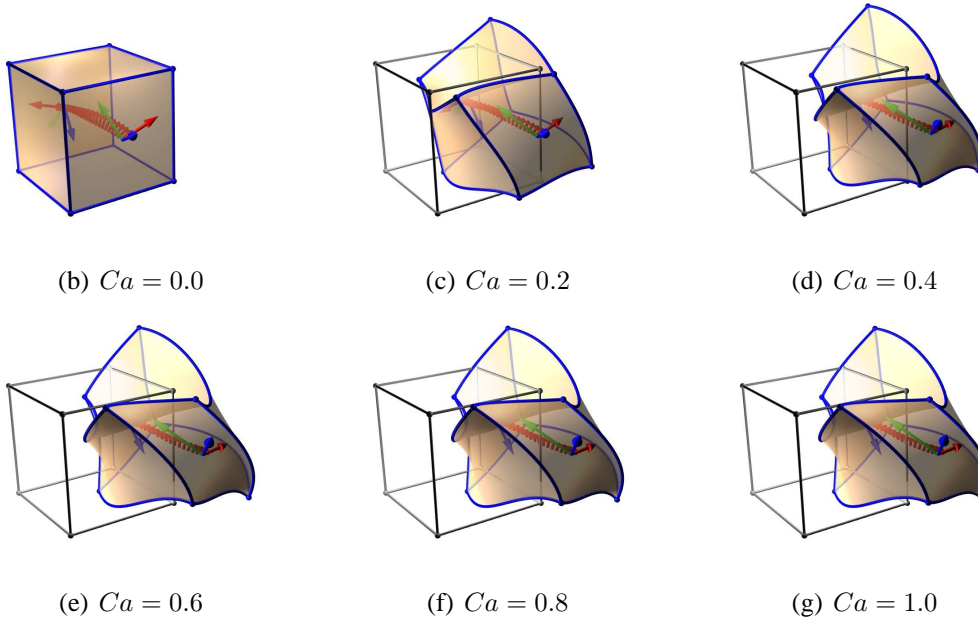
(h) Example extension ratios *vs.* calcium activation plot, taken from near the middle of the cube.
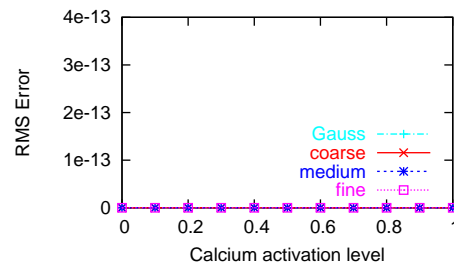
(i) RMS errors comparing the different grid schemes to the original Gauss point method.

FIGURE 3.11: Results from simulating the contraction of a 4x4x4 mm cube of cardiac tissue. The pole-zero material parameters used are given in Table 3.2. Figures (b)–(g) are the deformed solutions for the specified calcium activation levels, with the initial geometry superimposed (silver lines). (h) plots the calculated extension ratios against the calcium activation level and (i) plots the RMS errors for the different model configurations.

deformation is no longer homogeneous and the boundary conditions imposed on the model are perhaps less useful in terms of a real physiological problem. However, this simulation is only meant as a test of the implementation of the framework developed and we are more concerned in this case with being able to generate comparable results to those from the previous implementation. Once again, we note that conservation of mass is obeyed with the scalar product of the fibre, sheet, and normal extension ratios being equal to 1.0 at all calcium activation levels.

Figures 3.9(i) and 3.10(h) show that there are only very small (peak RMS $\sim 10^{-13}$, Equation (3.3.1)) differences between the deformations calculated using each of the grid based methods compared to the original model implemented in CMISS. Figure 3.11(i) shows no difference between all the grid based methods and the original method implemented. This shows that for these three, relatively simple, examples we can be confident that the new method based on CellML we have implemented in CMISS is capable of reproducing the results of the previous implementation. We now continue the evaluation of the implemented framework with a geometry and boundary conditions a bit closer to those of the heart.

3.3.2 A Ventricular Doughnut

Having gained a measure of confidence that the implementation of the framework developed in this thesis works for fairly simple models, we now test it further. The next model we test continues the use of the steady-state tension-length-calcium relationship used in the previous section and detailed in Section 2.5.6. We use this model of active tension in a doughnut shaped geometry representative of a section of a rat LV near the basal plane. The geometry used in the following models is presented in Figure 3.12.

In all the following simulations we use the same base set of mechanical boundary conditions, as described in Figure 3.12. The boundary conditions hold the "base" of the ventricular section in its initial geometry in the basal plane. This is representative of the connection between the basal skeleton of the ventricle with the rest of the body, which is assumed to remain unmoved during the contraction of the heart.

As with the above cube models, we compare the simulation results obtained from four different grid resolutions with those obtained from the original implementation of the model (Nash 1998). The four grid resolutions are illustrated in Figure 3.13 with a close-up view of two of the elements in the doughnut.
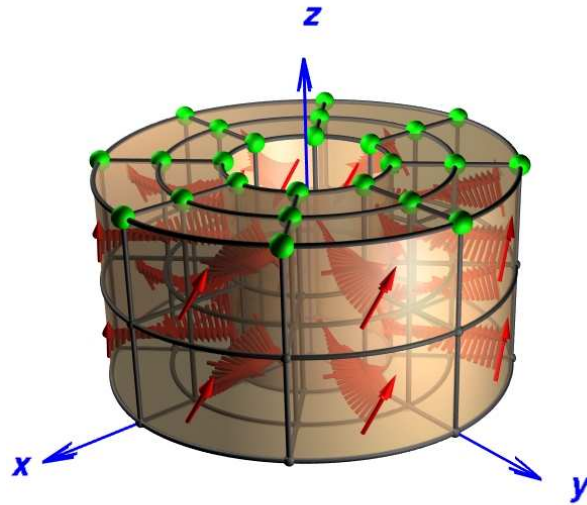
FIGURE 3.12: The geometric mesh of a doughnut shaped piece of cardiac tissue used in validation of the implementation of the simulation framework developed in this thesis. The inner diameter of the torus is 4 mm and the outer is 10 mm, with a height of 5 mm. The red arrows indicate the direction of the tissue fibres, rotating from $+60°$ at the epicardial surface through to $-60°$ on the endocardial surface (relative to the horizontal plane). Mechanical boundary conditions applied to this model fixed the coordinates of the basal nodes (green spheres) and also fixed the in-plane derivatives of these nodes.

Active contraction

The first model of the doughnut ventricular geometry given in Figure 3.12 simulates active contraction of the tissue using the steady-state tension-length-calcium relation. We assume all the tissue is activated at the same time and the calcium activation level is increased in a stepwise manner. The only boundary conditions are those described in Figure 3.12.

Figure 3.14 summarises the results obtained from this model. These results show the expected twist and wall thickening associated with contraction of the ventricular wall during normal cardiac rhythm.

As with the previous cube models we simulate the contraction using both the original implementation and several versions of the CellML based implementation using different resolutions for the GBFE (Figure 3.13). Comparisons of the deformation solutions for each of the different grid resolutions to those of the original implementation show the solutions are identical, with an RMS error of 0.0 (Equation (3.3.1)) for all grid resolutions (see Figure 3.11(i)).

(a) Gauss-based grid

(b) Coarse grid

(c) Medium grid

(d) Fine grid
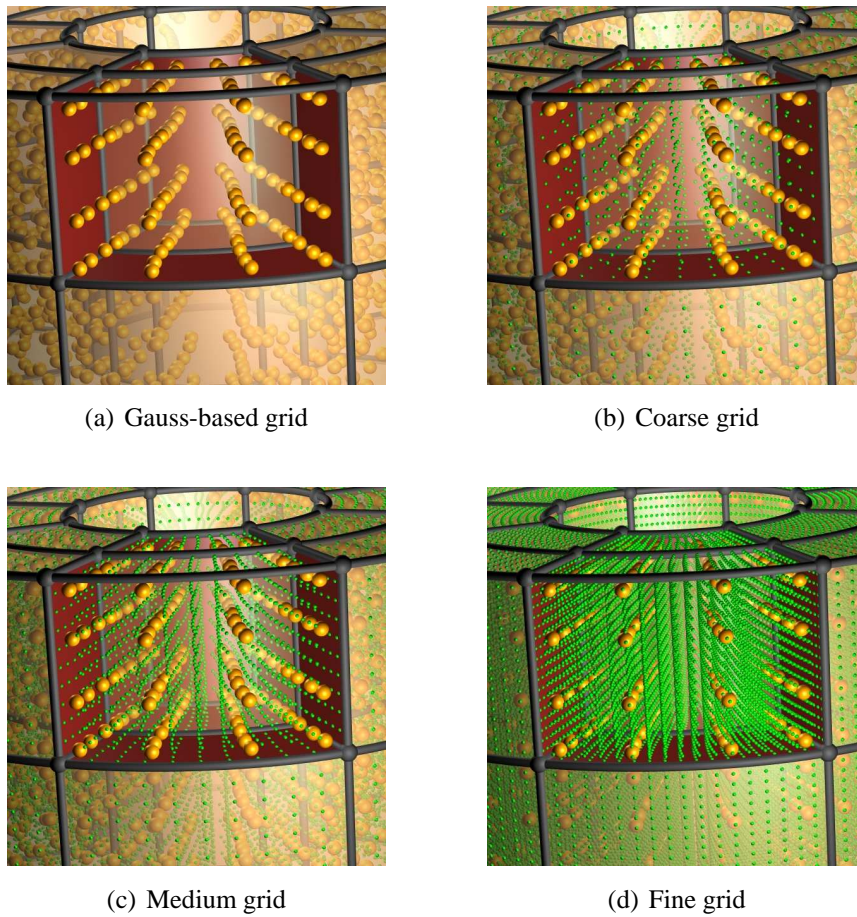
FIGURE 3.13: The five different configurations of the doughnut model shown in Figure 3.12. (a) shows the Gaussian quadrature points used in the solution of the finite elasticity model. The grid points for the lowest resolution grid lie at the same points in the elements. (b)–(d) show the increasing grid resolutions used in the simulations. The coarse grid has an average initial grid point spacing of 341 μm (9792 grid points), the medium of 245 μm (25200 grid points), and the fine grid 138 μm (133200 grid points).

(a) $Ca = 0.00$

(b) $Ca = 0.25$

(c) $Ca = 0.50$

(d) $Ca = 0.75$

(e) $Ca = 1.00$
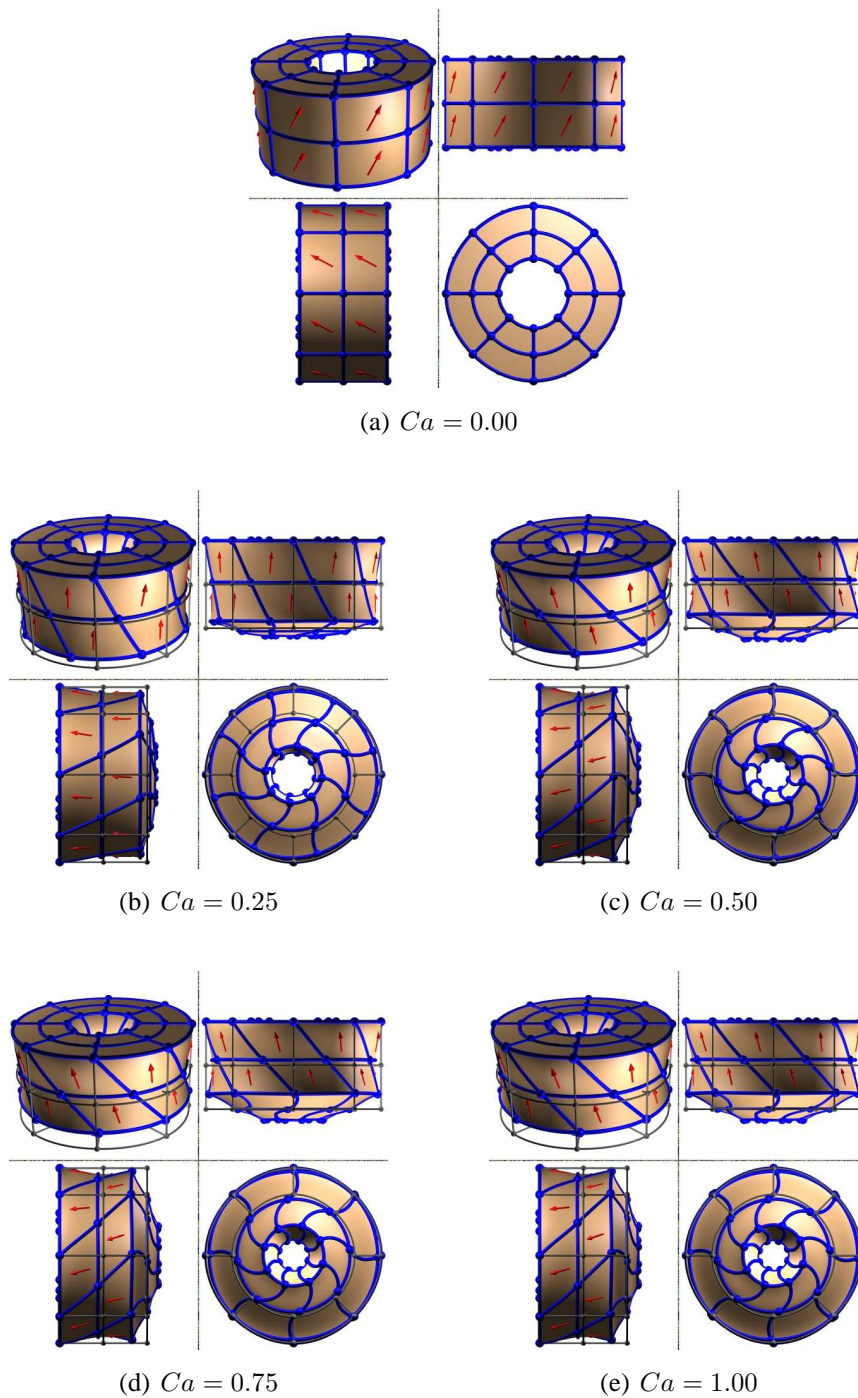
FIGURE 3.14: Results from simulating active contraction of the doughnut ventricular section. The red arrows indicate the deforming fibre directions on the epicardial surface of the model and figure captions give the corresponding calcium activation level. Boundary conditions are shown in Figure 3.12.

Application of a pressure boundary condition

The first phase of the cardiac cycle is the passive inflation of the LV as the ventricular cavity fills with blood. This is simulated in the doughnut model through the application of a pressure boundary condition to the endocardial surface of the doughnut. This has the effect of stretching the fibres before contraction begins.

Figure 3.15 presents the results of a simulation where the doughnut ventricular geometry is first inflated to a cavity pressure of 1.0 kPa and then allowed to freely contract using the same steady-state tension-length-calcium active tension model used above. As shown in this figure, the initial contraction is quite different from the non-inflated model (Figure 3.14). As the calcium activation level increases, however, the two models converge to the same solution as the active tension begins to have greater influence on the deformation than the applied pressure boundary condition. This is shown in Figure 3.15 by the merging of the blue and red lines as Ca approaches 1.0.

Like the previous doughnut model, all the different grid resolutions (Figure 3.13) result in identical deformations as the original model implementation. The RMS difference between the different implementations is 0.0, as calculated by Equation (3.3.1).

Isovolumic contraction

Following the passive inflation of the LV in the cardiac cycle, there is the period during which the excitation wavefront passes through the tissue and the ventricular wall begins to contract (Figure 5.2). During this period the pressure in the LV cavity increases until it overcomes the aortic impedance and blood begins to flow out through the aortic valve. This period before the opening of the aortic valve is known as isovolumic contraction.

We model this period in the doughnut by coupling a cavity volume region to the ventricular wall (Section 5.1.2). This allows for the solution of the pressure required to be applied to the ventricular wall to keep the cavity at a constant volume. Figure 3.16 provides some results from the isovolumic contraction of the doughnut following an initial inflation to a cavity pressure of 1.0 kPa.

While the results shown in Figure 3.16 continue significantly above the range of physiological pressure experienced by a normal ventricle, they serve the purpose of testing the im-

(a) $Ca = 0.00$

(b) Inflated to 1.0 kPa

(c) $Ca = 0.25$

(d) $Ca = 0.50$

(e) $Ca = 0.75$

(f) $Ca = 1.00$
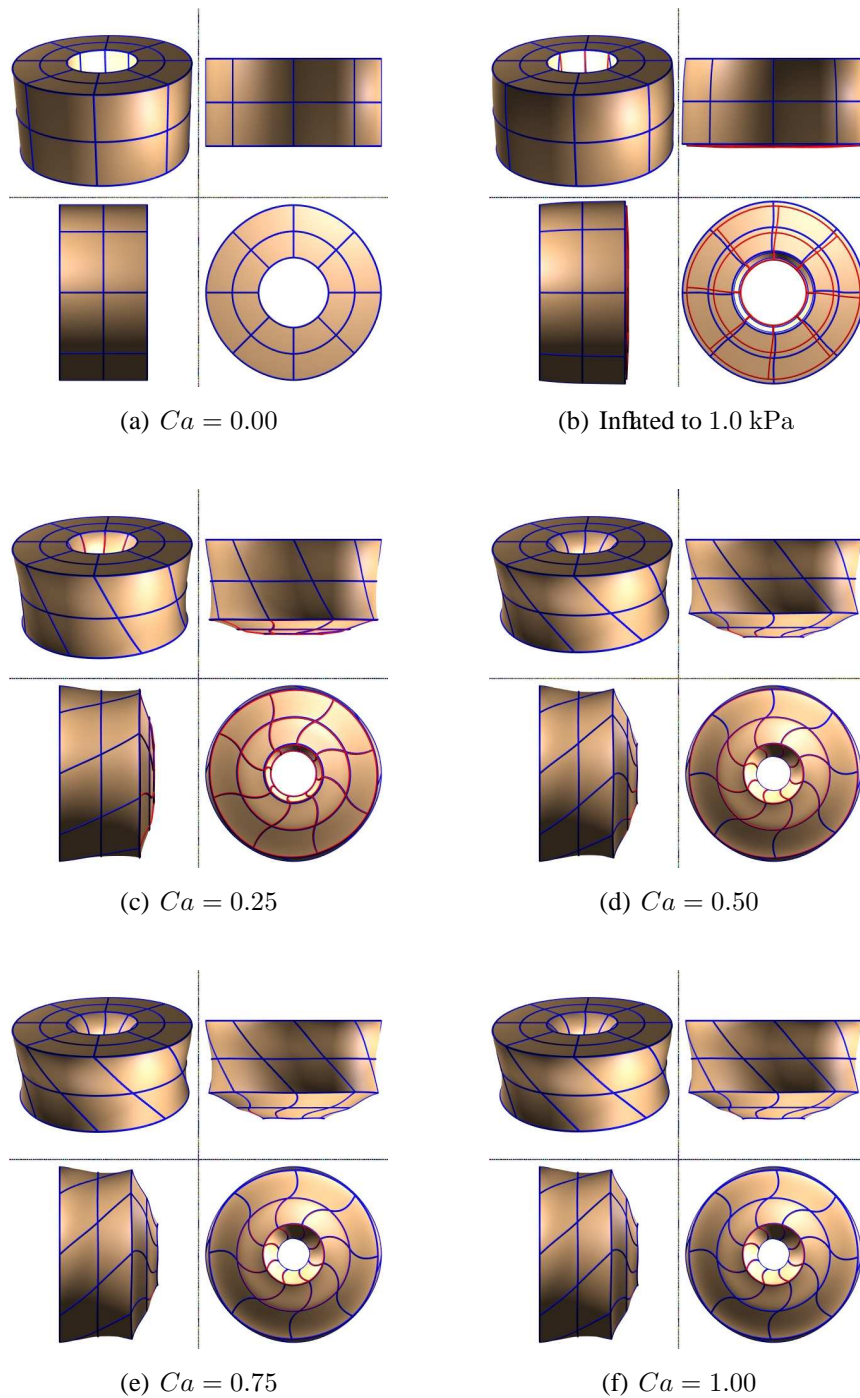
FIGURE 3.15: Results from simulating active contraction of the doughnut ventricular section following an initial inflation to a cavity pressure of 1.0 kPa. Displacement boundary conditions are shown in Figure 3.12. The red lines are the contraction solutions from Figure 3.14.

(a) $Ca = 0.0$ (b) Inflation to 1.0 kPa

(c) $Ca = 0.4 \rightarrow 21$ kPa   (d) $Ca = 0.6 \rightarrow 40$ kPa

(e) $Ca = 0.8 \rightarrow 51$ kPa   (f) $Ca = 1.0 \rightarrow 56$ kPa
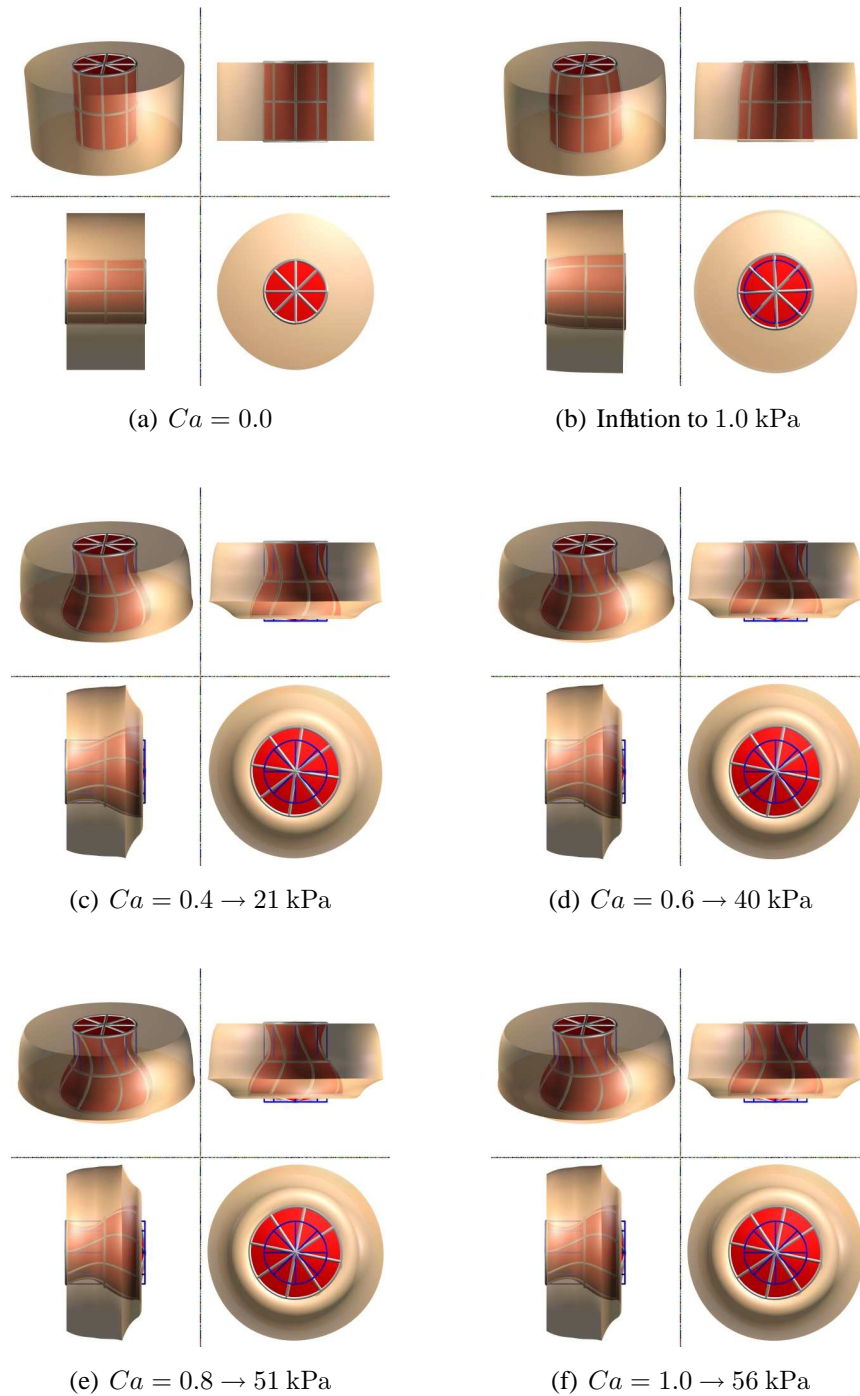
FIGURE 3.16: Results from simulating isovolumic contraction of the doughnut ventricular section following an initial inflation to a cavity pressure of 1.0 kPa. Displacement boundary conditions are shown in Figure 3.12. Red surface and silver lines show the deforming ventricular cavity mesh with the initial cavity mesh shown by the blue lines. The specified pressures are the cavity pressure for each calcium activation level.

plementation of the cellular based framework. For these results, we again see that the cellular based models achieve identical deformations compared to the original active contraction model implementation (Nash 1998). The RMS error from this comparison for all calcium activation levels and all the grid resolutions (Figure 3.13) is 0.0 (Equation (3.3.1)).

3.3.3   Summary

We have used the above cube and doughnut models to illustrate that the implementation of the cellular based framework developed in this thesis for active mechanics is capable of giving solutions quantitatively identical to those of the original implementation. These models have been used only to test the implementation under conditions similar to those expected to be found in various parts of more physiologically and anatomically based models.

In a departure from what has been previously possible in CMISS, we now examine the performance of the implemented framework with true models of coupled electro-mechanics. We first use a simplified cellular model to aid in the understanding of the ability and performance of the framework. This is followed by a model using a biophysically based cellular model to ensure that the framework is capable of handling the detailed and complex cellular models that are required to capture the behaviour necessary for some pathological conditions.

3.4   Cardiac Electro-Mechanics in a Cube

Having established confidence in the implementation of the simulation framework we have developed, we now test the ability of the framework with a real coupled model of cardiac electro-mechanics. The model presented here is the simple cube model (Figure 3.9(a)) using the orthotropic material parameters given in Table 3.2 and the tissue monodomain material properties are shown in Table 3.3. This simple geometric model is used to allow the understanding of the performance of the cellular models, material constitutive law, and the simulation framework without the complex behaviour of varying fibre axes and anatomically based geometry. Chapter 5 presents models which include these and other complexities with results from the simulations run with these models.

In this model the active contraction of the tissue is now driven by the propagating wave of electrical excitation initiated by the application of a stimulus current. This results in non-

uniform deformation throughout the cube dependent on the state of electrical activity in that region of tissue. To be able to resolve this deformation within the given convergence criteria, the geometric finite element mesh needed to be refined. The refined geometry is given in Figure 3.17 with the applied mechanical and electrical boundary conditions also shown.

(a)   (b)
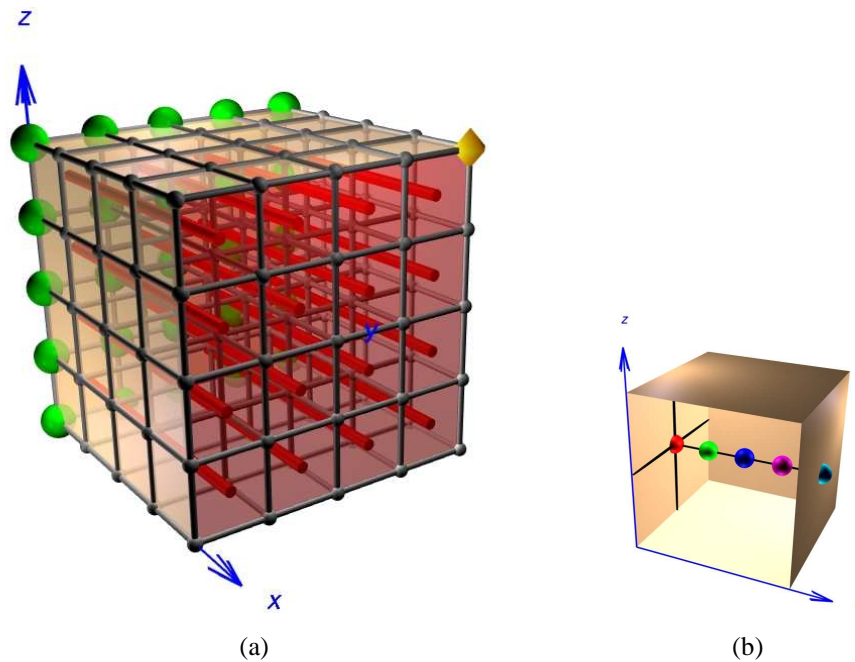
FIGURE 3.17: (a) shows the geometry and boundary conditions used for the cardiac cube model. The overall cube measures 4x4x4 mm, consisting of 64 unit cubes. The nodes represented by green spheres are fixed in the y-z plane and that represented by the gold diamond is restricted to slide along the x-axis. The solid cylinders within the cube indicate the fibre orientation. An electrical stimulus is applied on the $x = 4$ face, indicated by the red face of the cube. (b) provides the spatial locations for the cellular transients to be presented.

3.4.1 FK-HMT

We first test our framework using the epicardial version of the simplified FK-HMT cardiac cellular electro-mechanics model (Section 3.1.1). An electrical stimulus current of $150 \ \mu\text{A} \cdot \text{mm}^{-3}$ is applied with a duration of 1 ms and a period of 1000 ms, as illustrated in Figure 3.17. A summary of the results of this simulation is presented in Figure 3.18.

As shown by the cellular transients in Figure 3.18(d), the simulation results shown in Figure 3.18 are for the second contraction/relaxation cycle. This illustrates, at least for this model,

(a) $1000 \rightarrow 1080$ ms

(b) $\rightarrow 1220 \rightarrow 1300$ ms

(c) $\rightarrow 1400 \rightarrow 2000$ ms

(d) Cellular transients.
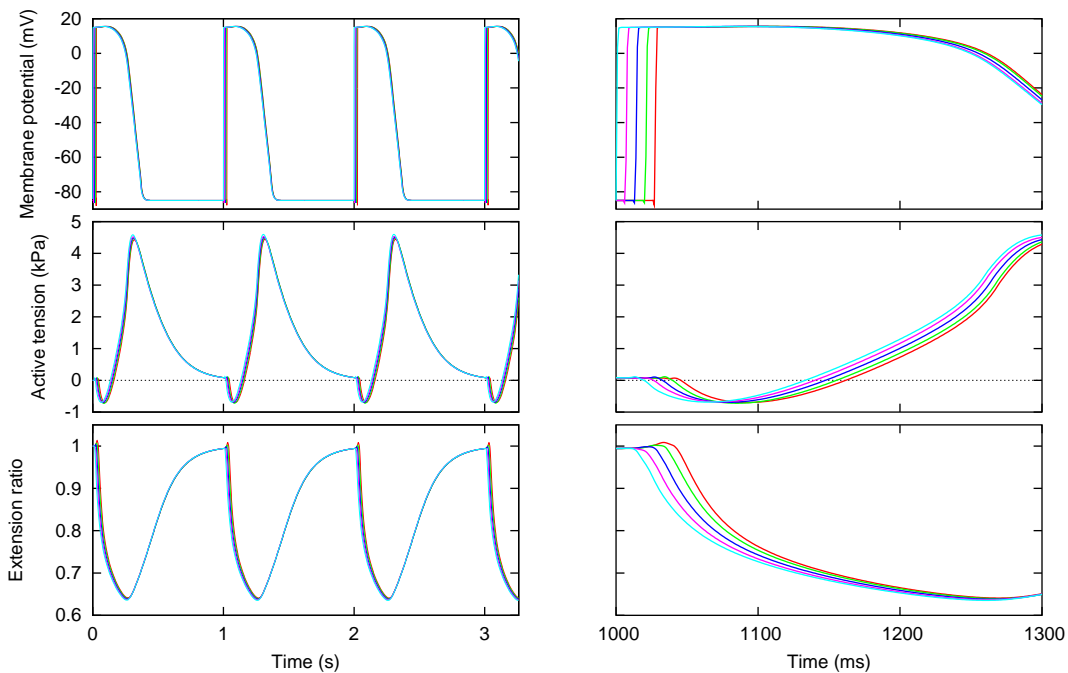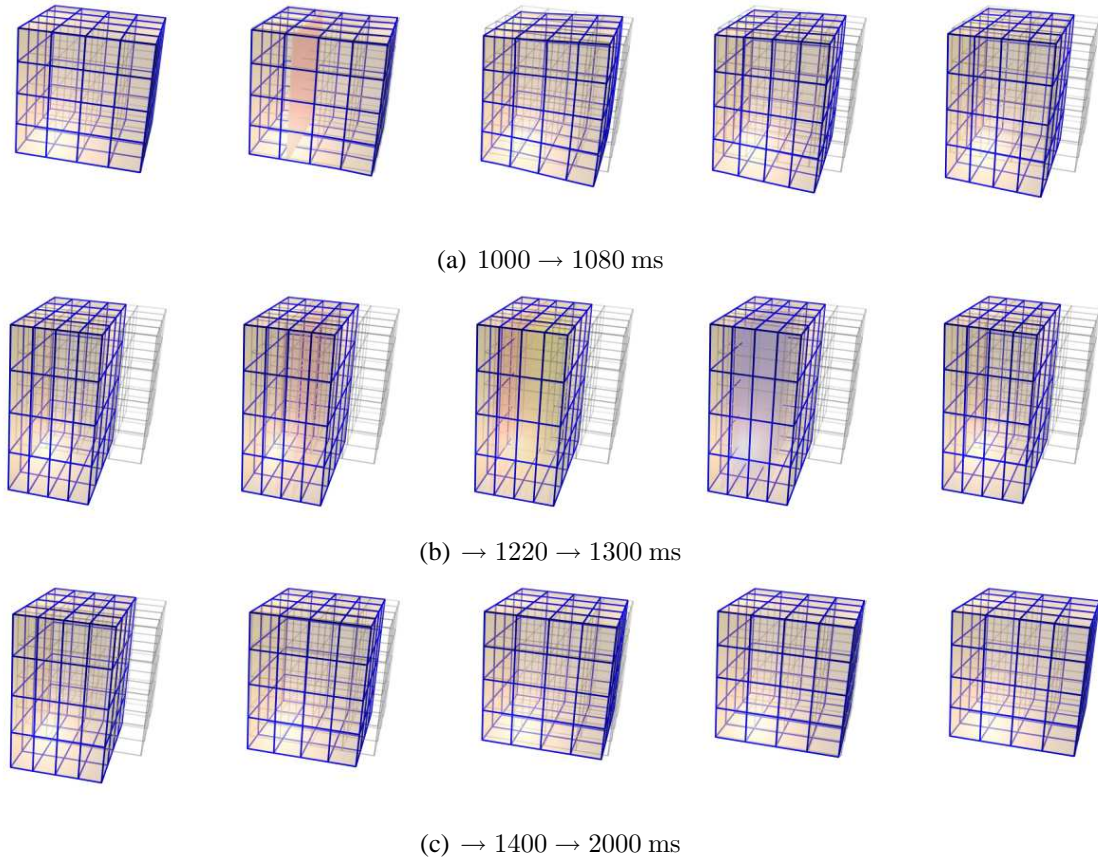
FIGURE 3.18: A sample of the simulation results from the FK-HMT based cube electro-mechanics model (with the epicardial material parameters). (a)–(c) show the deformation solutions in 20 ms (a,b) and 150 ms (c) time steps with transmembrane potential iso-surfaces passing through. (d) provides plots of three cellular parameters at the spatial locations indicated by the matching coloured sphere in Figure 3.17(b). See text for full description and Section D.3 for an animation of the simulation.

Material Axis	Parameter	Value
Fibre	σ_{11}	$0.01\,\text{mS} \cdot \text{mm}^{-1}$
Sheet	σ_{22}	$0.003\,\text{mS} \cdot \text{mm}^{-1}$
Normal	σ_{33}	$0.0015\,\text{mS} \cdot \text{mm}^{-1}$

TABLE 3.3: The orthotropic material parameters for the monodomain activation model in a cube. σ_{ii} are the intracellular conductivities in the given material axis.

that the framework is capable of simulating repetitive cycles. The coloured surfaces passing through the cube in Figures 3.18(a) and 3.18(b) represent the membrane potential range of $-15- + 5$ mV. The sharp activation wavefront appears in only one of the frames compressed into a barely discernible plane which is red (5 mV) on one side and blue (-15 mV on the other. The more dispersed repolarisation wave is more easily observed in several of the frames in Figure 3.18(c).

Figure 3.18(d) provides plots of membrane potential, active tension, and extension ratio for the five locations shown by the coloured spheres in Figure 3.17(b). The extension ratio plot illustrates the stretching that occurs within the tissue as the cube begins to contract in a spatially distributed manner. As the stimulated face of the cube begins to contract first the still passive tissue near the mechanically fixed boundary is stretched by the forces applied to it by the contraction of the active tissue. The closer the tissue is to the fixed boundary, the longer the period before the onset of contraction, and the more it is stretched. Despite these mechanical differences, the action potentials clearly show no effect of this stretching (or contraction), highlighting the lack of any mechano-electric feedback in the FK-HMT model. The slight differences observable in the action potentials from the different spatial locations can be attributed to the changing electrical diffusion properties of the tissue as the material shortens along the fibre axis while lengthening along the sheet and normal axes.

These results show the activation wave progressing with a finite velocity ($0.145\,\text{mm} \cdot \text{ms}^{-1}$) through the tissue, whereas the repolarisation wave is much more dispersed with the repolarisation phase of the cellular APs virtually indistinguishable (Figure 3.18(d)). This is followed by the tension and extension ratio transients, where the only significant differences at the cellular level are shown in the activation phase. Both sets of transients closely match between points through the cube during recovery to the resting state.

The simulation in Figure 3.18 used the algorithm described in Section 3.2.2 with the dynamic active tension (see the activation solution step in Section 3.2.2). Figure 3.19 shows a

comparison between this simulation and one performed using the non-dynamic active tension for the entire simulation (assumes a constant and homogeneous shortening velocity of 0). The
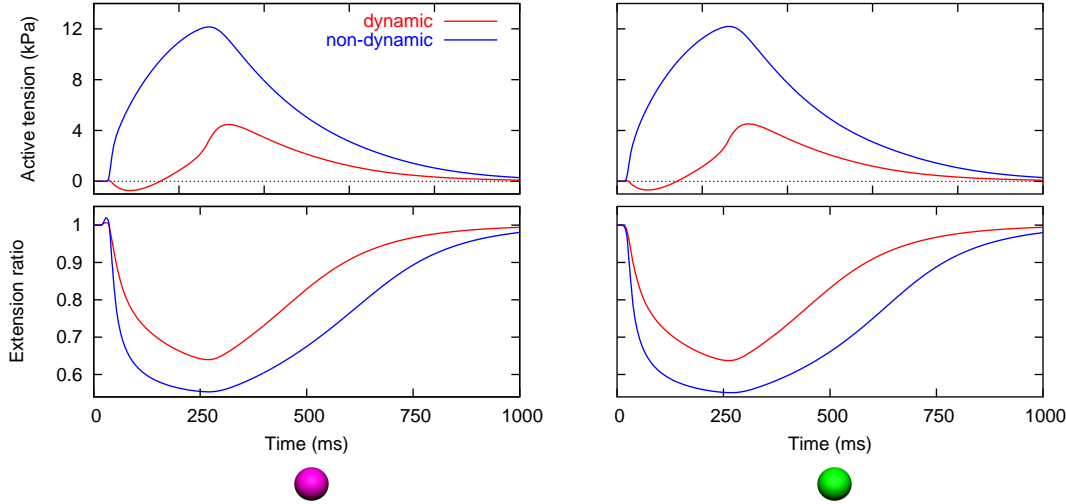
FIGURE 3.19: Comparison of the dynamic and non-dynamic active tension models (Section 3.2.2) at two spatial locations in the cube. The active tension and extension ratio transients are for the magenta (left) and green (right) cells shown in Figure 3.17(b).

dynamic tension uses the velocity history in the calculation of active tension and displays a prominent dip below zero for all the cells shown in Figures 3.18(d) and 3.19. The negative active tension indicates that the muscle tissue is shortening faster than the maximum shortening velocity of the cells, given in its simplest form and ignoring the high order rate constants by

$$\dot{\lambda}_{max} = \frac{\alpha_1}{aA_1}. \tag{3.4.1}$$

We initially suspected that the dip into negative active tension was a convergence issue with the use of active tension at the Gauss points smearing out the sharp wavefront shown in the GBFE domain (the cellular level of the model). This could result in more contraction than would be the case if the exact active tension at the cells was driving the contraction. Upon further investigation, however, we found this not to be the case. Refining the geometry to the point where the Gauss points were of a similar resolution as the GBFEs provided evidence that we did have a converged solution and that the dip is a real feature of the model rather than simply a numerical artifact. This leads to the material parameters of the three constituent component models (cellular, electrical activation, and finite elasticity). The material parameters for each of these components have largely been established in isolation from the others and few are based on a common animal species or tissue preparation. A mismatch in any of the model material parameters would explain the apparently overly rapid shortening of the tissue

in these simulations. In particular, the dynamic active tension at the cellular level needs to be matched to the passive elasticity at the tissue and organ levels. We discuss these issues further in Sections 6.1 and 6.2 but continue here with the existing material parameters. It is also worth noting that this is the first time the velocity dependent dynamic aspects of the HMT model have been incorporated into tissue models and these results suggest that further investigation of the cellular material parameters is required. A further point to note is that the model lacks any viscous damping, which has been found to significantly slow unloaded shortening (de Tombe & ter Keurs 1992). This suggests that inclusion of viscous damping may remove the negative dip in active tension.

3.4.2 N-LRd-HMT

Following successful demonstration of our modelling framework in a cube model using a fairly simple cellular model we now test the framework with the significantly more complex N-LRd-HMT cellular model. Like the simulation presented above, we are using the epicardial version of the N-LRd-HMT cellular electro-mechanics model. The cube is identical to that in the FK-HMT model with the only change being to increase the stimulus current to $250\,\mu\text{A}\cdot\text{mm}^{-3}$. A selection of results from this simulation are presented in Figure 3.20.

As with the results shown in Figure 3.18 for the FK-HMT based model, the initial activation wave passes through the cube very rapidly with all the membrane potential iso-surfaces compressed into a single plane. The epicardial N-LRd-HMT based model, however, has an AP profile with a spike-and-dome morphology. This morphology is shown in the simulation results by a more dispersed set of iso-surfaces passing through the cube following the initial activation wavefront as the cellular potentials drop back through the $-15-+5\,\text{mV}$ range of the iso-surfaces. The final set of iso-surfaces are even more dispersed and illustrate the repolarisation wavefront.

Comparing the cellular transients in Figure 3.20(d) with those in Figure 3.18(d), there are clear differences. While the most significant differences between the transients in Figure 3.20(d) occur during the initial electrical and mechanical activation there are also differences in the recovery phase. This is in contrast to the transient from the FK-HMT simulation in Figure 3.18(d) where the transients merge together as the cube returns to rest.

(a) $10 \rightarrow 50$ ms

(b) $\rightarrow 60 \rightarrow 100$ ms

(c) $\rightarrow 200 \rightarrow 600$ ms
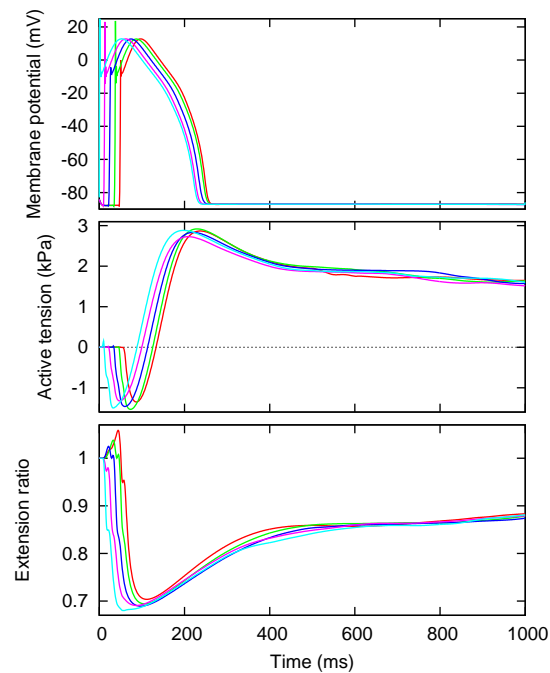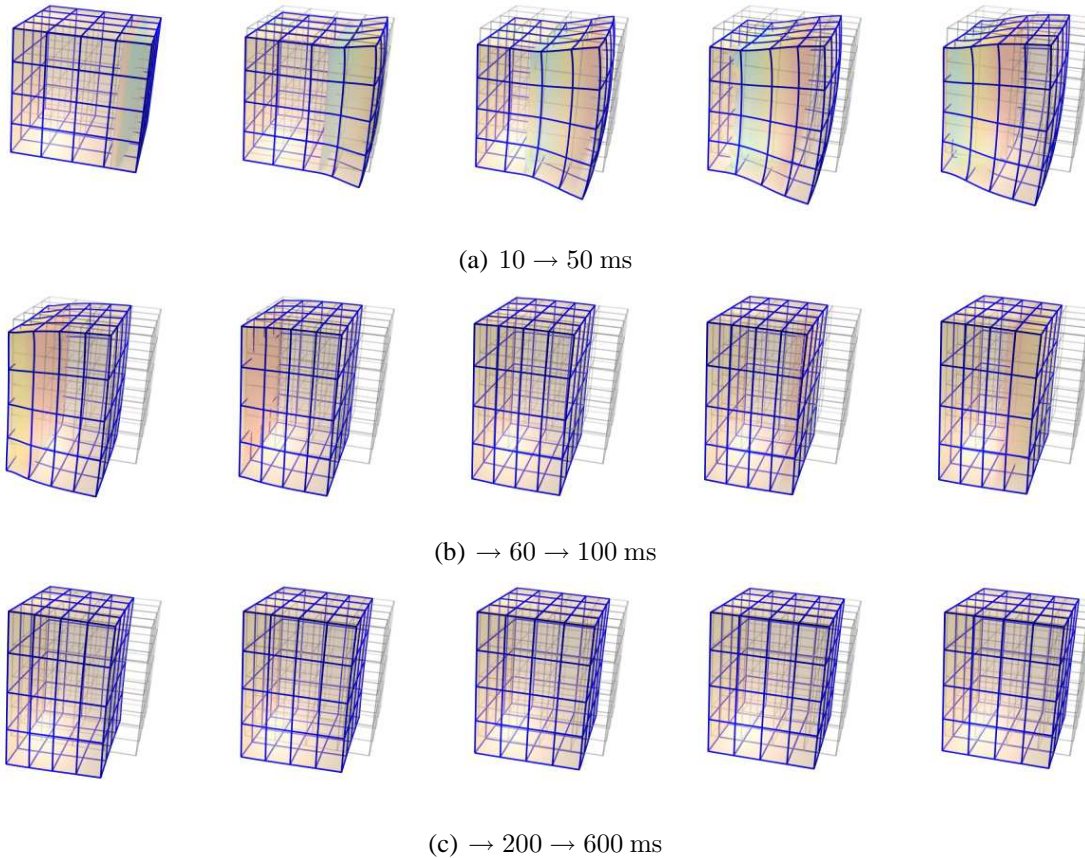
(d) Cellular transients.

FIGURE 3.20: A sample of the simulation results from the N-LRd-HMT based cube electro-mechanics model. (a)–(c) show the deformation solutions in 10 ms (a,b) and 100 ms (c) time steps with transmembrane potential iso-surfaces passing through. (d) provides plots of three cellular parameters at the spatial locations indicated by the matching coloured sphere in Figure 3.17(b). See text for full description.

3.4.3   Computational Performance

The models described in Sections 3.4.1 and 3.4.2 are very computationally demanding to solve, requiring a high performance computer for the numerical simulations. We performed these simulations on an IBM Regatta P690, consisting of 32 1.3 GHz Power 4 processors with 32 GB of physical memory. We present here a summary comparison of the computational cost of the two models given in Sections 3.4.1 and 3.4.2 over interval of the first 1000 ms simulation time.

Figure 3.21 plots the memory requirements for the two models over the first 100 ms of simulation time. This figure shows that the required memory initially climbs, but quickly reaches a plateau which is relatively constant for the remainder of the 1000 ms simulation. The FK-HMT based cube model plateaus at approximately 545 MB memory required while the N-LRd-HMT model requires three times that amount of memory with a plateau around 1.5 GB. This is a number which indicates the current implementation of our modelling framework based in CMISS is going to be extremely memory intensive as we move toward organ level models using a complex model like the N-LRd-HMT . After all, these simulations are for a 4x4x4 mm cube of tissue with a GBFE mesh resolution of 0.125 mm consisting of only 35, 937 nodes.
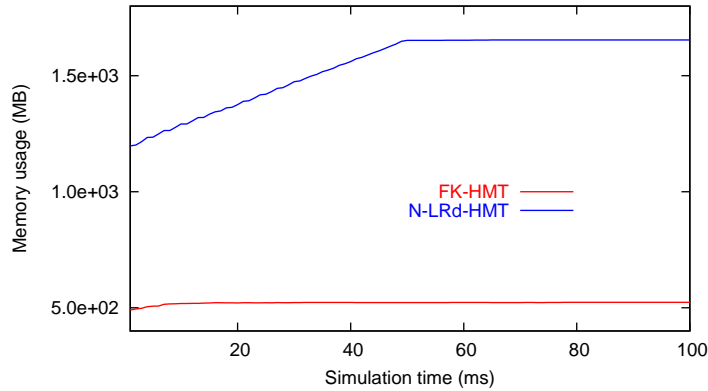
FIGURE 3.21: Comparison of the memory requirements for the FK-HMT and N-LRd-HMT based cube electro-mechanics models.

In Figure 3.22 we present a breakdown of the time taken in each of the cube models for the different steps in the solution algorithm (Figure 3.6). The three steps are: the update step, where the electrical activation model is updated from the deformed finite elasticity model; the activation model solution step; and the finite elasticity mechanics solution step.

Figure 3.22(a) presents the comparison of wall clock times for each of the models and Figure 3.22(b) compares the actual computational time (CPU), for each of the 1 ms solution intervals. The wall clock time is the actual *real world* time taken to run the simulation and the

computational time is the amount of time the process takes to run. The computational time is generally much larger since we are using multi-threaded software capable of running on more than one processor and the computational time is the sum over all the processors used in the simulation. The ratio of computational time to wall time can be used as a measure of the speed increase obtained by using multiple processors.

(a)

(b)
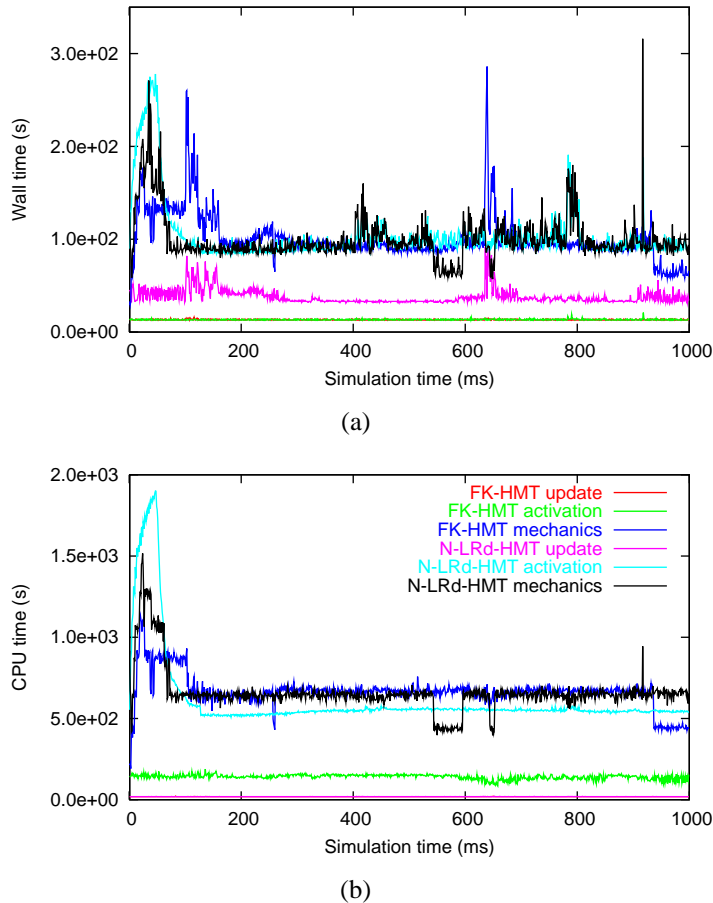
FIGURE 3.22: Comparison of the computational time for the FK-HMT and N-LRd-HMT based cube electro-mechanics models. (a) shows the comparison of wall clock times and (b) the actual computational times for each of the 1 ms solution intervals over an entire 1000 ms simulation. The same key is used in both graphs. See text for full description.

The FK-HMT cube simulation (Section 3.4.1) was performed using twelve processors on the IBM Regatta machine and the N-LRd-HMT simulation (Section 3.4.2) used eight processors. The plots shown in Figure 3.22 appear quite noisy due to the large dependence of these times on the load on the computer at the time of the simulation. This computer is a shared resource and as such there are numerous users running simulations and performing other tasks on the machine at any time, leading to a high load on the machine. The brief periods when the computational

times show sudden dips or increases can be attributed to the machine load changing for some unrelated reason rather than anything to do with the cube model simulations.

A clear illustration of the numerical complexity of the N-LRd-HMT model is provided by the huge peak in the activation model solution time in both Figures 3.22(a) and 3.22(b) during the first 150 ms of the simulation. This peak corresponds to the activation wavefront passing through the tissue electrically and mechanically activating all the cells in the model. The activation kinetics of the N-LRd-HMT cellular model are represented via a very stiff system of ODEs requiring far more time to numerically integrate than the recovery kinetics.

Figure 3.23 provides the cumulative total times for both models over the full 1000 ms simulation, again separated into the three components of the solution algorithm. Here the difference between computational and wall clock time is highlighted. As one would expect, the update times for both models shows no significant difference and has very little difference between wall clock and computational time (an obvious, but perhaps insignificant, area for improvement in implementation).
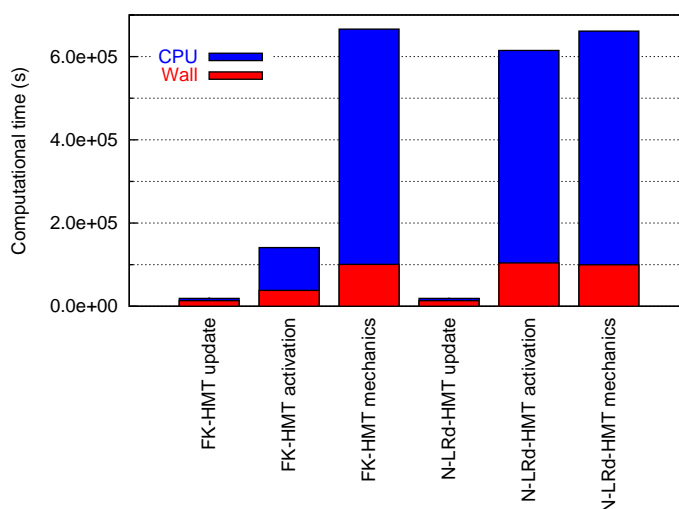
FIGURE 3.23: Comparison of the total computational times for the FK-HMT and N-LRd-HMT based cube electro-mechanics models. See text for full description.

The solution of the electrical activation model for the FK-HMT based model shows a 3.7 speed-up between total wall clock time and total computational time. The N-LRd-HMT based model has a 5.9 speed-up. Ideally we would want the speed-up factor to be close to the number of processors used in each of the simulations – 12 for the FK-HMT model and 8 for the N-LRd-HMT model. The activation model solution at each time involves two parts: the solution of a system of linear equations and the integration of the cellular model. The solution of the linear

equations requires the non-parallelised initial matrix assembly at each time step and will be the same for both models. Integration of the cellular model, however, is ideally suited to massive gains through the use of multiple processors. The total speed-up for a given activation step, therefore, will be dominated by the cellular model integration if the cell model is sufficiently complex to require a reasonable amount of numerical work in its integration (as for the N-LRd-HMT model). Otherwise, the non-parallelised matrix assembly will dominate (the case for the FK-HMT model). Section 5.5 provides data showing that for the case when the matrix assembly is not required at each time step (*i.e.*, when solving electrical activation only) the speed-up for the models is much closer to the ideal case (Figure 5.47).

Despite having much better multiprocessor performance, it is obvious from Figure 3.23 that activation solution of the N-LRd-HMT based model took much longer to solve. For a 1000 ms simulation, the FK-HMT model took 10.5 hours compared to 28.9 hours for the N-LRd-HMT based model (wall clock time).

Looking at the mechanics solution step, both Figures 3.22 and 3.23 show relatively similar times for the FK-HMT and N-LRd-HMT based models. This is despite the FK-HMT simulation being performed using 12 processors and the N-LRd-HMT model using 8 processors. The extra numerical complexity due to the stiffness of the N-LRd-HMT ODEs can be neglected here since the models are not integrated during the mechanics solution steps in these simulations. For the mechanics solution step the FK-HMT based model and the N-LRd-HMT based model both had a factor of 6.6 speed-up of total computational time over total wall clock time. The FK-HMT based model had a total wall clock time of 27.9 hours for the solution of the finite elasticity mechanics and the N-LRd-HMT based model 27.8 hours.

The total wall clock times for the two simulations were 42.2 hours for the FK-HMT based model and 60.3 hours for the N-LRd-HMT based model. Total computational time was 229 hours for the FK-HMT based model and 360 hours for the N-LRd-HMT based model, giving speed-up factors of approximately 5.4 and 6 over the full numerical simulations.

Chapter 4

Toward a Simulation Environment for the Physiome Project

The focus of this thesis is cardiac electro-mechanics and the development and implementation of a simulation framework suitable for this purpose in tissue and organ level models. The framework described in this thesis is, however, equally applicable to a wide range of physiological processes and organ systems. In particular, this work is seen as a crucial step in the development of an all-encompassing simulation environment for integrating from proteins through to organisms, a goal of the IUPS Physiome Project. More detail on the Physiome Project is given in Section 4.1, with a graphical overview provided by Figure 4.1.

The original idea for this framework was to "simply" extend existing simulation tools to include the full coupling of electro-mechanics between the cellular and tissue/organ levels of the modelling hierarchy. This approach was significantly enhanced by the decision to include in the framework the ability to specify cellular level models via CellML (Section 4.1.1). While it is hoped to further enhance the framework with the use of other markup languages currently under development (*e.g.,* FieldML (http://www.physiome.org.nz/fieldml/pages/) and AnatML (http://www.physiome.org.nz/anatml/pages/)), at this time they are not in a sufficiently stable or suitable state to allow inclusion in the framework.

The simulation framework developed here is built upon the extensive base provided by the CMISS software package developed in-house at the Bioengineering Institute at The University of Auckland. Section 4.2 provides an overview of this software and Section 4.4 describes how the framework developed here was integrated into the package.

4.1 The IUPS Physiome Project

The Physiome Project will provide a framework for modelling the human body, using computational methods that incorporate biochemical, biophysical, and anatomical information on cells, tissues, and organs. The main project goals are to use computational modelling to analyse integrative biological function and to provide a system for hypothesis testing (Hunter & Borg 2003). The term 'physiome' comes from 'physio' (life) and 'ome' (as a whole), and is intended to provide a *". . . quantitative description of physiological dynamics and functional behaviour of the intact organism"* (Bassingthwaighte 2000).

The Physiome Project has built upon the idea that no single model can possibly encompass the 10^9 dynamic range of spatial scales (*cf.* 1 nm pore size of an ion channel to the 1 m scale of the human body) or the 10^{15} range of temporal scales (*cf.* 1 μs typical of Brownian motion to the 70 year (10^9 s) typical human lifetime) (Hunter, Robbins & Noble 2002). Instead, a hierarchy of models is required where each model covers more limited spatial and temporal scales and then techniques are developed to link these models together (as this thesis is doing for the case of cardiac electro-mechanics). Figure 4.1 illustrates such a hierarchy specifically for the heart as used in this research, but a similar diagram can be drawn for any of the organ systems. Using this approach, at any given level in the hierarchy there is a 'black box' that groups all the detail at the level below into a mathematical expression. The parameters of this expression are determined from experiments, but can be related to another, more detailed, model at the finer spatial or temporal level (Hunter & Borg 2003). For the example of cardiac electro-mechanics, this results in a hierarchy ranging from gene networks, signal transduction pathways and stochastic models of single channels at the fine scale, up to systems of ordinary differential equations representing cell level function and partial differential equations representing the continuum properties of tissue and the heart, at the coarse scale (Hunter et al. 2002).

To link the rapidly growing knowledge-base of biological data into a physiome modelling framework, formal vocabularies need to be developed to reduce the growing heterogeneity of terms (Crampin, Halstead, Hunter, Nielsen, Noble, Smith & Tawhai 2004). Standards need to be developed to formalise the description of experimental data and mathematical models of physiological processes. Ontologies (taxonomies together with a set of domain specific rules for linking objects within a taxonomy) that incorporate semantic descriptions of modelling concepts make the modelling environment richer and unambiguous. To develop a framework for building tool-sets for the Physiome Project, computer based representations of models are required. To this end, various ontologies and representation languages which include these ontologies are be-
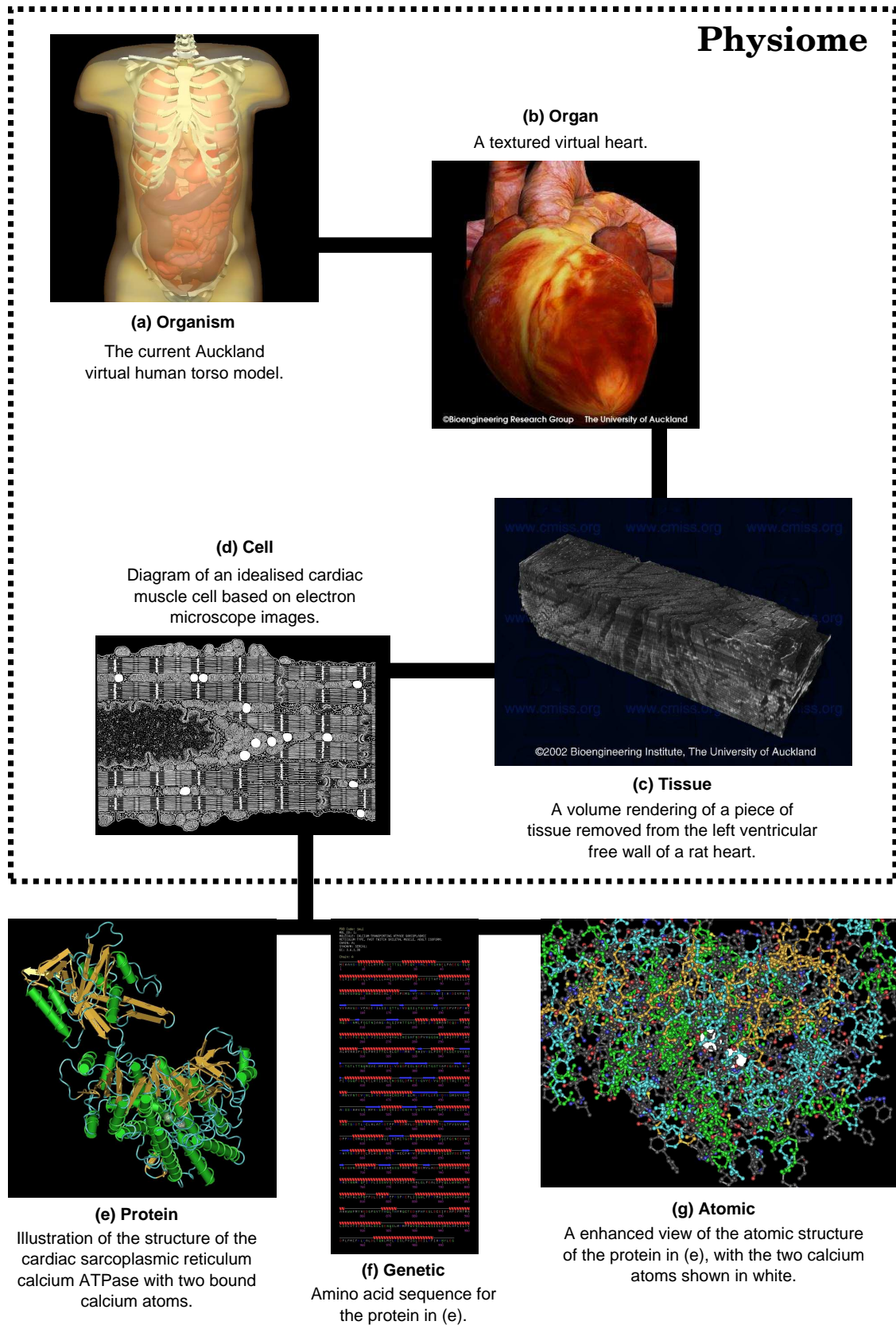
FIGURE 4.1: The hierarchy of modelling for the Physiome Project used in this research. Also shown is the link downward to the protein and molecular levels.

ing developed under the Physiome Project, helping to communicate biological models through tools for building, sharing, interpreting, and visualising models (Crampin et al. 2004). The most complete of these languages is CellML, which is used extensively in this research, and is covered in detail in the following section.

4.1.1   CellML

CellML– http://www.cellml.org – is a language developed at the Bioengineering Institute for the description and exchange of computer based biological models. It is a language built using eXtensible Markup Language (XML) developed by the World Wide Web consortium (W3C). More information on the W3C and the XML language can be found at http://www.w3c.org and http://www.w3c.org/XML, respectively. CellML began as a method for storing model configuration information for a computational simulation program of cardiac cellular models (Nickerson 1998). It was then redesigned and generalised. The CellML 1.0 recommendation was released on the 8th of August 2001 (Hedley, Nelson, Bullivant & Nielsen 2001, Hedley, Nelson, Bullivant, Cuellar, Ge, Grehlinger, Jim, Lett, Nickerson, Nielsen & Yu 2001) and the 1.1 specification is almost at the recommendation stage (Cuellar, Lloyd, Nielsen, Bullivant, Nickerson & Hunter 2003).

XML is a structured document format that is both human and machine readable. It is a format that is well supported by numerous software development teams with many free implementations of processors available that could be easily incorporated into CellML processing software. XML is also a format readily usable over the Internet, facilitating the exchange of models between databases and processing software. The XML specification also allows for the combination of multiple XML-based languages in one document. These are just a few of the reasons why XML was chosen as the metalanguage for CellML.

The philosophy behind the development of CellML was to use existing standards and languages wherever possible before resorting to creating native elements. Some examples of this are the use of: MathML 2.0 (http://www.w3c.org/Math) (Ausbrooks, Buswell, Carlisle, Dalmas, Devitt, Diaz, Froumentin, Hunter, Ion, Kohlhase, Miner, Poppelier, Smith, Soiffer, Sutor & Watt 2001) to specify the mathematical equations; RDF (http://www.w3c.org/RDF) as the basis of the metadata framework; and vCard (http://www.w3.org/TR/vcard-rdf) objects for the description of persons.

The root of a CellML document is always a model element. A model consists of a network

of interconnected components. Models are organised into the following structures.

- **Components**, which are the smallest functional units in a model. Each component contains the mathematics that describes the behaviour of the portion of the system represented by that component. The mathematics is specified using MathML and equations operate on variables defined in that component.
- **Connections**, which are used to connect components together and to map variables in one component to variables in another. The specification of such mappings includes directional information such that processing software can determine the correct data flow.
- **Groups**, which allow the modeller to indicate the existence of logical, physical, or user defined groups of components.
- **Metadata**, which provide context for the model (see below).

One of the key features ensuring robustness and re-usability of CellML components and models is the requirement that all variables and numbers be declared with units (Hedley, Nelson, Bullivant & Nielsen 2001). To achieve this, CellML includes a comprehensive specification of how to define dimensionality and an extension to MathML to provide specification of units for numerical constants given in equations. This includes a dictionary of standard units which consists of the International System of Units (SI) (Bureau International des Poids et Mesures 1998) and its derived units (Bureau International des Poids et Mesures 2000) plus some additional units commonly used in the cellular modelling community. CellML provides a facility for the definition of new units which can be defined in terms of the units defined in the dictionary. This functionality allows model authors to work in whatever set of units they feel most comfortable with, while still ensuring that their models can be integrated with those of other authors using a different set of units. With the definition of units, variables that are defined with differing units can still be connected as long as they have the same dimension.

Metadata is usually defined as "data about data". It is the supporting information that provides context to a resource. In CellML, the model (*i.e.,* the structure and mathematics of the model) is the resource, information that puts the model into a wider context is metadata. Metadata in CellML includes information such as the literature reference that supports the model, the identity of the creator(s) of the model, and the species for which the model is relevant. There is a full specification for CellML metadata available on the CellML website: http://www.cellml.org/public/metadata/cellml_metadata_specification.html.

Annotations for individual equations and variables can be incorporated in a CellML document through the use of CellML metadata. Appendix A provides numerous CellML models that

have been displayed in a format suitable for printing. The comments about the various components, variables, and equations in each model are obtained from the metadata of that model.

CellML 1.1 and future developments

The discussion above describes the basics of all CellML documents. There has, however, been continuing development of the CellML language and a CellML 1.1 specification is nearing the final recommendation version[1]. The main addition to CellML 1.1 over 1.0 is the ability to import units, variables, and components into one model from another. This import functionality makes use of the modular structure of the core CellML elements to provide model authors with the ability to reuse parts of other models (Cuellar et al. 2003).

With the CellML 1.1 specification, the core modelling representation language is approaching completeness. The focus of language development is now on the inclusion of Physiome ontologies in CellML. As part of the Physiome Project, structural and functional ontologies are being developed. The serialisation of such ontological information into a CellML model will be accomplished initially through the use of CellML metadata. Model authors will be able to use the appropriate ontological taxonomy to annotate their models, components, and equations using existing metadata structures or extensions of such structures. This additional information will allow much greater contextual data to be specified.

4.2 CMISS

CMISS is a computational package for modelling the structure and function of biological systems. It is designed to model the anatomy and material properties of organ systems (*e.g.,* cardiovascular, respiratory, and special sense organs) from the component organs (*e.g.,* heart, lungs, and eyes) down to the cellular and subcellular levels, including the coupling that occurs between and within all these levels. Equations derived from physical laws of conservation are solved to predict the integrative behaviour of an organ from knowledge of the anatomical structure and tissue properties. The tissue properties used in these organ simulations can incorporate tissue structure and cellular processes, together with spatial variation of the parameters characterising these processes. CMISS has facilities for fitting models to geometric data from various imaging modalities (*e.g.,* MRI, CT, and ultrasound) and has a rich set of tools for graphical interaction

---

[1] http://www.cellml.org/public/specification/20030930/cellml_specification.html

with the models and the display of simulation results. Control of CMISS is via graphical user interfaces, an interactive console based interpreter, or batch-mode scripting.

The origins of CMISS are based in the PhD work of Peter Hunter (Hunter 1975) as a finite element program for stress analysis of large deformations in the heart. It has since evolved into a general purpose biological systems modelling tool in the areas of **C**ontinuum **M**echanics, **I**mage analysis, **S**ignal processing, and **S**ystem identification. Recently, work has begun to modularise CMISS to enable the development of specialised and focused tools for various medical and other applications. The main academic goal of CMISS is to support the IUPS Physiome Project (Section 4.1). Figure 4.2 gives a few examples demonstrating some of the capabilities of CMISS, also see Christie, Bullivant, Blackett & Hunter (2002) for a detailed review of the abilities of CMISS in relation to the heart.

4.3 Incorporation of CellML into CMISS

Prior to this work, the standard method of implementing a new cellular model in CMISS was to hand-code the equations in Fortran and add this to the CMISS code base. This method has two main disadvantages: the author of the Fortran code is normally translating a published piece of work, which leads to errors in the translation and typographical errors; and the generated code is embedded in and specific to CMISS and thus not easily transferred to another modelling or simulation package. This assumes that the published model itself is free from error.

To avoid these problems, we decided to make CMISS capable of importing its cellular models from a CellML model representation. This provides the ability to store models in a free and open format, where the models could conceivably originate from various sources (for example, the original model publication could have provided a CellML version of the model, or it could have come from a public database or model repository; see Figure 4.3).

The first step in implementing this ability in CMISS was to develop CellML processing software capable of providing CMISS with all the information required from the model to be able to run computational simulations with the cellular models. In the spirit of the community development effort with the CellML project, we decided to develop our software in a sufficiently general way that it could be used as a generic CellML processor. To achieve this, a draft Application Program Interface (API) for use when accessing an in-memory computational representation of a CellML model was designed and an initial C++ implementation of this API was developed and
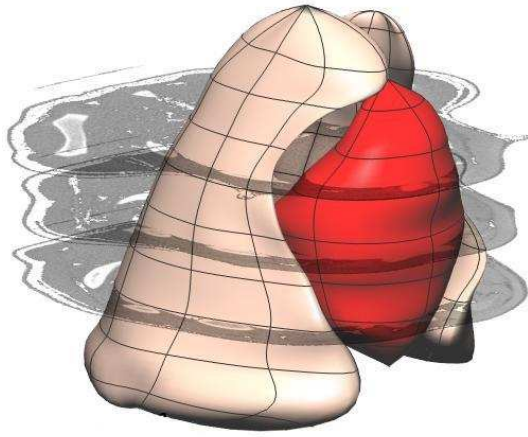
(a) A geometric mesh of the porcine lung and heart surfaces created from CT images.
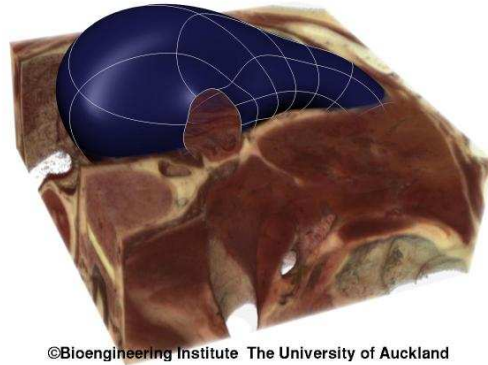
©Bioengineering Institute The University of Auckland

(b) A geometric mesh of the human stomach exterior surface embedded in a volume visualisation of the visible man data set from which the geometry was created.
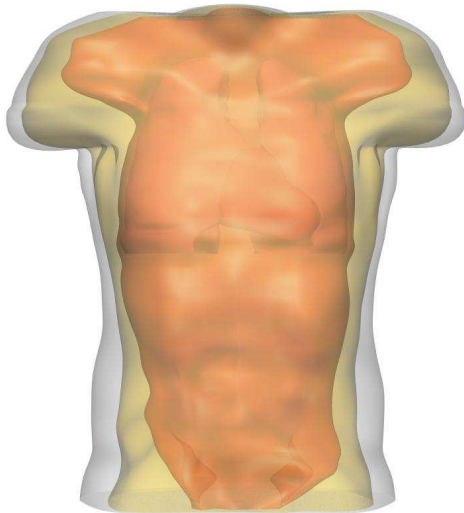
(c) A visualisation of the virtual human torso model showing the surface layers of skin, fat, muscle, lungs, and heart.
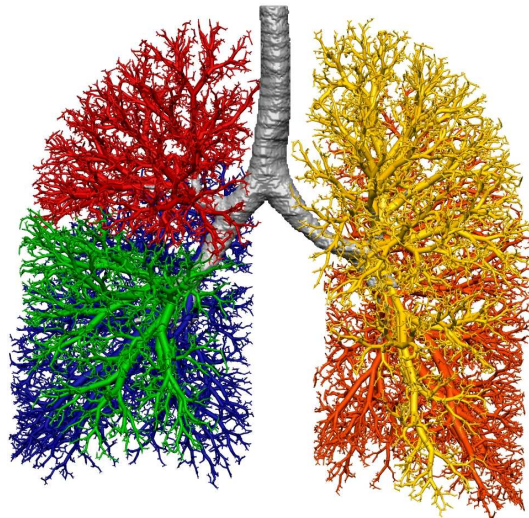
(d) A geometric mesh of the airways in the human lung.

FIGURE 4.2: Some examples of the capabilities of CMISS. The geometries illustrated in (a) and (c) are used in the forward and inverse problems of electrocardiography and equations of heat and mass transport can be solved using the lung geometry in (d).

made available (Section 4.3.1). At this stage the API is implemented for a subset of CellML 1.0 relevant to models of cellular electrophysiology and mechanics used in this work, but will be extended to cover the full CellML 1.1 specification.

With an API defined and implemented the ability to import CellML was added to CMISS, allowing the definition of cellular models via CellML. While the API implementation provided all the information required to run computational simulations, there still remains the problem of translating the mathematical equations, stored as MathML objects, into a format suitable for use inside CMISS. This translation is very specific to the target implementation of the equations and as such is outside the scope of a general CellML API implementation, although access to the MathML objects is through the API. Section 4.3.2 describes the process developed and implemented for the translation of a CellML model to a format suitable for CMISS.

Now cellular models no longer need to be hard-coded in Fortran in the CMISS code base. Scientists are free to develop their cellular model using software that is perhaps better suited to single cell modelling or any package they are comfortable with (Matlab, Mathematica, Lab-VIEW, *etc.*). Then, provided there exists a method for exporting CellML, it should be possible to take the cell model and perform tissue and whole heart simulations that are based on the model (Figure 4.3). With this framework, a cellular modeller/physiologist can work on their cell model and then very easily see the effect in a large scale tissue simulation.

Another important requirement for the use of CellML models in tissue modelling is the ability to specify spatial variation of models and parameters within a model. For example, when modelling the spread of excitation from the pacemaker cells in the sinus node into the atria a modeller would typically want to use different cellular electrophysiological models for each of the two regions of tissue. Another example is the variation of ion channel distributions through the ventricular wall, where the modeller might want the same model represented at all points in the ventricles but need to specify a spatial distribution of channel densities. While the specification of spatially dependent models and/or parameters is outside the scope of CellML, it was something that needed to be included in the incorporation of CellML into CMISS (Section 4.3.3).

4.3.1   The CellML 1.0 API

The aim of this part of the project was to develop a generic in-memory computational representation of a CellML model and to provide standard methods for accessing the data contained in the model. To achieve this, an initial draft Application Program Interface (API) for CellML
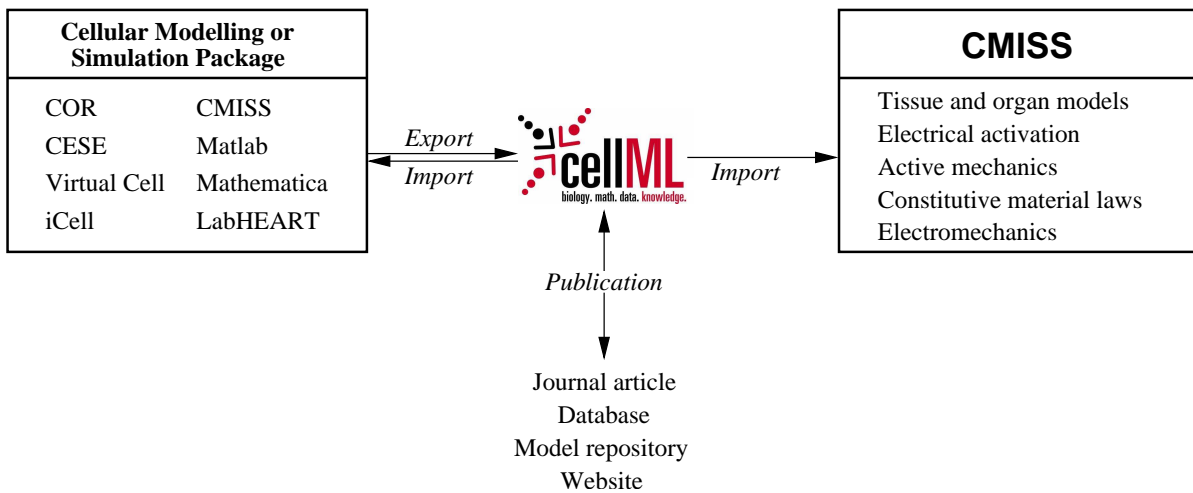
FIGURE 4.3: Here we illustrate how CellML can be used to allow the development of cellular models (and material constitutive laws) using software designed for this purpose, while allowing the models to be easily incorporated into tissue and organ level models. The cellular modelling and simulation packages listed are examples of software that can already understand CellML or are working on gaining that understanding. (COR - http://cor.physiol.ox.ac.uk; CESE - http://cese.sourceforge.net; Virtual Cell - http://www.nrcam.uchc.edu; iCell - http://ssd1.bme.memphis.edu/icell; LabHEART - http://www.lumen.luc.edu/lumen/DeptWebs/physio/bers.html).

1.0 was developed. The use of an API provides a layer of abstraction between an application and the implementation of a CellML processing library, which is a collection of subroutines and functions stored in one or more files, usually in compiled form, for linking with other programs. Documentation of the API is provided on the attached compact disc (Section D.1).

The API consists of classes that represent the structures defined by CellML (models, components, variables, *etc.*; Section 4.1.1) and a basic version of the W3C MathML Document Object Model (DOM) (http://www.w3c.org/Math/DOM) to enable interaction with the mathematics of the model. The class definitions specify the methods used to access and manipulate the data they contain.

This draft API has been implemented in C++ and the code has been "open-sourced" and made available on SourceForge.net, the world's largest Open Source software development website, under the CellML project: http://cellml.sourceforge.net. This implementation is designed to be compiled into a library which can be linked with an application to provide CellML processing capabilities. The implementation supports most of the CellML 1.0 API, and plans are currently under development to add support for the full CellML 1.1 specification.

The MathML DOM implementation currently in the API implementation is very basic, pro-

viding support for only the subset of MathML required for the models used in this thesis. It is hoped that more thorough implementations of the content MathML DOM will become available either through the CellML project or through the W3C math project. By using the MathML DOM specification in our CellML API implementation, we should be able to plug in such implementations quite easily.

Use of the CellML API implementation in CMISS first involves the parsing of the required model(s) into a standard XML in-memory representation (in this case we are using the DOM standard (http://www.w3c.org/DOM)). This representation of the CellML model is then processed by the API implementation into the native CellML memory model representation suitable for interaction with the model. Once the native memory model has been created for all the required models, the translation of the MathML can be performed to generate computable code as described in the following section.

4.3.2 Translation of CellML to Computable Code

As stated previously, translation from MathML data objects to something that is computable depends heavily on the target computational environment one wishes to aim at. During this research, several translation methods have been developed for different targets.

The first translation involved the use of an eXtensible Stylesheet Language Transformation (XSLT) to transform a CellML document directly into a document suitable for printing, as used to generate Appendix A from the various cellular models described in Chapter 2. A similar, but more detailed, translation to the Virtual Cell (Moraru, Schaff, Slepchenko & Loew 2002, Loew & Schaff 2001) internal VCML format was accomplished through the use of XSLT combined with custom Java classes. This transformation provided the basis for Virtual Cell to gain the ability to import cellular models into its MathModel interface.

While very useful for their given purposes, these XSLT-based translations are fairly limited in terms of computational usefulness. Translating MathML into LaTeX for compilation into a postscript file does not require a great deal of information about the equations, and the customised classes for the Virtual Cell transformation were quite complicated and specific to the Virtual Cell. A better, general purpose, method is to use generic CellML processing software, such as that described in the previous section, to abstract the application away from all the details of CellML. This allows an application to focus on processing the mathematics without needing to know anything about the internal working of CellML.

Using this approach, it is then possible to develop a math processor which can work directly with the MathML DOM data objects provided by the CellML API implementation. Such a processor can, in a target independent manner, produce a list of equations that contains the full mathematical model described in a given CellML model. This layer of abstraction from the MathML DOM provides the ability to add postprocessing functionality to the mathematical model. For example, it is potentially useful to simplify equations where possible to improve the efficiency of the model. A math processor is provided in the example applications that are included in the CellML API C++ implementation (Section D.1), which is the same processor as that used in CMISS.

Figure 4.4 summarises the work flow when using this approach. In this process, the CellML API implementation is responsible for providing a MathML document object that contains all the resolved mathematics for the model. The mathematics are resolved through the use of group and connection information to resolve variables used in equations and also any additional equations or expressions that need to be added to correct unit inconsistencies. From the resolved MathML document object, the math processor creates a list of equation objects, which currently provide a more simulation biased view of the MathML but provide for future addition of postprocessing of the mathematics. The list of equations is then written out into code specific to CMISS, this entails sorting the equations into an order correct for evaluation using Fortran (the language of CMISS) and writing out a subroutine that follows the CMISS specified interface for a cellular model. The platform's native compiler is then used to compile and link this subroutine into a dynamic object which can be loaded into the execution space of CMISS where it can be freely accessed during simulations.

The math writer described above and in Figure 4.4 was designed and implemented to write out code specific for use in CMISS. It was fairly easy, however, to develop a general interface for writing out the content MathML contained in the equation objects. Included in the C++ implementation of the CellML API is an example application which makes use of this interface to define a new format for writing out the equations. This application will take a CellML model and generate a Fortran program which, when linked with the RADAU integrator (Hairer & Wanner 1996, http://www.unige.ch/math/folks/hairer/software.html), is capable of integrating any of the electrophysiology models described in Chapter 2.

As mentioned previously, the implementation to date has only supported what was required for the models used in this research. There are three limitations of this implementation that need to be considered when using CellML models within the framework developed in this thesis. Firstly, no implementation of the units checking and conversion of either variables or equa-
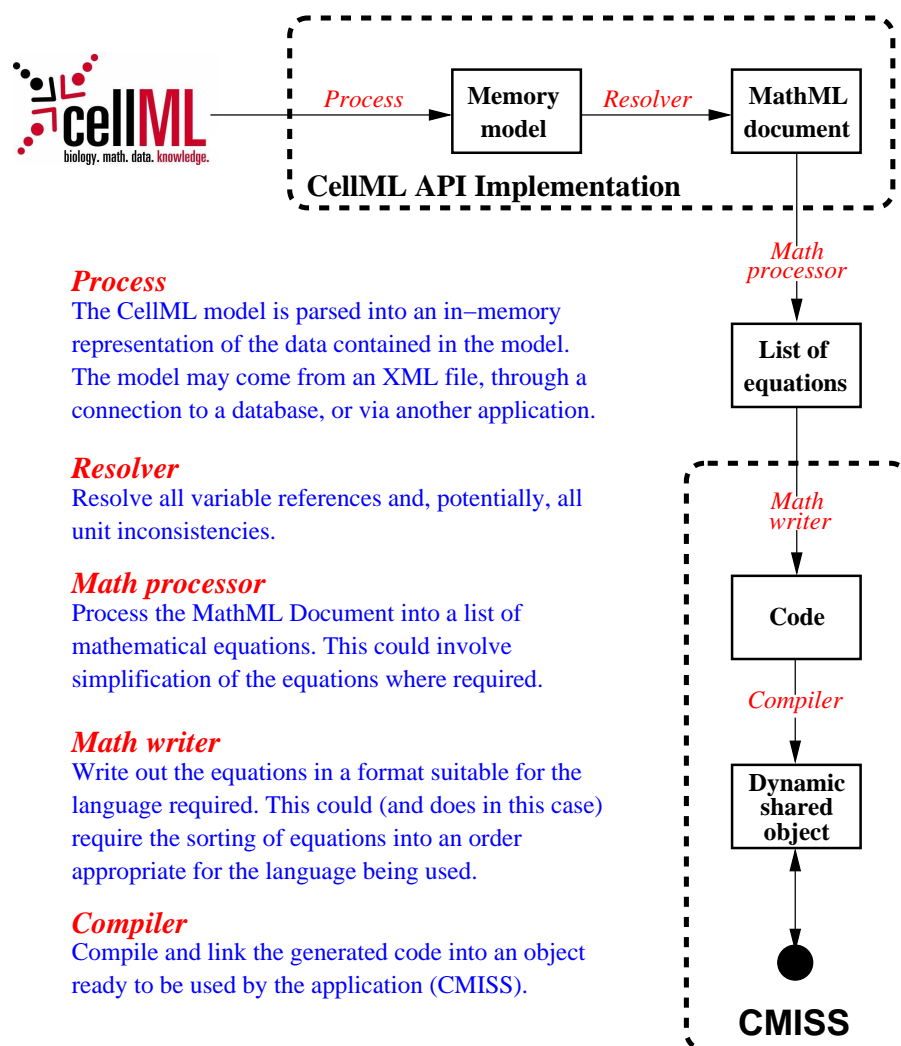
FIGURE 4.4: An illustration of the work flow involved in the generation of code suitable for use in CMISS from a CellML source. The upper dashed box encapsulates the processes that are internal to the CellML API Implementation, and the lower encapsulates those internal to CMISS. The math processor is independent and external to both of these.

tions has been implemented, it is assumed that all models conform to the units specified in Tables 2.1 and 2.2. Secondly, only the mathematical operators required by the models presented in Chapter 2 have been implemented (see Appendix A for the actual equations). Finally, the implementation requires that all expressions are in a standard "this variable equals that expression" format and all bound variables for the differential equations need to resolve to a common variable. Some examples that will work with the current implementation are:

$$\frac{\mathrm{d}V_m}{\mathrm{d}t} = -\frac{1.0}{C_m} \sum I_{ion};$$
$$g_K = \overline{g_K} \sqrt{\frac{[\mathrm{K}^+]_o}{5.4}},$$

$$(4.3.1)$$

whereas these equations would not work:

$$C_m \frac{\mathrm{d}V_m}{\mathrm{d}t} = -\sum I_{ion};$$
$$\overline{g_K} \sqrt{\frac{[\mathrm{K}^+]_o}{5.4}} = g_K.$$

$$(4.3.2)$$

With the development of postprocessing methods at the math processor stage of the process, these limitations would be relaxed.

4.3.3   Spatially Varying Models and Model Parameters

When implementing the ability to define cellular models in CMISS via CellML, the opportunity was taken to significantly re-factor the way CMISS handled the definition of multiple cell types within a single tissue model. Prior to this work, multiple cell types, or variants, were required to all be defined in a single model and each of the sub-models shared a common parameter space. This required all the variants to define all the parameters, which results in extra memory overheads if the models each have largely differing numbers of parameters. The sub-model to be used for each computational cell was defined through the use of a cell variant field defined over the tissue model which was used to switch to the correct sub-model in the full cellular model.

The process of implementing the use of CellML to define the cellular models provided the ability to modularise the cellular models with finer control. Thus, each cell variant now has its own CellML model and its own parameter space resulting in more efficient use of memory as each model only needs to keep its own parameters rather than the full set of all the models. Some examples where this functionality might be useful are shown in Figure 4.5.

(a)   (b)
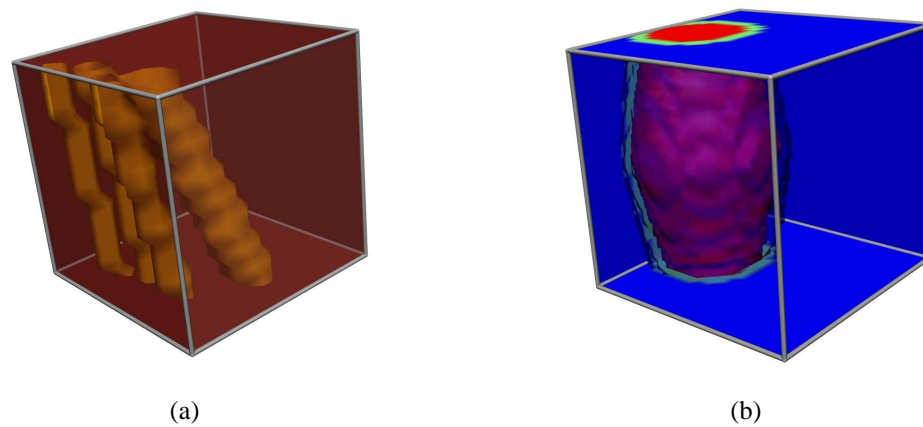
FIGURE 4.5: Here we illustrate two cases where the ability to define distinctly separate models might be useful. (a) shows a cube of tissue that has Purkinje-like fibres (gold) penetrating the tissue. Using the implemented framework, the fibres could be defined using a Purkinje fibre model (*e.g.,* Section 2.4.4) while the remainder of the tissue represented by normal myocytes (*e.g.,* Section 2.4.6). In (b), we show an ischaemic region of tissue (red) surrounded by a border-zone (green) and healthy tissue (blue). Depending on what is being modelled, it is possible that each of these regions could need their own specialised cellular model.

In addition to being able to specify a spatial distribution of cellular models, it is also necessary to have the ability to specify spatial variation of material parameters within models. As the implementation was extended to incorporate the spatial distribution of models discussed above, the specification of spatial variation of model parameters was similarly extended. Due to this work in CMISS, modellers are free to specify very detailed spatial distributions of model parameters. Examples of such parameter variation are discussed in Section 2.4.10 and Figure 4.6 provides some visualisations of these parameter variations.

4.4   Use Case: Cardiac Electro-Mechanics

We have described above a method for the generic specification of mathematical expressions in CellML and the dynamic incorporation of these expressions into CMISS. Focus is now shifted from the generic to the specific and we discuss the use of this framework in the context of modelling cardiac electro-mechanics. The algorithm developed in this thesis for computational modelling of cardiac electro-mechanics is summarised in Figure 3.6 and it is with reference to this algorithm that we now describe the implementation of our modelling and simulation
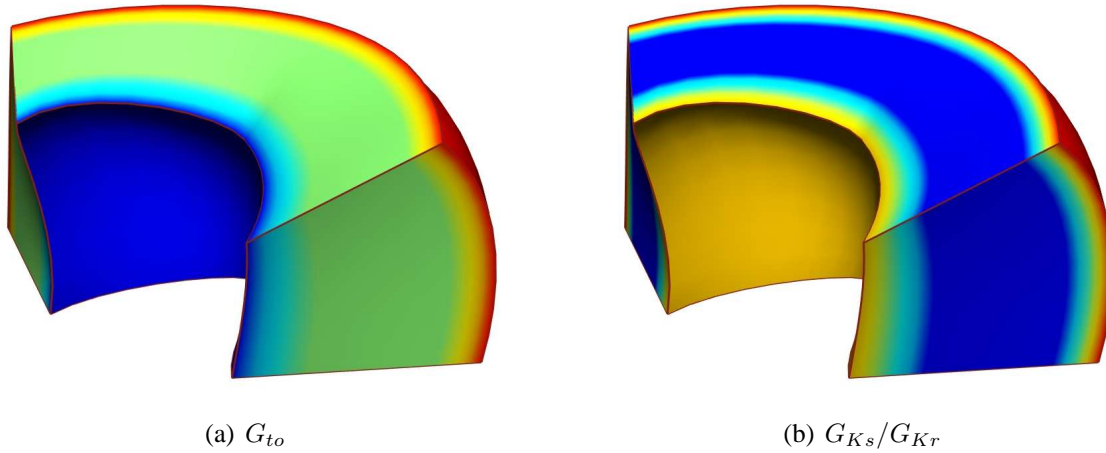
(a) G_{to}

(b) G_{Ks}/G_{Kr}

FIGURE 4.6: Examples showing the variation of the G_{to} and G_{Ks}/G_{Kr} parameters through the ventricular wall as given in Section 2.4.10. In (a), G_{to} is 0.0005 mS $\cdot$ mm^{-2} at the endocardial surface (blue), 0.005 mS $\cdot$ mm^{-2} in the midmyocardium, and 0.011 mS $\cdot$ mm^{-2} at the epicardial surface (red). In (b), G_{Ks}/G_{Kr} is 19 at the endocardial surface (yellow), 7 in the midmyocardium, and 23 at the epicardial surface (red). The geometry is a wedge taken from the LV free wall of the porcine ventricular model.

framework using CellML and CMISS.

Model specification

Standard CMISS methods are used to specify tissue and organ continuum models. This includes the specification of the finite element description of the model geometry and the interpolating basis functions to be used (Section 1.2). At this stage we also specify in CMISS that we wish to solve electrical activation and finite elasticity over this solution domain, and define the continuum material parameters and boundary conditions for these two components of the model.

Previously at this point in the model definition, CMISS users would be able to choose from a limited list of cellular models to describe the ionic current model used in the electrical activation model. We have now added enormous flexibility by allowing the user to choose to define their model in CellML. When specifying the model, all cellular models to be included in the model must be provided encoded as CellML files and then spatial distribution of these models can be described over the solution domain (Figure 4.5). The cellular model material parameters and boundary conditions are then specified, which could easily include the spatial distribution of parameter values within a model (Figure 4.6).

Solution procedure specification

With the model fully specified, we next need to define the methods that will be used to solve the model for a given simulation. This involves standard CMISS methods for choosing, for example, the linear solver to use when solving the GBFE method for the electrical activation model, or the integrator to be used to integrate the cellular model(s) ODEs. Each of these choices will lead to various parameter options dependent on the solvers chosen: iteration limits, maximum step sizes, matrix preconditioners, *etc.*.

In Figure 3.6 we include spatial discretization of the solution domain into the solution procedure specification. For the finite elasticity model this will be determined by the basis functions used to represent the deformation fields and is thus distinct from the actual model specification. In the case of the electrical activation model, however, the model specification relies on knowledge of the spatial discretization defined for the GBFEs to specify the cellular models. The GBFE nodes are treated as continuum cells and these nodes are used to define the spatial distribution of cellular models and model parameters. Ideally one would like to be able to specify the spatial distribution of cellular models and parameters based purely on the much coarser finite element geometry representation and have the GBFE nodes inherit this information from such a specification. Through the use of functional grouping methods in CMISS it is possible to almost hide the fact that these GBFE nodes are being used to define the spatial distribution, but this is not an ideal solution.

Initialisation

As discussed in Section 3.2.2, there is some initialisation that is performed once at the beginning of a electro-mechanics simulation. The framework we have implemented adds nothing here to the standard CMISS methods.

Activation solution step

Solution of the electrical activation model using the GBFE method has been well characterised elsewhere (see Appendix C for appropriate references). The piece of the solution that we have modified is the integration of the cellular model into the continuum propagation model.

The implementation of the electrical activation modelling in CMISS treats the cellular model as simply a black box which has an input of the applied diffusive pseudo stimulus current and an output of the temporal derivative of membrane potential. Traditionally, these black boxes have been described by specific cellular electrophysiology models embedded in routines directly in the CMISS code. Spatial distributions of cellular models was handled through the combination of the different cellular models into a single routine and the use of a spatially varying parameter to switch between the different models in the routine.

With the development of the CellML based approach in this work we have removed the need to hard code cellular models directly into CMISS. Through the implementation of a complete framework for specification of spatially varying cellular models we have removed the requirement to combine all cellular models for a given tissue model into a single cellular model. Now each GBFE node knows what model is being used at that location and the full parameter set for that model and spatial location. The CellML defined models can then be accessed through the dynamic shared object created for each model as they defined (Figure 4.4).

Mechanics solution step

We have discussed in Section 3.2.2 the requirement that the dynamic active tension is updated for every deformation applied to the solution domain during the mechanics solution step. This is achieved in our framework by updating the cellular model parameters at either the finite elasticity Gauss points or GBFE nodes (Figure 3.7) and directly calling the appropriate cellular model routine or performing a dummy integration of the cellular model.

This again illustrates the advantages of the CellML based approach we have developed in combination with the ability to describe spatial distribution of cellular models. At any location in the solution domain we can determine the appropriate cellular model for that location and interpolate the full model parameter set for that point in one-, two-, or three-dimensional space. These features meant it was trivial to implement method two from Figure 3.7, providing an enormous decrease in the computational time required for simulation runs – a very desirable feature given the time taken for some models (Section 5.5).

Update cellular and activation material parameters

The final step in the implementation of the modelling and simulation framework we have developed was the update step providing the coupling between the deforming finite elasticity model and the electrical activation model. At the continuum model level, this work had already been done (*e.g.,* the updating of the conductivity tensor and the spatial location of the GBFE nodes).

For use in our framework we needed to add methods to CMISS allowing for the updating of cellular model parameters which are dependent on deformation. In the work presented in this thesis the two parameters of interest are the fibre extension ratio and its temporal derivative (*i.e.,* velocity of shortening). These parameters are readily obtained from the local material strain tensor at the location of the GBFE node being updated which itself is calculated from the FE nodal displacements of the continuum model.

The methods developed for use at this point in the algorithm (Figure 3.6) for updating the global cellular material parameters at the completion of each time step are also used to keep the local model parameters updated during the mechanics solution step described above.

4.5 Other Applications

CellML is a language that can be used to describe any system of annotated mathematical equations. As described in Section 4.3 above, we have implemented a method in CMISS which essentially enables the dynamic specification of a set of equations specified in CellML to be accessible in CMISS at run-time.

This functionality has already been used for two applications outside the scope of the work presented in this thesis. The first application was in the modelling of substrate transport through the wall of a distal tubule model in the kidney. In this model, CMISS was used to model the fluid flow down the tubule with the substrate transport mechanisms described by models written in CellML that could be interpreted at run-time to give the equations defining the kinetics of substrate transport between the compartments represented in the model.

The second application is in the definition of finite elasticity material constitutive relationships. Previously, CMISS allowed the user to specify a spatial distribution of material parameters but due to various implementation details only one constitutive relationship could be spec-

ified for the entirety of the material. By allowing the constitutive relationships to be defined using CellML, the finite elasticity code in CMISS is now able to utilise the same code developed above for the distribution of cellular models and their parameters to describe a spatial distribution of material constitutive relationships and their parameters. The initial requirement for this ability came from a breast modelling project where a breast geometrical model consists of several different materials (skin, fat, muscle, and fibroglandular tissue) with distinct differences in material behaviour (Rajagopal, Nielsen & Nash 2004).

Further application of the work in this thesis has also begun in other organ systems which involve electro-mechanics. A large system in which modelling of electro-mechanics is becoming more important is the musculo-skeletal system. For obvious reasons the electrical excitation and mechanical contraction of skeletal muscles is nearly as important as that of the heart. While the detail of the skeletal muscle electro-mechanics differs from cardiac muscle, the underlying methods we have developed for the cardiac models is equally applicable to skeletal muscle (Fernandez & Hunter 2004). With CellML it is trivial to replace the cardiac cellular models with skeletal and simulations of, for example, knee flexion can be made (Fernandez, Buist, Nickerson & Hunter 2004).

Similar to skeletal muscle, smooth muscle also undergoes active contraction in response to stimuli. While skeletal and cardiac muscle are quite similar, smooth muscle is significantly different. Once again, however, the underlying modelling framework developed in this thesis should be capable of representing models of contracting smooth muscle. Initial investigation of this has recently begun in the area of modelling an active bronchial airway (Muttaiyah, Tawhai & Thorpe 2004).

Chapter 5

Toward a Whole Heart Model of Electro-Mechanics

In Chapter 3 we presented a modelling framework suitable for use in simulations of cardiac electro-mechanics. We demonstrated application of the framework to simulations using various configurations of tissue cube and doughnut geometric models (Section 3.3) and two examples of cellular electro-mechanics models (Section 3.4). Chapter 4 described the implementation of this simulation framework and its relevance to the IUPS Physiome Project.

We are now going to extend the modelling toward something more physiologically realistic, although still short of the desired full heart model. In this chapter, we present some results from simulations of electro-mechanics in a simple model of the LV. The LV geometry was primarily chosen due to the large number of recent publications examining cardiac resynchronisation therapy (CRT) and the electrical and mechanical effects of such therapy on the LV.

In the field of CRT there have been a large number of experimental (Usyk, Mazhari & McCulloch 2000, Kawaguchi, Murabayashi, Fetics, Nelson, Samejima, Nevo & Kass 2002, Leclercq, Faris, Tunin, Johnson, Kato, Evans, Spinelli, Halperin, McVeigh & Kass 2002, Wyman, Hunter, Prinzen, Faris & McVeigh 2002, Peschar, de Swart, Michels, Reneman & Prinzen 2003, Kerckhoffs, Faris, Bovendeerd, Prinzen, Smits, McVeigh & Arts 2003) and theoretical (Usyk et al. 2002, Kerckhoffs, Bovendeerd, Kotte, Prinzen, Smits & Arts 2003, Kerckhoffs, Faris, Bovendeerd, Prinzen, Smits, McVeigh & Arts 2003) studies examining LV pump function under normal sinus activation and activation via electrical stimulation by various pacing protocols. Experimental studies have also investigated intra-ventricular resynchronisation (Wyman,

Hunter, Prinzen & McVeigh 1999, Kawaguchi et al. 2002, Leclercq & Kass 2002, Verbeek, Vernooy, Peschar, Cornelussen & Prinzen 2003) and quantification of interventricular asynchrony (Wyman et al. 1999, Verbeek, Vernoot, Peschar, van der Nagel, van Hunnik & Prinzen 2003, Kass 2003) during left bundle branch block (LBBB) and CRT.

These experimental studies typically analyse their data through the use of a fairly stylised geometrical representation of an LV. The models also consist of a similar LV geometry, with Usyk et al. (2002) being an exception where they model both left and right ventricles. The LV is the most significant pumping chamber in the mammalian heart and, thus, understanding LV function and dysfunction is of critical importance.

Hence, through the application of our modelling framework to a similar LV model we are able to tap the wealth of experimental data available in the recent literature as well as having similar mathematical models to compare with. The basic LV geometry is shown in Figure 5.1. In order to compare to some of this data we first need to describe suitable boundary conditions for simulation of a *"typical"* cardiac cycle in the LV model. These are presented in Section 5.1.
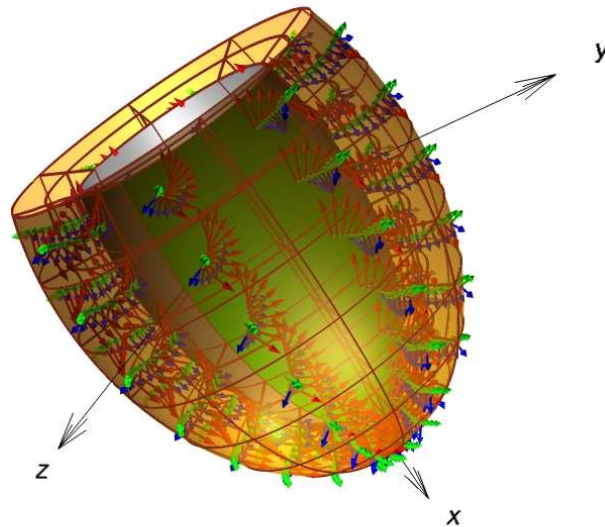
FIGURE 5.1: Simplified geometric model of the LV, showing the reference rectangular Cartesian axes. The red arrows indicate the material fibre axis, the green arrows are aligned with the sheet axis, and the blue matches the sheet-normal axis. The mid-septum region of the LV is indicated by the green endocardial surface.

In addition to the types of simulation data shown in Chapter 3 with cellular transients and deformed geometry solutions it is useful when discussing LV function to provide a more global measure of electrical and mechanical behaviour. The mechanical measures we will be using are

the volume and pressure changes of the LV cavity which can be easily calculated as described in Section 5.1. For the electrical behaviour we will be making use of some previous work in CMISS to allow the calculation of various clinical electrocardiogram (ECG) leads. A brief summary of how these are calculated is presented in Section 5.2.

5.1 The Cardiac Cycle

The cardiac cycle is classically described by a Wigger's diagram (Figure 5.2), which illustrates the relative temporal relationship between global mechanics and electrical transients. Of particular interest in Figure 5.2 are the clinical ECG and the LV pressure and volume transients. In this work we take a simplified view of the cardiac cycle and segment the mechanical cycle into three components: inflation, isovolumic contraction, and ejection.

5.1.1 Inflation

The first component of the cardiac cycle we consider is the final push of blood into the LV generated by contraction of the left atrium (LA) during atrial systole. This gives what we are calling the initial inflation of the LV which we model with the application of a pressure boundary condition to the endocardial surface of the LV model.

Some results demonstrating the application of such pressure boundary conditions are shown in Figures 3.15(b) and 3.16(b) for the ventricular doughnut model and in Figure 5.10 for the LV model. While the current implementation of the modelling framework allows for application of a spatially varying pressure boundary condition, the models presented in this thesis use a constant pressure applied over the entire endocardial surface.

5.1.2 Isovolumic Contraction

In our model, the end of the inflation phase coincides with the initiation of electrical activation of the LV. As shown in Sections 5.3 and 5.4 below, we have performed LV simulations using several different stimuli to initiate the electrical activation and drive the mechanical contraction of the LV.
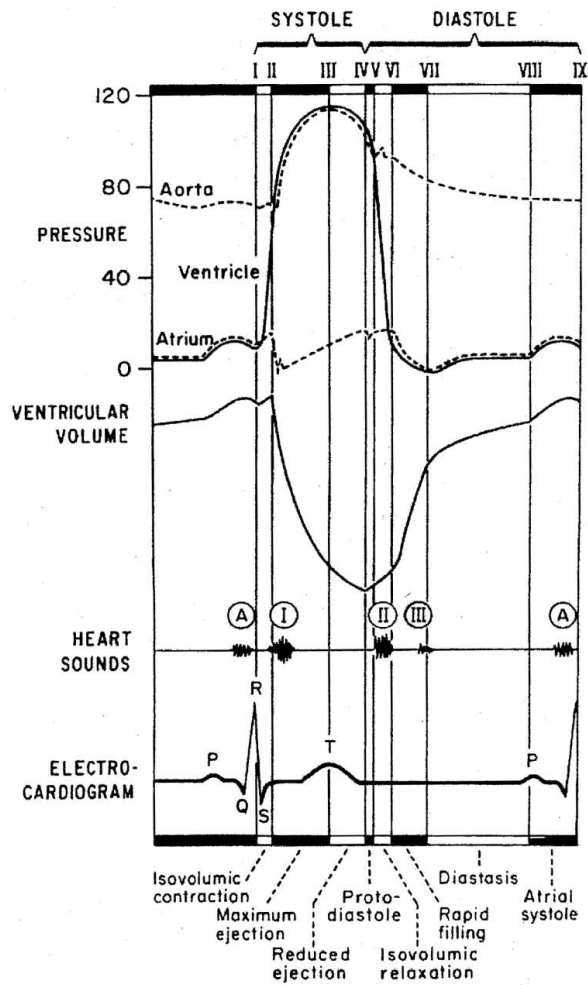
FIGURE 5.2: The Wigger's diagram, showing the nine phases of a cardiac cycle. The upper solid trace shows the LV cavity pressure with the LV cavity volume shown in the middle solid trace. An indication of the temporal relationship between the electrical activity of the heart and the mechanical is given by the stylised ECG trace at the bottom of the diagram. From Katz (1992).

The first period of contraction occurs with a constant volume of blood in the ventricular cavity (the mitral and aortic valves are closed) leading to this being the isovolumic contraction component of the cardiac cycle. As the wave of electrical activation moves through the ventricular tissue initiating mechanical contraction pressure in the LV cavity increases. Once the cavity pressure exceeds that in aorta the semilunar valves open and blood begins to flow out of the LV.

To model the effect of this constant volume of blood on the ventricular wall, we add a FE mesh representing this volume to the LV model and constrain these elements to have a constant total volume (Figure 5.3). Using the method developed by Nash (1998), this cavity region is coupled to the ventricular wall to act as feedback mechanisms to weakly constrain the deformation of the ventricular wall. Then as the ventricular wall contracts, the endocardial nodes shared between the wall and cavity meshes (blue spheres in Figure 5.3) deform with a tendency to reduce the size of the cavity mesh. The cavity model then calculates the pressure it must maintain to remain isovolumic and this pressure is then applied to the endocardial surface in a spatially homogeneous manner (Nash 1998). Figure 3.16 presents a series of isovolumic simulation results for the doughnut ventricular model using this method.
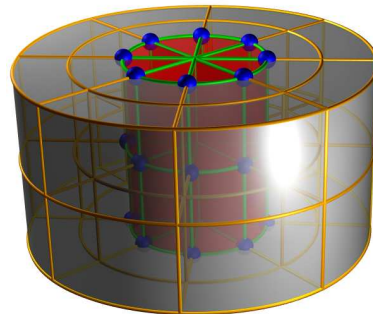
FIGURE 5.3: An example of a cylindrical ventricular wall mesh (gold/silver) coupled to a cavity region (green/red). The common nodes shared between the two meshes are shown as blue spheres.

5.1.3 Ejection

The end of isovolumic contraction is announced with the opening of the semilunar valves as the ventricular pressure surpasses the arterial impedance. As shown in Figure 5.2 there is initially a rapid ejection of blood from the LV which produces an abrupt decrease in LV volume. This is followed by a longer period of reduced ejection as the cavity pressure begins to lessen, the

end of this period marks the termination of ventricular systole and the closing of the semilunar valves. The first component of the diastolic phase is a period of isovolumic relaxation as the ventricle relaxes and pressure rapidly decreases. Once the LV cavity pressure drops below that in the LA the mitral valve opens and gives rise to rapid filling of the ventricle followed by a slower filling phase. The final period of diastole is the final push of blood into the ventricle caused by atrial systole, as described above in Section 5.1.1.

Simulation of the fluid dynamics during mechanical contraction and relaxation of the LV is a very computationally and numerically demanding problem. To make simulation of this phase of the cardiac cycle more tractable, various simplified fluid dynamics models have been used to model the flow of blood out of the LV. In an extension to the isovolumic model introduced above, Nash (1998) attaches one non-coupled cavity node to a variable impedance in one spatial axis while restricting any movement in the other two dimensions. By observing the volume of blood still enclosed by the ventricular wall this allows blood to be ejected from the ventricular cavity while still maintaining a constant total cavity mesh volume. Another common approach has been to use two-element (Usyk et al. 2002) and three-element (Bovendeerd, Arts, Huyghe, van Campen & Reneman 1992, Kerckhoffs, Bovendeerd, Kotte, Prinzen, Smits & Arts 2003, Kerckhoffs, Faris, Bovendeerd, Prinzen, Smits, McVeigh & Arts 2003) Windkessel models (Westerhof, Elzinga & Sipkema 1971, Westerhof, Elzinga & van den Bos 1973) to relate cavity dynamics to aortic flow and pressure.

In this work, we are focused on developing the framework for generalised coupled electro-mechanics in cardiac tissue. We are therefore more interested in a simple model for ejection capable of reproducing the general trends mentioned above with minimal additional computational expense. Thus, we have developed a method whereby the FE node in the LV cavity mesh (the silver sphere in Figure 5.4) has a displacement specified along the base-apex axis allowing for ejection of blood out of the ventricular cavity similar to the method developed by Nash (1998) but without any added degrees of freedom in the finite elasticity model. All other cavity nodes not coupled to the ventricular wall are fixed in all directions and derivatives. This is illustrated for a simple cylinder in Figure 5.4.

Using the method described in Figure 5.4 it is possible to control the volume of blood enclosed by the ventricular wall at a given point in the cardiac cycle. In order to perform simulations that represent something physiologically reasonable, we have proscribed a cavity volume transient obtained from that given in Figure 5.2. The starting point of the specified volume transient is the end of isovolumic contraction. The transient is specified as a volume fraction, so the absolute values are obtained based on the initial volume of the cavity at end diastole (*i.e.,* fol-

(a)   (b)
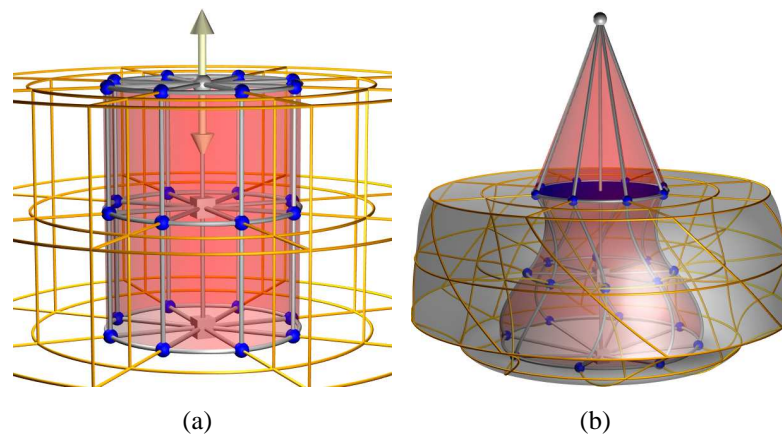
FIGURE 5.4: Illustration of the allowed movement of the free cavity FE node. The cavity nodes
shown as blue spheres are coupled to the ventricular wall mesh (gold lines/silver surface) and
those represented as silver cubes are fixed in all directions and derivatives. The free cavity node
is the silver sphere with its allowed movement in the base-apex axis illustrated by the arrows in
(a). This node is initially positioned in the basal plane of the ventricular geometry. (b) shows
an exaggerated contraction solution, where the free cavity node has been moved out of the basal
plane. The red surface is the boundary of the isovolumic mesh, with the volume of blood currently
ejected from the ventricle being the fraction of this volume above the blue basal plane.

lowing the initial inflation phase), and all values can be scaled to match a desired peak ejection
fraction. Using this method allows for the specification of the cavity volume at each point in
time but the cavity pressure remains a free parameter in the model.

5.2 Estimating Clinical ECGs

When describing whole heart electrical activity, by far the most common measurement is the
clinical ECG. The heart is one of the largest and most often electrically excited muscles in the
mammalian thorax. As such, electrical recordings from the surface of the torso will be domi-
nated by the electrical activity of the heart allowing inference of the heart's electrical behaviour
to be made from such recordings. Various methods for recording ECG signals have been devel-
oped (see Cheng (2001) for a review), with the most common being the 12-lead ECG.

   The standard 12-lead uses six precordial electrodes placed on the thorax at the heart level
and three extremity electrodes placed on the left leg and the right and left arms. The extremity
electrodes are used to derive a reference potential against which the other electrodes are mea-

sured relative to. A sample ECG can be seen in Figure 5.2 and the three extremity leads are illustrated in Figure 5.5.

Previous work in our group has looked at the forward problem of electrocardiography, where potential solutions at the heart surface are propagated through a torso model to produce ECG traces (Bradley 1998, Buist & Pullan 2001, Buist 2001, Buist & Pullan 2003). Methods have been developed that allow various heterogeneity and anisotropy to be included in the torso model (lungs, skeletal muscle and fat layers, *etc.*) and for the electrotonic load of the torso to be incorporated into the activation solution of the heart (see Buist & Pullan (2003) for a good review). Alternatively, simplified models have also been developed that allow equivalent cardiac source dipoles to be calculated from cellular dipoles that are calculated from the transmembrane potential gradients scaled by local tissue conductivity (Bradley 1998, Buist 2001, Buist & Pullan 2003).

In this work, we are after a global measure of cardiac electrical behaviour in order to compare between the different LV models presented in this chapter. We therefore use the simplified dipole source model for the forward problem. A single dipole source is calculated for each FE in the LV model for each solution time interval. These sources are then placed into a homogeneous and isotropic torso volume and the static Laplace equation is solved to obtain the torso surface potentials at each point in time (Bradley 1998, Buist 2001). The full set of leads from the 12-lead ECG can then be calculated by differencing the torso surface potentials from suitable spatial locations. Figure 5.5 shows the LV geometric model placed in the torso volume model with the electrode locations for the three extremity leads.

Using CMISS, the calculation of the source dipoles is easily incorporated into the electromechanics simulations of the LV models. The dipoles are then saved for use in the torso model separately to the LV simulations. The existing implementation of the dipole calculations in CMISS is almost completely serial (*i.e.,* not parallelised very well) and as such is a significant contributor to computational time when performing these simulations (Figure 5.47). We reduce this fixed cost by only evaluating the dipoles every second time step during the model solution, but significant improvement may be obtained through parallelisation of this code. Once the dipole solutions are obtained, the forward torso model can be solved using a normal desktop computer in a brief period of time (*i.e.,* approximately 5 minutes for a 1 second heart beat).

As stated, this method produces a potential field described over the torso surface at each time point in the solution domain. This potential field can then be drawn as illustrated in Figure 5.6 using the LV activation solution from the heterogeneous FK-HMT model. These potential maps
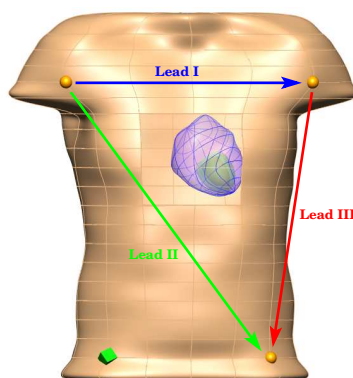
FIGURE 5.5: Illustration of the LV geometric model placed inside the torso volume model. The transparent blue surface shows the original human heart model created with the torso model, including left and right ventricles and the entire atria. The epicardial surface of the LV model is green and the endocardial surface is red. The locations of the extremity electrodes are given by the gold spheres and the reference electrode required for the model solution is given by the green cube. Leads I, II, and III from the standard 12-lead ECG are also shown.

are similar for the various simulations using the LV model presented below and we show the results in Figure 5.6 as an illustration of the results possible using this relatively simple method. For the purpose of analysing the simulation results we will focus on the ECG signals taken from these torso simulations.

5.3 Sinus Rhythm in a Left Ventricular Model

We first present simulations in which the LV model is paced in a manner representative of normal sinus rhythm. Buist (2001) has previously modelled initiation of electrical activation in a ventricular wedge model through the use of a Purkinje fibre network coupled to the myocardial tissue at the fibre end points. While such Purkinje activation would be closer to reality, here we follow the work of Tomlinson (2000) and specify the initial activation times at various points on the LV endocardial surface. A stimulus current is then applied at these points following the specified activation profile to give an initiation of Purkinje-like activation with no extra computational cost. The applied stimulus distribution is shown in Figure 5.7, where the stimulus times are derived from the initial activation times from the canine ventricular model of Tomlinson (2000). As shown in Figure 5.7 the earliest activation occurs in the lower mid-septal wall and the latest activation is toward the base of the free wall.

Using the Purkinje-like stimuli illustrated in Figure 5.7 we simulate normal sinus rhythm in

(a) 0 → 40 ms

(b) → 50 → 90 ms

(c) → 300 → 420 ms

(d) → 430 → 470 ms
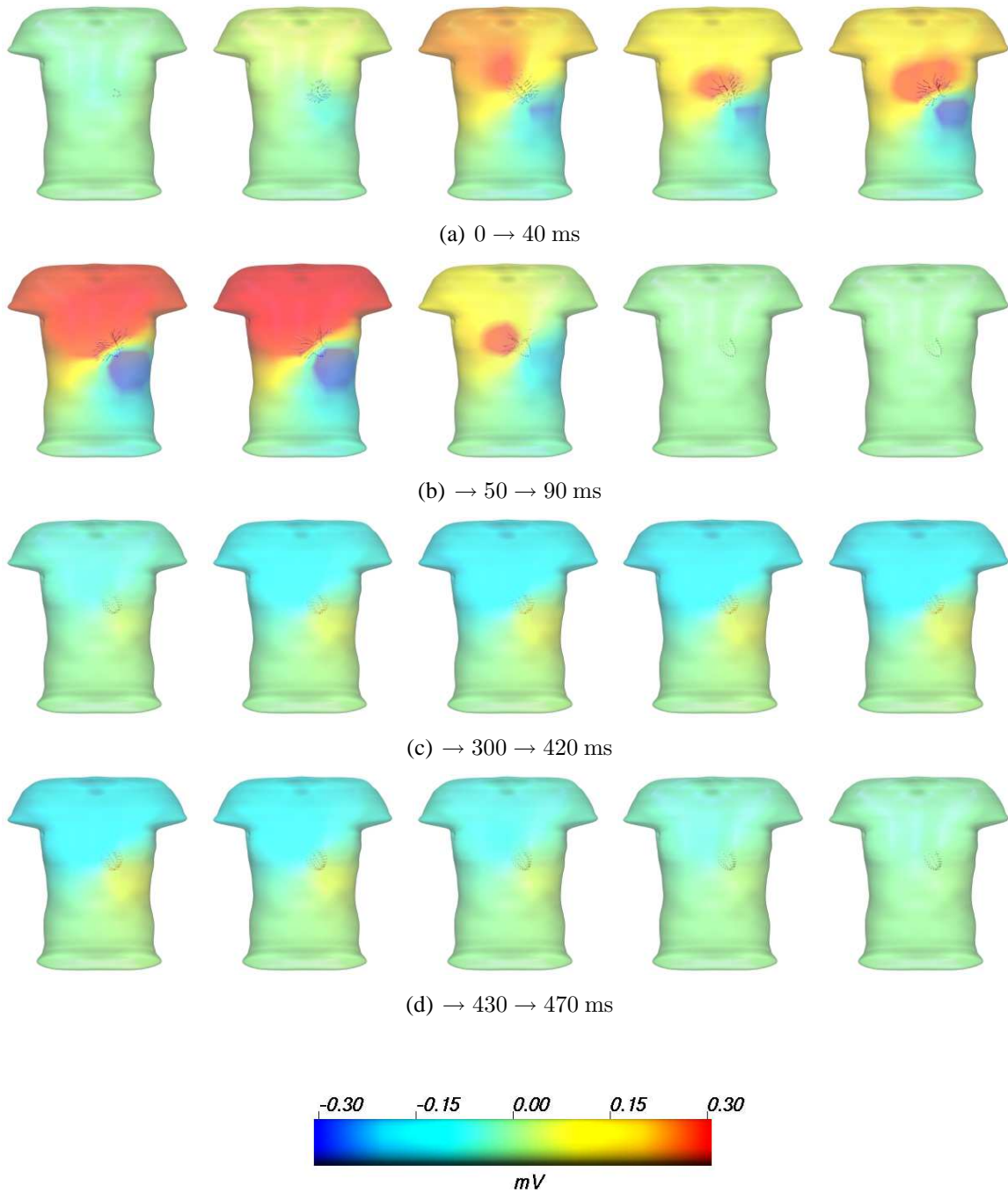
Figure 5.6: An illustration of torso surface potential solutions obtained using the method described in Section 5.2. These surface potentials are generated from the electrical activity in the heterogeneous FK-HMT sinus rhythm simulation in Figure 5.14. The torso surface is coloured with the potential calculated over the surface, using the scale given. Within the torso surface, the cellular based dipole sources are drawn as silver arrows, with the length of the arrow defined by the strength of the dipole.
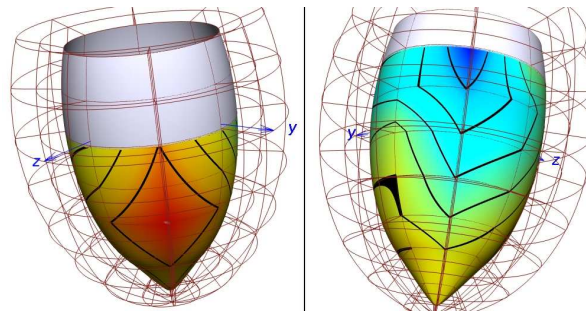
FIGURE 5.7: Illustration of the Purkinje-like stimulus used to approximate sinus rhythm in the LV model, the left panel shows the septal wall and the right is the LV free wall. The coloured endocardial surface shows the time of electrical stimulation of the endocardial surface, with red being the earliest activation at time 0 ms and blue the latest site of stimulation at 16 ms (the contour bands are in 2 ms intervals). The non-coloured regions of the endocardial surface have no stimulus current applied. A stimulus current of 150 μA · mm^{-3} is applied with a duration of 1 ms.

the LV geometry given in Figure 5.1. Following Section 5.1, the cardiac cycle is simulated with the following steps, subject to the displacement boundary conditions specified in Figure 5.8:

1. the LV is inflated to a cavity pressure of 1.0 kPa;
2. the time loop begins and electrical stimuli applied in sequence;
3. isovolumic contraction phase;
4. once cavity pressure exceeds arterial impedance (10 kPa), ejection begins and for each time step:
   (a) an isovolumic electro-mechanics solution step is performed;
   (b) the cavity free node displacement is adjusted to match the enclosed blood volume to that specified by the proscribed volume transient – for each displacement in these iterations a mechanics solution step is performed but the state of electrical activation remains constant;
   (c) final cavity pressure and volume values are determined for this time step and time is incremented.

The displacement boundary conditions illustrated in Figure 5.8 attempt to replicate similar conditions to the *in vivo* ventricle (Stevens 2002). The mitral and aortic valves are here combined into a single opening at the base of the LV where they are rigidly attached to the basal skeleton of the heart. With the given boundary conditions this valve ring is forced to maintain its location and shape. Since we are fixing the base of the ventricle we would like to leave the apex free to deform as dictated by contraction of the myocardium. When using the GBFE method
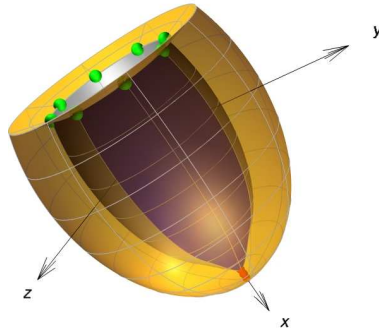
FIGURE 5.8: The displacement boundary conditions imposed on the LV model during sinus rhythm. The FE nodes represented by the green spheres are fixed in all three coordinate axes and their circumferential and transmural derivatives are also fixed. The red nodes at the apex are fixed in all coordinates and derivatives except the x-coordinate. The blue endocardial surface indicates the mid-septal region of the LV.

(Section C.3), however, there are numerical issues with the FE elements collapsing at the apex, issues which are very sensitive to certain modes of deformation. To restrict the occurrence of these deformations we are forced to restrain the apical nodes in a non-physiological manner. While this restriction probably does not interfere significantly with global ventricular function, there are implications for the mechanics of the tissue in close proximity to the apex which will be discussed below.

Tissue level material parameters for this model are summarised in Table 5.1 for the pole-zero mechanical material law and Table 5.2 presents the monodomain electrical conductivities. In the homogeneous model the FK-HMT cellular material parameters used are those described in Section 3.1.1 for the human epicardial cell type and the heterogeneous model uses all three cell type variants.

In setting the tissue conductivity values given in Table 5.2, we have decided to use transversely isotropic conductivities. Recent studies have shown that decisive evidence for the use of fully orthotropic conductivities in tissue level models is not yet available (Colli-Franzone, Guerri & Taccardi 2004). There is also wide variation reported in the literature for the values of the different conductivity components (Roth 1997). It has, however, been suggested that the ratio of fibre to cross-fibre conductivity is important, with a ratio of $10 : 1$ (longitudinal:transverse) estimated (Roth 1997) and used (Hooks et al. 2002, Hooks 2002). Note, however, that although in this model we are using transversely isotropic conductivities the simulation framework allows for the specification of orthotropic conductivities as well as spatial distribution of these parameters (as described in Figure 5.9 for the pole-zero parameters).

Type	Parameter	Apex	Sub-apex	Normal	Base
Coefficient	k_{11}			2.22 kPa	
	k_{22}			2.22 kPa	
	k_{33}			2.22 kPa	
	$k_{12} = k_{21}$	2.0 kPa	2.0 kPa	1.0 kPa	2.0 kPa
	$k_{13} = k_{31}$	2.0 kPa	2.0 kPa	1.0 kPa	2.0 kPa
	$k_{23} = k_{32}$	2.0 kPa	2.0 kPa	1.0 kPa	2.0 kPa
Pole	a_{11}	0.136	0.227	0.475	0.423
	a_{22}	0.136	0.227	0.619	0.555
	a_{33}	0.136	0.227	0.943	0.845
	$a_{12} = a_{21}$	0.3	0.4	0.8	0.4
	$a_{13} = a_{31}$	0.3	0.4	0.8	0.4
	$a_{23} = a_{32}$	0.3	0.4	0.8	0.4
Curvature	b_{11}	2.22	1.67	1.5	1.5
	b_{22}	2.22	1.67	1.5	1.5
	b_{33}	2.22	1.67	0.442	0.442
	$b_{12} = b_{21}$	1.5	1.0	1.2	1.0
	$b_{13} = b_{31}$	1.5	1.0	1.2	1.0
	$b_{23} = b_{32}$	1.5	1.0	1.2	1.0

TABLE 5.1: A summary of the pole-zero material parameters used in the sinus rhythm LV model. The parameters are based on those given by Remme et al. (2004) with modifications near the apex and base to aid convergence. The apex, sub-apex, normal, and base regions of the LV are described in Figure 5.9.
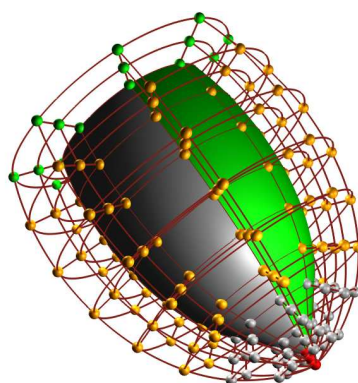
FIGURE 5.9: The different regions of the LV used in the pole-zero material parameter specification in Table 5.1. The apex nodes are shown as red spheres, the sub-apex as silver spheres, the normal nodes are gold spheres, and base nodes are green. The material parameters in Table 5.1 are specified at these nodes and linearly interpolated as required at intermediate spatial locations.

Material Axis	Parameter	Value
Fibre	σ_{11}	$0.263\,\mathrm{mS}\cdot\mathrm{mm}^{-1}$
Sheet	σ_{22}	$0.0263\,\mathrm{mS}\cdot\mathrm{mm}^{-1}$
Normal	σ_{33}	$0.0263\,\mathrm{mS}\cdot\mathrm{mm}^{-1}$

TABLE 5.2: The monodomain tissue conductivities for the sinus rhythm LV model, based on values given by Hooks et al. (2002).

5.3.1 Residual Strain and Atrial Systole

As described in Section 5.1.1 above, the first phase in our model of the cardiac cycle is atrial systole. During this phase the LA contracts and blood is forced into the diastolic LV. This is represented in the model by the application of a pressure boundary condition on the endocardial surface of the LV – here we apply a $1.0\,\mathrm{kPa}$ pressure.

Discussed in Section 3.2.2, an initial mechanics solution step is required if a model specifies residual strains to be incorporated. In the LV model, we specify a simple distribution of residual strain by setting the initial fibre extension ratios. At the apex and its surrounding tissue the initial fibre extension ratio is set to 1.0. Above the apex region, there is a linear transmural variation of initial fibre extension ratio from 0.95 at the endocardial surface to 1.05 at the epicardial surface.

Figure 5.10(a) provides the deformation solution obtained from inclusion of the residual strains and Figure 5.10(b) gives the deformed solution following the application of the endocardial surface pressure.

With an inflated model we can now move on to the next phase of the cardiac cycle and examine the active contraction of the myocardium and ejection of blood from the ventricle. First, however, we simulate electrical activation of the inflated geometry without any contraction to provide a comparison for the computational performance of the method developed as well as being able to compare the electrical activity of the contracting versus non-contracting models.

5.3.2 Electrical Activation

We now take the inflated model from Figure 5.10(b) and perform electrical activation simulations using the FK-HMT electro-mechanics model. In these simulations there is no contraction of the myocardium, we are focusing on the electrical activity of the model.

(a) Residual strain.   (b) Inflated to $1\,\mathrm{kPa}$.
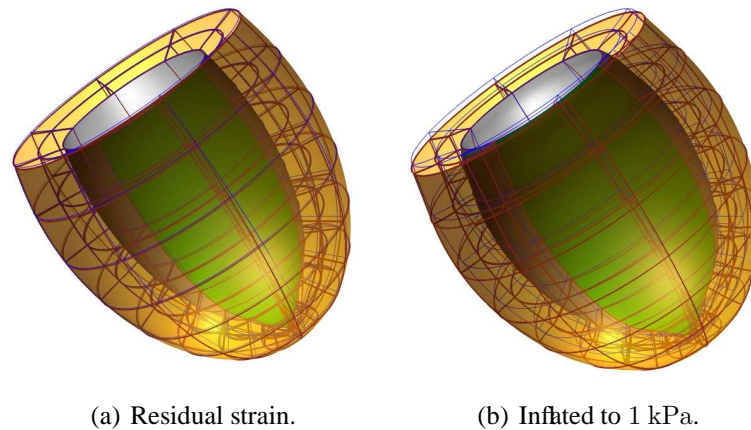
FIGURE 5.10: Results from simulating the deformation of the LV model through the application of a simple distribution of residual strain (a) and an applied pressure of $1.0\,\mathrm{kPa}$ on the endocardial surface. The blue lines represent the initial undeformed geometry and all other graphics are shown deformed.

Homogeneous FK-HMT

The first of the electrical activation simulations we present uses the epicardial cell type variant of the FK-HMT cellular electro-mechanics model (Section 3.1.1) with the inflated LV model. Figure 5.11 presents a summary of the results of this simulation, with a sampling of cellular AP signals from the simulation given in Figure 5.12.

In Figure 5.11(a) the sharp electrical activation wave can be seen progressing through the LV from the Purkinje-like endocardial stimulus, represented by the sharp transition between the blue resting potential and red plateau potential. The much smoother repolarisation wave is shown in Figures 5.11(b)–5.11(d) with a significantly more gradual transition back to the resting potential (coloured blue). Figure 5.11(e) shows that, as expected, without further electrical stimulus the ventricle completely returns to resting potential levels. From the selection of cellular AP signals presented in Figure 5.12, it is clear that they all have identical characteristics with the only difference being the time of initiation of the AP.

Following the method described above in Section 5.2, the electrical activation solution from this simulation can be used in a forward model to calculate torso surface potentials. These potential transients can then be used to calculate ECG signals as a measure of global electrical activity over the entire LV. See Figure 5.6 for an example of the surface potential images obtained from the torso model. The ECG signals from this model are given in Figure 5.16.

(a) $10 \rightarrow 50$ ms

(b) $\rightarrow 240 \rightarrow 280$ ms

(c) $\rightarrow 290 \rightarrow 330$ ms

(d) $\rightarrow 340 \rightarrow 380$ ms

(e) $\rightarrow 390 \rightarrow 430$ ms
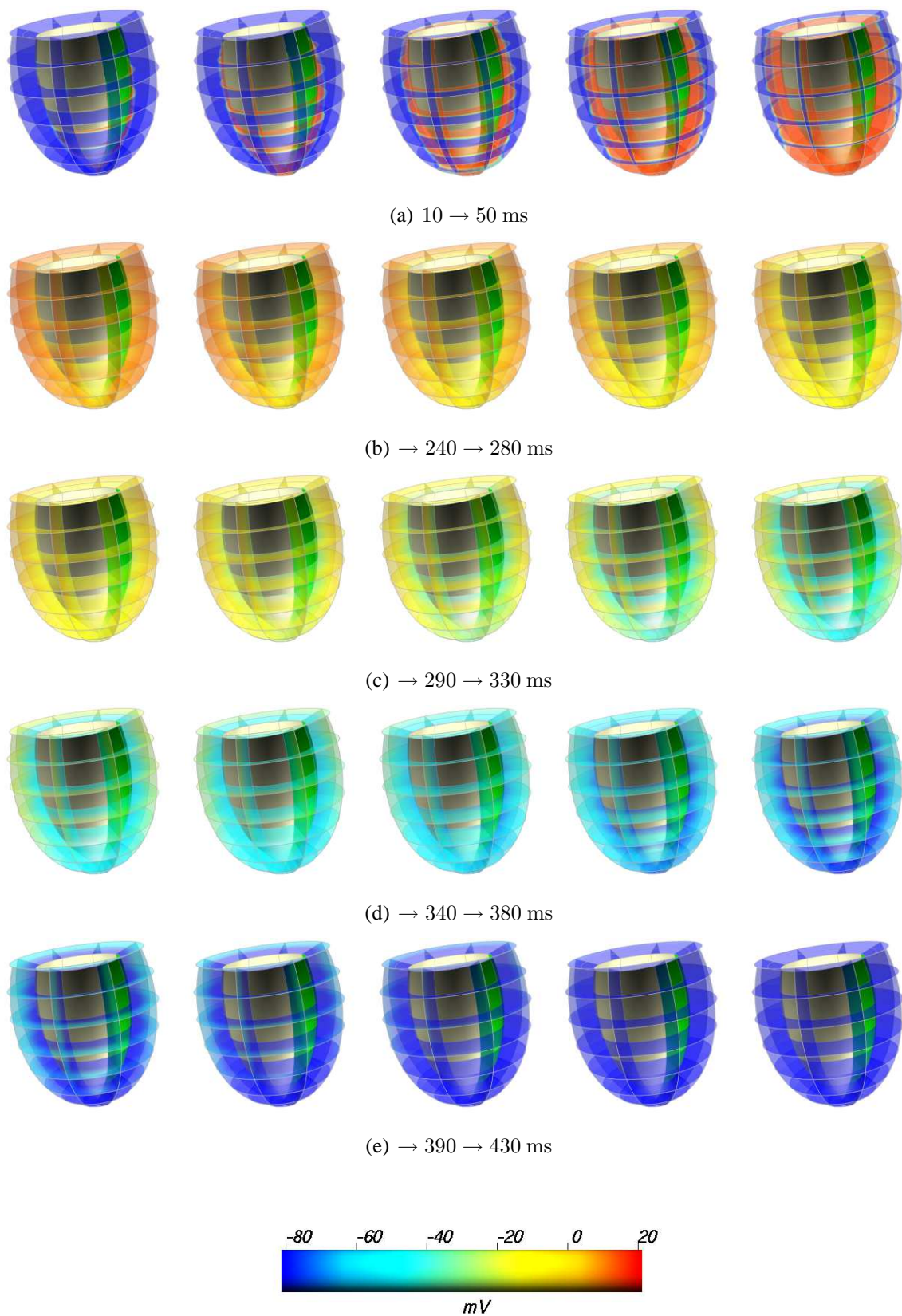
FIGURE 5.11: FK-HMT based activation of inflated homogeneous LV with Purkinje-like stimulus. Each image shows the internal element faces drawn as transparent surfaces coloured with the cellular transmembrane potential spectrum. The spectrum scale is shown in mV. See Figure 5.12 for a selection of cellular action potential signals from this simulation and Section D.3 for an animation of the full simulation results.

(a) Cellular action potentials.   (b) Spatial location of APs
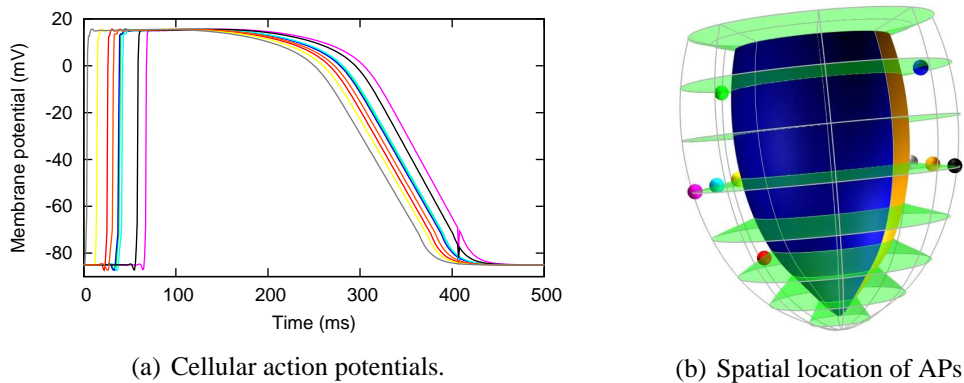
FIGURE 5.12: A selection of cellular AP signals from the homogeneous activation model presented in Figure 5.11. The colour of the action potentials in (a) matches the corresponding sphere in (b) which indicates the spatial location of the cell from which the signal is calculated.

Heterogeneous FK-HMT

The above sinus rhythm simulation is now repeated using a heterogeneous cell type distribution in the inflated LV model. We use a simple distribution of the epicardial, midmyocardial, and endocardial cell types described in Section 3.1.1 with the distribution throughout the LV illustrated in Figure 5.13. While this distribution of cell types is rather arbitrary and lacks any of the complex variation observed experimentally (Drouin et al. 1995), we are focused here on testing the implemented modelling framework and are less interested in modelling a specific physiological characteristic.
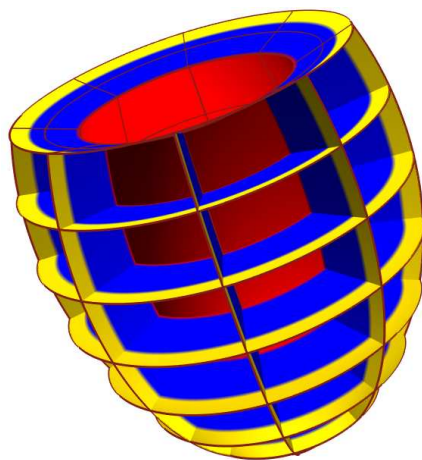
FIGURE 5.13: Distribution of the three cell types described by the FK-HMT model as used in the heterogeneous LV model. The epicardial cells are yellow, the midmyocardial blue, and the endocardial cells are drawn in red.

Note that the additional heterogeneity added to the LV model in this section is the spatial distribution of the three cell type variants described in Section 3.1.1. The previous model described above was obviously already heterogeneous, as shown by the material parameter variation given in Table 5.1. Thus, although not strictly correct, in this work when referring to the heterogeneous LV model we are referring to the model describing the distribution of different cellular phenotypes.

Results obtained from simulating only electrical activation using the heterogeneous distribution of FK-HMT cell types in the inflated LV are given in Figure 5.14. Cellular AP signals from a selection of cells throughout the ventricular wall are presented in Figure 5.15.

From Figure 5.14 the activation characteristics closely resemble those displayed by the homogeneous model in Figure 5.11. In the repolarisation phase, however, the effect of the greater APD of the midmyocardial cells is clearly displayed with the mid-wall region being the last to return to rest. This result is also shown by the cellular AP signals given in Figure 5.15 where the APD differences are more obvious in the mid-wall signals. Table 5.3 provides the actual APD values for both the homogeneous (Figure 5.12) and heterogeneous (Figure 5.15) activation simulations.

Location	Homogeneous model	Heterogeneous model
🔴	352 ms	416 ms
🟢	352 ms	423 ms
🔵	351 ms	423 ms
🟣	339 ms	367 ms
🔵	350 ms	417 ms
🟡	360 ms	434 ms
⚫	344 ms	367 ms
🟠	351 ms	418 ms
⚪	362 ms	437 ms

TABLE 5.3: The APD values for the cellular AP signals given in Figures 5.12 and 5.15, from the electrical activation only LV simulations. The coloured spheres match those used to provide signal locations in Figures 5.12(b) and 5.15(b).

The APD values given in Table 5.3 show that even for the homogeneous model there is variation of APD throughout the myocardium. This illustrates the effect of the electrotonic loading on each of the cells by their neighbouring cells. For the homogeneous model, all the APD values are close to the single cell APD of $352\,\mathrm{ms}$ for the epicardial cell type (Section 3.1.1).

(a) $10 \rightarrow 50$ ms

(b) $\rightarrow 240 \rightarrow 280$ ms

(c) $\rightarrow 290 \rightarrow 330$ ms

(d) $\rightarrow 340 \rightarrow 380$ ms

(e) $\rightarrow 390 \rightarrow 430$ ms

(f) $\rightarrow 440 \rightarrow 480$ ms
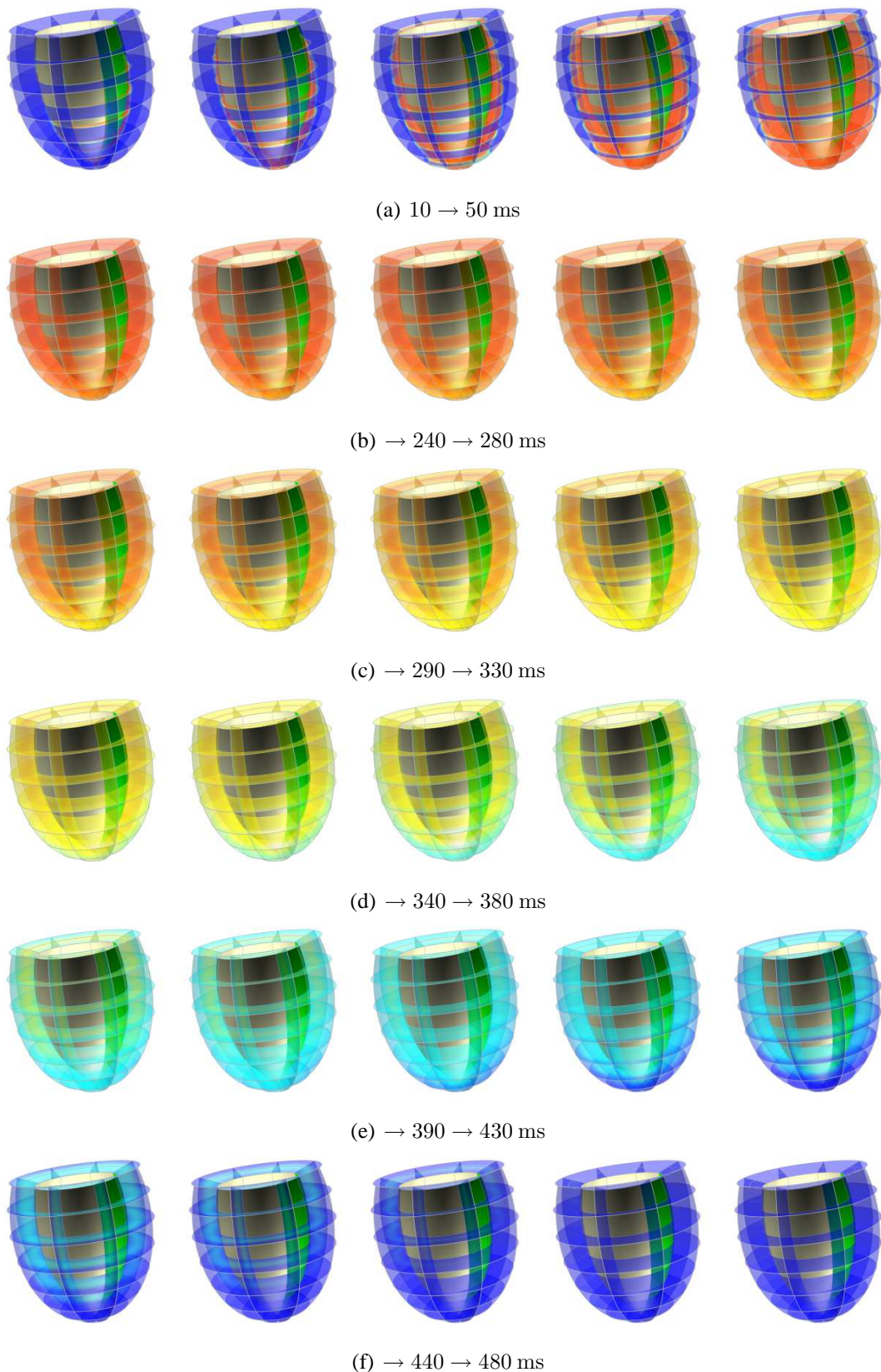
FIGURE 5.14: FK-HMT based activation of inflated LV with Purkinje-like stimulus and heterogeneous cell type distribution. Each image shows the internal element faces drawn as transparent surfaces coloured with the cellular transmembrane potential. The potential scale is given in Figure 5.11. See Figure 5.15 for a selection of cellular action potential signals from this simulation and Section D.3 for an animation of the full simulation results.

(a) Cellular action potentials.   (b) Spatial location of APs
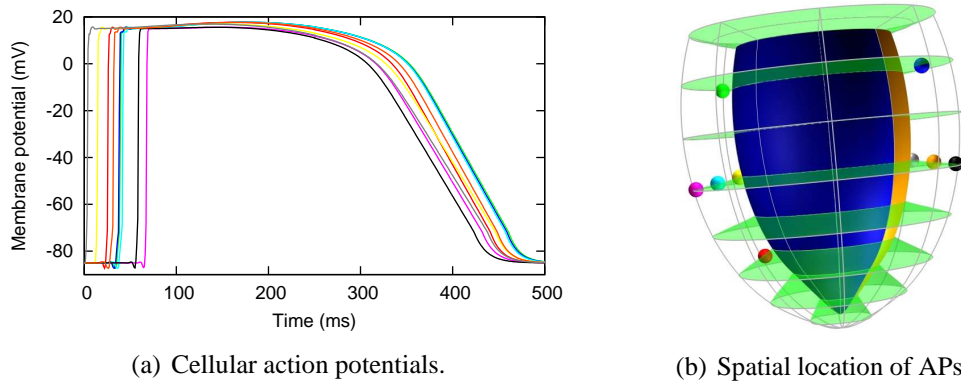
FIGURE 5.15: A selection of cellular AP signals from the heterogeneous activation model presented in Figure 5.11. The colour of the action potentials in (a) matches the corresponding sphere in (b) which indicates the spatial location of the cell from which the signal is calculated.

The heterogeneous model displays, as expected, greater variation of APD values through the ventricular wall. The first group of values (red, green, and blue) are all approximately in the mid-wall region and have APD values similar to those of the mid-wall cells from the transmural cell groups (cyan and orange). The two epicardial cells (magenta and black) show significantly longer AP signals in the heterogeneous model compared to the homogeneous, while the mid-wall cells (cyan and orange) have APDs slightly shorter than expected for the midmyocardial cells. The two endocardial cells (yellow and silver) show APD values higher than expected for even midmyocardial cells, suggesting that these are in fact midmyocardial cells rather than endocardial and that the comparatively low volume of endocardial cells places little current load on the midmyocardial cells close to the endocardial boundary. Conversely, the much larger volume of epicardial cells applies a significant current load on the midmyocardial cells nearer the epicardial cell boundary.

As with the homogeneous model, we can use the activation solution for the heterogeneous model to compute the torso surface potential field. The illustrative solutions presented in Figure 5.6 were computed from the activation solution from this heterogeneous LV model. From the torso potential solution ECG signals can be derived, with the three extremity leads given in Figure 5.16 for both the homogeneous and heterogeneous models.
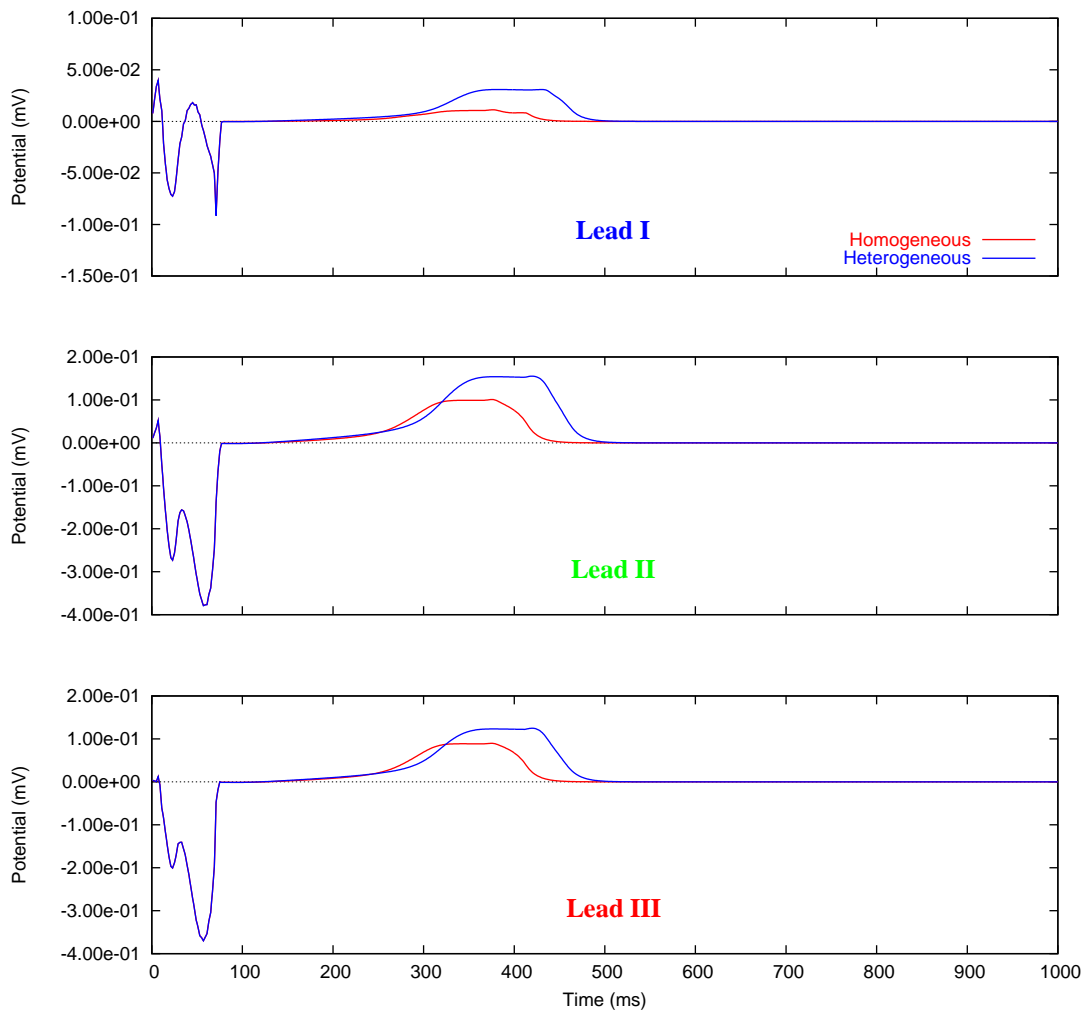
FIGURE 5.16: Comparison of Lead I, II, and III ECG signals between the homogeneous and heterogeneous LV activation models. The ECG signals are derived from torso potential solutions, such as those illustrated in Figure 5.6, from the activation model results given in Figures 5.11 and 5.14.

5.3.3 Coupled Electro-Mechanics

Progressing from the electrical activation models of sinus rhythm described in Section 5.3.2, we now present coupled electro-mechanics simulations using both the homogeneous and heterogeneous LV models of sinus rhythm. We are using the FK-HMT cellular electro-mechanics model with identical tissue level material parameters as described in Tables 5.1 and 5.2 and the Purkinje-like stimulus protocol (Figure 5.7).

Starting from the inflated LV model (Section 5.3.1) we perform steps $2 \rightarrow 4$ of the cardiac cycle algorithm as outlined on page 141. From the initial inflated geometry, the Purkinje-like sinus stimulus is applied to initiate contraction, resulting in the LV cavity pressure increasing. Once the pressure exceeds the 10 kPa arterial impedance imposed on the system the cavity volume begins to decrease as defined by the volume transient given in Figure 5.17, where we have arbitrarily set the peak ejection fraction at 50 % of the initial volume.
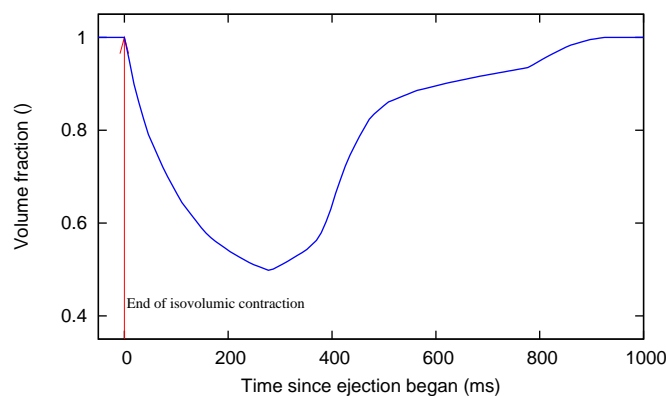
FIGURE 5.17: The volume transient used to control LV cavity volume during the ejection phase of the cardiac cycle, where 0 ms is the time at which the arterial impedance is overcome and ejection begins. The curve was digitised from the LV volume transient given in Figure 5.2. The volume fraction gives the instantaneous cavity volume as a fraction of the cavity volume following inflation to 1.0 kPa.

Homogeneous FK-HMT, no ejection

Before examining simulations of models of the cardiac cycle, we first present a simulation using the homogeneous LV sinus rhythm electro-mechanics model but with no ejection of blood from the ventricular cavity. This simulation is isovolumic for the duration of the cycle, and was primarily performed to test the behaviour of the simulation framework when adding the

mechanics to the activation models above without the added complexity of the cavity volume changes.

Results from this simulation are given in Figures 5.18 and 5.19 with a summary of the system dynamics given in Figure 5.20. In addition to testing the modelling and simulation framework we have developed, this particular simulation will be used to compare to the bi-ventricular (BiV) pacing protocol in Section 5.4.2 below.

Homogeneous FK-HMT

We now present results of cardiac cycle simulations of the LV model with the homogeneous FK-HMT model. Tissue and cellular material parameters and the stimulus protocol are identical to those described above (Tables 5.1 and 5.2, Figure 5.7, and the epicardial cell type from Section 3.1.1). The cavity volume is controlled to follow the transient given in Figure 5.17.

With the same layout as the isovolumic simulation above, Figures 5.21 and 5.22 present the results from this simulation, showing the transmembrane potential and deforming geometry of the LV. These figures also provide the LV cavity volume and pressure signals at corresponding temporal time intervals. Figure 5.23 summarises the organ and cellular level results from this simulation.

Heterogeneous FK-HMT

Similar to the homogeneous simulation above, we now present a simulation of the cardiac cycle in the heterogeneous LV model. This model uses the distribution shown in Figure 5.13 of the three cell types described by the FK-HMT cellular model (Section 3.1.1) with the specified LV cavity volume transient (Figure 5.17).

Results of this simulation are presented in Figures 5.24–5.26. Figures 5.24 and 5.25 provide the deformation solutions for the LV geometry at a selection of time points throughout the simulation as well as the distribution of transmembrane potential. Figure 5.26 summarises the cellular and organ level dynamics of this simulation.

(a) $10 \rightarrow 40$ ms

(b) $\rightarrow 50 \rightarrow 80$ ms

(c) $\rightarrow 90 \rightarrow 120$ ms

(d) $\rightarrow 130 \rightarrow 160$ ms

(e) $\rightarrow 170 \rightarrow 200$ ms

(f) $\rightarrow 210 \rightarrow 240$ ms
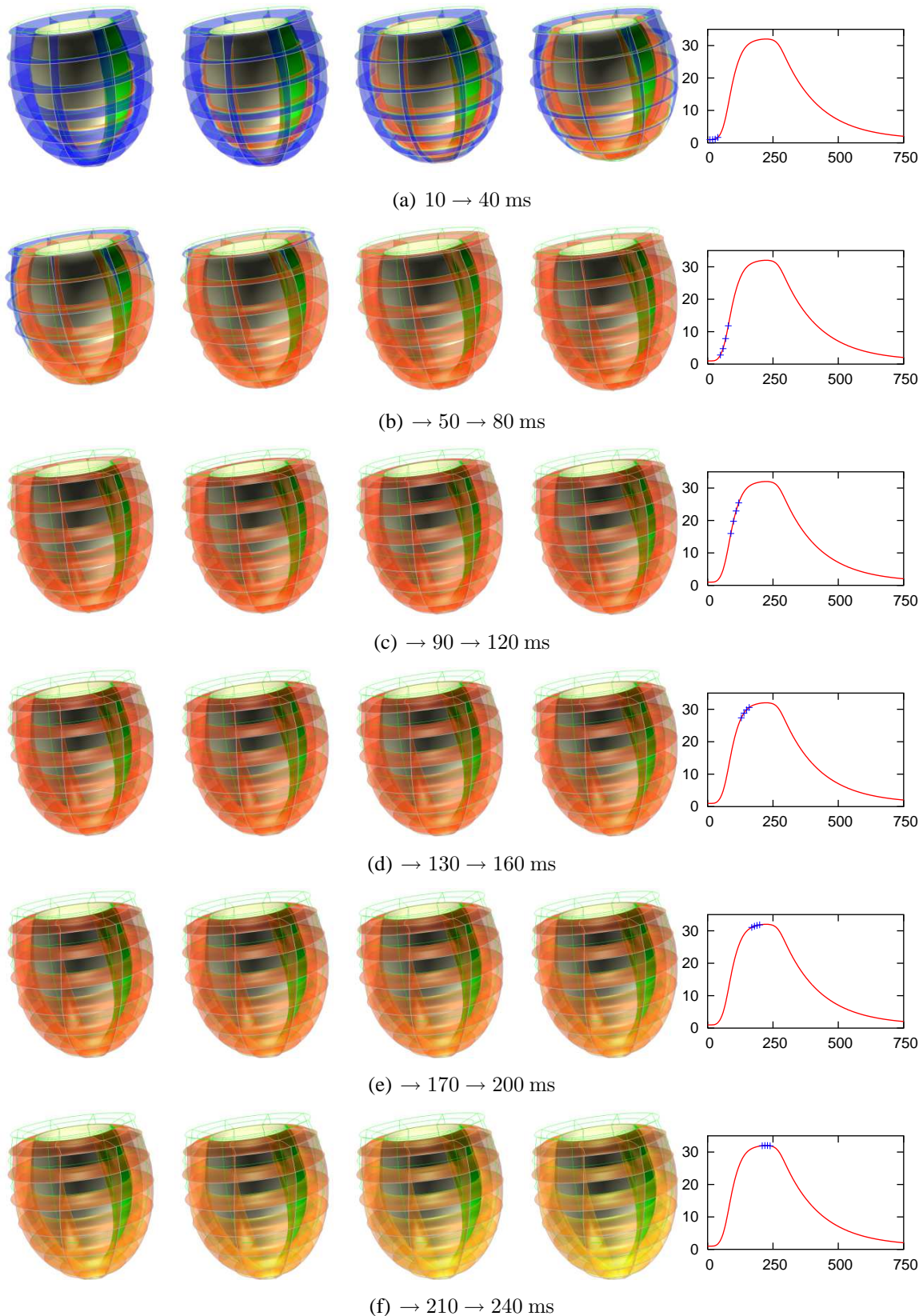
FIGURE 5.18: The first part of isovolumic contraction of the homogeneous LV electro-mechanics model of sinus rhythm. The graphs provide the cavity pressure at each of the time points shown, in kPa plotted against time in ms. This model has a constant cavity volume throughout the simulation. The green lines show the undeformed geometry and the element faces are coloured by the potential spectrum given in Figure 5.11. These results are continued in Figure 5.19.

(a) $250 \rightarrow 280$ ms

(b) $\rightarrow 290 \rightarrow 320$ ms

(c) $\rightarrow 330 \rightarrow 360$ ms

(d) $\rightarrow 370 \rightarrow 400$ ms

(e) $\rightarrow 410 \rightarrow 440$ ms

(f) $\rightarrow 450 \rightarrow 480$ ms
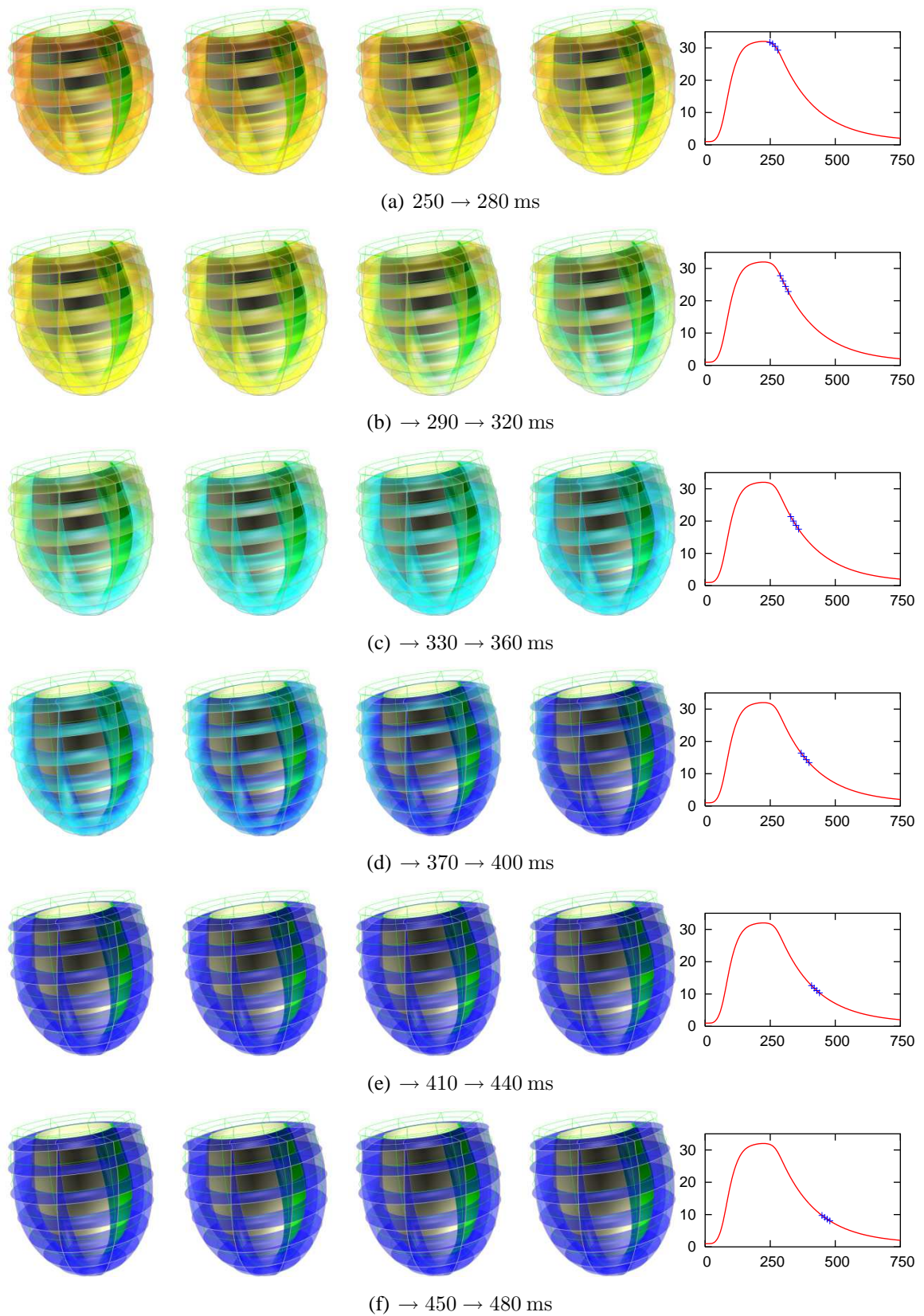
FIGURE 5.19: Continuing the results begun in Figure 5.18 with the homogeneous isovolumic contracting LV model. These results are summarised in Figure 5.20 and also see Section D.3.
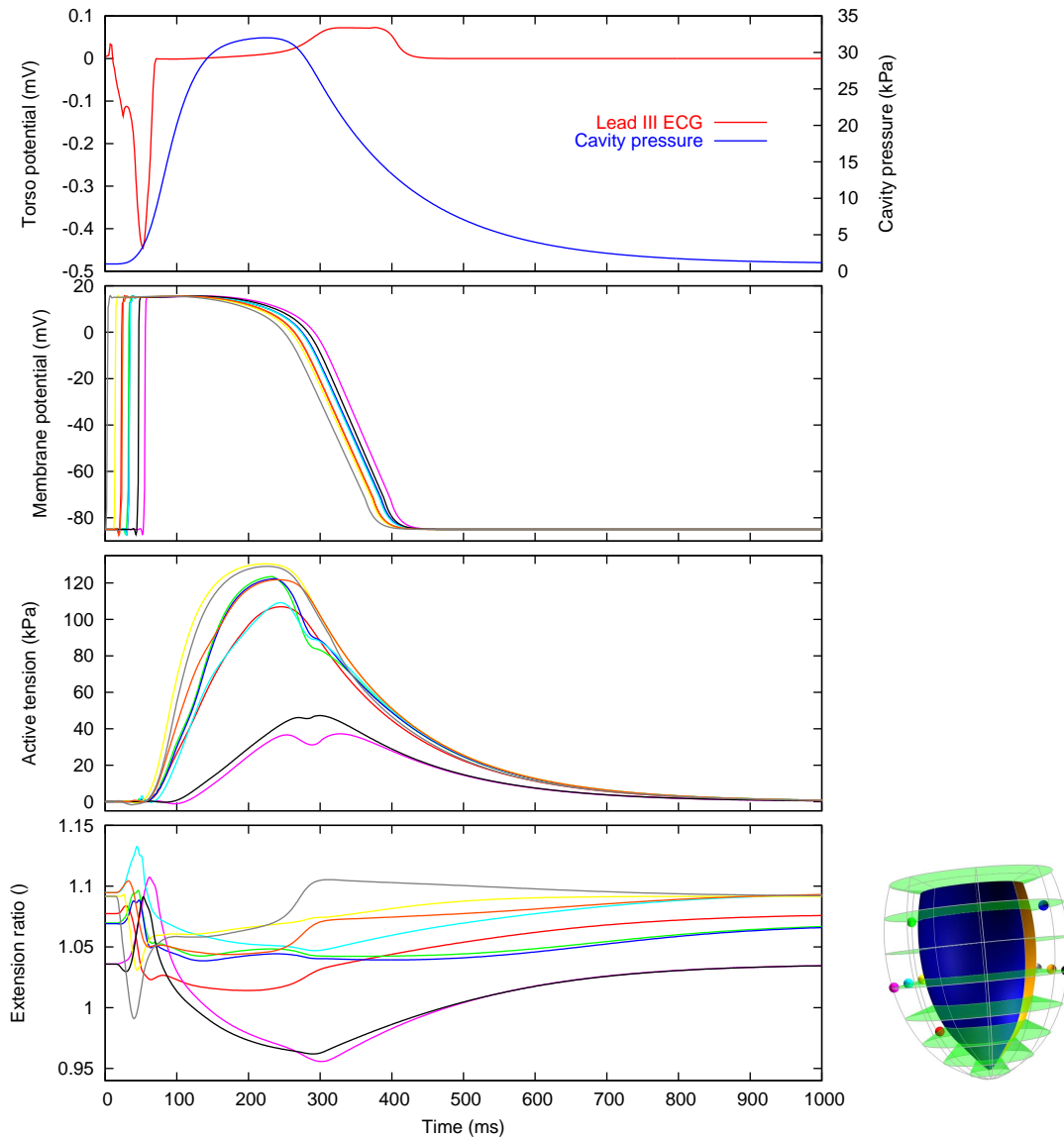
FIGURE 5.20: Summary of the results presented in Figures 5.18 and 5.19 of the simulation of electro-mechanics in the homogeneous LV model of sinus rhythm with no ejection. The top graph shows the lead III ECG signal (left axis) and the LV cavity pressure (right axis). The other graphs are the cellular AP, tension, and extension ratio signals, with signal colours matched to the coloured spheres in the accompanying LV image providing the spatial location of the signals.

(a) $10 \rightarrow 40$ ms

(b) $\rightarrow 50 \rightarrow 80$ ms

(c) $\rightarrow 90 \rightarrow 120$ ms

(d) $\rightarrow 130 \rightarrow 160$ ms

(e) $\rightarrow 170 \rightarrow 200$ ms

(f) $\rightarrow 210 \rightarrow 240$ ms
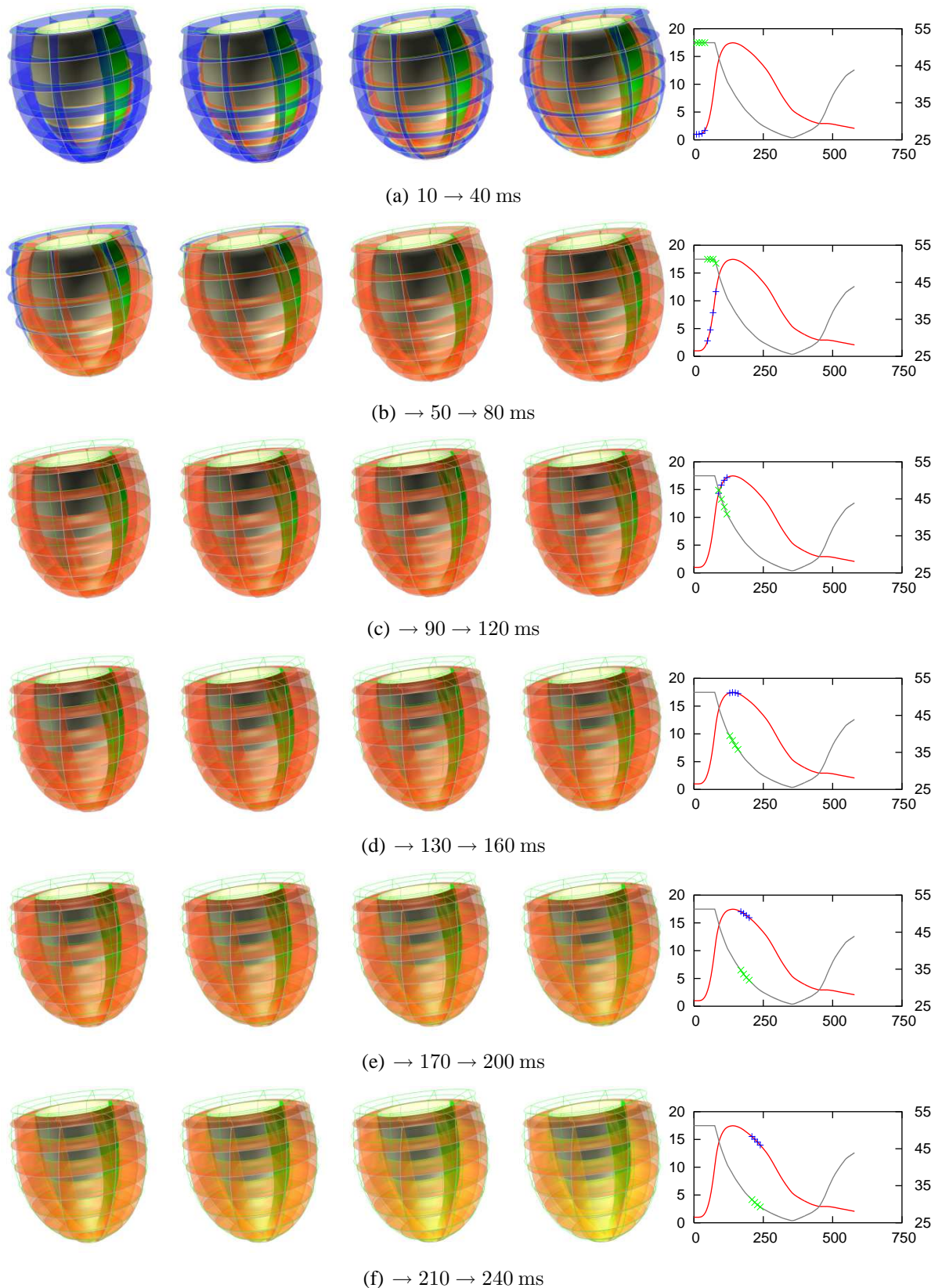
FIGURE 5.21: The first part of the cardiac cycle using the homogeneous LV electro-mechanics model of sinus rhythm. The graphs provide the cavity pressure (left scale, kPa) and volume (right scale, ml) at each of the time points shown. The green lines show the undeformed geometry and the element faces are coloured by the potential spectrum given in Figure 5.11. These results are continued in Figure 5.22.

(a) $250 \rightarrow 280$ ms

(b) $\rightarrow 290 \rightarrow 320$ ms

(c) $\rightarrow 330 \rightarrow 360$ ms

(d) $\rightarrow 370 \rightarrow 400$ ms

(e) $\rightarrow 410 \rightarrow 440$ ms

(f) $\rightarrow 450 \rightarrow 480$ ms
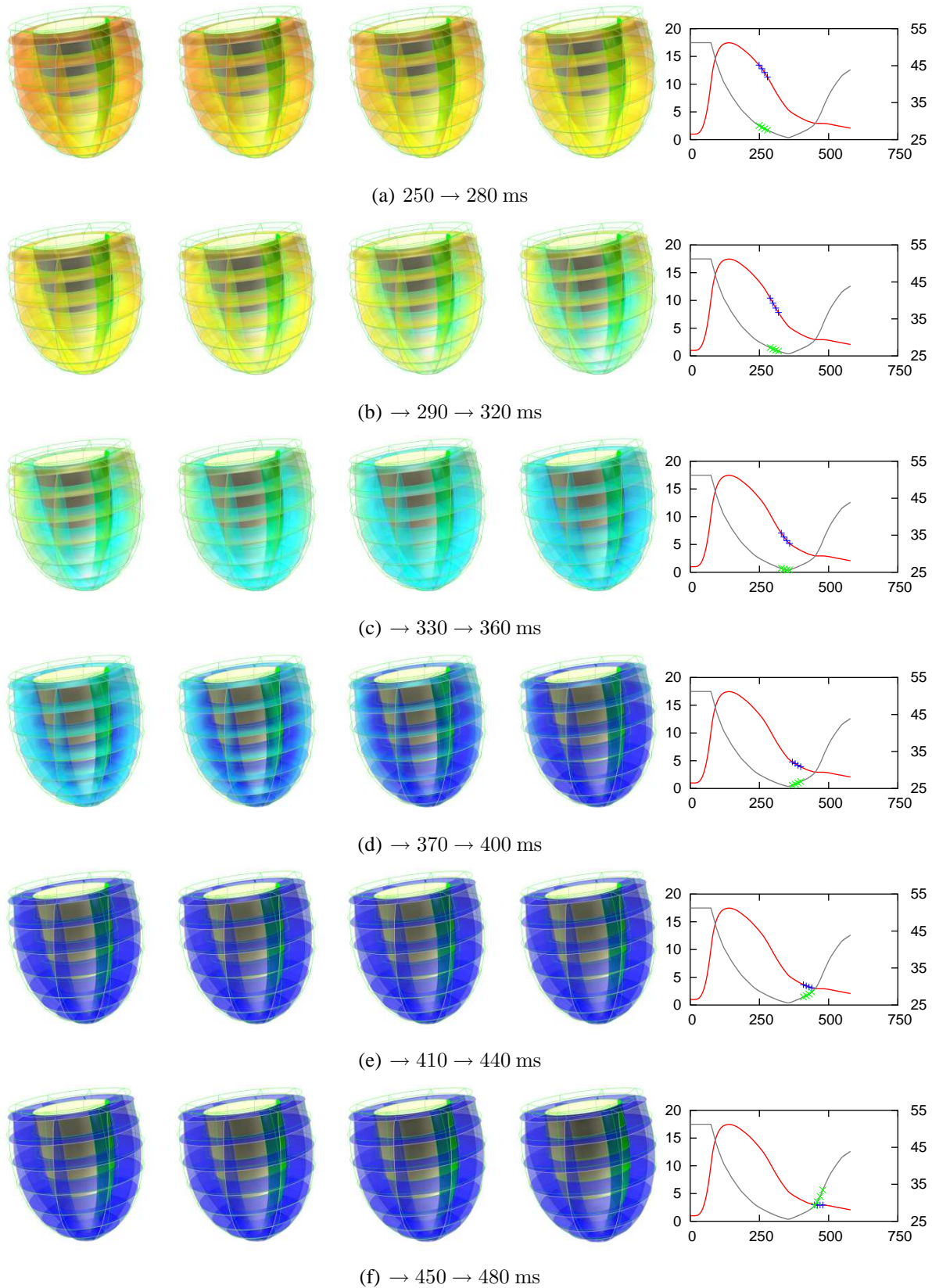
FIGURE 5.22: Continuation of the results begun in Figure 5.21 of the cardiac cycle model using the homogeneous LV electro-mechanics model of sinus rhythm. These results are summarised in Figure 5.23 and see Section D.3 for an animation of the simulation results.
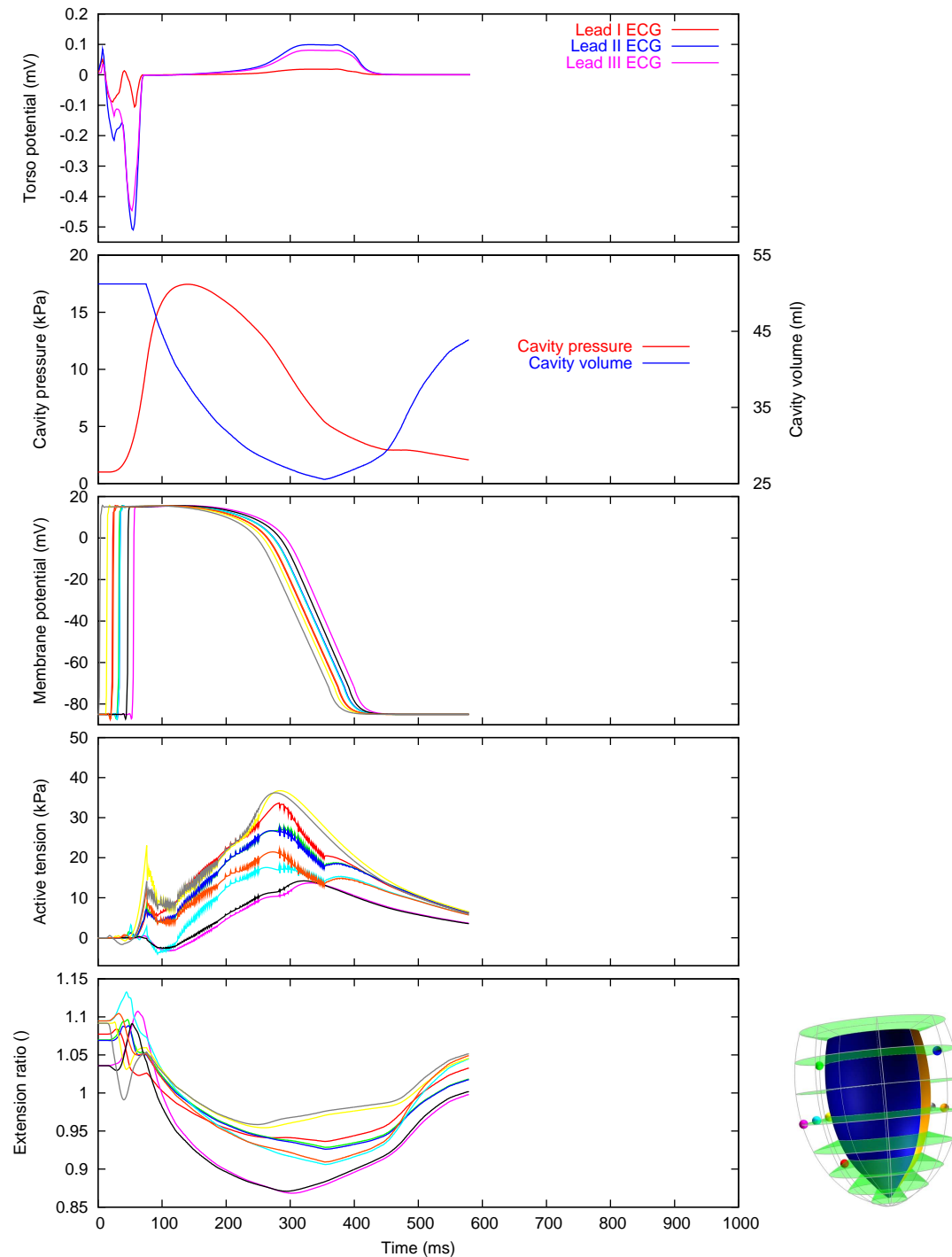
FIGURE 5.23: Summary of the results presented in Figures 5.21 and 5.22 of the simulation of the cardiac cycle in the homogeneous LV model of sinus rhythm. The top graph shows the ECG signals obtained from this simulation and the second graph plots the LV cavity pressure (left axis) and volume (right axis). The other graphs are the cellular AP, tension, and extension ratio signals, with signal colours matched to the coloured spheres in the accompanying LV image providing the spatial location of the signals.

(a) $10 \rightarrow 40$ ms

(b) $\rightarrow 50 \rightarrow 80$ ms

(c) $\rightarrow 90 \rightarrow 120$ ms

(d) $\rightarrow 130 \rightarrow 160$ ms

(e) $\rightarrow 170 \rightarrow 200$ ms

(f) $\rightarrow 210 \rightarrow 240$ ms
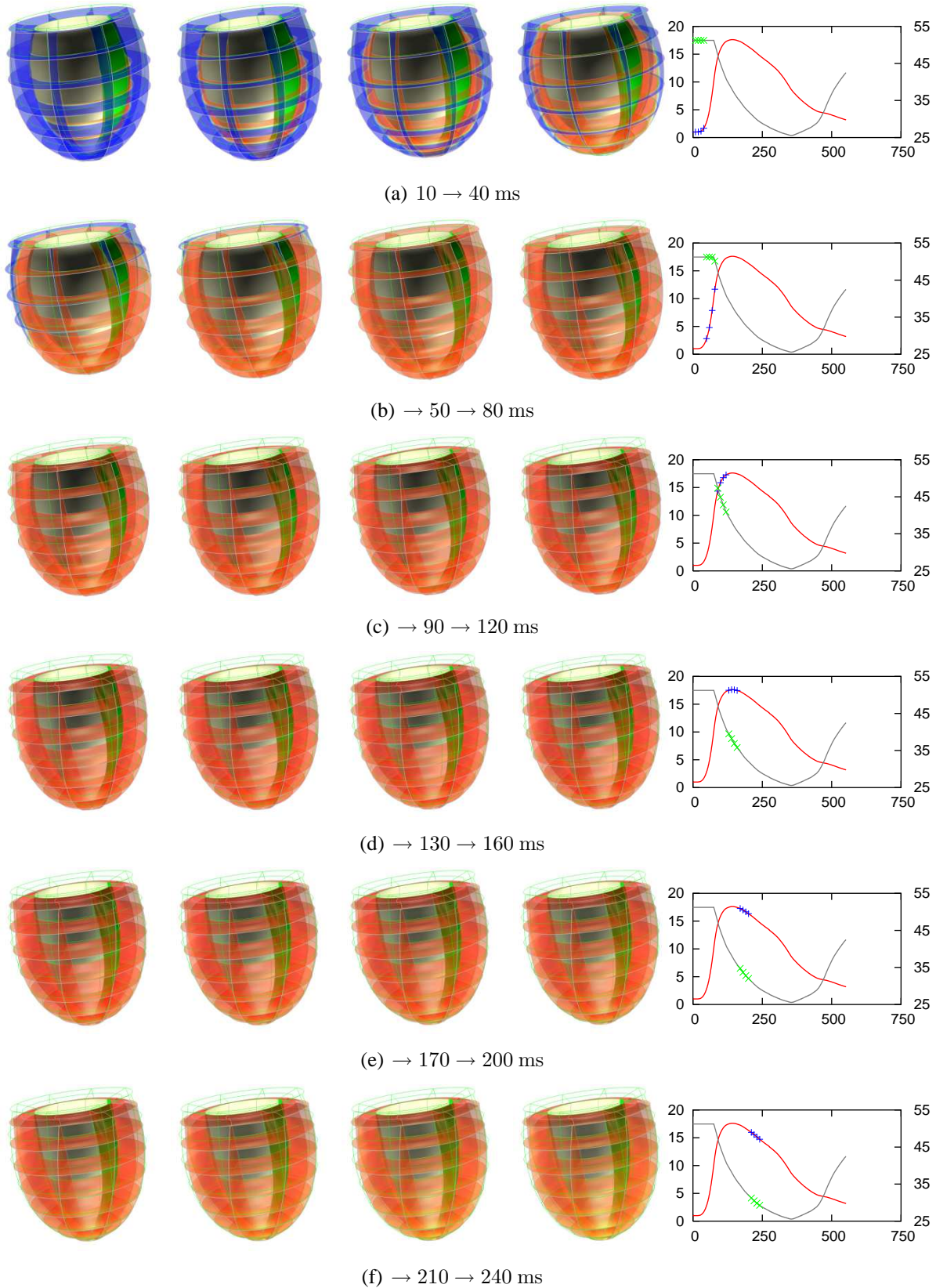
FIGURE 5.24: The first part of the cardiac cycle using the heterogeneous LV electro-mechanics model of sinus rhythm. The graphs provide the cavity pressure (left scale, kPa) and volume (right scale, ml) at each of the time points shown. The green lines show the undeformed geometry and the element faces are coloured by the potential spectrum given in Figure 5.11. These results are continued in Figure 5.25.

(a) 250 → 280 ms

(b) → 290 → 320 ms

(c) → 330 → 360 ms

(d) → 370 → 400 ms

(e) → 410 → 440 ms

(f) → 450 → 480 ms
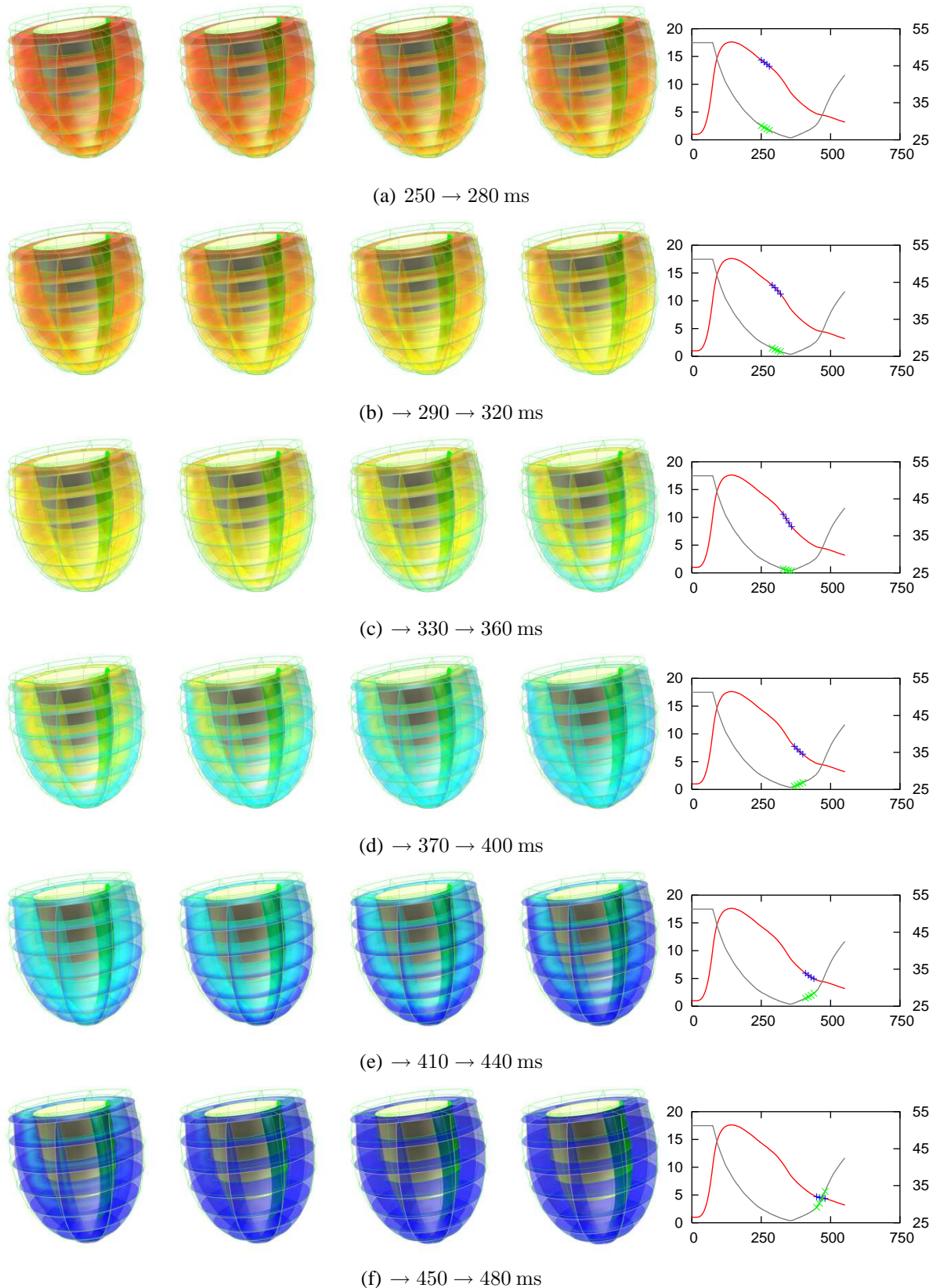
FIGURE 5.25: Continuation of the results begun in Figure 5.24 of the cardiac cycle model using the heterogeneous LV electro-mechanics model of sinus rhythm. These results are summarised in Figure 5.26 and see Section D.3 for an animation of the simulation results.
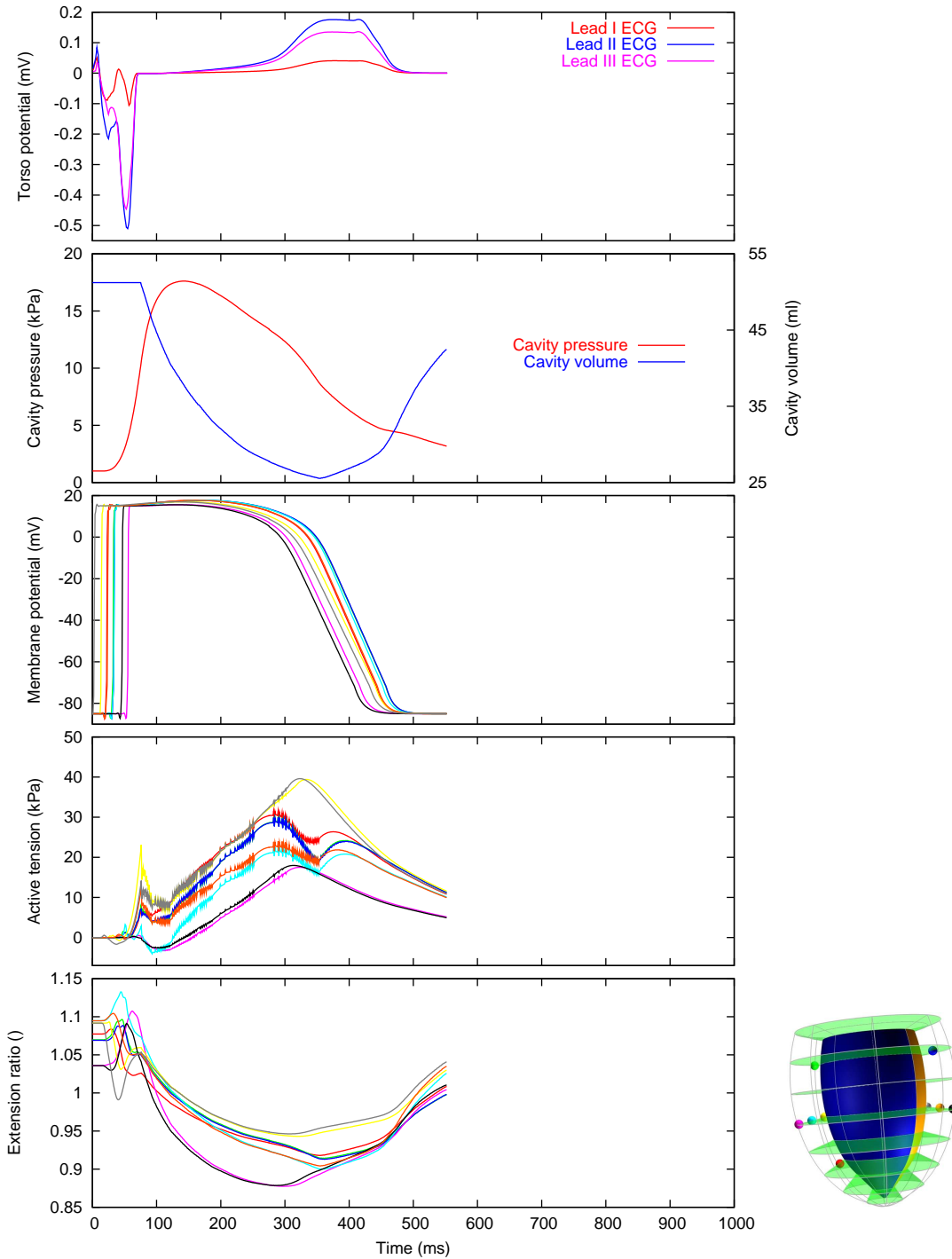
FIGURE 5.26: Summary of the results presented in Figures 5.24 and 5.25 of the simulation of the cardiac cycle in the heterogeneous LV model of sinus rhythm. The top graph shows the ECG signals obtained from this simulation and the second graph plots the LV cavity pressure (left axis) and volume (right axis). The other graphs are the cellular AP, tension, and extension ratio signals, with signal colours matched to the coloured spheres in the accompanying LV image providing the spatial location of the signals.

5.3.4   Discussion

The simulation results presented in Sections 5.3.2 and 5.3.3 above provide ample evidence that the modelling and simulation framework that we have developed and implemented works well for both electrical activation only models and coupled electro-mechanics models using the LV geometry given in Figure 5.1. The most significant drawback in the framework highlighted by these simulations is the shear amount of time taken to obtain these results. Section 5.5 provides a summarised view of this, but we note that the coupled electro-mechanics simulations of the homogeneous and heterogeneous LV models with ejection took on the order of three weeks to achieve the $550\,\mathrm{ms}$ of simulation time presented in this thesis.

In addition to demonstrating the successful application of our framework to a model more realistic than a the previous cube model (Section 3.4), these simulations demonstrate functionally reasonable solutions. Using the Purkinje-like sinus rhythm stimulus protocol given in Figure 5.7, the smooth transmural progression of electrical activation is clear in all these results with full ventricular activation in less than $70\,\mathrm{ms}$ for all of the models of sinus activation. With the simple transmural fibre variation illustrated in Figure 5.1 and the sequence of contraction solutions given in Figures 5.18(a)–5.18(c) we show that the LV initially deforms into a more spherical shape with just the endocardial region actively contracting. Then as the mechanical activation moves out through the wall to the circumferentially oriented mid-wall fibres the deformation becomes more longitudinal and the twisting motion begins. This is followed once more by a move toward more spherical deformation as the inclined epicardial fibres are activated and the twisting increases. These results are perhaps more easily observed in the animation of the simulation results given in Section D.3.

Sections 5.3.2 and 5.3.3 describe five sinus rhythm simulations based on the FK-HMT cellular model on the LV geometry. These are the electrical activation only models of the homogeneous and heterogeneous LV, coupled electro-mechanics in the LV with no ejection, and ejection models using the homogeneous and heterogeneous LV models. In all cases the homogeneous and heterogeneous models are identical during the electrical activation phase, as expected from the cellular model description, and differ during repolarisation. An important feature of the heterogeneous model is the reversal of the direction in which the repolarisation wave travels through the wall (compare, for example, Figures 5.22(c) and 5.22(d) with Figures 5.25(d) and 5.25(e)).

Figure 5.27 presents the three ECG extremity leads from each of the five sinus rhythm simulations. From these signals the similarity of the cellular activation phase between the models

can be seen on the torso surface. The two activation only models have initially identical ECG signals and the three electro-mechanics models are also identical to each other but different to the non-contracting models. These common portions of the ECG signals are followed by differing traces for all of the models during the tissue repolarisation phase. Most notably, the two heterogeneous models have significantly increased magnitudes of the T-wave regions of the ECG signals for the three leads and the contracting models have slightly faster kinetics. The cause of these differences can be seen in the AP signals given in Figure 5.28(a) which clearly show that all three electro-mechanics models activate earlier than the activation only models for each of the spatial locations shown. The T-wave changes are due to the differences in the repolarisation phases of the cellular APs which give rise to different APDs (Table 5.3).

Figure 5.27(d) presents a comparison of the pressure transients for the three sinus rhythm electro-mechanics models. As expected, the model with no ejection reaches a much higher peak pressure compared to the two models with ejection. Comparing the homogeneous and heterogeneous models that include ejection, we again see identical pressure values during the initial activation phase of the cycle followed by differences during repolarisation. The volume transient is identical for both models since it is essentially applied as a specified time varying boundary condition for both models (Section 5.1.3). The peak pressure achieved by the models with ejection is consistent with values reported is similar models (Usyk et al. 2002). During the repolarisation phase of the cycle the heterogeneous model maintains a higher cavity pressure due to the prolonged APs of the midmyocardial cells giving rise to increased active tension at the cellular level (Figure 5.28(b)).

5.4 Left Ventricular Pacing

The simulations presented in Section 5.3 above describe a fairly simple model developed to simulate a normal SAN initiated heart beat. In an extension to this, we now examine the applicability of the modelling and simulation framework we have developed to models which are a little less normal. In CRT studies there are some commonly used pacing sites that have been reported in the literature, chosen both for ease of access for placing the stimulus electrodes and for ability to aid mechanical resynchronisation of the LV pump.

Following the work of Wyman et al. (1999), we have chosen to present simulations examining two pacing sites in the LV. The first pacing site is located in the subendocardium near the base of the LV free wall and is referred to here as left ventricular base (LVb) pacing. The

(a) Lead I.

(b) Lead II.

(c) Lead III.

(d) Cavity pressure.
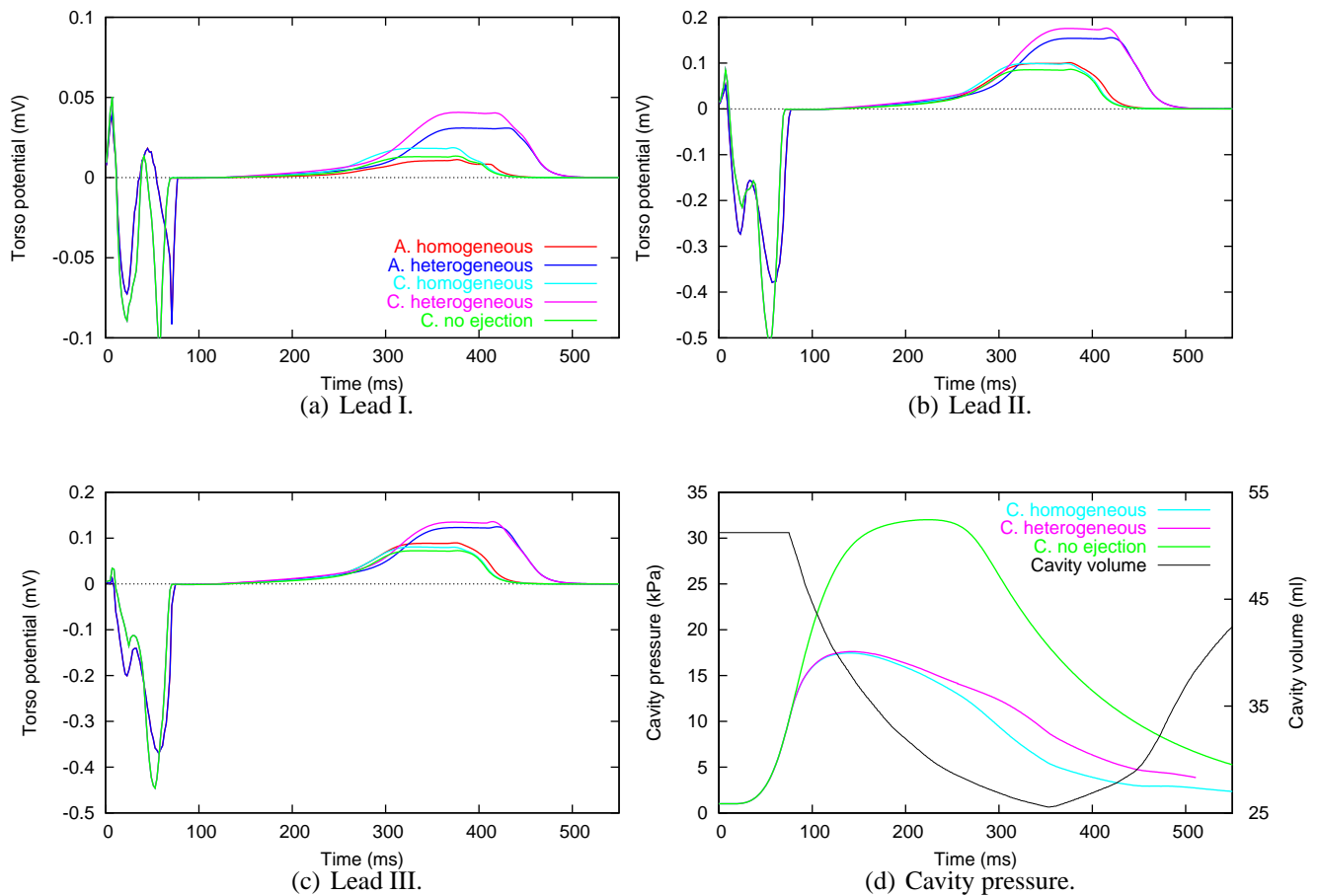
FIGURE 5.27: Comparison of the tissue level results from the sinus rhythm simulations. The full simulation results are given in Section 5.3.2 for the electrical activation only models (A. homogeneous and A. heterogeneous) and Section 5.3.3 for the coupled electro-mechanics models with the homogeneous (C. homogeneous) and heterogeneous (C. heterogeneous) models with ejection and the homogeneous model with no ejection (C. no ejection). (a)-(c) give the three extremity ECG signals and (d) the ventricular cavity pressure (and the volume for the two ejection models).
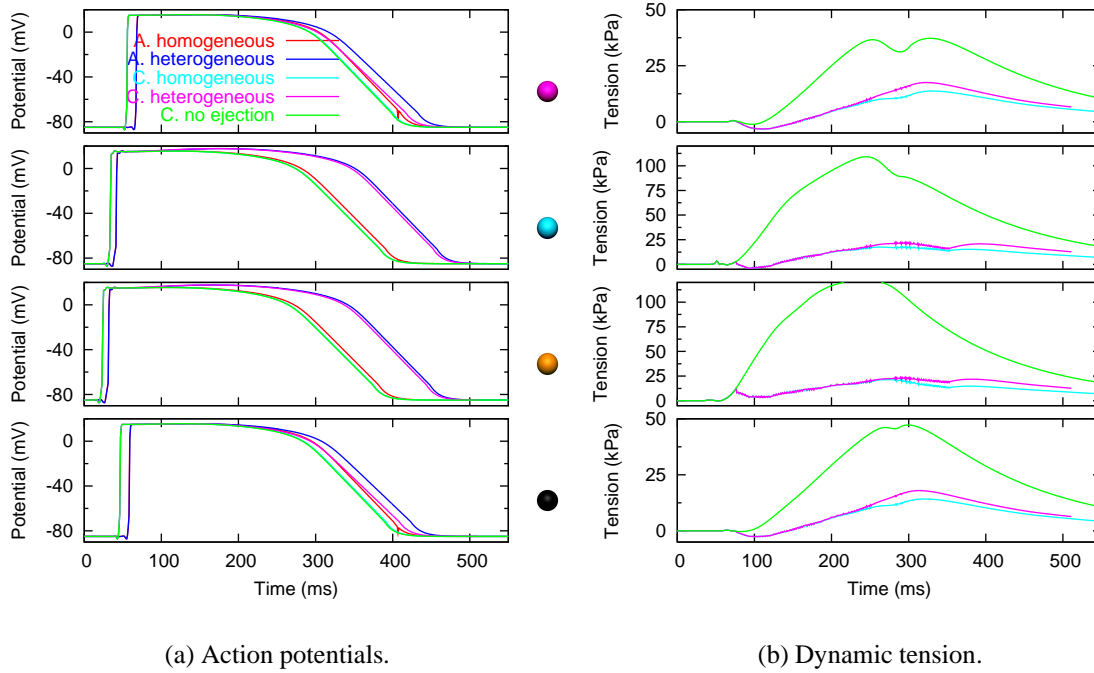
(a) Action potentials.

(b) Dynamic tension.
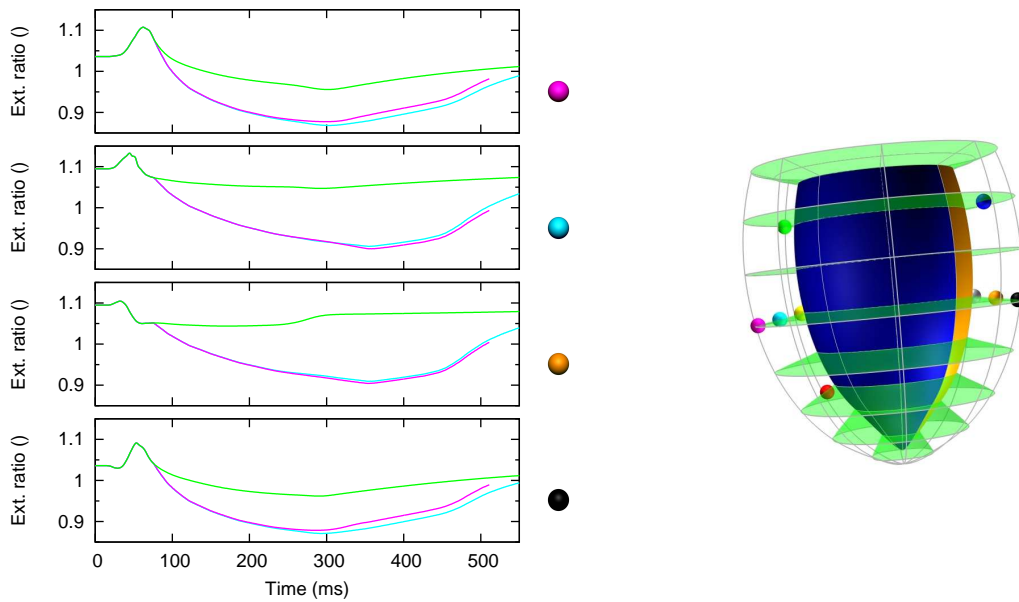
(c) Extension ratio.

FIGURE 5.28: Comparison of the cellular level results from the sinus rhythm simulations. The full simulation results are given in Section 5.3.2 for the electrical activation only models (A. homogeneous and A. heterogeneous) and Section 5.3.3 for the coupled electro-mechanics models with the homogeneous (C. homogeneous) and heterogeneous (C. heterogeneous) models with ejection and the homogeneous model with no ejection (C. no ejection). The coloured spheres give the location of each set of signals in the given LV image.

second location is the right ventricle (RV) apex which we model here as an epicardial stimulus in the LV model in the approximate location where we would expect the RV to terminate, and we term this right ventricular apex (RVa) pacing. A third pacing protocol is also investigated with the combination of the LVb and RVa pacing sites into what we call BiV pacing, which has been shown to be more beneficial in clinical studies (Kawaguchi et al. 2002, Leclercq & Kass 2002). The pacing locations are clear from the results given below.

5.4.1 Electrical Activation

As with the sinus rhythm simulations in Section 5.3.2, before launching into coupled simulations we first check the behaviour of the pacing models with electrical activation of the inflated LV. The inflation solution used is that from Figure 5.10 in Section 5.3.1, the tissue continuum material parameters are identical to those in Table 5.2, and we use the epicardial cell type of the FK-HMT cellular model (Section 3.1.1). For each of the pacing locations, a group of cells is stimulated with a current of $150\ \mu\mathrm{A} \cdot \mathrm{mm}^{-3}$ and a duration of $1.0\ \mathrm{ms}$.

Figures 5.29–5.31 present the activation solutions for the three pacing protocols. A summary of the organ and cellular dynamics is presented in Figure 5.32 where we provide a sampling of cellular AP signals and global ECGs.

5.4.2 BiV Electro-Mechanics

We now take the BiV paced LV model and examine its electro-mechanical behaviour. Here we first present a simulation where there is no ejection of blood from the LV cavity forcing the cavity volume to remain isovolumic for the duration of the $1000\ \mathrm{ms}$ simulated heart beat.

The simulation begins with the same inflated geometry as used above in the sinus simulation, shown in Figure 5.10(b), with the $150\ \mu\mathrm{A} \cdot \mathrm{mm}^{-3}$ BiV stimulus applied at time $0\ \mathrm{ms}$. The mechanical boundary conditions in this simulation are the same as those used above (Figure 5.8), as are the mechanical and electrical continuum material parameters (Tables 5.1 and 5.2). Once more, the epicardial variant of the FK-HMT cellular electro-mechanics model is used at the cellular level (Section 3.1.1).

Results from this simulation are given in Figures 5.33 and 5.34 with a summary of the system dynamics given in Figure 5.35. In addition to testing the modelling and simulation framework

(a) $10 \rightarrow 50$ ms

(b) $\rightarrow 60 \rightarrow 100$ ms

(c) $\rightarrow 110 \rightarrow 150$ ms

(d) $\rightarrow 300 \rightarrow 340$ ms

(e) $\rightarrow 350 \rightarrow 390$ ms

(f) $\rightarrow 400 \rightarrow 440$ ms
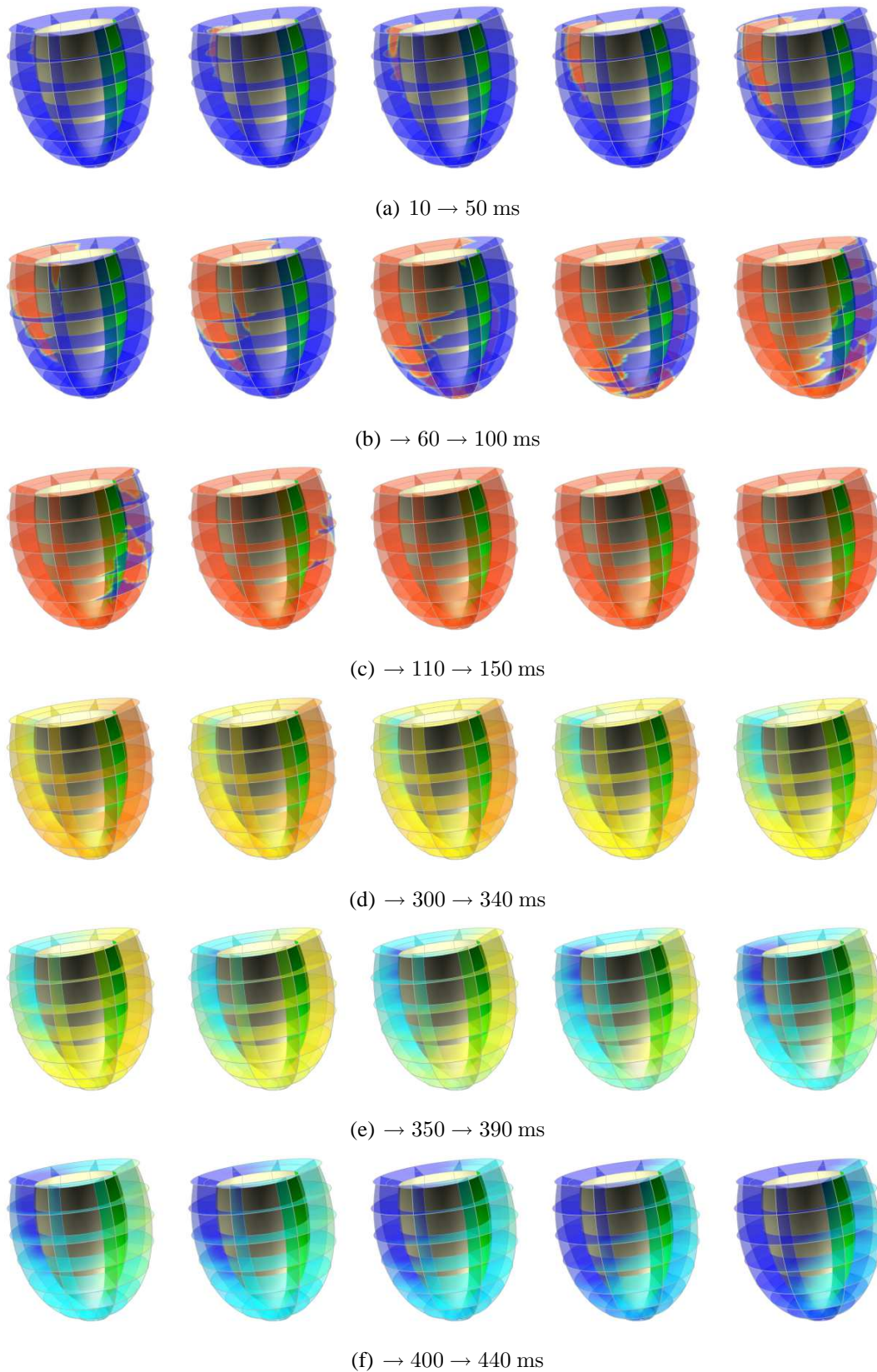
FIGURE 5.29: LVb paced electrical activation on the inflated homogeneous LV model. The green endocardial surface indicates the mid-septum region. Element faces are coloured by cellular transmembrane potential with the scale given in Figure 5.6. See Section D.3 for an animation of this simulation.

(a) $10 \rightarrow 50$ ms

(b) $\rightarrow 60 \rightarrow 100$ ms

(c) $\rightarrow 110 \rightarrow 150$ ms

(d) $\rightarrow 300 \rightarrow 340$ ms

(e) $\rightarrow 350 \rightarrow 390$ ms

(f) $\rightarrow 400 \rightarrow 440$ ms
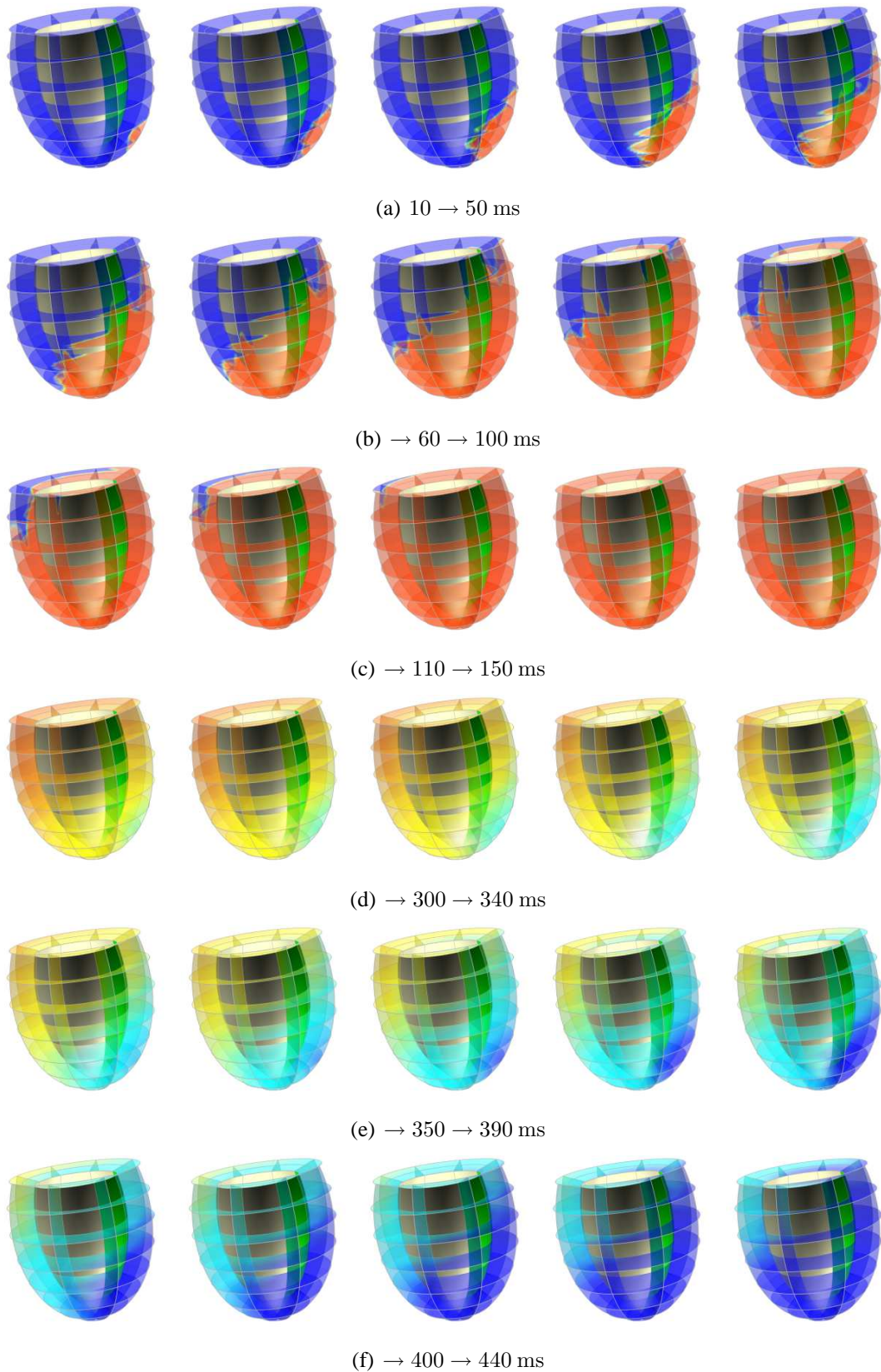
FIGURE 5.30: RVa paced electrical activation on the inflated homogeneous LV model. The green endocardial surface indicates the mid-septum region. Element faces are coloured by cellular transmembrane potential with the scale given in Figure 5.6. See Section D.3 for an animation of this simulation.

(a) $10 \rightarrow 50$ ms

(b) $\rightarrow 60 \rightarrow 100$ ms

(c) $\rightarrow 110 \rightarrow 150$ ms

(d) $\rightarrow 300 \rightarrow 340$ ms

(e) $\rightarrow 350 \rightarrow 390$ ms

(f) $\rightarrow 400 \rightarrow 440$ ms
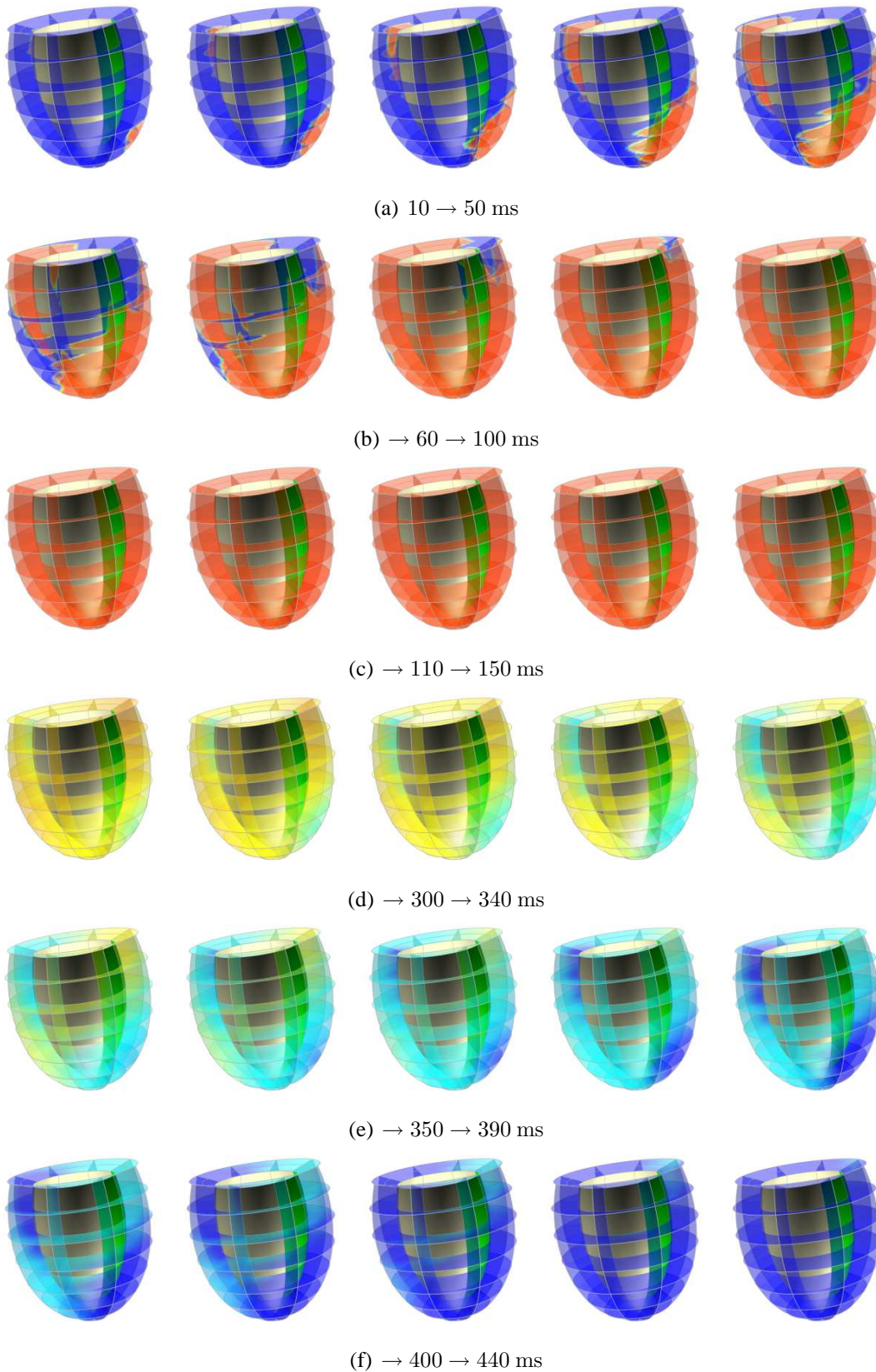
FIGURE 5.31: BiV paced electrical activation on the inflated homogeneous LV model. The green endocardial surface indicates the mid-septum region. Element faces are coloured by cellular transmembrane potential with the scale given in Figure 5.6. See Section D.3 for an animation of this simulation.

(a) LVb.

(b) RVa.

(c) BiV.

(d) Spatial location of APs.
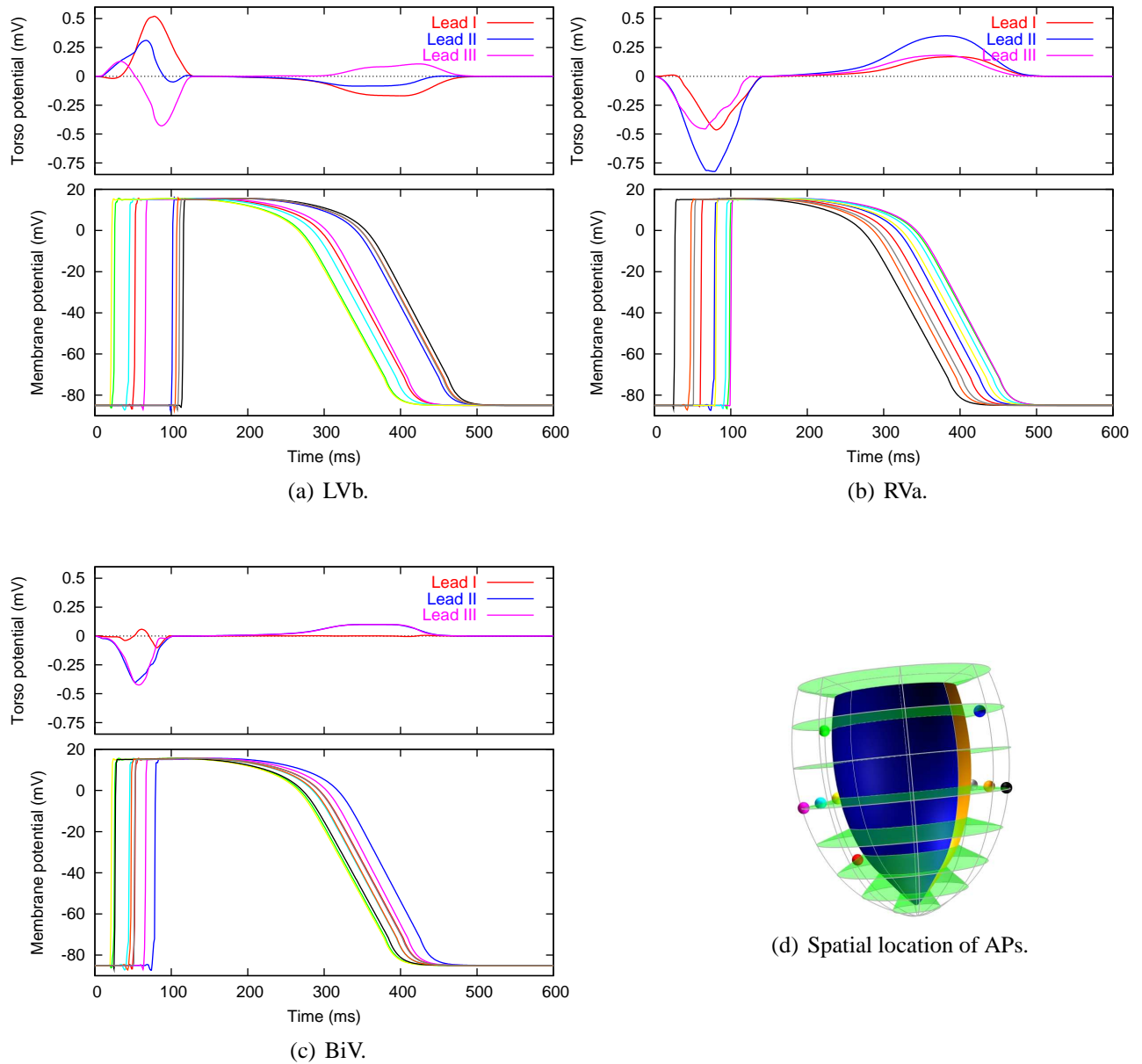
FIGURE 5.32: A summary of the simulation results from models of the electrical activation using the three LV pacing examined (Figures 5.29–5.31). (a)-(c) show the ECG and AP signals from each of the pacing protocols for a single stimulus applied at time 0 ms. The colours of the AP signals correspond to the spheres in (d) marking the spatial location of the presented signals in the LV geometry.

we have developed, this particular simulation will be used to compare to the sinus rhythm model in Section 5.3.3 above.

Having obtained some good results from the isovolumic simulation of a BiV paced heart beat (Figures 5.33–5.35), we proceeded to attempt a simulation of the full cardiac cycle (see page 141) initiated through the application of the BiV pacing protocol. Unfortunately, for reasons discussed below in Section 5.4.4, we were unable to obtain physiologically reasonable or numerically stable solutions past the early stages of ejection. The results we did obtain, however, are presented in Figures 5.36 and 5.37.

5.4.3 LVb and RVa Electro-Mechanics

To further test our framework, we attempted simulations of the cardiac cycle using the homogeneous LV model with contraction initiated via both the LVb and RVa pacing protocols. As with the BiV cycle simulation above, several issues of physiological reality and numerical stability surfaced during these simulations to wreak havoc with the solution process. These issues are discussed below in Section 5.4.4.

In both the LVb and RVa simulation, the most complete solutions were obtained by altering the mechanical boundary conditions applied to the LV. The boundary conditions described in Figure 5.8 were applied with the exception that some endocardial valve nodes were free to move in the vertical (x-axis) direction. For the LVb simulation the mid-septal valve nodes were released in the x-axis, and for the RVa simulation the mid free wall valve nodes were free to move vertically. These changes in boundary conditions resulted in altered deformed geometries following the inflation phase of the cardiac cycle and these solutions are shown in Figures 5.38(a) and 5.40(a) below.

The mechanical and electrical continuum material parameters in both these simulations are the same as those used previously (Tables 5.1 and 5.2). The epicardial variant of the FK-HMT cellular electro-mechanics model is used at the cellular level (Section 3.1.1).

Results from the LVb simulation are given in Figures 5.38 and 5.39 and those from the RVa simulation in Figures 5.40 and 5.41.

(a) $10 \to 40$ ms

(b) $\to 50 \to 80$ ms

(c) $\to 90 \to 120$ ms

(d) $\to 130 \to 160$ ms

(e) $\to 170 \to 200$ ms

(f) $\to 210 \to 240$ ms
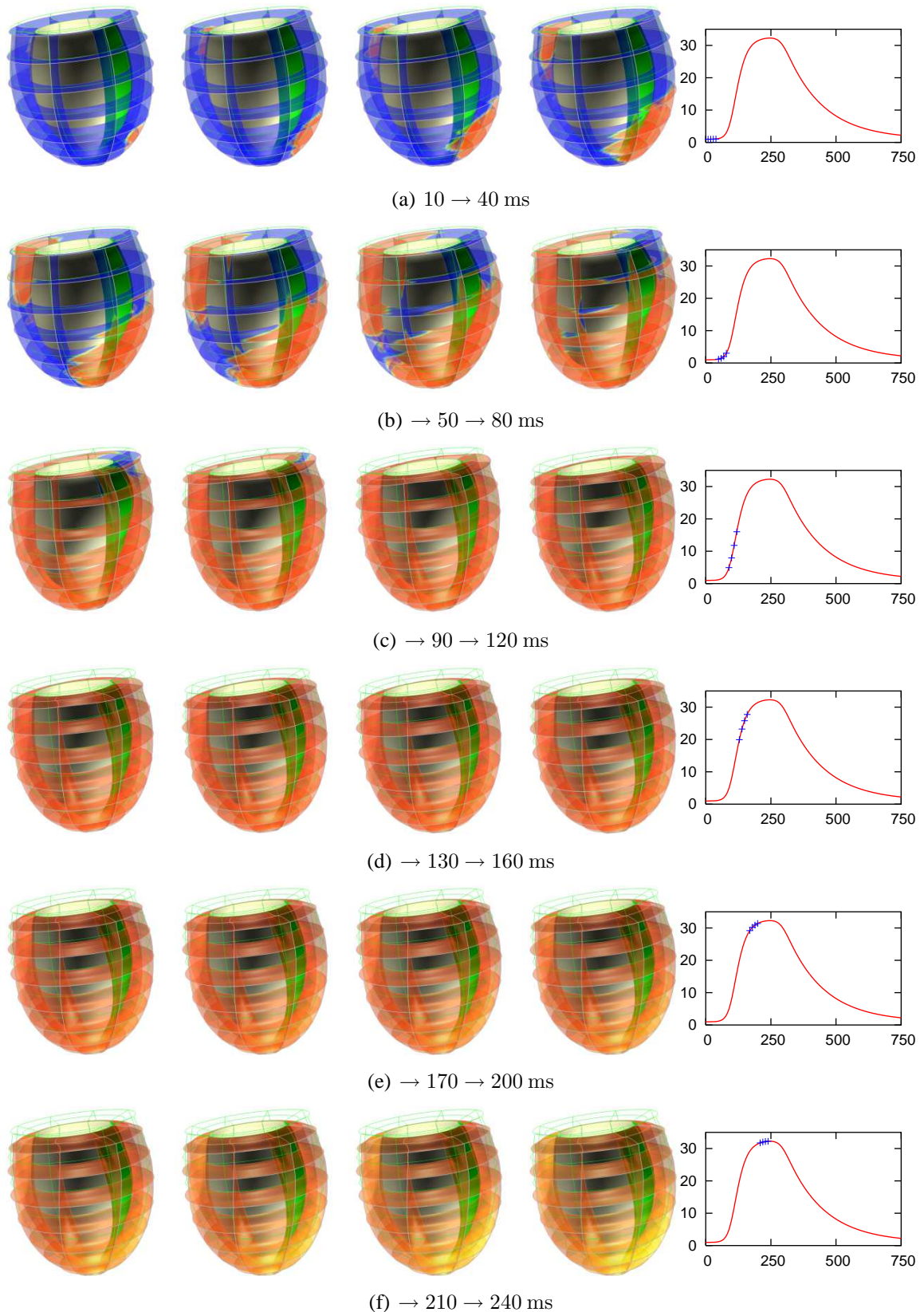
FIGURE 5.33: The first part of isovolumic contraction of the homogeneous LV electro-mechanics model of BiV pacing. The graphs provide the cavity pressure at each of the time points shown, in kPa plotted against time in ms. This model has a constant cavity volume throughout the simulation. The green lines show the undeformed geometry and the element faces are coloured by the potential spectrum given in Figure 5.11. These results are continued in Figure 5.34.

(a) $250 \rightarrow 280$ ms

(b) $\rightarrow 290 \rightarrow 320$ ms

(c) $\rightarrow 330 \rightarrow 360$ ms

(d) $\rightarrow 370 \rightarrow 400$ ms

(e) $\rightarrow 410 \rightarrow 440$ ms

(f) $\rightarrow 450 \rightarrow 480$ ms
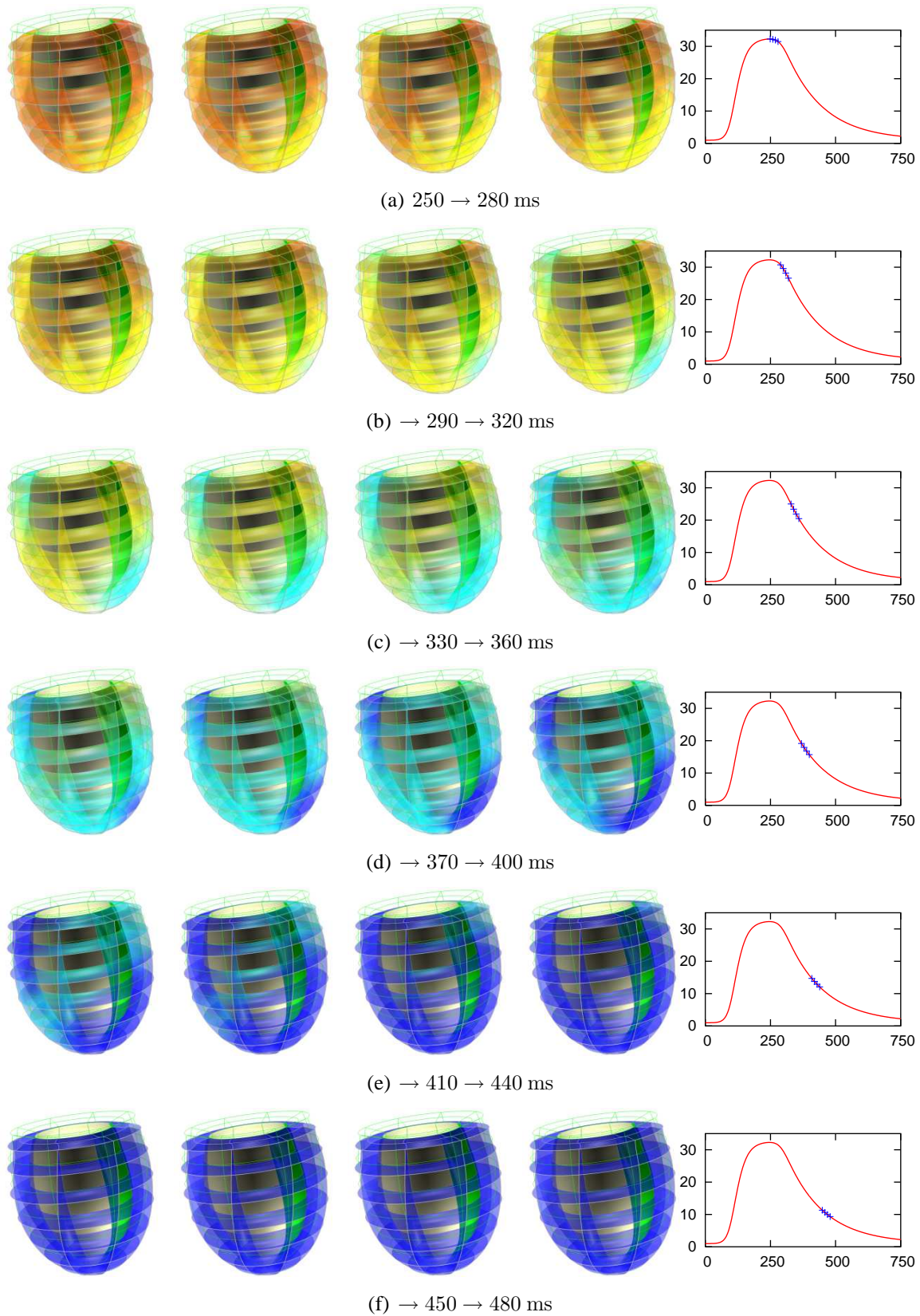
FIGURE 5.34: Continuing the results begun in Figure 5.33 with the BiV paced isovolumic con-
tracting LV model. These results are summarised in Figure 5.35 and also see Section D.3.
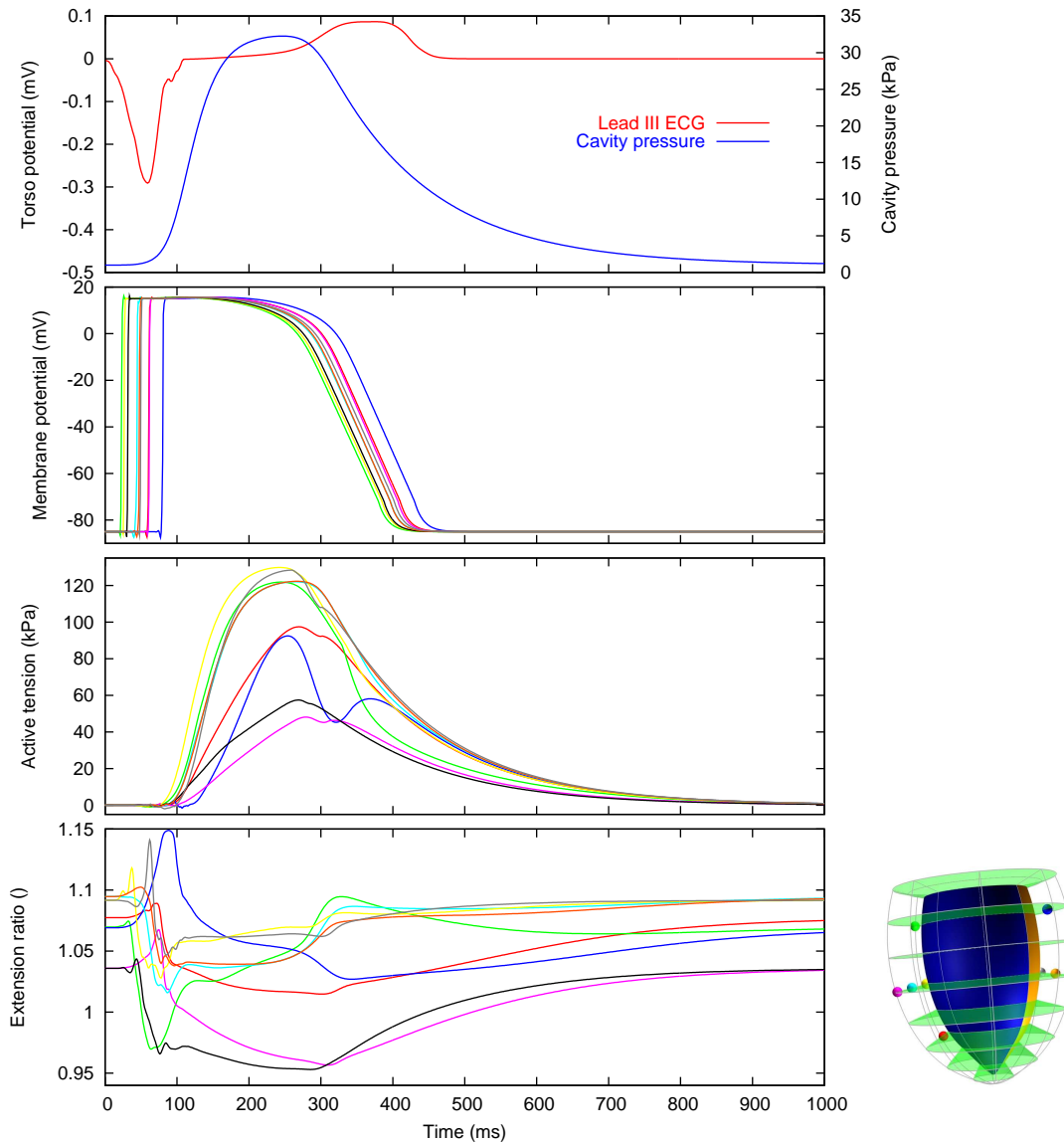
FIGURE 5.35: Summary of the results presented in Figures 5.33 and 5.34 of the simulation of electro-mechanics in the homogeneous LV model of BiV pacing with no ejection. The top graph shows the lead III ECG signal (left axis) and the LV cavity pressure (right axis). The other graphs are the cellular AP, tension, and extension ratio signals, with signal colours matched to the coloured spheres in the accompanying LV image providing the spatial location of the signals.

(a) $10 \to 40$ ms

(b) $\to 50 \to 80$ ms

(c) $\to 90 \to 120$ ms

(d) $\to 130$ ms
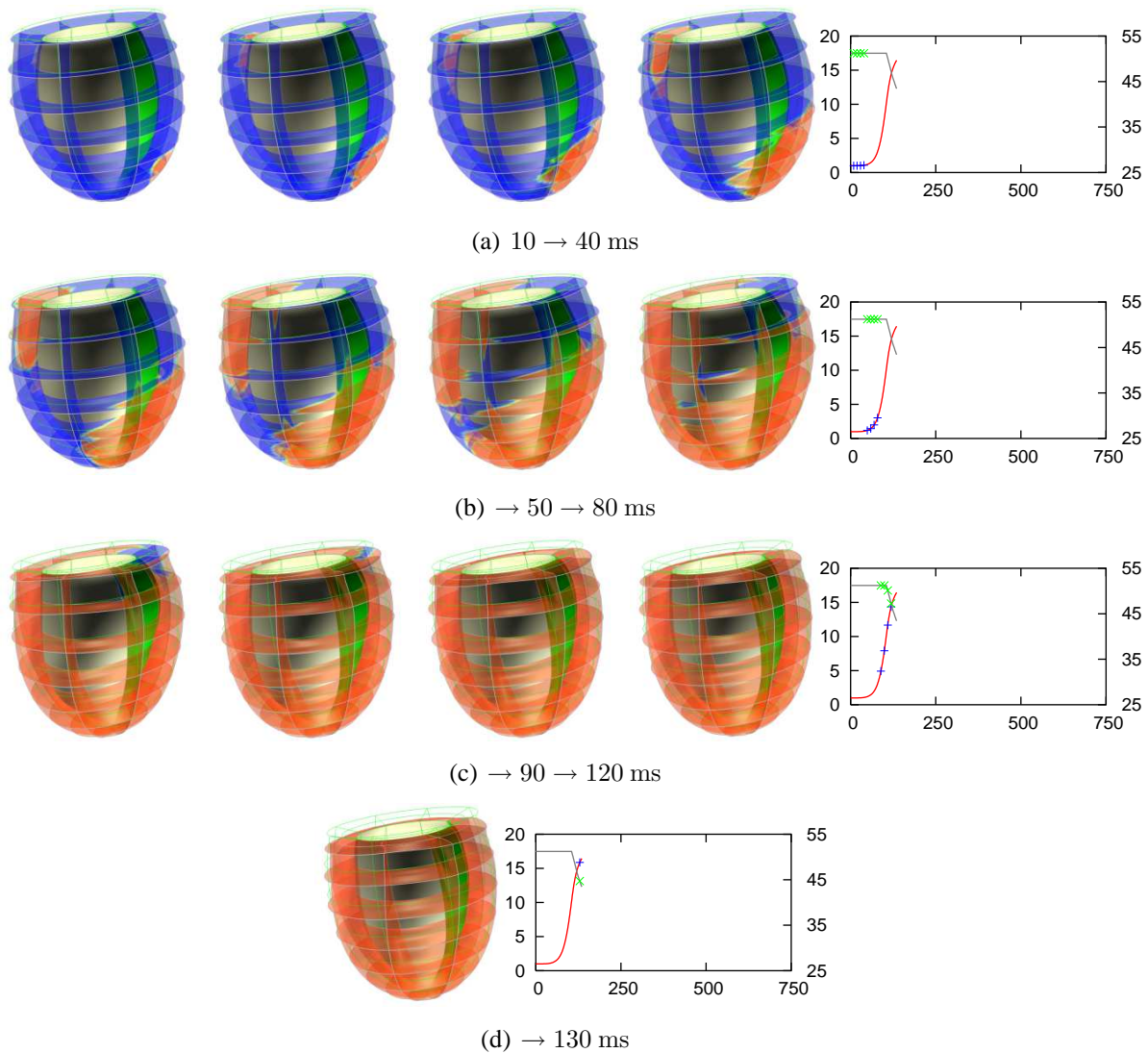
FIGURE 5.36: The working section of the cardiac cycle using the homogeneous LV electro-mechanics model of BiV pacing. The graphs provide the cavity pressure (left scale, kPa) and volume (right scale, ml) at each of the time points shown. The green lines show the undeformed geometry and the element faces are coloured by the potential spectrum given in Figure 5.11. See Figure 5.37 for a summary of the dynamics and Section D.3 for an animation of these results.
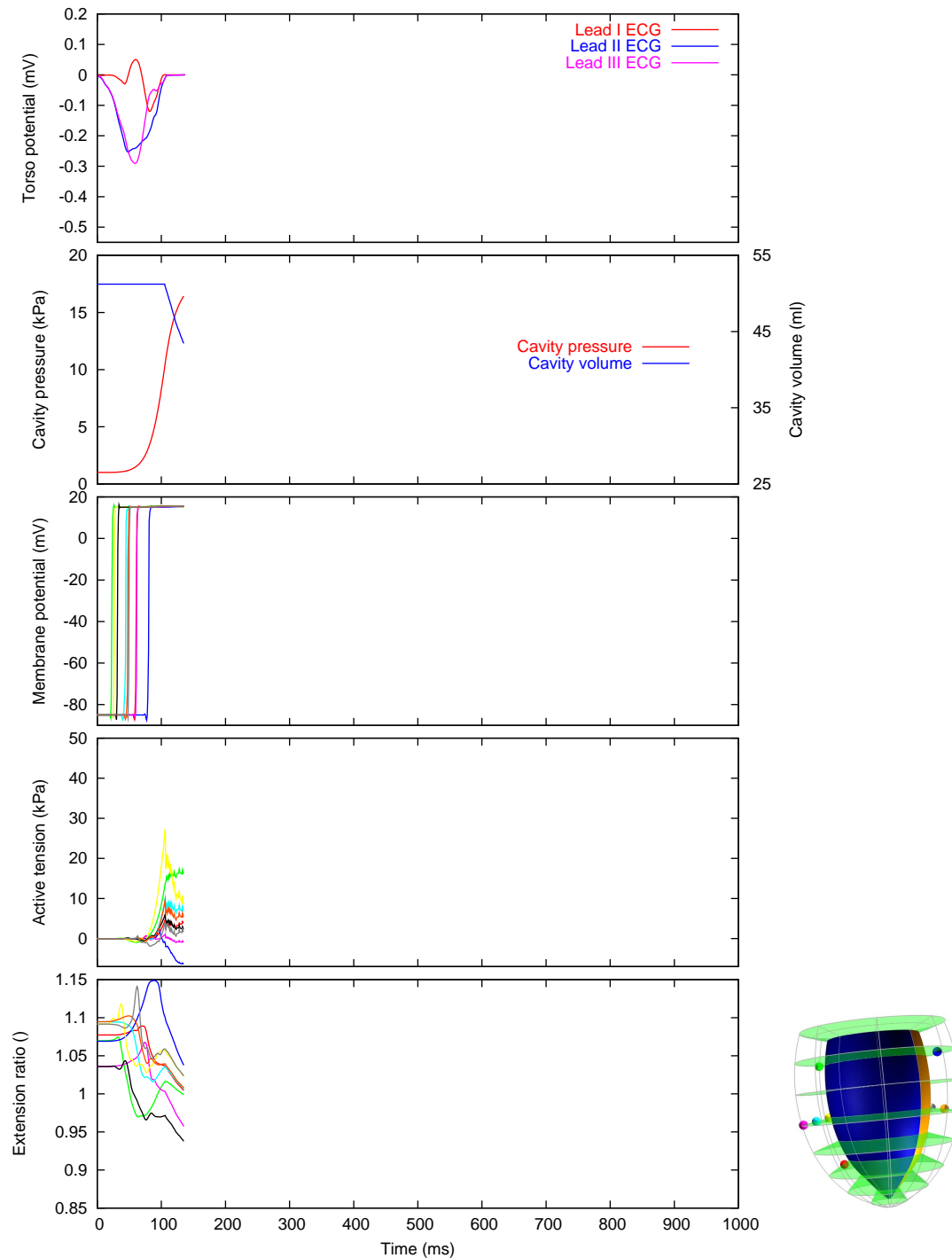
FIGURE 5.37: Summary of the results presented in Figure 5.36 of the simulation of the cardiac cycle in the homogeneous LV model of BiV pacing. The top graph shows the ECG signals obtained from this simulation and the second graph plots the LV cavity pressure (left axis) and volume (right axis). The other graphs are the cellular AP, tension, and extension ratio signals, with signal colours matched to the coloured spheres in the accompanying LV image providing the spatial location of the signals.

(a) $10 \rightarrow 40$ ms

(b) $\rightarrow 50 \rightarrow 80$ ms

(c) $\rightarrow 90 \rightarrow 110$ ms
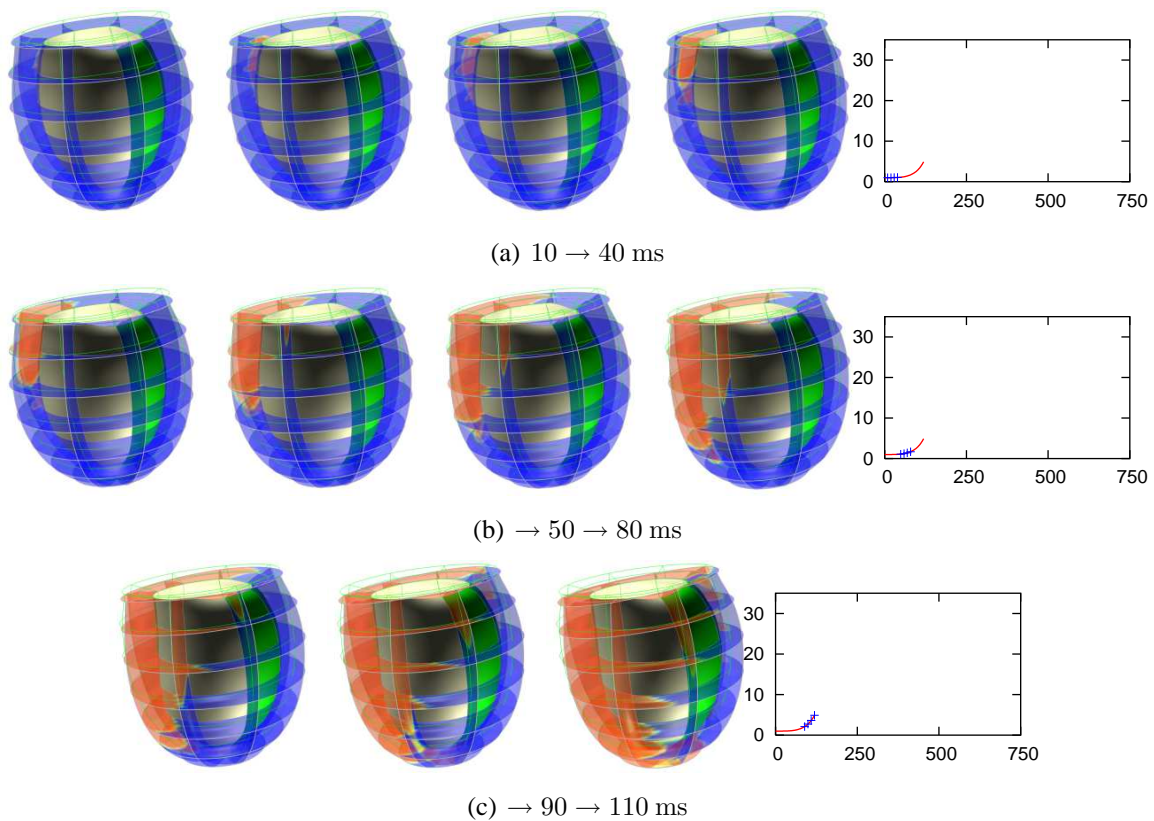
FIGURE 5.38: The working section of the cardiac cycle using the homogeneous LV electro-mechanics model of LVb pacing. The graphs provide the cavity pressure (left scale, kPa) and volume (right scale, ml) at each of the time points shown. The green lines show the undeformed geometry and the element faces are coloured by the potential spectrum given in Figure 5.11. See Figure 5.39 for a summary of the dynamics and Section D.3 for an animation of these results.
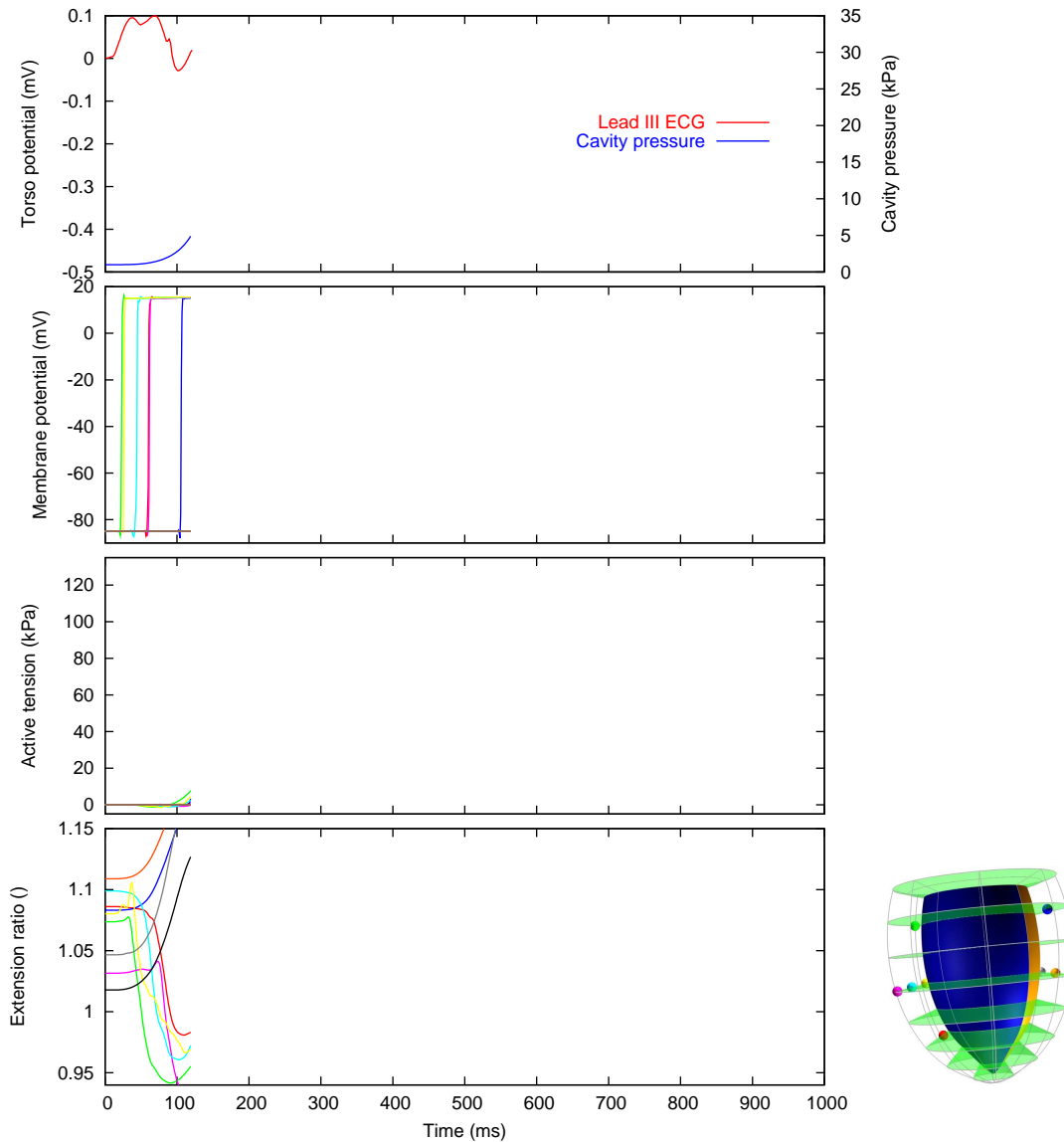
FIGURE 5.39: Summary of the results presented in Figure 5.38 of the simulation of the cardiac cycle in the homogeneous LV model of LVb pacing. The top graph shows the ECG signals obtained from this simulation and the second graph plots the LV cavity pressure (left axis) and volume (right axis). The other graphs are the cellular AP, tension, and extension ratio signals, with signal colours matched to the coloured spheres in the accompanying LV image providing the spatial location of the signals.

(a) $10 \to 40$ ms

(b) $\to 50 \to 80$ ms

(c) $\to 90 \to 110$ ms
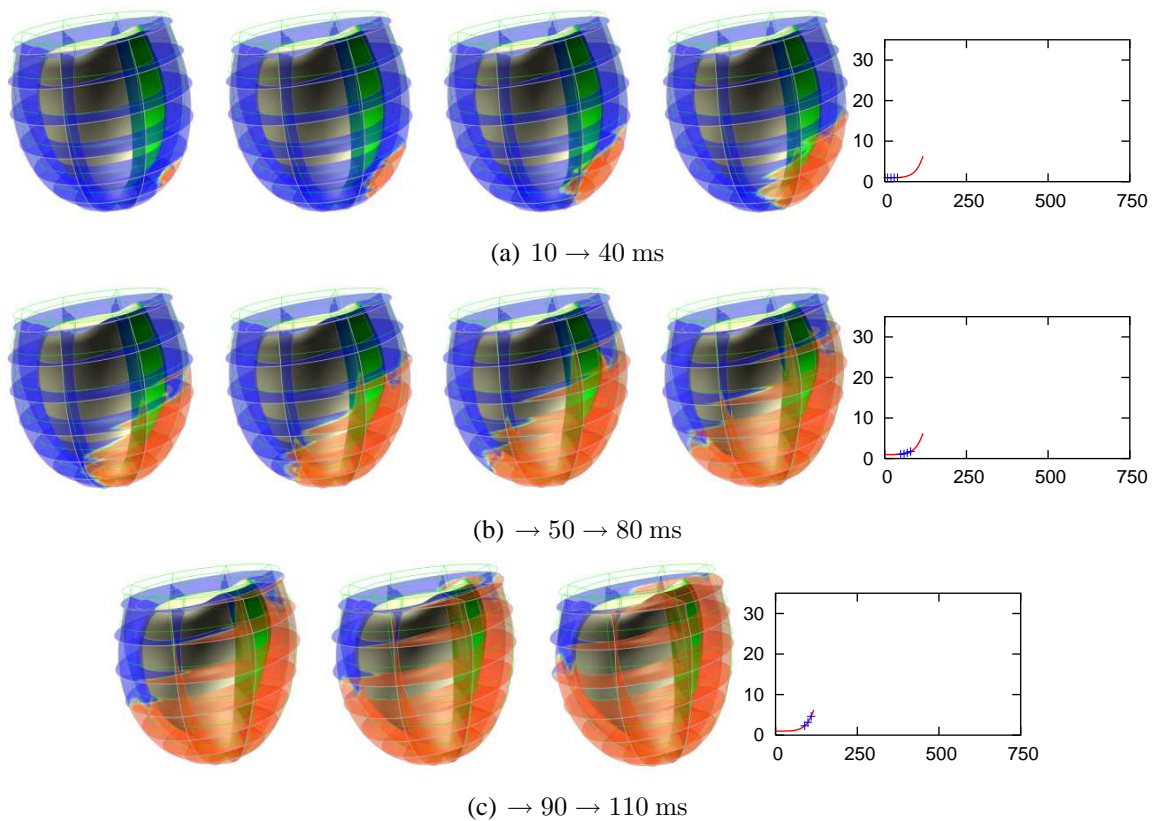
FIGURE 5.40: The working section of the cardiac cycle using the homogeneous LV electro-mechanics model of RVa pacing. The graphs provide the cavity pressure (left scale, kPa) and volume (right scale, ml) at each of the time points shown. The green lines show the undeformed geometry and the element faces are coloured by the potential spectrum given in Figure 5.11. See Figure 5.41 for a summary of the dynamics and Section D.3 for an animation of these results.
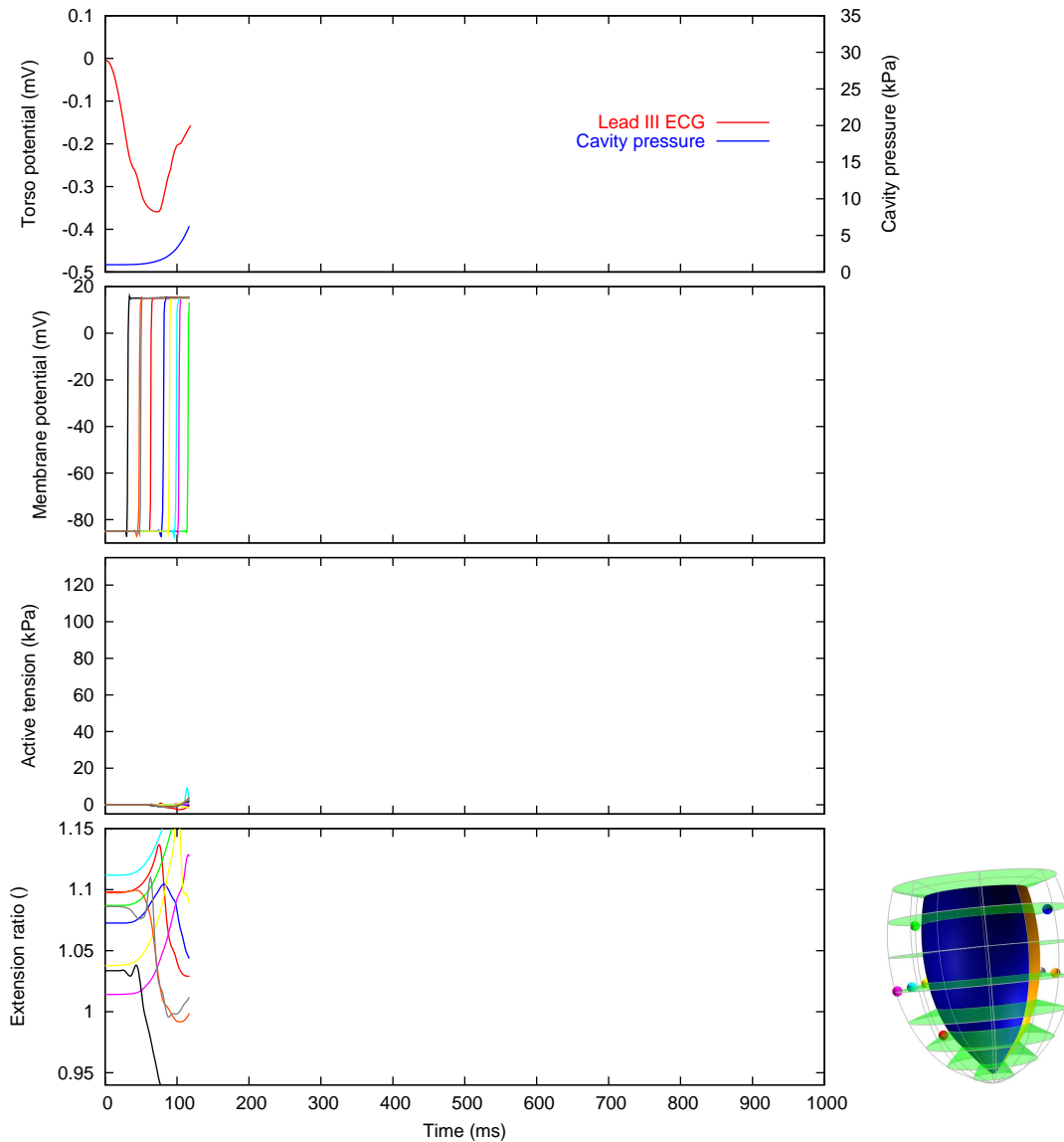
FIGURE 5.41: Summary of the results presented in Figure 5.40 of the simulation of the cardiac cycle in the homogeneous LV model of RVa pacing. The top graph shows the ECG signals obtained from this simulation and the second graph plots the LV cavity pressure (left axis) and volume (right axis). The other graphs are the cellular AP, tension, and extension ratio signals, with signal colours matched to the coloured spheres in the accompanying LV image providing the spatial location of the signals.

5.4.4 Discussion

In Sections 5.4.1–5.4.3 above, we have presented some preliminary results from attempts to model various pacing protocols used in CRT. We have successfully modelled the electrical activation of the LV model using the left ventricular base (LVb), right ventricular apex (RVa), and bi-ventricular (BiV) pacing protocols as well as isovolumic contraction of the homogeneous LV model with BiV pacing. Attempts to simulate electro-mechanics and ejection in the paced LV models have so far failed.

Figure 5.42 presents the three extremity ECG leads for the successful LV pacing simulations and the homogeneous sinus rhythm electro-mechanics model with no ejection (Section 5.3.3). From these results it is clear that BiV pacing is certainly much closer to a normal sinus rhythm beat as suggested in the literature (Wyman et al. 2002, Verbeek, Vernooy, Peschar, Cornelussen & Prinzen 2003), producing similar electrical and mechanical dynamics as our Purkinje-like stimulus protocol in a isovolumic model. The simulations of LVb and RVa pacing in a electrical activation model show significant differences to the normal sinus ECG leads.

The AP signals given in Figure 5.43(a) show clear differences in the activation sequence from the paced beats, especially the LVb and RVa protocols where the electrical wave propagation is no longer dominated by the transmural direction. The cellular tension and extension ratio signals shown in Figure 5.43 reinforce that BiV pacing in our homogeneous LV model results in behaviour close to the Purkinje-like sinus rhythm stimulus. Further work is required to determine if this similarity continues for models that include cellular heterogeneity and ejection.

In Section 5.4.3 we present results from attempted simulations of LV electro-mechanics using the LVb and RVa pacing protocols. These simulations failed before the developed cavity pressure reached the point where ejection would begin. As discussed in Section 5.4.3, the mechanical boundary conditions in these models were altered from those used in the sinus and BiV simulations in an attempt to improve the performance of these simulations. These changes allowed slight improvements in the simulations, but we still fail to achieve anything close to ejection in these paced models.

Further work is required to fully understand these failures, but we have some initial thoughts on possible explanations. These simulations fail because regions of the ventricular wall begin to be stretched to non-physiological lengths during the numerical solution of the finite elasticity model. This is illustrated in Figures 5.38 and 5.40 (and Section D.3) by the ventricular wall opposite the point stimulus beginning to bulge outwards as the tissue nearest the stimulus site

(a) Lead I.

(b) Lead II.

(c) Lead III.

(d) Cavity pressure.
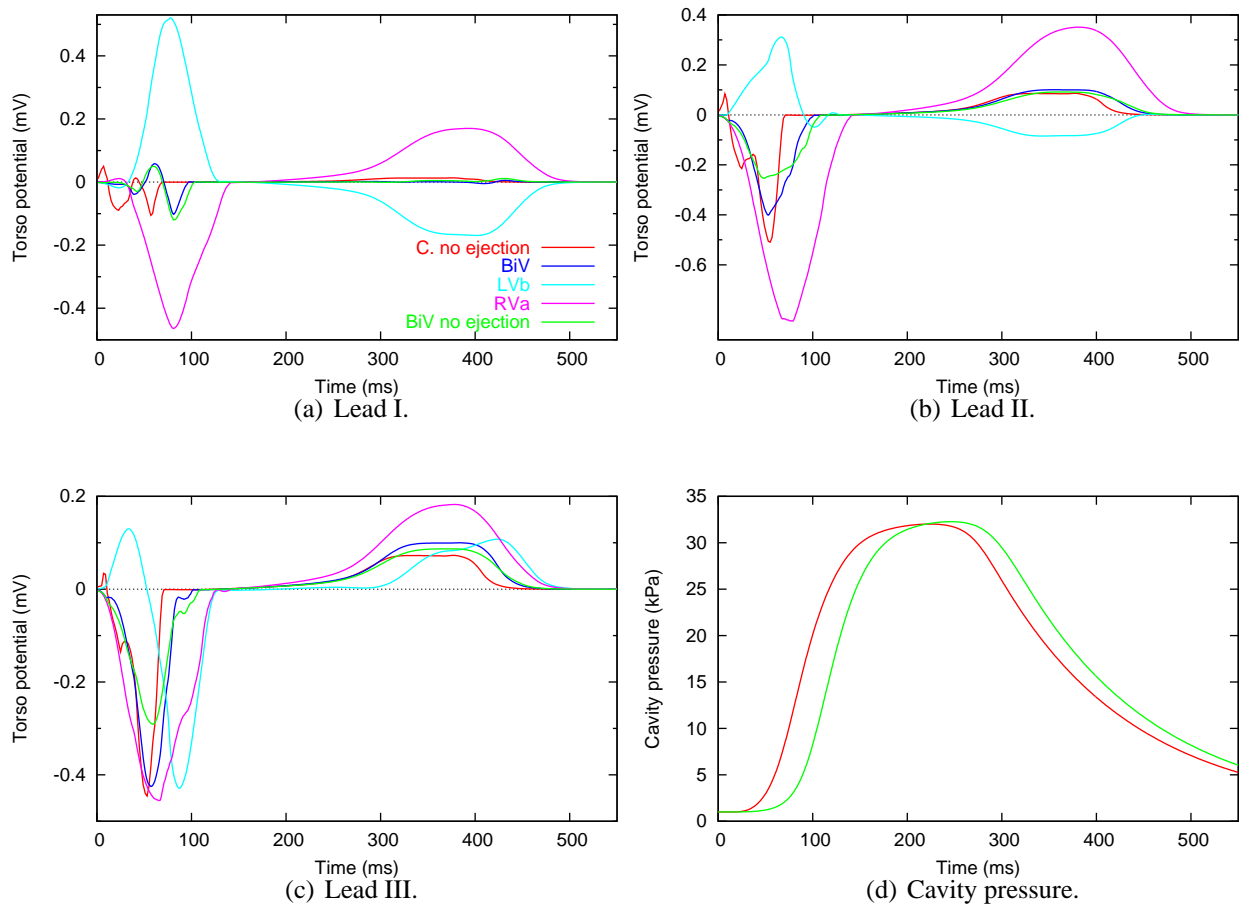
FIGURE 5.42: Comparison of the tissue level results from the LV pacing simulations. The full simulation results are given in Section 5.4.1 for the electrical activation only models (BiV, LVb, and RVa) and Section 5.4.2 for the coupled BiV electro-mechanics model (BiV no ejection) and Section 5.3.3 for the homogeneous sinus model with no ejection (C. no ejection). (a)-(c) give the three extremity ECG signals and (d) the ventricular cavity pressure.
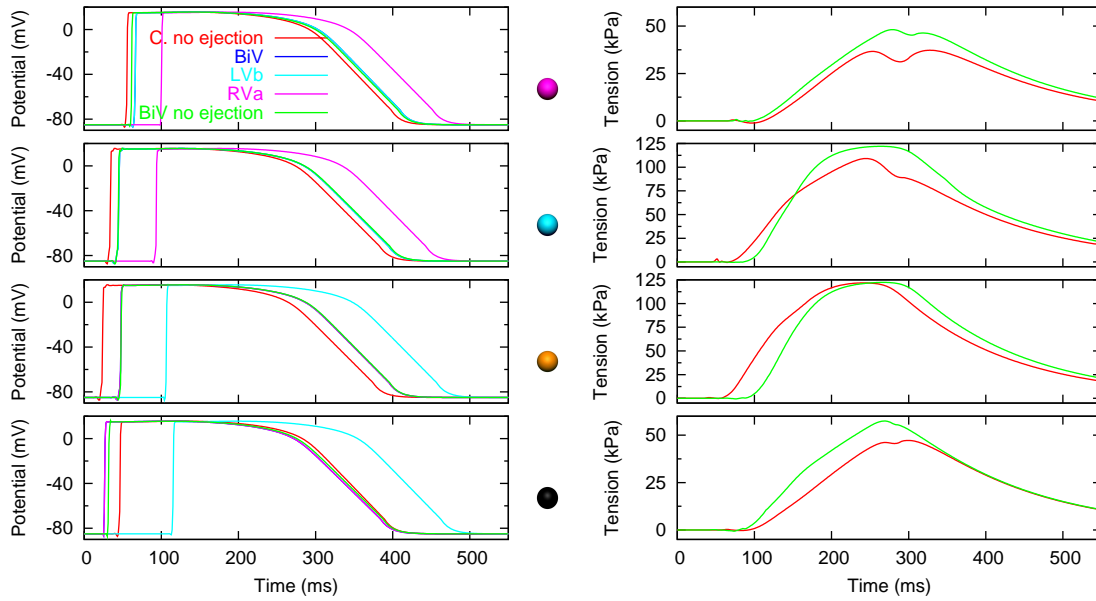
(a) Action potentials.

(b) Dynamic tension.
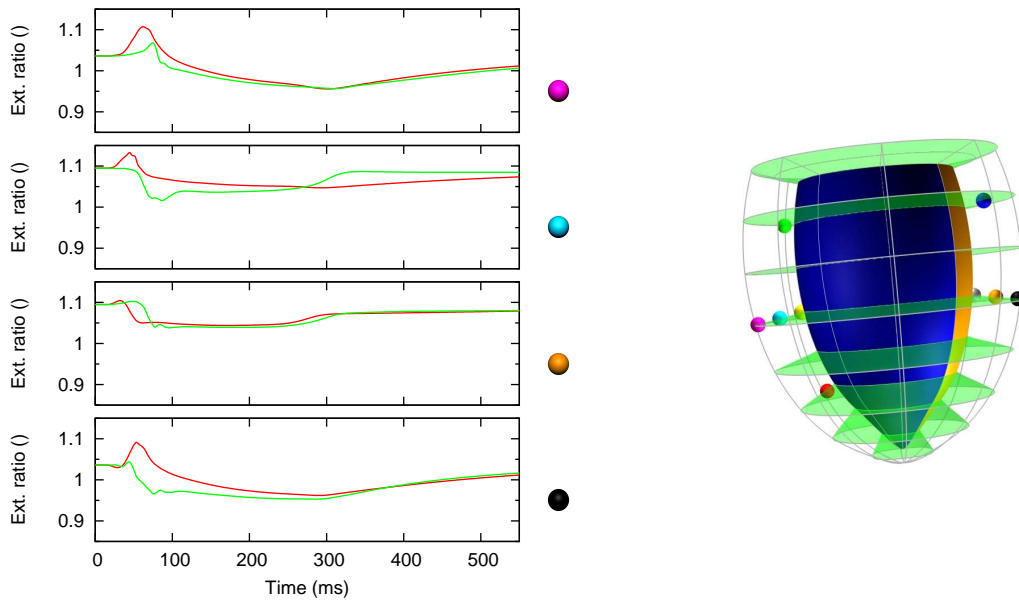
(c) Extension ratio.

FIGURE 5.43: Comparison of the cellular level results from the paced LV simulations. The full simulation results are given in Section 5.4.1 for the electrical activation only models (BiV, LVb, and RVa) and Section 5.4.2 for the coupled BiV electro-mechanics model (BiV no ejection) and Section 5.3.3 for the homogeneous sinus model with no ejection (C. no ejection). The coloured spheres give the location of each set of signals in the given LV image.

contracts (Figure 5.44). While such bulging is to be expected given the incompressible my-ocardium and isovolumic ventricular cavity, as the bulging increases the numerical solution of the finite elasticity model becomes unstable as the passive fibres which have been stretched are suddenly activated. Since active tension in the FK-HMT cellular model is proportional to the cellular extension ratio, these cells rapidly develop large active forces once they are activated. This causes a large instability which our simulation framework is currently unable to adequately handle. Thus, the instability could be due to either the cellular model or the numerical simula-tion framework.

5.5 Computational Performance

All the simulations presented above in Sections 5.3 and 5.4 were performed on an IBM Regatta P690, consisting of 32 $1.3\,\mathrm{GHz}$ Power 4 processors with $32\,\mathrm{GB}$ of physical memory. We present here a comparison of a coupled electro-mechanics model and a non-coupled electrical activation only model. The electro-mechanics model is the homogeneous FK-HMT LV model with no ejection (Figures 5.18–5.20) and we compare this to the electrical activation only version of the same model (Figures 5.11 and 5.12).

Figure 5.45 plots the memory requirements for the two models for the duration of the $1000\,\mathrm{ms}$ of simulation time. This figure shows that the required memory initially climbs, but quickly reaches a plateau which is relatively constant for the period when the myocardium is electrically active. For both models, once the tissue has returned to electrical rest the memory requirements drop to a very stable plateau of approximately $1.75\,\mathrm{GB}$ for the activation model and $2.25\,\mathrm{GB}$ for the coupled electro-mechanics model.

The LV model used in these simulations consists of approximately $320,000$ nodes in the GBFEs, compared to the $36,000$ nodes in the cube model presented in Section 3.4. Memory requirements for the FK-HMT cube model peaked at $0.55\,\mathrm{GB}$ and for the coupled LV model at $3.8\,\mathrm{GB}$. These data show that for a nine fold increase in the number of GBFE nodes there is a seven fold increase in the peak memory requirement. While $4\,\mathrm{GB}$ of memory is not pushing the limits of a modern scientific computer, it is important to note that the $320,000$ node GBFE discretization is not sufficient for a fully converged solution and this is also only a LV model.

In Figure 5.46 we present a breakdown of the time taken in the coupled LV electro-mechanics model for the different steps in the solution algorithm (Figure 3.6). The three steps are: the up-
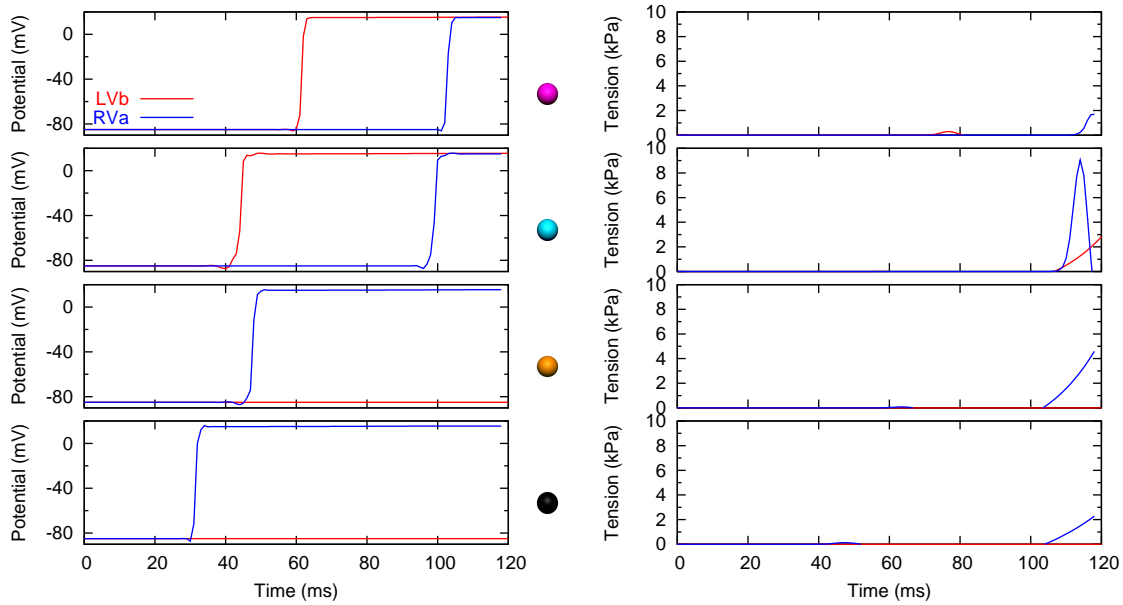
(a) Action potentials.

(b) Dynamic tension.
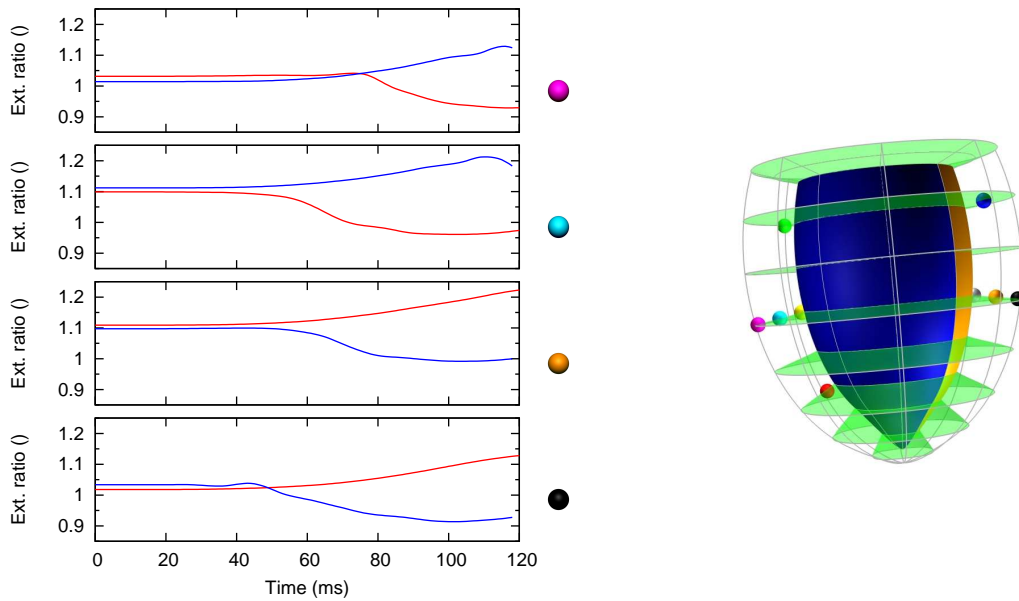
(c) Extension ratio.

FIGURE 5.44: Comparison of the cellular level results from the failed LV pacing simulations. The full results obtained from these simulations are presented in Section 5.4.3. The coloured spheres give the location of each set of signals in the given LV image.
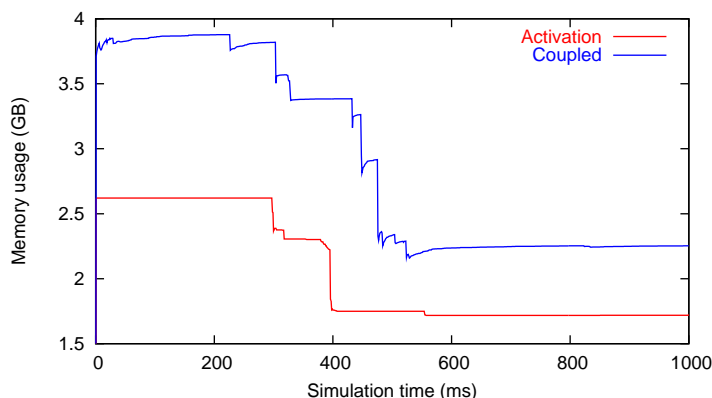
FIGURE 5.45: Comparison of the memory requirements for the FK-HMT and N-LRd-HMT based cube electro-mechanics models.

date step, where the electrical activation model is updated from the deformed finite elasticity model; the activation model solution step; and the finite elasticity mechanics solution step. Also shown are the solution time data for the activation only model.

Figure 5.46(a) presents the comparison of wall clock times for each of the models and Figure 5.46(b) compares the actual computational time (CPU), for each of the 1 ms solution intervals. The wall clock time is the actual *real world* time taken to run the simulation and the computational time is the amount of time the process takes to run. The computational time is generally much larger since we are using multi-threaded software capable of running on more than one processor and the computational time is the sum over all the processors used in the simulation. The ratio of computational time to wall time can be used as a measure of the speed increase obtained by using multiple processors.

The electro-mechanics LV simulation was performed using twelve processors on the IBM Regatta machine and the activation only simulation used eight processors. The plots shown in Figure 5.46 appear quite noisy due to the large dependence of these times on the load on the computer at the time of the simulation. This computer is a shared resource and as such there are numerous users running simulations and performing other tasks on the machine at any time, leading to a high load on the machine. The brief periods when the computational times show sudden dips or increases can be attributed to the machine load changing for some unrelated reason rather than anything to do with the model simulations.

Figure 5.47 provides some cumulative time data for both the coupled model and the electrical activation only model. Here the difference between computational and wall clock time is highlighted. As expected, the time for computing the cellular dipoles for use in the forward
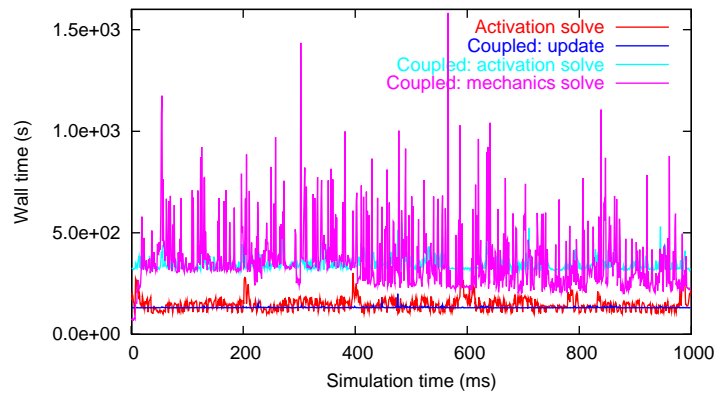
(a)
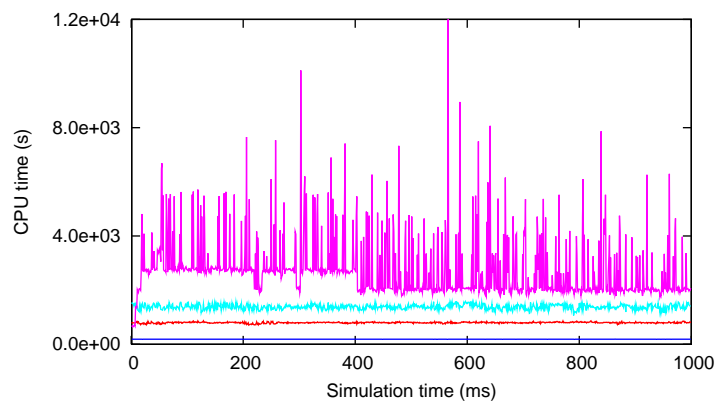
(b)

FIGURE 5.46: Comparison of the computational time for each of the steps in the solution algorithm for the FK-HMT based LV electro-mechanics model. Also shown is the solution times for the electrical activation only version of the model. (a) shows the comparison of wall clock times and (b) the actual computational times for each of the $1\ \mathrm{ms}$ solution intervals over the entire $1000\ \mathrm{ms}$ simulation. The same key is used in both graphs. See text for full description.

torso model is the same for both the coupled and electrical activation only models. It is also clear that there is no multiprocessing implemented for this section of the simulation framework.
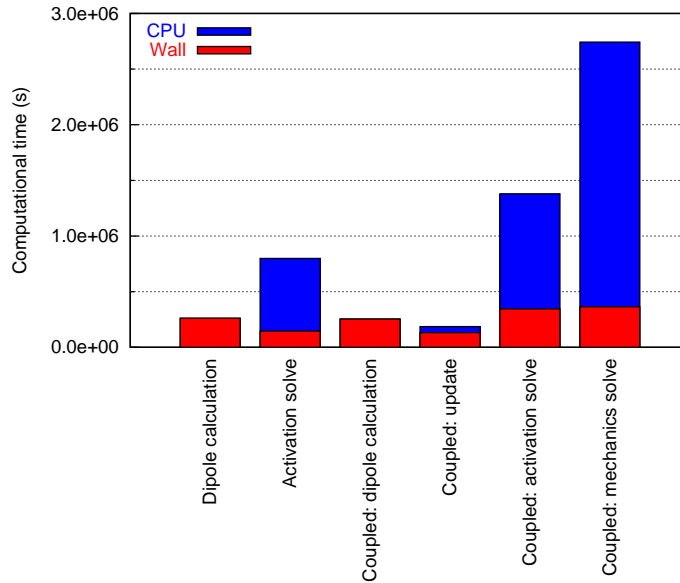
FIGURE 5.47: Comparison of the total computational times for the activation only LV model and the coupled electro-mechanics model. See text for full description.

The solution of the electrical activation model for the activation only model shows a 5.4 speed-up between total wall clock time and total computational time, whereas the coupled model has only a 4.0 speed-up. This is despite the coupled model being run using twelve processors compared to eight for the activation only simulation. This highlights the advantage of the activation only model not needing to perform the non-parallel matrix assembly at each time step (as discussed in Section 3.4.3).

For the mechanics solution step of the simulation algorithm we get a 7.5 speed-up. This is reasonable for this work, but significantly distant to the ideal linear speed-up (*i.e.,* a speed-up of 12 for this simulation). Section 3.4.3 contains discussion as to why we fall short of the desired linear speed-up for the different steps in the simulation.

Summing the contribution of each of the steps gives total wall clock times of 113 hours (4.5 days) for the activation only model and 304 hours (12.6 days) for the coupled electro-mechanics model. Total computation times were 293 and 1267 hours for the activation only and coupled models, respectively. This gives overall speed-up factors of 2.6 for the activation only model and 4.2 for the coupled model. These factors look particularly bad as they are heavily influenced by the completely serial dipole calculations.

Chapter 6

Conclusions

In this thesis we have developed a modelling and simulation framework which, for the first time, allows tight coupling between cellular, tissue, and organ level models of cardiac electro-mechanics. The framework developed is a crucial step along the path to a simulation and modelling environment for the IUPS Physiome Project and while the focus of this work has been on cardiac electro-mechanics we have demonstrated application of the framework to other physiological systems (Section 4.5).

An important feature of the framework we have developed is the use of CellML to dynamically specify cellular level mathematical models for use in distributed tissue and organ models. The framework implementation allows for specification of the spatial distribution of models themselves as well as material parameters within models. An example of this is the heterogeneous LV model described in Figure 5.13. This feature begins to provide a *plug-and-play* facility where a non-expert user can take a standard tissue or organ model and plug-in their favourite cellular model (or models) and see what happens. Using their CellML-enabled cell modelling software, such a user could tinker with their model, change parameters, add drug interactions, *etc.*, and then relatively easily step back into a tissue or whole heart model and instantly[1] see the effect of such changes on larger scale function.

We have demonstrated application of the implemented framework to various tissue (Section 3.4) and ventricular models (Chapter 5) with some very promising preliminary results. Using a fairly simple cellular model (Section 3.1.1) and a simplistic LV geometrical model (Figure 5.1) we have performed simulations of a normal sinus rhythm heart beat (Section 5.3)

---

[1]Instantly could be a time period of days or weeks depending on the simulations required.

and examined the behaviour of the LV under various pacing protocols (Section 5.4).

While we have obtained some reasonable results from the models developed in this thesis and developed a simulation framework capable of much more than just what we have presented, there are some limitations in our methods. Some of these are discussed in Sections 5.3.4 and 5.4.4. Other limitations are discussed in Section 6.1 below as well as some extensions to this work that would enhance our methods and overcome some of the limitations. Section 6.2 then presents some additional studies that could be performed using the methods developed in this thesis and Section 6.3 lists existing publications that have come from this work.

6.1   Limitations and Extensions

During the process of developing the methods and models presented in this thesis various desirable features have been mentioned but not included in this work for different reasons. In this section we discuss some of these limitations of our work and consider some extensions to this work that might relieve the limits.

Perhaps one of the most obvious limitations of the models described in this thesis is that we have used the monodomain approximation for all electrical activation models. This has been appropriate for the scope of this thesis as we have been developing the framework which enables the coupling of cellular level models into tissue and organ electro-mechanics models. In future studies, however, this approximation might no longer be appropriate. Because we have implemented our modelling framework in CMISS, we can easily use the full bidomain model when required (Sands 1997, Buist 2001).

As was mentioned in Section 5.3, due to numerical issues with the GBFE method (Section C.3) at the LV apex, we were forced to apply additional constraints on the ventricular deformation in order to obtain stable solutions for the electrical activation model in the myocardial tissue near the apex. This is primarily due to the implementation of the GBFE method used in this work being defined by regular quadrilateral-shaped elements that are collapsed along at least one face at the apex. A more efficient implementation of the method has been recently developed which allows non-regular GBFEs to be defined based on the collapsed host element. This implementation will hopefully aid in the numerical stability of the electrical activation model at the apex during mechanical deformation allowing the lifting of the undesirable apex deformation constraints. Testing of the new implementation is required to determine its effect

on coupled electro-mechanics models before we can claim the abolition of this limitation.

All of the cellular models reviewed and developed in this thesis have been developed based on experimental data from various animal species (with the possible exception of the FK-HMT model fitted to human APD measurements). To be clinically useful, however, models of cardiac function need to be developed based on human data. Recently, human cellular electrophysiology models have been published by Iyer, Mazhari & Winslow (2004) and ten Tusscher, Noble, Noble & Panfilov (2004). As discussed above, by using CellML in our modelling and simulation framework, model evolutions such as these can easily be incorporated into tissue and organ models. All that is required is the translation of the published model into CellML. Another issue related to material parameters is the need to ensure the parameters from the cellular, electrical activation, and finite elasticity models are all consistent with each other.

As models develop and become more complex we are beginning to see more models that take an existing model and then add significant detail to a specific mechanism in that model to enable the modelling of some new experimental observations. An example of this is the addition of Markov state models for the fast sodium and potassium channels to the dynamic Luo & Rudy (LRd) model by Clancy & Rudy that enabled the inclusion of specific genetic mutations into the whole cell electrophysiology model (Clancy & Rudy 2001, Clancy & Rudy 2002). The CellML version of these models included in this thesis, as the N-LRd model, uses version 1.0 of the CellML language. This results in large XML files that are largely duplicated between the wild-type and mutant versions of the model. By moving to version 1.1 of the CellML specification we could remove this code duplication by defining a single base model with the common components and then used the CellML 1.1 import facility to include the common components into a model which also defines either the wild-type or mutant fast sodium channel models. In fact, the base common model would probably also be the culmination of models that mirrors the development from the original Luo & Rudy (1991) model.

When implementing the simulation framework described in this thesis we have used the existing code base provided by CMISS (Section 4.4). In CMISS the definition and implementation of finite elasticity and electrical activation models is distinctly separate. This has resulted in our simulation framework consisting of quite separate components for the mechanics and activation with most of the work being in the coupling of these two parts of the CMISS code. By implementing the framework in this manner, we allow independent specification of the two constituent components of the coupled electro-mechanics model, which was thought to be a useful feature. As has been demonstrated in the various tissue and organ models presented in this thesis (Section 3.4 and Chapter 5) the coupling between the two parts of the code does not

always work perfectly. Further work is required to determine if greater integration of the finite elasticity and electrical activation sections of CMISS code would provide enhanced numerical stability and generality.

Another point to consider is inclusion of active material response directly into the finite elasticity constitutive relation. As described in Section 4.5, the methods developed in this thesis for incorporation of CellML into CMISS have been extended to allow specification of the material constitutive relationships. This extension uses all the same code in CMISS as the active contraction modelling and it should be relatively trivial to extend this to allow the inclusion of the active tension generation component directly into the constitutive relations rather than the current implementation where the active component is a separate addition to the finite elasticity stress tensor. If implementing this approach, however, the methods begin to get complicated when considering the electrophysiology aspects. The idea here would be to use cellular electro-mechanics models that include not only the electrophysiology and active tension but also the passive constitutive relations for the material(s) being modelled. While making the full cellular model more complex, CellML 1.1 could be used to define the master cell model which imports the standard electro-mechanics model as used in the current work and then defines the constitutive relationships and their connections with the active tension. This method would provide a method for a more transparent specification of the full tissue or organ electro-mechanics model.

A major deficiency in the Auckland heart models has always been the lack of physiologically realistic interaction between the ventricular cavity and the myocardium. The method developed by Nash (1998) and used in this work uses a separate cavity region FE mesh to model the cavity as a constant volume and then through volume conservation determine the hydrostatic pressure applied to the endocardial surface (Section 5.1). While this method can be used to simulate something reasonable it does not allow for a gradient of pressure within the cavity volume or realistic filling and ejection of blood from the ventricle. While the method we have used for ejection (Section 5.1.3) could equally be used to push blood into the ventricular cavity, this requires the specification of the cavity volume through time which is perhaps not the best aspect of the system to be controlling explicitly. A preferred boundary condition to impose on the system might be the vascular resistance or aortic flow and pressure. While the inclusion of a full computational fluid dynamics model for the blood flow in the ventricular cavity might add more complexity and computational requirements to the models than would be desirable, a more realistic model could be achieved with inclusion of simplified fluid dynamics models such as the Windkessel models used in several other studies (Bovendeerd et al. 1992, Usyk et al. 2002, Kerckhoffs, Bovendeerd, Kotte, Prinzen, Smits & Arts 2003, Kerckhoffs, Faris, Bovendeerd, Prinzen, Smits, McVeigh & Arts 2003). More work is required to determine the

effect of such fluid mechanics models on the behaviour of the ventricular tissue.

In Section 5.3 we model normal sinus activation of the LV through the application of electrical stimuli over most of the endocardial surface. The stimuli are applied following a specified sequence that mimics that observed experimentally following actual Purkinje fibre stimulus via the AVN originating at the SAN. While this produces a suitable pattern of activation for the purposes of this thesis, something more anatomically based might be desirable in different situations. Buist (2001) developed a method for growing a Purkinje fibre tree into a given host geometry and then incorporating this tree into the activation model where the fibres are only electrically connected to the myocardial tissue at the terminal points of the fibre branches. Once again, because our framework is based in CMISS we have access to this method although investigation is required to determine the behaviour of such a Purkinje fibre model during dynamic contraction of the tissue. Also, through the use of CellML the Purkinje fibres can easily be modelled using an actual Purkinje fibre model separately to the remainder of the myocardium.

The final limitation we discuss is the length of time these simulations take to run, especially the LV sinus rhythm electro-mechanics models that run for a full heart beat. We have shown that the implemented framework is capable of reasonable performance increases when using multiple processors for sections of the simulations (Section 5.5). An obvious and immediate method to decrease the total simulation time would be examine the parts of the simulations that do not scale well with the number of processors and see if the parallelism in the associated code can be improved. Some of the obvious targets for this are the dipole calculation and the evaluation of the cellular model to obtain updated active tension values following length perturbations.

If we could enhance the implementation to be as parallel as possible then the total simulation time should scale approximately with the number of processors. The current implementation of parallel code in CMISS requires the used of shared memory architectures, which has implications for the number of processors it is possible to use. The IBM Regatta machine that was used for the simulations in this thesis has a limit of 32 processors able to share a common memory pool. While other vendors, most notably SGI, have systems able to share memory between a much larger pool of processors most high processor count systems today are based on a distributed memory architecture. To capitalise on the number of processors in these systems would require significant redesign of the CMISS code to move to a distributed memory model.

In addition to making our framework run better on high performance machines there are also many fundamental algorithmic improvements that could be made. The implementation

of the framework developed in this thesis is very much a first draft – we now have the tools that are capable of these simulations but most of the new code added to CMISS was written with a goal of simply getting something that worked reasonably well but not particularly well designed. So the first step in improving the performance of our framework is to progressively work through the code checking for algorithmic improvements while ensuring that simulations we have already performed are not broken. Of course, this step is dependent on the outcome of some of the further work discussed above as some of them could easily result in significant changes to the existing code.

6.2 Future Studies

In this thesis we have developed a comprehensive method for tightly coupling cellular level models into tissue and organ models of cardiac electro-mechanics. Even without improving the current work with the extensions and further work described in Section 6.1 above, the framework we have developed is now capable of some significant studies. Here we briefly outline a few of the studies that could be performed using this work in the short term.

6.2.1 A Whole Heart Model

In this thesis we have developed a general modelling and simulation framework which allows tight coupling of cellular level processes into tissue and organ level continuum models. We presented some simulation studies based on a simplified LV geometry. While such studies are a useful aid for the interpretation of some experimental observations, the real predictive power of the methods we have developed will not be realised until we move to models based on real anatomical detail and include at least a RV and possibly the atria.

A detailed finite element model of the porcine left and right ventricles has recently been developed and the passive mechanical material parameters investigated (Stevens, Remme, LeGrice & Hunter 2003). Application of the methods developed in this thesis to model electro-mechanics in this geometry would be a good next step in the progression of this work. We are, unfortunately, currently limited by the computational cost of such a simulation. With further work on the methods developed, as described in Section 6.1 above, however, such a model should be possible.

Once we have a model of the porcine ventricles with which it is possible to perform simulations in a timely manner, we can begin to consider the inclusion of the atria into the geometric model to complete the full heart anatomically based geometry. Due to the complex structure of the atria, a first approximation may be to simply cap the ventricular geometry to provide a rough geometry for use with the cavity fluid dynamics models and actual SAN initiated electrical activation.

6.2.2 Material Parameter Analysis and Estimation

With some of the improvements discussed in Section 6.1, the LV simulations described in Chapter 5 should be able to be performed in significantly less time. Once we have this we will have a powerful tool for analysing and estimating material parameters for the cellular, tissue, and organ level models combined. This would allow, for example, additional constraints placed on an optimisation of the passive mechanical parameters at the tissue level that ensure the parameter space is restricted to those which are suitable for a given active tension model.

6.2.3 Investigation of the Epicardial Border Zone

Reentrant circuits capable of causing ventricular tachycardia (VT) are located in a thin layer of epicardial cells that survive a transmural infarct. This layer is known as the epicardial border zone.

Cabo & Boyden (2002) developed detailed cellular electrophysiology models for the electrical remodelling of the epicardial border zone, with separate models for normal (NZ) and epicardial border zone cells (IZ), based on the Winslow, Rice, Jafri, Marban & O'Rourke (1999) modified LRd model. They present AP simulations for varying $[K^+]_o$ and BCL's and examine conduction in a cable made by combining the two cell types, especially focused on the effective refractory period and how it affects the propagation of APs down the cable. Pollard, Cascio, Fast & Knisley (2002) present a model study of the modulation of triggered activity by uncoupling in the ischaemic border zone, a phenomena shown to coincide with the spontaneous occurrence of 1B-VT (de Groot 2002). Pollard et al. (2002) use modified LRd simulations to show that an intermediate amount of cellular uncoupling is an important contributor to phase 1B arrhythmogenesis. The results of Pollard et al. (2002) looked at single cell, two cell (ischaemic and control myocytes), and multicellular fibres (100 control cells (1 cm) coupled to 100 ischaemic

cells).

Using our framework we would be capable of reproducing the results given by Pollard et al. (2002) and Cabo & Boyden (2002) for the cellular and multicellular fibre models. We could then extend these models to three dimensional transmural myocardium sections and the complete LV model to investigate the effects of the conduction and AP changes on larger scale models of electrical activity.

6.2.4   The Genetic Basis of LQT

The N-LRd electrophysiology model was developed in Section 2.4.10 based on the models of Clancy & Rudy (Clancy & Rudy 2001, Clancy & Rudy 2002). In Clancy & Rudy (2002) they put forward a possible mechanism whereby a single fast sodium channel mutation is capable of causing both long-QT and Brugada syndromes. Their mechanism is based on simulations of the different cell types described by their model (epi-, mid-, and endocardial cell types) showing how the interaction between these cell types at different pacing rates would cause the changes at the whole heart and ECG level indicative of these abnormalities.

Using our framework we are capable of performing simulations using the LV geometry which would hopefully confirm the mechanism proposed by Clancy & Rudy (2002). The first step in such a study would be to perform more validation of the N-LRd model for each of the three cell types to confirm they behave as expected. We could then develop an anatomically accurate description of the distribution of these cell types throughout the LV model. Then simulations would be performed using the Purkinje-like stimulus protocol (Figure 5.7) at different pacing frequencies and the effect of the fast sodium channel mutation could be observed.

6.3   Publications

The work contained in this thesis has been presented in the following articles and conference proceedings:

- J. W. Fernandez, M. L. Buist, D. P. Nickerson and P. J. Hunter, "Modelling the passive and nerve activated response of the rectus femoris muscle to a flexion loading: A finite element framework," *Med. Eng. Phys.*, accepted, 2004.

- D. P. Nickerson and P. J. Hunter, "Cardiac electro-mechanics: From CellML to the whole heart," *J. Mol. Cell. Cardiol.*, **37**(1), 175, 2004.
- N. P. Smith, D. P. Nickerson, E. J. Crampin, and P. J. Hunter, "Multiscale computational modelling of the heart," *Acta Numerica*, **13**, 371–431, 2004.
- A. Cuellar, C. Lloyd, P. Nielson, M. Halstead, D. Bullivant, D. Nickerson, and P. Hunter, "An overview of CellML 1.1, a biological model description language," *Trans. Soc. Model Sim. Int.*, **79**(12), 740–747, 2003.
- D. P. Nickerson and P. J. Hunter, "Modelling cardiac electro-mechanics: From CellML to the whole heart," in Modelling and Control in Biomedical Systems 2003, D. D. Feng and E. R. Carson, Eds. International Federation of Automatic Control, 2003, pp. 47–50, Elsevier.
- D. P. Nickerson and P. J. Hunter, "Cardiac electromechanics: From CellML to the whole heart," in World Congress on Medical Physics and Biomedical Engineering, Sydney, Australia, 2003.
- M. P. Nash, D. P. Nickerson, N. P. Smith, and P. J. Hunter, "Computational electromechanics of the heart," in Mathematical and Computational Modeling of Biological Systems, J. Martins and E. B. Pires, Eds., chapter 2, pp. 39–85. Centro Internacional de Matematica, Coimbra Portugal, 2002.
- N. P. Smith, P. J. Mulquiney, M. P. Nash, C. P. Bradley, D. P. Nickerson, and P. J. Hunter, "Mathematical modelling of the heart: Cell to organ.," *Chaos, Solitons and Fractals*, **13**(8), 1613–1621, 2002.
- N. P. Smith, P. J. Mulquiney, M. P. Nash, C. P. Bradley, D. P. Nickerson, and P. J. Hunter, "Construction of a whole organ model of cardiac function.," in Computer Simulation and Experimental Assessment of Cardiac Function, chapter 14. Futura Publishing, 2001.
- D. P. Nickerson, N. P. Smith, and P. J. Hunter, "A model of cardiac cellular electromechanics," *Phil. Trans. R. Soc. Lond. A*, **359**(1783), 1159–1172, 2001.
- D. P. Nickerson and P. J. Hunter, "Modelling cardiac cellular electro-mechanics," in Proceedings of the Physiological Society of New Zealand, Christchurch, New Zealand, **20**(Supplement 1), p. 65, Proceedings of the XXXIV International Congress of Physiological Sciences, 2001.
- D. P. Nickerson, N. P. Smith, M. P. Nash, and P. J. Hunter, "Modelling cardiac tissue electro-mechanics," in Satellite Meeting of 34th International Congress of Physiological Sciences: The Integrated Heart: Cardiac Structure and Function, Queenstown, NZ, **20**, 66, 2001.
- D. P. Nickerson, P. Kohl, N. P. Smith, and P. J. Hunter, "Cardiac electro-mechanics: Cell and tissue modelling," in Proceedings of the BMES Annual Conference, Seattle, WA,

USA, 2000.

- D. P. Nickerson and P. J. Hunter, "Cardiac cell modelling," in ANZIAM 2000 - The 36th Applied Mathematics Conference, Waitangi, Bay of Islands, New Zealand, 2000.

- D. P. Nickerson and P. J. Hunter, "Cardiac electro-mechanics," in Proceedings of the Physiological Society of New Zealand, Waiheke Island, Auckland, New Zealand, **19**, 2000.

- D. P. Nickerson and P. J. Hunter, "Cardiac electro-mechanics," in ISHR Australasian Section - Engineering Cardiovascular Solutions, Pakatoa Island, NZ, **32**(3) 1999.

- D. P. Nickerson and P. J. Hunter, "Coupled cardiac electromechanics," in The FASEB Journal - Experimental Biology 99, Washington, D.C., USA, **13**, 1999.

Appendix A

CellML Models

The content of this appendix has been generated directly from the CellML models created and described in Chapter 2 and used in this research. This representation of the models is simply intended to provide a quick reference for the models for the purposes of this thesis – the actual models are all freely available from the CellML model repository available from http://cellml. sourceforge.net and http://www.cellml.org, and in the attached compact disc. In the simulations presented in this thesis, all variables with no initial value are assumed to be zero.

A.1 hill_1938_isometric

This is a CellML version of the model published in 1938 by Hill on the isometric contraction of skeletal muscle. The (default) initial values contained in this model are for frog satorius muscle at 0 degrees C.

Reference: Hill, A. V. (1938), 'The heat of shortening and the dynamic constants of muscle', *Proceedings of the Royal Society of London. Series B* **126**, 136–195.

"interface" component

We'll use this component as the 'interface' to the model, all other components are hidden via encapsulation in this component.

Initial values defined in this component

$a = 6.4 \times 10^9$ ng $\cdot$ mm^{-2} $\qquad\qquad$ $b = 0.59 \times 10^{-3}$ ms^{-1}

$alpha = 1.68 \times 10^{11}$ ng $\cdot$ mm^{-2} $\qquad\qquad$ $To = 1.68 \times 10^{10}$ ng $\cdot$ mm^{-2}

"isometric_contraction" component

The component which contains the isometric tension equation.

Equations defined in this component

The kinetics of the isometric tension development, from equation 1 on page 185 of the original publication.

$$\frac{\mathrm{d}(T)}{\mathrm{d}(t)} = \left(\frac{(To + a) * alpha * b}{(T + a)} - alpha * b \right) \tag{A.1.1}$$

The ratio of isometric tension to the maximum possible value.

$$ratio = \begin{cases} \frac{T}{To}; & \text{if } To > 0.0, \\ 0.0 & \text{otherwise.} \end{cases} \tag{A.1.2}$$

A.2   Hodgkin_Huxley_1952

This is a CellML version of the model published in 1952 by Hodgkin and Huxley on the electrical activation of squid axons.

Reference: Hodgkin, A. L. & Huxley, A. F. (1952), 'A quantitative description of membrane current and its application to conductance and excitation in nerve', *Journal of Physiology* **117**, 500–544.

"interface" component

We'll use this component as the 'interface' to the model, all other components are hidden via encapsulation in this component.

Initial values defined in this component

$Cm = 0.01 \ \mu\mathrm{F} \cdot \mathrm{mm}^{-2}$ $gK\_max = 36.0 \times 10^{-2} \ \mathrm{mS} \cdot \mathrm{mm}^{-2}$

$Er = -65.0 \ \mathrm{mV}$ $gleak\_max = 0.3 \times 10^{-2} \ \mathrm{mS} \cdot \mathrm{mm}^{-2}$

$gNa\_max = 120.0 \times 10^{-2} \ \mathrm{mS} \cdot \mathrm{mm}^{-2}$

Equations defined in this component

This is a dummy equation that we simply use to make grabbing the value in CMISS much easier.

$$IStimC = Istim \tag{A.2.1}$$

"membrane" component

The membrane component is the "real" parent component which physically contains its child components. This component defines the transmembrane potential.

Initial values defined in this component

$Vm = -65.0 \text{ mV}$

Equations defined in this component

This is the main equation for the model, describing the dependency of the time course of tranmembrane potential on the three ionic currents plus any applied stimulus current.

$$\frac{\mathrm{d}(Vm)}{\mathrm{d}(t)} = \frac{(Istim - (INa + IK + Ileak))}{Cm} \tag{A.2.2}$$

"sodium_channel" component

The sodium channel is the first of three membrane bound ionic channel proteins in this model. It is primarily responsible for the upstroke of the action potential.

Equations defined in this component

Calculation of the sodium current.

$$INa = gNa * (Vm - ENa) \tag{A.2.3}$$

Calculation of the sodium channel's current conductance based on the activation and inactivation gates.

$$gNa = gNa\_max * (m\_gate)^{3.0} * h \tag{A.2.4}$$

Calculation of the sodium channel's current equilibrium potential.

$$ENa = (Er + 115.0) \tag{A.2.5}$$

"sodium_channel_m_gate" component

This is the voltage dependent activation gate for the sodium channel.

Initial values defined in this component

$m = 0.0$

Equations defined in this component

Calculation of the opening rate of the activation gate of the sodium channel.

$$alpha = \frac{0.1 * (25.0 - V)}{(\exp(0.1 * (25.0 - V)) - 1.0)} \tag{A.2.6}$$

Calculation of the closing rate of the activation gate of the sodium channel.

$$beta = 4.0 * \exp\left(\frac{-V}{18.0}\right) \tag{A.2.7}$$

The rate of change of the activation gate of the sodium channel.

$$\frac{\mathrm{d}(m)}{\mathrm{d}(t)} = (alpha * (1.0 - m) - beta * m) \tag{A.2.8}$$

$$V = (Vm - Er) \tag{A.2.9}$$

"sodium_channel_h_gate" component

This is the voltage dependent inactivation gate for the sodium channel.

Initial values defined in this component
$h = 0.6$

Equations defined in this component

The closing rate of the inactivation gate.
$$beta = \frac{1.0}{(\exp(0.1 * (30.0 - V)) + 1.0)} \tag{A.2.10}$$

The opening rate of the inactivation gate.
$$alpha = 0.07 * \exp\left(\frac{-V}{20.0}\right) \tag{A.2.11}$$

The rate of change of the inactivation gate.
$$\frac{\mathrm{d}(h)}{\mathrm{d}(t)} = (alpha * (1.0 - h) - beta * h) \tag{A.2.12}$$

$$V = (Vm - Er) \tag{A.2.13}$$

"potassium_channel" component

The potassium channel is the second of three membrane bound ionic channels defined by this model. It is primarily responsible for the repolarisation phase of the action potential.

Equations defined in this component

Calculation of the potassium current.
$$IK = gK * (Vm - EK) \tag{A.2.14}$$

Calculation of the potassium channel conductance.
$$gK = gK\_max * (n)^{4.0} \tag{A.2.15}$$

Calculation of the potassium channel equilibrium potential.
$$EK = (Er - 12.0) \tag{A.2.16}$$

"potassium_channel_n_gate" component

The voltage dependent activation gate for the potassium channel.

Initial values defined in this component

$n = 0.3$

Equations defined in this component

Calculation of the opening rate of the activation gate for the potassium channel.

$$alpha = \frac{0.01 * (10.0 - V)}{(\exp(0.1 * (10.0 - V)) - 1.0)}$$ (A.2.17)

Calculation of the closing rate of the activation gate for the potassium channel.

$$beta = 0.125 * \exp\left(\frac{-V}{80.0}\right)$$ (A.2.18)

The rate of change in the activation gate of the potassium channel.

$$\frac{\mathrm{d}(n)}{\mathrm{d}(t)} = (alpha * (1.0 - n) - beta * n)$$ (A.2.19)

$$V = (Vm - Er)$$ (A.2.20)

"leak_channel" component

A small leakage current, made up by chloride and other ions, with a constant conductance.

Equations defined in this component

Calculation of the leakage current.

$$Ileak = gleak\_max * (Vm - Eleak)$$ (A.2.21)

Calculation of the equilibrium potential of the leak channel.

$$Eleak = (Er + 10.613)$$ (A.2.22)

A.3   FitzHugh_Nagumo_1961

This is a CellML version of the FitzHugh-Nagumo model, published separately by FitzHugh in 1961 and Nagumo et. al. in 1962. While the original two-variable model described a non-dimensional activation variable (x or u) and a non-dimensional recovery variable (y or v), here we formulate the model in terms of the 'real' action potential given by the time course of the transmembrane potential (Vm). In so doing, the time rate of change of the activation variable describes the total 'ionic current' through the membrane with the original model parameters adjusted to give the correct dimensionality.

Reference: Fitzhugh, R. A. (1961), 'Impulses and physiological states in theoretical models of nerve membrane', *Biophysical Journal* **1**, 445–466.

Reference: Nagumo, J., Animoto, S. & Yoshizawa, S. (1962), 'An active pulse transmission line simulating nerve axon', *Proceedings of the Institute of Radio Engineers* **50**, 2061–2070.

"interface" component

We'll use this component as the "interface" to the model, all other components are hidden via encapsulation in this component.

Initial values defined in this component

$Cm = 0.01 \, \mu\text{F} \cdot \text{mm}^{-2}$ $\qquad$ $c1 = 0.175 \, \mu\text{A} \cdot \text{mm}^{-2}$

$Vr = -85.0 \, \text{mV}$ $\qquad$ $c2 = 0.03 \, \mu\text{A} \cdot \text{mm}^{-2}$

$Vth = -75.0 \, \text{mV}$ $\qquad$ $b = 0.011 \, \text{ms}^{-1}$

$Vp = 15.0 \, \text{mV}$ $\qquad$ $d = 0.55$

Equations defined in this component

This is a dummy equation that we simply use to make grabbing the value in CMISS much easier.

$$IStimC = Istim \tag{A.3.1}$$

"membrane_potential" component

The component which defines the kinetics of the transmembrane potential.

Initial values defined in this component

$Vm = -85 \, \text{mV}$

Equations defined in this component

This equation describes the kinetics of the transmembrane, potential - the action potential.

$$\frac{\mathrm{d}(Vm)}{\mathrm{d}(t)} = \frac{(Istim - Iion)}{Cm} \tag{A.3.2}$$

The non-dimensional and scaled potential value.

$$u = \frac{(Vm - Vr)}{(Vp - Vr)} \tag{A.3.3}$$

"ionic_current" component

Here we define the total ionic current through the cellular membrane - equivalent to the temporal derivative of the original activation variable.

Initial values defined in this component

$Iion = 0.0 \, \mu\text{A} \cdot \text{mm}^{-2}$

Equations defined in this component

The calcuation of the total ionic current.
$$Iion = \left(c1 * u * \left(u - \frac{(Vth - Vr)}{(Vp - Vr)} \right) * (u - 1.0) + c2 * v \right) \tag{A.3.4}$$

"recovery_variable" component

Here we define the non-dimensional recovery variable, v.

Initial values defined in this component

$v = 0.0$

Equations defined in this component

The kinetics of the recovery variable.
$$\frac{d(v)}{d(t)} = b * (u - d * v) \tag{A.3.5}$$

A.4   noble_model_1962

This is the CellML description of Noble's 1962 mathematical model of Purkinje fibre action and pace-maker potentials. The equations formulated by Hodgkin and Huxley (1952) to describe the electrical activity of squid nerve have been modified to describe the action and pace-maker potentials of the Purkinje fibres of the heart.

Reference: Noble, D. (1962), 'A Modification of the Hodgkin-Huxley Equations Applicable to Purkinje Fibre Action and Pace-maker Potentials', *Journal of Physiology* **160**, 317–352.

"environment" component

"membrane" component

The main component of the model, containing the membrane currents and defining the transmembrane potential.

Initial values defined in this component

$V = -78.3 \, \text{mV}$ $Cm = 0.12 \, \mu\text{F} \cdot \text{mm}^{-2}$

Equations defined in this component

The kinetics of the transmembrane potential.
$$\frac{d(V)}{d(time)} = \frac{(I\_stim - (i\_Na + i\_K + i\_Leak))}{Cm} \tag{A.4.1}$$

This is a dummy equation that we simply use to make grabbing the value in CMISS much easier.

$$IStimC = I\_stim \tag{A.4.2}$$

"sodium_channel" component

The modified sodium current from the 1952 Hodgkin Huxley model.

Initial values defined in this component

$g\_Na\_max = 4.0 \, \text{mS} \cdot \text{mm}^{-2}$ $\qquad\qquad\qquad E\_Na = 40.0 \, \text{mV}$

Equations defined in this component

Calculation of the channel conductance.

$$g\_Na = (m)^{3.0} * h * g\_Na\_max \tag{A.4.3}$$

Calculation of the channel current.

$$i\_Na = \left(g\_Na\_max * (m)^{3.0} * h + 0.14 \times 10^{-2}\right) * (V - E\_Na) \tag{A.4.4}$$

"sodium_channel_m_gate" component

The voltage-dependent activation gate for the sodium channel - the m gate.

Initial values defined in this component

$m = 0.05$

Equations defined in this component

The opening rate for the m gate.

$$alpha\_m = \frac{0.1 * (-V - 48.0)}{\left(\exp\left(\frac{(-V-48.0)}{15.0}\right) - 1.0\right)} \tag{A.4.5}$$

The closing rate for the m gate.

$$beta\_m = \frac{0.12 * (V + 8.0)}{\left(\exp\left(\frac{(V+8.0)}{5.0}\right) - 1.0\right)} \tag{A.4.6}$$

The kinetics of the m gate.

$$\frac{\mathrm{d}(m)}{\mathrm{d}(time)} = (alpha\_m * (1.0 - m) - beta\_m * m) \tag{A.4.7}$$

"sodium_channel_h_gate" component

The voltage-dependent inactivation gate for the sodium channel - the h gate.

Initial values defined in this component

$h = 0.785$

Equations defined in this component

The opening rate for the h gate.
$$alpha\_h = 0.17 * \exp\left(\frac{(-V - 90.0)}{20.0}\right) \tag{A.4.8}$$

The closing rate for the h gate.
$$beta\_h = \frac{1.0}{\left(1.0 + \exp\left(\frac{(-V - 42.0)}{10.0}\right)\right)} \tag{A.4.9}$$

The kinetics of the h gate.
$$\frac{d(h)}{d(time)} = (alpha\_h * (1.0 - h) - beta\_h * h) \tag{A.4.10}$$

"potassium_channel" component

The modified Hodgkin Huxley 1952 potassium channel.

Equations defined in this component

Calculation of the potassium current. The g_K_add conductance term can be used to obtain a quiescent variant of the model by setting its value to 0.001 mS/mm2.
$$i\_K = (g\_K1 + g\_K2 + g\_K\_add) * (V + 100.0) \tag{A.4.11}$$

The conductance of the first 'type' of potassium channels present in this model, using an empirical formaulation.
$$g\_K1 = \left(1.2 \times 10^{-2} * \exp\left(\frac{(-V - 90.0)}{50.0}\right) + 0.015 \times 10^{-2} * \exp\left(\frac{(V + 90.0)}{60.0}\right)\right) \tag{A.4.12}$$

The conductance of the second 'type' of potassium channels present in this model, using the Hodgkin Huxley 1952 type kinetics.
$$g\_K2 = 1.2 \times 10^{-2} * (n)^{4.0} \tag{A.4.13}$$

"potassium_channel_n_gate" component

The voltage-dependent activation gate for the potassium channel - the n gate.

Initial values defined in this component
$n = 0.0935$

Equations defined in this component

The opening rate for the n gate.
$$alpha\_n = \frac{0.0001 * (-V - 50.0)}{\left(\exp\left(\frac{(-V - 50.0)}{10.0}\right) - 1.0\right)} \tag{A.4.14}$$

The closing rate for the n gate.

$$beta\_n = 0.002 * \exp\left(\frac{(-V - 90.0)}{80.0}\right)$$

(A.4.15)

The kinetics of the n gate.

$$\frac{\mathrm{d}(n)}{\mathrm{d}(time)} = (alpha\_n * (1.0 - n) - beta\_n * n)$$

(A.4.16)

"leakage_current" component

A non-specific background current attributed in part to chloride ions. Can be turned on by specifying an appropriate value for the conductance ($\sim$0.00075 mS/mm2).

Initial values defined in this component

$g\_L = 0.0\,\mathrm{mS} \cdot \mathrm{mm}^{-2}$ $\qquad\qquad\qquad\qquad$ $E\_L = -60.0\,\mathrm{mV}$

Equations defined in this component

$$i\_Leak = g\_L * (V - E\_L)$$

(A.4.17)

A.5 cubic_polynomial_1975

This is a CellML version of the cubic polynomial model of activation from the 1975 paper by Hunter et. al.

Reference: Hunter, P. J., McNaughton, P. A. & Noble, D. (1975), 'Analytical models of propagation in excitable cells', *Progress in Biophysics and Molecular Biology* **30**, 99–144.

"interface" component

We'll use this component as the "interface" to the model, all other components are hidden via encapsulation in this component.

Initial values defined in this component

$Cm = 0.01\,\mu\mathrm{F} \cdot \mathrm{mm}^{-2}$ $\qquad\qquad\qquad$ $Vm\_threshold = -75.0\,\mathrm{mV}$

$Vm\_rest = -85.0\,\mathrm{mV}$ $\qquad\qquad\qquad\qquad$ $membrane\_conductance = 0.004\,\mathrm{mS} \cdot \mathrm{mm}^{-2}$

$Vm\_plateau = 15.0\,\mathrm{mV}$

Equations defined in this component

This is a dummy equation that we simply use to make grabbing the value in CMISS much easier.

$$IStimC = Istim$$

(A.5.1)

"membrane" component

In this simple model we only have one component, which we call the membrane. It holds both the evaluation of the membrane potential ODE and the single current calculation.

Initial values defined in this component

$Vm = -85.0$ mV

Equations defined in this component

This is the main equation for the model, describing the dependency of the time course of tranmembrane potential on the single ionic current plus any applied stimulus current.

$$\frac{\mathrm{d}(Vm)}{\mathrm{d}(t)} = \frac{(Istim - I)}{Cm} \tag{A.5.2}$$

$$plateau = (Vm\_plateau - Vm\_rest) \tag{A.5.3}$$
$$threshold = (Vm\_threshold - Vm\_rest) \tag{A.5.4}$$
$$phi = (Vm - Vm\_rest) \tag{A.5.5}$$

This is the calculation of the single current in this model, and where the model name comes from.

$$I = membrane\_conductance * phi * \left(1.0 - \frac{phi}{threshold}\right) * \left(1.0 - \frac{phi}{plateau}\right) \tag{A.5.6}$$

A.6   mcallister_noble_tsien_model_1975

This is the CellML description of McAllister, Noble and Tsien's mathematical model of cardiac action potentials of Purkinje fibres. It describes transmembrane ionic currents in terms of Hodgkin-Huxley type equations. It is a significant development of the Noble (1962) model as more currents are added based on new experimental data.

Reference: McAllister, R. E., Noble, D. & Tsien, R. W. (1975), 'Reconstruction of the electrical activity of cardiac purkinje fibres', *Journal of Physiology* **251**, 1–59.

"environment" component

"membrane" component

The main component of the model, containing the definition of the model's action potential.

Initial values defined in this component

$V = -80.0$ mV $C = 0.1 \ \mu\mathrm{F} \cdot \mathrm{mm}^{-2}$

Equations defined in this component

The kinetics of the transmembrane potential, defi ned as the sum of the trans-sarcolemmal currents and an applied stimulus current.

$$\frac{\mathrm{d}(V)}{\mathrm{d}(time)} = \frac{(I\_stim - (i\_Na + i\_si + i\_K2 + i\_x1 + i\_x2 + i\_qr + i\_K1 + i\_Na\_b + i\_Cl\_b))}{C} \quad (\text{A.6.1})$$

This is a dummy equation that we simply use to make grabbing the value in CMISS much easier.

$$IStimC = I\_stim \quad (\text{A.6.2})$$

"fast_sodium_current" component

The fast sodium current, primarily responsible for the upstroke of the action potential.

Initial values defined in this component

$E\_Na = 40.0 \ \mathrm{mV}$ $g\_Na = 1.5 \ \mathrm{mS \cdot mm^{-2}}$

Equations defined in this component

Calculation of the fast sodium current.

$$i\_Na = g\_Na * (m)^{3.0} * h * (V - E\_Na) \quad (\text{A.6.3})$$

"fast_sodium_current_m_gate" component

The voltage-dependent activation gate for the fast sodium channel - the m gate.

Initial values defined in this component

$m = 0.019$

Equations defined in this component

The opening rate of the m gate.

$$alpha\_m = \frac{(V + 47.0)}{\left(1.0 - \exp\left(-\frac{(V+47.0)}{10.0}\right)\right)} \quad (\text{A.6.4})$$

The closing rate of the m gate.

$$beta\_m = 40.0 * \exp\left(-\frac{(V + 72.0)}{17.86}\right) \quad (\text{A.6.5})$$

The kinetics of the m gate.

$$\frac{\mathrm{d}(m)}{\mathrm{d}(time)} = (alpha\_m * (1.0 - m) - beta\_m * m) \quad (\text{A.6.6})$$

"fast_sodium_current_h_gate" component

The voltage-dependent inactivation gate for the fast sodium channel - the h gate.

Initial values defined in this component
$h = 0.863$

Equations defined in this component

The opening rate of the h gate.
$$alpha\_h = 0.0085 * \exp\left(-\frac{(V + 71.0)}{5.435}\right) \tag{A.6.7}$$

The closing rate of the h gate.
$$beta\_h = \frac{2.5}{\left(\exp\left(-\frac{(V+10.0)}{12.2}\right) + 1.0\right)} \tag{A.6.8}$$

The kinetics of the h gate.
$$\frac{d(h)}{d(time)} = (alpha\_h * (1.0 - h) - beta\_h * h) \tag{A.6.9}$$

"secondary_inward_current" component

The secondary (or sometimes slow) inward current activates much more slowly than the sodium current and it is responsible for holding up the plateau after the initial activation and for controlling the duration of the action potential. At the time of this model, it was assumed that the flux of both Na and Ca ions through the cell membrane was responsible for this current. This channel has an activation gate d and an inactivation gate f. It was observed in earlier experiments that a portion of this current would not completely inactivate. This is represented by the second term in the secondary current equation which has an activation variable d1, but no deactivation variable.

Initial values defined in this component

$g\_si = 0.008 \, \text{mS} \cdot \text{mm}^{-2}$ $\qquad\qquad$ $E\_si = 70.0 \, \text{mV}$
$g\_si\_ = 0.0004 \, \text{mS} \cdot \text{mm}^{-2}$

Equations defined in this component

Calculation of the second inward current.
$$i\_si = (g\_si * d * f * (V - E\_si) + g\_si\_ * d1 * (V - E\_si)) \tag{A.6.10}$$

"secondary_inward_current_d_gate" component

The voltage-dependent activation gate for the secondary inward current - the d gate.

Initial values defined in this component
$d = 0.002$

Equations defined in this component

The opening rate of the d gate.

$$alpha\_d = \frac{(V + 40.0)}{500.0 * \left(1.0 - \exp\left(-\frac{(V+40.0)}{10.0}\right)\right)} \tag{A.6.11}$$

The closing rate of the d gate.

$$beta\_d = 0.02 * \exp\left(-\frac{(V + 40.0)}{11.26}\right) \tag{A.6.12}$$

The kinetics of the d gate.

$$\frac{\mathrm{d}(d)}{\mathrm{d}(time)} = (alpha\_d * (1.0 - d) - beta\_d * d) \tag{A.6.13}$$

"secondary_inward_current_f_gate" component

The voltage-dependent inactivation gate for the secondary inward current - the f gate.

Initial values defined in this component

$f = 0.794$

Equations defined in this component

The opening rate of the f gate.

$$alpha\_f = 0.000987 * \exp\left(-\frac{(V + 60.0)}{25.0}\right) \tag{A.6.14}$$

The closing rate of the f gate.

$$beta\_f = \frac{0.02}{\left(\exp\left(-\frac{(V+26.0)}{11.5}\right) + 1.0\right)} \tag{A.6.15}$$

The kinetics of the f gate.

$$\frac{\mathrm{d}(f)}{\mathrm{d}(time)} = (alpha\_f * (1.0 - f) - beta\_f * f) \tag{A.6.16}$$

"secondary_inward_current_d1_gate" component

The activation variable for the slow component of the secondard inward current - the d1 gate (corresponds to the d' variable in the MNT paper.

Equations defined in this component

Calculation of the activation variable d1.

$$d1 = \frac{1.0}{\left(1.0 + \exp\left(-\frac{(V+40.0)}{6.667}\right)\right)} \tag{A.6.17}$$

"pacemaker_potassium_current" component

A potassium current activated over the 'pace-maker" range of potentials. Provides the pacemaker function of the model.

Initial values defined in this component
$E\_K = -110.0\,\mathrm{mV}$

Equations defined in this component

Calculation of the pacemaker current.

$$i\_K2 = I\_K2 * s \tag{A.6.18}$$

The maximal pacemaker current.

$$I\_K2 = 0.028 * \frac{\left(\exp\left(\frac{(V - E\_K)}{25.0}\right) - 1.0\right)}{\left(\exp\left(\frac{(V+60.0)}{12.5}\right) + \exp\left(\frac{(V+60.0)}{25.0}\right)\right)} \tag{A.6.19}$$

"pacemaker_potassium_current_s_gate" component

The voltage-dependent gating variable for the pacemaker current - the s gate.

Initial values defined in this component
$s = 0.763$ $\qquad\qquad\qquad E\_s = -52.0\,\mathrm{mV}$

Equations defined in this component

The opening rate of the s gate.

$$alpha\_s = \frac{0.001 * (V - E\_s)}{\left(1.0 - \exp\left(-\frac{(V - E\_s)}{5.0}\right)\right)} \tag{A.6.20}$$

The closing rate of the s gate.

$$beta\_s = 0.00005 * \exp\left(-\frac{(V - E\_s)}{15.0}\right) \tag{A.6.21}$$

The kinetics of the s gate.

$$\frac{\mathrm{d}(s)}{\mathrm{d}(time)} = (alpha\_s * (1.0 - s) - beta\_s * s) \tag{A.6.22}$$

"plateau_potassium_current1" component

The equations for the plateau potassium currents (x1 and x2) are based on experiments performed by Noble and Tsien (1969) which showed that additional potassium currents were activated in the plateau range of potentials. They appear to play an essential role in membrane repolarisation.

Equations defined in this component

Calculation of the first plateau potassium current.

$$i\_x1 = x1 * I\_x1 \tag{A.6.23}$$

Calculation of the maximal first plateau potassium current.

$$I\_x1 = 0.012 * \frac{\left(\exp\left(\frac{(V+95.0)}{25.0}\right) - 1.0\right)}{\exp\left(\frac{(V+45.0)}{25.0}\right)} \tag{A.6.24}$$

"plateau_potassium_current1_x1_gate" component

The voltage-dependent gating variable for the first plateau potassium current - the x1 gate.

Initial values defined in this component

$x1 = 0.051$

Equations defined in this component

The opening rate of the x1 gate.

$$alpha\_x1 = 5 \times 10^{-4} * \frac{\exp\left(\frac{(V+50.0)}{12.1}\right)}{\left(1.0 + \exp\left(\frac{(V+50.0)}{17.5}\right)\right)} \tag{A.6.25}$$

The closing rate of the x1 gate.

$$beta\_x1 = 0.0013 * \frac{\exp\left(-\frac{(V+20.0)}{16.67}\right)}{\left(1.0 + \exp\left(-\frac{(V+20.0)}{20.0}\right)\right)} \tag{A.6.26}$$

The kinetics of the x1 gate.

$$\frac{\mathrm{d}(x1)}{\mathrm{d}(time)} = (alpha\_x1 * (1.0 - x1) - beta\_x1 * x1) \tag{A.6.27}$$

"plateau_potassium_current2" component

The second of the plateau potassium currents.

Equations defined in this component

Calculation of the second plateau potassium current.

$$i\_x2 = x2 * I\_x2 \tag{A.6.28}$$

The linear maximal second plateau potassium current.

$$I\_x2 = (0.25 + 0.00385 * V) \tag{A.6.29}$$

"plateau_potassium_current2_x2_gate" component

The gating variable for the second plateau potassium current - the x2 gate.

Initial values defined in this component

$x2 = 0.006$

Equations defined in this component

The opening rate for the x2 gate.

$$alpha\_x2 = 0.000127 * \frac{1.0}{\left(1.0 + \exp\left(-\frac{(V+19.0)}{5.0}\right)\right)} \tag{A.6.30}$$

The closing rate for the x2 gate.

$$beta\_x2 = 0.0003 * \frac{\exp\left(-\frac{(V+20.0)}{16.67}\right)}{\left(1.0 + \exp\left(-\frac{(V+20.0)}{25.0}\right)\right)} \tag{A.6.31}$$

The kinetics of the x2 gate.

$$\frac{\mathrm{d}(x2)}{\mathrm{d}(time)} = (alpha\_x2 * (1.0 - x2) - beta\_x2 * x2) \tag{A.6.32}$$

"transient_chloride_current" component

The transient chloride current (i_qr) is responsible for the rapid repolarisation from the peak of the depolarisation spike of the action potential, to the start of the plateau. The current has 2 gating variables, q and r.

Initial values defined in this component

$E\_Cl = -70.0\,\mathrm{mV}$ $g\_qr = 0.05\,\mathrm{mS} \cdot \mathrm{mm}^{-2}$

Equations defined in this component

Calculation of the transient chloride current.

$$i\_qr = g\_qr * q * r * (V - E\_Cl) \tag{A.6.33}$$

"transient_chloride_current_q_gate" component

The voltage-dependent activation gate for the transient chloride channel - the q gate.

Initial values defined in this component

$q = 0.0$

Equations defined in this component

The opening rate for the q gate.

$$alpha\_q = 0.008 * \frac{V}{\left(1.0 - \exp\left(-\frac{V}{10.0}\right)\right)} \tag{A.6.34}$$

The closing rate for the q gate.

$$beta\_q = 0.08 * \exp\left(-\frac{V}{11.26}\right) \tag{A.6.35}$$

The kinetics of the q gate.

$$\frac{\mathrm{d}(q)}{\mathrm{d}(time)} = (alpha\_q * (1.0 - q) - beta\_q * q) \tag{A.6.36}$$

"transient_chloride_current_r_gate" component

The voltage-dependent inactivation gate for the transient chloride current - the r gate.

Initial values defined in this component
$r = 0.126$

Equations defined in this component

The opening rate for the r gate.

$$alpha\_r = 0.00018 * \exp\left(-\frac{(V + 80)}{25.0}\right) \tag{A.6.37}$$

The closing rate for the r gate.

$$beta\_r = \frac{0.02}{\left(\exp\left(-\frac{(V+26)}{11.5}\right) + 1.0\right)} \tag{A.6.38}$$

The kinetics of the r gate.

$$\frac{\mathrm{d}(r)}{\mathrm{d}(time)} = (alpha\_r * (1.0 - r) - beta\_r * r) \tag{A.6.39}$$

"time_independent_outward_current" component

The time-independent (background) current carried by potassium ions.

Initial values defined in this component
$E\_K1 = -30.0 \, \text{mV}$

Equations defined in this component

Calculation of the time-independent potassium current.

$$i\_K1 = \left(\frac{I\_K2}{2.8} + 0.002 * \frac{(V - E\_K1)}{\left(1.0 - \exp\left(-\frac{(V - E\_K1)}{25.0}\right)\right)}\right) \tag{A.6.40}$$

"sodium_background_current" component

The sodium background current is a time-independent diffusion of Na ions down their electrochemical gradient, through the cell surface membrane into the cytosol.

Initial values defined in this component

$g\_Nab = 0.00105 \, \text{mS} \cdot \text{mm}^{-2}$

Equations defined in this component

Calculation of the sodium background current.
$$i\_Na\_b = g\_Nab * (V - E\_Na) \tag{A.6.41}$$

"chloride_background_current" component

The chloride background current contributes to maintaining the plateau and helps to determine the action potential duration.

Initial values defined in this component

$g\_Clb = 0.0001 \, \text{mS} \cdot \text{mm}^{-2}$

Equations defined in this component

Calculation of the background chloride current.
$$i\_Cl\_b = g\_Clb * (V - E\_Cl) \tag{A.6.42}$$

A.7 beeler_reuter_model_1977

This is the CellML description of Beeler and Reuter's mathematical model of membrane action potentials of mammalian ventricular myocardial fibres. It describes four ionic currents in terms of Hodkin-Huxley type equations.

Reference: Beeler, G. W. & Reuter, H. (1977), 'Reconstruction of the action potential of ventricular myocardial fibres', *Journal of Physiology* **268**, 177–210.

"environment" component

This component is used to declare variables that are used by all or most of the other components, in this case just 'time'.

"membrane" component

This component is the 'root' node of our model. It defines the action potential variable 'V'.

Initial values defined in this component

$V = -84.624 \, \text{mV}$ $\qquad\qquad\qquad C = 0.01 \, \mu\text{F} \cdot \text{mm}^{-2}$

Equations defined in this component

The ODE governing the membrane potential – given by the summation of the ionic currents and an applied stimulus.

$$\frac{\text{d}(V)}{\text{d}(time)} = \frac{(Istim - (i\_Na + i\_s + i\_x1 + i\_K1))}{C} \tag{A.7.1}$$

This is a dummy equation that we simply use to make grabbing the value in CMISS much easier.

$$IStimC = Istim \tag{A.7.2}$$

"sodium_current" component

The "sodium_current" component contains the differential equations governing the influx of sodium ions through the cell surface membrane into the cell. This sodium current is primarily responsible for the rapid upstroke of the action potential during membrane depolarisation. Note that no initial values are needed on many variables as they are all directly dependent on the membrane voltage.

Initial values defined in this component

$g\_Na = 4.0 \times 10^{-2} \, \text{mS} \cdot \text{mm}^{-2}$ $\qquad\qquad g\_Nac = 3.0 \times 10^{-5} \, \text{mS} \cdot \text{mm}^{-2}$

$E\_Na = 50.0 \, \text{mV}$

Equations defined in this component

Calculation of the sodium current in terms of the conductance, membrane potential, and gating variables.

$$i\_Na = \left(g\_Na * (m)^{3.0} * h * j + g\_Nac \right) * (V - E\_Na) \tag{A.7.3}$$

"sodium_current_m_gate" component

The definition of the voltage-dependent activation gating kinetics for the sodium ion channel (the m gate).

Initial values defined in this component

$m = 0.011$

Equations defined in this component

The opening rate of the m gate.

$$alpha\_m = \frac{-1 * (V + 47.0)}{(\exp(-0.1 * (V + 47.0)) - 1.0)} \tag{A.7.4}$$

The closing rate of the m gate.

$$beta\_m = 40.0 * \exp(-0.056 * (V + 72.0)) \tag{A.7.5}$$

The actual kinetic equation for the m gate.

$$\frac{\mathrm{d}(m)}{\mathrm{d}(time)} = (alpha\_m * (1.0 - m) - beta\_m * m) \tag{A.7.6}$$

"sodium_current_h_gate" component

The voltage-dependent inactivation gate for the sodium channel - the h gate.

Initial values defined in this component

$h = 0.988$

Equations defined in this component

The opening rate of the h gate.

$$alpha\_h = 0.126 * \exp\left(-0.25 * (V + 77.0)\right) \tag{A.7.7}$$

The closing rate of the h gate.

$$beta\_h = \frac{1.7}{\left(\exp\left(-0.082 * (V + 22.5)\right) + 1.0\right)} \tag{A.7.8}$$

The gating kinetics of the h gate.

$$\frac{\mathrm{d}(h)}{\mathrm{d}(time)} = (alpha\_h * (1.0 - h) - beta\_h * h) \tag{A.7.9}$$

"sodium_current_j_gate" component

The voltage dependent slow inactivation sodium channel gate - the j gate.

Initial values defined in this component

$j = 0.975$

Equations defined in this component

The opening rate for the j gate.

$$alpha\_j = \frac{0.055 * \exp\left(-0.25 * (V + 78.0)\right)}{\left(\exp\left(-0.2 * (V + 78.0)\right) + 1.0\right)} \tag{A.7.10}$$

The closing rate for the j gate.

$$beta\_j = \frac{0.3}{\left(\exp\left(-0.1 * (V + 32.0)\right) + 1.0\right)} \tag{A.7.11}$$

The kinetics of the j gate.

$$\frac{\mathrm{d}(j)}{\mathrm{d}(time)} = (alpha\_j * (1.0 - j) - beta\_j * j) \tag{A.7.12}$$

"slow_inward_current" component

The "slow_inward_current" component contains the differential equations governing the transient inward ionic current. This current is predominately carried by calcium ions and it is largely responsible for maintaining the plateau of the action potential.

Initial values defined in this component

$g\_s = 9.0 \times 10^{-4}$ mS · mm^{-2} $\qquad\qquad\qquad\qquad$ $Cai = 1.0 \times 10^{-4}$ mM

Equations defined in this component

The reversal potential for the slow inward current.
$$E\_s = (-82.3 - 13.0287 * \ln{(Cai * 0.001)}) \tag{A.7.13}$$

Calculation of the slow inward current.
$$i\_s = g\_s * d * f * (V - E\_s) \tag{A.7.14}$$

The change in calcium ion concentration.
$$\frac{\mathrm{d}(Cai)}{\mathrm{d}(time)} = (-0.01 * i\_s + 0.07 * (0.0001 - Cai)) \tag{A.7.15}$$

"slow_inward_current_d_gate" component

The voltage-dependent activation gate for the slow inward current - the d gate.

Initial values defined in this component

$d = 0.003$

Equations defined in this component

The opening rate of the d gate.
$$alpha\_d = \frac{0.095 * \exp\left(-\frac{(V-5.0)}{100.0}\right)}{\left(1.0 + \exp\left(-\frac{(V-5.0)}{13.89}\right)\right)} \tag{A.7.16}$$

The closing rate of the d gate.
$$beta\_d = \frac{0.07 * \exp\left(-\frac{(V+44.0)}{59.0}\right)}{\left(1.0 + \exp\left(\frac{(V+44.0)}{20.0}\right)\right)} \tag{A.7.17}$$

The kinetics of the d gate.
$$\frac{\mathrm{d}(d)}{\mathrm{d}(time)} = (alpha\_d * (1.0 - d) - beta\_d * d) \tag{A.7.18}$$

"slow_inward_current_f_gate" component

The voltage-dependent inactivation gate for the slow inward current - the f gate.

Initial values defined in this component

$f = 0.994$

Equations defined in this component

The opening rate of the f gate.

$$alpha\_f = \frac{0.012 * \exp\left(-\frac{(V+28.0)}{125.0}\right)}{\left(1.0 + \exp\left(\frac{(V+28.0)}{6.67}\right)\right)}$$

(A.7.19)

The closing rate of the f gate.

$$beta\_f = \frac{0.0065 * \exp\left(-\frac{(V+30.0)}{50.0}\right)}{\left(1.0 + \exp\left(-\frac{(V+30.0)}{5.0}\right)\right)}$$

(A.7.20)

The kinetics of the f gate.

$$\frac{\mathrm{d}(f)}{\mathrm{d}(time)} = (alpha\_f * (1.0 - f) - beta\_f * f)$$

(A.7.21)

"time_dependent_outward_current" component

The 'time_dependent_outward_current" component contains the differential equations governing the voltage- and time-dependent outward current. This current is predominately carried by potassium ions and it is involved in the plateau of the action potential and in the re-polarisation phase.

Equations defined in this component

Calculation of the time-dependent outward current.

$$i\_x1 = x1 * 8.0 \times 10^{-3} * \frac{(\exp(0.04 * (V + 77.0)) - 1.0)}{\exp(0.04 * (V + 35.0))}$$

(A.7.22)

"time_dependent_outward_current_x1_gate" component

The voltage-dependent gating variable for the time-dependent outward current - the x1 gate.

Equations defined in this component

The opening rate of the x1 gate.

$$alpha\_x1 = 5 \times 10^{-4} * \frac{\exp\left(\frac{(V+50.0)}{12.1}\right)}{\left(1.0 + \exp\left(\frac{(V+50.0)}{17.5}\right)\right)}$$

(A.7.23)

The closing rate of the x1 gate.

$$beta\_x1 = 0.0013 * \frac{\exp\left(-\frac{(V+20.0)}{16.67}\right)}{\left(1.0 + \exp\left(-\frac{(V+20.0)}{25.0}\right)\right)} \tag{A.7.24}$$

The kinetics of the x1 gate.

$$\frac{\mathrm{d}(x1)}{\mathrm{d}(time)} = (alpha\_x1 * (1.0 - x1) - beta\_x1 * x1) \tag{A.7.25}$$

"time_independent_outward_current" component

The 'time_independent_outward_current"component contains the equations governing the voltage-dependent, time-independent outward current. This current is carried by potassium ions and it is involved in the plateau of the action potential and in the re-polarisation phase. Because the current is time-independent, it can also be described as a background current.

Equations defined in this component

Calculation of the time-independent outward current.

$$i\_K1 = 0.0035$$
$$* \left(4.0 * \frac{(\exp(0.04 * (V + 85.0)) - 1.0)}{(\exp(0.08 * (V + 53)) + \exp(0.04 * (V + 53.0)))} + 0.2 * \frac{(V + 23.0)}{(1.0 - \exp(-0.04 * (V + 23.0)))}\right) \tag{A.7.26}$$

A.8 ebihara_johnson_model_1980

This is the CellML description of Ebihara and Johnson's mathematical model of the fast sodium current in cardiac muscle (1980). It describes the ionic current with Hodgkin-Huxley formalism. This model was the first to specifically target a single channel and attempt to quantify its parameters.

Reference: Ebihara, L. & Johnson, E. A. (1980), 'Fast sodium current in cardiac muscle: A quantitative description', *Biophysical Journal* **32**, 779–790.

"environment" component

"membrane" component

In their 1980 paper, Ebihara and Johnson do not include all the ionic fluxes across the membrane of the cardiac muscle cell, they only describe the fast sodium current. The Ebihara-Johnson model can be coupled to the Beeler-Reuter model (1977) as a direct replacement for the sodium current. The other ionic currents were very similar to those found using the Beeler-Reuter model. I have included these equations from the Beeler-Reuter 1977 model in this CellML description.

Initial values defined in this component

$V = -87.0\,\text{mV}$ $\qquad\qquad\qquad\qquad\qquad\qquad\qquad\qquad C = 0.013\,\mu\text{F} \cdot \text{mm}^{-2}$

Equations defined in this component

The main differential equation for the model specifying the rate of change of the transmembrane potential as the sum of the ionic currents and an applied stimulus current.

$$\frac{\mathrm{d}(V)}{\mathrm{d}(time)} = \frac{(Istim - (i\_Na + i\_s + i\_x1 + i\_K1))}{C} \tag{A.8.1}$$

This is a dummy equation that we simply use to make grabbing the value in CMISS much easier.

$$IStimC = Istim \tag{A.8.2}$$

"fast_sodium_current" component

In the calculation of the fast sodium current there is no variable corresponding to the j gate used in the Beeler-Reuter model because the experimental results showed no need to include a second deactivation variable.

Initial values defined in this component

$g\_Na = 23.0 \times 10^{-2}\,\text{mS} \cdot \text{mm}^{-2}$ $\qquad\qquad\qquad\qquad E\_Na = 29.0\,\text{mV}$

Equations defined in this component

Calculation of the fast sodium current.

$$i\_Na = g\_Na * (m)^{3.0} * h * (V - E\_Na) \tag{A.8.3}$$

"fast_sodium_current_m_gate" component

The voltage-dependent activation gate for the fast sodium channel - the m gate.

Initial values defined in this component

$m = 0.0$

Equations defined in this component

The opening rate for the m gate. The equation for alpha-m was incorrectly stated in the original 1980 paper, but it appears as shown below in Spach and Heidlage (1993), who cite a later paper by Johnson as their source (Johnson, 1983).

$$alpha\_m = \frac{0.32 * (47.13 + V)}{(1.0 - \exp((-V - 47.13)))} \tag{A.8.4}$$

The closing rate for the m gate.

$$beta\_m = 0.08 * \exp\left(\frac{-V}{11.0}\right) \tag{A.8.5}$$

The gating kinetics of the m gate.

$$\frac{\mathrm{d}(m)}{\mathrm{d}(time)} = (alpha\_m * (1.0 - m) - beta\_m * m) \tag{A.8.6}$$

"fast_sodium_current_h_gate" component

The voltage-dependent inactivation gate of the fast sodium channel - the h gate.

Initial values defined in this component

$h = 0.18$

Equations defined in this component

The opening rate of the h gate.

$$alpha\_h = \begin{cases} 0.135 * \exp\left(\frac{(-80.0 - V)}{6.8}\right); & \text{if } V < -40.0, \\ 0.0 & \text{otherwise.} \end{cases} \tag{A.8.7}$$

The closing rate of the h gate.

$$beta\_h = \begin{cases} \left(3.56 * \exp\left(0.079 * V\right) + 3.1 \times 10^5 * \exp\left(0.35 * V\right)\right); & \text{if } V < -40.0, \\ \frac{1.0}{0.13 * \left(1.0 + \exp\left(\frac{-(V + 10.66)}{11.1}\right)\right)} & \text{otherwise.} \end{cases} \tag{A.8.8}$$

The kinetics of the h gate.

$$\frac{\mathrm{d}(h)}{\mathrm{d}(time)} = (alpha\_h * (1.0 - h) - beta\_h * h) \tag{A.8.9}$$

"slow_inward_current" component

The standard Beeler Reuter (1977) slow inward (calcium) current formulation.

Initial values defined in this component

$g\_s = 9.0 \times 10^{-4} \text{ mS} \cdot \text{mm}^{-2}$ $\qquad\qquad Cai = 0.000000177 \text{ mM}$

Equations defined in this component

$$E\_s = (-82.3 - 13.0287 * \ln(Cai * 0.001)) \tag{A.8.10}$$

$$i\_s = g\_s * d * f * (V - E\_s) \tag{A.8.11}$$

$$\frac{\mathrm{d}(Cai)}{\mathrm{d}(time)} = (-0.01 * i\_s + 0.07 * (0.0001 - Cai)) \tag{A.8.12}$$

"slow_inward_current_d_gate" component

The standard Beeler Reuter (1977) activation gate for the slow inward current.

Initial values defined in this component

$d = 0.003$

Equations defined in this component

$$alpha\_d = \frac{0.095 * \exp\left(-\frac{(V-5.0)}{100.0}\right)}{\left(1.0 + \exp\left(-\frac{(V-5.0)}{13.89}\right)\right)} \quad (A.8.13)$$

$$beta\_d = \frac{0.07 * \exp\left(-\frac{(V+44.0)}{59.0}\right)}{\left(1.0 + \exp\left(\frac{(V+44.0)}{20.0}\right)\right)} \quad (A.8.14)$$

$$\frac{d(d)}{d(time)} = (alpha\_d * (1.0 - d) - beta\_d * d) \quad (A.8.15)$$

"slow_inward_current_f_gate" component

The standard Beeler Reuter (1977) inactivation gate for the slow inward current.

Initial values defined in this component
$f = 0.994$

Equations defined in this component

$$alpha\_f = \frac{0.012 * \exp\left(-\frac{(V+28.0)}{125.0}\right)}{\left(1.0 + \exp\left(\frac{(V+28.0)}{6.67}\right)\right)} \quad (A.8.16)$$

$$beta\_f = \frac{0.0065 * \exp\left(-\frac{(V+30.0)}{50.0}\right)}{\left(1.0 + \exp\left(-\frac{(V+30.0)}{5.0}\right)\right)} \quad (A.8.17)$$

$$\frac{d(f)}{d(time)} = (alpha\_f * (1.0 - f) - beta\_f * f) \quad (A.8.18)$$

"time_dependent_outward_current" component

The standard Beeler Reuter (1977) time-dependent outward (potassium) current.

Equations defined in this component

$$i\_x1 = x1 * 8.0 \times 10^{-3} * \frac{(\exp(0.04 * (V + 77.0)) - 1.0)}{\exp(0.04 * (V + 35.0))} \quad (A.8.19)$$

"time_dependent_outward_current_x1_gate" component

The standard Beeler Reuter (1977) gating variable for the time-dependent outward potassium current.

Equations defined in this component

$$alpha\_x1 = 0.0005 * \frac{\exp\left(\frac{(V+50.0)}{12.1}\right)}{\left(1.0 + \exp\left(\frac{(V+50.0)}{17.5}\right)\right)} \tag{A.8.20}$$

$$beta\_x1 = 0.0013 * \frac{\exp\left(-\frac{(V+20.0)}{16.67}\right)}{\left(1.0 + \exp\left(-\frac{(V+20.0)}{25.0}\right)\right)} \tag{A.8.21}$$

$$\frac{d(x1)}{d(time)} = (alpha\_x1 * (1.0 - x1) - beta\_x1 * x1) \tag{A.8.22}$$

"time_independent_outward_current" component

The standard Beeler Reuter (1977) time-independent outward (potassium) current.

Equations defined in this component

$$i\_K1 = 0.0035$$
$$* \left(4.0 * \frac{(\exp(0.04 * (V + 85.0)) - 1.0)}{(\exp(0.08 * (V + 53)) + \exp(0.04 * (V + 53.0)))} + 0.2 * \frac{(V + 23.0)}{(1.0 - \exp(-0.04 * (V + 23.0)))}\right) \tag{A.8.23}$$

A.9 vanCapelle_Durrer_1980

This is a CellML version of the 1980 van Capelle & Durrer activation model. This model was designed to be used in simulations of arrhythmias in a network of coupled excitable elements. They developed a membrane kinetics model with two variables of state: the transmembrane potential, V; and a generalised excitability parameter, Y.

Reference: van Capelle, F. J. & Durrer, D. (1980), 'Computer Simulation of Arrhythmias in a Network of Coupled Excitable Elements', *Circulation Research* **47**, 454–466.

"interface" component

We'll use this component as the 'interface" to the model, all other components are hidden via encapsulation in this component.

Initial values defined in this component

$Cm = 0.01 \, \mu\text{F} \cdot \text{mm}^{-2}$

$T = 50.0 \, \text{ms}^{-1}$

$af = 3.837854 \times 10^{-5} \, \mu\text{A} \cdot \text{mm}^{-2} \cdot \text{mV}^{-3}$

$bf = 5.84649 \times 10^{-3} \, \mu\text{A} \cdot \text{mm}^{-2} \cdot \text{mV}^{-2}$

$cf = 0.2531834 \, \mu\text{A} \cdot \text{mm}^{-2} \cdot \text{mV}^{-1}$

$df = 2.356256 \, \mu\text{A} \cdot \text{mm}^{-2}$

Equations defined in this component

This is a dummy equation that we simply use to make grabbing the value in CMISS much easier.
$$IStimC = Istim \qquad (A.9.1)$$

"membrane_potential" component

The component which defines the kinetics of the transmembrane potential.

Initial values defined in this component

$Vm = -78.6$ mV

Equations defined in this component

This equation describes the kinetics of the transmembrane potential - the action potential.
$$\frac{\mathrm{d}(Vm)}{\mathrm{d}(t)} = \frac{(Istim - Iion)}{Cm} \qquad (A.9.2)$$

"ionic_current" component

Here we define the ionic current through the cellular membrane, defined as the summation of the two component currents weighted by the excitability variable.

Equations defined in this component

The calcuation of the total ionic current.
$$Iion = (Y * i1 + (1.0 - Y) * i0) \qquad (A.9.3)$$

The current-voltage relation for when the membrane is completely inexcitable. van Capelle & Durrer used a simple three segment piecewise linear function to represent this component of the total current.
$$i1 = \begin{cases} (0.05 + 0.005 * (Vm + 70.0)); & \text{if } Vm < -70.0, \\ (0.06 + 0.00425 * Vm); & \text{if } Vm > 0.0, \\ \left(0.05 + 0.01 * \frac{(Vm+70.0)}{70.0}\right) & \text{otherwise.} \end{cases} \qquad (A.9.4)$$

The current-voltage relation for when the membrane is maximally excitable. This is defined as the addition of a piecewise function, f, to the i1 component current. van Capelle & Durrer defined i0 as this to improve the efficiency of their algorithm.
$$i0 = (i1 + f) \qquad (A.9.5)$$

The function f, used to define the i0 component current, consists of three sections: two linear components joined by a cubic component. The function was fitted such that both the function value and its derivative df/dVm were

continuous.

$$f = \begin{cases} (0.0784 + 0.02 * (Vm + 74.3)); & \text{if } Vm < -74.3, \\ (-0.9884 + 0.0171 * (Vm + 27.8)); & \text{if } Vm > -27.8, \\ \left(af * (Vm)^{3.0} + bf * (Vm)^{2.0} + cf * Vm + df\right) & \text{otherwise.} \end{cases} \qquad \text{(A.9.6)}$$

"excitability_variable" component

Here we define the kinetics of the non-dimensional excitability variable.

Initial values defined in this component

$Y = 0.07$

Equations defined in this component

The kinetics of the excitability variable. The time constant, T, can be used to scale the duration of the action potential.

$$\frac{d(Y)}{d(t)} = \frac{1.0}{T} * (Yinf - Y) \qquad \text{(A.9.7)}$$

The voltage dependent steady-state value for the excitability variable. Must be an S-shaped function, increasing from zero when Vm is more negative than the resting potential to 1 at more positive values of Vm.

$$Yinf = \begin{cases} 0.0; & \text{if } Vm < -80.0, \\ 1.0; & \text{if } Vm > -60.0, \\ \frac{(Vm+80.0)}{20.0} & \text{otherwise.} \end{cases} \qquad \text{(A.9.8)}$$

A.10   difrancesco_noble_model_1985

This is the CellML description of Di Francesco and Noble's mathematical model of cardiac action potentials of Purkinje fibres. It is a significant development on the MNT model (1975), and it remains the most complete of all Purkinje fibre ionic current models to date. It is a complete replacement for the MNT model. In particular it considers changes in the interpretation of the i_K2 system, includes more accurate experimental data concerning the fast sodium current and it starts to account for fluctuations in ionic concentrations. In addition, a start is made on accounting for intracellular calcium movement between the sarcoplasmic reticulum and the myoplasm. Corrections for the model can be found in an appendix at the end of Earm & Noble, Proc. Roy. Soc. B, Vol 240(1297), 1990.

Reference: DiFrancesco, D. & Noble, D. (1985), 'A model of cardiac electrical activity incorporating ionic pumps and concentration changes', *Philosophical Transactions of the Royal Society of London Series B* **307**, 353–398.

"environment" component

"membrane" component

The membrane component is the main component for this model, containing the differential equation for the transmembrane potential (the action potential).

Initial values defined in this component

$V = -87.0 \text{ mV}$ $\qquad\qquad\qquad$ $F = 96485.3 \text{ nC} \cdot \text{nmol}^{-1}$

$R = 8314.41 \text{ pJ} \cdot \text{nmol}^{-1} \cdot \text{K}^{-1}$ $\qquad\qquad$ $C = 0.08466 \,\mu\text{F} \cdot \text{mm}^{-2}$

$T = 310.0 \text{ K}$

Equations defined in this component

The action potential equation consists of the sum of the trans-sarcolemmal currents plus an applied stimulus, which may be used to pace the cell model.

$$\frac{\text{d}(V)}{\text{d}(time)} = \frac{(I\_stim - (i\_f + i\_K + i\_K1 + i\_to + i\_Na\_b + i\_Ca\_b + i\_NaK + i\_NaCa + i\_Na + i\_si))}{C}$$

(A.10.1)

This is a dummy equation that we simply use to make grabbing the value in CMISS much easier.

$$IStimC = I\_stim \tag{A.10.2}$$

"hyperpolarising_activated_current" component

The 'funny' current - activated by hyperpolarisation rather than depolarisation, and consisting of sodium and potassium components.

Initial values defined in this component

$g\_f\_Na = 3.39 \times 10^{-3} \text{ mS} \cdot \text{mm}^{-2}$ $\qquad\qquad$ $Km\_f = 45.0 \text{ mM}$

$g\_f\_K = 3.39 \times 10^{-3} \text{ mS} \cdot \text{mm}^{-2}$

Equations defined in this component

The total current is simply the sum of the two component currents.

$$i\_f = (i\_fK + i\_fNa) \tag{A.10.3}$$

$$i\_fK = y * I\_fK \tag{A.10.4}$$
$$i\_fNa = y * I\_fNa \tag{A.10.5}$$

The maximal potassium current.

$$I\_fK = \frac{Kc}{(Kc + Km\_f)} * g\_f\_K * (V - E\_K) \tag{A.10.6}$$

The maximal sodium current.

$$I\_fNa = \frac{Kc}{(Kc + Km\_f)} * g\_f\_Na * (V - E\_Na) \tag{A.10.7}$$

The reversal potentials for the two ions.

$$E\_Na = \frac{R * T}{F} * \ln\left(\frac{Nao}{Nai}\right) \tag{A.10.8}$$

$$E\_K = \frac{R * T}{F} * \ln\left(\frac{Kc}{Ki}\right) \tag{A.10.9}$$

"hyperpolarising_activated_current_y_gate" component

The activation variable for the 'funny" current - the y gate.

Initial values defined in this component

$y = 0.2$

Equations defined in this component

The opening rate for the y gate.

$$alpha\_y = 0.05 \times 10^{-3} * \exp\left(-0.067 * (V + 42.0)\right) \tag{A.10.10}$$

The closing rate for the y gate.

$$beta\_y = \frac{1.0 \times 10^{-3} * (V + 42.0)}{(1.0 - \exp\left(-0.2 * (V + 42.0)\right))} \tag{A.10.11}$$

The Hodgkin-Huxley type kinetics for the y gate.

$$\frac{\mathrm{d}(y)}{\mathrm{d}(time)} = (alpha\_y * (1.0 - y) - beta\_y * y) \tag{A.10.12}$$

"time_dependent_potassium_current" component

The time-dependent potassium current, a current dependent on both potassium ion concentration and membrane potential.

Initial values defined in this component

$i\_K\_max = 0.2032\ \mu\mathrm{A} \cdot \mathrm{mm}^{-2}$

Equations defined in this component

Calculation of the time-dependent potassium current.

$$i\_K = x * I\_K \tag{A.10.13}$$

$$I\_K = i\_K\_max * \frac{\left(Ki - Kc * \exp\left(-\frac{V*F}{R*T}\right)\right)}{140.0} \tag{A.10.14}$$

"time_dependent_potassium_current_x_gate" component

The voltage-dependent activation variable for the time-dependent potassium current, the x gate.

Initial values defined in this component

$x = 0.01$

Equations defined in this component

The opening rate of the x gate.

$$alpha\_x = 0.5 \times 10^{-3} * \frac{\exp\left(\frac{(V+50.0)}{12.1}\right)}{\left(1.0 + \exp\left(\frac{(V+50.0)}{17.5}\right)\right)} \tag{A.10.15}$$

The closing rate of the x gate.

$$beta\_x = 1.3 \times 10^{-3} * \frac{\exp\left(-\frac{(V+20.0)}{16.67}\right)}{\left(1.0 + \exp\left(-\frac{(V+20.0)}{25.0}\right)\right)} \tag{A.10.16}$$

The kinetics of the x gate.

$$\frac{\mathrm{d}(x)}{\mathrm{d}(time)} = (alpha\_x * (1.0 - x) - beta\_x * x) \tag{A.10.17}$$

"time_independent_potassium_current" component

The time-independent background potassium current.

Initial values defined in this component

$g\_K1 = 1.0385 \text{ mS} \cdot \text{mm}^{-2}$ $\qquad\qquad Km\_K1 = 210.0 \text{ mM}$

Equations defined in this component

Calculation of the time-independent postassium current.

$$i\_K1 = g\_K1 * \frac{Kc}{(Kc + Km\_K1)} * \frac{(V - E\_K)}{\left(1.0 + \exp\left(\frac{((V+10.0) - E\_K)*F*2.0}{R*T}\right)\right)} \tag{A.10.18}$$

"transient_outward_current" component

The transient outward current (i_to) replaces the i_qr chloride-based current of the MNT model. This current is a calcium-activated, outward rectifier. It has an inactivation gate, r.

Initial values defined in this component

$Km\_to = 10.0 \text{ mM}$ $\qquad\qquad g\_to = 0.316 \times 10^{-3} \text{ mS} \cdot \text{mm}^{-2}$

$Km\_Ca = 0.5 \times 10^{-3} \text{ mM}$

Equations defined in this component

Calculation of the transient outward current.

$$i\_to = r * g\_to * \left(0.2 + \frac{Kc}{(Km\_to + Kc)}\right) * \frac{Cai}{(Km\_Ca + Cai)}$$
$$* \frac{(V + 10.0)}{(1.0 - \exp(-0.2 * (V + 10.0)))} * (Ki * \exp(0.02 * V) - Kc * \exp(-0.02 * V)) \quad \text{(A.10.19)}$$

"transient_outward_current_r_gate" component

The activation variable for the transient outward current.

Initial values defined in this component

$r = 1.0$

Equations defined in this component

The opening rate of the r gate.

$$alpha\_r = 0.033 \times 10^{-3} * \exp\left(\frac{-V}{17.0}\right) \quad \text{(A.10.20)}$$

The closing rate of the r gate.

$$beta\_r = \frac{33.0 \times 10^{-3}}{\left(1.0 + \exp\left(-\frac{(V+10.0)}{8.0}\right)\right)} \quad \text{(A.10.21)}$$

The kinetics for the r gate.

$$\frac{\mathrm{d}(r)}{\mathrm{d}(time)} = (alpha\_r * (1.0 - r) - beta\_r * r) \quad \text{(A.10.22)}$$

"sodium_background_current" component

A linear resting sodium flux.

Initial values defined in this component

$g\_Nab = 0.203 \times 10^{-3} \,\mathrm{mS \cdot mm^{-2}}$

Equations defined in this component

Calculation of the background sodium current.

$$i\_Na\_b = g\_Nab * (V - E\_Na) \quad \text{(A.10.23)}$$

"calcium_background_current" component

A resting background leakage calcium flux.

Initial values defined in this component

$g\_Cab = 0.0226 \times 10^{-3} \text{ mS} \cdot \text{mm}^{-2}$

Equations defined in this component

Calculation of the calcium leakage current.

$$i\_Ca\_b = g\_Cab * (V - E\_Ca) \tag{A.10.24}$$

The calcium reversal potential.

$$E\_Ca = \frac{R * T}{F * 2.0} * \ln\left(\frac{Cao}{Cai}\right) \tag{A.10.25}$$

"sodium_potassium_pump" component

The Na-K exchange pump couples the free energy released by the hydrolysis of ATP to transfer sodium and potassium ions across the cell membrane against their electrochemical gradients. 3 Na ions are pumped out for every 2 K ions pumped into the cell.

Initial values defined in this component

$I\_NaK = 0.141 \, \mu\text{A} \cdot \text{mm}^{-2}$ $\qquad\qquad K\_mNa = 40.0 \text{ mM}$

$K\_mK = 1.0 \text{ mM}$

Equations defined in this component

Calculation of the Na/K-pump current.

$$i\_NaK = I\_NaK * \frac{Kc}{(K\_mK + Kc)} * \frac{Nai}{(K\_mNa + Nai)} \tag{A.10.26}$$

"Na_Ca_exchanger" component

The DFN paper gives two alternative equations for the i_NaCa current. The simplest makes the current a sine function of the total energy gradient. The more realistic model uses an equation which is likely to reproduce better dependence of i_NaCa on intracellular calcium ions. We utilise the more complex version here.

Initial values defined in this component

$n\_NaCa = 3.0$ $\qquad\qquad d\_NaCa = 0.001$

$k\_NaCa = 0.0226 \times 10^{-3} \, \mu\text{A} \cdot \text{mm}^{-2}$ $\qquad\qquad gamma = 0.5$

Equations defined in this component

Calculation of the exchanger current.

$$i\_NaCa = k\_NaCa$$

$$* \left[\exp\left(\frac{gamma * (n\_NaCa - 2.0) * V * F}{R * T} \right) * (Nai)^{n\_NaCa} * Cao \right.$$

$$\left. - \exp\left(\frac{-1.0 * (1.0 - gamma) * (n\_NaCa - 2.0) * V * F}{R * T} \right) * (Nao)^{n\_NaCa} * Cai \right]$$

$$\Big/ \left(1.0 + d\_NaCa * \left(Cai * (Nao)^{n\_NaCa} + Cao * (Nai)^{n\_NaCa} \right) \right) \tag{A.10.27}$$

"fast_sodium_current" component

The DFN model retains a two-variable model of the sodium kinetics, with new equations for the gates m and h. It is acknowledged however that the model does not represent the slower components of Na inactivation and recovery. It is also assumed that the sodium channel shows a 12% permeability to K ions.

Initial values defined in this component

$g\_Na = 0.846 \text{ mS} \cdot \text{mm}^{-2}$

Equations defined in this component

Calculation of the fast sodium current.

$$i\_Na = g\_Na * (m)^{3.0} * h * (V - E\_mh) \tag{A.10.28}$$

The reversal potential of the fast sodium channel, assuming a 12% permeability of potassium ions.

$$E\_mh = \frac{R * T}{F} * \ln\left(\frac{(Nao + 0.12 * Kc)}{(Nai + 0.12 * Ki)} \right) \tag{A.10.29}$$

"fast_sodium_current_m_gate" component

The voltage-dependent activation gate for the fast sodium channel - the m gate.

Initial values defined in this component

$m = 0.01$

Equations defined in this component

The opening rate of the m gate.

$$alpha\_m = \frac{200.0 \times 10^{-3} * (V + 41.0)}{(1.0 - \exp(-0.1 * (V + 41.0)))} \tag{A.10.30}$$

The closing rate of the m gate.

$$beta\_m = 8000.0 \times 10^{-3} * \exp(-0.056 * (V + 66.0)) \tag{A.10.31}$$

The kinetics of the m gate.
$$\frac{d(m)}{d(time)} = (alpha\_m * (1.0 - m) - beta\_m * m) \tag{A.10.32}$$

"fast_sodium_current_h_gate" component

The voltage-dependent inactivation gate for the fast sodium current - the h gate.

Initial values defined in this component

$h = 0.98$

Equations defined in this component

The opening rate of the h gate.
$$alpha\_h = 20.0 \times 10^{-3} * \exp\left(-0.125 * (V + 75.0)\right) \tag{A.10.33}$$

The closing rate of the h gate.
$$beta\_h = \frac{2000.0 \times 10^{-3}}{(1.0 + 320.0 * \exp\left(-0.1 * (V + 75.0)\right))} \tag{A.10.34}$$

The kinetics of the h gate.
$$\frac{d(h)}{d(time)} = (alpha\_h * (1.0 - h) - beta\_h * h) \tag{A.10.35}$$

"secondary_inward_current" component

Like the MNT model, the kinetics of the secondary inward current are still described in terms of two gate variables d and f, but the time constants for activation and inactivation processes are much shorter. The fast component, i_si of this current has been divided into the individual ion movements of Ca, K and Na. This current would later be called the L-type calcium current.

Initial values defined in this component

$P\_Ca = 16.93 \times 10^{-3}\ \mu A \cdot mm^{-2} \cdot mM^{-1}$ $\qquad\qquad$ $P\_CaNa = 0.01$

$P\_CaK = 0.01$

Equations defined in this component

The total i_si current is simply the sum of the component calcium, potassium, and sodium currents.
$$i\_si = (i\_siCa + i\_siK + i\_siNa) \tag{A.10.36}$$

Calculation of the calcium component of the second inward current.
$$i\_siCa = d * f * f2 * \frac{4.0 * P\_Ca * (V - 50.0) * \frac{F}{R*T}}{\left(1.0 - \exp\left(\frac{-1.0*(V-50.0)*F*2.0}{R*T}\right)\right)}$$
$$* \left(Cai * \exp\left(\frac{50.0 * F * 2.0}{R * T}\right) - Cao * \exp\left(\frac{-2.0 * (V - 50.0) * F}{R * T}\right)\right) \tag{A.10.37}$$

Calculation of the potassium component of the second inward current.

$$i\_siK = d * f * f2 * \frac{P\_CaK * P\_Ca * (V - 50.0) * \frac{F}{R*T}}{\left(1.0 - \exp\left(\frac{-1.0*(V-50.0)*F}{R*T}\right)\right)}$$
$$* \left(Ki * \exp\left(\frac{50.0 * F}{R * T}\right) - Kc * \exp\left(\frac{-1.0 * (V - 50.0) * F}{R * T}\right)\right) \quad \text{(A.10.38)}$$

Calculation of the sodium component of the second inward current.

$$i\_siNa = d * f * f2 * \frac{P\_CaNa * P\_Ca * (V - 50.0) * \frac{F}{R*T}}{\left(1.0 - \exp\left(\frac{-1.0*(V-50.0)*F}{R*T}\right)\right)}$$
$$* \left(Nai * \exp\left(\frac{50.0 * F}{R * T}\right) - Nao * \exp\left(\frac{-1.0 * (V - 50.0) * F}{R * T}\right)\right) \quad \text{(A.10.39)}$$

"secondary_inward_current_d_gate" component

The voltage-dependent activation gate for the second inward current - the d gate.

Initial values defined in this component

$d = 0.005$

Equations defined in this component

The opening rate of the d gate.

$$alpha\_d = 30.0 \times 10^{-3} * \frac{(V + 19.0)}{\left(1.0 - \exp\left(\frac{-1.0*(V+19.0)}{4.0}\right)\right)} \quad \text{(A.10.40)}$$

The closing rate of the d gate.

$$beta\_d = 12.0 \times 10^{-3} * \frac{(V + 19.0)}{\left(\exp\left(\frac{(V+19.0)}{10.0}\right) - 1.0\right)} \quad \text{(A.10.41)}$$

The kinetics of the d gate.

$$\frac{d(d)}{d(time)} = (alpha\_d * (1.0 - d) - beta\_d * d) \quad \text{(A.10.42)}$$

"secondary_inward_current_f_gate" component

The voltage-dependent inactivation gate for the second inward current - the f gate.

Initial values defined in this component

$f = 1.0$

Equations defined in this component

The opening rate of the f gate.

$$alpha\_f = 6.25 \times 10^{-3} * \frac{(V + 34.0)}{\left(\exp\left(\frac{(V+34.0)}{4.0}\right) - 1.0\right)} \quad \text{(A.10.43)}$$

The closing rate of the f gate.

$$beta\_f = \frac{50.0 \times 10^{-3}}{\left(1.0 + \exp\left(\frac{-1.0*(V+34.0)}{4.0}\right)\right)}$$ (A.10.44)

The kinetics of the f gate.

$$\frac{\mathrm{d}(f)}{\mathrm{d}(time)} = (alpha\_f * (1.0 - f) - beta\_f * f)$$ (A.10.45)

"secondary_inward_current_f2_gate" component

The DFN model also includes a description of Ca-dependent inactivation. When calcium ions bind to a regulatory site on the channel protein, they induce a conformational change such that the channel no longer conducts, and the secondary current slows or ceases.

Initial values defined in this component

$f2 = 1.0$ $\hspace{5cm}$ $K\_mf2 = 1.0 \times 10^{-3}$ mM

$alpha\_f2 = 5.0 \times 10^{-3}$ ms^{-1}

Equations defined in this component

The kinetics of the f2 gate.

$$\frac{\mathrm{d}(f2)}{\mathrm{d}(time)} = (alpha\_f2 * (1.0 - f2) - beta\_f2 * f2)$$ (A.10.46)

$$beta\_f2 = \frac{Cai * alpha\_f2}{K\_mf2}$$ (A.10.47)

"extracellular_sodium_concentration" component

A representation of extracellular sodium ion concentration, held constant in this model.

Initial values defined in this component

$Nao = 140.0$ mM

"intracellular_sodium_concentration" component

This component contains the description of intracellular sodium concentration change.

Initial values defined in this component

$Nai = 8.0$ mM

Equations defined in this component

The rate of change of intracellular sodium concentration is the sum of the ions entering the intracellular volume via the sodium transmembrane currents.

$$\frac{\mathrm{d}(Nai)}{\mathrm{d}(time)} = \frac{-Am * \left(i\_Na + i\_Na\_b + i\_fNa + i\_siNa + i\_NaK * 3.0 + i\_NaCa * \frac{n\_NaCa}{(n\_NaCa-2.0)}\right)}{V\_i * F}$$

(A.10.48)

"extracellular_calcium_concentration" component

A representation of extracellular calcium ion concentration, held constant in this model.

Initial values defined in this component

$Cao = 2.0$ mM

"intracellular_calcium_concentration" component

Changes in [Ca]i were first modelled in the BR model and has only been slightly developed in the DFN model. Calcium is sequestered in the sarcoplasmic reticulum ([Ca]up). A fraction is transferred to a release store in the junctional SR ([Ca]rel) before being released into the intracellular space. The Ca concentrations in each of these various stores is modelled together with the transfer between the calcium sites and the Ca transfer across the cell membrane via the other ionic currents.

Initial values defined in this component

$Cai = 0.00005$ mM	$p = 1.0$
$Ca\_up = 2.0$ mM	$tau\_up = 25.0$ ms
$Ca\_rel = 1.0$ mM	$tau\_rep = 2.0 \times 10^{+3}$ ms
$Ca\_up\_max = 5.0$ mM	$tau\_rel = 50.0$ ms
$K\_mCa = 1.0 \times 10^{-6}$ mM^2	

Equations defined in this component

The calcium current into the uptake store.

$$i\_up = alpha\_up * Cai * (Ca\_up\_max - Ca\_up)$$

(A.10.49)

$$alpha\_up = \frac{1.0}{tau\_up * Ca\_up\_max}$$

(A.10.50)

The calcium current between the uptake and release stores, which uses a voltage-dependent activation variable - the p gate.

$$i\_tr = alpha\_tr * p * (Ca\_up - Ca\_rel)$$

(A.10.51)

$$alpha\_tr = \frac{1.0}{tau\_rep}$$

(A.10.52)

The opening rate of the p gate.
$$alpha\_p = 0.625 \times 10^{-3} * \frac{(V + 34.0)}{\left(\exp\left(\frac{(V+34.0)}{4.0}\right) - 1.0\right)} \tag{A.10.53}$$

The closing rate of the p gate.
$$beta\_p = \frac{5.0 \times 10^{-3}}{\left(1.0 + \exp\left(\frac{-1.0*(V+34.0)}{4.0}\right)\right)} \tag{A.10.54}$$

The kinetics of the p gate.
$$\frac{\mathrm{d}(p)}{\mathrm{d}(time)} = (alpha\_p * (1.0 - p) - beta\_p * p) \tag{A.10.55}$$

The calcium release current from the SR into the cytosol.
$$i\_rel = alpha\_rel * Ca\_rel * \frac{(Cai)^{2.0}}{\left((Cai)^{2.0} + K\_mCa\right)} \tag{A.10.56}$$

$$alpha\_rel = \frac{1.0}{tau\_rel} \tag{A.10.57}$$

The rate of change of calcium concentration in the uptake store.
$$\frac{\mathrm{d}(Ca\_up)}{\mathrm{d}(time)} = \left(i\_up * \frac{V\_i}{V\_up} - i\_tr * \frac{V\_rel}{V\_up}\right) \tag{A.10.58}$$

The rate of change of calcium concentration in the release store.
$$\frac{\mathrm{d}(Ca\_rel)}{\mathrm{d}(time)} = (i\_tr - i\_rel) \tag{A.10.59}$$

The rate of change of intracellular calcium concentration.
$$\frac{\mathrm{d}(Cai)}{\mathrm{d}(time)} = \left(i\_rel * \frac{V\_rel}{V\_i} - \left(i\_up + \frac{Am * \left((i\_siCa + i\_Ca\_b) - \frac{2.0*i\_NaCa}{(n\_NaCa-2.0)}\right)}{2.0 * V\_i * F}\right)\right) \tag{A.10.60}$$

"extracellular_potassium_concentration" component

A representation of extracellular potassium ion concentration based on a homogeneous three-compartment model.

Initial values defined in this component

$Kc = 4.0$ mM $\qquad\qquad\qquad\qquad P = 0.7$

$Kb = 4.0$ mM

Equations defined in this component

The rate of change in the cleft potassium concentration is the combination of potassium ions crossing the cellular membrane and ions diffusing into the volume from the bulk extracellular stores.
$$\frac{\mathrm{d}(Kc)}{\mathrm{d}(time)} = \left(-P * (Kc - Kb) + \frac{Am * i\_mK}{V\_i * F}\right) \tag{A.10.61}$$

The total transmembrane potassium current.
$$i\_mK = ((i\_K1 + i\_K + i\_fK + i\_siK + i\_to) - 2.0 * i\_NaK) \tag{A.10.62}$$

"intracellular_potassium_concentration" component

The change in intracellular potassium ion concentration.

Initial values defined in this component
$Ki = 140.0$ mM

Equations defined in this component

The rate of change of intracellular potassium concentration is the sum of the ions crossing the membrane.
$$\frac{\mathrm{d}(Ki)}{\mathrm{d}(time)} = \frac{-Am * i\_mK}{V\_i * F} \tag{A.10.63}$$

"volumes" component

A component used to group the geometry parameters and calculations.

Initial values defined in this component

$radius = 50 \times 10^{-3}$ mm	$V\_ecs = 0.1$
$length = 2$ mm	$Am = 40.0$ mm^{-1}

Equations defined in this component

The intracellular volume fraction.
$$V\_i = (1.0 - V\_ecs) \tag{A.10.64}$$

The extracellular volume fraction.
$$V\_e = V\_ecs \tag{A.10.65}$$

The calcium uptake store volume fraction.
$$V\_up = 0.05 * V\_i \tag{A.10.66}$$

The calcium release store volume fraction.
$$V\_rel = 0.02 * V\_i \tag{A.10.67}$$

A.11 drouhard_roberge_model_1987

This is the CellML description of Drouhard and Roberge's mathematical model of the fast sodium current in ventricular myocardial cells. It describes the ionic current with Hodgkin-Huxley formalism, but revises the original

parameters of the equation.

Reference: Drouhard, J. P. & Roberge, F. A. (1987), 'Revised formulation of the Hodgkin-Huxley representation of the sodium current in cardiac cells', *Computers and Biomedical Research* **20**, 333–350.

"environment" component

"membrane" component

Like the Ebihara-Johnson model (1980), the Drouhard-Roberge model can be used as a direct replacement for the sodium kinetics of the Beeler-Reuter model. The other ionic equations and membrane potential are quoted from the original 1977 paper.

Initial values defined in this component
$C = 0.013\,\mu\text{F} \cdot \text{mm}^{-2}$

Equations defined in this component

The main differential equation of the model which defines the change of membrane potential as a function of the total ionic current across the membrane plus an applied stimulus current.

$$\frac{\mathrm{d}(V)}{\mathrm{d}(time)} = \frac{(Istim - (i\_Na + i\_s + i\_x1 + i\_K1))}{C} \tag{A.11.1}$$

This is a dummy equation that we simply use to make grabbing the value in CMISS much easier.

$$IStimC = Istim \tag{A.11.2}$$

"fast_sodium_current" component

The Drouhard-Roberge model uses the Hodgkin-Huxley formulation for the sodium membrane current with only one inactivation variable (h) rather than the two (h and j) of the Beeler-Reuter model. At the time of the study (1987) there was still much uncertainty regarding the existence and function of the j gate.

Initial values defined in this component
$g\_Na = 0.15\,\text{mS} \cdot \text{mm}^{-2}$ $\qquad\qquad\qquad\qquad E\_Na = 40.0\,\text{mV}$

Equations defined in this component

Calculation of the modified sodium current.

$$i\_Na = g\_Na * (m)^{3.0} * h * (V - E\_Na) \tag{A.11.3}$$

"fast_sodium_current_m_gate" component

The modified voltage-dependent activation gate for the fast sodium channel - the m gate.

Initial values defined in this component

$m = 0.0$

Equations defined in this component

The opening rate of the m gate.

$$alpha\_m = \frac{0.9 * (V + 42.65)}{(1.0 - \exp{(-0.22 * (V + 42.65))})}$$
(A.11.4)

The closing rate of the m gate.

$$beta\_m = 1.437 * \exp{(-0.085 * (V + 39.75))}$$
(A.11.5)

The m gate kinetics.

$$\frac{\mathrm{d}(m)}{\mathrm{d}(time)} = (alpha\_m * (1.0 - m) - beta\_m * m)$$
(A.11.6)

"fast_sodium_current_h_gate" component

The modified inactivation gate for the fast sodium channel - the h gate.

Initial values defined in this component
$h = 0.99$

Equations defined in this component

The opening rate of the h gate.

$$alpha\_h = 0.1 * \exp{(-0.193 * (V + 79.65))}$$
(A.11.7)

The closing rate of the h gate.

$$beta\_h = \frac{1.7}{(1.0 + \exp{(-0.095 * (V + 20.5))})}$$
(A.11.8)

The h gate kinetics.

$$\frac{\mathrm{d}(h)}{\mathrm{d}(time)} = (alpha\_h * (1.0 - h) - beta\_h * h)$$
(A.11.9)

"slow_inward_current" component

The standard Beeler Reuter (1977) slow inward (calcium) current.

Initial values defined in this component
$g\_s = 9.0 \times 10^{-4} \; \mathrm{mS} \cdot \mathrm{mm}^{-2}$ $\qquad\qquad Cai = 0.000000177 \, \mathrm{mM}$

Equations defined in this component

$$E\_s = (-82.3 - 13.0287 * \ln{(0.001 * Cai)})$$
(A.11.10)

$$i\_s = g\_s * d * f * (V - E\_s) \tag{A.11.11}$$

$$\frac{\mathrm{d}(Cai)}{\mathrm{d}(time)} = (-0.01 * i\_s + 0.07 * (-0.0001 - Cai)) \tag{A.11.12}$$

"slow_inward_current_d_gate" component

The standard Beeler Reuter (1977) slow inward (calcium) current activation gate.

Initial values defined in this component

$d = 0.003$

Equations defined in this component

$$alpha\_d = \frac{0.095 * \exp\left(-\frac{(V-5.0)}{100.0}\right)}{\left(1.0 + \exp\left(-\frac{(V-5.0)}{13.89}\right)\right)} \tag{A.11.13}$$

$$beta\_d = \frac{0.07 * \exp\left(-\frac{(V+44.0)}{59.0}\right)}{\left(1.0 + \exp\left(\frac{(V+44.0)}{20.0}\right)\right)} \tag{A.11.14}$$

$$\frac{\mathrm{d}(d)}{\mathrm{d}(time)} = (alpha\_d * (1.0 - d) - beta\_d * d) \tag{A.11.15}$$

"slow_inward_current_f_gate" component

The standard Beeler Reuter (1977) slow inward (calcium) current inactivation gate.

Initial values defined in this component

$f = 0.994$

Equations defined in this component

$$alpha\_f = \frac{0.012 * \exp\left(-\frac{(V+28.0)}{125.0}\right)}{\left(1.0 + \exp\left(\frac{(V+28.0)}{6.67}\right)\right)} \tag{A.11.16}$$

$$beta\_f = \frac{0.0065 * \exp\left(-\frac{(V+30.0)}{50.0}\right)}{\left(1.0 + \exp\left(-\frac{(V+30.0)}{5.0}\right)\right)} \tag{A.11.17}$$

$$\frac{\mathrm{d}(f)}{\mathrm{d}(time)} = (alpha\_f * (1.0 - f) - beta\_f * f) \tag{A.11.18}$$

"time_dependent_outward_current" component

The standard Beeler Reuter (1977) time-dependent outward (potassium) current.

Equations defined in this component

$$i\_x1 = x1 * 8.0 \times 10^{-3} * \frac{(\exp{(0.04 * (V + 77.0))} - 1.0)}{\exp{(0.04 * (V + 35.0))}} \tag{A.11.19}$$

"time_dependent_outward_current_x1_gate" component

The standard Beeler Reuter (1977) time-dependent outward (potassium) current gating variable.

Equations defined in this component

$$alpha\_x1 = 5 \times 10^{-4} * \frac{\exp\left(\frac{(V+50.0)}{12.1}\right)}{\left(1.0 + \exp\left(\frac{(V+50.0)}{17.5}\right)\right)} \tag{A.11.20}$$

$$beta\_x1 = 0.0013 * \frac{\exp\left(-\frac{(V+20.0)}{16.67}\right)}{\left(1.0 + \exp\left(-\frac{(V+20.0)}{25.0}\right)\right)} \tag{A.11.21}$$

$$\frac{\mathrm{d}(x1)}{\mathrm{d}(time)} = (alpha\_x1 * (1.0 - x1) - beta\_x1 * x1) \tag{A.11.22}$$

"time_independent_outward_current" component

The standard Beeler Reuter (1977) time-independent outward (potassium) current.

Equations defined in this component

$$i\_K1 = 0.35 \times 10^{-2}$$
$$* \left(4.0 * \frac{(\exp{(0.04 * (V + 85.0))} - 1.0)}{(\exp{(0.08 * (V + 53))} + \exp{(0.04 * (V + 53.0))})} + 0.2 * \frac{(V + 23.0)}{(1.0 - \exp{(-0.04 * (V + 23.0))})}\right) \tag{A.11.23}$$

A.12   luo_rudy_I_model_1991

This is the CellML description of Luo and Rudy's mathematical model of the membrane action potential of the mammalian ventricular cell. It describes six ionic currents and it is a development of the Beeler-Reuter 1977 mammalian ventricular model, using Hodgkin-Huxley type equations.

Reference: Luo, C. & Rudy, Y. (1991), 'A Model of the Ventricular Cardiac Action Potential', *Circulation Research* **68**, 1501–1526.

"environment" component

"membrane" component

The parent component of the model - all other components are 'contained' in this one. Defines the transmembrane potential.

Initial values defined in this component

$V = -84.5\,\text{mV}$ $\hspace{3cm}$ $F = 96845.0\,\text{nC}\cdot\text{nmol}^{-1}$

$R = 8.314 \times 10^3\,\text{pJ}\cdot\text{nmol}^{-1}\cdot\text{K}^{-1}$ $\hspace{1cm}$ $C = 1.0 \times 10^{-2}\,\mu\text{F}\cdot\text{mm}^{-2}$

$T = 310.0\,\text{K}$

Equations defined in this component

The membrane potential kinetic equation.
$$\frac{\mathrm{d}(V)}{\mathrm{d}(time)} = \frac{(I\_stim - (i\_Na + i\_si + i\_K + i\_K1 + i\_Kp + i\_b))}{C} \tag{A.12.1}$$

This is a dummy equation that we simply use to make grabbing the value in CMISS much easier.
$$IStimC = I\_stim \tag{A.12.2}$$

"fast_sodium_current" component

The fast sodium current is primarily responsible for the upstroke of the action potential.

Initial values defined in this component

$g\_Na = 23.0 \times 10^{-2}\,\text{mS}\cdot\text{mm}^{-2}$ $\hspace{2cm}$ $E\_Na = 54.4\,\text{mV}$

Equations defined in this component

Evaluation of the fast sodium current.
$$i\_Na = g\_Na * (m)^{3.0} * h * j * (V - E\_Na) \tag{A.12.3}$$

"fast_sodium_current_m_gate" component

The voltage-dependent activation gate for the fast sodium channel - the m gate.

Initial values defined in this component

$m = 1.67 \times 10^{-3}$

Equations defined in this component

The opening rate of the m gate.
$$alpha\_m = \frac{0.32 * (V + 47.13)}{(1.0 - \exp(-0.1 * (V + 47.13)))} \tag{A.12.4}$$

The closing rate of the m gate.

$$beta\_m = 0.08 * \exp\left(\frac{-V}{11.0}\right) \qquad (A.12.5)$$

The kinetics of the m gate.

$$\frac{\mathrm{d}(m)}{\mathrm{d}(time)} = (alpha\_m * (1.0 - m) - beta\_m * m) \qquad (A.12.6)$$

"fast_sodium_current_h_gate" component

The voltage-dependent inactivation gate for the fast sodium channel - the h gate.

Initial values defined in this component
$h = 9.38 \times 10^{-1}$

Equations defined in this component

The opening rate of the h gate.

$$alpha\_h = \begin{cases} 0.135 * \exp\left(\frac{(-80.0-V)}{6.8}\right); & \text{if } V < -40.0, \\ 0.0 & \text{otherwise.} \end{cases} \qquad (A.12.7)$$

The closing rate of the h gate.

$$beta\_h = \begin{cases} (3.56 * \exp\left(0.079 * V\right) + 310000.0 * \exp\left(0.35 * V\right)); & \text{if } V < -40.0, \\ \frac{1.0}{0.13*\left(1.0+\exp\left(\frac{-(V+10.66)}{11.1}\right)\right)} & \text{otherwise.} \end{cases} \qquad (A.12.8)$$

The kinetics of the h gate.

$$\frac{\mathrm{d}(h)}{\mathrm{d}(time)} = (alpha\_h * (1.0 - h) - beta\_h * h) \qquad (A.12.9)$$

"fast_sodium_current_j_gate" component

The voltage-dependent slow inaction gate for the the fast sodium channel - the j gate.

Initial values defined in this component
$j = 1.0$

Equations defined in this component

The opening rate of the j gate.

$$alpha\_j = \begin{cases} (-127140.0 * \exp\left(0.2444 * V\right) - 0.00003474 * \exp\left(-0.04391 * V\right)) \\ \qquad\qquad\qquad * \frac{(V+37.78)}{(1.0+\exp(0.311*(V+79.23)))}; & \text{if } V < -40.0, \\ 0.0 & \text{otherwise.} \end{cases}$$

$$(A.12.10)$$

The closing rate of the j gate.

$$beta\_j = \begin{cases} 0.1212 * \frac{\exp(-0.01052*V)}{(1.0+\exp(-0.1378*(V+40.14)))}; & \text{if } V < -40.0, \\ 0.3 * \frac{\exp(-0.0000002535*V)}{(1.0+\exp(-0.1*(V+32.0)))} & \text{otherwise.} \end{cases} \quad \text{(A.12.11)}$$

The kinetics of the j gate.

$$\frac{\mathrm{d}(j)}{\mathrm{d}(time)} = (alpha\_j * (1.0 - j) - beta\_j * j) \quad \text{(A.12.12)}$$

"slow_inward_current" component

The slow inward (calcium) current is primarily responsible for the plateau pahse of the action potential.

Initial values defined in this component

$g\_si = 9.0 \times 10^{-4} \text{ mS} \cdot \text{mm}^{-2}$

Equations defined in this component

The reversal potential for the slow inward current.

$$E\_si = (7.7 - 13.0287 * \ln(Cai)) \quad \text{(A.12.13)}$$

Calculation of the slow inward current.

$$i\_si = g\_si * d * f * (V - E\_si) \quad \text{(A.12.14)}$$

"slow_inward_current_d_gate" component

The voltage-dependent activation gate for the slow inward current - the d gate.

Initial values defined in this component

$d = 2.98 \times 10^{-3}$

Equations defined in this component

The opening rate of the d gate.

$$alpha\_d = \frac{0.095 * \exp(-0.01 * (V - 5.0))}{(1.0 + \exp(-0.072 * (V - 5.0)))} \quad \text{(A.12.15)}$$

The closing rate of the d gate.

$$beta\_d = \frac{0.07 * \exp(-0.017 * (V + 44.0))}{(1.0 + \exp(0.05 * (V + 44.0)))} \quad \text{(A.12.16)}$$

The kinetics of the d gate.

$$\frac{\mathrm{d}(d)}{\mathrm{d}(time)} = (alpha\_d * (1.0 - d) - beta\_d * d) \quad \text{(A.12.17)}$$

"slow_inward_current_f_gate" component

The voltage-dependent inactivation gate of the slow inward channel - the f gate.

Initial values defined in this component

$f = 1.0$

Equations defined in this component

The opening rate of the f gate.

$$alpha\_f = \frac{0.012 * \exp\left(-0.008 * (V + 28.0)\right)}{(1.0 + \exp\left(0.15 * (V + 28.0)\right))} \tag{A.12.18}$$

The closing rate of the f gate.

$$beta\_f = \frac{0.0065 * \exp\left(-0.02 * (V + 30.0)\right)}{(1.0 + \exp\left(-0.2 * (V + 30.0)\right))} \tag{A.12.19}$$

The kinetics of the f gate.

$$\frac{\mathrm{d}(f)}{\mathrm{d}(time)} = (alpha\_f * (1.0 - f) - beta\_f * f) \tag{A.12.20}$$

"time_dependent_potassium_current" component

The time dependent potassium current contains a time-dependent activation gate (X) and a time-independent inactivation gate (Xi), neither of which are dependent on the extracellular concentration of potassium ions ([K]o).

Initial values defined in this component

$g\_K = 2.82 \times 10^{-3}\ \mathrm{mS \cdot mm^{-2}}$ $\qquad\qquad PR\_NaK = 0.01833$

Equations defined in this component

The maximum conductance for the channel.

$$g\_K\_max = g\_K * \sqrt{\frac{Ko}{5.4}} \tag{A.12.21}$$

The reversal potential for the channel.

$$E\_K = \frac{R * T}{F} * \ln\left(\frac{(Ko + PR\_NaK * Nao)}{(Ki + PR\_NaK * Nai)}\right) \tag{A.12.22}$$

Calculates the time-dependent potassium current in terms of the conductance, the membrane voltage and the gate variables.

$$i\_K = g\_K\_max * X * Xi * (V - E\_K) \tag{A.12.23}$$

"time_dependent_potassium_current_X_gate" component

Voltage- and time-dependent activation gate for the time-dependent potassium current - the X gate.

Initial values defined in this component

$X = 6.02 \times 10^{-3}$

Equations defined in this component

The opening rate for the X gate.

$$alpha\_X = 0.0005 * \frac{\exp{(0.083 * (V + 50.0))}}{(1.0 + \exp{(0.057 * (V + 50.0))})} \tag{A.12.24}$$

The closing rate for the X gate.

$$beta\_X = 0.0013 * \frac{\exp{(-0.06 * (V + 20.0))}}{(1.0 + \exp{(-0.04 * (V + 20.0))})} \tag{A.12.25}$$

The kinetics for the X gate.

$$\frac{\mathrm{d}(X)}{\mathrm{d}(time)} = (alpha\_X * (1.0 - X) - beta\_X * X) \tag{A.12.26}$$

"time_dependent_potassium_current_Xi_gate" component

The voltage-dependent and time-independent gate for the time-dependent potassium current - the Xi gate.

Equations defined in this component

The kinetics of the Xi gate.

$$Xi = \begin{cases} \frac{2.837*(\exp(0.04*(V+77.0))-1.0)}{(V+77.0)*\exp(0.04*(V+35.0))}; & \text{if } V > -100.0, \\ 1.0 & \text{otherwise.} \end{cases} \tag{A.12.27}$$

"time_independent_potassium_current" component

The time independent potassium current contains a single inactivation gate (K1) whose time constant is small enough that it can be approximated by its steady-state value K1_infinity.

Initial values defined in this component

$g\_K1 = 6.047 \times 10^{-3} \ \mathrm{mS \cdot mm^{-2}}$

Equations defined in this component

Calculation of the maximum conductance of the potassium channel.

$$g\_K1\_max = g\_K1 * \sqrt{\frac{Ko}{5.4}} \tag{A.12.28}$$

Calculation of the reversal potential of the potassium channel.

$$E\_K1 = \frac{R * T}{F} * \ln\left(\frac{Ko}{Ki}\right) \tag{A.12.29}$$

Calculation of the time-independent potassium current.

$$i\_K1 = g\_K1\_max * K1\_infinity * (V - E\_K1) \tag{A.12.30}$$

"timeindependentpotassiumcurrentK1gate" component

The voltage-dependent and time-independent gating variable for the time independent potassium current.

Equations defined in this component

The opening rate of the K1 gating variable.
$$alpha\_K1 = \frac{1.02}{(1.0 + \exp\left(0.2385 * ((V - E\_K1) - 59.215)\right))} \tag{A.12.31}$$

The closing rate of the K1 gating variable.
$$beta\_K1 = \frac{(0.49124 * \exp\left(0.08032 * ((V + 5.476) - E\_K1)\right) + \exp\left(0.06175 * (V - (E\_K1 + 594.31))\right))}{(1.0 + \exp\left(-0.5143 * ((V - E\_K1) + 4.753)\right))} \tag{A.12.32}$$

The steady-state approximation for the kinetics of the K1 gating variable.
$$K1\_infinity = \frac{alpha\_K1}{(alpha\_K1 + beta\_K1)} \tag{A.12.33}$$

"plateaupotassiumcurrent" component

The plateau potassium current component contains the equations which describe the contribution of a time-independent [K]o-insensitive channel at plateau potentials.

Initial values defined in this component
$g\_Kp = 1.83 \times 10^{-4}\ \mathrm{mS \cdot mm^{-2}}$

Equations defined in this component

The reversal potential is the same as the K1 channel.
$$E\_Kp = E\_K1 \tag{A.12.34}$$

The gating variable for the Kp channel.
$$Kp = \frac{1.0}{\left(1.0 + \exp\left(\frac{(7.488 - V)}{5.98}\right)\right)} \tag{A.12.35}$$

Calculation of the plateau potassium current.
$$i\_Kp = g\_Kp * Kp * (V - E\_Kp) \tag{A.12.36}$$

"backgroundcurrent" component

The background current describes an additional current which contributes at plateau potentials.

Initial values defined in this component
$E\_b = -59.87\ \mathrm{mV}$ $\qquad\qquad\qquad\qquad$ $g\_b = 3.921 \times 10^{-4}\ \mathrm{mS \cdot mm^{-2}}$

Equations defined in this component

Calculation of the background current.

$$i\_b = g\_b * (V - E\_b) \tag{A.12.37}$$

"ionic_concentrations" component

In their 1991 model for most ions, Luo and Rudy do not include equations to calculate changes in their concentrations. Instead they fix the variables and specify their values, as shown in this component. The only exception is for intracellular calcium concentrations which is defined by an equation. Extracellular calcium concentration is defined here but is not included in any of the ionic flux calculations. Therefore it has no public_interface.

Initial values defined in this component

Nao = 140.0 mM Ki = 145.0 mM

Nai = 18.0 mM Ko = 5.4 mM

Cao = 1.8 mM

"intracellular_calcium_concentration" component

The sole ionic concentration modelled is intracellular calcium, using the same equation as that used in the original Beller Reuter (1977) model.

Initial values defined in this component

Cai = 0.0002 mM

Equations defined in this component

The differential equation governing the intracellular calcium ion concentration.

$$\frac{\mathrm{d}(Cai)}{\mathrm{d}(time)} = (-0.01 * i\_si + 0.07 * (0.0001 - Cai)) \tag{A.12.38}$$

A.13   LR_II_model_1994

This is the CellML description of Luo and Rudy's mathematical model of the mammalian cardiac ventricular action potential. It is a significant development on their original 1991 model. While this version of the model qualitatively compares well to the LR II paper for the action potential, the intracellular calcium dynamics have not been included correctly - namely there is no calcium-induced calcium-release (CICR) process in this version of the model. The original version of the model simulates CICR via a mechanism whereby CICR is induced if and only if the calcium accumulated in the cell in the 2 ms following (dV/dt)max exceeds a given threshold. This sort of process is a bit tricky to include in the CellML (or at least in a way that will work with the CellML abilitites of CMISS) so has been left out for now.

Reference: Luo, C. & Rudy, Y. (1994), 'A Dynamic Model of the Cardiac Ventricular Action Potential I. Simula-

tions of Ionic Currents and Concentration Changes', *Circulation Research* **74**, 1071–1096.

"environment" component

"membrane" component

The main component for the model, contains all ionic currents and defi nes the transmembrane potential.

Initial values defined in this component

$V = -84.624 \text{ mV}$ $F = 96845.0 \text{ nC} \cdot \text{nmol}^{-1}$

$R = 8.3145 \times 10^3 \text{ pJ} \cdot \text{nmol}^{-1} \cdot \text{K}^{-1}$ $Cm = 0.01 \text{ } \mu\text{F} \cdot \text{mm}^{-2}$

$T = 310.0 \text{ K}$

Equations defined in this component

We need to use dV/dt in the calulation of calcium-induced calcium-release, so we make it accessible here.

$$dV\_dt = \left[I\_st - \left(i\_Na + i\_Ca\_L + i\_K + i\_K1 + i\_Kp + i\_NaCa \right.\right.$$
$$\left.\left. + i\_p\_Ca + i\_Na\_b + i\_Ca\_b + i\_NaK + i\_ns\_Ca \right) \right] \Big/ Cm \quad \text{(A.13.1)}$$

Assign the rate of change of potential for the differential equation.

$$\frac{\text{d}(V)}{\text{d}(time)} = dV\_dt \quad \text{(A.13.2)}$$

This is a dummy equation that we simply use to make grabbing the value in CMISS much easier.

$$IStimC = I\_st \quad \text{(A.13.3)}$$

"fast_sodium_current" component

The fast sodium current is primarily responsible for the upstroke of the action potential.

Initial values defined in this component

$g\_Na = 0.16 \text{ mS} \cdot \text{mm}^{-2}$

Equations defined in this component

Calculation of the fast sodium current.

$$i\_Na = g\_Na * (m)^{3.0} * h * j * (V - E\_Na) \quad \text{(A.13.4)}$$

Calculation of reversal potential for the fast sodium channel.

$$E\_Na = \frac{R * T}{F} * \ln\left(\frac{Nao}{Nai}\right) \quad \text{(A.13.5)}$$

"fast_sodium_current_m_gate" component

The voltage-dependent activation gate for the fast sodium channel - the m gate.

Initial values defined in this component

$m = 0.0$

Equations defined in this component

The opening rate for the m gate.

$$alpha\_m = \frac{0.32 * (V + 47.13)}{(1.0 - \exp(-0.1 * (V + 47.13)))} \tag{A.13.6}$$

The closing rate for the m gate.

$$beta\_m = 0.08 * \exp\left(\frac{-V}{11.0}\right) \tag{A.13.7}$$

The kinetics of the m gate.

$$\frac{\mathrm{d}(m)}{\mathrm{d}(time)} = (alpha\_m * (1.0 - m) - beta\_m * m) \tag{A.13.8}$$

"fast_sodium_current_h_gate" component

The voltage-dependent inactivation gate for the fast sodium channel - the h gate.

Initial values defined in this component

$h = 1.0$

Equations defined in this component

The opening rate for the h gate.

$$alpha\_h = \begin{cases} 0.135 * \exp\left(\frac{(80.0+V)}{-6.8}\right); & \text{if } V < -40.0, \\ 0.0 & \text{otherwise.} \end{cases} \tag{A.13.9}$$

The closing rate for the h gate.

$$beta\_h = \begin{cases} (3.56 * \exp(0.079 * V) + 310000.0 * \exp(0.35 * V)); & \text{if } V < -40.0, \\ \frac{1.0}{0.13 * \left(1.0 + \exp\left(\frac{(V+10.66)}{-11.1}\right)\right)} & \text{otherwise.} \end{cases} \tag{A.13.10}$$

The kinetics of the h gate.

$$\frac{\mathrm{d}(h)}{\mathrm{d}(time)} = (alpha\_h * (1.0 - h) - beta\_h * h) \tag{A.13.11}$$

"fast_sodium_current_j_gate" component

The voltage-dependent slow inactivation gate for the fast sodium channel - the j gate.

Initial values defined in this component

$j = 1.0$

Equations defined in this component

The opening rate for the j gate.

$$alpha\_j = \begin{cases} (-127140.0 * \exp\left(0.2444 * V\right) - 0.00003474 * \exp\left(-0.04391 * V\right)) \\ \qquad\qquad * \frac{(V+37.78)}{(1.0+\exp(0.311*(V+79.23)))}; & \text{if } V < -40.0, \\ 0.0 & \text{otherwise.} \end{cases}$$

(A.13.12)

The closing rate for the j gate.

$$beta\_j = \begin{cases} \frac{0.1212*\exp(-0.01052*V)}{(1.0+\exp(-0.1378*(V+40.14)))}; & \text{if } V < -40.0, \\ \frac{0.3*\exp(-0.0000002535*V)}{(1.0+\exp(-0.1*(V+32.0)))} & \text{otherwise.} \end{cases}$$

(A.13.13)

The kinetics of for the j gate.

$$\frac{\mathrm{d}(j)}{\mathrm{d}(time)} = (alpha\_j * (1.0 - j) - beta\_j * j)$$

(A.13.14)

"L_type_Ca_channel" component

The L-type calcium channel. Primarily a calcium specific channel, but with small potassium and sodium components, activated at plateau potentials.

Initial values defined in this component

$gamma\_Nai = 0.75$ $P\_Na = 6.75 \times 10^{-9} \text{ mm} \cdot \text{ms}^{-1}$

$gamma\_Nao = 0.75$ $P\_K = 1.93 \times 10^{-9} \text{ mm} \cdot \text{ms}^{-1}$

$gamma\_Ki = 0.75$ $gamma\_Cai = 1.0$

$gamma\_Ko = 0.75$ $gamma\_Cao = 0.34$

$P\_Ca = 5.4 \times 10^{-6} \text{ mm} \cdot \text{ms}^{-1}$

Equations defined in this component

The calcium component of the total L-type channel current.

$$i\_CaCa = d * f * f\_Ca * I\_CaCa$$

(A.13.15)

The sodium component of the total L-type channel current.

$$i\_CaNa = d * f * f\_Ca * I\_CaNa$$

(A.13.16)

The potassium component of the total L-type channel current.

$$i\_CaK = d * f * f\_Ca * I\_CaK$$

(A.13.17)

The maximum calcium component of the total L-type channel current.

$$I\_CaCa = P\_Ca * (2.0)^{2.0} * \frac{V * (F)^{2.0}}{R * T}$$
$$* \frac{\left(gamma\_Cai * Cai * \exp\left(\frac{2.0*V*F}{R*T}\right) - gamma\_Cao * Cao\right)}{\left(\exp\left(\frac{2.0*V*F}{R*T}\right) - 1.0\right)} \quad \text{(A.13.18)}$$

The maximum sodium component of the total L-type channel current.

$$I\_CaNa = P\_Na * (1.0)^{2.0} * \frac{V * (F)^{2.0}}{R * T}$$
$$* \frac{\left(gamma\_Nai * Nai * \exp\left(\frac{1.0*V*F}{R*T}\right) - gamma\_Nao * Nao\right)}{\left(\exp\left(\frac{1.0*V*F}{R*T}\right) - 1.0\right)} \quad \text{(A.13.19)}$$

The maximum potassium component of the total L-type channel current.

$$I\_CaK = P\_K * (1.0)^{2.0} * \frac{V * (F)^{2.0}}{R * T}$$
$$* \frac{\left(gamma\_Ki * Ki * \exp\left(\frac{1.0*V*F}{R*T}\right) - gamma\_Ko * Ko\right)}{\left(\exp\left(\frac{1.0*V*F}{R*T}\right) - 1.0\right)} \quad \text{(A.13.20)}$$

The total current of the L-type channel current.

$$i\_Ca\_L = (i\_CaCa + i\_CaK + i\_CaNa) \quad \text{(A.13.21)}$$

"L_type_Ca_channel_d_gate" component

The voltage-dependent activation gate for the L-type calcium channel - the d gate.

Initial values defined in this component
$d = 0.0$

Equations defined in this component

The opening rate of the d gate.

$$alpha\_d = \frac{d\_infinity}{tau\_d} \quad \text{(A.13.22)}$$

$$d\_infinity = \frac{1.0}{\left(1.0 + \exp\left(-\frac{(V+10.0)}{6.24}\right)\right)} \quad \text{(A.13.23)}$$

$$tau\_d = d\_infinity * \frac{\left(1.0 - \exp\left(-\frac{(V+10.0)}{6.24}\right)\right)}{0.035 * (V + 10.0)} \quad \text{(A.13.24)}$$

The closing rate of the d gate.

$$beta\_d = \frac{(1.0 - d\_infinity)}{tau\_d} \quad \text{(A.13.25)}$$

The kinetics of the d gate.

$$\frac{\mathrm{d}(d)}{\mathrm{d}(time)} = (alpha\_d * (1.0 - d) - beta\_d * d) \quad \text{(A.13.26)}$$

"L_type_Ca_channel_f_gate" component

The voltage-dependent inactivation gate for the L-type calcium channel - the f gate.

Initial values defined in this component

$f = 1.0$

Equations defined in this component

The opening rate of the f gate.

$$alpha\_f = \frac{f\_infinity}{tau\_f} \tag{A.13.27}$$

$$f\_infinity = \left(\frac{1.0}{\left(1.0 + \exp\left(\frac{(V+35.06)}{8.6}\right)\right)} + \frac{0.6}{\left(1.0 + \exp\left(\frac{(50.0-V)}{20.0}\right)\right)} \right) \tag{A.13.28}$$

$$tau\_f = \frac{1.0}{\left(0.0197 * \exp\left(-(0.0337 * (V+10.0))^{2.0}\right) + 0.02\right)} \tag{A.13.29}$$

The closing rate of the f gate.

$$beta\_f = \frac{(1.0 - f\_infinity)}{tau\_f} \tag{A.13.30}$$

The kinetics of the f gate.

$$\frac{\mathrm{d}(f)}{\mathrm{d}(time)} = (alpha\_f * (1.0 - f) - beta\_f * f) \tag{A.13.31}$$

"L_type_Ca_channel_f_Ca_gate" component

The calcium-dependent inactivation gate for the L-type calcium channel - the fCa gate.

Initial values defined in this component

$Km\_Ca = 0.6 \times 10^{-3}$ mM

Equations defined in this component

The kinetics of the fCa gate.

$$f\_Ca = \frac{1.0}{\left(1.0 + \left(\frac{Cai}{Km\_Ca}\right)^{2.0}\right)} \tag{A.13.32}$$

"time_dependent_potassium_current" component

The time-dependent potassium reploarisation current.

Initial values defined in this component

$g\_K\_max = 2.82 \times 10^{-3}$ mS $\cdot$ mm^{-2} $PR\_NaK = 0.01833$

Equations defined in this component

The conductance for the channel.

$$g\_K = g\_K\_max * \sqrt{\frac{Ko}{5.4}} \tag{A.13.33}$$

The reversal potential of the channel.

$$E\_K = \frac{R*T}{F} * \ln\left(\frac{(Ko + PR\_NaK * Nao)}{(Ki + PR\_NaK * Nai)}\right) \tag{A.13.34}$$

Calculation of the current.

$$i\_K = g\_K * (X)^{2.0} * Xi * (V - E\_K) \tag{A.13.35}$$

"time_dependent_potassium_current_X_gate" component

The time-dependent activation gate for the time-dependent potassium current - the X gate.

Initial values defined in this component

$X = 0.0$

Equations defined in this component

The opening rate for the X gate.

$$alpha\_X = \frac{0.0000719 * (V + 30.0)}{(1.0 - \exp(-0.148 * (V + 30.0)))} \tag{A.13.36}$$

The closing rate for the X gate.

$$beta\_X = \frac{0.000131 * (V + 30.0)}{(-1.0 + \exp(0.0687 * (V + 30.0)))} \tag{A.13.37}$$

The kinetics of the X gate.

$$\frac{d(X)}{d(time)} = (alpha\_X * (1.0 - X) - beta\_X * X) \tag{A.13.38}$$

"time_dependent_potassium_current_Xi_gate" component

The time-independent inactivation gate for the time-dependent potassium current - the Xi gate.

Equations defined in this component

The kinetics of the Xi gate.

$$Xi = \frac{1.0}{\left(1.0 + \exp\left(\frac{(V - 56.26)}{32.1}\right)\right)} \tag{A.13.39}$$

"time_independent_potassium_current" component

The time-independent potassium repolarisation current.

Initial values defined in this component

$g\_K1\_max = 7.5 \times 10^{-3} \text{ mS} \cdot \text{mm}^{-2}$

Equations defined in this component

Calculation of the channel conductance.

$$g\_K1 = g\_K1\_max * \sqrt{\frac{Ko}{5.4}} \tag{A.13.40}$$

Calculation of the channel reversal potential.

$$E\_K1 = \frac{R * T}{F} * \ln\left(\frac{Ko}{Ki}\right) \tag{A.13.41}$$

Calculation of the channel current.

$$i\_K1 = g\_K1 * K1\_infinity * (V - E\_K1) \tag{A.13.42}$$

"time_independent_potassium_current_K1_gate" component

The gating variable for the time-independent potassium current - the K1 gate.

Equations defined in this component

The opening rate for the K1 gate.

$$alpha\_K1 = \frac{1.02}{(1.0 + \exp(0.2385 * ((V - E\_K1) - 59.215)))} \tag{A.13.43}$$

The closing rate for the K1 gate.

$$beta\_K1 = \frac{(0.49124 * \exp(0.08032 * ((V + 5.476) - E\_K1)) + \exp(0.06175 * (V - (E\_K1 + 594.31))))}{(1.0 + \exp(-0.5143 * ((V - E\_K1) + 4.753)))} \tag{A.13.44}$$

The steady-state kinetics of the K1 gate.

$$K1\_infinity = \frac{alpha\_K1}{(alpha\_K1 + beta\_K1)} \tag{A.13.45}$$

"plateau_potassium_current" component

The potassium current active at plateau potentials.

Initial values defined in this component

$g\_Kp = 1.83 \times 10^{-4} \text{ mS} \cdot \text{mm}^{-2}$

Equations defined in this component

The reversal potential for the channel.

$$E\_Kp = E\_K1 \tag{A.13.46}$$

The gating kinetics for the channel.

$$Kp = \frac{1.0}{\left(1.0 + \exp\left(\frac{(7.488 - V)}{5.98}\right)\right)} \tag{A.13.47}$$

Calculation of the current.

$$i\_Kp = g\_Kp * Kp * (V - E\_Kp) \tag{A.13.48}$$

"sarcolemmal_calcium_pump" component

A calcium pump for removal of calcium from the cytosol to the extracellular space.

Initial values defined in this component

$K\_mpCa = 0.5 \times 10^{-3}$ mM $\qquad\qquad\qquad I\_pCa = 1.15 \times 10^{-2}$ μA $\cdot$ mm^{-2}

Equations defined in this component

The calcium pump current.

$$i\_p\_Ca = I\_pCa * \frac{Cai}{(K\_mpCa + Cai)} \tag{A.13.49}$$

"sodium_background_current" component

The background sodium current.

Initial values defined in this component

$g\_Nab = 1.41 \times 10^{-5}$ mS $\cdot$ mm^{-2}

Equations defined in this component

The reversal potential for the channel.

$$E\_NaN = E\_Na \tag{A.13.50}$$

Calculation of the current.

$$i\_Na\_b = g\_Nab * (V - E\_NaN) \tag{A.13.51}$$

"calcium_background_current" component

The background calcium current.

Initial values defined in this component

$g\_Cab = 3.016 \times 10^{-5}$ mS $\cdot$ mm^{-2}

Equations defined in this component

The reversal potential for the channel.

$$E\_CaN = \frac{R*T}{2.0*F} * \ln\left(\frac{Cao}{Cai}\right)$$ (A.13.52)

Calculation of the current.

$$i\_Ca\_b = g\_Cab * (V - E\_CaN)$$ (A.13.53)

"sodium_potassium_pump" component

The sodium/potassium exchanger current which extrudes three sodium ions from the cell in exchange for two potassium ions entering the cell.

Initial values defined in this component

$I\_NaK = 1.5 \times 10^{-2}\,\mu\text{A} \cdot \text{mm}^{-2}$ $\qquad\qquad K\_mKo = 1.5\,\text{mM}$

$K\_mNai = 10.0\,\text{mM}$

Equations defined in this component

$$f\_NaK = \frac{1.0}{\left(\left(1.0 + 0.1245 * \exp\left(-0.1 * \frac{V*F}{R*T}\right)\right) + 0.0365 * sigma * \exp\left(-\frac{V*F}{R*T}\right)\right)}$$ (A.13.54)

$$sigma = \frac{1.0}{7.0} * \left(\exp\left(\frac{Nao}{67.3}\right) - 1.0\right)$$ (A.13.55)

Calculation of the exchanger current.

$$i\_NaK = I\_NaK * f\_NaK * \frac{1.0}{\left(1.0 + \left(\frac{K\_mNai}{Nai}\right)^{1.5}\right)} * \frac{Ko}{(Ko + K\_mKo)}$$ (A.13.56)

"non_specific_calcium_activated_current" component

A non-specific calcium activated channel - assumed impermeable to calcium ions but permeable to sodium and potassium ions.

Initial values defined in this component

$P\_ns\_Ca = 1.75 \times 10^{-9}\,\text{mm} \cdot \text{ms}^{-1}$ $\qquad\qquad K\_m\_ns\_Ca = 1.2 \times 10^{-3}\,\text{mM}$

Equations defined in this component

The channel reversal potential.

$$EnsCa = \frac{R*T}{F} * \ln\left(\frac{(Ko + Nao)}{(Ki + Nai)}\right)$$ (A.13.57)

$$Vns = (V - EnsCa)$$ (A.13.58)

The sodium component of the channel's current.

$$i\_ns\_Na = I\_ns\_Na * \frac{1.0}{\left(1.0 + \left(\frac{K\_m\_ns\_Ca}{Cai}\right)^{3.0}\right)} \tag{A.13.59}$$

The potassium component of the channel's current.

$$i\_ns\_K = I\_ns\_K * \frac{1.0}{\left(1.0 + \left(\frac{K\_m\_ns\_Ca}{Cai}\right)^{3.0}\right)} \tag{A.13.60}$$

The total current through the channel.

$$i\_ns\_Ca = (i\_ns\_Na + i\_ns\_K) \tag{A.13.61}$$

The maximum sodium component of the channel's current.

$$I\_ns\_Na = P\_ns\_Ca * (1.0)^{2.0} * \frac{Vns * (F)^{2.0}}{R * T}$$
$$* \frac{\left(gamma\_Nai * Nai * \exp\left(\frac{1.0*Vns*F}{R*T}\right) - gamma\_Nao * Nao\right)}{\left(\exp\left(\frac{1.0*Vns*F}{R*T}\right) - 1.0\right)} \tag{A.13.62}$$

The maximum potassium component of the channel's current.

$$I\_ns\_K = P\_ns\_Ca * (1.0)^{2.0} * \frac{Vns * (F)^{2.0}}{R * T}$$
$$* \frac{\left(gamma\_Ki * Ki * \exp\left(\frac{1.0*Vns*F}{R*T}\right) - gamma\_Ko * Ko\right)}{\left(\exp\left(\frac{1.0*Vns*F}{R*T}\right) - 1.0\right)} \tag{A.13.63}$$

"Na_Ca_exchanger" component

The sodium-calcium exchanger current, exchanges three sodium ions for one calcium ion.

Initial values defined in this component

K_NaCa = 20.0 μA $\cdot$ mm^{-2} K_sat = 0.1

K_mNa = 87.5 mM   eta = 0.35

K_mCa = 1.38 mM

Equations defined in this component

Calculation of the exchanger current.

$$i\_NaCa = K\_NaCa * \frac{1.0}{\left((K\_mNa)^{3.0} + (Nao)^{3.0}\right)} * \frac{1.0}{(K\_mCa + Cao)}$$
$$* \frac{1.0}{\left(1.0 + K\_sat * \exp\left((eta - 1.0) * V * \frac{F}{R*T}\right)\right)}$$
$$* \left(\exp\left(eta * V * \frac{F}{R * T}\right) * (Nai)^{3.0} * Cao - \exp\left((eta - 1.0) * V * \frac{F}{R * T}\right) * (Nao)^{3.0} * Cai\right) \tag{A.13.64}$$

"calcium_fluxes_in_the_SR" component

The various calcium fluxes into and from the sarcoplasmic reticulum.

Initial values defined in this component

$G\_rel\_max = 60.0 \text{ ms}^{-1}$

$tau\_on = 2.0 \text{ ms}$

$tau\_off = 2.0 \text{ ms}$

$tau\_tr = 180.0 \text{ ms}$

$K\_mrel = 0.8 \times 10^{-3} \text{ mM}$

$K\_mup = 0.92 \times 10^{-3} \text{ mM}$

$I\_up = 0.005 \text{ mM} \cdot \text{ms}^{-1}$

$Ca\_NSR\_max = 15.0 \text{ mM}$

$delta\_Ca\_ith = 0.18 \times 10^{-3} \text{ mM}$

Equations defined in this component

The release flux from the junctional sarcoplasmic reticulum into the cytosol.

$$i\_rel = G\_rel * (Ca\_JSR - Cai) \qquad (A.13.65)$$

Calculation of the release channel conductance. This is incorrect as there is no CICR induced via the accumulation of calcium in the cytosol in the period following max(dV/dt)

$$G\_rel = G\_rel\_peak * \frac{(delta\_Ca\_i2 - delta\_Ca\_ith)}{((K\_mrel + delta\_Ca\_i2) - delta\_Ca\_ith)}$$
$$* \left(1.0 - \exp\left(-\frac{t\_CICR}{tau\_on}\right)\right) * \exp\left(-\frac{t\_CICR}{tau\_off}\right) \quad (A.13.66)$$

$$G\_rel\_peak = \begin{cases} 0.0; & \text{if } delta\_Ca\_i2 < delta\_Ca\_ith, \\ G\_rel\_max & \text{otherwise.} \end{cases} \qquad (A.13.67)$$

The uptake flux into the sarcoplasmic reticulum from the cytosol.

$$i\_up = I\_up * \frac{Cai}{(Cai + K\_mup)} \qquad (A.13.68)$$

Calcium leak flux from the network sarcoplasmic reticulum into the cytosol.

$$i\_leak = K\_leak * Ca\_NSR \qquad (A.13.69)$$

$$K\_leak = \frac{I\_up}{Ca\_NSR\_max} \qquad (A.13.70)$$

Translocation flux from the network to the junctional sarcoplasmic reticulum.

$$i\_tr = \frac{(Ca\_NSR - Ca\_JSR)}{tau\_tr} \qquad (A.13.71)$$

"ionic_concentrations" component

Component grouping together the differential equations for the various ionic concentrations that the model tracks.

Initial values defined in this component

$Nai = 10.0$ mM

$Nao = 140.0$ mM

$Cai = 0.12 \times 10^{-3}$ mM

$Cao = 1.8$ mM

$Ki = 145.0$ mM

$Ko = 5.4$ mM

$Ca\_JSR = 1.8$ mM

$Ca\_NSR = 1.8$ mM

$Am = 200$ mm^{-1}

$V\_myo = 0.68$

$V\_JSR = 0.0048$

$V\_NSR = 0.0552$

Equations defined in this component

The change in intracellular sodium concentration.
$$\frac{\mathrm{d}(Nai)}{\mathrm{d}(time)} = -(i\_Na + i\_CaNa + i\_Na\_b + i\_ns\_Na + i\_NaCa * 3.0 + i\_NaK * 3.0) * \frac{Am}{V\_myo * F}$$
(A.13.72)

The change in intracellular calcium concentration.
$$\frac{\mathrm{d}(Cai)}{\mathrm{d}(time)} = -((i\_CaCa + i\_p\_Ca + i\_Ca\_b) - i\_NaCa) * \frac{Am}{2.0 * V\_myo * F}$$
$$+ i\_rel * \frac{V\_JSR}{V\_myo} + (i\_leak - i\_up) * \frac{V\_NSR}{V\_myo} \quad (A.13.73)$$

The change in intracellular potassium concentration.
$$\frac{\mathrm{d}(Ki)}{\mathrm{d}(time)} = -(i\_CaK + i\_K + i\_K1 + i\_Kp + i\_ns\_K + -i\_NaK * 2.0) * \frac{Am}{V\_myo * F} \quad (A.13.74)$$

The change in calcium concentration in the junctional sarcoplasmic reticulum.
$$\frac{\mathrm{d}(Ca\_JSR)}{\mathrm{d}(time)} = -\left(i\_rel - i\_tr * \frac{V\_NSR}{V\_JSR} \right) \quad (A.13.75)$$

The change in calcium concentration in the network sarcoplasmic reticulum.
$$\frac{\mathrm{d}(Ca\_NSR)}{\mathrm{d}(time)} = -((i\_leak + i\_tr) - i\_up) \quad (A.13.76)$$

A.14   Rogers_McCulloch_1994

This is a CellML version of the modified FitzHugh-Nagumo model, published by Rogers and McCulloch in 1994. While the original two-variable model described a non-dimensional activation variable (u) and a non-dimensional recovery variable (v), here we formulate the model in terms of the 'real' action potential given by the time course of the transmembrane potential (Vm). In so doing, the time rate of change of the activation variable describes the total 'ionic current' through the membrane with the original model parameters adjusted to give the correct dimensionality.

Reference: Rogers, J. M. & McCulloch, A. D. (1994), 'A collocation–Galerkin finite element model of cardiac action potential propagation', *IEEE Transactions on Biomedical Engineering* **41**, 743–757.

"interface" component

We'll use this component as the "interface" to the model, all other components are hidden via encapsulation in this component.

Initial values defined in this component

$Cm = 0.01\ \mu\text{F} \cdot \text{mm}^{-2}$ $c1 = 0.26\ \mu\text{A} \cdot \text{mm}^{-2}$

$Vr = -85.0\ \text{mV}$ $c2 = 0.1\ \mu\text{A} \cdot \text{mm}^{-2}$

$Vth = -75.0\ \text{mV}$ $b = 0.013\ \text{ms}^{-1}$

$Vp = 15.0\ \text{mV}$ $d = 0.8$

Equations defined in this component

This is a dummy equation that we simply use to make grabbing the value in CMISS much easier.

$$IStimC = Istim \tag{A.14.1}$$

"membrane_potential" component

The component which defines the kinetics of the transmembrane potential.

Initial values defined in this component

$Vm = -85\ \text{mV}$

Equations defined in this component

This equation describes the kinetics of the transmembrane, potential - the action potential.

$$\frac{\mathrm{d}(Vm)}{\mathrm{d}(t)} = \frac{(Istim - Iion)}{Cm} \tag{A.14.2}$$

The non-dimensional and scaled potential value.

$$u = \frac{(Vm - Vr)}{(Vp - Vr)} \tag{A.14.3}$$

"ionic_current" component

Here we define the total ionic current through the cellular membrane - equivalent to the temporal derivative of the original activation variable. The modification of Rogers and McCulloch is in this equation, with the additional multiplication of recovery variable with the normalised potential.

Initial values defined in this component

$Iion = 0.0\ \mu\text{A} \cdot \text{mm}^{-2}$

Equations defined in this component

The calcuation of the total ionic current.

$$Iion = \left(c1 * u * \left(u - \frac{(Vth - Vr)}{(Vp - Vr)} \right) * (u - 1.0) + c2 * u * v \right) \tag{A.14.4}$$

"recovery_variable" component

Here we defi ne the non-dimensional recovery variable, v.

Initial values defined in this component
$v = 0.0$

Equations defined in this component

The kinetics of the recovery variable.

$$\frac{\mathrm{d}(v)}{\mathrm{d}(t)} = b * (u - d * v) \tag{A.14.5}$$

A.15   Aliev_Panfilov_1996

This is a CellML version of the modifi ed FitzHugh-Nagumo model, published by Aliev and Panfi lov in 1996. While the original two-variable model described a non-dimensional activation variable (u) and a non-dimensional recovery variable (v), here we formulate the model in terms of the 'real' action potential given by the time course of the transmembrane potential (Vm). In so doing, the time rate of change of the activation variable describes the total 'ionic current' through the membrane with the original model parameters adjusted to give the correct dimensionality.

Reference: Aliev, R. R. & Panfi lov, A. V. (1996), 'A Simple Two-variable Model of Cardiac Excitation', *Chaos, Solitons & Fractals* **7**, 293–301.

"interface" component

We'll use this component as the "interface" to the model, all other components are hidden via encapsulation in this component.

Initial values defined in this component

$Cm = 0.01 \, \mu\mathrm{F} \cdot \mathrm{mm}^{-2}$	$c1 = 8.0 \, \mu\mathrm{A} \cdot \mathrm{mm}^{-2}$
$Vr = -85.0 \, \mathrm{mV}$	$b = 0.000155 \, \mathrm{ms}^{-1}$
$Vth = -75.0 \, \mathrm{mV}$	$d = 0.0155 \, \mathrm{ms}^{-1}$
$Vp = 15.0 \, \mathrm{mV}$	$mu2 = 0.3$

Equations defined in this component

This is a dummy equation that we simply use to make grabbing the value in CMISS much easier.

$$IStimC = Istim \tag{A.15.1}$$

"membrane_potential" component

The component which defines the kinetics of the transmembrane potential.

Initial values defined in this component

$Vm = -85$ mV

Equations defined in this component

This equation describes the kinetics of the transmembrane, potential - the action potential.

$$\frac{\mathrm{d}(Vm)}{\mathrm{d}(t)} = \frac{(Istim - Iion)}{Cm} \tag{A.15.2}$$

The non-dimensional and scaled potential value.

$$u = \frac{(Vm - Vr)}{(Vp - Vr)} \tag{A.15.3}$$

"ionic_current" component

Here we define the total ionic current through the cellular membrane - equivalent to the temporal derivative of the original activation variable. One modification of Aliev and Panfilov is in this equation, with the additional multiplication of the recovery variable with the normalised potential and removal of the scalar multiplier.

Equations defined in this component

The calcuation of the total ionic current.

$$Iion = \left(c1 * u * \left(u - \frac{(Vth - Vr)}{(Vp - Vr)} \right) * (u - 1.0) + u * v \right) \tag{A.15.4}$$

"recovery_variable" component

Here we define the non-dimensional recovery variable, v. The kinetics of the recovery variable have been reworked by Aliev and Panfilov to provide more realistic restitution properties.

Initial values defined in this component

$v = 0.0$

Equations defined in this component

The kinetics of the recovery variable.

$$\frac{\mathrm{d}(v)}{\mathrm{d}(t)} = eps * (-v - rate * vstar * (Vm - Vr)) \tag{A.15.5}$$

$$eps = \left(b + \frac{d * v}{(u + mu2)} \right) \tag{A.15.6}$$

$$rate = \frac{c1}{((Vp - Vr))^{2.0}} \tag{A.15.7}$$

$$vstar = (Vm + ((Vr - Vp) - Vth)) \tag{A.15.8}$$

A.16   fenton_karma_model_1998

This is the CellML description of the Fenton-Karma simplified ionic model with three membrane currents, 1998. The default parameter values provided correspond to the modified-BR parameter set provided by Fenton and Karma in their corrected Table I.

Reference: Fenton, F. & Karma, A. (1998), 'Vortex dynamics in three-dimensional continuous myocardium with fiber rotation: Filament instability and fibrillation', *Chaos* **8**, 20–47.

"environment" component

"membrane" component

The main component of the model, defining both the actual transmembrane potential and it's non-dimensional representation used in the model.

Initial values defined in this component

$u = 0.0$	$V\_o = -85.0$ mV
$Cm = 0.01\ \mu\mathrm{F} \cdot \mathrm{mm}^{-2}$	$V\_fi = 15.0$ mV

Equations defined in this component

Convert the scaled currents to actual currents.

$$I\_fi = J\_fi * Cm * (V\_fi - V\_o) \tag{A.16.1}$$

$$I\_si = J\_si * Cm * (V\_fi - V\_o) \tag{A.16.2}$$

$$I\_so = J\_so * Cm * (V\_fi - V\_o) \tag{A.16.3}$$

Calculate the non-dimensional membrane potential variable.

$$u = \frac{(Vm - V\_o)}{(V\_fi - V\_o)}$$ (A.16.4)

The standard membrane action potential formulation.

$$\frac{\mathrm{d}(Vm)}{\mathrm{d}(time)} = \frac{(I\_stim - (I\_fi + I\_si + I\_so))}{Cm}$$ (A.16.5)

This is a dummy equation that we simply use to make grabbing the value in CMISS much easier.

$$IStimC = I\_stim$$ (A.16.6)

"p" component

Equivalent to the Heaviside step function H(u-uc) from the original paper.

Initial values defined in this component
$u\_c = 0.13$

Equations defined in this component

$$p = \begin{cases} 0.0; & \text{if } u < u\_c, \\ 1.0 & \text{otherwise.} \end{cases}$$ (A.16.7)

"q" component

Equivalent to the Heaviside step function H(u-uv) from the original paper.

Initial values defined in this component
$u\_v = 0.055$

Equations defined in this component

$$q = \begin{cases} 0.0; & \text{if } u < u\_v, \\ 1.0 & \text{otherwise.} \end{cases}$$ (A.16.8)

"fast_inward_current" component

Component representing the scaled fast inward current.

Initial values defined in this component
$g\_fi\_max = 0.04 \, \mathrm{mS} \cdot \mathrm{mm}^{-2}$

Equations defined in this component

Calculation of the current's time constant.

$$tau\_d = \frac{Cm}{g\_fi\_max} \tag{A.16.9}$$

Calculation of the current scaled fast inward current.

$$J\_fi = -v * p * (u - u\_c) * \frac{(1.0 - u)}{tau\_d} \tag{A.16.10}$$

"fast_inward_current_v_gate" component

The inactivation-reactivation gate for the fast inward current. Analogous in role to the product of the h and j gates of the BR and LR models.

Initial values defined in this component

$v = 1.0$ $tau\_v2\_minus = 19.2$ ms

$tau\_v1\_minus = 1000.0$ ms $tau\_v\_plus = 3.33$ ms

Equations defined in this component

The kinetics of the fast current's inactivation-reactivation variable.

$$\frac{\mathrm{d}(v)}{\mathrm{d}(time)} = \left((1.0 - p) * \frac{(1.0 - v)}{tau\_v\_minus} - \frac{p * v}{tau\_v\_plus} \right) \tag{A.16.11}$$

Fenton and Karma found it necessary to define the time constant that governs the reactivation of the fast inward current separately over two voltage ranges (uv<u<uc and u<uv).

$$tau\_v\_minus = (q * tau\_v1\_minus + (1.0 - q) * tau\_v2\_minus) \tag{A.16.12}$$

"slow_outward_current" component

The slow outward current, responsible for the repolarisation of the membrane.

Initial values defined in this component

$tau\_0 = 8.3$ ms $tau\_r = 50.0$ ms

Equations defined in this component

Calculation of the scaled slow outward current.

$$J\_so = \left(\frac{u * (1.0 - p)}{tau\_0} + \frac{p}{tau\_r} \right) \tag{A.16.13}$$

"slow_inward_current" component

The scaled slow inward current.

Initial values defined in this component

$tau\_si = 44.84$ ms $k = 10.0$

$u\_csi = 0.85$

Equations defined in this component

Calculation of the slow inward current.
$$J\_si = \frac{-w * (1.0 + \tanh(k * (u - u\_csi)))}{2.0 * tau\_si} \tag{A.16.14}$$

"slow_inward_current_w_gate" component

The inactivation-reactivation gate variable for the slow outward current, analogous to the f gate in the BR and LR models.

Initial values defined in this component

$w = 1.0$ $tau\_w\_plus = 667.0$ ms

$tau\_w\_minus = 11.0$ ms

Equations defined in this component

The kinetics of the inactivation-reactivation gate for the slow inward current.
$$\frac{\mathrm{d}(w)}{\mathrm{d}(time)} = \left((1.0 - p) * \frac{(1.0 - w)}{tau\_w\_minus} - \frac{p * w}{tau\_w\_plus} \right) \tag{A.16.15}$$

A.17   1998_HMT

This is a CellML version of the 1998 HMT cardiac contraction model.

Reference: Hunter, P. J., McCulloch, A. D. & ter Keurs, H. E. (1998), 'Modelling the mechanical properties of cardiac muscle', *Progress in Biophysics & Molecular Biology* **69**, 289–331.

"interface" component

We'll use this component as the 'interface" to the model, all other components are hidden via encapsulation in this component. With this model, we expect the intracellular calcium transient to be controlled externally to the model - i.e., the simulator needs to set the value of the Cai variable. Extension ratio should also be controlled externally for non-isometric simulations. Muscle velocity should also be set if you want to include the dynamic contribution of length changes.

Initial values defined in this component

$t = 0.0$ ms $rho0 = 100.0$ ms$^{-1} \cdot$ mM^{-1}

$Cai = 0.0$ mM $rho1 = 0.163$ ms^{-1}

$lambda = 1.0$ $gamma = 2.6$

$Cab\_max = 0.035$ mM $alpha0 = 2.0 \times 10^{-3}$ ms^{-1}

$n\_ref = 4.25$

$p50\_ref = 5.33$

$T\_ref = 125.0 \text{ kPa}$

$beta0 = 1.45$

$beta1 = 1.95$

$beta2 = 0.31$

$alpha1 = 0.033 \text{ ms}^{-1}$

$alpha2 = 2.85 \text{ ms}^{-1}$

$alpha3 = 2.85 \text{ ms}^{-1}$

$A1 = 50.0$

$A2 = 175.0$

$A3 = 175.0$

$a = 0.5$

$velocity = 0.0 \text{ ms}^{-1}$

Equations defined in this component

This is a dummy equation that we simply use to make grabbing the value in CMISS much easier.

$$CaiC = Cai \tag{A.17.1}$$

Another a dummy equation that we simply use to make grabbing the value in CMISS much easier.

$$lambdaC = lambda \tag{A.17.2}$$

Another a dummy equation that we simply use to make grabbing the value in CMISS much easier.

$$velocityC = velocity \tag{A.17.3}$$

"troponin_kinetics" component

The component which defines the kinetics of calcium binding to troponin-C. The binding has been shown to be tension dependent.

Initial values defined in this component

$Cab = 0.0 \text{ mM}$

Equations defined in this component

The kinetics of the tension-dependent calcium binding to troponin-C.

$$\frac{\mathrm{d}(Cab)}{\mathrm{d}(t)} = (rho0 * Cai * (Cab\_max - Cab) - rho1 * Cab * (1.0 - TTo)) \tag{A.17.4}$$

Calculate the tension dependent factor for calcium binding.

$$TTo = \begin{cases} \frac{T}{gamma*To}; & \text{if } To > 1.0 \times 10^{-8}, \\ 0.0 & \text{otherwise.} \end{cases} \tag{A.17.5}$$

"tropomyosin_kinetics" component

This component defines the kinetics of the length-dependent actin availability.

Initial values defined in this component

$z = 0.0$

Equations defined in this component

The kinetics of actin availability, z.

$$\frac{\mathrm{d}(z)}{\mathrm{d}(t)} = alpha0 * \left(\left(\frac{Cab}{C50} * Cab\_norm \right)^n * (1.0 - z) - z \right) \tag{A.17.6}$$

One of the Hill parameters used to fit the relationship between z and Cab at given sarcomere lengths, and defines part of the length dependence of the model.

$$n = n\_ref * (1.0 + beta1 * (lambda - 1.0)) \tag{A.17.7}$$

One of the Hill parameters used to fit the relationship between z and Cab at given sarcomere lengths, and defines part of the length dependence of the model.

$$p50 = p50\_ref * (1.0 + beta2 * (lambda - 1.0)) \tag{A.17.8}$$

The value of Cab that is required to achieve 50% availability, i.e., z = 0.5.

$$C50 = (10.0)^{(3.0 - p50)} \tag{A.17.9}$$

Normalised value of bound calcium.

$$Cab\_norm = \frac{Cab}{Cab\_max} \tag{A.17.10}$$

"isometric_tension" component

The component which defines the isometric tension.

Equations defined in this component

Calculation of the isometric tension.

$$To = T\_ref * (1.0 + beta0 * (lambda - 1.0)) * z \tag{A.17.11}$$

"dynamic_tension" component

We use the ODE equivalent to the fading memory hereditary (thanks Steve). The muscle velocity should be set outside of here, and will be controlled by the simulation environment.

Initial values defined in this component

$Q1 = 0.0$ ms $Q3 = 0.0$ ms

$Q2 = 0.0$ ms

Equations defined in this component

Calculation of the dynamic tension.

$$T = To * \frac{(1.0 + a * Q)}{(1.0 - Q)} \tag{A.17.12}$$

Calculate the value of the hereditary integral, with three rate constants.

$$Q = (Q1 + Q2 + Q3) \tag{A.17.13}$$

Calculation of the contribution of the first time constant to the hereditary integral, in the ODE form.

$$\frac{\mathrm{d}(Q1)}{\mathrm{d}(t)} = (A1 * velocity - alpha1 * Q1) \tag{A.17.14}$$

Calculation of the contribution of the second time constant to the hereditary integral, in the ODE form.

$$\frac{\mathrm{d}(Q2)}{\mathrm{d}(t)} = (A2 * velocity - alpha2 * Q2) \tag{A.17.15}$$

Calculation of the contribution of the third time constant to the hereditary integral, in the ODE form.

$$\frac{\mathrm{d}(Q3)}{\mathrm{d}(t)} = (A3 * velocity - alpha3 * Q3) \tag{A.17.16}$$

A.18   jafri_rice_winslow_model_1998

This is the CellML description of Jafri, Rice and Winslow's mathematical model for calcium regulation in the ventricular myocyte. It is based on an accurate model of the membrane currents and adds a more sophisticated model of calcium handling. The JRW model is based on the LR-II model for ventricular action potentials, with several modifications.

Reference: Jafri, M. S., Rice, J. J. & Winslow, R. L. (1998), 'Cardiac Ca2+ Dynamics: The Roles of Ryanodine Receptor Adaptation and Sarcoplasmic Reticulum Load', *Biophysical Journal* **74**, 1149–1168.

"environment" component

"membrane" component

The main component of the model which defines the action potential.

Initial values defined in this component

$V = -84.1638 \, \mathrm{mV}$ $F = 9.6845 \times 10^4 \, \mathrm{nC} \cdot \mathrm{nmol}^{-1}$

$R = 8.3145 \times 10^3 \, \mathrm{pJ} \cdot \mathrm{nmol}^{-1} \cdot \mathrm{K}^{-1}$ $Cm = 0.01 \, \mu\mathrm{F} \cdot \mathrm{mm}^{-2}$

$T = 310.0 \, \mathrm{K}$

Equations defined in this component

The kinetics of the transmembrane potential, defined as the sum of all the sarcolemmal currents and an applied stimulus current.

$$\frac{\mathrm{d}(V)}{\mathrm{d}(time)} = \Bigg[I\_stim - \big(i\_Na + i\_Ca\_L\_Ca + i\_Ca\_L\_K + i\_K + i\_NaCa + i\_K1 + $$

$$i\_Kp + i\_p\_Ca + i\_Na\_b + i\_Ca\_b + i\_NaK + i\_ns\_Ca \big) \Bigg] \Big/ Cm \tag{A.18.1}$$

This is a dummy equation that we simply use to make grabbing the value in CMISS much easier.

$$IStimC = I\_stim \tag{A.18.2}$$

"fast_sodium_current" component

The fast sodium current component contains the differential equations governing the influx of sodium ions through the cell surface membrane into the cell.

Initial values defined in this component

$g\_Na = 0.128 \text{ mS} \cdot \text{mm}^{-2}$

Equations defined in this component

Calculation of the fast sodium current using the three Hodkin-Huxley type voltage-dependent gating variables m, h, and j.

$$i\_Na = g\_Na * (m)^{3.0} * h * j * (V - E\_Na) \tag{A.18.3}$$

The sodium reversal potential.

$$E\_Na = \frac{R * T}{F} * \ln\left(\frac{Nao}{Nai}\right) \tag{A.18.4}$$

"fast_sodium_current_m_gate" component

The voltage-dependent activation gate for the fast sodium current - the m gate.

Initial values defined in this component

$m = 0.0328302$

Equations defined in this component

The opening rate of the m gate.

$$alpha\_m = \frac{0.32 * (V + 47.13)}{(1.0 - \exp(-0.1 * (V + 47.13)))} \tag{A.18.5}$$

The closing rate of the m gate.

$$beta\_m = 0.08 * \exp\left(\frac{-V}{11.0}\right) \tag{A.18.6}$$

The kinetics of the m gate.

$$\frac{\mathrm{d}(m)}{\mathrm{d}(time)} = (alpha\_m * (1.0 - m) - beta\_m * m) \tag{A.18.7}$$

"fast_sodium_current_h_gate" component

The voltage-dependent inactivation gate for the fast sodium current - the h gate.

Initial values defined in this component

$h = 0.988354$

Equations defined in this component

The opening rate of the h gate.

$$alpha\_h = \begin{cases} 0.135 * \exp\left(\frac{(80.0+V)}{-6.8}\right); & \text{if } V < -40.0, \\ 0.0 & \text{otherwise.} \end{cases} \tag{A.18.8}$$

The closing rate of the h gate.

$$beta\_h = \begin{cases} (3.56 * \exp(0.079 * V) + 310000.0 * \exp(0.35 * V)); & \text{if } V < -40.0, \\ \frac{1.0}{0.13*\left(1.0+\exp\left(\frac{(V+10.66)}{-11.1}\right)\right)} & \text{otherwise.} \end{cases} \tag{A.18.9}$$

The kinetics of the h gate.

$$\frac{d(h)}{d(time)} = (alpha\_h * (1.0 - h) - beta\_h * h) \tag{A.18.10}$$

"fast_sodium_current_j_gate" component

The voltage-dependent slow inactivation gate for the fast sodium current - the j gate.

Initial values defined in this component

$j = 0.992540$

Equations defined in this component

The opening rate of the j gate.

$$alpha\_j = \begin{cases} (-127140.0 * \exp(0.2444 * V) - 0.00003474 * \exp(-0.04391 * V)) \\ \qquad\qquad\qquad * \frac{(V+37.78)}{(1.0+\exp(0.311*(V+79.23)))}; & \text{if } V < -40.0, \\ 0.0 & \text{otherwise.} \end{cases} \tag{A.18.11}$$

The closing rate of the j gate.

$$beta\_j = \begin{cases} 0.1212 * \frac{\exp(-0.01052*V)}{(1.0+\exp(-0.1378*(V+40.14)))}; & \text{if } V < -40.0, \\ 0.3 * \frac{\exp(-0.0000002535*V)}{(1.0+\exp(-0.1*(V+32.0)))} & \text{otherwise.} \end{cases} \tag{A.18.12}$$

The kinetics of the j gate.

$$\frac{d(j)}{d(time)} = (alpha\_j * (1.0 - j) - beta\_j * j) \tag{A.18.13}$$

"L_type_Ca_channel" component

The JWR model creates a new mathematical model to describe the L-type calcium channel that is based on the experimentally observed mode-switching behaviour of the channel. Inactivation occurs as calcium ion binding

induces the channel to switch (from mode normal) to a mode in which transitions to open states are extremely slow (mode Ca). The channel has one voltage inactivation gate, y. As well as Ca, the channel is assumed permeable to K ions also.

Initial values defined in this component

$P\_Ca = 33.75 \times 10^{-6}$ mm $\cdot$ ms^{-1} $omega = 0.01$ ms^{-1}

$P\_K = 1.0 \times 10^{-9}$ mm $\cdot$ ms^{-1} $C0 = 0.997208$

$i\_Ca\_L\_Ca\_half = -4.58 \times 10^{-3}$ μA $\cdot$ mm^{-2} $C1 = 6.38897 \times 10^{-5}$

$O = 9.84546 \times 10^{-21}$ $C2 = 1.535 \times 10^{-9}$

$O\_Ca = 0.0$ $C3 = 1.63909 \times 10^{-14}$

$a = 2.0$ $C4 = 6.56337 \times 10^{-20}$

$b = 2.0$ $C\_Ca0 = 2.72826 \times 10^{-3}$

$g = 2.0$ ms^{-1} $C\_Ca1 = 6.99215 \times 10^{-7}$

$f = 0.3$ ms^{-1} $C\_Ca2 = 6.71989 \times 10^{-11}$

$g_- = 0.0$ ms^{-1} $C\_Ca3 = 2.87031 \times 10^{-15}$

$f_- = 0.0$ ms^{-1} $C\_Ca4 = 4.59752 \times 10^{-20}$

Equations defined in this component

Calculation of the calcium current component of the total channel current, given as the maximal current multiplied by the voltage-dependent inactivation gate and the open probability of the channel based on the mode-switching model.

$$i\_Ca\_L\_Ca = i\_Ca\_L\_Ca\_max * y * (O + O\_Ca) \tag{A.18.14}$$

Calculation of the potassium current component of the total channel current.

$$i\_Ca\_L\_K = p\_k * y * (O + O\_Ca) * \frac{V * (F)^{2.0}}{R * T} * \frac{\left(Ki * \exp\left(\frac{V*F}{R*T}\right) - Ko\right)}{\left(\exp\left(\frac{V*F}{R*T}\right) - 1.0\right)} \tag{A.18.15}$$

The potassium permeability of the channel, which depends on the calcium current component.

$$p\_k = \frac{P\_K}{\left(1.0 + \frac{i\_Ca\_L\_Ca\_max}{i\_Ca\_L\_Ca\_half}\right)} \tag{A.18.16}$$

The maximal calcium current through the channel.

$$i\_Ca\_L\_Ca\_max = P\_Ca * 4.0 * \frac{V * (F)^{2.0}}{R * T} * \frac{\left(0.001 * \exp\left(2.0 * V * \frac{F}{R*T}\right) - 0.341 * Cao\right)}{\left(\exp\left(2.0 * V * \frac{F}{R*T}\right) - 1.0\right)} \tag{A.18.17}$$

Rate constants for state changes in mode normal.

$$alpha = 0.4 * \exp\left(\frac{(V + 12.0)}{10.0}\right) \tag{A.18.18}$$

$$beta = 0.05 * \exp\left(\frac{(V + 12.0)}{-13.0}\right) \tag{A.18.19}$$

Rate constants for state changes in mode Ca (corresponding to alpha-prime and beta-prime in the JRW paper).

$$alpha\_a = alpha * a \tag{A.18.20}$$

$$beta\_b = \frac{beta}{b} \tag{A.18.21}$$

Rate constant for switching between mode normal and mode Ca.

$$gamma = 0.1875 * Ca\_SS \tag{A.18.22}$$

The kinetics of the state transitions in mode normal. In the normal mode, the calcium channel is able to make the transition to the open, conducting state (O) from the closed state (C) at a normal rate.

$$\frac{\mathrm{d}(C0)}{\mathrm{d}(time)} = ((beta * C1 + omega * C\_Ca0) - (4.0 * alpha + gamma) * C0) \tag{A.18.23}$$

$$\frac{\mathrm{d}(C1)}{\mathrm{d}(time)} = \left(4.0 * alpha * C0 + 2.0 * beta * C2 + \frac{omega}{b} * C\_Ca1\right)$$
$$- (beta + 3.0 * alpha + gamma * a) * C1 \tag{A.18.24}$$

$$\frac{\mathrm{d}(C2)}{\mathrm{d}(time)} = \left(3.0 * alpha * C1 + 3.0 * beta * C3 + \frac{omega}{(b)^{2.0}} * C\_Ca2\right)$$
$$- \left(beta * 2.0 + 2.0 * alpha + gamma * (a)^{2.0}\right) * C2 \tag{A.18.25}$$

$$\frac{\mathrm{d}(C3)}{\mathrm{d}(time)} = \left(2.0 * alpha * C2 + 4.0 * beta * C4 + \frac{omega}{(b)^{3.0}} * C\_Ca3\right)$$
$$- \left(beta * 3.0 + alpha + gamma * (a)^{3.0}\right) * C3 \tag{A.18.26}$$

$$\frac{\mathrm{d}(C4)}{\mathrm{d}(time)} = \left(alpha * C3 + g * O + \frac{omega}{(b)^{4.0}} * C\_Ca4\right)$$
$$- \left(beta * 4.0 + f + gamma * (a)^{4.0}\right) * C4 \tag{A.18.27}$$

$$\frac{\mathrm{d}(O)}{\mathrm{d}(time)} = (f * C4 - g * O) \tag{A.18.28}$$

The kinetics of the state transitions in mode Ca. Calcium binding to the Ca channel induces a conformational change from normal mode to mode Ca. This effectively inhibits the conduction of calcium ions because in mode Ca, the calcium channel makes the transition to the open, conducting state (O) extremely slowly.

$$\frac{\mathrm{d}(C\_Ca0)}{\mathrm{d}(time)} = ((beta\_b * C\_Ca1 + gamma * C\_Ca0) - (4.0 * alpha\_a + omega) * C\_Ca0) \tag{A.18.29}$$

$$\frac{\mathrm{d}(C\_Ca1)}{\mathrm{d}(time)} = (4.0 * alpha\_a * C\_Ca0 + 2.0 * beta\_b * C\_Ca2 + gamma * a * C1)$$
$$- \left(beta\_b + 3.0 * alpha\_a + \frac{omega}{b}\right) * C\_Ca1 \tag{A.18.30}$$

$$\frac{\mathrm{d}(C\_Ca2)}{\mathrm{d}(time)} = \left(3.0 * alpha\_a * C\_Ca1 + 3.0 * beta\_b * C\_Ca3 + gamma * (a)^{2.0} * C2\right)$$
$$- \left(beta\_b * 2.0 + 2.0 * alpha\_a + \frac{omega}{(b)^{2.0}}\right) * C\_Ca2 \tag{A.18.31}$$

$$\frac{\mathrm{d}(C\_Ca3)}{\mathrm{d}(time)} = \left(2.0 * alpha\_a * C\_Ca2 + 4.0 * beta\_b * C\_Ca4 + gamma * (a)^{3.0} * C3\right)$$

$$- \left(beta\_b * 3.0 + alpha\_a + \frac{omega}{(b)^{3.0}}\right) * C\_Ca3 \quad \text{(A.18.32)}$$

$$\frac{\mathrm{d}(C\_Ca4)}{\mathrm{d}(time)} = \left(alpha\_a * C\_Ca3 + g\_ * O\_Ca + gamma * (a)^{4.0} * C4\right)$$

$$- \left(beta\_b * 4.0 + f\_ + \frac{omega}{(b)^{4.0}}\right) * C\_Ca4 \quad \text{(A.18.33)}$$

$$\frac{\mathrm{d}(O\_Ca)}{\mathrm{d}(time)} = (f\_ * C\_Ca4 - g\_ * O\_Ca) \quad \text{(A.18.34)}$$

"L_type_Ca_channel_y_gate" component

The voltage-dependent inactivation gate for the L-type calcium channel - the y gate.

Initial values defined in this component
$y = 0.998983$

Equations defined in this component

The kinetics of the y gate.

$$\frac{\mathrm{d}(y)}{\mathrm{d}(time)} = \frac{(y\_infinity - y)}{tau\_y} \quad \text{(A.18.35)}$$

$$y\_infinity = \left(\frac{1.0}{\left(1.0 + \exp\left(\frac{(V+55.0)}{7.5}\right)\right)} + \frac{0.1}{\left(1.0 + \exp\left(\frac{(-V+21.0)}{6.0}\right)\right)}\right) \quad \text{(A.18.36)}$$

$$tau\_y = \left(20.0 + \frac{600.0}{\left(1.0 + \exp\left(\frac{(V+30.0)}{9.5}\right)\right)}\right) \quad \text{(A.18.37)}$$

"time_dependent_potassium_current" component

The time-dependent potassium current has an X^2 dependence on it's activation gate, and an Xi inactivation gate. This channel is also assumed permeable to sodium ions.

Initial values defined in this component
$g\_K\_max = 0.001128 \, \mathrm{mS \cdot mm^{-2}}$ $\qquad\qquad$ $P\_NaK = 0.01833$

Equations defined in this component

Calculation of the maximal channel conductance, dependent on extracellular potassium concentration.

$$g\_K = g\_K\_max * \sqrt{\frac{Ko}{5.4}} \quad \text{(A.18.38)}$$

The reversal potential of the channel.

$$E\_K = \frac{R*T}{F} * \ln\left(\frac{(Ko + P\_NaK * Nao)}{(Ki + P\_NaK * Nai)}\right) \quad \text{(A.18.39)}$$

Calculation of the time-dependent potassium current.

$$i\_K = g\_K * Xi * (X)^{2.0} * (V - E\_K) \quad \text{(A.18.40)}$$

"time_dependent_potassium_current_X_gate" component

The voltage- and time-dependent activation gate for the time-dependent potassium current - the X gate.

Initial values defined in this component

X = 0.000928836

Equations defined in this component

The opening rate of the X gate.

$$alpha\_X = 0.0000719 * \frac{(V + 30.0)}{(1.0 - \exp(-0.148 * (V + 30.0)))} \quad \text{(A.18.41)}$$

The closing rate of the X gate.

$$beta\_X = 0.000131 * \frac{(V + 30.0)}{(-1.0 + \exp(0.0687 * (V + 30.0)))} \quad \text{(A.18.42)}$$

The kinetics of the X gate.

$$\frac{d(X)}{d(time)} = (alpha\_X * (1.0 - X) - beta\_X * X) \quad \text{(A.18.43)}$$

"time_dependent_potassium_current_Xi_gate" component

The time-independent inactivation gate for the time-dependent potassium channel.

Equations defined in this component

Xi is the inward rectification parameter and is given by the following equation.

$$Xi = \frac{1.0}{\left(1.0 + \exp\left(\frac{(V - 56.26)}{32.1}\right)\right)} \quad \text{(A.18.44)}$$

"time_independent_potassium_current" component

The time-independent potassium current.

Initial values defined in this component

g_K1_max = 7.5×10^{-3} mS · mm^{-2}

Equations defined in this component

Calculation of the maximal channel conductance, dependent on extracellular potassium concentration.

$$g\_K1 = g\_K1\_max * \sqrt{\frac{Ko}{5.4}} \tag{A.18.45}$$

The following equation calculates the reversal potential of the time-independent potassium current.

$$E\_K1 = \frac{R * T}{F} * \ln\left(\frac{Ko}{Ki}\right) \tag{A.18.46}$$

Calculate the current.

$$i\_K1 = g\_K1 * K1\_infinity * (V - E\_K1) \tag{A.18.47}$$

"time_independent_potassium_current_K1_gate" component

The time constants for the K1 gate are small enough that the gating variable can be approximated with it's steady-state value.

Equations defined in this component

The opening rate of the K1 gate.

$$alpha\_K1 = \frac{1.02}{(1.0 + \exp\left(0.2385 * ((V - E\_K1) - 59.215)\right))} \tag{A.18.48}$$

The closing rate of the K1 gate.

$$beta\_K1 = \frac{(0.49124 * \exp\left(0.08032 * ((V + 5.476) - E\_K1)\right) + \exp\left(0.06175 * (V - (E\_K1 + 594.31))\right))}{(1.0 + \exp\left(-0.5143 * ((V - E\_K1) + 4.753)\right))} \tag{A.18.49}$$

The steady-state approximation for the K1 gating kinetics.

$$K1\_infinity = \frac{alpha\_K1}{(alpha\_K1 + beta\_K1)} \tag{A.18.50}$$

"plateau_potassium_current" component

The plateau potassium current component contains the equations which describe the contribution of a time independent [K]o-insensitive channel at plateau potentials.

Initial values defined in this component

$g\_Kp = 8.28 \times 10^{-5} \text{ mS} \cdot \text{mm}^{-2}$

Equations defined in this component

The channel's reversal potential.

$$E\_Kp = E\_K1 \tag{A.18.51}$$

The activation variable.

$$Kp = \frac{1.0}{\left(1.0 + \exp\left(\frac{(7.488-V)}{5.98}\right)\right)} \tag{A.18.52}$$

Calculation of the plateau potassium current.

$$i\_Kp = g\_Kp * Kp * (V - E\_Kp) \tag{A.18.53}$$

"Na_Ca_exchanger" component

The Na/Ca exchanger component describes how a protein molecule in the cell surface membrane transports Na ions into the cytosol and exports Ca ions into the extracellular volume, in a ratio of 3:1 respectively.

Initial values defined in this component

$k\_NaCa = 50.0\ \mu A \cdot mm^{-2}$ $k\_sat = 0.1$

$K\_mNa = 87.5\ mM$ $eta = 0.35$

$K\_mCa = 1.38\ mM$

Equations defined in this component

Calculation of the Na/Ca exchanger current.

$$i\_NaCa = k\_NaCa * \frac{1.0}{\left((K\_mNa)^{3.0} + (Nao)^{3.0}\right)} * \frac{1.0}{(K\_mCa + Cao)}$$
$$* \frac{1.0}{\left(1.0 + k\_sat * \exp\left((eta - 1.0) * V * \frac{F}{R*T}\right)\right)}$$
$$* \left(\exp\left(eta * V * \frac{F}{R*T}\right) * (Nai)^{3.0} * Cao - \exp\left((eta - 1.0) * V * \frac{F}{R*T}\right) * (Nao)^{3.0} * Cai\right) \tag{A.18.54}$$

"sarcolemmal_calcium_pump" component

The sarcolemmal calcium pump is an additional mechanism for removing Ca ions from the myoplasm to help maintain a low intracellular calcium concentration when at rest.

Initial values defined in this component

$K\_mpCa = 0.5 \times 10^{-3}\ mM$ $I\_pCa = 1.15 \times 10^{-2}\ \mu A \cdot mm^{-2}$

Equations defined in this component

The calcium pump current.

$$i\_p\_Ca = I\_pCa * \frac{Cai}{(K\_mpCa + Cai)} \tag{A.18.55}$$

"sodium_background_current" component

The sodium background current is a time-independent diffusion of Na ions down their electrochemical gradient, through the cell surface membrane into the cytosol.

Initial values defined in this component

$g\_Nab = 1.41 \times 10^{-5}$ mS $\cdot$ mm^{-2}

Equations defined in this component

The reversal potential for the background sodium channel.
$$E\_NaN = E\_Na \tag{A.18.56}$$

Calculation of the background sodium current.
$$i\_Na\_b = g\_Nab * (V - E\_NaN) \tag{A.18.57}$$

"calcium_background_current" component

The calcium background current describes a time-independent diffusion of Ca ions down their electrochemical gradient through the cell surface membrane into the cytosol. However, calcium is not allowed to accumulate to high intracellular concentrations. This influx is balanced by the Ca ion extrusion through the Na-Ca exchanger and the sarcolemmal Ca pump.

Initial values defined in this component

$g\_Cab = 6.032 \times 10^{-5}$ mS $\cdot$ mm^{-2}

Equations defined in this component

The reversal potential for the background calcium current.
$$E\_CaN = \frac{R * T}{2.0 * F} * \ln\left(\frac{Cao}{Cai}\right) \tag{A.18.58}$$

Calculation of the background calcium current.
$$i\_Ca\_b = g\_Cab * (V - E\_CaN) \tag{A.18.59}$$

"sodium_potassium_pump" component

The sodium potassium pump is an active protein in the cell membrane which couples the free energy released by the hydrolysis of ATP to the movement of Na and K ions against their electrochemical gradients through the cell membrane.

Initial values defined in this component

$I\_NaK = 0.013$ μA $\cdot$ mm^{-2} $\qquad\qquad$ $K\_mKo = 1.5$ mM

$K\_mNai = 10.0$ mM

Equations defined in this component

Calculation of the Na/K pump current.

$$f\_NaK = \frac{1.0}{\left(\left(1.0 + 0.1245 * \exp\left(\frac{-0.1*V*F}{R*T}\right)\right) + 0.0365 * sigma * \exp\left(\frac{-V*F}{R*T}\right)\right)} \tag{A.18.60}$$

$$sigma = \frac{1.0}{7.0} * \left(\exp\left(\frac{Nao}{67.3}\right) - 1.0\right) \tag{A.18.61}$$

$$i\_NaK = I\_NaK * f\_NaK * \frac{1.0}{\left(1.0 + \left(\frac{K\_mNai}{Nai}\right)^{1.5}\right)} * \frac{Ko}{(Ko + K\_mKo)} \tag{A.18.62}$$

"non_specific_calcium_activated_current" component

The nonspecific calcium activated current describes a channel which is activated by calcium ions, but is permeable to only sodium and potassium ions.

Initial values defined in this component

$K\_m\_ns\_Ca = 1.2 \times 10^{-3}$ mM $\qquad\qquad P\_ns\_Ca = 1.75 \times 10^{-9}$ mm $\cdot$ ms^{-1}

Equations defined in this component

The reversal potential of the channel.

$$EnsCa = \frac{R*T}{F} * \ln\left(\frac{(Ko + Nao)}{(Ki + Nai)}\right) \tag{A.18.63}$$

The potential offset for the channel.

$$VnsCa = (V - EnsCa) \tag{A.18.64}$$

The sodium component of the channel's current.

$$i\_ns\_Na = I\_ns\_Na * \frac{1.0}{\left(1.0 + \left(\frac{K\_m\_ns\_Ca}{Cai}\right)^{3.0}\right)} \tag{A.18.65}$$

The potassium component of the channel's current.

$$i\_ns\_K = I\_ns\_K * \frac{1.0}{\left(1.0 + \left(\frac{K\_m\_ns\_Ca}{Cai}\right)^{3.0}\right)} \tag{A.18.66}$$

The total nonspecific calcium activated current.

$$i\_ns\_Ca = (i\_ns\_Na + i\_ns\_K) \tag{A.18.67}$$

The maximal sodium component current.

$$I\_ns\_Na = P\_ns\_Ca * (1.0)^{2.0} * \frac{VnsCa * (F)^{2.0}}{R*T} * \frac{\left(0.75 * Nai * \exp\left(\frac{VnsCa*F}{R*T}\right) - 0.75 * Nao\right)}{\left(\exp\left(\frac{VnsCa*F}{R*T}\right) - 1.0\right)} \tag{A.18.68}$$

The maximal potassium component current.

$$I\_ns\_K = P\_ns\_Ca * (1.0)^{2.0} * \frac{VnsCa * (F)^{2.0}}{R*T} * \frac{\left(0.75 * Ki * \exp\left(\frac{VnsCa*F}{R*T}\right) - 0.75 * Ko\right)}{\left(\exp\left(\frac{VnsCa*F}{R*T}\right) - 1.0\right)} \tag{A.18.69}$$

"calcium_subsystem" component

In the JRW model, subcellular calcium regulatory mechanisms are described in detail. There are six calcium fluxes to consider; J_rel, J_leak, J_up, J_tr, J_xfer and J_trpn. In addition, three membrane current fluxes are also necessary for the formulation of calcium regulation; i_p_Ca, i_Ca_L_Ca and i_NaCa.

Initial values defined in this component

$Cai = 9.94893 \times 10^{-11}$ mM

$Ca\_SS = 1.36058 \times 10^{-4}$ mM

$Am = 546.69$ mm^{-1}

$V\_myo = 0.92$

$P\_O1 = 1.19168 \times 10^{-3}$

$P\_O2 = 6.30613 \times 10^{-9}$

$P\_C1 = 0.762527$

$P\_C2 = 0.236283$

$v1 = 1.8$ ms^{-1}

$v2 = 0.58 \times 10^{-4}$ ms^{-1}

$v3 = 1.8 \times 10^{-3}$ mM · ms^{-1}

$nCa = 4.0$

$mCa = 3.0$

$k\_a\_plus = 1.215 \times 10^{10}$ mM^{-4} · ms^{-1}

$k\_a\_minus = 0.1425$ ms^{-1}

$k\_b\_plus = 4.05 \times 10^{7}$ mM^{-3} · ms^{-1}

$k\_b\_minus = 1.930$ ms^{-1}

$k\_c\_plus = 0.018$ ms^{-1}

$k\_c\_minus = 0.0008$ ms^{-1}

$k\_htrpn\_plus = 20.0$ mM^{-1} · ms^{-1}

$k\_htrpn\_minus = 0.066 \times 10^{-3}$ ms^{-1}

$k\_ltrpn\_plus = 40.0$ mM^{-1} · ms^{-1}

$k\_ltrpn\_minus = 0.04$ ms^{-1}

$tau\_tr = 34.48$ ms

$Ca\_JSR = 1.17504$ mM

$Ca\_NSR = 1.243891$ mM

$K\_mup = 0.5 \times 10^{-3}$ mM

$K\_mCMDN = 2.38 \times 10^{-3}$ mM

$K\_mCSQN = 0.8$ mM

$tau\_xfer = 3.125$ ms

$HTRPN\_tot = 0.14$ mM

$LTRPN\_tot = 0.07$ mM

$HTRPNCa = 0.13598$ mM

$LTRPNCa = 0.00635$ mM

$CSQN\_tot = 15.0$ mM

$CMDN\_tot = 0.05$ mM

Equations defined in this component

Calculate some volume fractions as proportions of the total myoplasmic volume.

$$V\_SS = 5.828 \times 10^{-5} * V\_myo \tag{A.18.70}$$

$$V\_NSR = 0.081 * V\_myo \tag{A.18.71}$$

$$V\_JSR = 0.00464 * V\_myo \tag{A.18.72}$$

The calcium release flux from the JSR into the restricted subspace is governed by the fraction of RyR channels in an open state.

$$J\_rel = v1 * RyR\_open * (Ca\_JSR - Ca\_SS) \tag{A.18.73}$$

The "open" RyR's are those P_O1 and P_O2 states.

$$RyR\_open = (P\_O1 + P\_O2) \tag{A.18.74}$$

The kinetic equations governing the transitions between the four states used to model the RyR's.

$$\frac{\mathrm{d}(P\_C1)}{\mathrm{d}(time)} = \Big(-k\_a\_plus * (Ca\_SS)^{nCa} * P\_C1 + k\_a\_minus * P\_O1\Big) \tag{A.18.75}$$

$$\frac{\mathrm{d}(P\_O1)}{\mathrm{d}(time)} = \Big[k\_a\_plus * (Ca\_SS)^{nCa} * P\_C1$$

$$- \Big(k\_a\_minus * P\_O1 + k\_b\_plus * (Ca\_SS)^{mCa} * P\_O1 + k\_c\_plus * P\_O1\Big)\Big]$$

$$+ k\_b\_minus * P\_O2 + k\_c\_minus * P\_C2 \tag{A.18.76}$$

$$\frac{\mathrm{d}(P\_O2)}{\mathrm{d}(time)} = \Big(k\_b\_plus * (Ca\_SS)^{mCa} * P\_O1 - k\_b\_minus * P\_O2\Big) \tag{A.18.77}$$

$$\frac{\mathrm{d}(P\_C2)}{\mathrm{d}(time)} = (k\_c\_plus * P\_O1 - k\_c\_minus * P\_C2) \tag{A.18.78}$$

Calculate the leakage flux from the NSR into the myoplasm.

$$J\_leak = v2 * (Ca\_NSR - Cai) \tag{A.18.79}$$

Calculate the uptake flux into the NSR from the myoplasm.

$$J\_up = v3 * \frac{(Cai)^{2.0}}{\Big((K\_mup)^{2.0} + (Cai)^{2.0}\Big)} \tag{A.18.80}$$

Calculate the translocation flux between the uptake (NSR) and release (JSR) stores.

$$J\_tr = \frac{(Ca\_NSR - Ca\_JSR)}{tau\_tr} \tag{A.18.81}$$

Calculate the calcium flux from the diffusion of calcium out of the restricted subspace into the myoplasm.

$$J\_xfer = \frac{(Ca\_SS - Cai)}{tau\_xfer} \tag{A.18.82}$$

The kinetics of calcium binding to the myoplasm buffer troponin - both high and low affinity binding sites.

$$J\_htrpn = (k\_htrpn\_plus * Cai * (HTRPN\_tot - HTRPNCa) - k\_htrpn\_minus * HTRPNCa) \tag{A.18.83}$$

$$J\_ltrpn = (k\_ltrpn\_plus * Cai * (LTRPN\_tot - LTRPNCa) - k\_ltrpn\_minus * LTRPNCa) \tag{A.18.84}$$

$$J\_trpn = (J\_htrpn + J\_ltrpn) \tag{A.18.85}$$

Keep track of the concentration of calcium ions bound to high and low affinity troponin binding sites.

$$\frac{\mathrm{d}(HTRPNCa)}{\mathrm{d}(time)} = J\_htrpn \tag{A.18.86}$$

$$\frac{\mathrm{d}(LTRPNCa)}{\mathrm{d}(time)} = J\_ltrpn \tag{A.18.87}$$

Calcium is buffered by calmodulin (CMDN) in the subspace and myoplasm, and by calsequestrin (CSQN) in the JSR. These are fast buffers and their effect is modelled using the rapid buffering approximation.

$$Bi = \frac{1.0}{\Big(1.0 + \frac{CMDN\_tot * K\_mCMDN}{((K\_mCMDN + Cai))^{2.0}}\Big)} \tag{A.18.88}$$

$$B\_SS = \frac{1.0}{\left(1.0 + \frac{CMDN\_tot * K\_mCMDN}{((K\_mCMDN + Ca\_SS))^{2.0}}\right)} \tag{A.18.89}$$

$$B\_JSR = \frac{1.0}{\left(1.0 + \frac{CSQN\_tot * K\_mCSQN}{((K\_mCSQN + Ca\_JSR))^{2.0}}\right)} \tag{A.18.90}$$

The kinetics of the calcium ion concentration changes in the various compartments of the model.

$$\frac{d(Cai)}{d(time)} = Bi * \Bigg[(J\_leak + J\_xfer)$$
$$- \left(J\_up + J\_trpn + ((i\_Ca\_b - 2.0 * i\_NaCa) + i\_p\_Ca) * \frac{Am}{2.0 * V\_myo * F} \right) \Bigg] \tag{A.18.91}$$

$$\frac{d(Ca\_SS)}{d(time)} = B\_SS * \left(\left(J\_rel * \frac{V\_JSR}{V\_SS} - J\_xfer * \frac{V\_myo}{V\_SS} \right) - i\_Ca\_L\_Ca * \frac{Am}{2.0 * V\_SS * F} \right) \tag{A.18.92}$$

$$\frac{d(Ca\_JSR)}{d(time)} = B\_JSR * (J\_tr - J\_rel) \tag{A.18.93}$$

$$\frac{d(Ca\_NSR)}{d(time)} = \left((J\_up - J\_leak) * \frac{V\_myo}{V\_NSR} - J\_tr * \frac{V\_JSR}{V\_NSR} \right) \tag{A.18.94}$$

"ionic_concentrations" component

The descriptions of the rate of change of [Na]i and [K]i are the same as the LR-II model.

Initial values defined in this component

$Nai = 10.2042$ mM $\qquad\qquad Ko = 5.4$ mM

$Nao = 140.0$ mM $\qquad\qquad Cao = 1.8$ mM

$Ki = 143.727$ mM

Equations defined in this component

The rate of change of intracellular sodium ion concentration.

$$\frac{d(Nai)}{d(time)} = -(i\_Na + i\_Na\_b + i\_ns\_Na + i\_NaCa * 3.0 + i\_NaK * 3.0) * \frac{Am}{V\_myo * F} \tag{A.18.95}$$

The rate of change of intracellular potassium ion concentration.

$$\frac{d(Ki)}{d(time)} = -(i\_Ca\_L\_K + i\_K + i\_K1 + i\_Kp + i\_ns\_K + -i\_NaK * 2.0) * \frac{Am}{V\_myo * F} \tag{A.18.96}$$

The rate of change of extracellular potassium ion concentration.

$$\frac{d(Ko)}{d(time)} = (i\_Ca\_L\_K + i\_K + i\_K1 + i\_Kp + i\_ns\_K + -i\_NaK * 2.0) * \frac{Am}{V\_myo * F} \tag{A.18.97}$$

A.19   nash_1998

This is a CellML version of the steady-state length-tension-calcium relationship described by Martyn Nash in his thesis.

"interface" component

We'll use this component as the "interface" to the model, all other components are hidden via encapsulation in this component. With this model, we expect the extension ratio to be controlled externally for non-isometric simulations.

Initial values defined in this component

$time = 0.0$ ms $c50 = 0.5$ mM

$lambda = 1.0$ $h = 3.0$

$Ca\_max = 1.0$ mM $T\_ref = 100.0$ kPa

$beta = 1.45$

Equations defined in this component

A dummy equation that we simply use to make grabbing the value in CMISS much easier.
$$lambdaC = lambda \tag{A.19.1}$$

We need a dummy ODE to establish time as the bound variable to get things to work properly with CMISS.
$$\frac{\mathrm{d}(Vm)}{\mathrm{d}(time)} = 0.0 \tag{A.19.2}$$

"active_contraction" component

Initial values defined in this component

$T = 0.0$ kPa $Ca\_actn = 0.0$ mM

Equations defined in this component

The kinetics of the active tension development using the steady-state description from the Nash model.
$$T = \frac{Ca\_max * (Ca\_actn)^h}{\left((Ca\_actn)^h + (c50)^h\right)} * T\_ref * (1.0 + beta * (lambda - 1.0)) \tag{A.19.3}$$

Here we define the calcium activation transient which simply goes from 0 to 1 and back to 0 over a period of 2ms.
$$Ca\_actn = \begin{cases} time * Ca\_max; & \text{if } time \leq 5.0, \\ (2.0 - time) * Ca\_max; & \text{if } time \leq 2.0, \\ 0.0 & \text{otherwise.} \end{cases} \tag{A.19.4}$$

A.20   noble_model_1998

This is the CellML description of Noble's 1998 improved guinea-pig ventricular cell model. It incorporates a diadic space, rapid and slow potassium currents and length- and tension-dependent processes.

Reference: Noble, D., Varghese, A., Kohl, P. & Noble, P. (1998), 'Improved guinea-pig ventricular cell model incorporating a diadic space, IKr and IKs, and length- and tension-dependent processes', *Canadian Journal of Cardiology* **14**, 123–134.

"environment" component

This component is used to declare variables that are used by all or most of the other components, in this case just 'time'.

"membrane" component

This component is the 'root' node of our model. It defines the action potential variable 'V'.

Initial values defined in this component

$V = -92.499 \, \text{mV}$ $F = 96485.0 \, \text{nC} \cdot \text{nmol}^{-1}$

$R = 8314.472 \, \text{pJ} \cdot \text{nmol}^{-1} \cdot \text{K}^{-1}$ $Cm = 0.014651 \, \mu\text{F} \cdot \text{mm}^{-2}$

$T = 310.0 \, \text{K}$

Equations defined in this component

A dummy equation used to get the total stimulus current into CMISS.
$$IStimC = IStim \tag{A.20.1}$$

The ODE governing the membrane potential – given by the summation of the ionic currents and an applied stimulus.

$$\begin{aligned}
\frac{\mathrm{d}(V)}{\mathrm{d}(time)} = \Big[IStim - \Big(&i\_K1 + i\_to + i\_K + i\_K\_ATP + i\_b\_K + i\_NaK + i\_Na + i\_b\_Na \\
&+ i\_p\_Na + i\_NaCa + i\_NaCa\_ds + i\_Ca\_L\_Ca + i\_Ca\_L\_Ca\_ds + i\_Ca\_L\_K + i\_Ca\_L\_K\_ds \\
&+ i\_Ca\_L\_Na + i\_Ca\_L\_Na\_ds + i\_b\_Ca + i\_Na\_stretch + i\_K\_stretch + i\_Ca\_stretch \\
&+ i\_Ns\_stretch + i\_An\_stretch + i\_K\_ACh \Big) \Big] \Big/ Cm
\end{aligned} \tag{A.20.2}$$

"reversal_potentials" component

A component that conveniently keeps the reversal potential calculations together.

Initial values defined in this component

$P\_kna = 0.03$ $P\_nak = 0.12$

Equations defined in this component

Calculation of the sodium reversal potential from the current intra- and extracellular concentration of sodium ions.

$$E\_Na = \frac{R * T}{F} * \ln\left(\frac{Na\_o}{Na\_i}\right) \tag{A.20.3}$$

Calculation of the potassium reversal potential from the current intra- and extracellular concentration of potassium ions.

$$E\_K = \frac{R * T}{F} * \ln\left(\frac{K\_o}{K\_i}\right) \tag{A.20.4}$$

Calculation of the potassium reversal potential for the slow component of the delayed rectifi er.

$$E\_Ks = \frac{R * T}{F} * \ln\left(\frac{(K\_o + P\_kna * Na\_o)}{(K\_i + P\_kna * Na\_i)}\right) \tag{A.20.5}$$

Calculation of the calcium reversal potential.

$$E\_Ca = 0.5 * \frac{R * T}{F} * \ln\left(\frac{Ca\_o}{Ca\_i}\right) \tag{A.20.6}$$

Calculation of the reversal potential for the fast sodium channel.

$$E\_mh = \frac{R * T}{F} * \ln\left(\frac{(Na\_o + P\_nak * K\_o)}{(Na\_i + P\_nak * K\_i)}\right) \tag{A.20.7}$$

"time_independent_potassium_current" component

Description of the time independent inward potassium current.

Initial values defined in this component

K_mk1 = 10.0 mM $\qquad\qquad\qquad$ g_K1 = 77.11×10^{-3} mS · mm^{-2}

Equations defined in this component

Calculation of the time independent potassium current.

$$i\_K1 = g\_K1 * \frac{K\_o}{(K\_o + K\_mk1)} * \frac{(V - E\_K)}{\left(1.0 + \exp\left(\frac{1.25*(V-(E\_K+10.0))}{\frac{R*T}{F}}\right)\right)} \tag{A.20.8}$$

"total_potassium_current" component

A component to group the potassium currents.

Equations defined in this component

Simple summation of the individual potassium currents into a single current.

$$i\_K = (i\_Kr + i\_Ks + i\_KNa) \tag{A.20.9}$$

"rapid_time_dependent_potassium_current" component

The rapid component of the delayed rectifier current.

Initial values defined in this component

$g\_Kr1 = 0.32386 \times 10^{-3} \; \text{mS} \cdot \text{mm}^{-2}$ $\qquad\qquad$ $g\_Kr2 = 0.20049 \times 10^{-3} \; \text{mS} \cdot \text{mm}^{-2}$

Equations defined in this component

Calculation of the rapid component of the delayed rectifier current.

$$i\_Kr = (g\_Kr1 * Xr1 + g\_Kr2 * Xr2) * \frac{1.0}{\left(1.0 + \exp\left(\frac{(V+9.0)}{22.4}\right)\right)} * (V - E\_K) \qquad (A.20.10)$$

"rapid_time_dependent_potassium_current_Xr1_gate" component

The fast activation gate for the rapid component of the delayed rectifier.

Initial values defined in this component

$Xr1 = 0.01428$

Equations defined in this component

The gating kinetics for the fast gate of the rapid component of the delayed rectifier.

$$\frac{\mathrm{d}(Xr1)}{\mathrm{d}(time)} = \left(\frac{0.05}{\left(1.0 + \exp\left(\frac{-(V-5.0)}{9.0}\right)\right)} * (1.0 - Xr1) - 0.00005 * \exp\left(-\frac{(V-20.0)}{15.0}\right) * Xr1 \right) \quad (A.20.11)$$

"rapid_time_dependent_potassium_current_Xr2_gate" component

The slow gate of the rapid component of the delayed rectifier.

Initial values defined in this component

$Xr2 = 0.5$

Equations defined in this component

Gating kinetics for the slow gate of the rapid component of the delayed rectifier.

$$\frac{\mathrm{d}(Xr2)}{\mathrm{d}(time)} = \left(\frac{0.05}{\left(1.0 + \exp\left(\frac{-(V-5.0)}{9.0}\right)\right)} * (1.0 - Xr2) - 0.0004 * \exp\left(-\left(\frac{(V+30.0)}{30.0}\right)^{3.0}\right) * Xr2 \right)$$
$$(A.20.12)$$

"slow_time_dependent_potassium_current" component

The slow component of the delayed rectifier current.

Initial values defined in this component

$g\_Ks = 0.40097 \times 10^{-3}$ mS · mm^{-2}

Equations defined in this component

Calculation of the slow component current of the delayed rectifi er.

$$i\_Ks = g\_Ks * (Xs)^{2.0} * (V - E\_Ks) \tag{A.20.13}$$

"slow_time_dependent_potassium_current_Xs_gate" component

The gate for the slow component of the delayed rectifi er current.

Initial values defined in this component

$Xs = 0.5$

Equations defined in this component

The gating kinetics for the slow component of the delayed rectifi er current.

$$\frac{\mathrm{d}(Xs)}{\mathrm{d}(time)} = \left(\frac{0.014}{\left(1.0 + \exp\left(\frac{-(V-40.0)}{9.0}\right)\right)} * (1.0 - Xs) - Xs * 0.001 * \exp\left(\frac{-V}{45.0}\right) \right) \tag{A.20.14}$$

"potassium_background_current" component

Background potassium current.

Initial values defined in this component

$g\_bk = 0.0$ mS · mm^{-2}

Equations defined in this component

Calculation of the background potassium current.

$$i\_b\_K = g\_bk * (V - E\_K) \tag{A.20.15}$$

"ATP_dependent_potassium_current" component

An ATP dependent potassium current. Included here for completeness, but this current is only used when modelling ischaemia - and this version of the model has not been tested for this.

Initial values defined in this component

$g\_K\_ATP = 0.0$ mS · mm^{-2} $\qquad\qquad\qquad\qquad ATP = 5.0$ mM

$K\_ATP = 0.1$ mM

Equations defined in this component

Calculation of the ATP dependent potassium current.

$$i\_K\_ATP = \frac{g\_K\_ATP * (V + 80.0)}{\left(1.0 + \left(\frac{ATP}{K\_ATP}\right)^{2.0}\right)}$$

(A.20.16)

"sodium_activated_potassium_current" component

A sodium activated potassium current. Again, included for completeness but generally not used and untested.

Initial values defined in this component

$g\_K\_Na = 0.0 \text{ mS} \cdot \text{mm}^{-2}$ $\qquad\qquad K\_kna = 20.0 \text{ mM}$

Equations defined in this component

Calculation of the sodium activated potassium current.

$$i\_KNa = g\_K\_Na * \frac{Na\_i}{(Na\_i + K\_kna)} * (V - E\_K)$$

(A.20.17)

"fast_sodium_current" component

The fast sodium current - the driving force of the upstroke of the cardiac action potential.

Initial values defined in this component

$g\_Na = 385.5 \times 10^{-3} \text{ mS} \cdot \text{mm}^{-2}$

Equations defined in this component

Calculation of the fast sodium current.

$$i\_Na = g\_Na * (m)^{3.0} * h * (V - E\_mh)$$

(A.20.18)

"fast_sodium_current_m_gate" component

The activation gate for the fast sodium current.

Initial values defined in this component

$m = 0.0017$

Equations defined in this component

The gating kinetics for the activation gate of the fast sodium current.

$$\frac{\mathrm{d}(m)}{\mathrm{d}(time)} = (alpha * (1.0 - m) - beta * m)$$

(A.20.19)

Calculation of the opening rate of the activation gate for the fast sodium current.

$$alpha = \begin{cases} 2.0; & \text{if } |(V + 41.0)| < 0.1 \times 10^{-4}, \\ \frac{0.2*(V+41.0)}{(1.0-\exp(-0.1*(V+41.0)))} & \text{otherwise.} \end{cases} \quad \text{(A.20.20)}$$

Calculation of the closing rate of the activation gate for the fast sodium current.

$$beta = 8.0 * \exp\left(-0.055556 * (V + 66.0)\right) \quad \text{(A.20.21)}$$

"fast_sodium_current_h_gate" component

The inactivation gate for the fast sodium current.

Initial values defined in this component

$h = 0.9939474$

Equations defined in this component

The gating kinetics for the inactivation gate of the fast sodium current.

$$\frac{\mathrm{d}(h)}{\mathrm{d}(time)} = 0.02 * \exp\left(-0.125 * (V + 75.0)\right) * (1.0 - h)$$
$$- h * \frac{2.0}{(1.0 + 320.0 * \exp\left(-0.1 * (V + 75.0)\right))} \quad \text{(A.20.22)}$$

"persistent_sodium_current" component

The persistent sodium current.

Initial values defined in this component

$g\_pna = 0.61688 \times 10^{-3} \, \text{mS} \cdot \text{mm}^{-2}$

Equations defined in this component

Calculation of the persistent sodium current.

$$i\_p\_Na = g\_pna * \frac{1.0}{\left(1.0 + \exp\left(-\frac{(V+52.0)}{8.0}\right)\right)} * (V - E\_Na) \quad \text{(A.20.23)}$$

"sodium_background_current" component

The background sodium current.

Initial values defined in this component

$g\_bna = 0.092532 \times 10^{-3} \, \text{mS} \cdot \text{mm}^{-2}$

Equations defined in this component

Calculation of the sodium background current.

$$i\_b\_Na = g\_bna * (V - E\_Na) \tag{A.20.24}$$

"L_type_Ca_channel" component

This component describes an inward ionic current which is the sum of calcium, sodium and potassium ions through the membrane channel. The channel has one activation gate (d) and two inactivation gates (f and f2 (or f2ds in the diadic space)). A fraction of these channels (ICaLfract) open into the diadic subspace, with the remainder being evenly distributed throughout the membrane area.

Initial values defined in this component

$P\_ca = 15.422 \times 10^{-3} \, \mu\text{A} \cdot \text{mm}^{-2} \cdot \text{mM}^{-1}$ $\qquad$ $ICaLfract = 1.0$

$P\_caK = 0.002$ $\qquad$ $K\_cachoff = 0.001 \, \text{mM}$

$P\_caNa = 0.01$ $\qquad$ $K\_AChICaL = 0.2 \times 10^{-6} \, \text{mM}$

Equations defined in this component

The calcium ion component of the total current through the channel into the bulk myoplasm.

$$i\_Ca\_L\_Ca = (1.0 - ICaLfract) * 4.0 * P\_ca * d * f * f2 * \frac{\frac{(V-50.0)}{\frac{R*T}{F}}}{\left(1.0 - \exp\left(\frac{-(V-50.0)}{\frac{R*T}{2.0*F}}\right)\right)}$$
$$* \left(Ca\_i * \exp\left(\frac{50.0}{\frac{R*T}{2.0*F}}\right) - Ca\_o * \exp\left(\frac{-(V-50.0)}{\frac{R*T}{2.0*F}}\right)\right) * \left(1.0 - \frac{ACh}{(ACh + K\_AChICaL)}\right) \tag{A.20.25}$$

The potassium ion component of the total current through the channel into the bulk myoplasm.

$$i\_Ca\_L\_K = (1.0 - ICaLfract) * P\_caK * P\_ca * d * f * f2$$
$$* \left(K\_i * \exp\left(\frac{50.0}{\frac{R*T}{F}}\right) - K\_o * \exp\left(\frac{-(V-50.0)}{\frac{R*T}{F}}\right)\right) * \left(1.0 - \frac{ACh}{(ACh + K\_AChICaL)}\right) \tag{A.20.26}$$

The sodium ion component of the total current through the channel into the bulk myoplasm.

$$i\_Ca\_L\_Na = (1.0 - ICaLfract) * P\_caNa * P\_ca * d * f * f2$$
$$* \left(Na\_i * \exp\left(\frac{50.0}{\frac{R*T}{F}}\right) - Na\_o * \exp\left(\frac{-(V-50.0)}{\frac{R*T}{F}}\right)\right) * \left(1.0 - \frac{ACh}{(ACh + K\_AChICaL)}\right) \tag{A.20.27}$$

The calcium ion component of the total current through the channel into the diadic subspace.

$$i\_Ca\_L\_Ca\_ds = ICaLfract * 4.0 * P\_ca * d * f * f2ds * \frac{\frac{(V-50.0)}{\frac{R*T}{F}}}{\left(1.0 - \exp\left(\frac{-(V-50.0)}{\frac{R*T}{2.0*F}}\right)\right)}$$
$$* \left(Ca\_ds * \exp\left(\frac{50.0}{\frac{R*T}{2.0*F}}\right) - Ca\_o * \exp\left(\frac{-(V-50.0)}{\frac{R*T}{2.0*F}}\right)\right) * \left(1.0 - \frac{ACh}{(ACh + K\_AChICaL)}\right) \tag{A.20.28}$$

The potassium ion component of the total current through the channel into the diadic subspace.

$$i\_Ca\_L\_K\_ds = ICaLfract * P\_caK * P\_ca * d * f * f2ds$$
$$* \left(K\_i * \exp\left(\frac{50.0}{\frac{R*T}{F}}\right) - K\_o * \exp\left(\frac{-(V-50.0)}{\frac{R*T}{F}}\right) \right) * \left(1.0 - \frac{ACh}{(ACh + K\_AChICaL)} \right) \quad \text{(A.20.29)}$$

The sodium ion component of the total current through the channel into the diadic subspace.

$$i\_Ca\_L\_Na\_ds = ICaLfract * P\_caNa * P\_ca * d * f * f2ds$$
$$* \left(Na\_i * \exp\left(\frac{50.0}{\frac{R*T}{F}}\right) - Na\_o * \exp\left(\frac{-(V-50.0)}{\frac{R*T}{F}}\right) \right) * \left(1.0 - \frac{ACh}{(ACh + K\_AChICaL)} \right) \quad \text{(A.20.30)}$$

"L_type_Ca_channel_d_gate" component

The activation gate of the L-type calcium channel.

Initial values defined in this component

$d = 0.0$

Equations defined in this component

The gating kinetics for the activation gate.
$$\frac{\mathrm{d}(d)}{\mathrm{d}(time)} = (alpha * (1.0 - d) - beta * d) \quad \text{(A.20.31)}$$

The opening rate for the activation gate.
$$alpha = \begin{cases} 0.36; & \text{if } |(V + 19.0)| < 1.0 \times 10^{-3}, \\ \frac{0.09*(V+19.0)}{\left(1.0 - \exp\left(\frac{-(V+19.0)}{4.0}\right)\right)} & \text{otherwise.} \end{cases} \quad \text{(A.20.32)}$$

The closing rate for the activation gate.
$$beta = \begin{cases} 0.36; & \text{if } |(V + 19.0)| < 1.0 \times 10^{-3}, \\ \frac{-0.036*(V+19.0)}{\left(1.0 - \exp\left(\frac{(V+19.0)}{10.0}\right)\right)} & \text{otherwise.} \end{cases} \quad \text{(A.20.33)}$$

"L_type_Ca_channel_f_gate" component

The first inactivation gate for the L-type calcium channel.

Initial values defined in this component

$f = 1.0$

Equations defined in this component

The gating kinetics for the first inactivation gate.
$$\frac{\mathrm{d}(f)}{\mathrm{d}(time)} = (alpha * (1.0 - f) - beta * f) \quad \text{(A.20.34)}$$

The opening rate for the inactivation gate.

$$alpha = \begin{cases} 0.0075; & \text{if } |(V + 34.0)| < 1.0 \times 10^{-3}, \\ -0.001875 * \frac{(V+34.0)}{\left(1.0 - \exp\left(\frac{(V+34.0)}{4.0}\right)\right)} & \text{otherwise.} \end{cases} \quad \text{(A.20.35)}$$

The closing rate for the inactivation gate.

$$beta = \frac{0.0036}{\left(1.0 + \exp\left(-\frac{(V+34.0)}{4.0}\right)\right)} \quad \text{(A.20.36)}$$

"L_type_Ca_channel_f2_gate" component

The second inactivation gate for L-type calcium channels in the membrane outside the diadic subspace.

Initial values defined in this component

$f2 = 1.0$ $\qquad\qquad\qquad$ $CaInact = 0.02 \text{ ms}^{-1}$

Equations defined in this component

The gating kinetics for the inactivation gate.

$$\frac{\mathrm{d}(f2)}{\mathrm{d}(time)} = CaInact * \left(1.0 - \left(\frac{Ca\_i}{(K\_cachoff + Ca\_i)} + f2\right)\right) \quad \text{(A.20.37)}$$

"L_type_Ca_channel_f2ds_gate" component

The second inactivation gate for L-type calcium channels in the membrane when open into the diadic subspace.

Initial values defined in this component

$f2ds = 1.0$ $\qquad\qquad\qquad$ $CaInactDS = 0.02 \text{ ms}^{-1}$
$K\_dsoff = 0.001 \text{ mM}$

Equations defined in this component

The gating kinetics for the inactivation gate.

$$\frac{\mathrm{d}(f2ds)}{\mathrm{d}(time)} = CaInactDS * \left(1.0 - \left(\frac{Ca\_ds}{(K\_dsoff + Ca\_ds)} + f2ds\right)\right) \quad \text{(A.20.38)}$$

"calcium_background_current" component

The background calcium current.

Initial values defined in this component

$g\_bca = 0.038555 \times 10^{-3} \text{ mS} \cdot \text{mm}^{-2}$

Equations defined in this component

Calculation of the background calcium current.

$$i\_b\_Ca = g\_bca * (V - E\_Ca) \tag{A.20.39}$$

"transient_outward_current" component

The doubly gated transient outward current.

Initial values defined in this component

$g\_to = 0.77100 \times 10^{-3} \ \mathrm{mS \cdot mm^{-2}}$ $\qquad\qquad g\_tos = 0.0$

Equations defined in this component

Evaluation of the transient outward current.

$$i\_to = g\_to * (g\_tos + s * (1.0 - g\_tos)) * r * (V - E\_K) \tag{A.20.40}$$

"transient_outward_current_s_gate" component

The first gate of the transient outward current.

Initial values defined in this component

$s = 0.9950485$

Equations defined in this component

The gating kinetics.

$$\frac{\mathrm{d}(s)}{\mathrm{d}(time)} = \left(0.000033 * \exp\left(\frac{-V}{17.0}\right) * (1.0 - s) - \frac{0.033}{\left(1.0 + \exp\left(\frac{-(V+10.0)}{8.0}\right)\right)} * s \right) \tag{A.20.41}$$

"transient_outward_current_r_gate" component

The second of the two gates for the transient outward current.

Initial values defined in this component

$r = 0.0$

Equations defined in this component

The gating kinetics for the r gate.

$$\frac{\mathrm{d}(r)}{\mathrm{d}(time)} = 0.333 * (r\_ss - r) \tag{A.20.42}$$

Calculation of the steady-state component of the gating kinetics for the r gate.

$$r\_ss = \frac{1.0}{(1.0 + \exp(-0.2 * (V + 4.0)))}$$

(A.20.43)

"ACh_dependent_potassium_current" component

Acetylcholine (ACh) dependent potassium current. Once more, this current has been included for completeness with respect to the original publication but is usually left out of simulations. It is useful for simulating specific cellular conditions, but this formulation has not been tested.

Initial values defined in this component

$g\_KACh = 0.0 \text{ mS} \cdot \text{mm}^{-2}$ $K\_ACh = 0.2795 \times 10^{-6} \text{ mM}$

$ACh = 0.0 \text{ mM}$ $K\_KACh = 10.0 \text{ mM}$

Equations defined in this component

Evaluation of the ACh dependent potassium current.

$$i\_K\_ACh = g\_KACh * \frac{K\_o}{(K\_o + K\_KACh)} * x\_ACh1 * x\_ACh2$$
$$* \frac{(ACh)^{1.4969}}{\left((ACh)^{1.4969} + (K\_ACh)^{1.4969}\right)} * \frac{(V - E\_K)}{\left(1.0 + \exp\left(\frac{0.4*(V-(E\_K+140.0))}{\frac{R*T}{F}}\right)\right)}$$

(A.20.44)

"ACh_dependent_potassium_current_xACh1_gate" component

The first of two gates for the ACh dependent potassium current.

Initial values defined in this component

$x\_ACh1 = 0.5$ $alpha\_ACh = 0.003684211 \text{ ms}^{-1}$

Equations defined in this component

Gating kinetics for the first gate.

$$\frac{\mathrm{d}(x\_ACh1)}{\mathrm{d}(time)} = \left(alpha\_ACh * (1.0 - x\_ACh1) - \frac{0.00582}{\left(1.0 + \exp\left(-\frac{(V+50.0)}{15.0}\right)\right)} * x\_ACh1\right)$$

(A.20.45)

"ACh_dependent_potassium_current_xACh2_gate" component

The second of the two gates for the ACh dependent potassium current.

Initial values defined in this component

$x\_ACh2 = 0.5$ $alpha\_ACh = 0.07309924 \text{ ms}^{-1}$

Equations defined in this component

Gating kinetics for the second gate.

$$\frac{\mathrm{d}(x\_ACh2)}{\mathrm{d}(time)} = \left(alpha\_ACh * (1.0 - x\_ACh2) - \frac{0.12}{\left(1.0 + \exp\left(-\frac{(V+50.0)}{15.0}\right)\right)} * x\_ACh2 \right) \quad \text{(A.20.46)}$$

"sodium_potassium_pump" component

The sodium potassium pump.

Initial values defined in this component

$i\_NaK\_max = 107.95 \times 10^{-3} \ \mu\text{A} \cdot \text{mm}^{-2}$ $\qquad K\_mNa = 40.0 \ \text{mM}$

$K\_mk = 1.0 \ \text{mM}$

Equations defined in this component

Calculation of the sodium potassium pump current.

$$i\_NaK = i\_NaK\_max * \frac{K\_o}{(K\_o + K\_mk)} * \frac{Na\_i}{(Na\_i + K\_mNa)} \quad \text{(A.20.47)}$$

"sodium_calcium_pump" component

The sodium calcium exchanger. A fraction of the Na-Ca exchangers (INaCaFract) are assumed to emmpty into the diadic subspace, while the remainder of the channels open into the bulk cytosol.

Initial values defined in this component

$K\_NaCa = 0.07711 \times 10^{-3} \ \mu\text{A} \cdot \text{mm}^{-2} \cdot \text{mM}^{-4}$ $\qquad gamma = 0.5$

$d\_NaCa = 0.0 \ \text{mM}^{-4}$ $\qquad INaCaFract = 0.001$

Equations defined in this component

Calculation of the sodium calcium exchanger current for the channels exposed to the bulk myoplasm.

$$i\_NaCa = (1.0 - INaCaFract) * K\_NaCa$$
$$* \frac{\left(\exp\left(gamma * \frac{V}{\frac{R*T}{F}}\right) * (Na\_i)^{3.0} * Ca\_o - \exp\left((gamma - 1.0) * \frac{V}{\frac{R*T}{F}}\right) * (Na\_o)^{3.0} * Ca\_i\right)}{\left(1.0 + d\_NaCa * \left(Ca\_i * (Na\_o)^{3.0} + Ca\_o * (Na\_i)^{3.0}\right)\right)}$$
$$* \frac{1.0}{\left(1.0 + \frac{Ca\_i}{0.0069}\right)} \quad \text{(A.20.48)}$$

Calculation of the sodium calcium exchanger current for the channels opening into the diadic subspace.

$$i\_NaCa\_ds = INaCaFract * K\_NaCa$$

$$* \frac{\left(\exp\left(gamma * \frac{V}{\frac{R*T}{F}}\right) * (Na\_i)^{3.0} * Ca\_o - \exp\left((gamma - 1.0) * \frac{V}{\frac{R*T}{F}}\right) * (Na\_o)^{3.0} * Ca\_ds\right)}{\left(1.0 + d\_NaCa * \left(Ca\_ds * (Na\_o)^{3.0} + Ca\_o * (Na\_i)^{3.0}\right)\right)}$$

$$* \frac{1.0}{\left(1.0 + \frac{Ca\_ds}{0.0069}\right)} \quad (A.20.49)$$

"calcium_uptake_from_myoplasm_to_NSR" component

The sarcoplasmic reticulum calcium pump which transports calcium from the bulk myoplasm into the network SR.

Initial values defined in this component

$K\_cyca = 0.0003$ mM $\qquad\qquad$ $K\_srca = 0.5$ mM

$K\_xcs = 0.4$

Equations defined in this component

Calculation of the calcium uptake flux.

$$i\_up = \frac{\left(0.0004 * Ca\_i - 0.00003 * Ca\_up * \frac{K\_cyca * K\_xcs}{K\_srca}\right)}{\left(Ca\_i + Ca\_up * \frac{K\_cyca * K\_xcs}{K\_srca} + K\_cyca * K\_xcs + K\_cyca\right)} \quad (A.20.50)$$

"calcium_transfer_from_NSR_to_JSR" component

Diffusion down the concentration gradient to transfer calcium from the uptake stores in the network SR to the release stores in the junctional SR.

Equations defined in this component

Calculation of the transfer flux between the uptake and release calcium stores.

$$i\_tr = 0.05 * (Ca\_up - Ca\_rel) \quad (A.20.51)$$

"length_dependence" component

This component describes the addition of length dependence to the Noble models. However, in this implementation of the model, it is unused - sarcomere length (SL) is a constant 0, resulting in the removal of length dependence from the model.

Initial values defined in this component

$SL = 0.0$ mm $\qquad\qquad$ $gamma\_SR\_SL = 1.5 \times 10^{+3}$ mm^{-1}

$SLRef = 2.0 \times 10^{-3}$ mm $\qquad\qquad$ $gamma\_SAC\_SL = 2.5 \times 10^{+3}$ mm^{-1}

Equations defined in this component

Calculation of the scaling factor for the stretch activated currents based on the change in length from the reference state.

$$f\_stretch = \frac{1.0}{(1.0 + \exp{(-2.0 * gamma\_SAC\_SL * (SL - SLRef)))}} \tag{A.20.52}$$

"calcium_leak_from_SR" component

The length dependent leakage of calcium from the junctional SR into the cytolsol.

Initial values defined in this component

$alpha\_SRleak = 0.00005 \text{ ms}^{-1}$

Equations defined in this component

$$i\_leak = \exp{(gamma\_SR\_SL * SL)} * alpha\_SRleak * Ca\_rel \tag{A.20.53}$$

"ds_decay_flux" component

Description of the diffusion of calcium out of the diadic subspace into the bulk cytosol.

Initial values defined in this component

$alpha\_ca\_ds\_decay = 0.01 \text{ ms}^{-1}$

Equations defined in this component

Calculation of the flux of calcium out of the diadic subspace.

$$i\_decay = alpha\_ca\_ds\_decay * Ca\_ds \tag{A.20.54}$$

"calcium_release_from_SR" component

The calcium induced calcium release from the junctional SR into the bulk myoplasm. Assumed that activation of calcium release sites by the diadic subspace calcium triggers calcium release in the whole cytosol.

Initial values defined in this component

$ActivatorFract = 0.00191$ $K\_mca\_ds = 0.01 \text{ mM}$

$ProductFract = 0.28546$ $alpha\_rel = 0.25 \text{ ms}^{-1}$

$K\_mca = 0.0005 \text{ mM}$

Equations defined in this component

The fraction of release sites in the open state.
$$OpenReleaseChannelFract = \left(\frac{ActivatorFract}{(ActivatorFract + 0.25)} \right)^{2.0} \quad \text{(A.20.55)}$$

Calculation of the calcium release flux from the JSR into the cytosol.
$$i\_rel = alpha\_rel * OpenReleaseChannelFract * Ca\_rel \quad \text{(A.20.56)}$$

Regulatory binding sites.
$$RegulatoryBindingSite =$$
$$\left(\left(\frac{Ca\_i}{(Ca\_i + K\_mca)} + \left(1.0 - \frac{Ca\_i}{(Ca\_i + K\_mca)} \right) * \frac{Ca\_ds}{(Ca\_ds + K\_mca\_ds)} \right) \right)^{2.0} \quad \text{(A.20.57)}$$

Fraction of release channels in the precursor state.
$$PrecursorFract = (1.0 - (ActivatorFract + ProductFract)) \quad \text{(A.20.58)}$$

$$alpha\_act = 0.5 * RegulatoryBindingSite \quad \text{(A.20.59)}$$
$$alpha\_inact = (0.06 + 0.5 * RegulatoryBindingSite) \quad \text{(A.20.60)}$$
$$SR\_speed\_factor = \begin{cases} 5.0; & \text{if } V < -50.0, \\ 1.0 & \text{otherwise.} \end{cases} \quad \text{(A.20.61)}$$
$$\frac{\mathrm{d}(ActivatorFract)}{\mathrm{d}(time)} = SR\_speed\_factor * (alpha\_act * PrecursorFract - alpha\_inact * ActivatorFract) \quad \text{(A.20.62)}$$
$$\frac{\mathrm{d}(ProductFract)}{\mathrm{d}(time)} = SR\_speed\_factor * (alpha\_inact * ActivatorFract - 0.001 * ProductFract) \quad \text{(A.20.63)}$$

"stretch_dependent_Ca_current" component

A stretch activated calcium current. Unused and untested in this implementation, but included for completeness.

Initial values defined in this component

$g\_Ca\_stretch = 154.22 \times 10^{-3} \text{ mS} \cdot \text{mm}^{-2}$

Equations defined in this component

Calculation of the current.
$$i\_Ca\_stretch = g\_Ca\_stretch * f\_stretch * (V - E\_Ca) \quad \text{(A.20.64)}$$

"stretch_dependent_K_current" component

Stretch activated potassium current - unused and untested, but included for completeness.

Initial values defined in this component

$g\_K\_stretch = 154.22 \times 10^{-3} \ \mathrm{mS \cdot mm^{-2}}$

Equations defined in this component

Calculation of the current.

$$i\_K\_stretch = g\_K\_stretch * f\_stretch * (V - E\_K) \tag{A.20.65}$$

"stretch_dependent_Na_current" component

A stretch activated sodium current - unused and untested, but included for completeness.

Initial values defined in this component

$g\_Na\_stretch = 154.22 \times 10^{-3} \ \mathrm{mS \cdot mm^{-2}}$

Equations defined in this component

Calculation of the current.

$$i\_Na\_stretch = g\_Na\_stretch * f\_stretch * (V - E\_Na) \tag{A.20.66}$$

"stretch_dependent_Ns_current" component

A non-specifi c stretch activated current. Not used and untested, but included for completeness.

Initial values defined in this component

$g\_Ns\_stretch = 154.22 \times 10^{-3} \ \mathrm{mS \cdot mm^{-2}}$ $\qquad\qquad$ $E\_Ns\_stretch = -30.0 \ \mathrm{mV}$

Equations defined in this component

Calculation of the current.

$$i\_Ns\_stretch = g\_Ns\_stretch * f\_stretch * (V - E\_Ns\_stretch) \tag{A.20.67}$$

"stretch_dependent_An_current" component

A anion specifi c stretch ativated current - unused and untested, but included for completeness.

Initial values defined in this component

$g\_An\_stretch = 154.22 \times 10^{-3} \ \mathrm{mS \cdot mm^{-2}}$ $\qquad\qquad$ $E\_An\_stretch = -20.0 \ \mathrm{mV}$

Equations defined in this component

Calculation of the current.

$$i\_An\_stretch = g\_An\_stretch * f\_stretch * (V - E\_An\_stretch) \tag{A.20.68}$$

"ionic_concentrations" component

A convenient grouping of all the ionic concentration differential equations.

Initial values defined in this component

$Na\_i = 5.5997$ mM	$CALM = 0.02$ mM
$Na\_o = 140.0$ mM	$TROP = 0.05$ mM
$K\_i = 139.3050$ mM	$alpha\_trop = 100.0$ mM$^{-1} \cdot$ ms^{-1}
$K\_o = 4.0$ mM	$beta\_trop = 0.2$ ms^{-1}
$Ca\_i = 0.0000082$ mM	$gamma\_trop\_SL = 2.5 \times 10^{+3}$ mm^{-1}
$Ca\_o = 2.0$ mM	$V\_i = 0.49$
$Ca\_ds = 0.0000171$ mM	$V\_rel = 0.1$
$Ca\_up = 0.2872393$ mM	$V\_ds = 0.1$
$Ca\_rel = 0.2846761$ mM	$V\_up = 0.01$
$Ca\_calmod = 0.0003258$ mM	$V\_ecs = 0.3$
$Ca\_troponin = 0.0002060$ mM	$Am = 193.69$ mm^{-1}

Equations defined in this component

The rate of change of intracellular sodium concentration.

$$\frac{\mathrm{d}(Na\_i)}{\mathrm{d}(time)} = -\frac{Am}{V\_i * F} * \left(i\_Na + i\_p\_Na + i\_b\_Na * \frac{Na\_o}{140.0} + i\_NaK * 3.0 + i\_NaCa * 3.0 \right.$$
$$\left. + i\_NaCa\_ds * 3.0 + i\_Ca\_L\_Na + i\_Ca\_L\_Na\_ds + i\_Na\_stretch \right) \quad \text{(A.20.69)}$$

The rate of change of intracellular potassium concentration.

$$\frac{\mathrm{d}(K\_i)}{\mathrm{d}(time)} = -\frac{Am}{V\_i * F} * \left(i\_K1 + i\_to + i\_b\_K + i\_K + i\_K\_stretch + i\_Ca\_L\_K \right.$$
$$\left. + i\_Ca\_L\_K\_ds + i\_K\_ACh + i\_K\_ATP - i\_NaK * 2.0 \right) \quad \text{(A.20.70)}$$

The rate of change of intracellular calcium concentration.

$$\frac{\mathrm{d}(Ca\_i)}{\mathrm{d}(time)} = \left[-\frac{Am}{2.0 * V\_i * F} * ((i\_Ca\_L\_Ca + i\_b\_Ca + i\_Ca\_stretch) - i\_NaCa * 2.0) \right.$$
$$\left. + i\_rel * \frac{V\_rel}{V\_i} + i\_leak * \frac{V\_rel}{V\_i} + i\_decay * \frac{V\_ds}{V\_i} \right] - (i\_up + dy\_Ca\_calmod + dy\_Ca\_troponin)$$
$$\text{(A.20.71)}$$

The rate of change of calcium concentration in the diadic subspace.

$$\frac{\mathrm{d}(Ca\_ds)}{\mathrm{d}(time)} = \left(-\frac{Am}{2.0 * V\_ds * F} * (i\_Ca\_L\_Ca\_ds - i\_NaCa\_ds * 2.0) - i\_decay \right) \quad \text{(A.20.72)}$$

The rate of change of calcium concentration in the network SR uptake store.

$$\frac{\mathrm{d}(Ca\_up)}{\mathrm{d}(time)} = \left(\frac{V\_i}{V\_up} * i\_up - i\_tr \right) \quad \text{(A.20.73)}$$

The rate of change of calcium concentration in the junctional SR release store.

$$\frac{\mathrm{d}(Ca\_rel)}{\mathrm{d}(time)} = \left(\frac{V\_up}{V\_rel} * i\_tr - (i\_rel + i\_leak) \right) \tag{A.20.74}$$

The rate of change of calcium bound to calmodulin.

$$dy\_Ca\_calmod = (100.0 * Ca\_i * (CALM - Ca\_calmod) - 0.05 * Ca\_calmod) \tag{A.20.75}$$

$$\frac{\mathrm{d}(Ca\_calmod)}{\mathrm{d}(time)} = dy\_Ca\_calmod \tag{A.20.76}$$

The rate of change of calcium bound to troponin.

$$dy\_Ca\_troponin = (alpha\_trop * Ca\_i * (TROP - Ca\_troponin) - beta\_trop * Ca\_troponin) \tag{A.20.77}$$

$$\frac{\mathrm{d}(Ca\_troponin)}{\mathrm{d}(time)} = dy\_Ca\_troponin \tag{A.20.78}$$

A.21 defibrillation_model_1999

This is the CellML description of the defibrillation Beeler-Reuter model. The original Beeler-Reuter model was modified by Drouhard and Roberge (1987) to improve the fast sodium kinetics. This model was then further modified by Skouibine et al (1999) to handle potentials outside the range of normal physiological activity, allowing the model to be used in defibrillation studies.

Reference: Skouibine, K. B., Trayanova, N. A. & Moore, P. K. (1999), 'Anode/cathode make and break phenomena in a model of defibrillation', *IEEE Trans Biomed Eng.* **46**, 769–777.

"environment" component

"membrane" component

The main component for the model, defining the transmembrane potential.

Initial values defined in this component

$V = -86.9 \, \mathrm{mV}$ $\qquad\qquad\qquad\qquad\qquad C = 1.0 \times 10^{-2} \, \mu\mathrm{F} \cdot \mathrm{mm}^{-2}$

Equations defined in this component

The main differential equation for the model, specifying membrane potential as the summation of all ionic currents and an applied stimulus current.

$$\frac{\mathrm{d}(V)}{\mathrm{d}(time)} = \frac{(I\_stim - (i\_Na + i\_s + i\_x1 + i\_K1))}{C} \tag{A.21.1}$$

"fast_sodium_current" component

The fast sodium current, primarily responsible for the upstroke of the action potential.

Initial values defined in this component

$g\_Na = 0.15 \, \text{mS} \cdot \text{mm}^{-2}$ $E\_Na = 40.0 \, \text{mV}$

Equations defined in this component

Calculation of the fast sodium current.
$$i\_Na = g\_Na * (m)^{3.0} * h * (V - E\_Na) \tag{A.21.2}$$

"fast_sodium_current_m_gate" component

The voltage-dependent activation gate for the fast sodium channel - the m gate.

Initial values defined in this component

$m = 0.0$

Equations defined in this component

The opening rate for the m gate.
$$alpha\_m = \begin{cases} 890.9437890 * \frac{\exp((0.0486479*V-4.8647916))}{(1.0+5.93962526*\exp((0.0486479*V-4.8647916)))}; & \text{if } V > 100.0, \\ 0.9 * \frac{(V+42.65)}{(1.0-\exp((-0.22*V-9.3830)))} & \text{otherwise.} \end{cases} \tag{A.21.3}$$

The closing rate for the m gate.
$$beta\_m = \begin{cases} 1.437 * \exp\left((-0.085 * V - 3.37875)\right); & \text{if } V > -85.0, \\ \frac{100.0}{(1.0+0.486479*\exp((0.2597504*V+22.0787804)))} & \text{otherwise.} \end{cases} \tag{A.21.4}$$

The kinetics of the m gate.
$$\frac{\mathrm{d}(m)}{\mathrm{d}(time)} = (alpha\_m * (1.0 - m) - beta\_m * m) \tag{A.21.5}$$

"fast_sodium_current_h_gate" component

The voltage-dependent inactivation gate for the fast sodium channel - the h gate.

Initial values defined in this component

$h = 0.99$

Equations defined in this component

The opening rate for the h gate.

$$alpha\_h = \begin{cases} 0.1 * \exp\left((-0.193 * V - 15.37245)\right); & \text{if } V > -90.0, \\ (-12.0662845 - 0.1422598 * V) & \text{otherwise.} \end{cases} \tag{A.21.6}$$

The closing rate for the h gate.

$$beta\_h = \frac{1.7}{(1.0 + \exp\left((-0.095 * V - 1.9475)\right))} \tag{A.21.7}$$

The kinetics of the h gate.

$$\frac{\mathrm{d}(h)}{\mathrm{d}(time)} = (alpha\_h * (1.0 - h) - beta\_h * h) \tag{A.21.8}$$

"time_independent_outward_current" component

The formula for the time independent outward potassium current of the defibrillation Beeler-Reuter model is the same as for the original Beeler-Reuter (1977) model.

Equations defined in this component

$$i\_K1 = 0.35 \times 10^{-2}$$
$$* \left(4.0 * \frac{(\exp\left(0.04 * (V + 85.0)\right) - 1.0)}{(\exp\left(0.08 * (V + 53)\right) + \exp\left(0.04 * (V + 53.0)\right))} + 0.2 * \frac{(V + 23.0)}{(1.0 - \exp\left(-0.04 * (V + 23.0)\right))} \right) \tag{A.21.9}$$

"time_dependent_outward_current" component

While the governing equations for the time dependent outward potassium current are unchanged, the gating variables (alpha_x1 and beta_x1) are modified.

Equations defined in this component

$$i\_x1 = x1 * 0.8 \times 10^{-2} * \frac{(\exp\left(0.04 * (V + 77.0)\right) - 1.0)}{\exp\left(0.04 * (V + 35.0)\right)} \tag{A.21.10}$$

"time_dependent_outward_current_x1_gate" component

The gating variable for the time-dependent outward potassium current - the x1 gate.

Initial values defined in this component

$x1 = 0.0$

Equations defined in this component

The opening rate of the x1 gate.

$$alpha\_x1 = \begin{cases} 151.7994692 * \frac{\exp((0.0654679*V - 26.1871448))}{(1.0 + 1.5179947 * \exp((0.0654679*V - 26.1871448)))}; & \text{if } V > 400.0, \\ 0.0005 * \frac{\exp((V*0.083 + 4.150))}{(1.0 + \exp((0.057*V + 2.850)))} & \text{otherwise.} \end{cases}$$

(A.21.11)

The closing rate of the x1 gate.

$$beta\_x1 = 0.0013 * \frac{\exp((V * -0.06 - 1.2))}{(1.0 + \exp((-0.04 * V - 0.8)))}$$

(A.21.12)

The kinetics of the x1 gate.

$$\frac{\mathrm{d}(x1)}{\mathrm{d}(time)} = (alpha\_x1 * (1.0 - x1) - beta\_x1 * x1)$$

(A.21.13)

"slow_inward_current" component

A minor change is made to the intracellular calcium ion tracking to limit the movement of calcium ions at large potentials. In addition to these changes, a scale factor can be added to the time dependent d and f gates to allow the scaling of the action potential duration. This enables a better representation of an action potential from ischemic tissue.

Initial values defined in this component

$g\_s = 9.0 \times 10^{-4} \text{ mS} \cdot \text{mm}^{-2}$ $\qquad\qquad Cai = 1.0 \times 10^{-4} \text{ mM}$

Equations defined in this component

Calculation of the reversal potential for the slow inward current.

$$E\_s = (-82.3 - 13.0287 * \ln(Cai * 0.001))$$

(A.21.14)

Calculation of the slow inward current.

$$i\_s = g\_s * d * f * (V - E\_s)$$

(A.21.15)

The time rate of change of intracellular calcium concentration.

$$\frac{\mathrm{d}(Cai)}{\mathrm{d}(time)} = \begin{cases} 0.0; & \text{if } V > 200.0, \\ (i\_s * -0.01 + 0.07 * (0.0001 - Cai)) & \text{otherwise.} \end{cases}$$

(A.21.16)

"slow_inward_current_d_gate" component

The voltage-dependent activation gate for the slow inward current - the d gate.

Initial values defined in this component

$d = 0.0$ $\qquad\qquad R\_d = 1.0$

Equations defined in this component

The opening rate of the d gate.

$$alpha\_d = \frac{0.095 * \exp\left(-\frac{(V-5.0)}{100.0}\right)}{\left(1.0 + \exp\left(-\frac{(V-5.0)}{13.89}\right)\right)} \tag{A.21.17}$$

The closing rate of the d gate.

$$beta\_d = \frac{0.07 * \exp\left(-\frac{(V+44.0)}{59.0}\right)}{\left(1.0 + \exp\left(\frac{(V+44.0)}{20.0}\right)\right)} \tag{A.21.18}$$

The kinetics of the d gate.

$$\frac{\mathrm{d}(d)}{\mathrm{d}(time)} = \left(\frac{alpha\_d}{R\_d} * (1.0 - d) - beta\_d * d\right) \tag{A.21.19}$$

"slow_inward_current_f_gate" component

The voltage-dependent inactivation gate for the slow inward current - the f gate.

Initial values defined in this component

$f = 1.0$ $\qquad\qquad\qquad\qquad\qquad R\_f = 1.0$

Equations defined in this component

The opening rate of the f gate.

$$alpha\_f = \frac{0.012 * \exp\left(-\frac{(V+28.0)}{125.0}\right)}{\left(1.0 + \exp\left(\frac{(V+28.0)}{6.67}\right)\right)} \tag{A.21.20}$$

The closing rate of the f gate.

$$beta\_f = \frac{0.0065 * \exp\left(-\frac{(V+30.0)}{50.0}\right)}{\left(1.0 + \exp\left(-\frac{(V+30.0)}{5.0}\right)\right)} \tag{A.21.21}$$

The kinetics of the f gate.

$$\frac{\mathrm{d}(f)}{\mathrm{d}(time)} = \left(\frac{alpha\_f}{R\_f} * (1.0 - f) - beta\_f * f\right) \tag{A.21.22}$$

A.22   2004_FK_HMT

A model which couples the Fenton-Karma activation model to the HMT mechanics model via a calcium transient which depends on the slow inward current. The calcium transient definition is taken from the original Beeler-Reuter (1977) model. The default parameter values provided correspond to the modified-LR I parameter set provided by Fenton and Karma in their corrected Table I.

Reference: Fenton, F. & Karma, A. (1998), 'Vortex dynamics in three-dimensional continuous myocardium with fiber rotation: Filament instability and fibrillation', *Chaos* **8**, 20–47.

Reference: Beeler, G. W. & Reuter, H. (1977), 'Reconstruction of the action potential of ventricular myocardial fibres', *Journal of Physiology* **268**, 177–210.

Reference: Hunter, P. J., McCulloch, A. D. & ter Keurs, H. E. (1998), 'Modelling the mechanical properties of cardiac muscle', *Progress in Biophysics & Molecular Biology* **69**, 289–331.

"environment" component

"membrane" component

The main component of the activation model, defining both the actual transmembrane potential and it's non-dimensional representation used in the model.

Initial values defined in this component

$u = 0.0$ $\qquad\qquad$ $V\_o = -85.0 \, \text{mV}$

$Cm = 0.01 \, \mu\text{F} \cdot \text{mm}^{-2}$ $\qquad\qquad$ $V\_fi = 15.0 \, \text{mV}$

$Vm = -85.0 \, \text{mV}$

Equations defined in this component

Convert the scaled currents to actual currents.
$$I\_fi = J\_fi * Cm * (V\_fi - V\_o) \tag{A.22.1}$$

$$I\_si = J\_si * Cm * (V\_fi - V\_o) \tag{A.22.2}$$
$$I\_so = J\_so * Cm * (V\_fi - V\_o) \tag{A.22.3}$$

Calculate the non-dimensional membrane potential variable.
$$u = \frac{(Vm - V\_o)}{(V\_fi - V\_o)} \tag{A.22.4}$$

The standard membrane action potential formulation.
$$\frac{\mathrm{d}(Vm)}{\mathrm{d}(time)} = \frac{(I\_stim - (I\_fi + I\_si + I\_so))}{Cm} \tag{A.22.5}$$

This is a dummy equation that we simply use to make grabbing the value in CMISS much easier.
$$IStimC = I\_stim \tag{A.22.6}$$

"p" component

Equivalent to the Heaviside step function H(u-uc) from the original paper.

Initial values defined in this component

$u\_c = 0.13$

Equations defined in this component

$$p = \begin{cases} 0.0; & \text{if } u < u\_c, \\ 1.0 & \text{otherwise.} \end{cases} \tag{A.22.7}$$

"q" component

Equivalent to the Heaviside step function H(u-uv) from the original paper.

Initial values defined in this component
$u\_v = 0.0$

Equations defined in this component

$$q = \begin{cases} 0.0; & \text{if } u < u\_v, \\ 1.0 & \text{otherwise.} \end{cases} \tag{A.22.8}$$

"fast_inward_current" component

Component representing the scaled fast inward current.

Initial values defined in this component
$g\_fi\_max = 0.058 \ \text{mS} \cdot \text{mm}^{-2}$

Equations defined in this component

Calculation of the current's time constant.
$$tau\_d = \frac{Cm}{g\_fi\_max} \tag{A.22.9}$$

Calculation of the current scaled fast inward current.
$$J\_fi = -v * p * (u - u\_c) * \frac{(1.0 - u)}{tau\_d} \tag{A.22.10}$$

"fast_inward_current_v_gate" component

The inactivation-reactivation gate for the fast inward current. Analogous in role to the product of the h and j gates of the BR and LR models.

Initial values defined in this component
$v = 1.0$ $\qquad\qquad\qquad tau\_v1\_minus = 18.2 \ \text{ms}$

$tau\_v2\_minus = 18.2$ ms $tau\_v\_plus = 10.0$ ms

Equations defined in this component

The kinetics of the fast current's inactivation-reactivation variable.
$$\frac{\mathrm{d}(v)}{\mathrm{d}(time)} = \left((1.0 - p) * \frac{(1.0 - v)}{tau\_v\_minus} - \frac{p * v}{tau\_v\_plus} \right) \tag{A.22.11}$$

Fenton and Karma found it necessary to define the time constant that governs the reactivation of the fast inward current separately over two voltage ranges (uv<u<uc and u<uv).
$$tau\_v\_minus = (q * tau\_v1\_minus + (1.0 - q) * tau\_v2\_minus) \tag{A.22.12}$$

"slow_outward_current" component

The slow outward current, responsible for the repolarisation of the membrane.

Initial values defined in this component

$tau\_0 = 12.5$ ms $tau\_r = 130.0$ ms

Equations defined in this component

Calculation of the scaled slow outward current.
$$J\_so = \left(\frac{u * (1.0 - p)}{tau\_0} + \frac{p}{tau\_r} \right) \tag{A.22.13}$$

"slow_inward_current" component

The scaled slow inward current.

Initial values defined in this component

$tau\_si = 127.0$ ms $k = 10.0$

$u\_csi = 0.85$

Equations defined in this component

Calculation of the slow inward current.
$$J\_si = \frac{-w * (1.0 + \tanh(k * (u - u\_csi)))}{2.0 * tau\_si} \tag{A.22.14}$$

"slow_inward_current_w_gate" component

The inactivation-reactivation gate variable for the slow outward current, analogous to the f gate in the BR and LR models.

Initial values defined in this component

$w = 1.0$ $tau\_w\_plus = 1020.0$ ms

$tau\_w\_minus = 80.0$ ms

Equations defined in this component

The kinetics of the inactivation-reactivation gate for the slow inward current.
$$\frac{\mathrm{d}(w)}{\mathrm{d}(time)} = \left((1.0 - p) * \frac{(1.0 - w)}{tau\_w\_minus} - \frac{p * w}{tau\_w\_plus} \right)$$
(A.22.15)

"calcium_dynamics" component

Here we define the calcium dynamics given by Beeler & Reuter (1977). We are assuming that the slow inward current component is the sole carrier of calcium ions. The BR model also included a calcium dependence in the reversal potential of the slow inward current - should we add this somehow to the FK model ? We have also scaled down the transient to lie within the 0.1 -> 1.0 uM range.

Initial values defined in this component

$Cai = 1.0 \times 10^{-4}$ mM $I\_si\_multiplier = -0.0085$

Equations defined in this component

The intracellular calcium dynamics.
$$\frac{\mathrm{d}(Cai)}{\mathrm{d}(time)} = (I\_si\_multiplier * I\_si + 0.07 * (0.0001 - Cai))$$
(A.22.16)

"mechanics_interface" component

Initial values defined in this component

$lambda = 1.0$	$beta1 = 1.95$
$Cab\_max = 0.035$ mM	$beta2 = 0.31$
$rho0 = 100.0 \, \mathrm{ms}^{-1} \cdot \mathrm{mM}^{-1}$	$alpha1 = 0.033 \, \mathrm{ms}^{-1}$
$rho1 = 0.163 \, \mathrm{ms}^{-1}$	$alpha2 = 2.85 \, \mathrm{ms}^{-1}$
$gamma = 2.6$	$alpha3 = 2.85 \, \mathrm{ms}^{-1}$
$alpha0 = 7.0 \times 10^{-3} \, \mathrm{ms}^{-1}$	$A1 = 50.0$
$n\_ref = 4.25$	$A2 = 175.0$
$p50\_ref = 5.33$	$A3 = 175.0$
$T\_ref = 125.0$ kPa	$a = 0.5$
$beta0 = 1.45$	$velocity = 0.0 \, \mathrm{ms}^{-1}$

Equations defined in this component

Another a dummy equation that we simply use to make grabbing the value in CMISS much easier.
$$lambdaC = lambda$$
(A.22.17)

Another a dummy equation that we simply use to make grabbing the value in CMISS much easier.
$$velocityC = velocity$$
(A.22.18)

"troponin_kinetics" component

The component which defines the kinetics of calcium binding to troponin-C. The binding has been shown to be tension dependent.

Initial values defined in this component

$Cab = 0.0$ mM

Equations defined in this component

The kinetics of the tension-dependent calcium binding to troponin-C.
$$\frac{\mathrm{d}(Cab)}{\mathrm{d}(t)} = (rho0 * Cai * (Cab\_max - Cab) - rho1 * Cab * (1.0 - TTo)) \tag{A.22.19}$$

Calculate the tension dependent factor for calcium binding.
$$TTo = \begin{cases} \frac{T}{gamma * To}; & \text{if } To > 1.0 \times 10^{-8}, \\ 0.0 & \text{otherwise.} \end{cases} \tag{A.22.20}$$

"tropomyosin_kinetics" component

This component defines the kinetics of the length-dependent actin availability.

Initial values defined in this component

$z = 0.0$

Equations defined in this component

The kinetics of actin availability, z.
$$\frac{\mathrm{d}(z)}{\mathrm{d}(t)} = alpha0 * \left(\left(\frac{Cab}{C50} * Cab\_norm \right)^n * (1.0 - z) - z \right) \tag{A.22.21}$$

One of the Hill parameters used to fit the relationship between z and Cab at given sarcomere lengths, and defines part of the length dependence of the model.
$$n = n\_ref * (1.0 + beta1 * (lambda - 1.0)) \tag{A.22.22}$$

One of the Hill parameters used to fit the relationship between z and Cab at given sarcomere lengths, and defines part of the length dependence of the model.
$$p50 = p50\_ref * (1.0 + beta2 * (lambda - 1.0)) \tag{A.22.23}$$

The value of Cab that is required to achieve 50% availability, i.e., z = 0.5.
$$C50 = (10.0)^{(3.0 - p50)} \tag{A.22.24}$$

Normalised value of bound calcium.
$$Cab\_norm = \frac{Cab}{Cab\_max} \tag{A.22.25}$$

"isometric_tension" component

The component which defines the isometric tension.

Equations defined in this component

Calculation of the isometric tension.
$$To = T\_ref * (1.0 + beta0 * (lambda - 1.0)) * z \qquad \text{(A.22.26)}$$

"dynamic_tension" component

We use the ODE equivalent to the fading memory hereditary (thanks Steve). The muscle velocity should be set outside of here, and will be controlled by the simulation environment.

Initial values defined in this component

$Q1 = 0.0$ ms $Q3 = 0.0$ ms

$Q2 = 0.0$ ms

Equations defined in this component

Calculation of the dynamic tension.
$$T = To * \frac{(1.0 + a * Q)}{(1.0 - Q)} \qquad \text{(A.22.27)}$$

Calculate the value of the hereditary integral, with three rate constants.
$$Q = (Q1 + Q2 + Q3) \qquad \text{(A.22.28)}$$

Calculation of the contribution of the first time constant to the hereditary integral, in the ODE form.
$$\frac{\mathrm{d}(Q1)}{\mathrm{d}(t)} = (A1 * velocity - alpha1 * Q1) \qquad \text{(A.22.29)}$$

Calculation of the contribution of the second time constant to the hereditary integral, in the ODE form.
$$\frac{\mathrm{d}(Q2)}{\mathrm{d}(t)} = (A2 * velocity - alpha2 * Q2) \qquad \text{(A.22.30)}$$

Calculation of the contribution of the third time constant to the hereditary integral, in the ODE form.
$$\frac{\mathrm{d}(Q3)}{\mathrm{d}(t)} = (A3 * velocity - alpha3 * Q3) \qquad \text{(A.22.31)}$$

A.23   Nash_Panfilov_2004

This is a CellML version of the modified FitzHugh-Nagumo model, published by Aliev and Panfilov in 1996. While the original two-variable model described a non-dimensional activation variable (u) and a non-dimensional recovery variable (v), here we formulate the model in terms of the 'real' action potential given by the time course of the transmembrane potential (Vm). In so doing, the time rate of change of the activation variable describes the

total 'ionic current' through the membrane with the original model parameters adjusted to give the correct dimensionality. This model has been further modified by Nash and Panfilov 2004 to include active tension development.

Reference: Nash, M. P. & Panfilov, A. V. (2004), 'Electromechanical model of excitable tissue to study reentrant cardiac arrhythmias', *Prog. Biophys. Molec. Biol.* **85**, 501–522.

"interface" component

We'll use this component as the 'interface" to the model, all other components are hidden via encapsulation in this component.

Initial values defined in this component

$Cm = 0.01 \ \mu\text{F} \cdot \text{mm}^{-2}$

$Vr = -85.0 \ \text{mV}$

$Vth = -75.0 \ \text{mV}$

$Vp = 15.0 \ \text{mV}$

$c1 = 8.0 \ \mu\text{A} \cdot \text{mm}^{-2}$

$b = 0.000155 \ \text{ms}^{-1}$

$d = 0.0155 \ \text{ms}^{-1}$

$mu2 = 0.3$

$e0 = 1.0$

$kTa = 47.9 \ \text{kPa}$

Equations defined in this component

This is a dummy equation that we simply use to make grabbing the value in CMISS much easier.

$$IStimC = Istim \tag{A.23.1}$$

"membrane_potential" component

The component which defines the kinetics of the transmembrane potential.

Initial values defined in this component

$Vm = -85 \ \text{mV}$

Equations defined in this component

This equation describes the kinetics of the transmembrane, potential - the action potential.

$$\frac{\mathrm{d}(Vm)}{\mathrm{d}(t)} = \frac{(Istim - Iion)}{Cm} \tag{A.23.2}$$

The non-dimensional and scaled potential value.

$$u = \frac{(Vm - Vr)}{(Vp - Vr)} \tag{A.23.3}$$

"ionic_current" component

Here we define the total ionic current through the cellular membrane - equivalent to the temporal derivative of the original activation variable. One modification of Aliev and Panfilov is in this equation, with the additional multiplication of the recovery variable with the normalised potential and removal of the scalar multiplier.

Equations defined in this component

The calcuation of the total ionic current.
$$Iion = \left(c1 * u * \left(u - \frac{(Vth - Vr)}{(Vp - Vr)} \right) * (u - 1.0) + u * v \right) \tag{A.23.4}$$

"recovery_variable" component

Here we defi ne the non-dimensional recovery variable, v. The kinetics of the recovery variable have been reworked by Aliev and Panfi lov to provide more realistic restitution properties.

Initial values defined in this component
$v = 0.0$

Equations defined in this component

The kinetics of the recovery variable.
$$\frac{\mathrm{d}(v)}{\mathrm{d}(t)} = eps * (-v - rate * vstar * (Vm - Vr)) \tag{A.23.5}$$

$$eps = \left(b + \frac{d * v}{(u + mu2)} \right) \tag{A.23.6}$$

$$rate = \frac{c1}{((Vp - Vr))^{2.0}} \tag{A.23.7}$$

$$vstar = (Vm + ((Vr - Vp) - Vth)) \tag{A.23.8}$$

"active_tension" component

This is the active tension relation from the Nash and Panfi lov article.

Initial values defined in this component
$Ta = 0.0$ kPa

Equations defined in this component

The kinetics of the active tension.
$$\frac{\mathrm{d}(Ta)}{\mathrm{d}(t)} = e * (kTa * u - Ta) \tag{A.23.9}$$

$$e = \begin{cases} 100.0 * e0; & \text{if } u < 0.05, \\ 10.0 * e0 & \text{otherwise.} \end{cases} \tag{A.23.10}$$

A.24 N_LRd

This is the CellML description of a cellular electrophysiology and calcium dynamics model based on the Luo & Rudy model given in Clancy & Rudy (2001), with the Markov state model for IKr. This model also uses the wild-type INa Markov state model of Clancy & Rudy (2002) and the calcium subsystem of Jafri et. al. (1998). The default intitial values included in this CellML model description are for the wild-type epicardial cell type.

Reference: Clancy, C. E. & Rudy, Y. (2002), 'Na+ Channel Mutation That Causes Both Brugada and Long-QT Syndrome Phenotypes: A Simulation Study of Mechanism', *Circulation* **105**, 1208–1213.

Reference: Clancy, C. E. & Rudy, Y. (2001), 'Cellular consequences of HERG mutations in the long QT syndrome: precursors to sudden cardiac death', *Cardiovascular Research* **50**, 301–313.

Reference: Jafri, M. S., Rice, J. J. & Winslow, R. L. (1998), 'Cardiac Ca2+ Dynamics: The Roles of Ryanodine Receptor Adaptation and Sarcoplasmic Reticulum Load', *Biophysical Journal* **74**, 1149–1168.

"environment" component

"membrane" component

The main component of the model which defines the action potential.

Initial values defined in this component

$V = -84.1638 \, \text{mV}$ $F = 9.6845 \times 10^4 \, \text{nC} \cdot \text{nmol}^{-1}$

$R = 8.3145 \times 10^3 \, \text{pJ} \cdot \text{nmol}^{-1} \cdot \text{K}^{-1}$ $Cm = 0.01 \, \mu\text{F} \cdot \text{mm}^{-2}$

$T = 310.0 \, \text{K}$

Equations defined in this component

The kinetics of the transmembrane potential, defined as the sum of all the sarcolemmal currents and an applied stimulus current.

$$\frac{\mathrm{d}(V)}{\mathrm{d}(time)} = \left[I\_stim - \left(i\_Na + i\_Ca\_L\_Ca + i\_Ca\_L\_K + i\_Ca\_T + i\_Kr + i\_Ks + i\_NaCa \right. \right.$$
$$\left. \left. + i\_K1 + i\_Kp + i\_p\_Ca + i\_Na\_b + i\_Ca\_b + i\_NaK + i\_ns\_Ca + i\_to \right) \right] \Big/ Cm \quad \text{(A.24.1)}$$

This is a dummy equation that we simply use to make grabbing the value in CMISS much easier.

$$IStimC = I\_stim \quad \text{(A.24.2)}$$

$$i\_K = (i\_Kr + i\_Ks) \quad \text{(A.24.3)}$$
$$i\_Ca\_L = (i\_Ca\_L\_Ca + i\_Ca\_L\_K) \quad \text{(A.24.4)}$$

"transient_outward_potassium_current" component

The transient outward current. The g_to given here is for epicardial cells. Use g_to=0.005 mS.mm^-2 for M cells and 0.0005 mS.mm^-2 for endocardial cells.

Initial values defined in this component

$g\_to = 0.011 \text{ mS} \cdot \text{mm}^{-2}$

Equations defined in this component

$$i\_to = g\_to * (z)^{3.0} * y * R\_to * (V - E\_K) \tag{A.24.5}$$

$$R\_to = \exp\left(\frac{V}{100.0}\right) \tag{A.24.6}$$

$$E\_K = \frac{R * T}{F} * \ln\left(\frac{Ko}{Ki}\right) \tag{A.24.7}$$

"transient_outward_potassium_current_z_gate" component

Initial values defined in this component

$z = 0.0120892$

Equations defined in this component

$$\frac{\mathrm{d}(z)}{\mathrm{d}(time)} = (alpha\_z * (1.0 - z) - beta\_z * z) \tag{A.24.8}$$

$$alpha\_z = \frac{10.0 * \exp\left(\frac{(V-40.0)}{25.0}\right)}{\left(1.0 + \exp\left(\frac{(V-40.0)}{25.0}\right)\right)} \tag{A.24.9}$$

$$beta\_z = \frac{10.0 * \exp\left(-\frac{(V+90.0)}{25.0}\right)}{\left(1.0 + \exp\left(-\frac{(V+90.0)}{25.0}\right)\right)} \tag{A.24.10}$$

"transient_outward_potassium_current_y_gate" component

Initial values defined in this component

$y = 0.999978$

Equations defined in this component

$$\frac{\mathrm{d}(y)}{\mathrm{d}(time)} = (alpha\_y * (1.0 - y) - beta\_y * y) \tag{A.24.11}$$

$$alpha\_y = \frac{0.015}{\left(1.0 + \exp\left(\frac{(V+60.0)}{5.0}\right)\right)} \tag{A.24.12}$$

$$beta\_y = \frac{0.1 * \exp\left(\frac{(V+25.0)}{5.0}\right)}{\left(1.0 + \exp\left(\frac{(V+25.0)}{5.0}\right)\right)} \tag{A.24.13}$$

"fast_sodium_current" component

Initial values defined in this component

$g\_Na = 0.235 \, \mathrm{mS} \cdot \mathrm{mm}^{-2}$

Equations defined in this component

$$i\_Na = g\_Na * P\_O\_Na * (V - E\_Na) \tag{A.24.14}$$

$$E\_Na = \frac{R * T}{F} * \ln\left(\frac{Nao}{Nai}\right) \tag{A.24.15}$$

"Na_channel_states" component

Initial values defined in this component

$P\_O\_Na = 2.67 \times 10^{-7}$　　　　　$P\_IC3\_Na = 0.261$

$P\_C1\_Na = 0.000159$　　　　　$P\_IC2\_Na = 0.0062$

$P\_C2\_Na = 0.0169$　　　　　$P\_IM1\_Na = 8.05 \times 10^{-5}$

$P\_C3\_Na = 0.713$　　　　　$P\_IM2\_Na = 0.00245$

$P\_IF\_Na = 5.82 \times 10^{-5}$

Equations defined in this component

$$\frac{d(P\_C3\_Na)}{d(time)} = (-(beta\_3 + alpha\_11) * P\_C3\_Na + alpha\_3 * P\_IC3\_Na + beta\_11 * P\_C2\_Na) \tag{A.24.16}$$

$$\frac{d(P\_C2\_Na)}{d(time)} = -(beta\_11 + beta\_3 + alpha\_12) * P\_C2\_Na + alpha\_11 * P\_C3\_Na$$
$$+ beta\_12 * P\_C1\_Na + alpha\_3 * P\_IC2\_Na \tag{A.24.17}$$

$$\frac{d(P\_C1\_Na)}{d(time)} = -(beta\_12 + alpha\_13 + beta\_3) * P\_C1\_Na + alpha\_12 * P\_C2\_Na$$
$$+ beta\_13 * P\_O\_Na + alpha\_3 * P\_IF\_Na \tag{A.24.18}$$

$$\frac{d(P\_O\_Na)}{d(time)} = (-(alpha\_2 + beta\_13) * P\_O\_Na + beta\_2 * P\_IF\_Na + alpha\_13 * P\_C1\_Na) \tag{A.24.19}$$

$$\frac{d(P\_IF\_Na)}{d(time)} = -(beta\_2 + alpha\_3 + alpha\_4 + beta\_12) * P\_IF\_Na + beta\_3 * P\_C1\_Na$$
$$+ beta\_4 * P\_IM1\_Na + alpha\_2 * P\_O\_Na + alpha\_12 * P\_IC2\_Na \tag{A.24.20}$$

$$\frac{d(P\_IC3\_Na)}{d(time)} = (-(alpha\_3 + alpha\_11) * P\_IC3\_Na + beta\_3 * P\_C3\_Na + beta\_11 * P\_IC2\_Na) \tag{A.24.21}$$

$$\frac{\mathrm{d}(P\_IC2\_Na)}{\mathrm{d}(time)} = -\left(alpha\_3 + alpha\_12 + beta\_11\right) * P\_IC2\_Na + beta\_3 * P\_C2\_Na$$

$$+ beta\_12 * P\_IF\_Na + alpha\_11 * P\_IC3\_Na \quad \text{(A.24.22)}$$

$$\frac{\mathrm{d}(P\_IM1\_Na)}{\mathrm{d}(time)} = \left(-\left(alpha\_5 + beta\_4\right) * P\_IM1\_Na + beta\_5 * P\_IM2\_Na + alpha\_4 * P\_IF\_Na\right)$$

$$\text{(A.24.23)}$$

$$\frac{\mathrm{d}(P\_IM2\_Na)}{\mathrm{d}(time)} = \left(alpha\_5 * P\_IM1\_Na - beta\_5 * P\_IM2\_Na\right) \quad \text{(A.24.24)}$$

$$alpha\_11 = \frac{3.802}{\left(0.1027 * \exp\left(\frac{-V}{17.0}\right) + 0.20 * \exp\left(\frac{-V}{150.0}\right)\right)} \quad \text{(A.24.25)}$$

$$alpha\_12 = \frac{3.802}{\left(0.1027 * \exp\left(\frac{-V}{15.0}\right) + 0.23 * \exp\left(\frac{-V}{150.0}\right)\right)} \quad \text{(A.24.26)}$$

$$alpha\_13 = \frac{3.802}{\left(0.1027 * \exp\left(\frac{-V}{12.0}\right) + 0.25 * \exp\left(\frac{-V}{150.0}\right)\right)} \quad \text{(A.24.27)}$$

$$beta\_11 = 0.1917 * \exp\left(\frac{-V}{20.3}\right) \quad \text{(A.24.28)}$$

$$beta\_12 = 0.20 * \exp\left(\frac{-(V - 5.0)}{20.3}\right) \quad \text{(A.24.29)}$$

$$beta\_13 = 0.22 * \exp\left(\frac{-(V - 10.0)}{20.3}\right) \quad \text{(A.24.30)}$$

$$alpha\_2 = 9.178 * \exp\left(\frac{V}{29.68}\right) \quad \text{(A.24.31)}$$

$$beta\_2 = \frac{alpha\_13 * alpha\_2 * alpha\_3}{beta\_13 * beta\_3} \quad \text{(A.24.32)}$$

$$alpha\_3 = 3.7933E - 7 * \exp\left(\frac{-V}{7.7}\right) \quad \text{(A.24.33)}$$

$$beta\_3 = \left(0.0084 + 0.00002 * V\right) \quad \text{(A.24.34)}$$

$$alpha\_4 = \frac{alpha\_2}{100.0} \quad \text{(A.24.35)}$$

$$beta\_4 = alpha\_3 \quad \text{(A.24.36)}$$

$$alpha\_5 = \frac{alpha\_2}{9.5E5} \quad \text{(A.24.37)}$$

$$beta\_5 = \frac{alpha\_3}{50} \quad \text{(A.24.38)}$$

"L_type_Ca_channel" component

The JWR model creates a new mathematical model to describe the L-type calcium channel that is based on the experimentally observed mode-switching behaviour of the channel. Inactivation occurs as calcium ion binding induces the channel to switch (from mode normal) to a mode in which transitions to open states are extremely slow (mode Ca). The channel has one voltage inactivation gate, y. As well as Ca, the channel is assumed permeable to K ions also. The value of P_Ca varies depending on the cell type being modelled. The default value is 33.75e-6 mm.ms^-1 from the JRW model, but this needs to be reduced by 50 percent for RV epicardial cells and 20 percent for LV epicardial cells (following Dumaine et. al. 1999), to allow for the i_to current. From Clancy and Rudy 2002, P_Ca should also be reduced for M-cells and endocardial cells. Since the default in this model is epicardial cells, we used the 50 percent reduced value to match the defualt value of g_to.

Initial values defined in this component

$P\_Ca = 1.6875 \times 10^{-5} \text{ mm} \cdot \text{ms}^{-1}$ $O = 9.84546 \times 10^{-21}$

$P\_K = 1.0 \times 10^{-9} \text{ mm} \cdot \text{ms}^{-1}$ $O\_Ca = 0.0$

$i\_Ca\_L\_Ca\_half = -4.58 \times 10^{-3} \text{ } \mu\text{A} \cdot \text{mm}^{-2}$ $a = 2.0$

$b = 2.0$

$g = 2.0 \text{ ms}^{-1}$

$f = 0.3 \text{ ms}^{-1}$

$g_- = 0.0 \text{ ms}^{-1}$

$f_- = 0.0 \text{ ms}^{-1}$

$omega = 0.01 \text{ ms}^{-1}$

$C0 = 0.997208$

$C1 = 6.38897 \times 10^{-5}$

$C2 = 1.535 \times 10^{-9}$

$C3 = 1.63909 \times 10^{-14}$

$C4 = 6.56337 \times 10^{-20}$

$C\_Ca0 = 2.72826 \times 10^{-3}$

$C\_Ca1 = 6.99215 \times 10^{-7}$

$C\_Ca2 = 6.71989 \times 10^{-11}$

$C\_Ca3 = 2.87031 \times 10^{-15}$

$C\_Ca4 = 4.59752 \times 10^{-20}$

Equations defined in this component

Calculation of the calcium current component of the total channel current, given as the maximal current multiplied by the voltage-dependent inactivation gate and the open probability of the channel based on the mode-switching model.

$$i\_Ca\_L\_Ca = i\_Ca\_L\_Ca\_max * y * (O + O\_Ca) \tag{A.24.39}$$

Calculation of the potassium current component of the total channel current.

$$i\_Ca\_L\_K = p\_k * y * (O + O\_Ca) * \frac{V * (F)^{2.0}}{R * T} * \frac{\left(Ki * \exp\left(\frac{V*F}{R*T}\right) - Ko\right)}{\left(\exp\left(\frac{V*F}{R*T}\right) - 1.0\right)} \tag{A.24.40}$$

The potassium permeability of the channel, which depends on the calcium current component.

$$p\_k = \frac{P\_K}{\left(1.0 + \frac{i\_Ca\_L\_Ca\_max}{i\_Ca\_L\_Ca\_half}\right)} \tag{A.24.41}$$

The maximal calcium current through the channel.

$$i\_Ca\_L\_Ca\_max = P\_Ca * 4.0 * \frac{V * (F)^{2.0}}{R * T} * \frac{\left(0.001 * \exp\left(2.0 * V * \frac{F}{R*T}\right) - 0.341 * Cao\right)}{\left(\exp\left(2.0 * V * \frac{F}{R*T}\right) - 1.0\right)} \tag{A.24.42}$$

Rate constants for state changes in mode normal.

$$alpha = 0.4 * \exp\left(\frac{(V + 12.0)}{10.0}\right) \tag{A.24.43}$$

$$beta = 0.05 * \exp\left(\frac{(V + 12.0)}{-13.0}\right) \tag{A.24.44}$$

Rate constants for state changes in mode Ca (corresponding to alpha-prime and beta-prime in the JRW paper).

$$alpha\_a = alpha * a \tag{A.24.45}$$

$$beta\_b = \frac{beta}{b} \tag{A.24.46}$$

Rate constant for switching between mode normal and mode Ca.

$$gamma = 0.1875 * Ca\_SS \tag{A.24.47}$$

The kinetics of the state transitions in mode normal. In the normal mode, the calcium channel is able to make the

transition to the open, conducting state (O) from the closed state (C) at a normal rate.

$$\frac{\mathrm{d}(C0)}{\mathrm{d}(time)} = ((beta * C1 + omega * C\_Ca0) - (4.0 * alpha + gamma) * C0) \tag{A.24.48}$$

$$\frac{\mathrm{d}(C1)}{\mathrm{d}(time)} = \left(4.0 * alpha * C0 + 2.0 * beta * C2 + \frac{omega}{b} * C\_Ca1 \right)$$
$$- (beta + 3.0 * alpha + gamma * a) * C1 \tag{A.24.49}$$

$$\frac{\mathrm{d}(C2)}{\mathrm{d}(time)} = \left(3.0 * alpha * C1 + 3.0 * beta * C3 + \frac{omega}{(b)^{2.0}} * C\_Ca2 \right)$$
$$- \left(beta * 2.0 + 2.0 * alpha + gamma * (a)^{2.0} \right) * C2 \tag{A.24.50}$$

$$\frac{\mathrm{d}(C3)}{\mathrm{d}(time)} = \left(2.0 * alpha * C2 + 4.0 * beta * C4 + \frac{omega}{(b)^{3.0}} * C\_Ca3 \right)$$
$$- \left(beta * 3.0 + alpha + gamma * (a)^{3.0} \right) * C3 \tag{A.24.51}$$

$$\frac{\mathrm{d}(C4)}{\mathrm{d}(time)} = \left(\left(alpha * C3 + g * O + \frac{omega}{(b)^{4.0}} * C\_Ca4 \right) - \left(beta * 4.0 + f + gamma * (a)^{4.0} \right) * C4 \right) \tag{A.24.52}$$

$$\frac{\mathrm{d}(O)}{\mathrm{d}(time)} = (f * C4 - g * O) \tag{A.24.53}$$

The kinetics of the state transitions in mode Ca. Calcium binding to the Ca channel induces a conformational change from normal mode to mode Ca. This effectively inhibits the conduction of calcium ions because in mode Ca, the calcium channel makes the transition to the open, conducting state (O) extremely slowly.

$$\frac{\mathrm{d}(C\_Ca0)}{\mathrm{d}(time)} = ((beta\_b * C\_Ca1 + gamma * C\_Ca0) - (4.0 * alpha\_a + omega) * C\_Ca0) \tag{A.24.54}$$

$$\frac{\mathrm{d}(C\_Ca1)}{\mathrm{d}(time)} = (4.0 * alpha\_a * C\_Ca0 + 2.0 * beta\_b * C\_Ca2 + gamma * a * C1)$$
$$- \left(beta\_b + 3.0 * alpha\_a + \frac{omega}{b} \right) * C\_Ca1 \tag{A.24.55}$$

$$\frac{\mathrm{d}(C\_Ca2)}{\mathrm{d}(time)} = \left(3.0 * alpha\_a * C\_Ca1 + 3.0 * beta\_b * C\_Ca3 + gamma * (a)^{2.0} * C2 \right)$$
$$- \left(beta\_b * 2.0 + 2.0 * alpha\_a + \frac{omega}{(b)^{2.0}} \right) * C\_Ca2 \tag{A.24.56}$$

$$\frac{\mathrm{d}(C\_Ca3)}{\mathrm{d}(time)} = \left(2.0 * alpha\_a * C\_Ca2 + 4.0 * beta\_b * C\_Ca4 + gamma * (a)^{3.0} * C3 \right)$$
$$- \left(beta\_b * 3.0 + alpha\_a + \frac{omega}{(b)^{3.0}} \right) * C\_Ca3 \tag{A.24.57}$$

$$\frac{\mathrm{d}(C\_Ca4)}{\mathrm{d}(time)} = \left(alpha\_a * C\_Ca3 + g\_ * O\_Ca + gamma * (a)^{4.0} * C4 \right)$$
$$- \left(beta\_b * 4.0 + f\_ + \frac{omega}{(b)^{4.0}} \right) * C\_Ca4 \tag{A.24.58}$$

$$\frac{\mathrm{d}(O\_Ca)}{\mathrm{d}(time)} = (f\_ * C\_Ca4 - g\_ * O\_Ca) \tag{A.24.59}$$

"L_type_Ca_channel_y_gate" component

The voltage-dependent inactivation gate for the L-type calcium channel - the y gate.

Initial values defined in this component

$y = 0.998983$

Equations defined in this component

The kinetics of the y gate.

$$\frac{\mathrm{d}(y)}{\mathrm{d}(time)} = \frac{(y\_infinity - y)}{tau\_y} \tag{A.24.60}$$

$$y\_infinity = \left(\frac{1.0}{\left(1.0 + \exp\left(\frac{(V+55.0)}{7.5}\right)\right)} + \frac{0.1}{\left(1.0 + \exp\left(\frac{(-V+21.0)}{6.0}\right)\right)} \right) \tag{A.24.61}$$

$$tau\_y = \left(20.0 + \frac{600.0}{\left(1.0 + \exp\left(\frac{(V+30.0)}{9.5}\right)\right)} \right) \tag{A.24.62}$$

"T_type_Ca_channel" component

Initial values defined in this component

$g\_Ca\_T = 1.25 \times 10^{-5} \ \mathrm{mS \cdot mm^{-2}}$

Equations defined in this component

$$i\_Ca\_T = g\_Ca\_T * (b)^{2.0} * g * (V - E\_Ca) \tag{A.24.63}$$

$$E\_Ca = \frac{R*T}{2.0*F} * \ln\left(\frac{Cao}{Cai}\right) \tag{A.24.64}$$

"T_type_Ca_channel_b_gate" component

Initial values defined in this component

$b = 0.000970231$

Equations defined in this component

$$\frac{\mathrm{d}(b)}{\mathrm{d}(time)} = \frac{(b\_infinity - b)}{tau\_b} \tag{A.24.65}$$

$$b\_infinity = \frac{1.0}{\left(1.0 + \exp\left(-\frac{(V+14.0)}{10.8}\right)\right)} \tag{A.24.66}$$

$$tau\_b = \frac{(3.7 + 6.1)}{\left(1.0 + \exp\left(\frac{(25.0+V)}{4.5}\right)\right)} \tag{A.24.67}$$

"T_type_Ca_channel_g_gate" component

Initial values defined in this component

$g = 0.994305$

Equations defined in this component

$$\frac{\mathrm{d}(g)}{\mathrm{d}(time)} = \frac{(g\_infinity - g)}{tau\_g} \tag{A.24.68}$$

$$g\_infinity = \frac{1.0}{\left(1.0 + \exp\left(\frac{(V+60.0)}{5.6}\right)\right)} \tag{A.24.69}$$

$$tau\_g = \begin{cases} 12.0; & \text{if } V > 0.0, \\ (-0.875 * V + 12.0) & \text{otherwise.} \end{cases} \tag{A.24.70}$$

"rapid_time_dependent_potassium_current" component

The P_NaK_Kr factor is zero for the default wild-type IKr channel, but is non-zero for some genetic mutations.

Initial values defined in this component

$g\_Kr\_max = 0.000135 \, \mathrm{mS} \cdot \mathrm{mm}^{-2}$ $P\_NaK\_Kr = 0.0$

Equations defined in this component

$$i\_Kr = g\_Kr * P\_O\_Kr * (V - E\_Kr) \tag{A.24.71}$$

$$g\_Kr = g\_Kr\_max * (Ko)^{0.59} \tag{A.24.72}$$

$$E\_Kr = \frac{R * T}{F} * \ln\left(\frac{(Ko + P\_NaK\_Kr * Nao)}{(Ki + P\_NaK\_Kr * Nai)}\right) \tag{A.24.73}$$

"Kr_channel_states" component

The model for cardiac i_Kr includes three closed states (C3, C2, C1) an open state (O) and an inactivation state (I). P_i is the probability of a channel occupying a particular state (i), which is determined by a system of linear first oder differential equations. The default initial values below are for the wild-type channel.

Initial values defined in this component

$P\_O\_Kr = 6.11 \times 10^{-7}$ $beta\_in = 1.077 \, \mathrm{ms}^{-1}$

$P\_C1\_Kr = 0.00116$ $alpha\_V\_shift = -12.0 \, \mathrm{mV}$

$P\_C2\_Kr = 0.000574$ $alpha\_alpha\_V\_shift = -36.0 \, \mathrm{mV}$

$P\_C3\_Kr = 0.938$ $beta\_scale = 1.0$

$P\_I\_Kr = 2.55 \times 10^{-7}$ $beta\_beta\_scale = 1.0$

$alpha\_in = 2.172 \, \mathrm{ms}^{-1}$ $beta\_i\_scale = 1.0$

Equations defined in this component

$$\frac{\mathrm{d}(P\_C3\_Kr)}{\mathrm{d}(time)} = (beta * P\_C2\_Kr - alpha * P\_C3\_Kr) \tag{A.24.74}$$

$$\frac{\mathrm{d}(P\_C2\_Kr)}{\mathrm{d}(time)} = (-(beta + alpha\_in) * P\_C2\_Kr + alpha * P\_C3\_Kr + beta\_in * P\_C1\_Kr) \tag{A.24.75}$$

$$\frac{\mathrm{d}(P\_C1\_Kr)}{\mathrm{d}(time)} = -(beta\_in + alpha\_alpha + alpha\_alpha) * P\_C1\_Kr + alpha\_in * P\_C2\_Kr$$

$$+ beta\_beta * P\_O\_Kr + mu * P\_I\_Kr \tag{A.24.76}$$

$$\frac{\mathrm{d}(P\_O\_Kr)}{\mathrm{d}(time)} = (-(beta\_beta + beta\_i) * P\_O\_Kr + alpha\_alpha * P\_C1\_Kr + alpha\_i * P\_I\_Kr) \tag{A.24.77}$$

$$\frac{\mathrm{d}(P\_I\_Kr)}{\mathrm{d}(time)} = (-(mu + alpha\_i) * P\_I\_Kr + alpha\_alpha * P\_C1\_Kr + beta\_i * P\_O\_Kr) \tag{A.24.78}$$

$$alpha = 55.5 \times 10^{-3} * \exp\left(0.05547153 * (V + alpha\_V\_shift)\right) \tag{A.24.79}$$

$$beta = 0.002357 * \exp\left(-0.036588 * V\right) * beta\_scale \tag{A.24.80}$$

$$alpha\_alpha = 65.5 \times 10^{-3} * \exp\left(0.05547153 * (V + alpha\_alpha\_V\_shift)\right) \tag{A.24.81}$$

$$beta\_beta = 0.0029357 * \exp\left(-0.02158 * V\right) * beta\_beta\_scale \tag{A.24.82}$$

$$alpha\_i = 0.439 * \exp\left(-0.02352 * (V + 25.0)\right) * \frac{4.5}{Ko} \tag{A.24.83}$$

$$beta\_i = 0.656 * \exp\left(0.000942 * V\right) * \frac{(4.5)^{0.3}}{(Ko)^{0.3}} * beta\_i\_scale \tag{A.24.84}$$

$$mu = \begin{cases} \frac{alpha\_i*beta\_beta*alpha\_alpha}{alpha\_alpha*beta\_i}; & \text{if } |beta\_i| > 0.0, \\ \frac{alpha\_i*beta\_beta*alpha\_alpha}{alpha\_alpha} & \text{otherwise.} \end{cases} \tag{A.24.85}$$

"slow_time_dependent_potassium_current" component

The slowly activating component of the time dependent potassium current. g_Ks_max can be varied to give representations of the different cell types described in the various LR models. The default value here is for epicardial cells from the Clancy and Rudy (2002) model - corresponding to a ratio GKs/GKr = 23. From this model, ratios of 17 and 19 should be used for M-cells and endocardial cells, respectively.

Initial values defined in this component

gKs_gKr_ratio = 23.0   P_NaK = 0.01833

Equations defined in this component

$$g\_Ks = g\_Ks\_max * \left(1.0 + \frac{0.6}{\left(1.0 + \left(\frac{0.38 \times 10^{-4}}{Cai}\right)^{1.4}\right)}\right) \tag{A.24.86}$$

$$g\_Ks\_max = g\_Kr\_max * gKs\_gKr\_ratio \tag{A.24.87}$$

$$E\_Ks = \frac{R*T}{F} * \ln\left(\frac{(Ko + P\_NaK * Nao)}{(Ki + P\_NaK * Nai)}\right) \tag{A.24.88}$$

$$i\_Ks = g\_Ks * Xs1 * Xs2 * (V - E\_Ks) \tag{A.24.89}$$

$$Xs = Xs1 * Xs2 \tag{A.24.90}$$

"slow_time_dependent_potassium_current_Xs1_gate" component

Initial values defined in this component

$Xs1 = 0.00445683$

Equations defined in this component

$$\frac{\mathrm{d}(Xs1)}{\mathrm{d}(time)} = \frac{(Xs\_infinity - Xs1)}{tau\_Xs1} \tag{A.24.91}$$

$$Xs\_infinity = \frac{1.0}{\left(1.0 + \exp\left(-\frac{(V-1.5)}{16.7}\right)\right)} \tag{A.24.92}$$

$$tau\_Xs1 = \frac{1.0}{\left(\frac{0.0000719*(V+30.0)}{(1.0-\exp(-0.148*(V+30.0)))} + \frac{0.000131*(V+30.0)}{(\exp(0.0687*(V+30.0))-1.0)}\right)} \tag{A.24.93}$$

"slow_time_dependent_potassium_current_Xs2_gate" component

Initial values defined in this component

$Xs2 = 0.00445683$

Equations defined in this component

$$\frac{\mathrm{d}(Xs2)}{\mathrm{d}(time)} = \frac{(Xs\_infinity - Xs2)}{tau\_Xs2} \tag{A.24.94}$$

$$tau\_Xs2 = 4.0 * tau\_Xs1 \tag{A.24.95}$$

"time_independent_potassium_current" component

The time-independent potassium current.

Initial values defined in this component

$g\_K1\_max = 7.5 \times 10^{-3} \ \mathrm{mS \cdot mm^{-2}}$

Equations defined in this component

Calculation of the maximal channel conductance, dependent on extracellular potassium concentration.

$$g\_K1 = g\_K1\_max * \sqrt{\frac{Ko}{5.4}} \tag{A.24.96}$$

The following equation calculates the reversal potential of the time-independent potassium current.

$$E\_K1 = \frac{R * T}{F} * \ln\left(\frac{Ko}{Ki}\right) \tag{A.24.97}$$

Calculate the current.

$$i\_K1 = g\_K1 * K1\_infinity * (V - E\_K1) \tag{A.24.98}$$

"time_independent_potassium_current_K1_gate" component

The time constants for the K1 gate are small enough that the gating variable can be approximated with it's steady-state value.

Equations defined in this component

The opening rate of the K1 gate.
$$alpha\_K1 = \frac{1.02}{(1.0 + \exp{(0.2385 * ((V - E\_K1) - 59.215)))}} \tag{A.24.99}$$

The closing rate of the K1 gate.
$$beta\_K1 = \frac{(0.49124 * \exp{(0.08032 * ((V + 5.476) - E\_K1))} + \exp{(0.06175 * (V - (E\_K1 + 594.31)))})}{(1.0 + \exp{(-0.5143 * ((V - E\_K1) + 4.753))})} \tag{A.24.100}$$

The steady-state approximation for the K1 gating kinetics.
$$K1\_infinity = \frac{alpha\_K1}{(alpha\_K1 + beta\_K1)} \tag{A.24.101}$$

"plateau_potassium_current" component

The plateau potassium current component contains the equations which describe the contribution of a time independent [K]o-insensitive channel at plateau potentials.

Initial values defined in this component
$g\_Kp = 8.28 \times 10^{-5} \text{ mS} \cdot \text{mm}^{-2}$

Equations defined in this component

The channel's reversal potential.
$$E\_Kp = E\_K1 \tag{A.24.102}$$

The activation variable.
$$Kp = \frac{1.0}{\left(1.0 + \exp{\left(\frac{(7.488 - V)}{5.98}\right)}\right)} \tag{A.24.103}$$

Calculation of the plateau potassium current.
$$i\_Kp = g\_Kp * Kp * (V - E\_Kp) \tag{A.24.104}$$

"Na_Ca_exchanger" component

The Na/Ca exchanger component describes how a protein molecule in the cell surface membrane transports Na ions into the cytosol and exports Ca ions into the extracellular volume, in a ratio of 3:1 respectively.

Initial values defined in this component

$k\_NaCa = 50.0\ \mu\text{A} \cdot \text{mm}^{-2}$ \hspace{3cm} $k\_sat = 0.1$

$K\_mNa = 87.5\ \text{mM}$ \hspace{3.5cm} $eta = 0.35$

$K\_mCa = 1.38\ \text{mM}$

Equations defined in this component

Calculation of the Na/Ca exchanger current.

$$
i\_NaCa = k\_NaCa * \frac{1.0}{\left((K\_mNa)^{3.0} + (Nao)^{3.0}\right)} * \frac{1.0}{(K\_mCa + Cao)}
$$
$$
* \frac{1.0}{\left(1.0 + k\_sat * \exp\left((eta - 1.0) * V * \frac{F}{R*T}\right)\right)}
$$
$$
* \left(\exp\left(eta * V * \frac{F}{R*T}\right) * (Nai)^{3.0} * Cao - \exp\left((eta - 1.0) * V * \frac{F}{R*T}\right) * (Nao)^{3.0} * Cai\right)
$$
$$
\text{(A.24.105)}
$$

"sarcolemmal_calcium_pump" component

The sarcolemmal calcium pump is an additional mechanism for removing Ca ions from the myoplasm to help maintain a low intracellular calcium concentration when at rest.

Initial values defined in this component

$K\_mpCa = 0.5 \times 10^{-3}\ \text{mM}$ \hspace{3cm} $I\_pCa = 1.15 \times 10^{-2}\ \mu\text{A} \cdot \text{mm}^{-2}$

Equations defined in this component

The calcium pump current.

$$
i\_p\_Ca = I\_pCa * \frac{Cai}{(K\_mpCa + Cai)} \tag{A.24.106}
$$

"sodium_background_current" component

The sodium background current is a time-independent diffusion of Na ions down their electrochemical gradient, through the cell surface membrane into the cytosol.

Initial values defined in this component

$g\_Nab = 1.41 \times 10^{-5}\ \text{mS} \cdot \text{mm}^{-2}$

Equations defined in this component

The reversal potential for the background sodium channel.

$$
E\_NaN = E\_Na \tag{A.24.107}
$$

Calculation of the background sodium current.

$$
i\_Na\_b = g\_Nab * (V - E\_NaN) \tag{A.24.108}
$$

"calcium_background_current" component

The calcium background current describes a time-independent diffusion of Ca ions down their electrochemical gradient through the cell surface membrane into the cytosol. However, calcium is not allowed to accumulate to high intracellular concentrations. This influx is balanced by the Ca ion extrusion through the Na-Ca exchanger and the sarcolemmal Ca pump.

Initial values defined in this component

$g\_Cab = 6.032 \times 10^{-5} \text{ mS} \cdot \text{mm}^{-2}$

Equations defined in this component

The reversal potential for the background calcium current.
$$E\_CaN = \frac{R * T}{2.0 * F} * \ln\left(\frac{Cao}{Cai}\right) \tag{A.24.109}$$

Calculation of the background calcium current.
$$i\_Ca\_b = g\_Cab * (V - E\_CaN) \tag{A.24.110}$$

"sodium_potassium_pump" component

The sodium potassium pump is an active protein in the cell membrane which couples the free energy released by the hydrolysis of ATP to the movement of Na and K ions against their electrochemical gradients through the cell membrane.

Initial values defined in this component

$I\_NaK = 0.013 \ \mu\text{A} \cdot \text{mm}^{-2}$ $\qquad\qquad K\_mKo = 1.5 \text{ mM}$

$K\_mNai = 10.0 \text{ mM}$

Equations defined in this component

Calculation of the Na/K pump current.
$$f\_NaK = \frac{1.0}{\left(\left(1.0 + 0.1245 * \exp\left(\frac{-0.1*V*F}{R*T}\right)\right) + 0.0365 * sigma * \exp\left(\frac{-V*F}{R*T}\right)\right)} \tag{A.24.111}$$

$$sigma = \frac{1.0}{7.0} * \left(\exp\left(\frac{Nao}{67.3}\right) - 1.0\right) \tag{A.24.112}$$

$$i\_NaK = I\_NaK * f\_NaK * \frac{1.0}{\left(1.0 + \left(\frac{K\_mNai}{Nai}\right)^{1.5}\right)} * \frac{Ko}{(Ko + K\_mKo)} \tag{A.24.113}$$

"non_specific_calcium_activated_current" component

The nonspecific calcium activated current describes a channel which is activated by calcium ions, but is permeable to only sodium and potassium ions.

Initial values defined in this component

$K\_m\_ns\_Ca = 1.2 \times 10^{-3}$ mM $\qquad\qquad\qquad P\_ns\_Ca = 1.75 \times 10^{-9}$ mm $\cdot$ ms^{-1}

Equations defined in this component

The reversal potential of the channel.

$$EnsCa = \frac{R * T}{F} * \ln\left(\frac{(Ko + Nao)}{(Ki + Nai)}\right) \tag{A.24.114}$$

The potential offset for the channel.

$$VnsCa = (V - EnsCa) \tag{A.24.115}$$

The sodium component of the channel's current.

$$i\_ns\_Na = I\_ns\_Na * \frac{1.0}{\left(1.0 + \left(\frac{K\_m\_ns\_Ca}{Cai}\right)^{3.0}\right)} \tag{A.24.116}$$

The potassium component of the channel's current.

$$i\_ns\_K = I\_ns\_K * \frac{1.0}{\left(1.0 + \left(\frac{K\_m\_ns\_Ca}{Cai}\right)^{3.0}\right)} \tag{A.24.117}$$

The total nonspecifi c calcium activated current.

$$i\_ns\_Ca = (i\_ns\_Na + i\_ns\_K) \tag{A.24.118}$$

The maximal sodium component current.

$$I\_ns\_Na = P\_ns\_Ca * (1.0)^{2.0} * \frac{VnsCa * (F)^{2.0}}{R * T} * \frac{\left(0.75 * Nai * \exp\left(\frac{VnsCa*F}{R*T}\right) - 0.75 * Nao\right)}{\left(\exp\left(\frac{VnsCa*F}{R*T}\right) - 1.0\right)} \tag{A.24.119}$$

The maximal potassium component current.

$$I\_ns\_K = P\_ns\_Ca * (1.0)^{2.0} * \frac{VnsCa * (F)^{2.0}}{R * T} * \frac{\left(0.75 * Ki * \exp\left(\frac{VnsCa*F}{R*T}\right) - 0.75 * Ko\right)}{\left(\exp\left(\frac{VnsCa*F}{R*T}\right) - 1.0\right)} \tag{A.24.120}$$

"calcium_subsystem" component

In the JRW model, subcellular calcium regulatory mechanisms are described in detail. There are six calcium fluxes to consider; J_rel, J_leak, J_up, J_tr, J_xfer and J_trpn. In addition, three membrane current fluxes are also necessary for the formulation of calcium regulation; i_p_Ca, i_Ca_L_Ca and i_NaCa.

Initial values defined in this component

$Cai = 9.94893 \times 10^{-11}$ mM	$v1 = 1.8$ ms^{-1}
$Ca\_SS = 1.36058 \times 10^{-4}$ mM	$v2 = 0.58 \times 10^{-4}$ ms^{-1}
$Am = 546.69$ mm^{-1}	$v3 = 1.8 \times 10^{-3}$ mM $\cdot$ ms^{-1}
$V\_myo = 0.92$	$nCa = 4.0$
$P\_O1 = 1.19168 \times 10^{-3}$	$mCa = 3.0$
$P\_O2 = 6.30613 \times 10^{-9}$	$k\_a\_plus = 1.215 \times 10^{10}$ mM$^{-4} \cdot$ ms^{-1}
$P\_C1 = 0.762527$	$k\_a\_minus = 0.1425$ ms^{-1}
$P\_C2 = 0.236283$	$k\_b\_plus = 4.05 \times 10^{7}$ mM$^{-3} \cdot$ ms^{-1}

$k\_b\_minus = 1.930 \text{ ms}^{-1}$ $K\_mup = 0.5 \times 10^{-3} \text{ mM}$

$k\_c\_plus = 0.018 \text{ ms}^{-1}$ $K\_mCMDN = 2.38 \times 10^{-3} \text{ mM}$

$k\_c\_minus = 0.0008 \text{ ms}^{-1}$ $K\_mCSQN = 0.8 \text{ mM}$

$k\_htrpn\_plus = 20.0 \text{ mM}^{-1} \cdot \text{ms}^{-1}$ $tau\_xfer = 3.125 \text{ ms}$

$k\_htrpn\_minus = 0.066 \times 10^{-3} \text{ ms}^{-1}$ $HTRPN\_tot = 0.14 \text{ mM}$

$k\_ltrpn\_plus = 40.0 \text{ mM}^{-1} \cdot \text{ms}^{-1}$ $LTRPN\_tot = 0.07 \text{ mM}$

$k\_ltrpn\_minus = 0.04 \text{ ms}^{-1}$ $HTRPNCa = 0.13598 \text{ mM}$

$tau\_tr = 34.48 \text{ ms}$ $LTRPNCa = 0.00635 \text{ mM}$

$Ca\_JSR = 1.17504 \text{ mM}$ $CSQN\_tot = 15.0 \text{ mM}$

$Ca\_NSR = 1.243891 \text{ mM}$ $CMDN\_tot = 0.05 \text{ mM}$

Equations defined in this component

Calculate some volume fractions as proportions of the total myoplasmic volume.
$$V\_SS = 5.828 \times 10^{-5} * V\_myo \tag{A.24.121}$$

$$V\_NSR = 0.081 * V\_myo \tag{A.24.122}$$
$$V\_JSR = 0.00464 * V\_myo \tag{A.24.123}$$

The calcium release flux from the JSR into the restricted subspace is governed by the fraction of RyR channels in an open state.
$$J\_rel = v1 * RyR\_open * (Ca\_JSR - Ca\_SS) \tag{A.24.124}$$

The "open" RyR's are those P_O1 and P_O2 states.
$$RyR\_open = (P\_O1 + P\_O2) \tag{A.24.125}$$

The kinetic equations governing the transitions between the four states used to model the RyR's.
$$\frac{\mathrm{d}(P\_C1)}{\mathrm{d}(time)} = \left(-k\_a\_plus * (Ca\_SS)^{nCa} * P\_C1 + k\_a\_minus * P\_O1 \right) \tag{A.24.126}$$

$$\frac{\mathrm{d}(P\_O1)}{\mathrm{d}(time)} = \Big[k\_a\_plus * (Ca\_SS)^{nCa} * P\_C1$$
$$- \left(k\_a\_minus * P\_O1 + k\_b\_plus * (Ca\_SS)^{mCa} * P\_O1 + k\_c\_plus * P\_O1 \right) \Big]$$
$$+ k\_b\_minus * P\_O2 + k\_c\_minus * P\_C2 \tag{A.24.127}$$

$$\frac{\mathrm{d}(P\_O2)}{\mathrm{d}(time)} = \left(k\_b\_plus * (Ca\_SS)^{mCa} * P\_O1 - k\_b\_minus * P\_O2 \right) \tag{A.24.128}$$

$$\frac{\mathrm{d}(P\_C2)}{\mathrm{d}(time)} = (k\_c\_plus * P\_O1 - k\_c\_minus * P\_C2) \tag{A.24.129}$$

Calculate the leakage flux from the NSR into the myoplasm.
$$J\_leak = v2 * (Ca\_NSR - Cai) \tag{A.24.130}$$

Calculate the uptake flux into the NSR from the myoplasm.

$$J\_up = v3 * \frac{(Cai)^{2.0}}{\left((K\_mup)^{2.0} + (Cai)^{2.0}\right)} \tag{A.24.131}$$

Calculate the translocation flux between the uptake (NSR) and release (JSR) stores.

$$J\_tr = \frac{(Ca\_NSR - Ca\_JSR)}{tau\_tr} \tag{A.24.132}$$

Calculate the calcium flux from the diffusion of calcium out of the restricted subspace into the myoplasm.

$$J\_xfer = \frac{(Ca\_SS - Cai)}{tau\_xfer} \tag{A.24.133}$$

The kinetics of calcium binding to the myoplasm buffer troponin - both high and low affinity binding sites.

$$J\_htrpn = (k\_htrpn\_plus * Cai * (HTRPN\_tot - HTRPNCa) - k\_htrpn\_minus * HTRPNCa) \tag{A.24.134}$$

$$J\_ltrpn = (k\_ltrpn\_plus * Cai * (LTRPN\_tot - LTRPNCa) - k\_ltrpn\_minus * LTRPNCa) \tag{A.24.135}$$

$$J\_trpn = (J\_htrpn + J\_ltrpn) \tag{A.24.136}$$

Keep track of the concentration of calcium ions bound to high and low affinity troponin binding sites.

$$\frac{\mathrm{d}(HTRPNCa)}{\mathrm{d}(time)} = J\_htrpn \tag{A.24.137}$$

$$\frac{\mathrm{d}(LTRPNCa)}{\mathrm{d}(time)} = J\_ltrpn \tag{A.24.138}$$

Calcium is buffered by calmodulin (CMDN) in the subspace and myoplasm, and by calsequestrin (CSQN) in the JSR. These are fast buffers and their effect is modelled using the rapid buffering approximation.

$$Bi = \frac{1.0}{\left(1.0 + \frac{CMDN\_tot * K\_mCMDN}{((K\_mCMDN + Cai))^{2.0}}\right)} \tag{A.24.139}$$

$$B\_SS = \frac{1.0}{\left(1.0 + \frac{CMDN\_tot * K\_mCMDN}{((K\_mCMDN + Ca\_SS))^{2.0}}\right)} \tag{A.24.140}$$

$$B\_JSR = \frac{1.0}{\left(1.0 + \frac{CSQN\_tot * K\_mCSQN}{((K\_mCSQN + Ca\_JSR))^{2.0}}\right)} \tag{A.24.141}$$

The kinetics of the calcium ion concentration changes in the various compartments of the model.

$$\frac{\mathrm{d}(Cai)}{\mathrm{d}(time)} = Bi * \left[(J\_leak + J\_xfer) \right.$$
$$\left. - \left(J\_up + J\_trpn + ((i\_Ca\_b - 2.0 * i\_NaCa) + i\_Ca\_T + i\_p\_Ca) * \frac{Am}{2.0 * V\_myo * F} \right) \right] \tag{A.24.142}$$

$$\frac{\mathrm{d}(Ca\_SS)}{\mathrm{d}(time)} = B\_SS * \left(\left(J\_rel * \frac{V\_JSR}{V\_SS} - J\_xfer * \frac{V\_myo}{V\_SS} \right) - i\_Ca\_L\_Ca * \frac{Am}{2.0 * V\_SS * F} \right) \tag{A.24.143}$$

$$\frac{\mathrm{d}(Ca\_JSR)}{\mathrm{d}(time)} = B\_JSR * (J\_tr - J\_rel) \tag{A.24.144}$$

$$\frac{\mathrm{d}(Ca\_NSR)}{\mathrm{d}(time)} = \left((J\_up - J\_leak) * \frac{V\_myo}{V\_NSR} - J\_tr * \frac{V\_JSR}{V\_NSR} \right) \tag{A.24.145}$$

"ionic_concentrations" component

The descriptions of the rate of change of [Na]i and [K]i are the same as the LR-II model.

Initial values defined in this component

$Nai = 10.2042$ mM $\qquad\qquad Ko = 4.5$ mM

$Nao = 140.0$ mM $\qquad\qquad Cao = 1.8$ mM

$Ki = 143.727$ mM

Equations defined in this component

The rate of change of intracellular sodium ion concentration.

$$\frac{\mathrm{d}(Nai)}{\mathrm{d}(time)} = -(i\_Na + i\_Na\_b + i\_ns\_Na + i\_NaCa * 3.0 + i\_NaK * 3.0) * \frac{Am}{V\_myo * F} \tag{A.24.146}$$

The rate of change of intracellular potassium ion concentration.

$$\frac{\mathrm{d}(Ki)}{\mathrm{d}(time)} = -(i\_Ca\_L\_K + i\_Kr + i\_Ks + i\_K1 + i\_Kp + i\_ns\_K + i\_to + -i\_NaK * 2.0) * \frac{Am}{V\_myo * F} \tag{A.24.147}$$

A.25 N_LRd_1795insD_mutant

This is the CellML description of a cellular electrophysiology and calcium dynamics model based on the Luo & Rudy model given in Clancy & Rudy (2001), with the Markov state model for IKr. This model also uses the 1795insD muntant INa Markov state model of Clancy & Rudy (2002) and the calcium subsystem of Jafri et. al. (1998). The default intitial values included in this CellML model description are for the wild-type epicardial cell type, except for the mutant INa channel model.

Reference: Clancy, C. E. & Rudy, Y. (2002), 'Na+ Channel Mutation That Causes Both Brugada and Long-QT Syndrome Phenotypes: A Simulation Study of Mechanism', *Circulation* **105**, 1208–1213.

Reference: Clancy, C. E. & Rudy, Y. (2001), 'Cellular consequences of HERG mutations in the long QT syndrome: precursors to sudden cardiac death', *Cardiovascular Research* **50**, 301–313.

Reference: Jafri, M. S., Rice, J. J. & Winslow, R. L. (1998), 'Cardiac Ca2+ Dynamics: The Roles of Ryanodine Receptor Adaptation and Sarcoplasmic Reticulum Load', *Biophysical Journal* **74**, 1149–1168.

"environment" component

"membrane" component

The main component of the model which defines the action potential.

Initial values defined in this component

$V = -84.1638\,\mathrm{mV}$ $\qquad\qquad$ $F = 9.6845 \times 10^4\,\mathrm{nC \cdot nmol^{-1}}$

$R = 8.3145 \times 10^3\,\mathrm{pJ \cdot nmol^{-1} \cdot K^{-1}}$ $\qquad$ $Cm = 0.01\,\mathrm{\mu F \cdot mm^{-2}}$

$T = 310.0\,\mathrm{K}$

Equations defined in this component

The kinetics of the transmembrane potential, defined as the sum of all the sarcolemmal currents and an applied stimulus current.

$$\frac{\mathrm{d}(V)}{\mathrm{d}(time)} = \Big[I\_stim - \big(i\_Na + i\_Ca\_L\_Ca + i\_Ca\_L\_K + i\_Ca\_T + i\_Kr + i\_Ks + i\_NaCa $$
$$+ i\_K1 + i\_Kp + i\_p\_Ca + i\_Na\_b + i\_Ca\_b + i\_NaK + i\_ns\_Ca + i\_to \big) \Big] \Big/ Cm \quad \text{(A.25.1)}$$

This is a dummy equation that we simply use to make grabbing the value in CMISS much easier.

$$IStimC = I\_stim \qquad\qquad\qquad\qquad \text{(A.25.2)}$$

$$i\_K = (i\_Kr + i\_Ks) \qquad\qquad\qquad\qquad \text{(A.25.3)}$$
$$i\_Ca\_L = (i\_Ca\_L\_Ca + i\_Ca\_L\_K) \qquad\qquad\qquad \text{(A.25.4)}$$

"transient_outward_potassium_current" component

The transient outward current. The g_to given here is for epicardial cells. Use g_to=0.005 mS.mm^-2 for M cells and 0.0005 mS.mm^-2 for endocardial cells.

Initial values defined in this component

$g\_to = 0.011\,\mathrm{mS \cdot mm^{-2}}$

Equations defined in this component

$$i\_to = g\_to * (z)^{3.0} * y * R\_to * (V - E\_K) \qquad\qquad \text{(A.25.5)}$$
$$R\_to = \exp\left(\frac{V}{100.0}\right) \qquad\qquad\qquad\qquad \text{(A.25.6)}$$
$$E\_K = \frac{R * T}{F} * \ln\left(\frac{Ko}{Ki}\right) \qquad\qquad\qquad \text{(A.25.7)}$$

"transient_outward_potassium_current_z_gate" component

Initial values defined in this component

$z = 0.0120892$

Equations defined in this component

$$\frac{d(z)}{d(time)} = (alpha\_z * (1.0 - z) - beta\_z * z) \tag{A.25.8}$$

$$alpha\_z = \frac{10.0 * \exp\left(\frac{(V - 40.0)}{25.0}\right)}{\left(1.0 + \exp\left(\frac{(V - 40.0)}{25.0}\right)\right)} \tag{A.25.9}$$

$$beta\_z = \frac{10.0 * \exp\left(-\frac{(V + 90.0)}{25.0}\right)}{\left(1.0 + \exp\left(-\frac{(V + 90.0)}{25.0}\right)\right)} \tag{A.25.10}$$

"transient_outward_potassium_current_y_gate" component

Initial values defined in this component

$y = 0.999978$

Equations defined in this component

$$\frac{d(y)}{d(time)} = (alpha\_y * (1.0 - y) - beta\_y * y) \tag{A.25.11}$$

$$alpha\_y = \frac{0.015}{\left(1.0 + \exp\left(\frac{(V + 60.0)}{5.0}\right)\right)} \tag{A.25.12}$$

$$beta\_y = \frac{0.1 * \exp\left(\frac{(V + 25.0)}{5.0}\right)}{\left(1.0 + \exp\left(\frac{(V + 25.0)}{5.0}\right)\right)} \tag{A.25.13}$$

"fast_sodium_current" component

Initial values defined in this component

$g\_Na = 0.235 \, \text{mS} \cdot \text{mm}^{-2}$

Equations defined in this component

$$i\_Na = g\_Na * P\_O\_Na * (V - E\_Na) \tag{A.25.14}$$

$$E\_Na = \frac{R * T}{F} * \ln\left(\frac{Nao}{Nai}\right) \tag{A.25.15}$$

"Na_channel_states" component

Initial values defined in this component

$P\_LO\_Na = 1.19 \times 10^{-11}$ $P\_UC3\_Na = 0.477$

$P\_UO\_Na = 1.87 \times 10^{-7}$ $P\_UIC3\_Na = 0.445$

$P\_LC1\_Na = 6.95 \times 10^{-9}$ $P\_UIC2\_Na = 0.0107$

$P\_LC2\_Na = 7.31 \times 10^{-7}$ $P\_UIM1\_Na = 0.00297$

$P\_LC3\_Na = 3.04 \times 10^{-5}$ $P\_UIM2\_Na = 0.0525$

$P\_UIF\_Na = 0.000103$ $alpha\_UL = 1.0 \times 10^{-7} \text{ ms}^{-1}$

$P\_UC1\_Na = 1.09 \times 10^{-4}$ $beta\_LU = 9.5 \times 10^{-4} \text{ ms}^{-1}$

$P\_UC2\_Na = 0.0115$

Equations defined in this component

$$P\_O\_Na = (P\_LO\_Na + P\_UO\_Na) \tag{A.25.16}$$

$$\frac{\mathrm{d}(P\_LC3\_Na)}{\mathrm{d}(time)} = -(beta\_LU + alpha\_11) * P\_LC3\_Na + alpha\_UL * P\_UC3\_Na$$
$$+ beta\_11 * P\_LC2\_Na \tag{A.25.17}$$

$$\frac{\mathrm{d}(P\_LC2\_Na)}{\mathrm{d}(time)} = -(beta\_11 + beta\_LU + alpha\_12) * P\_LC2\_Na + alpha\_11 * P\_LC3\_Na$$
$$+ beta\_12 * P\_LC1\_Na + alpha\_UL * P\_UC2\_Na \tag{A.25.18}$$

$$\frac{\mathrm{d}(P\_LC1\_Na)}{\mathrm{d}(time)} = -(beta\_12 + alpha\_13 + beta\_LU) * P\_LC1\_Na + alpha\_12 * P\_LC2\_Na$$
$$+ beta\_13 * P\_LO\_Na + alpha\_UL * P\_UC1\_Na \tag{A.25.19}$$

$$\frac{\mathrm{d}(P\_LO\_Na)}{\mathrm{d}(time)} = (-(beta\_LU + beta\_13) * P\_LO\_Na + alpha\_UL * P\_UO\_Na + alpha\_13 * P\_LC1\_Na)$$
$$\tag{A.25.20}$$

$$\frac{\mathrm{d}(P\_UIF\_Na)}{\mathrm{d}(time)} = -(beta\_2 + alpha\_3 + alpha\_4 + beta\_12) * P\_UIF\_Na + beta\_3 * P\_UC1\_Na$$
$$+ beta\_4 * P\_UIM1\_Na + alpha\_2 * P\_UO\_Na + alpha\_12 * P\_UIC2\_Na \tag{A.25.21}$$

$$\frac{\mathrm{d}(P\_UIC3\_Na)}{\mathrm{d}(time)} = -(alpha\_3 + alpha\_11) * P\_UIC3\_Na + beta\_3 * P\_UC3\_Na$$
$$+ beta\_11 * P\_UIC2\_Na \tag{A.25.22}$$

$$\frac{\mathrm{d}(P\_UIC2\_Na)}{\mathrm{d}(time)} = -(alpha\_3 + alpha\_12 + beta\_11) * P\_UIC2\_Na + beta\_3 * P\_UC2\_Na$$
$$+ beta\_12 * P\_UIF\_Na + alpha\_11 * P\_UIC3\_Na \tag{A.25.23}$$

$$\frac{\mathrm{d}(P\_UIM1\_Na)}{\mathrm{d}(time)} = -(alpha\_5 + beta\_4) * P\_UIM1\_Na + beta\_5 * P\_UIM2\_Na$$
$$+ alpha\_4 * P\_UIF\_Na \tag{A.25.24}$$

$$\frac{\mathrm{d}(P\_UIM2\_Na)}{\mathrm{d}(time)} = (alpha\_5 * P\_UIM1\_Na - beta\_5 * P\_UIM2\_Na) \tag{A.25.25}$$

$$\frac{\mathrm{d}(P\_UC3\_Na)}{\mathrm{d}(time)} = -(beta\_3 + alpha\_11 + alpha\_UL) * P\_UC3\_Na + alpha\_3 * P\_UIC3\_Na$$
$$+ beta\_11 * P\_UC2\_Na + beta\_LU * P\_LC3\_Na \quad \text{(A.25.26)}$$

$$\frac{\mathrm{d}(P\_UC2\_Na)}{\mathrm{d}(time)} = -(beta\_11 + beta\_3 + alpha\_12 + alpha\_UL) * P\_UC2\_Na$$
$$+ alpha\_11 * P\_UC3\_Na + beta\_12 * P\_UC1\_Na + alpha\_3 * P\_UIC2\_Na + beta\_LU * P\_LC2\_Na$$
$$\text{(A.25.27)}$$

$$\frac{\mathrm{d}(P\_UC1\_Na)}{\mathrm{d}(time)} = -(beta\_12 + alpha\_13 + beta\_3 + alpha\_UL) * P\_UC1\_Na$$
$$+ alpha\_12 * P\_UC2\_Na + beta\_13 * P\_UO\_Na + alpha\_3 * P\_UIF\_Na + beta\_LU * P\_LC1\_Na$$
$$\text{(A.25.28)}$$

$$\frac{\mathrm{d}(P\_UO\_Na)}{\mathrm{d}(time)} = -(alpha\_2 + beta\_13 + alpha\_UL) * P\_UO\_Na + beta\_2 * P\_UIF\_Na$$
$$+ alpha\_13 * P\_UC1\_Na + beta\_LU * P\_LO\_Na \quad \text{(A.25.29)}$$

$$alpha\_11 = \frac{3.802}{\left(0.1027 * \exp\left(\frac{-V}{17.0}\right) + 0.20 * \exp\left(\frac{-V}{150.0}\right)\right)} \quad \text{(A.25.30)}$$

$$alpha\_12 = \frac{3.802}{\left(0.1027 * \exp\left(\frac{-V}{15.0}\right) + 0.23 * \exp\left(\frac{-V}{150.0}\right)\right)} \quad \text{(A.25.31)}$$

$$alpha\_13 = \frac{3.802}{\left(0.1027 * \exp\left(\frac{-V}{12.0}\right) + 0.25 * \exp\left(\frac{-V}{150.0}\right)\right)} \quad \text{(A.25.32)}$$

$$beta\_11 = 0.1917 * \exp\left(\frac{-V}{20.3}\right) \quad \text{(A.25.33)}$$

$$beta\_12 = 0.20 * \exp\left(\frac{-(V - 5.0)}{20.3}\right) \quad \text{(A.25.34)}$$

$$beta\_13 = 0.22 * \exp\left(\frac{-(V - 10.0)}{20.3}\right) \quad \text{(A.25.35)}$$

$$alpha\_2 = 9.178 * \exp\left(\frac{V}{29.68}\right) \quad \text{(A.25.36)}$$

$$beta\_2 = \frac{alpha\_13 * alpha\_2 * alpha\_3}{beta\_13 * beta\_3} \quad \text{(A.25.37)}$$

$$alpha\_3 = \frac{3.7933E - 7 * \exp\left(\frac{-V}{7.7}\right)}{2.5} \quad \text{(A.25.38)}$$

$$beta\_3 = (0.0084 + 0.00002 * V) \quad \text{(A.25.39)}$$

$$alpha\_4 = \frac{alpha\_2}{100.0} \quad \text{(A.25.40)}$$

$$beta\_4 = alpha\_3 \quad \text{(A.25.41)}$$

$$alpha\_5 = \frac{alpha\_2}{3.5E4} \quad \text{(A.25.42)}$$

$$beta\_5 = \frac{alpha\_3}{20} \quad \text{(A.25.43)}$$

"L_type_Ca_channel" component

The JWR model creates a new mathematical model to describe the L-type calcium channel that is based on the experimentally observed mode-switching behaviour of the channel. Inactivation occurs as calcium ion binding induces the channel to switch (from mode normal) to a mode in which transitions to open states are extremely slow (mode Ca). The channel has one voltage inactivation gate, y. As well as Ca, the channel is assumed permeable to K ions also. The value of P_Ca varies depending on the cell type being modelled. The default value is 33.75e-6 mm.ms^-1from the JRW model, but this needs to be reduced by 50 percent for RV epicardial cells and 20 percent

for LV epicardial cells (following Dumaine et. al. 1999), to allow for the i_to current. From Clancy and Rudy 2002, P_Ca should also be reduced for M-cells and endocardial cells. Since the default in this model is epicardial cells, we used the 50 percent reduced value to match the defualt value of g_to.

Initial values defined in this component

$P\_Ca = 1.6875 \times 10^{-5} \; \mathrm{mm} \cdot \mathrm{ms}^{-1}$ $omega = 0.01 \; \mathrm{ms}^{-1}$

$P\_K = 1.0 \times 10^{-9} \; \mathrm{mm} \cdot \mathrm{ms}^{-1}$ $C0 = 0.997208$

$i\_Ca\_L\_Ca\_half = -4.58 \times 10^{-3} \; \mu\mathrm{A} \cdot \mathrm{mm}^{-2}$ $C1 = 6.38897 \times 10^{-5}$

$O = 9.84546 \times 10^{-21}$ $C2 = 1.535 \times 10^{-9}$

$O\_Ca = 0.0$ $C3 = 1.63909 \times 10^{-14}$

$a = 2.0$ $C4 = 6.56337 \times 10^{-20}$

$b = 2.0$ $C\_Ca0 = 2.72826 \times 10^{-3}$

$g = 2.0 \; \mathrm{ms}^{-1}$ $C\_Ca1 = 6.99215 \times 10^{-7}$

$f = 0.3 \; \mathrm{ms}^{-1}$ $C\_Ca2 = 6.71989 \times 10^{-11}$

$g\_ = 0.0 \; \mathrm{ms}^{-1}$ $C\_Ca3 = 2.87031 \times 10^{-15}$

$f\_ = 0.0 \; \mathrm{ms}^{-1}$ $C\_Ca4 = 4.59752 \times 10^{-20}$

Equations defined in this component

Calculation of the calcium current component of the total channel current, given as the maximal current multiplied by the voltage-dependent inactivation gate and the open probability of the channel based on the mode-switching model.

$$i\_Ca\_L\_Ca = i\_Ca\_L\_Ca\_max * y * (O + O\_Ca) \tag{A.25.44}$$

Calculation of the potassium current component of the total channel current.

$$i\_Ca\_L\_K = p\_k * y * (O + O\_Ca) * \frac{V * (F)^{2.0}}{R * T} * \frac{\left(Ki * \exp\left(\frac{V*F}{R*T}\right) - Ko\right)}{\left(\exp\left(\frac{V*F}{R*T}\right) - 1.0\right)} \tag{A.25.45}$$

The potassium permeability of the channel, which depends on the calcium current component.

$$p\_k = \frac{P\_K}{\left(1.0 + \frac{i\_Ca\_L\_Ca\_max}{i\_Ca\_L\_Ca\_half}\right)} \tag{A.25.46}$$

The maximal calcium current through the channel.

$$i\_Ca\_L\_Ca\_max = P\_Ca * 4.0 * \frac{V * (F)^{2.0}}{R * T} * \frac{\left(0.001 * \exp\left(2.0 * V * \frac{F}{R*T}\right) - 0.341 * Cao\right)}{\left(\exp\left(2.0 * V * \frac{F}{R*T}\right) - 1.0\right)} \tag{A.25.47}$$

Rate constants for state changes in mode normal.

$$alpha = 0.4 * \exp\left(\frac{(V + 12.0)}{10.0}\right) \tag{A.25.48}$$

$$beta = 0.05 * \exp\left(\frac{(V + 12.0)}{-13.0}\right) \tag{A.25.49}$$

Rate constants for state changes in mode Ca (corresponding to alpha-prime and beta-prime in the JRW paper).

$$alpha\_a = alpha * a \tag{A.25.50}$$

$$beta\_b = \frac{beta}{b} \tag{A.25.51}$$

Rate constant for switching between mode normal and mode Ca.

$$gamma = 0.1875 * Ca\_SS \tag{A.25.52}$$

The kinetics of the state transitions in mode normal. In the normal mode, the calcium channel is able to make the transition to the open, conducting state (O) from the closed state (C) at a normal rate.

$$\frac{\mathrm{d}(C0)}{\mathrm{d}(time)} = ((beta * C1 + omega * C\_Ca0) - (4.0 * alpha + gamma) * C0) \tag{A.25.53}$$

$$\frac{\mathrm{d}(C1)}{\mathrm{d}(time)} = \left(4.0 * alpha * C0 + 2.0 * beta * C2 + \frac{omega}{b} * C\_Ca1\right)$$
$$- (beta + 3.0 * alpha + gamma * a) * C1 \tag{A.25.54}$$

$$\frac{\mathrm{d}(C2)}{\mathrm{d}(time)} = \left(3.0 * alpha * C1 + 3.0 * beta * C3 + \frac{omega}{(b)^{2.0}} * C\_Ca2\right)$$
$$- \left(beta * 2.0 + 2.0 * alpha + gamma * (a)^{2.0}\right) * C2 \tag{A.25.55}$$

$$\frac{\mathrm{d}(C3)}{\mathrm{d}(time)} = \left(2.0 * alpha * C2 + 4.0 * beta * C4 + \frac{omega}{(b)^{3.0}} * C\_Ca3\right)$$
$$- \left(beta * 3.0 + alpha + gamma * (a)^{3.0}\right) * C3 \tag{A.25.56}$$

$$\frac{\mathrm{d}(C4)}{\mathrm{d}(time)} = \left(\left(alpha * C3 + g * O + \frac{omega}{(b)^{4.0}} * C\_Ca4\right) - \left(beta * 4.0 + f + gamma * (a)^{4.0}\right) * C4\right)$$
$$\tag{A.25.57}$$

$$\frac{\mathrm{d}(O)}{\mathrm{d}(time)} = (f * C4 - g * O) \tag{A.25.58}$$

The kinetics of the state transitions in mode Ca. Calcium binding to the Ca channel induces a conformational change from normal mode to mode Ca. This effectively inhibits the conduction of calcium ions because in mode Ca, the calcium channel makes the transition to the open, conducting state (O) extremely slowly.

$$\frac{\mathrm{d}(C\_Ca0)}{\mathrm{d}(time)} = ((beta\_b * C\_Ca1 + gamma * C\_Ca0) - (4.0 * alpha\_a + omega) * C\_Ca0) \tag{A.25.59}$$

$$\frac{\mathrm{d}(C\_Ca1)}{\mathrm{d}(time)} = (4.0 * alpha\_a * C\_Ca0 + 2.0 * beta\_b * C\_Ca2 + gamma * a * C1)$$
$$- \left(beta\_b + 3.0 * alpha\_a + \frac{omega}{b}\right) * C\_Ca1 \tag{A.25.60}$$

$$\frac{\mathrm{d}(C\_Ca2)}{\mathrm{d}(time)} = \left(3.0 * alpha\_a * C\_Ca1 + 3.0 * beta\_b * C\_Ca3 + gamma * (a)^{2.0} * C2\right)$$
$$- \left(beta\_b * 2.0 + 2.0 * alpha\_a + \frac{omega}{(b)^{2.0}}\right) * C\_Ca2 \tag{A.25.61}$$

$$\frac{\mathrm{d}(C\_Ca3)}{\mathrm{d}(time)} = \left(2.0 * alpha\_a * C\_Ca2 + 4.0 * beta\_b * C\_Ca4 + gamma * (a)^{3.0} * C3\right)$$
$$- \left(beta\_b * 3.0 + alpha\_a + \frac{omega}{(b)^{3.0}}\right) * C\_Ca3 \tag{A.25.62}$$

$$\frac{d(C\_Ca4)}{d(time)} = \left(alpha\_a * C\_Ca3 + g\_ * O\_Ca + gamma * (a)^{4.0} * C4 \right)$$

$$- \left(beta\_b * 4.0 + f\_ + \frac{omega}{(b)^{4.0}} \right) * C\_Ca4 \quad \text{(A.25.63)}$$

$$\frac{d(O\_Ca)}{d(time)} = (f\_ * C\_Ca4 - g\_ * O\_Ca) \quad \text{(A.25.64)}$$

"L_type_Ca_channel_y_gate" component

The voltage-dependent inactivation gate for the L-type calcium channel - the y gate.

Initial values defined in this component

$y = 0.998983$

Equations defined in this component

The kinetics of the y gate.

$$\frac{d(y)}{d(time)} = \frac{(y\_infinity - y)}{tau\_y} \quad \text{(A.25.65)}$$

$$y\_infinity = \left(\frac{1.0}{\left(1.0 + \exp\left(\frac{(V+55.0)}{7.5} \right) \right)} + \frac{0.1}{\left(1.0 + \exp\left(\frac{(-V+21.0)}{6.0} \right) \right)} \right) \quad \text{(A.25.66)}$$

$$tau\_y = \left(20.0 + \frac{600.0}{\left(1.0 + \exp\left(\frac{(V+30.0)}{9.5} \right) \right)} \right) \quad \text{(A.25.67)}$$

"T_type_Ca_channel" component

Initial values defined in this component

$g\_Ca\_T = 1.25 \times 10^{-5} \text{ mS} \cdot \text{mm}^{-2}$

Equations defined in this component

$$i\_Ca\_T = g\_Ca\_T * (b)^{2.0} * g * (V - E\_Ca) \quad \text{(A.25.68)}$$

$$E\_Ca = \frac{R * T}{2.0 * F} * \ln\left(\frac{Cao}{Cai} \right) \quad \text{(A.25.69)}$$

"T_type_Ca_channel_b_gate" component

Initial values defined in this component

$b = 0.000970231$

Equations defined in this component

$$\frac{\mathrm{d}(b)}{\mathrm{d}(time)} = \frac{(b\_infinity - b)}{tau\_b} \tag{A.25.70}$$

$$b\_infinity = \frac{1.0}{\left(1.0 + \exp\left(-\frac{(V+14.0)}{10.8}\right)\right)} \tag{A.25.71}$$

$$tau\_b = \frac{(3.7 + 6.1)}{\left(1.0 + \exp\left(\frac{(25.0+V)}{4.5}\right)\right)} \tag{A.25.72}$$

"T_type_Ca_channel_g_gate" component

Initial values defined in this component

$g = 0.994305$

Equations defined in this component

$$\frac{\mathrm{d}(g)}{\mathrm{d}(time)} = \frac{(g\_infinity - g)}{tau\_g} \tag{A.25.73}$$

$$g\_infinity = \frac{1.0}{\left(1.0 + \exp\left(\frac{(V+60.0)}{5.6}\right)\right)} \tag{A.25.74}$$

$$tau\_g = \begin{cases} 12.0; & \text{if } V > 0.0, \\ (-0.875 * V + 12.0) & \text{otherwise.} \end{cases} \tag{A.25.75}$$

"rapid_time_dependent_potassium_current" component

The P_NaK_Kr factor is zero for the default wild-type IKr channel, but is non-zero for some genetic mutations.

Initial values defined in this component

$g\_Kr\_max = 0.000135 \, \mathrm{mS \cdot mm^{-2}}$ $P\_NaK\_Kr = 0.0$

Equations defined in this component

$$i\_Kr = g\_Kr * P\_O\_Kr * (V - E\_Kr) \tag{A.25.76}$$

$$g\_Kr = g\_Kr\_max * (Ko)^{0.59} \tag{A.25.77}$$

$$E\_Kr = \frac{R * T}{F} * \ln\left(\frac{(Ko + P\_NaK\_Kr * Nao)}{(Ki + P\_NaK\_Kr * Nai)}\right) \tag{A.25.78}$$

"Kr_channel_states" component

The model for cardiac i_Kr includes three closed states (C3, C2, C1) an open state (O) and an inactivation state (I). P_i is the probability of a channel occupying a particular state (i), which is determined by a system of linear first oder differential equations. The default initial values below are for the wild-type channel.

Initial values defined in this component

$P\_O\_Kr = 6.11 \times 10^{-7}$ $beta\_in = 1.077\,\mathrm{ms}^{-1}$

$P\_C1\_Kr = 0.00116$ $alpha\_V\_shift = -12.0\,\mathrm{mV}$

$P\_C2\_Kr = 0.000574$ $alpha\_alpha\_V\_shift = -36.0\,\mathrm{mV}$

$P\_C3\_Kr = 0.938$ $beta\_scale = 1.0$

$P\_I\_Kr = 2.55 \times 10^{-7}$ $beta\_beta\_scale = 1.0$

$alpha\_in = 2.172\,\mathrm{ms}^{-1}$ $beta\_i\_scale = 1.0$

Equations defined in this component

$$\frac{\mathrm{d}(P\_C3\_Kr)}{\mathrm{d}(time)} = (beta * P\_C2\_Kr - alpha * P\_C3\_Kr) \tag{A.25.79}$$

$$\frac{\mathrm{d}(P\_C2\_Kr)}{\mathrm{d}(time)} = (-(beta + alpha\_in) * P\_C2\_Kr + alpha * P\_C3\_Kr + beta\_in * P\_C1\_Kr) \tag{A.25.80}$$

$$\frac{\mathrm{d}(P\_C1\_Kr)}{\mathrm{d}(time)} = -(beta\_in + alpha\_alpha + alpha\_alpha) * P\_C1\_Kr$$
$$+ alpha\_in * P\_C2\_Kr + beta\_beta * P\_O\_Kr + mu * P\_I\_Kr \tag{A.25.81}$$

$$\frac{\mathrm{d}(P\_O\_Kr)}{\mathrm{d}(time)} = (-(beta\_beta + beta\_i) * P\_O\_Kr + alpha\_alpha * P\_C1\_Kr + alpha\_i * P\_I\_Kr) \tag{A.25.82}$$

$$\frac{\mathrm{d}(P\_I\_Kr)}{\mathrm{d}(time)} = (-(mu + alpha\_i) * P\_I\_Kr + alpha\_alpha * P\_C1\_Kr + beta\_i * P\_O\_Kr) \tag{A.25.83}$$

$$alpha = 55.5 \times 10^{-3} * \exp\left(0.05547153 * (V + alpha\_V\_shift)\right) \tag{A.25.84}$$

$$beta = 0.002357 * \exp\left(-0.036588 * V\right) * beta\_scale \tag{A.25.85}$$

$$alpha\_alpha = 65.5 \times 10^{-3} * \exp\left(0.05547153 * (V + alpha\_alpha\_V\_shift)\right) \tag{A.25.86}$$

$$beta\_beta = 0.0029357 * \exp\left(-0.02158 * V\right) * beta\_beta\_scale \tag{A.25.87}$$

$$alpha\_i = 0.439 * \exp\left(-0.02352 * (V + 25.0)\right) * \frac{4.5}{Ko} \tag{A.25.88}$$

$$beta\_i = 0.656 * \exp\left(0.000942 * V\right) * \frac{(4.5)^{0.3}}{(Ko)^{0.3}} * beta\_i\_scale \tag{A.25.89}$$

$$mu = \begin{cases} \frac{alpha\_i * beta\_beta * alpha\_alpha}{alpha\_alpha * beta\_i}; & \text{if } |beta\_i| > 0.0, \\ \frac{alpha\_i * beta\_beta * alpha\_alpha}{alpha\_alpha} & \text{otherwise.} \end{cases} \tag{A.25.90}$$

"slow_time_dependent_potassium_current" component

The slowly activating component of the time dependent potassium current. g_Ks_max can be varied to give representations of the different cell types described in the various LR models. The default value here is for epicardial cells from the Clancy and Rudy (2002) model - corresponding to a ratio GKs/GKr = 23. From this model, ratios of 17 and 19 should be used for M-cells and endocardial cells, respectively.

Initial values defined in this component

$gKs\_gKr\_ratio = 23.0$ $P\_NaK = 0.01833$

Equations defined in this component

$$g\_Ks = g\_Ks\_max * \left(1.0 + \frac{0.6}{\left(1.0 + \left(\frac{0.38 \times 10^{-4}}{Cai} \right)^{1.4} \right)} \right) \quad \text{(A.25.91)}$$

$$g\_Ks\_max = g\_Kr\_max * gKs\_gKr\_ratio \quad \text{(A.25.92)}$$

$$E\_Ks = \frac{R * T}{F} * \ln\left(\frac{(Ko + P\_NaK * Nao)}{(Ki + P\_NaK * Nai)} \right) \quad \text{(A.25.93)}$$

$$i\_Ks = g\_Ks * Xs1 * Xs2 * (V - E\_Ks) \quad \text{(A.25.94)}$$

$$Xs = Xs1 * Xs2 \quad \text{(A.25.95)}$$

"slow_time_dependent_potassium_current_Xs1_gate" component

Initial values defined in this component

$Xs1 = 0.00445683$

Equations defined in this component

$$\frac{\mathrm{d}(Xs1)}{\mathrm{d}(time)} = \frac{(Xs\_infinity - Xs1)}{tau\_Xs1} \quad \text{(A.25.96)}$$

$$Xs\_infinity = \frac{1.0}{\left(1.0 + \exp\left(-\frac{(V - 1.5)}{16.7} \right) \right)} \quad \text{(A.25.97)}$$

$$tau\_Xs1 = \frac{1.0}{\left(\frac{0.0000719 * (V + 30.0)}{(1.0 - \exp(-0.148 * (V + 30.0)))} + \frac{0.000131 * (V + 30.0)}{(\exp(0.0687 * (V + 30.0)) - 1.0)} \right)} \quad \text{(A.25.98)}$$

"slow_time_dependent_potassium_current_Xs2_gate" component

Initial values defined in this component

$Xs2 = 0.00445683$

Equations defined in this component

$$\frac{\mathrm{d}(Xs2)}{\mathrm{d}(time)} = \frac{(Xs\_infinity - Xs2)}{tau\_Xs2} \quad \text{(A.25.99)}$$

$$tau\_Xs2 = 4.0 * tau\_Xs1 \quad \text{(A.25.100)}$$

"time_independent_potassium_current" component

The time-independent potassium current.

Initial values defined in this component

$g\_K1\_max = 7.5 \times 10^{-3} \ \mathrm{mS} \cdot \mathrm{mm}^{-2}$

Equations defined in this component

Calculation of the maximal channel conductance, dependent on extracellular potassium concentration.

$$g\_K1 = g\_K1\_max * \sqrt{\frac{Ko}{5.4}} \tag{A.25.101}$$

The following equation calculates the reversal potential of the time-independent potassium current.

$$E\_K1 = \frac{R * T}{F} * \ln\left(\frac{Ko}{Ki}\right) \tag{A.25.102}$$

Calculate the current.

$$i\_K1 = g\_K1 * K1\_infinity * (V - E\_K1) \tag{A.25.103}$$

"time_independent_potassium_current_K1_gate" component

The time constants for the K1 gate are small enough that the gating variable can be approximated with it's steady-state value.

Equations defined in this component

The opening rate of the K1 gate.

$$alpha\_K1 = \frac{1.02}{(1.0 + \exp(0.2385 * ((V - E\_K1) - 59.215)))} \tag{A.25.104}$$

The closing rate of the K1 gate.

$$beta\_K1 = \frac{(0.49124 * \exp(0.08032 * ((V + 5.476) - E\_K1)) + \exp(0.06175 * (V - (E\_K1 + 594.31))))}{(1.0 + \exp(-0.5143 * ((V - E\_K1) + 4.753)))} \tag{A.25.105}$$

The steady-state approximation for the K1 gating kinetics.

$$K1\_infinity = \frac{alpha\_K1}{(alpha\_K1 + beta\_K1)} \tag{A.25.106}$$

"plateau_potassium_current" component

The plateau potassium current component contains the equations which describe the contribution of a time independent [K]o-insensitive channel at plateau potentials.

Initial values defined in this component

$g\_Kp = 8.28 \times 10^{-5}$ mS $\cdot$ mm^{-2}

Equations defined in this component

The channel's reversal potential.

$$E\_Kp = E\_K1 \tag{A.25.107}$$

The activation variable.

$$Kp = \frac{1.0}{\left(1.0 + \exp\left(\frac{(7.488 - V)}{5.98}\right)\right)} \qquad (A.25.108)$$

Calculation of the plateau potassium current.

$$i\_Kp = g\_Kp * Kp * (V - E\_Kp) \qquad (A.25.109)$$

"Na_Ca_exchanger" component

The Na/Ca exchanger component describes how a protein molecule in the cell surface membrane transports Na ions into the cytosol and exports Ca ions into the extracellular volume, in a ratio of 3:1 respectively.

Initial values defined in this component

$k\_NaCa = 50.0 \ \mu A \cdot mm^{-2}$ $k\_sat = 0.1$

$K\_mNa = 87.5 \ mM$ $eta = 0.35$

$K\_mCa = 1.38 \ mM$

Equations defined in this component

Calculation of the Na/Ca exchanger current.

$$i\_NaCa = k\_NaCa * \frac{1.0}{\left((K\_mNa)^{3.0} + (Nao)^{3.0}\right)} * \frac{1.0}{(K\_mCa + Cao)}$$
$$* \frac{1.0}{\left(1.0 + k\_sat * \exp\left((eta - 1.0) * V * \frac{F}{R*T}\right)\right)}$$
$$* \left(\exp\left(eta * V * \frac{F}{R*T}\right) * (Nai)^{3.0} * Cao - \exp\left((eta - 1.0) * V * \frac{F}{R*T}\right) * (Nao)^{3.0} * Cai\right)$$
$$(A.25.110)$$

"sarcolemmal_calcium_pump" component

The sarcolemmal calcium pump is an additional mechanism for removing Ca ions from the myoplasm to help maintain a low intracellular calcium concentration when at rest.

Initial values defined in this component

$K\_mpCa = 0.5 \times 10^{-3} \ mM$ $I\_pCa = 1.15 \times 10^{-2} \ \mu A \cdot mm^{-2}$

Equations defined in this component

The calcium pump current.

$$i\_p\_Ca = I\_pCa * \frac{Cai}{(K\_mpCa + Cai)} \qquad (A.25.111)$$

"sodium_background_current" component

The sodium background current is a time-independent diffusion of Na ions down their electrochemical gradient, through the cell surface membrane into the cytosol.

Initial values defined in this component

$g\_Nab = 1.41 \times 10^{-5} \text{ mS} \cdot \text{mm}^{-2}$

Equations defined in this component

The reversal potential for the background sodium channel.
$$E\_NaN = E\_Na \tag{A.25.112}$$

Calculation of the background sodium current.
$$i\_Na\_b = g\_Nab * (V - E\_NaN) \tag{A.25.113}$$

"calcium_background_current" component

The calcium background current describes a time-independent diffusion of Ca ions down their electrochemical gradient through the cell surface membrane into the cytosol. However, calcium is not allowed to accumulate to high intracellular concentrations. This influx is balanced by the Ca ion extrusion through the Na-Ca exchanger and the sarcolemmal Ca pump.

Initial values defined in this component

$g\_Cab = 6.032 \times 10^{-5} \text{ mS} \cdot \text{mm}^{-2}$

Equations defined in this component

The reversal potential for the background calcium current.
$$E\_CaN = \frac{R * T}{2.0 * F} * \ln\left(\frac{Cao}{Cai}\right) \tag{A.25.114}$$

Calculation of the background calcium current.
$$i\_Ca\_b = g\_Cab * (V - E\_CaN) \tag{A.25.115}$$

"sodium_potassium_pump" component

The sodium potassium pump is an active protein in the cell membrane which couples the free energy released by the hydrolysis of ATP to the movement of Na and K ions against their electrochemical gradients through the cell membrane.

Initial values defined in this component

$I\_NaK = 0.013 \, \mu\text{A} \cdot \text{mm}^{-2}$ $K\_mKo = 1.5 \text{ mM}$

$K\_mNai = 10.0 \text{ mM}$

Equations defined in this component

Calculation of the Na/K pump current.

$$f\_NaK = \frac{1.0}{\left(\left(1.0 + 0.1245 * \exp\left(\frac{-0.1*V*F}{R*T}\right)\right) + 0.0365 * sigma * \exp\left(\frac{-V*F}{R*T}\right)\right)} \quad (A.25.116)$$

$$sigma = \frac{1.0}{7.0} * \left(\exp\left(\frac{Nao}{67.3}\right) - 1.0\right) \quad (A.25.117)$$

$$i\_NaK = I\_NaK * f\_NaK * \frac{1.0}{\left(1.0 + \left(\frac{K\_mNai}{Nai}\right)^{1.5}\right)} * \frac{Ko}{(Ko + K\_mKo)} \quad (A.25.118)$$

"non_specific_calcium_activated_current" component

The nonspecific calcium activated current describes a channel which is activated by calcium ions, but is permeable to only sodium and potassium ions.

Initial values defined in this component

$K\_m\_ns\_Ca = 1.2 \times 10^{-3}$ mM $\qquad\qquad P\_ns\_Ca = 1.75 \times 10^{-9}$ mm $\cdot$ ms^{-1}

Equations defined in this component

The reversal potential of the channel.

$$EnsCa = \frac{R*T}{F} * \ln\left(\frac{(Ko + Nao)}{(Ki + Nai)}\right) \quad (A.25.119)$$

The potential offset for the channel.

$$VnsCa = (V - EnsCa) \quad (A.25.120)$$

The sodium component of the channel's current.

$$i\_ns\_Na = I\_ns\_Na * \frac{1.0}{\left(1.0 + \left(\frac{K\_m\_ns\_Ca}{Cai}\right)^{3.0}\right)} \quad (A.25.121)$$

The potassium component of the channel's current.

$$i\_ns\_K = I\_ns\_K * \frac{1.0}{\left(1.0 + \left(\frac{K\_m\_ns\_Ca}{Cai}\right)^{3.0}\right)} \quad (A.25.122)$$

The total nonspecific calcium activated current.

$$i\_ns\_Ca = (i\_ns\_Na + i\_ns\_K) \quad (A.25.123)$$

The maximal sodium component current.

$$I\_ns\_Na = P\_ns\_Ca * (1.0)^{2.0} * \frac{VnsCa * (F)^{2.0}}{R*T} * \frac{\left(0.75 * Nai * \exp\left(\frac{VnsCa*F}{R*T}\right) - 0.75 * Nao\right)}{\left(\exp\left(\frac{VnsCa*F}{R*T}\right) - 1.0\right)} \quad (A.25.124)$$

The maximal potassium component current.

$$I\_ns\_K = P\_ns\_Ca * (1.0)^{2.0} * \frac{VnsCa * (F)^{2.0}}{R*T} * \frac{\left(0.75 * Ki * \exp\left(\frac{VnsCa*F}{R*T}\right) - 0.75 * Ko\right)}{\left(\exp\left(\frac{VnsCa*F}{R*T}\right) - 1.0\right)} \quad (A.25.125)$$

"calcium_subsystem" component

In the JRW model, subcellular calcium regulatory mechanisms are described in detail. There are six calcium fluxes to consider; J_rel, J_leak, J_up, J_tr, J_xfer and J_trpn. In addition, three membrane current fluxes are also necessary for the formulation of calcium regulation; i_p_Ca, i_Ca_L_Ca and i_NaCa.

Initial values defined in this component

$Cai = 9.94893 \times 10^{-11}$ mM

$Ca\_SS = 1.36058 \times 10^{-4}$ mM

$Am = 546.69$ mm^{-1}

$V\_myo = 0.92$

$P\_O1 = 1.19168 \times 10^{-3}$

$P\_O2 = 6.30613 \times 10^{-9}$

$P\_C1 = 0.762527$

$P\_C2 = 0.236283$

$v1 = 1.8$ ms^{-1}

$v2 = 0.58 \times 10^{-4}$ ms^{-1}

$v3 = 1.8 \times 10^{-3}$ mM $\cdot$ ms^{-1}

$nCa = 4.0$

$mCa = 3.0$

$k\_a\_plus = 1.215 \times 10^{10}$ mM^{-4} $\cdot$ ms^{-1}

$k\_a\_minus = 0.1425$ ms^{-1}

$k\_b\_plus = 4.05 \times 10^{7}$ mM^{-3} $\cdot$ ms^{-1}

$k\_b\_minus = 1.930$ ms^{-1}

$k\_c\_plus = 0.018$ ms^{-1}

$k\_c\_minus = 0.0008$ ms^{-1}

$k\_htrpn\_plus = 20.0$ mM^{-1} $\cdot$ ms^{-1}

$k\_htrpn\_minus = 0.066 \times 10^{-3}$ ms^{-1}

$k\_ltrpn\_plus = 40.0$ mM^{-1} $\cdot$ ms^{-1}

$k\_ltrpn\_minus = 0.04$ ms^{-1}

$tau\_tr = 34.48$ ms

$Ca\_JSR = 1.17504$ mM

$Ca\_NSR = 1.243891$ mM

$K\_mup = 0.5 \times 10^{-3}$ mM

$K\_mCMDN = 2.38 \times 10^{-3}$ mM

$K\_mCSQN = 0.8$ mM

$tau\_xfer = 3.125$ ms

$HTRPN\_tot = 0.14$ mM

$LTRPN\_tot = 0.07$ mM

$HTRPNCa = 0.13598$ mM

$LTRPNCa = 0.00635$ mM

$CSQN\_tot = 15.0$ mM

$CMDN\_tot = 0.05$ mM

Equations defined in this component

Calculate some volume fractions as proportions of the total myoplasmic volume.

$$V\_SS = 5.828 \times 10^{-5} * V\_myo \tag{A.25.126}$$

$$V\_NSR = 0.081 * V\_myo \tag{A.25.127}$$

$$V\_JSR = 0.00464 * V\_myo \tag{A.25.128}$$

The calcium release flux from the JSR into the restricted subspace is governed by the fraction of RyR channels in an open state.

$$J\_rel = v1 * RyR\_open * (Ca\_JSR - Ca\_SS) \tag{A.25.129}$$

The "open"RyR's are those P_O1 and P_O2 states.

$$RyR\_open = (P\_O1 + P\_O2) \tag{A.25.130}$$

The kinetic equations governing the transitions between the four states used to model the RyR's.

$$\frac{\mathrm{d}(P\_C1)}{\mathrm{d}(time)} = \left(-k\_a\_plus * (Ca\_SS)^{nCa} * P\_C1 + k\_a\_minus * P\_O1\right) \tag{A.25.131}$$

$$\frac{\mathrm{d}(P\_O1)}{\mathrm{d}(time)} = \Big[k\_a\_plus * (Ca\_SS)^{nCa} * P\_C1$$

$$- \left(k\_a\_minus * P\_O1 + k\_b\_plus * (Ca\_SS)^{mCa} * P\_O1 + k\_c\_plus * P\_O1\right)\Big]$$

$$+ k\_b\_minus * P\_O2 + k\_c\_minus * P\_C2 \tag{A.25.132}$$

$$\frac{\mathrm{d}(P\_O2)}{\mathrm{d}(time)} = \left(k\_b\_plus * (Ca\_SS)^{mCa} * P\_O1 - k\_b\_minus * P\_O2\right) \tag{A.25.133}$$

$$\frac{\mathrm{d}(P\_C2)}{\mathrm{d}(time)} = (k\_c\_plus * P\_O1 - k\_c\_minus * P\_C2) \tag{A.25.134}$$

Calculate the leakage flux from the NSR into the myoplasm.

$$J\_leak = v2 * (Ca\_NSR - Cai) \tag{A.25.135}$$

Calculate the uptake flux into the NSR from the myoplasm.

$$J\_up = v3 * \frac{(Cai)^{2.0}}{\left((K\_mup)^{2.0} + (Cai)^{2.0}\right)} \tag{A.25.136}$$

Calculate the translocation flux between the uptake (NSR) and release (JSR) stores.

$$J\_tr = \frac{(Ca\_NSR - Ca\_JSR)}{tau\_tr} \tag{A.25.137}$$

Calculate the calcium flux from the diffusion of calcium out of the restricted subspace into the myoplasm.

$$J\_xfer = \frac{(Ca\_SS - Cai)}{tau\_xfer} \tag{A.25.138}$$

The kinetics of calcium binding to the myoplasm buffer troponin - both high and low affinity binding sites.

$$J\_htrpn = (k\_htrpn\_plus * Cai * (HTRPN\_tot - HTRPNCa) - k\_htrpn\_minus * HTRPNCa) \tag{A.25.139}$$

$$J\_ltrpn = (k\_ltrpn\_plus * Cai * (LTRPN\_tot - LTRPNCa) - k\_ltrpn\_minus * LTRPNCa) \tag{A.25.140}$$

$$J\_trpn = (J\_htrpn + J\_ltrpn) \tag{A.25.141}$$

Keep track of the concentration of calcium ions bound to high and low affinity troponin binding sites.

$$\frac{\mathrm{d}(HTRPNCa)}{\mathrm{d}(time)} = J\_htrpn \tag{A.25.142}$$

$$\frac{\mathrm{d}(LTRPNCa)}{\mathrm{d}(time)} = J\_ltrpn \tag{A.25.143}$$

Calcium is buffered by calmodulin (CMDN) in the subspace and myoplasm, and by calsequestrin (CSQN) in the

JSR. These are fast buffers and their effect is modelled using the rapid buffering approximation.

$$Bi = \frac{1.0}{\left(1.0 + \frac{CMDN\_tot * K\_mCMDN}{((K\_mCMDN + Cai))^{2.0}}\right)} \tag{A.25.144}$$

$$B\_SS = \frac{1.0}{\left(1.0 + \frac{CMDN\_tot * K\_mCMDN}{((K\_mCMDN + Ca\_SS))^{2.0}}\right)} \tag{A.25.145}$$

$$B\_JSR = \frac{1.0}{\left(1.0 + \frac{CSQN\_tot * K\_mCSQN}{((K\_mCSQN + Ca\_JSR))^{2.0}}\right)} \tag{A.25.146}$$

The kinetics of the calcium ion concentration changes in the various compartments of the model.

$$\frac{\mathrm{d}(Cai)}{\mathrm{d}(time)} = Bi * \Bigg[(J\_leak + J\_xfer)$$
$$- \left(J\_up + J\_trpn + ((i\_Ca\_b - 2.0 * i\_NaCa) + i\_Ca\_T + i\_p\_Ca) * \frac{Am}{2.0 * V\_myo * F}\right)\Bigg] \tag{A.25.147}$$

$$\frac{\mathrm{d}(Ca\_SS)}{\mathrm{d}(time)} = B\_SS * \left(\left(J\_rel * \frac{V\_JSR}{V\_SS} - J\_xfer * \frac{V\_myo}{V\_SS}\right) - i\_Ca\_L\_Ca * \frac{Am}{2.0 * V\_SS * F}\right)$$
$$\tag{A.25.148}$$

$$\frac{\mathrm{d}(Ca\_JSR)}{\mathrm{d}(time)} = B\_JSR * (J\_tr - J\_rel) \tag{A.25.149}$$

$$\frac{\mathrm{d}(Ca\_NSR)}{\mathrm{d}(time)} = \left((J\_up - J\_leak) * \frac{V\_myo}{V\_NSR} - J\_tr * \frac{V\_JSR}{V\_NSR}\right) \tag{A.25.150}$$

"ionic_concentrations" component

The descriptions of the rate of change of [Na]i and [K]i are the same as the LR-II model.

Initial values defined in this component

Nai = 10.2042 mM
Nao = 140.0 mM
Ki = 143.727 mM

Ko = 4.5 mM
Cao = 1.8 mM

Equations defined in this component

The rate of change of intracellular sodium ion concentration.

$$\frac{\mathrm{d}(Nai)}{\mathrm{d}(time)} = -(i\_Na + i\_Na\_b + i\_ns\_Na + i\_NaCa * 3.0 + i\_NaK * 3.0) * \frac{Am}{V\_myo * F} \tag{A.25.151}$$

The rate of change of intracellular potassium ion concentration.

$$\frac{\mathrm{d}(Ki)}{\mathrm{d}(time)} = -(i\_Ca\_L\_K + i\_Kr + i\_Ks + i\_K1 + i\_Kp + i\_ns\_K + i\_to + -i\_NaK * 2.0) * \frac{Am}{V\_myo * F}$$
$$\tag{A.25.152}$$

A.26   N_LRd_HMT

This is the CellML description of a cellular electrophysiology and calcium dynamics model based on the Luo & Rudy model given in Clancy & Rudy (2001), with the Markov state model for IKr. This model also uses the wild-type INa Markov state model of Clancy & Rudy (2002) and the calcium subsystem of Jafri et. al. (1998). The default intitial values included in this CellML model description are for the wild-type epicardial cell type. The electrophysiological model is coupled to the HMT cardiac mechanics model via the JRW calcium binding to low affinity troponin-C, which has been modified to include the tension dependent release of Ca from TnC.

Reference: Clancy, C. E. & Rudy, Y. (2002), 'Na+ Channel Mutation That Causes Both Brugada and Long-QT Syndrome Phenotypes: A Simulation Study of Mechanism', *Circulation* **105**, 1208–1213.

Reference: Clancy, C. E. & Rudy, Y. (2001), 'Cellular consequences of HERG mutations in the long QT syndrome: precursors to sudden cardiac death', *Cardiovascular Research* **50**, 301–313.

Reference: Jafri, M. S., Rice, J. J. & Winslow, R. L. (1998), 'Cardiac Ca2+ Dynamics: The Roles of Ryanodine Receptor Adaptation and Sarcoplasmic Reticulum Load', *Biophysical Journal* **74**, 1149–1168.

Reference: Hunter, P. J., McCulloch, A. D. & ter Keurs, H. E. (1998), 'Modelling the mechanical properties of cardiac muscle', *Progress in Biophysics & Molecular Biology* **69**, 289–331.

"environment" component

"membrane" component

The main component of the model which defines the action potential.

Initial values defined in this component

$V = -84.1638\,\mathrm{mV}$ $\qquad\qquad\qquad$ $F = 9.6845 \times 10^4\,\mathrm{nC} \cdot \mathrm{nmol}^{-1}$

$R = 8.3145 \times 10^3\,\mathrm{pJ} \cdot \mathrm{nmol}^{-1} \cdot \mathrm{K}^{-1}$ $\qquad$ $Cm = 0.01\,\mu\mathrm{F} \cdot \mathrm{mm}^{-2}$

$T = 310.0\,\mathrm{K}$

Equations defined in this component

The kinetics of the transmembrane potential, defined as the sum of all the sarcolemmal currents and an applied stimulus current.

$$\frac{\mathrm{d}(V)}{\mathrm{d}(time)} = \Big[I\_stim - \big(i\_Na + i\_Ca\_L\_Ca + i\_Ca\_L\_K + i\_Ca\_T + i\_Kr + i\_Ks + i\_NaCa$$
$$+\, i\_K1 + i\_Kp + i\_p\_Ca + i\_Na\_b + i\_Ca\_b + i\_NaK + i\_ns\_Ca + i\_to\big)\Big]\Big/ Cm \quad \text{(A.26.1)}$$

This is a dummy equation that we simply use to make grabbing the value in CMISS much easier.

$$IStimC = I\_stim \qquad\qquad\qquad\qquad\qquad\qquad \text{(A.26.2)}$$

$$i\_K = (i\_Kr + i\_Ks) \tag{A.26.3}$$
$$i\_Ca\_L = (i\_Ca\_L\_Ca + i\_Ca\_L\_K) \tag{A.26.4}$$

"transient_outward_potassium_current" component

The transient outward current. The g_to given here is for epicardial cells. Use g_to=0.005 mS.mm^-2 for M cells and 0.0005 mS.mm^-2 for endocardial cells.

Initial values defined in this component

$g\_to = 0.011 \text{ mS} \cdot \text{mm}^{-2}$

Equations defined in this component

$$i\_to = g\_to * (z)^{3.0} * y * R\_to * (V - E\_K) \tag{A.26.5}$$
$$R\_to = \exp\left(\frac{V}{100.0}\right) \tag{A.26.6}$$
$$E\_K = \frac{R*T}{F} * \ln\left(\frac{Ko}{Ki}\right) \tag{A.26.7}$$

"transient_outward_potassium_current_z_gate" component

Initial values defined in this component

$z = 0.0120892$

Equations defined in this component

$$\frac{\mathrm{d}(z)}{\mathrm{d}(time)} = (alpha\_z * (1.0 - z) - beta\_z * z) \tag{A.26.8}$$
$$alpha\_z = \frac{10.0 * \exp\left(\frac{(V-40.0)}{25.0}\right)}{\left(1.0 + \exp\left(\frac{(V-40.0)}{25.0}\right)\right)} \tag{A.26.9}$$
$$beta\_z = \frac{10.0 * \exp\left(-\frac{(V+90.0)}{25.0}\right)}{\left(1.0 + \exp\left(-\frac{(V+90.0)}{25.0}\right)\right)} \tag{A.26.10}$$

"transient_outward_potassium_current_y_gate" component

Initial values defined in this component

$y = 0.999978$

Equations defined in this component

$$\frac{d(y)}{d(time)} = (alpha\_y * (1.0 - y) - beta\_y * y) \quad \text{(A.26.11)}$$

$$alpha\_y = \frac{0.015}{\left(1.0 + \exp\left(\frac{(V+60.0)}{5.0}\right)\right)} \quad \text{(A.26.12)}$$

$$beta\_y = \frac{0.1 * \exp\left(\frac{(V+25.0)}{5.0}\right)}{\left(1.0 + \exp\left(\frac{(V+25.0)}{5.0}\right)\right)} \quad \text{(A.26.13)}$$

"fast_sodium_current" component

Initial values defined in this component

$g\_Na = 0.235 \, \text{mS} \cdot \text{mm}^{-2}$

Equations defined in this component

$$i\_Na = g\_Na * P\_O\_Na * (V - E\_Na) \quad \text{(A.26.14)}$$

$$E\_Na = \frac{R * T}{F} * \ln\left(\frac{Nao}{Nai}\right) \quad \text{(A.26.15)}$$

"Na_channel_states" component

Initial values defined in this component

$P\_O\_Na = 2.67 \times 10^{-7}$ $P\_IC3\_Na = 0.261$

$P\_C1\_Na = 0.000159$ $P\_IC2\_Na = 0.0062$

$P\_C2\_Na = 0.0169$ $P\_IM1\_Na = 8.05 \times 10^{-5}$

$P\_C3\_Na = 0.713$ $P\_IM2\_Na = 0.00245$

$P\_IF\_Na = 5.82 \times 10^{-5}$

Equations defined in this component

$$\frac{d(P\_C3\_Na)}{d(time)} = (-(beta\_3 + alpha\_11) * P\_C3\_Na + alpha\_3 * P\_IC3\_Na + beta\_11 * P\_C2\_Na)$$
$$\text{(A.26.16)}$$

$$\frac{d(P\_C2\_Na)}{d(time)} = -(beta\_11 + beta\_3 + alpha\_12) * P\_C2\_Na + alpha\_11 * P\_C3\_Na$$
$$+ beta\_12 * P\_C1\_Na + alpha\_3 * P\_IC2\_Na \quad \text{(A.26.17)}$$

$$\frac{d(P\_C1\_Na)}{d(time)} = -(beta\_12 + alpha\_13 + beta\_3) * P\_C1\_Na + alpha\_12 * P\_C2\_Na$$
$$+ beta\_13 * P\_O\_Na + alpha\_3 * P\_IF\_Na \quad \text{(A.26.18)}$$

$$\frac{d(P\_O\_Na)}{d(time)} = (-(alpha\_2 + beta\_13) * P\_O\_Na + beta\_2 * P\_IF\_Na + alpha\_13 * P\_C1\_Na)$$
$$\text{(A.26.19)}$$

$$\frac{d(P\_IF\_Na)}{d(time)} = -(beta\_2 + alpha\_3 + alpha\_4 + beta\_12) * P\_IF\_Na + beta\_3 * P\_C1\_Na$$

$$+ beta\_4 * P\_IM1\_Na + alpha\_2 * P\_O\_Na + alpha\_12 * P\_IC2\_Na \quad \text{(A.26.20)}$$

$$\frac{d(P\_IC3\_Na)}{d(time)} = (-(alpha\_3 + alpha\_11) * P\_IC3\_Na + beta\_3 * P\_C3\_Na + beta\_11 * P\_IC2\_Na)$$

$$\text{(A.26.21)}$$

$$\frac{d(P\_IC2\_Na)}{d(time)} = -(alpha\_3 + alpha\_12 + beta\_11) * P\_IC2\_Na + beta\_3 * P\_C2\_Na$$

$$+ beta\_12 * P\_IF\_Na + alpha\_11 * P\_IC3\_Na \quad \text{(A.26.22)}$$

$$\frac{d(P\_IM1\_Na)}{d(time)} = (-(alpha\_5 + beta\_4) * P\_IM1\_Na + beta\_5 * P\_IM2\_Na + alpha\_4 * P\_IF\_Na)$$

$$\text{(A.26.23)}$$

$$\frac{d(P\_IM2\_Na)}{d(time)} = (alpha\_5 * P\_IM1\_Na - beta\_5 * P\_IM2\_Na) \quad \text{(A.26.24)}$$

$$alpha\_11 = \frac{3.802}{\left(0.1027 * \exp\left(\frac{-V}{17.0}\right) + 0.20 * \exp\left(\frac{-V}{150.0}\right)\right)} \quad \text{(A.26.25)}$$

$$alpha\_12 = \frac{3.802}{\left(0.1027 * \exp\left(\frac{-V}{15.0}\right) + 0.23 * \exp\left(\frac{-V}{150.0}\right)\right)} \quad \text{(A.26.26)}$$

$$alpha\_13 = \frac{3.802}{\left(0.1027 * \exp\left(\frac{-V}{12.0}\right) + 0.25 * \exp\left(\frac{-V}{150.0}\right)\right)} \quad \text{(A.26.27)}$$

$$beta\_11 = 0.1917 * \exp\left(\frac{-V}{20.3}\right) \quad \text{(A.26.28)}$$

$$beta\_12 = 0.20 * \exp\left(\frac{-(V - 5.0)}{20.3}\right) \quad \text{(A.26.29)}$$

$$beta\_13 = 0.22 * \exp\left(\frac{-(V - 10.0)}{20.3}\right) \quad \text{(A.26.30)}$$

$$alpha\_2 = 9.178 * \exp\left(\frac{V}{29.68}\right) \quad \text{(A.26.31)}$$

$$beta\_2 = \frac{alpha\_13 * alpha\_2 * alpha\_3}{beta\_13 * beta\_3} \quad \text{(A.26.32)}$$

$$alpha\_3 = 3.7933E - 7 * \exp\left(\frac{-V}{7.7}\right) \quad \text{(A.26.33)}$$

$$beta\_3 = (0.0084 + 0.00002 * V) \quad \text{(A.26.34)}$$

$$alpha\_4 = \frac{alpha\_2}{100.0} \quad \text{(A.26.35)}$$

$$beta\_4 = alpha\_3 \quad \text{(A.26.36)}$$

$$alpha\_5 = \frac{alpha\_2}{9.5E5} \quad \text{(A.26.37)}$$

$$beta\_5 = \frac{alpha\_3}{50} \quad \text{(A.26.38)}$$

"L_type_Ca_channel" component

The JWR model creates a new mathematical model to describe the L-type calcium channel that is based on the experimentally observed mode-switching behaviour of the channel. Inactivation occurs as calcium ion binding induces the channel to switch (from mode normal) to a mode in which transitions to open states are extremely slow (mode Ca). The channel has one voltage inactivation gate, y. As well as Ca, the channel is assumed permeable to K ions also. The value of P_Ca varies depending on the cell type being modelled. The default value is 33.75e-6 mm.ms^-1from the JRW model, but this needs to be reduced by 50 percent for RV epicardial cells and 20 percent for LV epicardial cells (following Dumaine et. al. 1999), to allow for the i_to current. From Clancy and Rudy 2002, P_Ca should also be reduced for M-cells and endocardial cells. Since the default in this model is epicardial

cells, we used the 50 percent reduced value to match the defualt value of g_to.

Initial values defined in this component

$P\_Ca = 1.6875 \times 10^{-5}$ mm $\cdot$ ms^{-1}

$P\_K = 1.0 \times 10^{-9}$ mm $\cdot$ ms^{-1}

$i\_Ca\_L\_Ca\_half = -4.58 \times 10^{-3}$ μA $\cdot$ mm^{-2}

$O = 9.84546 \times 10^{-21}$

$O\_Ca = 0.0$

$a = 2.0$

$b = 2.0$

$g = 2.0$ ms^{-1}

$f = 0.3$ ms^{-1}

$g\_ = 0.0$ ms^{-1}

$f\_ = 0.0$ ms^{-1}

$omega = 0.01$ ms^{-1}

$C0 = 0.997208$

$C1 = 6.38897 \times 10^{-5}$

$C2 = 1.535 \times 10^{-9}$

$C3 = 1.63909 \times 10^{-14}$

$C4 = 6.56337 \times 10^{-20}$

$C\_Ca0 = 2.72826 \times 10^{-3}$

$C\_Ca1 = 6.99215 \times 10^{-7}$

$C\_Ca2 = 6.71989 \times 10^{-11}$

$C\_Ca3 = 2.87031 \times 10^{-15}$

$C\_Ca4 = 4.59752 \times 10^{-20}$

Equations defined in this component

Calculation of the calcium current component of the total channel current, given as the maximal current multiplied by the voltage-dependent inactivation gate and the open probability of the channel based on the mode-switching model.

$$i\_Ca\_L\_Ca = i\_Ca\_L\_Ca\_max * y * (O + O\_Ca) \tag{A.26.39}$$

Calculation of the potassium current component of the total channel current.

$$i\_Ca\_L\_K = p\_k * y * (O + O\_Ca) * \frac{V * (F)^{2.0}}{R * T} * \frac{\left(Ki * \exp\left(\frac{V*F}{R*T}\right) - Ko\right)}{\left(\exp\left(\frac{V*F}{R*T}\right) - 1.0\right)} \tag{A.26.40}$$

The potassium permeability of the channel, which depends on the calcium current component.

$$p\_k = \frac{P\_K}{\left(1.0 + \frac{i\_Ca\_L\_Ca\_max}{i\_Ca\_L\_Ca\_half}\right)} \tag{A.26.41}$$

The maximal calcium current through the channel.

$$i\_Ca\_L\_Ca\_max = P\_Ca * 4.0 * \frac{V * (F)^{2.0}}{R * T} * \frac{\left(0.001 * \exp\left(2.0 * V * \frac{F}{R*T}\right) - 0.341 * Cao\right)}{\left(\exp\left(2.0 * V * \frac{F}{R*T}\right) - 1.0\right)} \tag{A.26.42}$$

Rate constants for state changes in mode normal.

$$alpha = 0.4 * \exp\left(\frac{(V + 12.0)}{10.0}\right) \tag{A.26.43}$$

$$beta = 0.05 * \exp\left(\frac{(V + 12.0)}{-13.0}\right) \tag{A.26.44}$$

Rate constants for state changes in mode Ca (corresponding to alpha-prime and beta-prime in the JRW paper).

$$alpha\_a = alpha * a \tag{A.26.45}$$

$$beta\_b = \frac{beta}{b} \tag{A.26.46}$$

Rate constant for switching between mode normal and mode Ca.
$$gamma = 0.1875 * Ca\_SS \tag{A.26.47}$$

The kinetics of the state transitions in mode normal. In the normal mode, the calcium channel is able to make the transition to the open, conducting state (O) from the closed state (C) at a normal rate.
$$\frac{\mathrm{d}(C0)}{\mathrm{d}(time)} = ((beta * C1 + omega * C\_Ca0) - (4.0 * alpha + gamma) * C0) \tag{A.26.48}$$

$$\frac{\mathrm{d}(C1)}{\mathrm{d}(time)} = \left(4.0 * alpha * C0 + 2.0 * beta * C2 + \frac{omega}{b} * C\_Ca1\right)$$
$$- (beta + 3.0 * alpha + gamma * a) * C1 \tag{A.26.49}$$

$$\frac{\mathrm{d}(C2)}{\mathrm{d}(time)} = \left(3.0 * alpha * C1 + 3.0 * beta * C3 + \frac{omega}{(b)^{2.0}} * C\_Ca2\right)$$
$$- \left(beta * 2.0 + 2.0 * alpha + gamma * (a)^{2.0}\right) * C2 \tag{A.26.50}$$

$$\frac{\mathrm{d}(C3)}{\mathrm{d}(time)} = \left(2.0 * alpha * C2 + 4.0 * beta * C4 + \frac{omega}{(b)^{3.0}} * C\_Ca3\right)$$
$$- \left(beta * 3.0 + alpha + gamma * (a)^{3.0}\right) * C3 \tag{A.26.51}$$

$$\frac{\mathrm{d}(C4)}{\mathrm{d}(time)} = \left(\left(alpha * C3 + g * O + \frac{omega}{(b)^{4.0}} * C\_Ca4\right) - \left(beta * 4.0 + f + gamma * (a)^{4.0}\right) * C4\right)$$
$$\tag{A.26.52}$$

$$\frac{\mathrm{d}(O)}{\mathrm{d}(time)} = (f * C4 - g * O) \tag{A.26.53}$$

The kinetics of the state transitions in mode Ca. Calcium binding to the Ca channel induces a conformational change from normal mode to mode Ca. This effectively inhibits the conduction of calcium ions because in mode Ca, the calcium channel makes the transition to the open, conducting state (O) extremely slowly.
$$\frac{\mathrm{d}(C\_Ca0)}{\mathrm{d}(time)} = ((beta\_b * C\_Ca1 + gamma * C\_Ca0) - (4.0 * alpha\_a + omega) * C\_Ca0) \tag{A.26.54}$$

$$\frac{\mathrm{d}(C\_Ca1)}{\mathrm{d}(time)} = (4.0 * alpha\_a * C\_Ca0 + 2.0 * beta\_b * C\_Ca2 + gamma * a * C1)$$
$$- \left(beta\_b + 3.0 * alpha\_a + \frac{omega}{b}\right) * C\_Ca1 \tag{A.26.55}$$

$$\frac{\mathrm{d}(C\_Ca2)}{\mathrm{d}(time)} = \left(3.0 * alpha\_a * C\_Ca1 + 3.0 * beta\_b * C\_Ca3 + gamma * (a)^{2.0} * C2\right)$$
$$- \left(beta\_b * 2.0 + 2.0 * alpha\_a + \frac{omega}{(b)^{2.0}}\right) * C\_Ca2 \tag{A.26.56}$$

$$\frac{\mathrm{d}(C\_Ca3)}{\mathrm{d}(time)} = \left(2.0 * alpha\_a * C\_Ca2 + 4.0 * beta\_b * C\_Ca4 + gamma * (a)^{3.0} * C3\right)$$
$$- \left(beta\_b * 3.0 + alpha\_a + \frac{omega}{(b)^{3.0}}\right) * C\_Ca3 \tag{A.26.57}$$

$$\frac{\mathrm{d}(C\_Ca4)}{\mathrm{d}(time)} = \left(alpha\_a * C\_Ca3 + g\_ * O\_Ca + gamma * (a)^{4.0} * C4 \right)$$

$$- \left(beta\_b * 4.0 + f\_ + \frac{omega}{(b)^{4.0}} \right) * C\_Ca4 \quad \text{(A.26.58)}$$

$$\frac{\mathrm{d}(O\_Ca)}{\mathrm{d}(time)} = (f\_ * C\_Ca4 - g\_ * O\_Ca) \quad \text{(A.26.59)}$$

"L_type_Ca_channel_y_gate" component

The voltage-dependent inactivation gate for the L-type calcium channel - the y gate.

Initial values defined in this component

$y = 0.998983$

Equations defined in this component

The kinetics of the y gate.

$$\frac{\mathrm{d}(y)}{\mathrm{d}(time)} = \frac{(y\_infinity - y)}{tau\_y} \quad \text{(A.26.60)}$$

$$y\_infinity = \left(\frac{1.0}{\left(1.0 + \exp\left(\frac{(V+55.0)}{7.5}\right)\right)} + \frac{0.1}{\left(1.0 + \exp\left(\frac{(-V+21.0)}{6.0}\right)\right)} \right) \quad \text{(A.26.61)}$$

$$tau\_y = \left(20.0 + \frac{600.0}{\left(1.0 + \exp\left(\frac{(V+30.0)}{9.5}\right)\right)} \right) \quad \text{(A.26.62)}$$

"T_type_Ca_channel" component

Initial values defined in this component

$g\_Ca\_T = 1.25 \times 10^{-5} \; \mathrm{mS \cdot mm^{-2}}$

Equations defined in this component

$$i\_Ca\_T = g\_Ca\_T * (b)^{2.0} * g * (V - E\_Ca) \quad \text{(A.26.63)}$$

$$E\_Ca = \frac{R * T}{2.0 * F} * \ln\left(\frac{Cao}{Cai}\right) \quad \text{(A.26.64)}$$

"T_type_Ca_channel_b_gate" component

Initial values defined in this component

$b = 0.000970231$

Equations defined in this component

$$\frac{\mathrm{d}(b)}{\mathrm{d}(time)} = \frac{(b\_infinity - b)}{tau\_b} \tag{A.26.65}$$

$$b\_infinity = \frac{1.0}{\left(1.0 + \exp\left(-\frac{(V+14.0)}{10.8}\right)\right)} \tag{A.26.66}$$

$$tau\_b = \frac{(3.7 + 6.1)}{\left(1.0 + \exp\left(\frac{(25.0+V)}{4.5}\right)\right)} \tag{A.26.67}$$

"T_type_Ca_channel_g_gate" component

Initial values defined in this component

$g = 0.994305$

Equations defined in this component

$$\frac{\mathrm{d}(g)}{\mathrm{d}(time)} = \frac{(g\_infinity - g)}{tau\_g} \tag{A.26.68}$$

$$g\_infinity = \frac{1.0}{\left(1.0 + \exp\left(\frac{(V+60.0)}{5.6}\right)\right)} \tag{A.26.69}$$

$$tau\_g = \begin{cases} 12.0; & \text{if } V > 0.0, \\ (-0.875 * V + 12.0) & \text{otherwise.} \end{cases} \tag{A.26.70}$$

"rapid_time_dependent_potassium_current" component

The P_NaK_Kr factor is zero for the default wild-type IKr channel, but is non-zero for some genetic mutations.

Initial values defined in this component

$g\_Kr\_max = 0.000135\,\mathrm{mS \cdot mm^{-2}}$ $\qquad\qquad$ $P\_NaK\_Kr = 0.0$

Equations defined in this component

$$i\_Kr = g\_Kr * P\_O\_Kr * (V - E\_Kr) \tag{A.26.71}$$

$$g\_Kr = g\_Kr\_max * (Ko)^{0.59} \tag{A.26.72}$$

$$E\_Kr = \frac{R * T}{F} * \ln\left(\frac{(Ko + P\_NaK\_Kr * Nao)}{(Ki + P\_NaK\_Kr * Nai)}\right) \tag{A.26.73}$$

"Kr_channel_states" component

The model for cardiac i_Kr includes three closed states (C3, C2, C1) an open state (O) and an inactivation state (I). P_i is the probability of a channel occupying a particular state (i), which is determined by a system of linear first oder differential equations. The default initial values below are for the wild-type channel.

Initial values defined in this component

$P\_O\_Kr = 6.11 \times 10^{-7}$ $beta\_in = 1.077 \, \text{ms}^{-1}$

$P\_C1\_Kr = 0.00116$ $alpha\_V\_shift = -12.0 \, \text{mV}$

$P\_C2\_Kr = 0.000574$ $alpha\_alpha\_V\_shift = -36.0 \, \text{mV}$

$P\_C3\_Kr = 0.938$ $beta\_scale = 1.0$

$P\_I\_Kr = 2.55 \times 10^{-7}$ $beta\_beta\_scale = 1.0$

$alpha\_in = 2.172 \, \text{ms}^{-1}$ $beta\_i\_scale = 1.0$

Equations defined in this component

$$\frac{\mathrm{d}(P\_C3\_Kr)}{\mathrm{d}(time)} = (beta * P\_C2\_Kr - alpha * P\_C3\_Kr) \tag{A.26.74}$$

$$\frac{\mathrm{d}(P\_C2\_Kr)}{\mathrm{d}(time)} = (-(beta + alpha\_in) * P\_C2\_Kr + alpha * P\_C3\_Kr + beta\_in * P\_C1\_Kr) \tag{A.26.75}$$

$$\frac{\mathrm{d}(P\_C1\_Kr)}{\mathrm{d}(time)} = -(beta\_in + alpha\_alpha + alpha\_alpha) * P\_C1\_Kr$$
$$+ alpha\_in * P\_C2\_Kr + beta\_beta * P\_O\_Kr + mu * P\_I\_Kr \tag{A.26.76}$$

$$\frac{\mathrm{d}(P\_O\_Kr)}{\mathrm{d}(time)} = (-(beta\_beta + beta\_i) * P\_O\_Kr + alpha\_alpha * P\_C1\_Kr + alpha\_i * P\_I\_Kr) \tag{A.26.77}$$

$$\frac{\mathrm{d}(P\_I\_Kr)}{\mathrm{d}(time)} = (-(mu + alpha\_i) * P\_I\_Kr + alpha\_alpha * P\_C1\_Kr + beta\_i * P\_O\_Kr) \tag{A.26.78}$$

$$alpha = 55.5 \times 10^{-3} * \exp(0.05547153 * (V + alpha\_V\_shift)) \tag{A.26.79}$$

$$beta = 0.002357 * \exp(-0.036588 * V) * beta\_scale \tag{A.26.80}$$

$$alpha\_alpha = 65.5 \times 10^{-3} * \exp(0.05547153 * (V + alpha\_alpha\_V\_shift)) \tag{A.26.81}$$

$$beta\_beta = 0.0029357 * \exp(-0.02158 * V) * beta\_beta\_scale \tag{A.26.82}$$

$$alpha\_i = 0.439 * \exp(-0.02352 * (V + 25.0)) * \frac{4.5}{Ko} \tag{A.26.83}$$

$$beta\_i = 0.656 * \exp(0.000942 * V) * \frac{(4.5)^{0.3}}{(Ko)^{0.3}} * beta\_i\_scale \tag{A.26.84}$$

$$mu = \begin{cases} \frac{alpha\_i*beta\_beta*alpha\_alpha}{alpha\_alpha*beta\_i}; & \text{if } |beta\_i| > 0.0, \\ \frac{alpha\_i*beta\_beta*alpha\_alpha}{alpha\_alpha} & \text{otherwise.} \end{cases} \tag{A.26.85}$$

"slow_time_dependent_potassium_current" component

The slowly activating component of the time dependent potassium current. g_Ks_max can be varied to give representations of the different cell types described in the various LR models. The default value here is for epicardial cells from the Clancy and Rudy (2002) model - corresponding to a ratio GKs/GKr = 23. From this model, ratios of 17 and 19 should be used for M-cells and endocardial cells, respectively.

Initial values defined in this component

$gKs\_gKr\_ratio = 23.0$ $P\_NaK = 0.01833$

Equations defined in this component

$$g\_Ks = g\_Ks\_max * \left(1.0 + \frac{0.6}{\left(1.0 + \left(\frac{0.38 \times 10^{-4}}{Cai} \right)^{1.4} \right)} \right) \tag{A.26.86}$$

$$g\_Ks\_max = g\_Kr\_max * gKs\_gKr\_ratio \tag{A.26.87}$$

$$E\_Ks = \frac{R * T}{F} * \ln \left(\frac{(Ko + P\_NaK * Nao)}{(Ki + P\_NaK * Nai)} \right) \tag{A.26.88}$$

$$i\_Ks = g\_Ks * Xs1 * Xs2 * (V - E\_Ks) \tag{A.26.89}$$

$$Xs = Xs1 * Xs2 \tag{A.26.90}$$

"slow_time_dependent_potassium_current_Xs1_gate" component

Initial values defined in this component

Xs1 = 0.00445683

Equations defined in this component

$$\frac{d(Xs1)}{d(time)} = \frac{(Xs\_infinity - Xs1)}{tau\_Xs1} \tag{A.26.91}$$

$$Xs\_infinity = \frac{1.0}{\left(1.0 + \exp \left(-\frac{(V - 1.5)}{16.7} \right) \right)} \tag{A.26.92}$$

$$tau\_Xs1 = \frac{1.0}{\left(\frac{0.0000719 * (V + 30.0)}{(1.0 - \exp(-0.148 * (V + 30.0)))} + \frac{0.000131 * (V + 30.0)}{(\exp(0.0687 * (V + 30.0)) - 1.0)} \right)} \tag{A.26.93}$$

"slow_time_dependent_potassium_current_Xs2_gate" component

Initial values defined in this component

Xs2 = 0.00445683

Equations defined in this component

$$\frac{d(Xs2)}{d(time)} = \frac{(Xs\_infinity - Xs2)}{tau\_Xs2} \tag{A.26.94}$$

$$tau\_Xs2 = 4.0 * tau\_Xs1 \tag{A.26.95}$$

"time_independent_potassium_current" component

The time-independent potassium current.

Initial values defined in this component

g_K1_max = 7.5×10^{-3} mS · mm^{-2}

Equations defined in this component

Calculation of the maximal channel conductance, dependent on extracellular potassium concentration.

$$g\_K1 = g\_K1\_max * \sqrt{\frac{Ko}{5.4}} \qquad (A.26.96)$$

The following equation calculates the reversal potential of the time-independent potassium current.

$$E\_K1 = \frac{R*T}{F} * \ln\left(\frac{Ko}{Ki}\right) \qquad (A.26.97)$$

Calculate the current.

$$i\_K1 = g\_K1 * K1\_infinity * (V - E\_K1) \qquad (A.26.98)$$

"time_independent_potassium_current_K1_gate" component

The time constants for the K1 gate are small enough that the gating variable can be approximated with it's steady-state value.

Equations defined in this component

The opening rate of the K1 gate.

$$alpha\_K1 = \frac{1.02}{(1.0 + \exp(0.2385 * ((V - E\_K1) - 59.215)))} \qquad (A.26.99)$$

The closing rate of the K1 gate.

$$beta\_K1 = \frac{(0.49124 * \exp(0.08032 * ((V + 5.476) - E\_K1)) + \exp(0.06175 * (V - (E\_K1 + 594.31))))}{(1.0 + \exp(-0.5143 * ((V - E\_K1) + 4.753)))} \qquad (A.26.100)$$

The steady-state approximation for the K1 gating kinetics.

$$K1\_infinity = \frac{alpha\_K1}{(alpha\_K1 + beta\_K1)} \qquad (A.26.101)$$

"plateau_potassium_current" component

The plateau potassium current component contains the equations which describe the contribution of a time independent [K]o-insensitive channel at plateau potentials.

Initial values defined in this component

$g\_Kp = 8.28 \times 10^{-5} \ \mathrm{mS \cdot mm^{-2}}$

Equations defined in this component

The channel's reversal potential.

$$E\_Kp = E\_K1 \qquad (A.26.102)$$

The activation variable.

$$Kp = \frac{1.0}{\left(1.0 + \exp\left(\frac{(7.488-V)}{5.98}\right)\right)} \tag{A.26.103}$$

Calculation of the plateau potassium current.

$$i\_Kp = g\_Kp * Kp * (V - E\_Kp) \tag{A.26.104}$$

"Na_Ca_exchanger" component

The Na/Ca exchanger component describes how a protein molecule in the cell surface membrane transports Na ions into the cytosol and exports Ca ions into the extracellular volume, in a ratio of 3:1 respectively.

Initial values defined in this component

$k\_NaCa = 50.0 \ \mu\text{A} \cdot \text{mm}^{-2}$ $\qquad k\_sat = 0.1$

$K\_mNa = 87.5 \ \text{mM}$ $\qquad eta = 0.35$

$K\_mCa = 1.38 \ \text{mM}$

Equations defined in this component

Calculation of the Na/Ca exchanger current.

$$i\_NaCa = k\_NaCa * \frac{1.0}{\left((K\_mNa)^{3.0} + (Nao)^{3.0}\right)} * \frac{1.0}{(K\_mCa + Cao)}$$
$$* \frac{1.0}{\left(1.0 + k\_sat * \exp\left((eta - 1.0) * V * \frac{F}{R*T}\right)\right)}$$
$$* \left(\exp\left(eta * V * \frac{F}{R*T}\right) * (Nai)^{3.0} * Cao - \exp\left((eta - 1.0) * V * \frac{F}{R*T}\right) * (Nao)^{3.0} * Cai\right) \tag{A.26.105}$$

"sarcolemmal_calcium_pump" component

The sarcolemmal calcium pump is an additional mechanism for removing Ca ions from the myoplasm to help maintain a low intracellular calcium concentration when at rest.

Initial values defined in this component

$K\_mpCa = 0.5 \times 10^{-3} \ \text{mM}$ $\qquad I\_pCa = 1.15 \times 10^{-2} \ \mu\text{A} \cdot \text{mm}^{-2}$

Equations defined in this component

The calcium pump current.

$$i\_p\_Ca = I\_pCa * \frac{Cai}{(K\_mpCa + Cai)} \tag{A.26.106}$$

"sodium_background_current" component

The sodium background current is a time-independent diffusion of Na ions down their electrochemical gradient, through the cell surface membrane into the cytosol.

Initial values defined in this component
$g\_Nab = 1.41 \times 10^{-5} \text{ mS} \cdot \text{mm}^{-2}$

Equations defined in this component

The reversal potential for the background sodium channel.
$$E\_NaN = E\_Na \qquad\qquad (A.26.107)$$

Calculation of the background sodium current.
$$i\_Na\_b = g\_Nab * (V - E\_NaN) \qquad\qquad (A.26.108)$$

"calcium_background_current" component

The calcium background current describes a time-independent diffusion of Ca ions down their electrochemical gradient through the cell surface membrane into the cytosol. However, calcium is not allowed to accumulate to high intracellular concentrations. This influx is balanced by the Ca ion extrusion through the Na-Ca exchanger and the sarcolemmal Ca pump.

Initial values defined in this component
$g\_Cab = 6.032 \times 10^{-5} \text{ mS} \cdot \text{mm}^{-2}$

Equations defined in this component

The reversal potential for the background calcium current.
$$E\_CaN = \frac{R * T}{2.0 * F} * \ln\left(\frac{Cao}{Cai}\right) \qquad\qquad (A.26.109)$$

Calculation of the background calcium current.
$$i\_Ca\_b = g\_Cab * (V - E\_CaN) \qquad\qquad (A.26.110)$$

"sodium_potassium_pump" component

The sodium potassium pump is an active protein in the cell membrane which couples the free energy released by the hydrolysis of ATP to the movement of Na and K ions against their electrochemical gradients through the cell membrane.

Initial values defined in this component

$I\_NaK = 0.013 \ \mu\text{A} \cdot \text{mm}^{-2}$　　　　　　　　$K\_mKo = 1.5 \text{ mM}$
$K\_mNai = 10.0 \text{ mM}$

Equations defined in this component

Calculation of the Na/K pump current.

$$f\_NaK = \frac{1.0}{\left(\left(1.0 + 0.1245 * \exp\left(\frac{-0.1*V*F}{R*T}\right)\right) + 0.0365 * sigma * \exp\left(\frac{-V*F}{R*T}\right)\right)} \quad (A.26.111)$$

$$sigma = \frac{1.0}{7.0} * \left(\exp\left(\frac{Nao}{67.3}\right) - 1.0\right) \quad (A.26.112)$$

$$i\_NaK = I\_NaK * f\_NaK * \frac{1.0}{\left(1.0 + \left(\frac{K\_mNai}{Nai}\right)^{1.5}\right)} * \frac{Ko}{(Ko + K\_mKo)} \quad (A.26.113)$$

"non_specifi c_ calcium_ activated_ current" component

The nonspecifi c calcium activated current describes a channel which is activated by calcium ions, but is permeable to only sodium and potassium ions.

Initial values defined in this component

$K\_m\_ns\_Ca = 1.2 \times 10^{-3}$ mM $\qquad\qquad P\_ns\_Ca = 1.75 \times 10^{-9}$ mm $\cdot$ ms^{-1}

Equations defined in this component

The reversal potential of the channel.

$$EnsCa = \frac{R*T}{F} * \ln\left(\frac{(Ko + Nao)}{(Ki + Nai)}\right) \quad (A.26.114)$$

The potential offset for the channel.

$$VnsCa = (V - EnsCa) \quad (A.26.115)$$

The sodium component of the channel's current.

$$i\_ns\_Na = I\_ns\_Na * \frac{1.0}{\left(1.0 + \left(\frac{K\_m\_ns\_Ca}{Cai}\right)^{3.0}\right)} \quad (A.26.116)$$

The potassium component of the channel's current.

$$i\_ns\_K = I\_ns\_K * \frac{1.0}{\left(1.0 + \left(\frac{K\_m\_ns\_Ca}{Cai}\right)^{3.0}\right)} \quad (A.26.117)$$

The total nonspecifi c calcium activated current.

$$i\_ns\_Ca = (i\_ns\_Na + i\_ns\_K) \quad (A.26.118)$$

The maximal sodium component current.

$$I\_ns\_Na = P\_ns\_Ca * (1.0)^{2.0} * \frac{VnsCa * (F)^{2.0}}{R*T} * \frac{\left(0.75 * Nai * \exp\left(\frac{VnsCa*F}{R*T}\right) - 0.75 * Nao\right)}{\left(\exp\left(\frac{VnsCa*F}{R*T}\right) - 1.0\right)} \quad (A.26.119)$$

The maximal potassium component current.

$$I\_ns\_K = P\_ns\_Ca * (1.0)^{2.0} * \frac{VnsCa * (F)^{2.0}}{R*T} * \frac{\left(0.75 * Ki * \exp\left(\frac{VnsCa*F}{R*T}\right) - 0.75 * Ko\right)}{\left(\exp\left(\frac{VnsCa*F}{R*T}\right) - 1.0\right)} \quad (A.26.120)$$

"calcium_subsystem" component

In the JRW model, subcellular calcium regulatory mechanisms are described in detail. There are six calcium fluxes to consider; J_rel, J_leak, J_up, J_tr, J_xfer and J_trpn. In addition, three membrane current fluxes are also necessary for the formulation of calcium regulation; i_p_Ca, i_Ca_L_Ca and i_NaCa. We have added the tension dependent release of Ca from TnC as part of the coupling to HMT mechanics.

Initial values defined in this component

$Cai = 9.94893 \times 10^{-11}$ mM

$Ca\_SS = 1.36058 \times 10^{-4}$ mM

$Am = 546.69$ mm^{-1}

$V\_myo = 0.92$

$HTRPN\_tot = 0.14$ mM

$LTRPN\_tot = 0.07$ mM

$HTRPNCa = 0.13598$ mM

$LTRPNCa = 0.00635$ mM

$P\_O1 = 1.19168 \times 10^{-3}$

$P\_O2 = 6.30613 \times 10^{-9}$

$P\_C1 = 0.762527$

$P\_C2 = 0.236283$

$v1 = 1.8$ ms^{-1}

$v2 = 0.58 \times 10^{-4}$ ms^{-1}

$v3 = 1.8 \times 10^{-3}$ mM $\cdot$ ms^{-1}

$nCa = 4.0$

$mCa = 3.0$

$k\_a\_plus = 1.215 \times 10^{10}$ mM$^{-4} \cdot$ ms^{-1}

$k\_a\_minus = 0.1425$ ms^{-1}

$k\_b\_plus = 4.05 \times 10^{7}$ mM$^{-3} \cdot$ ms^{-1}

$k\_b\_minus = 1.930$ ms^{-1}

$k\_c\_plus = 0.018$ ms^{-1}

$k\_c\_minus = 0.0008$ ms^{-1}

$k\_htrpn\_plus = 20.0$ mM$^{-1} \cdot$ ms^{-1}

$k\_htrpn\_minus = 0.066 \times 10^{-3}$ ms^{-1}

$k\_ltrpn\_plus = 40.0$ mM$^{-1} \cdot$ ms^{-1}

$k\_ltrpn\_minus = 0.04$ ms^{-1}

$tau\_tr = 34.48$ ms

$Ca\_JSR = 1.17504$ mM

$Ca\_NSR = 1.243891$ mM

$K\_mup = 0.5 \times 10^{-3}$ mM

$K\_mCMDN = 2.38 \times 10^{-3}$ mM

$K\_mCSQN = 0.8$ mM

$tau\_xfer = 3.125$ ms

$CSQN\_tot = 15.0$ mM

$CMDN\_tot = 0.05$ mM

Equations defined in this component

Calculate some volume fractions as proportions of the total myoplasmic volume.
$$V\_SS = 5.828 \times 10^{-5} * V\_myo \tag{A.26.121}$$

$$V\_NSR = 0.081 * V\_myo \tag{A.26.122}$$
$$V\_JSR = 0.00464 * V\_myo \tag{A.26.123}$$

The calcium release flux from the JSR into the restricted subspace is governed by the fraction of RyR channels in an open state.
$$J\_rel = v1 * RyR\_open * (Ca\_JSR - Ca\_SS) \tag{A.26.124}$$

The "open" RyR's are those P_O1 and P_O2 states.
$$RyR\_open = (P\_O1 + P\_O2) \tag{A.26.125}$$

The kinetic equations governing the transitions between the four states used to model the RyR's.

$$\frac{\mathrm{d}(P\_C1)}{\mathrm{d}(time)} = \left(-k\_a\_plus * (Ca\_SS)^{nCa} * P\_C1 + k\_a\_minus * P\_O1\right) \tag{A.26.126}$$

$$\frac{\mathrm{d}(P\_O1)}{\mathrm{d}(time)} = \Bigg[k\_a\_plus * (Ca\_SS)^{nCa} * P\_C1$$
$$- \left(k\_a\_minus * P\_O1 + k\_b\_plus * (Ca\_SS)^{mCa} * P\_O1 + k\_c\_plus * P\_O1\right) \Bigg]$$
$$+ k\_b\_minus * P\_O2 + k\_c\_minus * P\_C2 \tag{A.26.127}$$

$$\frac{\mathrm{d}(P\_O2)}{\mathrm{d}(time)} = \left(k\_b\_plus * (Ca\_SS)^{mCa} * P\_O1 - k\_b\_minus * P\_O2\right) \tag{A.26.128}$$

$$\frac{\mathrm{d}(P\_C2)}{\mathrm{d}(time)} = (k\_c\_plus * P\_O1 - k\_c\_minus * P\_C2) \tag{A.26.129}$$

Calculate the leakage flux from the NSR into the myoplasm.

$$J\_leak = v2 * (Ca\_NSR - Cai) \tag{A.26.130}$$

Calculate the uptake flux into the NSR from the myoplasm.

$$J\_up = v3 * \frac{(Cai)^{2.0}}{\left((K\_mup)^{2.0} + (Cai)^{2.0}\right)} \tag{A.26.131}$$

Calculate the translocation flux between the uptake (NSR) and release (JSR) stores.

$$J\_tr = \frac{(Ca\_NSR - Ca\_JSR)}{tau\_tr} \tag{A.26.132}$$

Calculate the calcium flux from the diffusion of calcium out of the restricted subspace into the myoplasm.

$$J\_xfer = \frac{(Ca\_SS - Cai)}{tau\_xfer} \tag{A.26.133}$$

Calculate the tension dependent factor for calcium binding.

$$TTo = \begin{cases} \frac{T}{gamma*To}; & \text{if } To > 1.0 \times 10^{-8}, \\ 0.0 & \text{otherwise.} \end{cases} \tag{A.26.134}$$

The kinetics of calcium binding to the myoplasm buffer troponin - both high and low affinity binding sites.

$$J\_htrpn = (k\_htrpn\_plus * Cai * (HTRPN\_tot - HTRPNCa) - k\_htrpn\_minus * HTRPNCa) \tag{A.26.135}$$

$$J\_ltrpn = k\_ltrpn\_plus * Cai * (LTRPN\_tot - LTRPNCa)$$
$$- k\_ltrpn\_minus * (1.0 - TTo) * LTRPNCa \tag{A.26.136}$$

$$J\_trpn = (J\_htrpn + J\_ltrpn) \tag{A.26.137}$$

Keep track of the concentration of calcium ions bound to high and low affinity troponin binding sites.

$$\frac{\mathrm{d}(HTRPNCa)}{\mathrm{d}(time)} = J\_htrpn \tag{A.26.138}$$

$$\frac{\mathrm{d}(LTRPNCa)}{\mathrm{d}(time)} = J\_ltrpn \tag{A.26.139}$$

Calcium is buffered by calmodulin (CMDN) in the subspace and myoplasm, and by calsequestrin (CSQN) in the JSR. These are fast buffers and their effect is modelled using the rapid buffering approximation.

$$Bi = \frac{1.0}{\left(1.0 + \frac{CMDN\_tot*K\_mCMDN}{((K\_mCMDN+Cai))^{2.0}}\right)} \tag{A.26.140}$$

$$B\_SS = \frac{1.0}{\left(1.0 + \frac{CMDN\_tot*K\_mCMDN}{((K\_mCMDN+Ca\_SS))^{2.0}}\right)} \tag{A.26.141}$$

$$B\_JSR = \frac{1.0}{\left(1.0 + \frac{CSQN\_tot*K\_mCSQN}{((K\_mCSQN+Ca\_JSR))^{2.0}}\right)} \tag{A.26.142}$$

The kinetics of the calcium ion concentration changes in the various compartments of the model.

$$\frac{\mathrm{d}(Cai)}{\mathrm{d}(time)} = Bi * \left[(J\_leak + J\_xfer) \right.$$
$$\left. - \left(J\_up + J\_trpn + ((i\_Ca\_b - 2.0 * i\_NaCa) + i\_Ca\_T + i\_p\_Ca) * \frac{Am}{2.0 * V\_myo * F} \right) \right] \tag{A.26.143}$$

$$\frac{\mathrm{d}(Ca\_SS)}{\mathrm{d}(time)} = B\_SS * \left(\left(J\_rel * \frac{V\_JSR}{V\_SS} - J\_xfer * \frac{V\_myo}{V\_SS} \right) - i\_Ca\_L\_Ca * \frac{Am}{2.0 * V\_SS * F} \right) \tag{A.26.144}$$

$$\frac{\mathrm{d}(Ca\_JSR)}{\mathrm{d}(time)} = B\_JSR * (J\_tr - J\_rel) \tag{A.26.145}$$

$$\frac{\mathrm{d}(Ca\_NSR)}{\mathrm{d}(time)} = \left((J\_up - J\_leak) * \frac{V\_myo}{V\_NSR} - J\_tr * \frac{V\_JSR}{V\_NSR} \right) \tag{A.26.146}$$

"ionic_concentrations" component

The descriptions of the rate of change of [Na]i and [K]i are the same as the LR-II model.

Initial values defined in this component

Nai = 10.2042 mM	*Ko* = 4.5 mM
Nao = 140.0 mM	*Cao* = 1.8 mM
Ki = 143.727 mM	

Equations defined in this component

The rate of change of intracellular sodium ion concentration.

$$\frac{\mathrm{d}(Nai)}{\mathrm{d}(time)} = -(i\_Na + i\_Na\_b + i\_ns\_Na + i\_NaCa * 3.0 + i\_NaK * 3.0) * \frac{Am}{V\_myo * F} \tag{A.26.147}$$

The rate of change of intracellular potassium ion concentration.

$$\frac{\mathrm{d}(Ki)}{\mathrm{d}(time)} = -(i\_Ca\_L\_K + i\_Kr + i\_Ks + i\_K1 + i\_Kp + i\_ns\_K + i\_to + -i\_NaK * 2.0) * \frac{Am}{V\_myo * F} \tag{A.26.148}$$

"mechanics_interface" component

Initial values defined in this component

$lambda = 1.0$ $alpha2 = 2.85 \text{ ms}^{-1}$

$alpha0 = 7.0 \times 10^{-3} \text{ ms}^{-1}$ $alpha3 = 2.85 \text{ ms}^{-1}$

$n\_ref = 4.25$ $A1 = 50.0$

$p50\_ref = 5.33$ $A2 = 175.0$

$T\_ref = 125.0 \text{ kPa}$ $A3 = 175.0$

$beta0 = 1.45$ $a = 0.5$

$beta1 = 1.95$ $velocity = 0.0 \text{ ms}^{-1}$

$beta2 = 0.31$ $gamma = 2.6$

$alpha1 = 0.033 \text{ ms}^{-1}$

Equations defined in this component

Another a dummy equation that we simply use to make grabbing the value in CMISS much easier.
$$lambdaC = lambda \tag{A.26.149}$$

Another a dummy equation that we simply use to make grabbing the value in CMISS much easier.
$$velocityC = velocity \tag{A.26.150}$$

"tropomyosin_kinetics" component

This component defines the kinetics of the length-dependent actin availability.

Initial values defined in this component

$z = 0.0$

Equations defined in this component

The kinetics of actin availability, z.
$$\frac{\mathrm{d}(z)}{\mathrm{d}(t)} = alpha0 * \left(\left(\frac{Cab}{C50} * Cab\_norm \right)^{n} * (1.0 - z) - z \right) \tag{A.26.151}$$

One of the Hill parameters used to fit the relationship between z and Cab at given sarcomere lengths, and defines part of the length dependence of the model.
$$n = n\_ref * (1.0 + beta1 * (lambda - 1.0)) \tag{A.26.152}$$

One of the Hill parameters used to fit the relationship between z and Cab at given sarcomere lengths, and defines part of the length dependence of the model.
$$p50 = p50\_ref * (1.0 + beta2 * (lambda - 1.0)) \tag{A.26.153}$$

The value of Cab that is required to achieve 50% availability, i.e., z = 0.5.
$$C50 = (10.0)^{(3.0 - p50)} \tag{A.26.154}$$

Normalised value of bound calcium.

$$Cab\_norm = \frac{Cab}{Cab\_max} \tag{A.26.155}$$

"isometric_tension" component

The component which defines the isometric tension.

Equations defined in this component

Calculation of the isometric tension.

$$To = T\_ref * (1.0 + beta0 * (lambda - 1.0)) * z \tag{A.26.156}$$

"dynamic_tension" component

We use the ODE equivalent to the fading memory hereditary (thanks Steve). The muscle velocity should be set outside of here, and will be controlled by the simulation environment.

Initial values defined in this component

$Q1 = 0.0$ ms $\qquad\qquad Q3 = 0.0$ ms
$Q2 = 0.0$ ms

Equations defined in this component

Calculation of the dynamic tension.

$$T = To * \frac{(1.0 + a * Q)}{(1.0 - Q)} \tag{A.26.157}$$

Calculate the value of the hereditary integral, with three rate constants.

$$Q = (Q1 + Q2 + Q3) \tag{A.26.158}$$

Calculation of the contribution of the first time constant to the hereditary integral, in the ODE form.

$$\frac{\mathrm{d}(Q1)}{\mathrm{d}(t)} = (A1 * velocity - alpha1 * Q1) \tag{A.26.159}$$

Calculation of the contribution of the second time constant to the hereditary integral, in the ODE form.

$$\frac{\mathrm{d}(Q2)}{\mathrm{d}(t)} = (A2 * velocity - alpha2 * Q2) \tag{A.26.160}$$

Calculation of the contribution of the third time constant to the hereditary integral, in the ODE form.

$$\frac{\mathrm{d}(Q3)}{\mathrm{d}(t)} = (A3 * velocity - alpha3 * Q3) \tag{A.26.161}$$

Appendix B

Finite Deformation Elasticity

Understanding and predicting the deformation of tissue under varying distributions of applied stresses and strains is fundamental to understanding its function. To deal with the nonlinear constitutive mechanical behaviour requires a framework based on finite deformation elasticity.

B.1 Kinematics

We begin by introducing the kinematic relations required to track material based properties through large deformations. Let $\mathbf{x} = (x_1, x_2, x_3)$ give the present position in rectangular Cartesian coordinates of a material particle that occupied the position $\mathbf{X} = (X_1, X_2, X_3)$ in the reference state.

In standard finite deformation theory (x_1, x_2, x_3) are considered as material coordinates and a *deformation gradient tensor* $\mathbf{F}$ is defined, which carries the undeformed line segment, $d\mathbf{X}$, to the corresponding deformed line segment $d\mathbf{x} = \mathbf{F}d\mathbf{X}$, or in component form:

$$dx^i = F^i_M dX^M \tag{B.1.1}$$

where

$$F^i_M = \frac{\partial x_i}{\partial X_M} \tag{B.1.2}$$

Polar decomposition, $\mathbf{F} = \mathbf{R}\mathbf{U}$, splits $\mathbf{F}$ into the product of an orthogonal rotation tensor, $\mathbf{R}$, and a symmetric positive definite stretch tensor, $\mathbf{U}$, which contains a complete description of the material strain, independent of any rigid body motion (Atkin & Fox 1980).

For inhomogeneous, anisotropic materials the orientation of the material axes may vary with location, for example fibre direction changes spatially throughout the myocardium. Thus it is no longer practical to identify the material axes in the undeformed body with the reference coordinates (X_1, X_2, X_3). Instead, a new material coordinate system (ν_1, ν_2, ν_3) is introduced which is aligned with the microstructural features of the material, as described in Figure 1.3. For myocardium, a natural set of material axes are formed by identifying ν_1 with the muscle fibre direction, ν_2 with the sheet direction, and ν_3 with the normal direction.

It is useful to choose the base vectors for the ν_α-coordinate system to be orthogonal in the reference state. This is convenient in myocardium, for example, where the ν_α-coordinates are chosen to line up with the fibre, sheet and normal directions, which are defined to be orthogonal in the undeformed state. However, the ensuing deformation means that they are not, in general, orthogonal in the deformed configuration.

$\mathbf{A}_\alpha^{(\nu)}$, $\mathbf{A}_{(\nu)}^\alpha$ and $\mathbf{a}_\alpha^{(\nu)}$, $\mathbf{a}_{(\nu)}^\alpha$ denote the covariant and contravariant base vectors in the undeformed and deformed configurations, respectively. The corresponding metric tensors are denoted by $A_{\alpha\beta}^{(\nu)}$, $A_{(\nu)}^{\alpha\beta}$ and $a_{\alpha\beta}^{(\nu)}$, $a_{(\nu)}^{\alpha\beta}$. The undeformed covariant base vectors, $\mathbf{A}_\alpha^{(\nu)}$, are defined to be unit vectors by choosing the ν_α-coordinates to be a measure of physical arclength in the undeformed state. The base vectors and metric tensors for the ν_α-coordinate system are:

$$\mathbf{A}_\alpha^{(\nu)} = \frac{\partial X_k}{\partial \nu_\alpha} \mathbf{g}_k^{(x)} \qquad\qquad \mathbf{a}_\alpha^{(\nu)} = \frac{\partial x_k}{\partial \nu_\alpha} \mathbf{g}_k^{(x)}$$
$$A_{\alpha\beta}^{(\nu)} = \mathbf{A}_\alpha^{(\nu)} \cdot \mathbf{A}_\beta^{(\nu)} \qquad\qquad a_{\alpha\beta}^{(\nu)} = \mathbf{a}_\alpha^{(\nu)} \cdot \mathbf{a}_\beta^{(\nu)} \qquad\qquad \text{(B.1.3)}$$

where $\mathbf{g}_k^{(x)}$ are the base vectors of the rectangular Cartesian reference axes. The Green strain tensor, defining the kinematics of large deformation for an inhomogeneous anisotropic material, is then

$$E_{\alpha\beta} = \frac{1}{2}\left(a_{\alpha\beta}^{(\nu)} - A_{\alpha\beta}^{(\nu)}\right). \qquad\qquad \text{(B.1.4)}$$

B.2   Stress Equilibrium and the Principle of Virtual Work

The governing equations for elastostatics can be derived from a physically appealing argument. For equilibrium, the work done by the external surface forces in moving through a virtual displacement is equal to the work done by the stress vector in moving through a compatible set of virtual displacements. Using this principle (known as the principle of virtual work) the stress

equilibrium can be expressed via the following equation (Nash & Hunter 2000):

$$\int\limits_{V_0} T^{\alpha\beta} F_\beta^j \, \delta v_j|_\alpha \, dV_0 = \int\limits_{V_0} \rho_0 \left(b^j - f^j\right) \delta v_j \, dV_0 + \int\limits_{S_2} p_{(appl)} \frac{g_{(\xi)}^{3M}}{\sqrt{g_{(\xi)}^{33}}} \frac{\partial x_j}{\partial \xi_M} \delta v_j \, dS \qquad \text{(B.2.1)}$$

where $T^{\alpha\beta}$ are second Piola-Kirchhoff stresses expressed relative to the fibre-sheet material coordinates; $|_\alpha$ is a covariant derivative; $\delta\mathbf{v} \;=\; \delta v_j \mathbf{i}_j$ are virtual displacements expressed relative to the reference coordinate system (Malvern 1969); b^j and f^j are the components of the body force and acceleration vectors, respectively; $p_{(appl)}$ is the pressure applied to the surface S_2 with normal direction ξ_3; ρ_0 is the tissue density; and $g_{(\xi)}^{MN}$ are contravariant metric tensors for the ξ_i-coordinate system. Covariant base vectors and metric tensors for the ξ_M-coordinate system are defined for the undeformed and deformed states as follows:

$$\mathbf{G}_M^{(\xi)} = \frac{\partial X_k}{\partial \xi_M} \mathbf{g}_k^{(x)} \qquad\qquad\qquad \mathbf{g}_M^{(\xi)} = \frac{\partial x_k}{\partial \xi_M} \mathbf{g}_k^{(x)}$$

$$G_{MN}^{(\xi)} = \mathbf{G}_M^{(\xi)} \cdot \mathbf{G}_N^{(\xi)} = \frac{\partial X_k}{\partial \xi_M} \frac{\partial X_k}{\partial \xi_N} \qquad g_{MN}^{(\xi)} = \mathbf{g}_M^{(\xi)} \cdot \mathbf{g}_N^{(\xi)} = \frac{\partial x_k}{\partial \xi_M} \frac{\partial x_k}{\partial \xi_N} \qquad \text{(B.2.2)}$$

Equation (B.2.1) is the starting point for the analysis of a body undergoing large elastic deformations. For further detail see, for example, Costa, Hunter, Rogers, Guccione, Waldman & McCulloch (1996) and Costa, Hunter, Wayne, Waldman, Guccione & McCulloch (1996).

B.3   Finite Element Solution Techniques

Using the interpolation functions ψ_n from Section 1.2 we can define virtual displacement fields δv_j as

$$\delta v_j = \psi_n \left(\xi_1, \xi_2, \xi_3\right) \delta v_j^n \qquad\qquad \text{(B.3.1)}$$

where δv_j^n are arbitrary virtual nodal displacements. Substituting Equation (B.3.1) into the equilibrium equations (Equation (B.2.1)) and setting the coefficient of each component δv_j^n to zero, gives

$$\int\limits_{V_0} T^{\alpha\beta} F_\beta^j \, \psi_n|_\alpha \, dV_0 = \int\limits_{V_0} \rho_0 \left(b^j - f^j\right) \psi_n \, dV_0 + \int\limits_{S_2} p_{(appl)} \frac{g_{(\xi)}^{3M}}{\sqrt{g_{(\xi)}^{33}}} \frac{\partial x_j}{\partial \xi_M} \psi_n \, dS \qquad \text{(B.3.2)}$$

To evaluate the integrals in Equation (B.3.2), they must first be transformed from the reference coordinate space to the element ξ_M-coordinate space using the appropriate Jacobian. The

transformed integrals are written in Equation (B.3.3).

$$\iiint_{V_0} T^{\alpha\beta} F_\beta^j \, \psi_n|_\alpha \sqrt{G^{(\xi)}} \, d\xi_3 d\xi_2 d\xi_1 = \iiint_{V_0} \rho_0 \left(b^j - f^j \right) \psi_n \sqrt{G^{(\xi)}} \, d\xi_3 d\xi_2 d\xi_1$$

$$+ \iint_{S_2} p_{(appl)} \, g_{(\xi)}^{3M} \, \frac{\partial \theta_j}{\partial \xi_M} \, \psi_n \sqrt{g^{(\xi)}} \, d\xi_2 d\xi_1 \quad \text{(B.3.3)}$$

where $\sqrt{G^{(\xi)}} = \sqrt{\det\{G_{ij}^{(\xi)}\}}$ and $\sqrt{g^{(\xi)}} = \sqrt{\det\{g_{ij}^{(\xi)}\}}$ are the Jacobians of the three-dimensional coordinate transformation with respect to the undeformed and deformed configurations, respectively. Note that the surface integral is transformed by substituting $J_{2D}d\xi_2d\xi_1$ for dS, where the two-dimensional Jacobian with respect to deformed coordinates is given by $J_{2D} = \sqrt{g^{(\xi)}g_{(\xi)}^{33}}$ (Oden 1972).

The three-dimensional integrals in Equation (B.3.3) are evaluated over the undeformed volume and the two-dimensional integral is computed over the portion of the deformed surface (denoted S_2) for which external pressure loads are applied. These integrals are replaced by a sum of integrals over the collection of element domains which constitute the finite element model. Element integrals are evaluated numerically using Gaussian quadrature. Components of the second Piola-Kirchhoff stress tensor, $T^{\alpha\beta}$, are evaluated at each Gauss point using (Malvern 1969)

$$T^{\alpha\beta} = \frac{1}{2} \left(\frac{\partial W}{\partial E_{\alpha\beta}} + \frac{\partial W}{\partial E_{\beta\alpha}} \right) - p a_{(\nu)}^{\alpha\beta} \quad \text{(B.3.4)}$$

where p is hydrostatic pressure and the derivatives of the strain energy function W with respect to the components of $\boldsymbol{E}$ are determined using a constitutive relation.

The strain energy functions of cardiac tissue have been characterised and applied by a number of authors (Guccione, McCulloch & Waldman 1991, Emery, Omens & McCulloch 1997, Usyk et al. 2002) using a generic exponential relation of the form:

$$W = \frac{1}{2}\boldsymbol{C}(e^Q - 1) \quad \text{(B.3.5)}$$

Where $\boldsymbol{C}$ is the right Cauchy-Green strain tensor and Q is a function in which the strain components of $\boldsymbol{E}$ are referred to the local structure-based coordinates. Guccione et al. (1991) defined the form of Q such that myocardium was assumed to be transversely isotropic and incompressible. More recently Usyk et al. (2000) have developed and applied (Usyk et al. 2002) a fully orthotropic model in the form of Equation (B.3.5) within a three-dimensional model of cardiac mechanics. Difficulties lie in assigning unique parameter values in the complex forms of Q required to fully represent the orthotropic behaviour of myocardium via Equation (B.3.5).

The passive myocardial characteristics have also been encapsulated via an alternative pole-zero strain energy function for the myocardium (Hunter, Smaill & Hunter 1995) given by:

$$
\begin{aligned}
W \quad = \quad & k_{11}\frac{E_{11}^2}{|a_{11}-E_{11}|^{b_{11}}}+ \quad k_{22}\frac{E_{22}^2}{|a_{22}-E_{22}|^{b_{22}}}+ \quad k_{33}\frac{E_{33}^2}{|a_{33}-E_{33}|^{b_{33}}} \\
+ \quad & k_{12}\frac{E_{12}^2}{|a_{12}-E_{12}|^{b_{12}}}+ \quad k_{13}\frac{E_{13}^2}{|a_{13}-E_{13}|^{b_{13}}}+ \quad k_{23}\frac{E_{23}^2}{|a_{23}-E_{23}|^{b_{23}}}
\end{aligned}
\tag{B.3.6}
$$

where the constitutive parameters (a's, b's and k's) are fitted from biaxial testing of tissue slices cut parallel with the fibre axis at several transmural sites throughout the myocardium (Novak, Yin & Humphrey 1994). Within Equation (B.3.6) $a_{\alpha\beta}$ denote limiting strain or poles, $b_{\alpha\beta}$ relate the curvature of the uni-axial stress-strain relationships and $k_{\alpha\beta}$ weight the contribution of the corresponding mode of deformation to the total strain energy of the material.

For incompressible materials, an additional scalar hydrostatic pressure field is introduced into the constitutive equations. The extra constraint necessary to determine the parameters of the hydrostatic pressure field arise from the requirement that the third strain invariant (I_3) equals one for incompressible materials.

For a Galerkin formulation, the form of the incompressibility constraints is given in Equation (B.3.7).

$$
\iiint\limits_{V_e} \left(\sqrt{I_3}-1\right)\psi^p\,\sqrt{G^{(\xi)}}\,d\xi_3 d\xi_2 d\xi_1 = 0
\tag{B.3.7}
$$

where V_e denotes the domain of the element and ψ^p are the basis functions used to approximate the three-dimensional hydrostatic pressure field. Note that the undeformed three-dimensional Jacobian, $\sqrt{G^{(\xi)}}$, is introduced since the integrals are evaluated with respect to the undeformed configuration.

B.3.1 Explicit Pressure Boundary Conditions

In this formulation, the hydrostatic pressure field is quadratically interpolated across each element in the ξ_3-direction. This is described as

$$
p^e\left(\xi_3\right) = \sum_{i=0}^{2} p_i^e\psi_i^p\left(\xi_3\right)
\tag{B.3.8}
$$

where

$$
\psi_0^p\left(\xi_3\right)=1 \qquad \psi_1^p\left(\xi_3\right)=\xi_3 \qquad \psi_1^p\left(\xi_3\right)=2\xi_3\left(\xi_3-1\right)
\tag{B.3.9}
$$

With the application of external pressure boundary loads, the constant hydrostatic pressure element variables, p_0^e, remain unchanged and are determined using an element constraint of the

form in Equation (B.3.7). p_1^e and p_2^e are determined by introducing the following explicit surface traction constraints into the global system.

$$
\begin{aligned}
\sigma_{wall}^{33}\big|_{\xi_3=0} + p_{in} &= 0 \\
\sigma_{wall}^{33}\big|_{\xi_3=1} + p_{out} &= 0
\end{aligned}
\tag{B.3.10}
$$

p_{in} and p_{out} are the applied pressure loads at the centre of the $\xi_3 = 0$ and $\xi_3 = 1$ element faces, respectively, and $\sigma_{wall}^{33}\big|_{\xi_3=0}$ is the physical component of the Cauchy stress normal to the centre of the deformed element (ξ_1, ξ_2) face (Nash 1998, Stevens 2002).

B.3.2   Model Solution

Simulation using the FE method for finite elasticity requires the solution of a system of nonlinear equations over the domain of interest. This system of equations comes from the combination of Equations (B.3.3) and (B.3.7), with additional equations from Equation (B.3.10) if pressure boundary conditions are specified. It is convenient to rearrange the complete nonlinear system of equations into a set of residuals which must be minimised with respect to the set of solution variables. The solution to this system of equations is now a set of solution variables which give a zero residual. Such a set of solution variables can be found using a nonlinear, multi-dimensional, root finding technique. The Newton method has been found to work well with these models (Nash 1998, Stevens 2002).

Coupling the dynamic active tension from the cellular model(s) into the mechanics is integral to the solution of this nonlinear system of equations, so a brief overview of Newton's method is presented here (Section 3.2.2).

Consider the system of n nonlinear equations of the form $f_i(\boldsymbol{x}) = 0, (i = 1, \ldots, n)$, where $\boldsymbol{x}$ are the solution variables. Given an initial estimate of the solution, $\{x_i\} = \{a_i\}$, each function can be expanded about $\boldsymbol{a}$ using a Taylor's series approximation. Retaining only the linear terms in this expansion yields

$$
\begin{aligned}
f_1(\boldsymbol{a}) &+ \frac{\partial f_1}{\partial x_1}(\boldsymbol{a})\,\delta_1 &+ \frac{\partial f_1}{\partial x_2}(\boldsymbol{a})\,\delta_2 &+ \ldots &+ \frac{\partial f_1}{\partial x_n}(\boldsymbol{a})\,\delta_n &= 0 \\[2mm]
f_2(\boldsymbol{a}) &+ \frac{\partial f_2}{\partial x_1}(\boldsymbol{a})\,\delta_1 &+ \frac{\partial f_2}{\partial x_2}(\boldsymbol{a})\,\delta_2 &+ \ldots &+ \frac{\partial f_2}{\partial x_n}(\boldsymbol{a})\,\delta_n &= 0 \\[1mm]
&\vdots & & & &\vdots \\[1mm]
f_n(\boldsymbol{a}) &+ \frac{\partial f_n}{\partial x_1}(\boldsymbol{a})\,\delta_1 &+ \frac{\partial f_n}{\partial x_2}(\boldsymbol{a})\,\delta_2 &+ \ldots &+ \frac{\partial f_n}{\partial x_n}(\boldsymbol{a})\,\delta_n &= 0
\end{aligned}
\tag{B.3.11}
$$

where $\{\delta_i\}$ represents the deviations from $\boldsymbol{a}$. Equation (B.3.11) may be rewritten

$$\boldsymbol{J}(\boldsymbol{a})\,\boldsymbol{\delta} = -\boldsymbol{f}(\boldsymbol{a}) \tag{B.3.12}$$

where $\boldsymbol{J}$ is the Jacobian of derivatives evaluated at $\boldsymbol{a}$, and is defined in terms of the solution variables $\boldsymbol{x}$ as

$$\boldsymbol{J}(\boldsymbol{x}) = \begin{pmatrix} \dfrac{\partial f_1}{\partial x_1} & \dfrac{\partial f_1}{\partial x_2} & \cdots & \dfrac{\partial f_1}{\partial x_n} \\[2mm] \dfrac{\partial f_2}{\partial x_1} & \dfrac{\partial f_2}{\partial x_2} & \cdots & \dfrac{\partial f_2}{\partial x_n} \\[2mm] \vdots & & & \vdots \\[2mm] \dfrac{\partial f_n}{\partial x_1} & \dfrac{\partial f_n}{\partial x_2} & \cdots & \dfrac{\partial f_n}{\partial x_n} \end{pmatrix} \tag{B.3.13}$$

Equation (B.3.12) is a system of linear equations that can be solved using standard linear methods to give the set of deviations, $\{\delta_i\}$. The deviations are used to update the approximation of the solution variables to the nonlinear system of equations from the initial solutions, $\{a_i\}$,

$$x_i = a_i + \delta_i. \tag{B.3.14}$$

The initial solution for the FE equations for finite elasticity is chosen to be the unloaded geometry. For small loads, which produce small displacements, Newton's method will converge quadratically to the solution. Newton's method, however, is not guaranteed to converge for larger loads which give larger displacements. Thus, such loadings may be split into several incremental load steps which are applied sequentially. Newton's method can then be applied with greater confidence of a converged solution being obtained for a load step which can then be used as the initial solution for the subsequent load each step. In this formulation of the finite elasticity equations, the solution variables are the nodal displacements and hydrostatic pressure variables for each node in the solution domain plus any derivatives of these quantities depending on the element interpolation functions.

B.4   Numerical and Computational Issues

There are a number of numerical and computational challenges which must be overcome for the effective and efficient application of the finite element method to the finite deformation elasticity equations described above. The first of these is in the implementation of numerical techniques to find the roots of the system of nonlinear equations obtained by evaluating the

integrals in Equations (B.3.3) and (B.3.7) for each element in the mesh. The Newton-Raphson method can be used for this root-finding process. The calculation of the Newton step vector at each iteration requires the solution of a sparse set of linear equations, for which the *SuperLU* method (Demmel, Eisenstat, Gilbert, Li & Liu 1999, Demmel, Gilbert & Li 1999) has been found to perform well.

Oden (1972) suggests that the interpolation scheme chosen to describe the deformed geometric coordinates (ψ_n in Equation (B.3.3)) should be of higher order than those chosen to approximate the hydrostatic pressure field (ψ^p in Equation (B.3.7)). The strain energy contribution to stress components is related to the first derivatives of the geometric displacement fields, whereas the hydrostatic pressure directly contributes to the stress components. For consistency, and to avoid numerical ill-conditioning when calculating components of the stress tensor, the two contributions should vary in a similar manner.

The computational issues associated with modelling finite deformation mechanics centre around the exploitation of parallel architectures. In particular, the determination of groups of element stiffness matrices can be allocated across multiple processors while incurring only a small computational overhead. Furthermore, the *SuperLU* algorithm provides close to linear scalability for the Newton step calculations. The scalability of two such major components of the method means that with increased processor count close to linear speed-up is exhibited for the whole algorithm. The ease of implementation and code maintenance for shared memory architectures is well suited to finite deformation mechanics simulations, and indeed this has been the preferred platform. However, recent improvements in availability and the ongoing optimisation of specific algorithms (Li & Demmel 2003) has meant that distributed memory systems now provide an increasingly attractive alternative computational platform.

Appendix C

Modelling Electrical Activation and Propagation

Cardiac tissue consists of countless numbers of discrete cells which electrically interact to varying degrees. While we are not yet capable of modelling the complexity of such a huge interacting system, we can average the electrical properties of the individual cells over a length scale greater than that of single cells. The use of such averaging techniques leads to a continuum model of cardiac tissue. If we then assume that the tissue has three orthogonal directions of conductivity (Figure 1.3) we can incorporate the electrical connectivity and preferential conduction between cells (Section 1.1) through the use of an orthogonal conductivity tensor. The components of this tensor can be varied spatially throughout a geometric model and represent the underlying tissue microstructure.

Provided below is a brief overview of the full bidomain activation model and the simplified monodomain approximation. This is followed by a description of the numerical formulation used in simulations of electrical activation and propagation in cardiac tissue and whole heart models.

C.1 The Bidomain Model of Electrical Activation

One continuum approach is to use the bidomain model of multicellular volume conductors, which has been used extensively in models of the spread of electrical activity in excitable tissues

(Fischer, Tilg, Modre, Huiskamp, Fetzer, Rucker & Wach 2000, Henriquez 1993, Muzikant & Henriquez 1998, Plonsey & Barr 1984, Roth & Wikswo 1986, Roth 1997, Skouibine et al. 2000, Trayanova 1994). The bidomain model of cardiac tissue consists of two interpenetrating domains representing cells and the space surrounding them. The intracellular domain represents the region inside the cells and is given the subscript i, and the extracellular domain represents the space between cells and is given the subscript e. The key to the model is that these two domains are assumed to both exist at all points in the physical solution domain. Detailed derivation of the bidomain model can be found elsewhere (Schmitt 1969, Tung 1978, Krassowska & Neu 1994). Here we state the equations and show how they are transformed to finite element coordinates in order to study electrical propagation on a deforming finite element mesh.

We let ϕ_i and ϕ_e be the electric potentials in the intracellular and extracellular domains, respectively, and $V_m = \phi_i - \phi_e$ is the transmembrane potential. Associated with these domains are the macroscopic tensor quantities σ_i and σ_e, representing the local volume averaged conductivities in the intra- and extracellular spaces respectively. Tensors σ_i and σ_e are each separately anisotropic and are assumed to be diagonal in the material coordinates based on the fibrous structure of muscle tissue (Figure 1.3).

The bidomain model consists of two equations. The first describes the conservation of current:

$$\nabla \cdot \left((\sigma_i + \sigma_e)\, \nabla \phi_e \right) = -\nabla \cdot (\sigma_i \nabla V_m) + I_{s1}, \tag{C.1.1}$$

that given a transmembrane potential distribution is used to solve for the extracellular potential. The second equation describes the current flow across the cellular membrane composed of ionic and capacitive currents (the cell membrane acts as a parallel capacitance):

$$\nabla \cdot (\sigma_i \nabla V_m) + \nabla \cdot (\sigma_i \nabla \phi_e) = A_m \left(C_m \frac{\partial V_m}{\partial t} + I_{ion} \right) - I_{s2}, \tag{C.1.2}$$

and is used to calculate the transmembrane potential distribution. A_m is the surface to volume ratio of the cell membrane, C_m is the membrane capacitance per unit area, and I_{ion} is a nonlinear function representing the sum of all the transmembrane ionic currents. Externally applied volume stimulus currents can be imposed in both the extracellular (I_{s1}) and intracellular (I_{s2}) domains.

It is assumed that there is no current flow between the intracellular domain and the external region so the boundary condition applied to V_m on the solution domain boundary is

$$(\sigma_i \nabla V_m) \cdot \boldsymbol{n} = -(\sigma_i \nabla \phi_e) \cdot \boldsymbol{n}, \tag{C.1.3}$$

where $\boldsymbol{n}$ is a unit vector outwardly normal to the domain boundary. For the extracellular domain the current must balance between the extracellular domain and the surrounding external regions

$$(\sigma_e \nabla \phi_e) \cdot \boldsymbol{n} = - (\sigma_o \nabla \phi_o) \cdot \boldsymbol{n}. \tag{C.1.4}$$

where σ_o signifies the conductivity of the surrounding region. The negative sign accounts for the direction of current flow as both sides of the equations use outward normal vectors. The boundary extracellular potential must also match the potential of the boundary of the external regions,

$$\phi_e = \phi_o. \tag{C.1.5}$$

In the absence of an external region any combination of current and potential boundary conditions can be used to specify the required physical problem, with the restriction that at least one extracellular boundary point has a potential boundary condition to provide a reference potential (and hence a unique solution to the bidomain equations).

C.2 The Monodomain Model of Electrical Activation

In an effort to further reduce the computational cost of the activation modelling, the extracellular domain is sometimes assumed to be highly conducting or, alternatively, both domains are assumed equally anisotropic. With either of these assumptions the transmembrane potential is equal to the intracellular potential, and the bidomain equations simplify to

$$\nabla \cdot (\sigma \nabla V_m) = A_m \left(C_m \frac{\partial V_m}{\partial t} + I_{ion} \right) - I_{stim}, \tag{C.2.1}$$

as the gradient of the extracellular potential field is effectively zero in either of these approximations. This monodomain model is suitable for situations such as computations on an isolated heart. When the extracellular electrical state is important the full bidomain model needs to be used, for example electrical current propagating from the heart to the torso in body surface potential forward simulations or the application of defibrillation type extracellular stimuli.

For the monodomain model, there is no connection between the intracellular domain and any surrounding media. Therefore, no current can flow out of the solution domain giving rise to the boundary condition

$$(\sigma \nabla V_m) \cdot \boldsymbol{n} = 0. \tag{C.2.2}$$

C.3   Grid-Based Finite Element Method

Numerous techniques have been developed and applied to the numerical simulation of the bidomain and monodomain electrical activation models. Previously, detailed cardiac models have been constructed using a FE derived finite difference (FD) method (Sands 1997, Buist 2001, Buist, Sands, Hunter & Pullan 2003). This method involves embedding a high resolution FD grid in a FE geometric model. Finite difference approximations of the partial derivatives in the activation equations can then be solved over this computational grid. An advantage of this method over traditional FD methods, is that the FD grid is tied to the FE geometrical model allowing the FD grid to deform with any deformation of the geometrical model – such as that which occurs when the heart contracts.

A new method has recently been developed and implemented in CMISS which is based on a FE formulation of the bidomain or monodomain models (Hooks et al. 2002, Hooks 2002). This method, named here as the GBFE method, uses the same technique of embedding a high resolution computational grid in a FE geometric model. Rather than a FD approximation of the partial derivatives in the activation equations this method uses a FE formulation of the activation equations to integrate the equations over linear FEs defined by the high resolution grid. A significant advantage of the GBFE method over the FE derived FD method is its ability to exactly represent the Neumann condition (zero flux normal to boundary surfaces) at all boundaries. This is an important factor in models containing detailed microstructual information, such as the internal cleavage planes between sheets of cardiac myocytes (Hooks et al. 2002).

Illustration of the specification of a GBFE model is provided in Figure C.1. A typically high order FE geometry is first defined. Grid points are defined such that they are regularly spaced in element ξ-space (Figure 1.6). These grid points are the nodes for the linear FEs constructed for solution of the activation equations. The FE formulation of the activation equations can then be integrated over these linear elements.

Derivation of the FE formulation of the full bidomain equations can be found in Hooks (2002). Given the work in this thesis uses only the monodomain model, we present here a brief derivation of the FE formulation of the monodomain equation.

We begin with the FE weighted residual of the monodomain equation, Equation (C.2.1):

$$\int_{\Omega} \left(\nabla \cdot (\sigma \nabla V_m) - A_m C_m \frac{\partial V_m}{\partial t} - A_m I_{ion} - I_{stim} \right) \omega \, d\Omega = 0, \qquad \text{(C.3.1)}$$

(a) Geometric FE model

(b) Generated grid points

(c) Grid-based finite elements
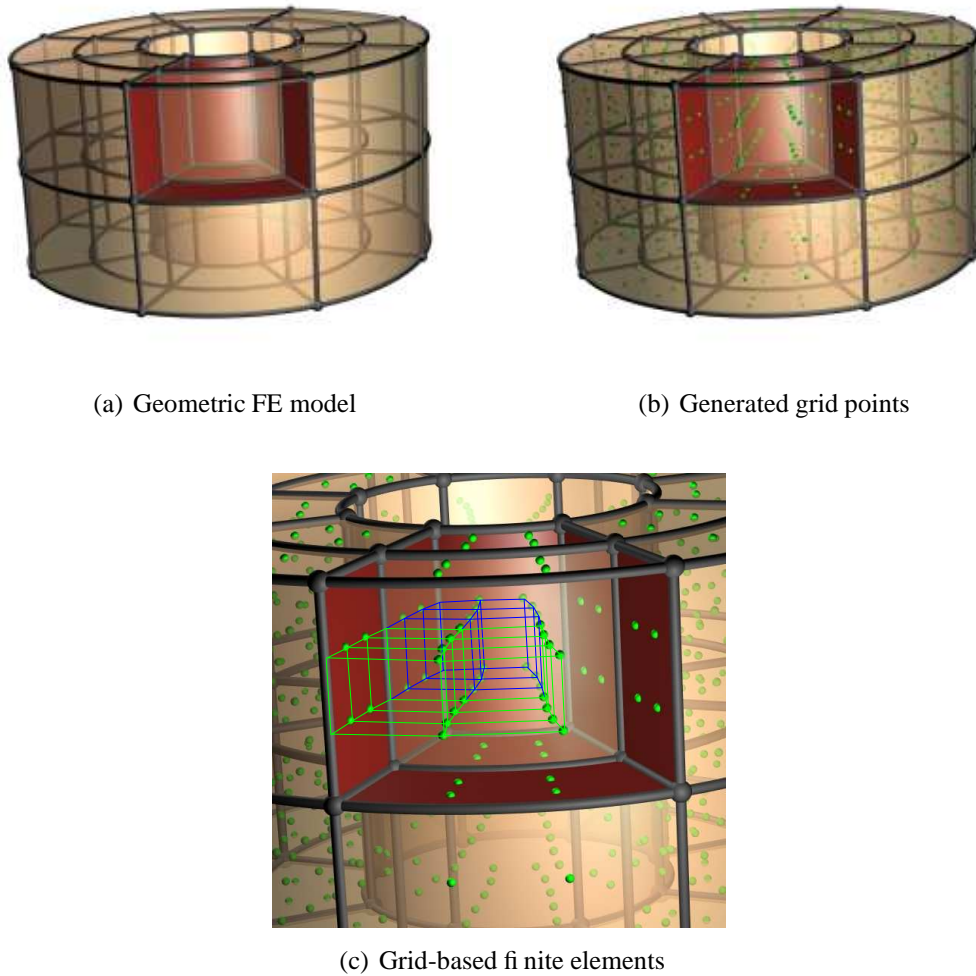
FIGURE C.1: An illustration of the specification of a GBFE model. The tricubic Hermite geometry is shown in (a) and the high resolution grid embedded in the geometric model is added in (b) (in this example a coarse grid has been used to enhance the presentation). In (c) we have given a close-up view of two of the geometric FEs and marked some of the trilinear grid-based elements defined for the solution of the activation model over this geometric domain (the blue lines represent elements embedded in the rear geometric element and the green those in the front element).

where ω is a weighting function and Ω is the solution domain. The order of the potential spatial derivative can be reduced through the use of the Green-Gauss theorem:

$$\int_{\Omega} \nabla \cdot (\sigma \nabla V_m)\, \omega\, d\Omega = -\int_{\Omega} (\sigma \nabla V_m) \cdot \nabla \omega\, d\Omega + \int_{\Gamma} \nabla V_m \cdot \sigma \boldsymbol{n} \omega\, d\Gamma, \qquad \text{(C.3.2)}$$

where $\boldsymbol{n}$ is the outward pointing normal to the domain boundary Γ. Substituting back into Equation (C.3.1) and expanding gives

$$-\int_{\Omega} (\sigma \nabla V_m) \cdot \nabla \omega\, d\Omega - \int_{\Omega} A_m C_m \frac{\partial V_m}{\partial t} \omega\, d\Omega =$$

$$-\int_{\Gamma} \nabla V_m \cdot \sigma \boldsymbol{n} \omega\, d\Gamma + \int_{\Omega} A_m I_{ion} \omega\, d\Omega + \int_{\Omega} I_{stim} \omega\, d\Omega. \quad \text{(C.3.3)}$$

Using the finite element method we can numerically evaluate these integrals by dividing the solution domain Ω, bounded by Γ, into a number of elements (Section 1.2). The membrane potential field, $V_m(\boldsymbol{x})$, is represented through the nodal values at the N nodes in the solution domain ($V_m{}^n$, $n = 1..N$). The potential field is interpolated over element $\boldsymbol{\xi}$-space using trilinear Lagrange basis functions, such that

$$V_m(\boldsymbol{x}(\boldsymbol{\xi})) = V_m{}^n \psi^n(\boldsymbol{\xi}). \qquad \text{(C.3.4)}$$

where n is now a local node number for the given element and the eight trilinear basis functions are:

$$
\begin{aligned}
\psi^1(\boldsymbol{\xi}) &= (1 - \xi_1)(1 - \xi_2)(1 - \xi_3) & \psi^2(\boldsymbol{\xi}) &= \xi_1(1 - \xi_2)(1 - \xi_3) \\
\psi^3(\boldsymbol{\xi}) &= (1 - \xi_1)\xi_2(1 - \xi_3) & \psi^4(\boldsymbol{\xi}) &= \xi_1\xi_2(1 - \xi_3) \\
\psi^5(\boldsymbol{\xi}) &= (1 - \xi_1)(1 - \xi_2)\xi_3 & \psi^6(\boldsymbol{\xi}) &= \xi_1(1 - \xi_2)\xi_3 \\
\psi^7(\boldsymbol{\xi}) &= (1 - \xi_1)\xi_2\xi_3 & \psi^8(\boldsymbol{\xi}) &= \xi_1\xi_2\xi_3
\end{aligned}
\qquad \text{(C.3.5)}
$$

The Galerkin FE method puts $\omega = \psi^m$, which can be substituted into the left hand side of Equation (C.3.3),

$$\text{LHS} = -\int_{\Omega} \sigma_{ij} \frac{\partial(V_m{}^n \psi^n)}{\partial x_j} \frac{\partial \psi^m}{\partial x_i}\, d\Omega - \int_{\Omega} A_m C_m \frac{\partial(V_m{}^n \psi^n)}{\partial t} \psi^m\, d\Omega, \qquad \text{(C.3.6)}$$

and transformed to element $\boldsymbol{\xi}$-space

$$\text{LHS} = -V_m \sum_e \left(\int_{\Omega_e} \sigma_{ij} \frac{\partial \psi^n}{\partial \xi_k} \frac{\partial \xi_k}{\partial x_j} \frac{\partial \psi^m}{\partial \xi_d} \frac{\partial \xi_d}{\partial x_i} \boldsymbol{J}\, d\boldsymbol{\xi} \right) - \sum_e \left(\left(\frac{\partial V_m}{\partial t} \right)^n \int_{\Omega_e} A_m C_m \psi^n \psi^m\, d\boldsymbol{\xi} \right),$$

$$\text{(C.3.7)}$$

where $\boldsymbol{J}$ is the Jacobian of transformation from global $\boldsymbol{x}$-space to element $\boldsymbol{\xi}$-space and e is summed over all elements Ω_e in the solution domain Ω. Equation (C.3.7) can be written

$$\text{LHS} = \boldsymbol{K}\boldsymbol{v} + \boldsymbol{M}\frac{\mathrm{d}\boldsymbol{v}}{\mathrm{d}t}, \tag{C.3.8}$$

where $\boldsymbol{K}$ and $\boldsymbol{M}$ are the global stiffness and mass matrices, respectively, and $\boldsymbol{v}$ is a vector of global nodal unknown membrane potentials ($V_m{}^n$). The time domain is discretized to approximate the membrane potential time derivative

$$\text{LHS} = \boldsymbol{K}\left(\theta\boldsymbol{v}^{i+1} + (1-\theta)\,\boldsymbol{v}^i\right) + \boldsymbol{M}\left(\frac{\boldsymbol{v}^{i+1} - \boldsymbol{v}^i}{\Delta t}\right), \tag{C.3.9}$$

where θ is a weighting factor satisfying $0 < \theta < 1$, and i denotes the ith time step of size Δt. For $\theta = 0.5$ the method is known as the Crank-Nicholson-Galerkin method and errors arising from the time discretization are O (Δt).

Similar transformations can be performed for terms two and three in the right hand side of Equation (C.3.3), giving

$$\int\limits_{\Omega} A_m I_{ion}\omega\, d\Omega = I_{ion}{}^n \sum_e \int\limits_{\Omega_e} A_m\psi^n\psi^m\, d\boldsymbol{\xi} = \boldsymbol{L}\boldsymbol{I_{ion}}, \tag{C.3.10}$$

and

$$\int\limits_{\Omega} I_{stim}\omega\, d\Omega = I_{stim}{}^n \sum_e \int\limits_{\Omega_e} \psi^n\psi^m\, d\boldsymbol{\xi} = \boldsymbol{Q}\boldsymbol{I_{stim}}. \tag{C.3.11}$$

Substituting Equations (C.3.9)–(C.3.11) into Equation (C.3.3) and approximating $\boldsymbol{I_{ion}}$ and $\boldsymbol{I_{stim}}$ by their values at the ith time step, we can write

$$(\boldsymbol{M} + \theta\Delta t\boldsymbol{K})\,\boldsymbol{v}^{i+1} = (\boldsymbol{M} - (1-\theta)\,\Delta t\boldsymbol{K})\,\boldsymbol{v}^i + \boldsymbol{L}\boldsymbol{I_{ion}}^i + \boldsymbol{Q}\boldsymbol{I_{stim}}^i - \int\limits_{\Gamma} \nabla V_m \cdot \sigma\boldsymbol{n}\omega\, d\Gamma, \tag{C.3.12}$$

where the boundary integral term is equal to zero in the case of Neumann boundary conditions. Standard linear algebra solution techniques can be used to solve this system of equations for $\boldsymbol{v}^{i+1}$ to give the membrane potential nodal values for the next time step.

$\boldsymbol{I_{ion}}$ is given at each node by the cellular electrophysiological model given at that node. The work in this thesis allows for any CellML based model to be defined at any node, thus providing for a very general specification of underlying cellular models.

C.4   Numerical and Computational Issues

The wave of electrical activation propagates through cardiac tissue with a very steep wavefront due to the fast response of ventricular cells to electrical stimulation. This leads to high spatial gradients of electrical potential in the region around the wavefront, requiring the use of a very high density grid to accurately resolve the wavefront. Various sources recommend a spatial resolution of between 10–$200 \ \mu$m for the grid (Sands 1997, Buist 2001, Pollard 2003, Hunter et al. 2003). Ahead of the wavefront and behind the activation wave, however, tissue is inactive and recovering, respectively, and a lower density grid is sufficient to resolve the slower electrical activity. Therefore the use of a uniformly high resolution FE grid results in a large computational overhead for the inactive and recovering regions of tissue. Adaptive grid techniques are well suited to this type of problem, where only the region of tissue about the activation wavefront is solved using the high resolution grid, while inactive regions use lower resolution meshes and recovering regions use a medium density mesh. Currently, testing is underway of an implementation of a multi-grid technique (McCormick 1989) which allows for the specification of multiple grid '*levels*', with stepping between these levels during model simulation.

Numerical solution of the electrical activation model requires two steps: integration of a system of ordinary differential equations for the cellular processes at each point to calculate I_{ion} and solution of the monodomain model (C.2.1) for V_m. Using anything other than the simplest cellular models, the first of these steps will have significantly greater computational demands than the solution of the advection-diffusion equation (Pollard (2003) recommends that the action potential upstroke is broken into several time steps, requiring Δt to be on the order of 1–$10 \ \mu$s, also needed to be able to resolve the fast sodium current). This is a prime target for parallelisation. The cellular ODEs at each grid point can be integrated independently for a given time step, suggesting that this integration is an ideal candidate for multiprocessing. Given no communication between grid points during a time step the integration of the cell model should scale linearly with the number of processors in a shared memory system, while the communication between the cellular and continuum models represents a fixed cost which may restrict the scalability on distributed memory systems. Work is beginning examining the ability of these models to scale across distributed memory systems as well as large scale grid computing as part of the Integrative Biology Grid – http://www.integrativebiology.ox.ac.uk/.

Appendix D

Description of Attached Compact Disc

Attached to this thesis is a compact disc containing additional data relevant to this thesis. Here we provide a brief description of the contents of the disc as an aid to finding the data as referenced in the preceding chapters.

The disc is divided into three top level directories (or folders) relating to: the CellML API code we have developed and implemented; the repository of cellular models we have developed, tested, and used in this work; and a collection of movies providing animations of some of the simulations performed in this thesis. In the following description, we denote the compact disc drive (MS Windows) or Unix mount point as X and indicate paths from this root.

D.1 CellML API

Documentation of the CellML Application Program Interface (API) we developed as part of the process of enabling the use of CellML in CMISS is provided in X/cellml-api/. We provide a browsable version in X/cellml-api/html/, just point your favourite web-browser at: X/cellml-api/html/index.html. A print version is also provided in the Adobe portable document format at X/cellml-api/api.pdf. The LaTeX source generated directly from the API code and used to create the PDF is given in X/cellml-api/latex/.

The latest API code and sample applications is always available from http://cellml.sourceforge. net. Of particular note is the ODE integration application which is capable of generating code

from the CellML models used in this thesis and integrating these models.

D.2   CellML Models

All cellular models used in this thesis are made available encoded in CellML. They can be found at X/cellml-models/ with file names that are self explanatory. These versions of the models are exactly what are used in all simulations in this work, with the code generated directly from the CellML. Boundary and initial conditions and parameter changes for specific simulations are given with the simulation results in the preceding chapters.

D.3   Simulation Animations

In the preceding chapters we have attempted to describe all simulation results for the models we have developed in this thesis using static images. When discussing large scale tissue and organ level models, a static image sometimes fails to convey the full impact of the simulation. By providing animations of the simulation results, therefore, we hope to be able to impart a more understandable summary of the various simulations.

All movies are provided in the MPEG 2 format and we have tried to create movies that play on most major platforms.

We provide an animation of the FK-HMT based cube model at X/movies/cube-FK-HMT.mpg. This animation shows the cube undergoing three consecutive stimuli, as shown in Figure 3.18. In addition to the animation of the cube, in this movie we show cellular potential, tension, and extension ratio transients for several points in the cube. The electrical wave can be seen propagating through the tissue with a spectrum ranging from -15 mV (blue) to $+5$ mV (red).

Animations are provided for all the LV simulations described in Sections 5.3 and 5.4. These movies show animations of the LV model contracting and the cellular transmembrane activation and repolarisation waves travelling through the tissue (same spectrum as the cube animation above). Shown in conjunction with the LV are cellular potential, tension, and extension ratio transients and the cavity pressure and volume transients. A key to the movies is given in Fig-

ure D.1, where the vertical scales indicated are constant for all movies but the horizontal time scale is variable. The electrical activation only models display only the cellular membrane potential transients as the other transients have no effect on these models.
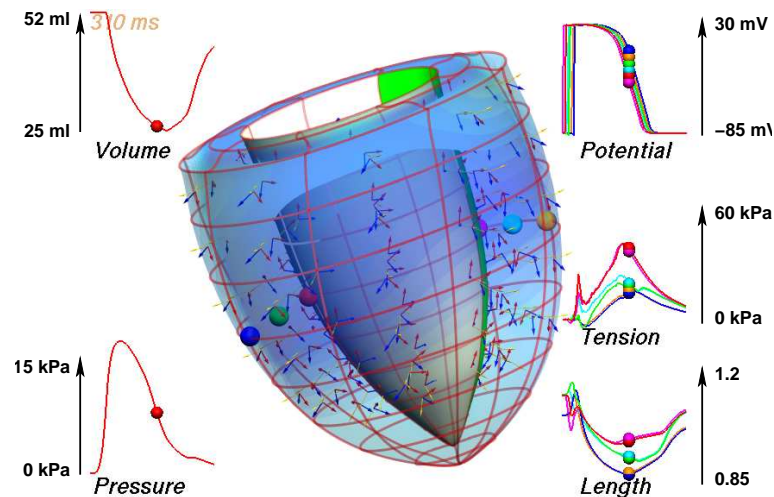

FIGURE D.1: The key to describe the LV simulation animations. The vertical scales for each of the graphs gives an indication of the scale for each of the plots which is consistent for all movies. Shown in the top left corner of each of the movies is the time for each of the movie frames. The transients on the right are all from the cellular level and those on the left are for the ventricular cavity. The colour of the cellular transients match the sphere in the ventricular wall placed at the spatial location of the cell from which the transient originated. The sphere plot markers indicate the values for the current time as the movie progresses.

The movies are all given in X/movies/ and the file names correspond to the simulations as given below.

- cube-FK-HMT.mpg: the FK-HMT based cube model.
- lv-activation-purkinje.mpg: electrical activation in the LV from the Purkinje-like sinus rhythm stimulus.
- lv-activation-purkinje-heterogeneous.mpg: electrical activation in the LV from the Purkinje-like sinus rhythm stimulus with the heterogeneous cellular model specification.
- lv-activation-BiV.mpg: electrical activation in the LV from the BiV pacing protocol.
- lv-activation-LVb.mpg: electrical activation in the LV from the LVb pacing protocol.
- lv-activation-RVa.mpg: electrical activation in the LV from the RVa pacing protocol.
- lv-electromechanics-purkinje.mpg: electro-mechanics in the LV from the Purkinje-like sinus rhythm stimulus.
- lv-electromechanics-purkinje-heterogeneous.mpg: electro-mechanics in the LV from the Purkinje-like sinus rhythm stimulus with the heterogeneous cellular model specification.

- lv-electromechanics-BiV-noEjection.mpg: electro-mechanics in the LV from the BiV pacing protocol and no ejection.
- lv-electromechanics-BiV.mpg: electro-mechanics in the LV from the BiV pacing protocol with ejection.
- lv-electromechanics-LVb.mpg: electro-mechanics in the LV from the LVb pacing protocol.
- lv-electromechanics-RVa.mpg: electro-mechanics in the LV from the RVa pacing protocol.

References

Aliev, R. R. & Panfilov, A. V. (1996), 'A simple two-variable model of cardiac excitation', *Chaos Solitons Fractals* **7**(3), 293–301.

Antzelevitch, C., Sicouri, S., Litovsky, S. H., Lukas, A., Krishnan, S. C., Di Diego, J. M., Gintant, G. A. & Liu, D.-W. (1991), 'Heterogeneity within the ventricular wall. Electrophysiology and pharmacology of epicardial, endocardial, and M cells', *Circ. Res.* **69**(6), 1427–1449.

Atkin, R. J. & Fox, N. (1980), *An Introduction to the Theory of Elasticity*, Longman Group Ltd., London.

Ausbrooks, R., Buswell, S., Carlisle, D., Dalmas, S., Devitt, S., Diaz, A., Froumentin, M., Hunter, R., Ion, P., Kohlhase, M., Miner, R., Poppelier, N., Smith, B., Soiffer, N., Sutor, R. & Watt, S. (2001), 'Mathematical markup language (MathML) version 2.0 (second edition)', http://www.w3.org/TR/MathML2/.

Barritt, G. & Rychkov, G. (2005), 'TRPs as mechanosensitive channels', *Nat. Cell Biol.* **7**(2), 105–107.

Bassingthwaighte, J. B. (2000), 'Stategies for the physiome project', *Ann. Biomed. Eng.* **28**(8), 1043–1058.

Beeler, G. W. & Reuter, H. (1977), 'Reconstruction of the action potential of ventricular myocardial fibres', *J. Physiol.* **268**, 177–210.

Bergel, D. A. & Hunter, P. J. (1979), The mechanics of the heart, *in* N. H. C. Hwang, D. R. Gross & D. J. Patel, eds, 'Quantitative Cardiovascular Studies, Clinical and Research Applications of Engineering Principles', University Park Press, Baltimore, chapter 4, pp. 151–213.

Berne, R. M. & Levy, M. N., eds (1993), *Physiology*, 3rd edn, Mosby, 11830 Westline Industrial Drive, St. Louis, Missouri 63146.

Bovendeerd, P. H. M., Arts, T., Huyghe, J. M., van Campen, D. H. & Reneman, R. S. (1992), 'Dependence of local left ventricular wall mechanics on myocardial fiber orientation: a model study', *J. Biomech.* **25**(10), 1129–1140.

Bradley, C. P. (1998), A three-dimensional torso model for electrocardiology, PhD thesis, The University of Auckland, Auckland, New Zealand.

Bradley, C. P., Pullan, A. J. & Hunter, P. J. (1997), 'Geometric modelling of the human torso using cubic Hermite elements', *Ann. Biomed. Eng.* **76**(7), 96–111.

Brown, H. & Kozlowski, R. (1997), *Physiology and Pharmacology of the Heart*, Blackwell Science.

Buist, M. L. (2001), Modelling Cardiac Activation from Cell to Body Surface, PhD thesis, The University of Auckland, Auckland, New Zealand.

Buist, M. L. & Pullan, A. J. (2001), 'From cell to body surface: A fully coupled approach', *J. Electrocardiol.* **34**(Suppl.), 191–195.

Buist, M. L. & Pullan, A. J. (2003), 'Effect of torso impedance on body surface and epicardial potentials', *IEEE Trans. Biomed. Eng.* **50**(7), 816–824.

Buist, M., Sands, G., Hunter, P. & Pullan, A. (2003), 'A deformable finite element derived finite difference method for cardiac activation problems', *Ann. Biomed. Eng.* **31**(5), 577–588.

Bureau International des Poids et Mesures (1998), 'The international system of units (SI)', http://www1.bipm.org/utils/en/pdf/si-brochure.pdf.

Bureau International des Poids et Mesures (2000), 'The international system of units (SI). Supplement 2000: addenda and corrigenda to the 7th edition', http://www1.bipm.org/utils/en/pdf/si-supplement2000.pdf.

Cabo, C. & Boyden, P. A. (2002), 'Electrical remodeling of the epicardial border zone in the canine infarcted heart: a computational analysis', *Am. J. Physiol. Heart Circ. Physiol.* **284**, H372–H384.

Cheng, L. K. (2001), Non-invasive Electrical Imaging of the Heart, PhD thesis, The University of Auckland, Auckland, New Zealand.

Christie, G. R., Bullivant, D., Blackett, S. & Hunter, P. J. (2002), 'Modelling and visualising the heart', *Comput. Visual. Sci.* **4**, 227–235.

Clancy, C. E. & Rudy, Y. (1999), 'Linking a genetic defect to its cellular phenotype in a cardiac arrhythmia', *Nature* **400**, 566–569.

Clancy, C. E. & Rudy, Y. (2001), 'Cellular consequences of HERG mutations in the long QT syndrome: Precursors to sudden cardiac death', *Cardiovasc. Res.* **50**(2), 301–313.

Clancy, C. E. & Rudy, Y. (2002), 'Na^+ channel mutation that causes both Brugada and long-QT syndrome phenotypes: a simulation study of mechanism', *Circulation* **105**(10), 1208–1213.

Colatsky, T. J. (1980), 'Voltage clamp measurement of sodium channel properties in rabbit cardiac Purkinje fibre', *J. Physiol. Lond.* **305**, 215–234.

Colli-Franzone, P., Guerri, L. & Taccardi, B. (2004), 'Modeling ventricular excitation: axial and orthotropic anisotropy effects on wavefronts and potentials', *Math. Biosci.* **188**, 191–205.

Costa, K. D., Hunter, P. J., Rogers, J. M., Guccione, J. M., Waldman, L. K. & McCulloch, A. D. (1996), 'A three-dimensional finite element method for large elastic deformations of ventricular myocardium: Part I – Cylindrical and spherical polar coordinates', *ASME J. Biomech. Eng.* **118**(4), 452–463.

Costa, K. D., Hunter, P. J., Wayne, J. S., Waldman, L. K., Guccione, J. M. & McCulloch, A. D. (1996), 'A three-dimensional finite element method for large elastic deformations of ventricular myocardium: Part II – Prolate spheroidal coordinates', *ASME J. Biomech. Eng.* **118**(4), 464–472.

Costa, K. D., May-Newman, K., Farr, D., O'Dell, W. G., McCulloch, A. & Omens, J. H. (1997), 'Three-dimensional residual strain in midanterior canine left ventricle', *Am. J. Physiol.* **273**, H1968–H1976.

Crampin, E. J., Halstead, M., Hunter, P., Nielsen, P., Noble, D., Smith, N. & Tawhai, M. (2004), 'Computational physiology and the physiome project', *Exp. Physiol.* **89**(1), 1–26.

Cuellar, A. A., Lloyd, C. M., Nielsen, P. F., Bullivant, D. P., Nickerson, D. P. & Hunter, P. J. (2003), 'An overview of CellML 1.1, a biological model description language', *Simulation* **79**(12), 740–747.

de Groot, J. R. (2002), 'A little gap junctional uncoupling too much', *Cardiovasc. Res.* **56**, 350–352.

de Tombe, P. P. & ter Keurs, H. E. (1992), 'An internal viscous element limits unloaded velocity of sarcomere shortening in rat myocardium', *J. Physiol.* **454**, 619–642.

Demmel, J., Eisenstat, S., Gilbert, J., Li, X. & Liu, J. (1999), 'A supernodal approach to sparse partial pivoting', *SIAM J. Mat. Anal. Appl.* **20**(3), 720–755.

Demmel, J., Gilbert, J. & Li, X. (1999), 'An asynchronous parallel supernodal algorithm for sparse gaussian elimination', *SIAM J. Mat. Anal. Appl.* **20**(4), 915–952.

DiFrancesco, D. & Noble, D. (1985), 'A model of cardiac electrical activity incorporating ionic pumps and concentration changes', *Phil. Trans. R. Soc. Lond. B* **307**(1133), 353–398.

Dokos, S., Smaill, B. H., Young, A. & LeGrice, I. (2002), 'Shear properties of passive ventricular myocardium', *Am. J. Physiol.* **283**, H2650–H2659.

Drouhard, J.-P. & Roberge, F. A. (1987), 'Revised formulation of the Hodgkin-Huxley representation of the sodium current in cardiac cells', *Comput. Biomed. Res.* **20**(4), 333–350.

Drouin, E., Charpentier, F., Gauthier, C., Laurent, K. & Le Marec, H. (1995), 'Electrophysiologic characteristics of cells spanning the left ventricular wall of human heart: evidence for presence of M cells', *J. Am. Coll. Cardiol.* **26**(1), 185–192.

Dumaine, R., Towbin, J. A., Brugada, P., Vatta, M., Nesterenko, D. V., Nesterenko, V. V., Brugada, J., Brugada, R. & Antzelevitch, C. (1999), 'Ionic mechanisms responsible for the electrocardiographic phenotype of the brugada syndrome are temperature dependent', *Circ. Res.* **85**(9), 803–809.

Earm, Y. E. & Noble, D. (1990), 'A model of the single atrial cell: relation between calcium current and calcium release', *Proc. R. Soc. Lond. B* **240**(1297), 83–96.

Ebihara, L. & Johnson, E. A. (1980), 'Fast sodium current in cardiac muscle. A quantitative description', *Biophys. J.* **32**, 779–790.

Emery, J. L., Omens, J. H. & McCulloch, A. D. (1997), 'Biaxial mechanics of the passively overstretched left ventricle.', *Am. J. Physiol.* **272**, H2299–30.

Faber, G. M. & Rudy, Y. (2000), 'Action potential and contractility changes in $[Na^+]_i$ overloaded cardiac myocytes: A simulation study', *Biophys. J.* **78**(5), 2392–2404.

Fabiato, A. & Fabiato, F. (1975), 'Contractions induced by a calcium-triggered release of calcium from the sarcoplasmic reticulum of single skinned cardiac cells', *J. Physiol. Lond.* **249**(3), 469–495.

Fenton, F. & Karma, A. (1998), 'Vortex dynamics in three-dimensional continuous myocardium with fiber rotation: Filament instability and fibrillation', *Chaos* **8**, 20–47.

Fernandez, J. W., Buist, M. L., Nickerson, D. P. & Hunter, P. J. (2004), 'Modelling the passive and nerve activated response of the rectus femoris muscle to a flexion loading: A finite element framework', *Med. Eng. Phys.* **accepted**.

Fernandez, J. W. & Hunter, P. J. (2004), 'An anatomically based finite element model of patella articulation: Towards a diagnostic tool', *Biomechan. Model. Mechanobiol.* **accepted**.

Fischer, G., Tilg, B., Modre, R., Huiskamp, G. J. M., Fetzer, J., Rucker, W. & Wach, P. (2000), 'A bidomain model based BEM-FEM coupling formulation for anisotropic cardiac tissue', *Ann. Biomed. Eng.* **28**(10), 1229–1243.

FitzHugh, R. (1961), 'Impulses and physiological states in theoretical models of nerve membrane', *Biophys. J.* **1**, 445–466.

Fozzard, H. A. & Lipkind, G. (1995), Ion channels and pumps in cardiac function, *in* S. Sideman & R. Beyar, eds, 'Molecular and Subcellular Cardiology: Effects of Structure and Function', Plenum Press, chapter 1, pp. 3–10.

Gadsby, D. C. (1980), 'Activation of electrogenic Na+/K+ exchange by extracellular K+ in canine cardiac purkinje fibers', *Proc. Natl. Acad. Sci. USA* **77**(7), 4035–4039.

Guccione, J. M. & McCulloch, A. (1993), 'Mechanics of active contraction in cardiac muscle: Part I - constitutive relations for fiber stress that describe deactivation', *J. Biomed. Eng.* **115**(81).

Guccione, J. M., McCulloch, A. D. & Waldman, L. K. (1991), 'Passive material properties of intact ventricular myocardium determined from a cylindrical model', *ASME J. Biomech. Eng.* **113**, 42–55.

Guccione, J., Motabarzadeh, I. & Zahalak, G. I. (1998), 'A distribution-moment model of deactivation in cardiac muscle', *J. Biomech.* **31**(11), 1069–1073.

Hairer, E. & Wanner, G. (1996), *Solving Ordinary Differential Equations II. Stiff and Differential-Algebraic Problems.*, Vol. 14 of *Springer Series in Computational Mathematics*, 2nd edn, Springer-Verlag.

Hedley, W., Nelson, M., Bullivant, D., Cuellar, A., Ge, Y., Grehlinger, M., Jim, K., Lett, S., Nickerson, D., Nielsen, P. & Yu, H. (2001), 'CellML 1.0 Specification', http://www.cellml.org/public/specification/20010810/cellml_specification.html.

Hedley, W., Nelson, M. R., Bullivant, D. & Nielsen, P. (2001), 'A short introduction to CellML', *Phil. Trans. R. Soc. Lond. A* **359**(1783), 1073–1089.

Henriquez, C. S. (1993), 'Simulating the electrical behaviour of cardiac tissue using the bidomain model', *Crit. Rev. Biomed. Eng.* **21**(1), 1–77.

Henry, H. & Rappel, W.-J. (2004), 'The role of M cells and the long QT syndrome in cardiac arrhythmias: Simulation studies of reentrant excitations using a detailed electrophysiological model', *CHAOS* **14**(1), 172–182.

Hilgemann, D. W. & Noble, D. (1987), 'Excitation-contraction coupling and extracellular calcium transients in rabbit atrium: Reconstruction of basic cellular mechanisms', *Proc. R. Soc. Lond. B* **230**(1259), 163–205.

Hill, A. V. (1938), 'Heat of shortening and the dynamic constants of muscle', *Proc. R. Soc. Lond. B* **126**, 136–195.

Hill, A. V. (1970), *First and Last Experiments in Muscle Mechanics*, Cambridge University Press.

Hindmarsh, A. C. (1983), ODEPACK, a systematized collection of ODE solvers, *in* R. S. Stepleman, ed., 'Scientific Computing', North Holland, Amsterdam, pp. 55–64.

Hodgkin, A. L. & Huxley, A. F. (1952), 'A quantitative description of membrane current and its application to conductance and excitation in nerve', *J. Physiol.* **117**, 500–544.

Hooks, D. (2002), Three-dimensional mapping of electrical propagation in the heart: experimental and mathematical model based analysis, PhD thesis, The University of Auckland, Auckland, New Zealand.

Hooks, D., Tomlinson, K., Marsden, S. G., LeGrice, I., Smaill, B. H., Pullan, A. J. & Hunter, P. J. (2002), 'Cardiac microstructure: Implications for electrical propagation and defibrillation in the heart', *Circ. Res.* **91**, 331–338.

Hunter, P. J. (1975), Finite element analysis of cardiac muscle mechanics., PhD thesis, University of Oxford, Oxford, UK.

Hunter, P. J. (1995), Myocardial constitutive laws for continuum mechanics models of the heart, *in* S. Sideman & R. Beyar, eds, 'Molecular and Subcellular Cardiology: Effects of Structure and Function', Plenum Press, chapter 30, pp. 303–318.

Hunter, P. J. & Borg, T. (2003), 'Integration from proteins to organs: the Physiome Project', *Nature Rev. Mol. Cell Biol.* **4**, 237–243.

Hunter, P. J., McCulloch, A. & ter Keurs, H. E. D. J. (1998), 'Modelling the mechanical properties of cardiac muscle', *Prog. Biophys. Molec. Biol.* **69**, 289–331.

Hunter, P. J., McNaughton, P. A. & Noble, D. (1975), 'Analytical models of propagation in excitable cells', *Prog. Biophys. Molec. Biol.* **30**(2/3), 99–144.

Hunter, P. J., Nash, M. P. & Sands, G. B. (1997), Computational electromechanics of the heart, *in* A. V. Panfilov & A. V. Holden, eds, 'Computational Biology of the Heart', John Wiley & Sons Ltd, West Sussex, England, chapter 12, pp. 345–407.

Hunter, P. J., Pullan, A. J. & Smaill, B. H. (2003), 'Modeling total heart function', *Annu. Rev. Biomed. Eng.* **5**, 147–177.

Hunter, P. J., Robbins, P. & Noble, D. (2002), 'The IUPS human physiome project', *Pflgers Arch - Eur. J. Physiol.* **445**, 1–9.

Hunter, P. J., Smaill, B. H. & Hunter, I. W. (1995), 'A "pole-zero" constitutive law for myocardium', *ASME J. Biomech. Eng.* **382**, 303–18.

Huxley, A. F. (1957), 'Muscle structure and theories of contraction', *Prog. Biophys. Chem.* **7**, 255–318.

Huxley, H. E. (1953), 'Electron microscope studies of the organisation of the filaments in striated muscle', *Biochim. Biophys. Acta* **12**(3), 387–394.

Huxley, H. E. & Hanson, J. (1954), 'Changes in the cross-striations of muscle during contraction and stretch and their structural interpretation', *Nature* **173**, 973–976.

Imredy, J. P. & Yue, D. T. (1994), 'Mechanism of Ca^{2+}-sensitive inactivation of L-type Ca^{2+} channels', *Neuron* **12**, 1301–1318.

Iyer, V., Mazhari, R. & Winslow, R. L. (2004), 'A computational model of the human left-ventricular epicardial myocyte', *Biophys. J.* **87**(3), 1507–1525.

Izakov, V., Katsnelson, L., Blyakhman, F., Markhasin, V. & Shklyar, T. F. (1991), 'Cooperative effects due to calcium binding by troponin and their consequences for contraction and relaxation of cardiac muscle under various conditions of mechanical loading', *Circ. Res.* **69**(5), 1171–1184.

Jafri, M. S., Rice, J. J. & Winslow, R. L. (1998), 'Cardiac Ca^{2+} dynamics: The role of ryanodine receptor adaptation and sarcoplasmic reticulum load', *Biophys. J.* **74**(3), 1149–1168.

Kass, D. A. (2003), 'Ventricular resynchronization: pathophysiology and identification of responders', *Rev. Cardiovasc. Med.* **4**(suppl 2), S3–S13.

Katsnelson, L. B., Izakov, V. & Markhasin, V. S. (1990), 'Heart muscle: mathematical modelling of the mechanical activity and modelling of mechanochemical uncoupling', *Gen. Physiol. Biophys.* **9**(3), 219–243.

Katz, A. M. (1992), *Physiology of the Heart*, 2 edn, Raven Press.

Kawaguchi, M., Murabayashi, T., Fetics, B. J., Nelson, G. S., Samejima, H., Nevo, E. & Kass, D. A. (2002), 'Quantitation of basal dyssynchrony and acute resynchronization from left or biventricular pacing by novel echo-contrast variability imaging', *J. Am. Coll. Cardiol.* **39**(12), 2052–2058.

Keizer, J. & Levine, L. (1996), 'Ryanodine receptor adaptation and Ca^{2+}-induced Ca^{2+} release-dependent Ca^{2+} oscillations', *Biophys. J.* **71**, 3477–3487.

Kerckhoffs, R. C. P., Bovendeerd, P. H. M., Kotte, J. C. S., Prinzen, F. W., Smits, K. & Arts, T. (2003), 'Homogeneity of cardiac contraction despite physiological asynchrony of depolarization: a model study', *Ann. Biomed. Eng.* **31**, 536–547.

Kerckhoffs, R. C. P., Faris, O. P., Bovendeerd, P. H. M., Prinzen, F. W., Smits, K., McVeigh, E. R. & Arts, T. (2003), 'Timing of depolarization and contraction in the paced canine left ventricle: model and experiment', *J. Cardiovasc. Electrophysiol.* **14**(Suppl.), S188–S195.

Kimura, J., Noma, A. & Irisawa, H. (1986), 'Na-Ca exchange current in mammalian heart cells', *Nature* **319**(6054), 596–597.

Kléber, A. G. & Rudy, Y. (2004), 'Basic mechanisms of cardiac impulse propagation and associated arrhythmias', *Physiol. Rev.* **84**, 431–488.

Kohl, P. (1995), 'Mechano-electric feedback: Impact on heart rhythm', *Futura* (4), 240–252.

Krassowska, W. & Neu, J. C. (1994), 'Effective boundary conditions for syncytial tissues', *IEEE Trans. Biomed. Eng.* **41**(2), 143–150.

Leclercq, C., Faris, O., Tunin, R., Johnson, J., Kato, R., Evans, F., Spinelli, J., Halperin, H., McVeigh, E. & Kass, D. A. (2002), 'Systolic improvement and mechanical resynchronization does not require electrical synchrony in the dilated failing heart with left bundle-branch block.', *Circulation* **106**(14), 1760–1763.

Leclercq, C. & Kass, D. A. (2002), 'Retiming the failing heart: principles and current clinical status of cardiac resynchronization', *J. Am. Coll. Cardiol.* **39**(2), 194–201.

LeGrice, I., Hunter, P. J., Young, A. & Smaill, B. H. (2001), 'The architecture of the heart: a data-based model', *Phil. Trans. R. Soc. Lond. A* **359**(1783), 1217–1232.

LeGrice, I., Smaill, B. H., Chai, L. Z., Edgar, S. G., Gavin, J. B. & Hunter, P. J. (1995), 'Laminar structure of the heart: Ventricular myocyte arrangement and connective tissue architecture in the dog', *Am. J. Physiol. Heart Circ. Physiol.* **269**(38), H571–H582.

Li, X. S. & Demmel, J. W. (2003), 'Superlu_dist: A scalable distributed-memory sparse direct solver for unsymmetric linear systems', *ACM Trans. Math. Software* **29**(2), 110–140.

Loew, L. M. & Schaff, J. C. (2001), 'The virtual cell: A software environment for computational cell biology', *Trends in Biotechnology* **19**(10), 401–406.

Luo, C.-H. & Rudy, Y. (1991), 'A model of the ventricular cardiac action potential. Depolarisation, repolarisation, and their interaction', *Circ. Res.* **68**(6), 1501–1526.

Luo, C.-H. & Rudy, Y. (1994), 'A dynamic model of the cardiac ventricular action potential. I. Simulations of ionic currents and concentration changes', *Circ. Res.* **74**(6), 1071–1096.

Malvern, L. E. (1969), *Introduction to the Mechanics of a Continuous Medium*, Prentice-Hall, Inc., New Jersey.

Markhasin, V. S., Solovyova, O., Katsnelson, L. B., Protsenko, Y., Kohl, P. & Noble, D. (2003), 'Mechano-electric interactions in heterogeneous myocardium: development of fundamental experimental and theoretical models', **82**, 207–220.

McAllister, R. E., Noble, D. & Tsien, R. W. (1975), 'Reconstruction of the electrical activity of cardiac purkinje fibres', *J. Physiol.* **251**(1), 1–59.

McCormick, S. F. (1989), *Multilevel Adaptive Methods for Partial Differential Equations*, SIAM.

Moraru, I. I., Schaff, J. C., Slepchenko, B. M. & Loew, L. M. (2002), 'The virtual cell: an integrated modeling environment for experimental and computational cell biology', *Ann. N. Y. Acad. Sci.* **971**, 595–596.

Muttaiyah, S., Tawhai, M. & Thorpe, W. (2004), Modelling an active bronchial airway, Part iv biomedical engineering project, Bioengineering Institute, The University of Auckland, Auckland, New Zealand.

Muzikant, A. L. & Henriquez, C. S. (1998), 'Bipolar stimulation of a three-dimensional bidomain incorporating rotational anisotropy', *IEEE Trans. Biomed. Eng.* **45**(4), 449–462.

Nagumo, J., Animoto, S. & Yoshizawa, S. (1962), 'An active pulse transmission line simulating nerve axon', *Proc. Inst. Radio Engineers* **50**, 2061–2070.

Nash, M. P. (1998), Mechanics and Material Properties of the Heart using an Anatomically Accurate Mathematical Model, PhD thesis, The University of Auckland, Auckland, New Zealand.

Nash, M. P. & Hunter, P. J. (2000), 'Computational mechanics of the heart', *J. Elasticity* **61**, 112–141.

Nash, M. P. & Panfilov, A. V. (2004), 'Electromechanical model of excitable tissue to study reentrant cardiac arrhythmias', *Prog. Biophys. Mol. Biol.* **85**, 501–522.

Nickerson, D. P. (1998), Electro-mechanical modelling of cardiac cells, Master's thesis, The University of Auckland, Auckland, New Zealand.

Nickerson, D. P., Smith, N. P. & Hunter, P. J. (2001), 'A model of cardiac cellular electromechanics', *Phil. Trans. R. Soc. Lond. A* **359**(1783), 1159–1172.

Nielsen, P., LeGrice, I., Smaill, B. H. & Hunter, P. J. (1991), 'Mathematical model of geometry and fibrous structure of the heart', *Am. J. Physiol. Heart Circ. Physiol.* **260**(29), H1365–H1378.

Noble, D. (1962), 'A modification of the Hodgkin-Huxley equation applicable to Purkinje fibre action and pace-maker potentials', *J. Physiol.* **160**, 317–352.

Noble, D., Noble, S. J., Bett, G. C. L., Earm, Y. E., Ho, W. K. & So, I. K. (1991), 'The role of sodium-calcium exchange during the cardiac action potential', *Ann. N. Y. Acad. Sci.* **639**, 334–353.

Noble, D. & Rudy, Y. (2001), 'Models of cardiac ventricular action potentials: Iterative interaction between experiment and simulation', *Phil. Trans. R. Soc. Lond. A* **359**(1783), 1127–1142.

Noble, D., Varghese, A., Kohl, P. & Noble, P. (1998), 'Improved guinea-pig ventricular cell model incorporating a diadic space, i_{Kr} and i_{Ks}, length- and tension-dependent processes', *Can. J. Cardiol.* **14**(1), 123–134.

Novak, V. P., Yin, F. C. P. & Humphrey, J. D. (1994), 'Regional mechanical properties of passive myocardium', *J. Biomech.* **27**(4), 403–412.

Oden, J. T. (1972), *Finite Elements of Nonlinear Continua*, McGraw-Hill, Inc., New York.

Omens, J. H. & Fung, Y. C. (1990), 'Residual strain in the rat left ventricle', *Circ. Res.* **66**(1), 37–45.

Peschar, M., de Swart, H., Michels, K. J., Reneman, R. S. & Prinzen, F. W. (2003), 'Left ventricular septal and apex pacing for optimal pump function in canine hearts', *J. Am. Coll. Cardiol.* **41**(7), 1218–1226.

Plonsey, R. & Barr, R. C. (1984), 'Current flow patterns in two-dimensional anisotropic bisyncytia with normal and extreme conductivities', *Biophys. J.* **45**(3), 557–571.

Pollard, A. E. (2003), 'From myocardial cell models to action potential propagation', *J. Electrocardiol.* **36**(Supplement).

Pollard, A. E., Cascio, W. E., Fast, V. G. & Knisley, S. B. (2002), 'Modulation of triggered activity by uncoupling in the ischemic border: A model study with phase 1b-like conditions', *Cardiovasc. Res.* **56**, 381–392.

Rajagopal, V., Nielsen, P. M. F. & Nash, M. P. (2004), Development of a three-dimensional finite element model of breast mechanics, *in* '26th Annual International Conference of the IEEE Engineering in Medicine and Biology Society'.

Remme, E. W., Nash, M. P. & Hunter, P. J. (2004), Distributions of sarcomere stretch, stress and work in a model of the beating ventricles, *in* P. Kohl, M. Franz & F. Sachs, eds, 'Cardiac Mechano-Electric Feedback and Arrhythmias: From Pipette to Patient', Unknown, chapter 44.

Rodriguez, E. K., Omens, J. H., Waldman, L. K. & McCulloch, A. (1993), 'Effect of residual stress on transmural sarcomere length distributions in rat left ventricle', *Am. J. Physiol.* **264**(4), H1048–H1096.

Rogers, J. M. & McCulloch, A. (1994), 'A collocation-Galerkin finite element model of cardiac action potential propagation', *IEEE Trans. Biomed. Eng.* **41**(8), 743–757.

Roth, B. J. (1997), 'Electrical conductivity values used with the bidomain model of cardiac tissue', *IEEE Trans. Biomed. Eng.* **44**(4), 326–328.

Roth, B. J. & Wikswo, Jr., J. P. (1986), 'A bidomain model for the extracellular potential and magnetic field of cardiac tissue', *IEEE Trans. Biomed. Eng.* **33**(4), 467–469.

Sands, G. B. (1997), Mathematical Model of Ventricular Activation in an Anatomically Accurate Deforming Heart, PhD thesis, The University of Auckland, Auckland, New Zealand.

Schmitt, O. H. (1969), Biological information processing using the concept of interpenetrating domains, *in* K. N. Leibovic, ed., 'Information Processing in the Nervous System', Springer-Verlag, New York, pp. 325–331.

Simmons, R. M. & Jewel, B. R. (1974), Mechanics and models of muscular contraction, *in* R. J. Linden, ed., 'Recent Advances in Physiology', Vol. 9, Churchill Livingstone Ltd., London, pp. 87–147.

Skouibine, K. B., Trayanova, N. A. & Moore, P. K. (2000), 'A numerically efficient model for simulation of defibrillation in an active bidomain sheet of myocardium', *Math. Biosci.* **166**(1), 85–100.

Smith, N. P., Nickerson, D. P., Crampin, E. J. & Hunter, P. J. (2004), 'Multiscale computational modelling of the heart', *Acta Numerica* **13**, 371–431.

Solovyova, O., Vikulova, N., Katsnelson, L. B., Markhasin, V. S., Noble, P. J., Garny, A. F., Kohl, P. & Noble, D. (2003), 'Mechanical interaction of heterogeneous cardiac muscle segments in silico: effects on Ca^{2+} handling and action potential', *Int. J. Bifurc. Chaos* **13**(12), 3757–3782.

Spach, M. S. & Heidlage, J. F. (1993), A multidimensional model of cellular effects on the spread of electrotonic currents and on propagating action potentials, *in* T. C. Pilkington, B. Loftis, J. F. Thompson, S. L.-Y. Woo, T. C. Palmer & T. F. Budinger, eds, 'High-Performance Computing in Biomedical Research', CRC Press Inc., chapter 11, pp. 289–317.

Stevens, C. (2002), An Anatomically-based Computational Study of Cardiac Mechanics and Myocardial Infarction, PhD thesis, The University of Auckland, Auckland, New Zealand.

Stevens, C., Remme, E., LeGrice, I. & Hunter, P. J. (2003), 'Ventricular mechanics in diastole: material parameter sensitivity.', *J. Biomech.* **36**, 737–748.

ten Tusscher, K. H. W. J., Noble, D., Noble, P. J. & Panfilov, A. V. (2004), 'A model for human ventricular tissue', *Am. J. Physiol. Heart Circ. Physiol.* **286**(4), H1573–H1589.

Tomlinson, K. (2000), Finite element solution of an eikonal equation for excitation wavefront propagation in ventricular myocardium, PhD thesis, The University of Auckland, Auckland, New Zealand.

Tomlinson, K., Pullan, A. J. & Hunter, P. J. (2002), 'A finite element method for an eikonal equation model of mycardial excitation wavefront propagation', *SIAM J. Appl. Math.* **63**(1), 324–350.

Trayanova, N. A. (1994), 'A bidomain model for ring stimulation of a cardiac strand', *IEEE Trans. Biomed. Eng.* **41**(4), 393–397.

Tung, L. (1978), A Bidomain Model for Describing Ischemic Myocardial D-C Potentials, PhD thesis, M.I.T., Boston, MA.

Usyk, T. P., LeGrice, I. J. & McCulloch, A. D. (2002), 'Computational model of three-dimensional cardiac electromechanics', *Comput. Visual Sci.* **4**, 249–257.

Usyk, T. P., Mazhari, R. & McCulloch, A. D. (2000), 'Effect of laminar orthotropic myofiber architecture on regional stress and strain in the canine left ventricle', *J. Elasticity* **61**, 143–164.

van Capelle, F. J. L. & Durrer, D. (1980), 'Computer simulation of arrhythmias in a network of coupled excitable elements', *Circ. Res.* **47**(3), 454–466.

Verbeek, X. A. A. M., Vernoot, K., Peschar, M., van der Nagel, T., van Hunnik, A. & Prinzen, F. W. (2003), 'Quantification of interventricular asynchrony during LBBB and ventricular pacing', *Am. J. Physiol. Heart Circ. Physiol.* **283**, H1370–H1378.

Verbeek, X. A. A. M., Vernooy, K., Peschar, M., Cornelussen, R. N. M. & Prinzen, F. W. (2003), 'Intra-ventricular resyynchronization for optimal left ventricular function during pacing in experimental left bundle branch block', *J. Am. Coll. Cardiol.* **42**(3), 558–567.

Viswanathan, P. C., Shaw, R. M. & Rudy, Y. (1999), 'Effects of i_{Kr} and i_{Ks} heterogeneity on action potential duration and its rate dependence', *Circulation* **99**(18), 2466–2474.

Westerhof, N., Elzinga, G. & Sipkema, P. (1971), 'An artificial arterial system for pumping hearts', *J. Appl. Physiol.* **31**(5), 776–781.

Westerhof, N., Elzinga, G. & van den Bos, G. C. (1973), 'Influence of central and peripheral changes on the hydraulic input impedance of the systemic arterial tree', *Med. Biol. Eng.* **11**(6), 710–723.

Winslow, R. L., Rice, J., Jafri, S., Marban, E. & O'Rourke, B. (1999), 'Mechanisms of altered excitation-contraction coupling in canine tachycardia-induced heart failure, II: Model studies', *Circ. Res.* **84**(5), 571–586.

Winslow, R. L., Scollan, D. F., Holmes, A., Yung, C. K., Zhang, J. & Jafri, M. S. (2000), 'Electrophysiological modeling of cardiac ventricular function: From cell to organ', *Annu. Rev. Biomed. Eng.* **2**, 119–155.

World Health Organization (2002), *The World Health Report : 2002 : Reducing risks, promoting healthy life*, World Health Organization.

Wyman, B. T., Hunter, W. C., Prinzen, F. W., Faris, O. P. & McVeigh, E. R. (2002), 'Effects of single- and biventricular pacing on temporal and spatial dynamics of ventricular contraction', *Am. J. Physiol. Heart Circ. Physiol.* **282**, H372–H379.

Wyman, B. T., Hunter, W. C., Prinzen, F. W. & McVeigh, E. R. (1999), 'Mapping propagation of mechanical activation in the paced heart with MRI tagging', *Am. J. Physiol. Heart Circ. Physiol.* **276**, H881–H891.

Yan, G.-X., Shimizu, W. & Antzelevitch, C. (1998), 'Characteristics and distribution of m cells in arterially perfused canine left ventricular wedge preparations', *Circulation* **98**, 1921–1927.

Yue, D. T. & Marban, E. (1988), 'A novel cardiac potassium channel that is active and conductive at depolarized potentials', *Pflueg. Arch.* **413**(2), 127–133.

Zahalak, G. I. & Ma, S.-P. (1990), 'Muscle activation and contraction: Constitutive relations based directly on cross-bridge kinetics', *J. Biomech. Eng.* **112**, 52–62.

Zahalak, G. I. & Motabarzadeh, I. (1997), 'A re-examination of calcium activation in the Huxley cross-bridge model', *J. Biomech. Eng.* **119**, 20–29.

Zeng, J., Laurita, K. R., Rosenbaum, D. S. & Rudy, Y. (1995), 'Two components of the delayed rectifier k^+ current in ventricular myocytes of the guinea pig type: Theoretical formulation and their role in repolarization', *Circ. Res.* **77**(1), 140–152.

Zienkiewicz, O. C. & Taylor, R. L. (1994), *The Finite Element Method. I. Basic Formulation and Linear Problems.*, fourth edn, McGraw-Hill Book Company, Berkshire, UK.